AGARD-R-819

AGARD

ADVISORY GROUP FOR AEROSPACE RESEARCH & DEVELOPMENT
7 RUE ANCELLE, 92200 NEUILLY-SUR-SEINE, FRANCE

AGARD REPORT 819

Turbulence in Compressible Flows

(la Turbulence dans les écoulements compressibles)

This report is a compilation of the edited proceedings of the "Turbulence in Compressible Flows" course held at the von Kármán Institute for Fluid Dynamics (VKI) in Rhode-Saint-Genèse, Belgium, 2-6 June 1997, and in Newport News, Virginia, USA, 20-24 October 1997.

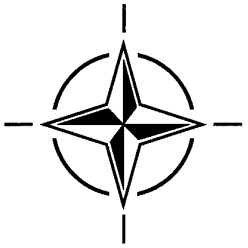

NORTH ATLANTIC TREATY ORGANIZATION

DISTRIBUTION STATEMENT A
Approved for public release;
Distribution Unlimited

Published June 1997

Distribution and Availability on Back Cover

AGARD-R-819

AGARD

ADVISORY GROUP FOR AEROSPACE RESEARCH & DEVELOPMENT

7 RUE ANCELLE, 92200 NEUILLY-SUR-SEINE, FRANCE

AGARD REPORT 819

Turbulence in Compressible Flows

(la Turbulence dans les écoulements compressibles)

This report is a compilation of the edited proceedings of the "Turbulence in Compressible Flows" course held at the von Kármán Institute for Fluid Dynamics (VKI) in Rhode-Saint-Genèse, Belgium, 2-6 June 1997, and in Newport News, Virginia, USA, 20-24 October 1997.

DTIC QUALITY INSPECTED 4

North Atlantic Treaty Organization
Organisation du Traité de l'Atlantique Nord

DISTRIBUTION STATEMENT A
Approved for public release;
Distribution Unlimited

19970710 087

The Mission of AGARD

According to its Charter, the mission of AGARD is to bring together the leading personalities of the NATO nations in the fields of science and technology relating to aerospace for the following purposes:

- Recommending effective ways for the member nations to use their research and development capabilities for the common benefit of the NATO community;
- Providing scientific and technical advice and assistance to the Military Committee in the field of aerospace research and development (with particular regard to its military application);
- Continuously stimulating advances in the aerospace sciences relevant to strengthening the common defence posture;
- Improving the co-operation among member nations in aerospace research and development;
- Exchange of scientific and technical information;
- Providing assistance to member nations for the purpose of increasing their scientific and technical potential;
- Rendering scientific and technical assistance, as requested, to other NATO bodies and to member nations in connection with research and development problems in the aerospace field.

The highest authority within AGARD is the National Delegates Board consisting of officially appointed senior representatives from each member nation. The mission of AGARD is carried out through the Panels which are composed of experts appointed by the National Delegates, the Consultant and Exchange Programme and the Aerospace Applications Studies Programme. The results of AGARD work are reported to the member nations and the NATO Authorities through the AGARD series of publications of which this is one.

Participation in AGARD activities is by invitation only and is normally limited to citizens of the NATO nations.

The content of this publication has been reproduced
directly from material supplied by AGARD or the authors.

Published June 1997

Copyright © AGARD 1997
All Rights Reserved

ISBN 92-836-1057-1

Printed by Canada Communication Group Inc.
(A St. Joseph Corporation Company)
45 Sacré-Cœur Blvd., Hull (Québec), Canada K1A 0S7

Turbulence in Compressible Flows

(AGARD R-819)

Executive Summary

This report is a compilation of the edited proceedings of the "Turbulence in Compressible Flows" course held at the von Kármán Institute for Fluid Dynamics (VKI) in Rhode-Saint-Genèse, Belgium, 2-6 June 1997, and in Newport News, Virginia, USA, under the sponsorship of NASA Langley Research Center, 20-24 October 1997.

Computational Fluid Dynamics is not an exact technology. While its basic framework consists of a well-established set of partial differential equations describing fluid motion, this framework is not self-contained and must be combined with approximate theoretical models describing the physical processes in question. Turbulence and the transition from laminar to turbulent flow are central phenomena, and a proper prediction of these phenomena is a prerequisite to accuracy improvements of any numerical method.

This series of lectures, supported by the AGARD Fluid Dynamics Panel and the von Kármán Institute for Fluid Dynamics, reviewed the state of knowledge of turbulence in compressible flows, with specific focus on fundamental physical understanding, modeling and application to engineering systems. The following topics were covered: Compressible Turbulent Boundary Layers, Compressible Turbulent Free Shear Layers, Turbulent Combustion, DNS/LES and RANS Simulations of Compressible Turbulent Flows, and Case Studies of Applications of Turbulence in Aerospace.

La turbulence dans les écoulements compressibles

(AGARD R-819)

Synthèse

Ce rapport est un recueil des comptes rendus officiels du Cours sur la turbulence dans les écoulements compressibles, tenu à l'Institut von Kármán (VKI) à Rhodes-Saint-Genèse, en Belgique, du 2 au 6 juin 1997, et à l'Omni Hotel, Newport News Virginia, sous l'égide du NASA Langley Research Center, du 20 au 24 octobre 1997.

L'aérodynamique numérique n'est pas une technologie exacte. Si les grandes lignes du domaine consistent en un système d'équations aux dérivées partielles bien définies décrivant le comportement des fluides, ce cadre général n'est pas suffisant et doit être associé à la modélisation théorique approchée des processus physiques en question. La turbulence et la transition de l'écoulement laminaire à l'écoulement tourbillonnaire sont des phénomènes essentiels et toute amélioration de la précision d'une méthode numérique quelconque passe par la prévision correcte de ces phénomènes.

Ce cycle de conférences, présenté sous l'égide du Panel AGARD de la dynamique des fluides et de l'Institut von Kármán, a fait le point de l'état actuel des connaissances dans le domaine de la turbulence dans les écoulements compressibles, en privilégiant les aspects physiques fondamentaux, la modélisation et les applications aux systèmes opérationnels.

Les sujets suivants ont été abordés :

Les couches limites tourbillonnaires compressibles, les zones de mélange tourbillonnaires compressibles, la combustion tourbillonnaire, les simulations DNS/LES et RANS des écoulements tourbillonnaires compressibles et des cas d'essai d'applications de la turbulence dans le domaine aérospatial.

Contents

	Page
Executive Summary	iii
Synthèse	iv
Special Course Staff	vi
Recent Publications of the Fluid Dynamics Panel	vii
	Reference
Compressible Turbulent Boundary Layers by A.J. Smits	1
Compressible Turbulent Free Shear Layers by J.C. Dutton	2
Turbulent Combustion by K. Bray	3
Large-Eddy Simulations of Compressible Turbulent Flows by M. Lesieur and P. Comte	4
Numerical Simulation of Compressible Turbulent Flows Using the Reynolds-Averaged Navier-Stokes Equations by D.D. Knight	5
Case Studies of Applications of Turbulence Models in Aerospace by W. Haase	6

Special Course Staff

COURSE DIRECTOR

D. Knight
Rutgers University
P.O. Box 909
Piscataway, New Jersey
08855-0909
United States

LECTURERS

J. Smits
Princeton University
P.O. Box CN5263
Princeton, New Jersey
08544-5263
United States

K. Bray
University of Cambridge
Cambridge CB2 1PZ
United Kingdom

C. Dutton
University of Illinois
at Urbana-Champaign
Urbana, Illinois
61801
United States

M. Lesieur
Institut Universitaire de France
LEGI/IMG - BP 53
38041 Grenoble Cedex 9
France

W. Haase
Daimler-Benz Aerospace . AG
Postfach 11 48
D-85073 Manching
Germany

NATIONAL COORDINATORS

G. Degrez
von Kármán Institute
Chausée de Waterloo, 72
1640 Rhode-Saint-Genèse
Belgium

T. Gatski
NASA Langley Research Center
Hampton, Virginia
23681
United States

PANEL EXECUTIVE

J.K. Molloy

Mail from Europe:
AGARD-OTAN
Attn. FDP Executive
92200 Neuilly-sur-Seine
France

Mail from US and Canada:
Attn. FDP Executive
PSC 116
AGARD/NATO
APO AE 09777

Recent Publications of the Fluid Dynamics Panel

AGARDOGRAPHS (AG)

Turbulent Boundary Layers in Subsonic and Supersonic Flow
AGARD AG-335, July 1996

Computational Aerodynamics Based on the Euler Equations
AGARD AG-325, September 1994

Scale Effects on Aircraft and Weapon Aerodynamics
AGARD AG-323 (E), July 1994

Design and Testing of High-Performance Parachutes
AGARD AG-319, November 1991

Experimental Techniques in the Field of Low Density Aerodynamics
AGARD AG-318 (E), April 1991

Techniques Expérimentales Liées à l'Aérodynamique à Basse Densité
AGARD AG-318 (FR), April 1990

A Survey of Measurements and Measuring Techniques in Rapidly Distorted Compressible Turbulent Boundary Layers
AGARD AG-315, May 1989

REPORTS (R)

Advances in Cryogenic Wind Tunnel Technology
AGARD R-812, Special Course Notes, January 1997

Aerothermodynamics and Propulsion Integration for Hypersonic Vehicles
AGARD R-813, Special Course Notes, October 1996

Parallel Computing in CFD
AGARD R-807, Special Course Notes, October 1995

Optimum Design Methods for Aerodynamics
AGARD R-803, Special Course Notes, November 1994

Missile Aerodynamics
AGARD R-804, Special Course Notes, May 1994

Progress in Transition Modelling
AGARD R-793, Special Course Notes, April 1994

Shock-Wave/Boundary-Layer Interactions in Supersonic and Hypersonic Flows
AGARD R-792, Special Course Notes, August 1993

Unstructured Grid Methods for Advection Dominated Flows
AGARD R-787, Special Course Notes, May 1992

Skin Friction Drag Reduction
AGARD R-786, Special Course Notes, March 1992

Engineering Methods in Aerodynamic Analysis and Design of Aircraft
AGARD R-783, Special Course Notes, January 1992

ADVISORY REPORTS (AR)

Cooperative Programme on Dynamic Wind Tunnel Experiments for Manoeuvering Aircraft
AGARD AR-305, Report of WG-16, October 1996

Hypersonic Experimental and Computational Capability, Improvement and Validation
AGARD AR-319, Vol. I, Report of WG-18, May 1996

Aerodynamics of 3-D Aircraft Afterbodies
AGARD AR-318, Report of WG-17, September 1995

A Selection of Experimental Test Cases for the Validation of CFD Codes
AGARD AR-303, Vols. I and II, Report of WG-14, August 1994

Quality Assessment for Wind Tunnel Testing
AGARD AR-304, Report of WG-15, July 1994

Air Intakes of High Speed Vehicles
AGARD AR-270, Report of WG-13, September 1991

Appraisal of the Suitability of Turbulence Models in Flow Calculations
AGARD AR-291, Technical Status Review, July 1991

Rotary-Balance Testing for Aircraft Dynamics
AGARD AR-265, Report of WG11, December 1990

Calculation of 3D Separated Turbulent Flows in Boundary Layer Limit
AGARD AR-255, Report of WG10, May 1990

Adaptive Wind Tunnel Walls: Technology and Applications
AGARD AR-269, Report of WG12, April 1990

CONFERENCE PROCEEDINGS (CP)

The Characterization & Modification of Wakes from Lifting Vehicles in Fluids
AGARD CP-584, November 1996

Progress and Challenges in CFD Methods and Algorithms
AGARD CP-578, April 1996

Aerodynamics of Store Integration and Separation
AGARD CP-570, February 1996

Aerodynamics and Aeroacoustics of Rotorcraft
AGARD CP-552, August 1995

Application of Direct and Large Eddy Simulation to Transition and Turbulence
AGARD CP-551, December 1994

Wall Interference, Support Interference, and Flow Field Measurements
AGARD CP-535, July 1994

Computational and Experimental Assessment of Jets in Cross Flow
AGARD CP-534, November 1993

High-Lift System Aerodynamics
AGARD CP-515, September 1993

Theoretical and Experimental Methods in Hypersonic Flows
AGARD CP-514, April 1993

Aerodynamic Engine/Airframe Integration for High Performance Aircraft and Missiles
AGARD CP-498, September 1992

Effects of Adverse Weather on Aerodynamics
AGARD CP-496, December 1991

Manoeuvering Aerodynamics
AGARD CP-497, November 1991

Vortex Flow Aerodynamics
AGARD CP-494, July 1991

Missile Aerodynamics
AGARD CP-493, October 1990

Aerodynamics of Combat Aircraft Controls and of Ground Effects
AGARD CP-465, April 1990

Computational Methods for Aerodynamic Design (Inverse) and Optimization
AGARD CP-463, March 1990

Applications of Mesh Generation to Complex 3-D Configurations
AGARD CP-464, March 1990

Fluid Dynamics of Three-Dimensional Turbulent Shear Flows and Transition
AGARD CP-438, April 1989

Validation of Computational Fluid Dynamics
AGARD CP-437, December 1988

Aerodynamic Data Accuracy and Quality: Requirements and Capabilities in Wind Tunnel Testing
AGARD CP-429, July 1988

Compressible Turbulent Boundary Layers

A.J. Smits
Department of Mechanical and Aerospace Engineering
Princeton University, Princeton, NJ 08544-0710

Abstract

These notes review what is currently known about the structure of zero-pressure-gradient, flat-plate turbulent boundary layers. The behavior of boundary layers in subsonic and supersonic flows is discussed, with a particular emphasis on scaling laws with respect to Reynolds number and Mach number.

1 Introduction

The most important parameter in the description of incompressible turbulent boundary layer behavior is, of course, the Reynolds number. Engineering applications cover an extremely wide range and values based on the streamwise distance can vary from 10^5 to 10^9. Most laboratory experiments are performed at the lower end of this range, and to be able to predict the behavior at very high Reynolds numbers, as found in the flow over aircraft and ships, it is therefore important to understand how turbulent boundary layers scale with Reynolds number.

For compressible flows, the Mach number becomes an additional scaling parameter. Because of the no-slip condition, however, a subsonic region persists near the wall, although the sonic line is located very close to the wall at high Mach number. Furthermore, a significant temperature gradient develops across the boundary layer at supersonic speeds due to the high levels of viscous dissipation near the wall. In fact, the static-temperature variation can be very large even in an adiabatic flow, resulting in a low-density, high-viscosity region near the wall. In turn, this leads to a skewed mass-flux profile, a thicker boundary layer, and a region in which viscous effects are somewhat more important than at an equivalent Reynolds number in subsonic flow.

Figure 1 shows two sets of air boundary layer profiles at about the same Reynolds number, one set measured on an adiabatic wall, the other measured on an isothermal wall. The momentum thickness Reynolds number R_θ is approximately 2200 when based on the freestream velocity u_e, and the kinematic viscosity evaluated at the freestream temperature ν_e, in accord with usual practice. That is, $R_\theta = \theta u_e/\nu_e$. The temperature of the air increases near the wall, even for the adiabatic wall case, since the dissipation of kinetic energy by friction is an important source of heat in supersonic shear layers. Somewhat surprisingly, the velocity, temperature and mass-flux profiles for these two flows appear very much the same, even though the boundary conditions, Mach numbers and heat transfer parameters differ considerably. The velocity profiles in the outer region, in fact, follow a 1/7th power law distribution quite well, just as a subsonic velocity profile would at this Reynolds number. With increasing Mach number, however, the elevated temperature near the the wall means that the bulk of the mass flux is increasingly found toward the outer edge of the boundary layer. This effect is strongly evident in the boundary-layer profiles shown in figure 2, where the freestream Mach number was 10 for a helium flow on an adiabatic wall. For this case, the temperature ratio between the wall and the boundary layer edge was about 30.

If the total temperature T_o was constant across the layer, then from the definition of the total temperature, $T_o = T + U^2/2C_p$, we see that there is a very simple relationship between the temperature T and the velocity u. Since there is never an exact balance between frictional heating and conduction (unless the Prandtl number equals one), the total temperature is not quite constant, even in an adiabatic flow, and the wall temperature depends on the recovery factor r. Hence:

$$\frac{T_w}{T_e} = 1 + r\frac{\gamma - 1}{2}M_e^2$$

where M is the Mach number, the subscript w denotes conditions at the wall, and the subscript e denotes conditions at the edge of the boundary layer, that is, in the local freestream. Since $r \approx 0.9$ for a turbulent boundary layer, the temperature at the wall in an adiabatic flow is nearly equal to the freestream total temperature. For example, at a freestream Mach number of 3, the ratio $T_w/T_0 = 0.93$.

As a result of these large variations of temperature through the layer, the fluid properties are far from constant. To the boundary layer approximation, the static pressure variation across the layer is constant, as in subsonic flow, and therefore for the examples shown in figure 1 the density varies by about a factor of 5. The viscosity varies by somewhat less than that: if we assume some form of Sutherland's law to express the temperature dependence of viscosity, for instance $(\mu/\mu_e) = (T/T_e)^\omega$ where $\omega = 0.765$, then the viscosity varies by a factor of 3.4. Since the density increases and the viscosity decreases with distance from the wall, the kinematic viscosity decreases by a factor of about 17 across the layer.

Paper presented at the AGARD FDP Special Course on "Turbulence in Compressible Flows", held at the von Kármán Institute for Fluid Dynamics (VKI) in Rhode-Saint-Genèse, Belgium, 2-6 June 1997, and in Newport News, Virginia, USA, 20-24 October 1997, and published in R-819.

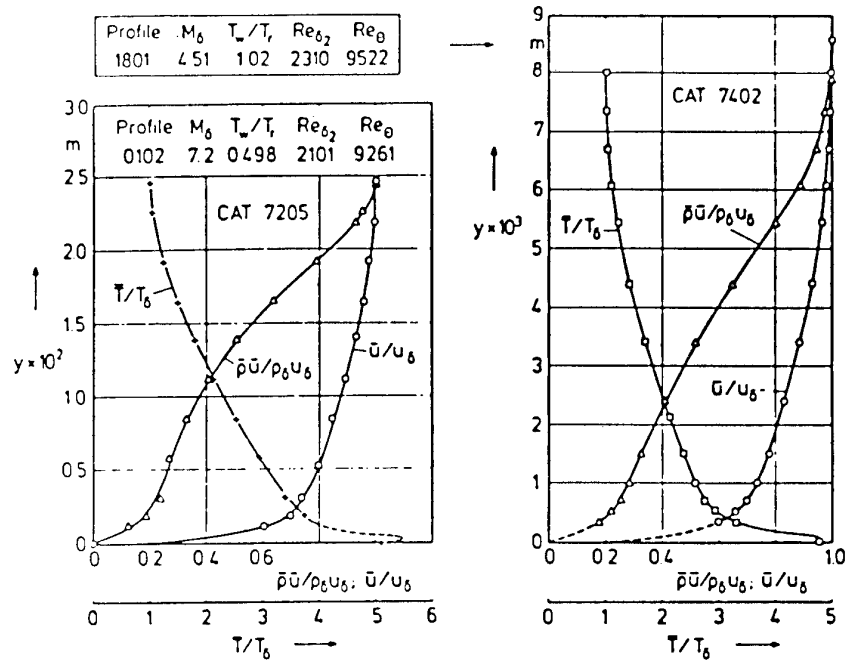

Figure 1: Turbulent boundary layer profiles in air ($T_\delta = T_e$). From Fernholz & Finley (1980), where catalog numbers are referenced.

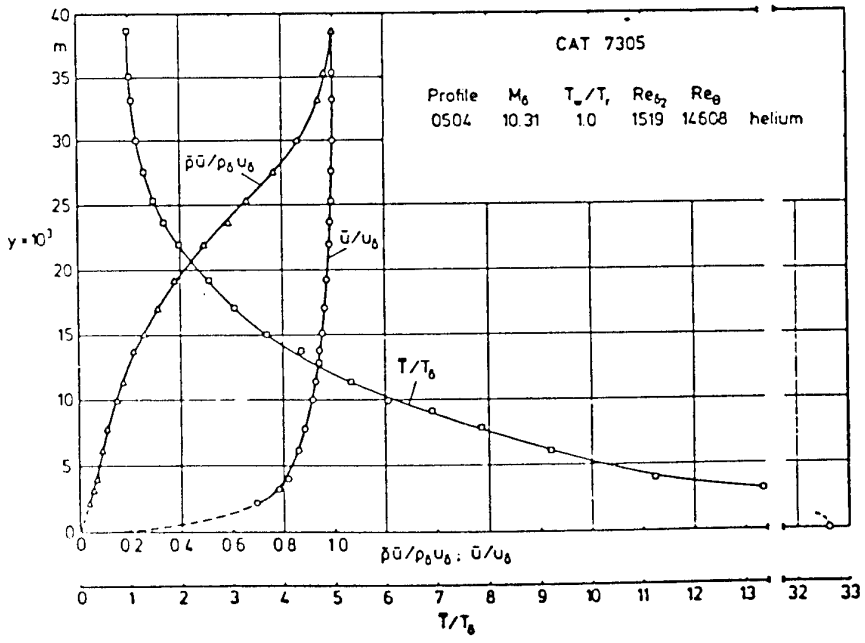

Figure 2: Turbulent boundary layer profiles in helium ($T_\delta = T_e$). Figure from Fernholz & Finley (1980), where catalog numbers are referenced. Original data from Watson *et al.* (1973).

M_∞	T_w/T_∞	ρ_w/ρ_∞	μ_w/μ_∞	ν_w/ν_∞
2.9 (air)[a]	3	0.33	1.4	4.2
4.5 (air)[b]	5	0.2	2.9	14
10.3 (He)[c]	33	0.03	9.6	320

[a] Spina & Smits 1987.
[b] Mabey et al 1974.
[c] Watson et al 1973.

Table 1: The ratio of fluid properties across three boundary layers in supersonic flow on adiabatic walls. Table from Spina *et al.* (1994).

Typical wall-to-freestream ratios of some flow properties are provided in table 1 for three different Mach numbers.

It is therefore difficult to assign a single Reynolds number to describe the state of the boundary layer. Of course, even in a subsonic boundary layer the Reynolds number varies through the layer since the length scale depends (in a general sense) on the distance from the wall. But here the variation is more complex in that the non-dimensionalizing fluid properties also change with wall distance. One consequence is that the relative thickness of the viscous sublayer depends not only on the Reynolds number, but also on the Mach number and heat transfer rate since these will influence the distribution of the fluid properties. At very high Mach numbers, most of the layer may become viscous-dominated. Now the boundary layers at the lower Mach numbers shown in figure 1 are certainly turbulent, but the Mach 10 boundary layer shown in figure 2 may well be transitional. For that case, the Reynolds number based on freestream fluid properties (for example, $R_\theta = \rho_e U_e \theta/\mu_e$ suggests a fully turbulent flow, but when the Reynolds number is based on fluid properties evaluated at the wall temperature ($R_{\delta 2} = \rho_e U_e \theta/\mu_w$) it suggests a laminar flow. The difference between Re_θ and $R_{\delta 2}$ increases steadily with Mach number and heat transfer, and can become very significant at high Mach number (for a full discussion, see Fernholz & Finley, 1976).

We can see that any comparisons we try to make between subsonic and supersonic boundary layers must take into account the variations in fluid properties, which may be strong enough to lead to unexpected physical phenomena, as well as the gradients in Mach number. Intuitively, one would expect to see significant dynamical differences between subsonic and supersonic boundary layers. However, it appears that many of these differences can be explained by simply accounting for the fluid-property variations that accompany the temperature variation, as would be the case in a heated incompressible boundary layer. This suggests a rather passive role for the density differences in these flows, most clearly expressed by Morkovin's hypothesis (Morkovin, 1962): the dynamics of a compressible boundary layer follow the incompressible pattern closely, as long as the Mach number associated with the fluctuations remains small. That is, the fluctuating Mach number, M', must remain small, where M' is the r.m.s.

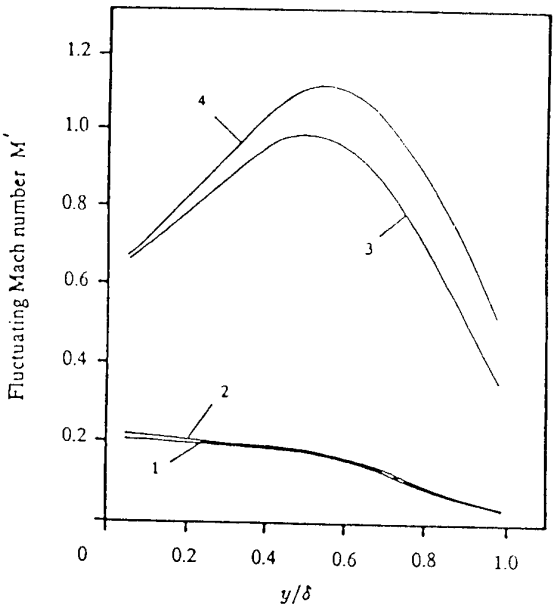

Figure 3: Fluctuating Mach number distributions. Flow 1: $M_e = 2.32$, $Re_\theta = 4,700$, adiabatic wall (Eléna & Lacharme, 1988); Flow 2: $M_e = 2.87$, $Re_\theta = 80,000$, adiabatic wall (Spina & Smits, 1987); Flow 3: $M_e = 7.2$, $Re_\theta = 7,100$, $T_w/T_r = 0.2$ (Owen & Horstman, 1972); Flow 4: $M_e = 9.4$, $Re_\theta = 40,000$, $T_w/T_r = 0.4$ (Laderman & Demetriades, 1974). Figure from Spina *et al.* (1994).

perturbation of the instantaneous Mach number from its mean value, taking into account the variations in velocity and sound speed with time. If M' approaches unity at any point, we would expect direct compressibility effects such as local "shocklets" and pressure fluctuations to become important. If we take $M' = 0.3$ as the point where compressibility effects become important for the turbulence behavior, we find that for zero-pressure-gradient adiabatic boundary layers at moderately high Reynolds numbers this point will be reached with a freestream Mach number of about 4 or 5 (see figure 3).

Recently, some measurements in moderately supersonic boundary layers ($M_\infty < 5$) have indicated subtle differences in the instantaneous behavior of certain quantities and parameters as compared to subsonic flow. These differences do not seem to be due simply to fluid-property variations. In particular, differences in turbulence length and velocity scales, the intermittency of the outer layer, and the structure of the large-scale shear-stress containing motions may indicate that the turbulence dynamics are affected at a lower fluctuating Mach number than previously believed. It is also possible that some of these changes in the turbulence structure are due to Reynolds number effects. As pointed out earlier, the characteristic Reynolds numbers encountered in high-speed flow can cover a very large range, extending well beyond values of the Reynolds number typically found in the laboratory. Furthermore, the temperature gradients which are found in the boundary layer in supersonic flow lead to variations in Reynolds number across the layer which must be con-

sidered along with the usual variations in the streamwise direction.

We begin these notes by reviewing the boundary layer equations in section 2. In section 3, we discuss the structure of boundary layers in supersonic flow, and in section 4 we consider their behavior in flows with pressure gradient and wall curvature. Shock-wave boundary layer interactions are reviewed in section 5, and a brief summary is given in section 6. These notes are based largely on the recent AGARDograph by Dussauge *et al.* (1996) and the monograph by Smits & Dussauge (1996), supplemented by more recent data obtained at Princeton and elsewhere.

2 Boundary-Layer Equations

Detailed derivations of the equations for compressible turbulent boundary layers have been provided in kinematic variables by van Driest (1951), Schubauer & Tchen (1959), Cebeci & Smith (1974) and Fernholz & Finley (1980). While it is well-known that the inclusion of density as an instantaneous variable is to add terms other than $-\overline{\rho u' v'}$ to the Reynolds-averaged boundary layer equations, the interpretation of these terms and their significance is not universally agreed upon. One of the reasons is that these terms do not appear in the mass-averaged (Favre-averaged) equations, as shown by, for example, Morkovin (1962), Favre (1965), and Rubesin & Rose (1973). A critical review of the equations of compressible turbulent flow and a discussion of the relative merits of the mass-averaged form is given by Lele (1994).

2.1 Continuity

The Reynolds-averaged, stationary, two-dimensional continuity equation for compressible flow is:

$$\frac{\partial}{\partial x}(\overline{\rho}U) + \frac{\partial}{\partial y}(\overline{\rho}V) + \frac{\partial}{\partial y}(\overline{\rho' v'}) + \frac{\partial}{\partial y}(\overline{\rho' u'}) = 0. \qquad (1)$$

The additional terms in this equation, $\frac{\partial}{\partial y}(\overline{\rho' v'})$ and $\frac{\partial}{\partial y}(\overline{\rho' u'})$, act as apparent sources/sinks to the mean flow (Schubauer & Tchen, 1959). To the boundary-layer approximation, $\frac{\partial}{\partial y}(\overline{\rho' u'})$ is negligible, and a simple mixing-length argument indicates that $\overline{\rho' v'}$ is negative. The absolute magnitudes of ρ' and v' increase with y near the wall before decreasing with y in the outer part of the boundary layer, and therefore $\frac{\partial}{\partial y}(\overline{\rho' v'})$ acts as a mass-flux source in the inner layer and as a sink in the outer region of the boundary layer. The presence of a source term in the continuity equation indicates that the physics of the flowfield are not well represented (see also Smits & Dussauge, 1996).

An alternative approach uses "Favre-averaging", where the instantaneous variable is decomposed into the sum of a mass-weighted average, $\tilde{\alpha}$, and a fluctuation, α'' (Favre, 1965). The use of mass-averaged variables leaves the continuity equation devoid of turbulent mass transport terms:

$$\frac{\partial}{\partial x}(\overline{\rho}\tilde{u}) + \frac{\partial}{\partial y}(\overline{\rho}\tilde{v}) = 0. \qquad (2)$$

2.2 Momentum

For two-dimensional compressible flow, the y-component (wall-normal) momentum equation contains many terms associated with density and velocity fluctuations. For zero-pressure-gradient boundary layers in a steady supersonic flow, however, the usual order-of-magnitude arguments show that the pressure across the layer can be taken as constant, as for subsonic flows. The pressure is then a function only of streamwise distance, so that $\partial\overline{p}/\partial x$ may be replaced by $d\overline{p}/dx$ in the x-momentum equation. Hence, the mean pressure is considered to be "imposed" on the boundary layer in that it appears as a boundary condition rather than as an independent variable.

If the continuity equation is multiplied by the streamwise velocity, added to the boundary-layer approximation of the x-momentum equation, and the resulting equation Reynolds-averaged, we obtain:

$$\frac{\partial}{\partial x}(\overline{\rho}U^2) + \frac{\partial}{\partial y}(\overline{\rho}UV) = \frac{-d\overline{p}}{dx} + \frac{\partial}{\partial y}(\mu\frac{\partial U}{\partial y} - \overline{\rho u' v'} - U\overline{\rho' v'} - V\overline{\rho' u'} - \overline{\rho' u' v'}). \qquad (3)$$

Equation 3 is the most general form of the compressible boundary layer equation. The triple-product term may be neglected since it is one order of magnitude smaller than the other terms, and $V\overline{\rho' u'}$ can be neglected since it is smaller than $U\overline{\rho' v'}$ ($\overline{\rho' u'}$ and $\overline{\rho' v'}$ are assumed to be the same order and $V << U$). The resulting equation is:

$$\frac{\partial}{\partial x}(\overline{\rho}U^2) + \frac{\partial}{\partial y}(\overline{\rho}UV) = \frac{-d\overline{p}}{dx} + \frac{\partial}{\partial y}(\mu\frac{\partial U}{\partial y} - \overline{\rho u' v'} - U\overline{\rho' v'}). \qquad (4)$$

Alternatively, the boundary-layer form of the compressible x-momentum equation can be written:

$$\overline{\rho u}\frac{\partial}{\partial x}U + \overline{\rho v}\frac{\partial}{\partial y}U = \frac{-d\overline{p}}{dx} + \frac{\partial}{\partial y}(\mu\frac{\partial U}{\partial y} - \overline{\rho u' v'}), \qquad (5)$$

where $\overline{\rho u} = \overline{\rho}U + \overline{\rho' u'}$ and $\overline{\rho v} = \overline{\rho}V + \overline{\rho' v'}$, and $\overline{\rho' u'}$ can usually be neglected. When the Favre-averaged form of the x-momentum equation is considered, that is,

$$\frac{\partial}{\partial x}(\overline{\rho}\tilde{u}^2) + \frac{\partial}{\partial y}(\overline{\rho}\tilde{u}\tilde{v}) = \frac{-d\overline{p}}{dx} + \frac{\partial}{\partial y}(\overline{\tau}_{yx} - \overline{\rho u'' v''}), \qquad (6)$$

it is clear that three different forms of the equation exist, and some physical insight regarding the differences is necessary.

In equation 4 the traditional Reynolds stress and another "apparent" stress, $-U\overline{\rho' v'}$, comprise the turbulent shear stress. Now, $U\overline{\rho' v'}$ is not a "true" Reynolds stress, but simply a consequence of the type of averaging used. Nevertheless, its contribution to the total stress cannot be discounted. The correlations $\overline{\rho u' v'}$ and $U\overline{\rho' v'}$ are both negative (as evident from a mixing-length argument), and thus $U\overline{\rho' v'}$ acts in addition to the "incompressible" Reynolds shear stress. Assuming small pressure fluctuations and using the Strong Reynolds Analogy (SRA) (Morkovin, 1962) (see section 2.3), it is a simple matter to express the ratio of $U\overline{\rho' v'}$ to $\overline{\rho u' v'}$ as $(\gamma - 1)M^2$ ((see, for example, Spina *et al.*, 1991a). Of course, this expression is subject to the inaccuracies inherent in the SRA (see below), but it is a good approximation to at least $M = 5$, and provides an order-of-magnitude comparison even at higher Mach numbers. This relation indicates how quickly

$U\overline{\rho' v'}$ becomes important in the boundary layer. For a Mach 3 adiabatic-wallboundary layer with $Re_\theta = 80,000$, $(\gamma - 1)M^2$ rises to a value of 1.0 at approximately 0.05δ ($\sim 500y^+$), and asymptotes to a value of 3.5 at the boundary layer edge (Spina, 1988). Since the Mach number is small across much of the constant-stress layer, Schubauer & Tchen (1959) neglected the "second-order term" when developing a skin-friction theory, but this should not be considered a general result.

The correlation $U\overline{\rho' v'}$ also appears in the turbulent kinetic energy (TKE) equation for a compressible boundary layer. This equation is much more complex than the incompressible TKE equation, with eight production terms, including one due to the Reynolds shear stress, $-\overline{\rho} \overline{u'v'} \frac{\partial U}{\partial y}$, and one due to the "fictitious" stress, $-U\overline{\rho' v'} \frac{\partial V}{\partial x}$. A comparison between these two terms indicates that the production of turbulent kinetic energy due to the Reynolds shear stress is two orders-of-magnitude greater than that due to the term in question (in fact, there are three other terms that are an order-of-magnitude larger than $-U\overline{\rho' v'} \frac{\partial V}{\partial x}$). This indicates that $U\overline{\rho' v'}$ is less important than the other terms in determining the energy flow in a compressible boundary layer because it interacts with a considerably smaller mean strain.

If the convective terms are written as the product of the average instantaneous mass flux and a strain (as in equation 5), the only additional term (in addition to those found in laminar flow) is the traditional Reynolds stress, $\overline{\rho} \overline{u'v'}$. This form of the equation was advocated by Morkovin (1962) to isolate the turbulent momentum transport, and the new parts of the convective terms represent the fact that there is no mean mass transfer between mean streamlines. Since $U\overline{\rho' v'}$ may be thought of as a turbulent mass-transport term, it is not surprising that this form of the equation is free from this term, and the interpretation of the equation is physically and intuitively attractive.

The major drawback to writing the x-momentum equation in Favre-averaged variables (equation 6) is that $\overline{\tau}_{yx}$ is more complex than for incompressible boundary layers (Rubesin & Rose, 1973). Expressing the instantaneous stress tensor in mass-weighted variables, expanding, and time-averaging results in:

$$\overline{\tau}_{ij} = \tilde{\mu} \tilde{S}_{ij} + \tilde{\mu} \overline{S''}_{ij}$$

where $S_{ij} = [(u_{i,j} + u_{j,i}) - \frac{2}{3} \delta_{ij} u_{k,k}]$. This expression contains additional terms that are not amenable to a simple physical interpretation, but the similarity of the Favre-averaged representation of the compressible momentum equation to that of the incompressible equation makes its use nevertheless attractive, especially in computations.

2.3 Energy and the Strong Reynolds Analogy

The mean energy equation was developed in terms of the stagnation enthalpy by Young (1951) (see Howarth, 1953, Gaviglio, 1987) in the forms corresponding to the Reynolds-averaged and Favre-averaged variables, respectively. In Reynolds-averaged variables, the boundary-layer approximation for the equation is:

$$\overline{\rho u} \frac{\partial \overline{H}}{\partial x} + \overline{\rho v} \frac{\partial \overline{H}}{\partial y} = \frac{\partial}{\partial y} \left[\frac{k}{c_p} \frac{\partial \overline{H}}{\partial y} + \mu \left(1 - \frac{1}{Pr} \right) \frac{\partial}{\partial y} \left(\frac{U^2}{2} \right) - \overline{\rho v' H'} \right], \quad (7)$$

where, neglecting higher-order terms, $\overline{H} = \overline{h} + \frac{1}{2} U^2$, and $H' = h' + Uu'$. As in the development of the mean x-momentum equation (equation 5), there are no additional terms beyond those found in incompressible flow, although the convective terms are slightly altered, as noted by Morkovin.

A useful relation for the reduction of experimental data and the comparison of compressible to incompressible results is the Strong Reynolds Analogy [first identified as such by Morkovin (1962), but primarily due to Young (1951)]. This analogy, leading to simplified solutions of the energy equation, is based upon the similarity between equations 5 and 7 when $Pr = 1$ (or when molecular effects are negligible compared to turbulent processes) and the similarity of the boundary conditions for $\overline{T_0}$ and U, and T_0' and u'. For zero-pressure-gradient flow of a perfect gas with heat transfer, the equations admit the solutions:

$$c_p(\overline{T}_0 - T_w) = \frac{\overline{q}_w}{\overline{\tau}_w} U, \quad (8)$$

$$c_p T_0' = \frac{\overline{q}_w}{\overline{\tau}_w} u', \quad (9)$$

where the heat-transfer rate and shear stress at the wall enter through the boundary conditions. For adiabatic flows, it follows that

$$T_0' = 0, \quad (10)$$

$$\frac{T'}{\overline{T}} = -(\gamma - 1) M^2 \frac{u'}{U}, \quad (11)$$

$$\text{and} \quad R_{uT} = -1. \quad (12)$$

The solution given by $\overline{T}_0 = T_w$ and equation 10 satisfies the energy equation independently, and therefore may be applied for any pressure gradient (Gaviglio, 1987).

Gaviglio notes that these relations (equations 8 - 12) are so strict (that is, they apply in an instantaneous sense) that they cannot be expected to hold exactly. Morkovin (1962) gives a "milder" form of the SRA that relates the r.m.s. of the static temperature fluctuations to that of the velocity fluctuations (also see Spina *et al.*, 1991a)). Morkovin (1962) and Gaviglio (1987) tested the time-averaged form of the SRA and found that R_{uT} is not -1.0 but is closer to -0.8 or -0.9. Still, this high correlation level indicates that large-scale eddies moving away from the wall in a supersonic flow almost always contain warmer, lower-speed fluid than the average values found at that distance from the wall. As for the instantaneous form of the SRA (equation 10), Morkovin & Phinney (1958), Kistler (1959), Dussauge & Gaviglio (1987), and Smith & Smits (1993a) have shown that T_0' is not negligible, but that the results derived from such an assumption still represent very good approximations. The instantaneous form of the SRA has been validated to a freestream Mach number of 3 (Smith & Smits, 1993a), but the only limit to its first-order approximation at higher

Mach number may be the increasing importance of low-Reynolds-number effects near the wall at higher hypersonic Mach numbers (Morkovin, 1962). There is also the fact that $T'/\bar{T}$ is bounded, which means there exists an upper Mach number limit on the SRA unless $u'/\bar{U}$ approaches very small values at the same time.

3 Flat Plate Boundary Layers

At supersonic Mach numbers, viscous energy dissipation makes a significant contribution to the energy budget. As a result, the temperature rises and significant temperature gradients occur within the boundary layer. In a turbulent boundary layer in supersonic flow, therefore, the mean temperature and velocity vary, and significant temperature and velocity fluctuations occur. Pressure fluctuations are usually small at supersonic speeds but may become important at Mach numbers exceeding 5.

3.1 Stagnation-temperature distribution

The stagnation-temperature profile must be known to calculate the velocity distribution. Measurements and theory often seem to conflict, however, and a truly representative stagnation-temperature profile is difficult to define, particularly at high Mach number. The measurement difficulty stems from the compromise that must be made between spatial resolution and accuracy when selecting a stagnation-temperature probe (see, for example, Fernholz & Finley, 1980). Since approximately one-half of the decrease in $\overline{T_0}$ to the wall-recovery value occurs in the inner layer of near-unity Prandtl-number gases (Morkovin, 1962), this compromise leads to a kind of uncertainty principle on the accuracy of the data.

As for theoretical stagnation-temperature distributions, Fernholz & Finley (1980) present and discuss many of the energy-equation solutions commonly applied to supersonic turbulent boundary layers. They note that many of the relations are applied beyond their range of validity when used to benchmark experimental data. The two most widely discussed stagnation-temperature distributions in the literature are the "linear" and "quadratic" solutions. It has been commonly assumed that $(T_0 - T_w)/(T_{0_e} - T_w) \equiv \Theta = U/U_e$ is the proper distribution for flat-plate flows, while $\Theta = (U/U_e)^2$ is the appropriate tunnel/nozzle wall solution. It has been claimed that the quadratic nature of the measurements along tunnel walls is due to the upstream history of the flow (significant dT/dx and dp/dx) and the resultant local non-equilibrium. While Feller (1973), Bushnell *et al.* (1969), and Beckwith (1970) offer convincing arguments for flow-history effects, there is little experimental evidence that the linear profile is the equilibrium stagnation-temperature distribution in supersonic, turbulent boundary layers.

The classic (linear) Crocco solution, $\Theta = U/U_e$, is derived from the energy and momentum equations for laminar flow with $Pr = 1$, zero pressure gradient, and an isothermal wall. The Crocco solution is extended to turbulent flows under the same conditions with the additional assumption of unity turbulent Prandtl number (Pr_t). However, it has been shown that Pr_t is less than 1.0 across the outer layer for both near-adiabatic walls (Meier & Rotta, 1971) and cold walls (Owen *et al.*, 1975). Fernholz & Finley (1980) show that the origins of a quadratic profile for turbulent flow lie in a solution by Walz (1966):

$$\Theta = \beta\frac{U}{U_e} + (1-\beta)\left(\frac{U}{U_e}\right)^2, \qquad (13)$$

where $\beta = (T_{aw} - T_w)/(T_{0_e} - T_w)$. The assumptions inherent in this solution are zero pressure gradient, isothermal wall, and a constant "mixed" Prandtl number, $Pr_M \equiv c_p(\mu + \mu_t)/(k + k_t)$ between 0.7 and 1.0. The linear profile therefore holds only for $\beta = 1$, that is, $T_{0_e} = T_{aw}$, and the purely quadratic profile holds only for a zero-pressure-gradient flow, with constrained Pr_M, and an isothermal (also adiabatic) wall ($\beta = 0$). The range of validity of the quadratic relation is often extended improperly to flows with pressure gradients because of the similarity of the equation to one that is valid for laminar and turbulent adiabatic flows with pressure gradients. Perhaps due to the relaxed constraint on the Prandtl number (as compared to the linear solution), much of the stagnation-temperature data appears to be characterized by a quadratic trend (Bushnell *et al.*, 1969, Bertram & Neal, 1965, Wallace, 1969, Hopkins & Keener, 1972).

A critical shortcoming is the dearth of near-wall T_0 measurements, which are critical for determination of the wall heat-transfer rate. The lack of data makes it impossible to determine whether these temperature-velocity relations, or even those provided by Bradshaw (1977) to represent the inner layer, accurately describe the near-wall behavior of the stagnation temperature. For flows with non-isothermal walls and significant pressure gradients the situation is much worse, however, as no theoretical temperature-velocity relations exist for these conditions. Much of the confusion surrounding stagnation-temperature distributions is due to comparison between data taken under these conditions and theoretical relations that are applied beyond their range of validity.

3.2 Mean-velocity scaling

When the mean velocity in a supersonic boundary layer is plotted as U/U_e *vs.* y/δ, the profile appears qualitatively similar to that of an incompressible flow. When the velocity is replotted in classic inner- or outer-layer coordinates, however, the velocity does not follow the familiar incompressible scaling laws for these regions. But a modified scaling that accounts for the fluid-property variations correlates much of the existing compressible mean-velocity data with the "universal" incompressible distribution. This velocity scaling was first employed in the viscous sublayer and the logarithmic region by van Driest (1951), was extended to the wake region and to velocity-defect scaling by Maise & McDonald (1968), and to Coles' universal wall-wake scaling by Mathews *et al.* (1970). The following outline of the scaling arguments for supersonic turbulent boundary layers is based largely on the discussion given by Fernholz & Finley (1980).

The usual derivation of the velocity distribution in the inner region is based on the assumptions:

(1) that the convective term $\partial/\partial x$ in the equation of motion is small compared with the viscous term,

(2) that the pressure gradient term can be ignored so as to simplify the discussion, and

(3) that the total stress $\tau_T = \mu\left(\partial\bar{U}/\partial y\right) - \bar{\rho}\overline{u'v'}$ is constant in the inner region and equals τ_w.

(4) Morkovin's hypothesis holds, in that the structure of the turbulence does not change significantly due to compressibility effects up to about a freestream Mach number of about 5.

> "The dominating factor in the compressible turbulent-boundary layer problem is apparently then the effect of high temperature on the velocity profile near the wall and therefore on the shear stress. This latter observation was first advanced by von Kármán in 1935 but has been somewhat neglected in favour of interpolation formulae or of elaborate generalizations of the mixing length hypothesis" (Part I of Coles, 1953).

The increased dissipation rate in the viscous sublayer has the effect that at a fixed Reynolds number the sublayer thickness increases with increasing Mach number. The same effect is of course responsible for the observed increase in the thickness of the laminar boundary layer at high Mach numbers (see, for example, van Driest, 1951).

If one assumes that in the viscous sublayer the molecular shear stress $\mu\left(\partial\bar{U}/\partial y\right)$ is large compared with the Reynolds shear stress $-\bar{\rho}\overline{u'v'}$ and equal to the skin friction τ_w, then one obtains for the velocity gradient

$$\frac{\partial\bar{U}}{\partial y} = \frac{u_\tau^2}{\nu_w}\left(\frac{T_w}{\bar{T}}\right)^\omega \tag{14}$$

in which the variation of the viscosity with temperature is taken to be given by

$$\frac{\mu}{\mu_w} = \left(\frac{\bar{T}}{T_w}\right)^\omega \tag{15}$$

Using equation 13 for the temperature distribution (valid under the assumptions $dp/dx = 0$ and T_w = constant), equation 14 yields:

$$\frac{\overline{U^s}}{u_\tau} = \frac{yu_\tau}{\nu_w} \tag{16}$$

where the transformed mean velocity in the sublayers $\overline{U^s}$ is defined by

$$\overline{U^s} = \int_0^U \left(\frac{T}{T_w}\right)^\omega dU. \tag{17}$$

Hence, with $\omega = 1$:

$$\overline{U^s} = \bar{U}\left[1 + \frac{1}{2}a\frac{\bar{U}}{U_e} - \frac{1}{3}b^2\left(\frac{\bar{U}}{U_e}\right)^2\right] \tag{18}$$

in which

$$a = \left(1 + r\frac{\gamma-1}{2}M_e^2\right)\frac{T_e}{T_w} - 1 \tag{19}$$

$$b^2 = r\frac{\gamma-1}{2}M_e^2\frac{T_e}{T_w}. \tag{20}$$

We see that the transformed velocity $\overline{U^s}$ has a linear distribution similar to the linear velocity distribution in the viscous sublayer of an incompressible turbulent boundary layer, and to which it reduces for $\bar{T} = T_w$ and $M_e = 0$.

Between the viscous sublayer and the outer layer there exist a region, defined by $y^+ >> 1$ and $\eta << 1$, where the Reynolds shear stress $-\bar{\rho}\overline{u'v'}$ is dominant and is approximately equal to the skin friction τ_w. If it is assumed that Prandtl's mixing length theory is also valid for compressible turbulent boundary layers, then from $\tau_w = -\bar{\rho}\overline{u'v'} = \rho\ell^2\left(\partial\bar{U}/\partial y\right)^2$ we obtain:

$$\frac{\partial\bar{U}}{\partial y} = \frac{\sqrt{\tau_w/\rho}}{\kappa y} \tag{21}$$

where κ is von Kármán's constant and ℓ is Prandtl's mixing length (assumed to be equal to κy, as in subsonic flows). This result is independent of Mach number. Since the pressure is constant in the wall-normal direction, we have, for a perfect gas:

$$\frac{\partial\bar{U}}{\partial y} = \frac{u_\tau}{\kappa y}\sqrt{\left(\frac{\bar{T}}{T_w}\right)} \tag{22}$$

We can again use equation 13 to substitute for the temperature ratio in equation 17 and obtain (Fernholz, 1969):

$$\frac{\overline{U^*}}{u_\tau} = \frac{1}{\kappa}\ln\frac{yu_\tau}{\nu_w} + C^* \tag{23}$$

where

$$\overline{U^*} = \int_{U_1^+}^{U^+}\sqrt{\frac{T_w}{\bar{T}}}dU^+. \tag{24}$$

Hence:

$$\overline{U^*} = \frac{U_e}{b}\sin^{-1}\left[\frac{2b^2\frac{U}{U_e} - a}{\sqrt{(a^2+4b^2)}}\right] \tag{25}$$

and

$$C^* = \frac{1}{\kappa}\ln\frac{y_1u_\tau}{\nu_w} + \frac{U_e}{u_\tau}\frac{1}{b}\sin^{-1}\left[\frac{2b^2\frac{\overline{U_1}}{U_e} - a}{\sqrt{(a^2+4b^2)}}\right]$$

where a and b are given by equations 19 and 20, and the suffix 1 denotes a boundary condition at the lower end of the validity range of the log-law (which can in principle only be found by experiment).

For an adiabatic wall, T_w becomes the recovery temperature T_r, and $a = 0$. In this case experiments show that $\overline{U_1}/U_e$ lies in the range $0.3 \le \overline{U_1}/U_e \le 0.6$. With a value for $\overline{U_1}/U_e = 0.5$ one can show that arcsin can be replaced by its argument for Mach numbers up to 8 with a relative error of -4% or less. Then C^* reduces to

$$C^*_{ad} \approx \frac{\overline{U_1}}{u_\tau} - \frac{1}{\kappa}\ln\frac{yu_\tau}{\nu_w} \approx C, \tag{26}$$

that is, the same value as for the incompressible case. This result was also confirmed by the measurements discussed by Fernholz & Finley (1980) and by general computational experience (Bushnell *et al.*, 1976).

Fernholz & Finley (1980) concluded that velocity profiles in compressible turbulent boundary layers are well represented by equation 23 within the limits set by the assumptions. A comparison between measurements in transformed and un-transformed coordinates is given in figure 4.

The first approach to this type of transformation was suggested by van Driest (1951) who derived a relationship similar to equation 23 also using the mixing length concept. He assumed Prandtl number unity and so a recovery factor equal to one and determined the constant C so that for the limit $M_e \rightarrow 0$ and $(T_w/T_e) \rightarrow 1$ the well-established relationship for the incompressible case should result. Van Driest's equation for the logarithmic law then reads the same as equation 23, except that $r = 1$ in the definitions of a and b.

The differences likely to appear if the alternative transformation is used can be seen in figure 5. Here three sets of profile data are plotted using firstly equation 25 with $r = 0.896$ and secondly equation 25 with $r = 1.0$ which then reduces to van Driest's transformation. The differences, although systematic, are small when compared to experimental error, particularly in the determination of C_f. Given the uncertainties in the transformation approach, and the experimental difficulties in obtaining accurate values for C_f, there is little that can be said for any given set of log-law constants and their possible variation with Reynolds number or Mach number. It is equally difficult to say anything meaningful regarding the existence of power law similarity, rather than log-law similarity, as discussed in Dussauge *et al.* (1996).

The empirical validity of Morkovin's hypothesis offers some support for the concept behind the van Driest transform (and similarly that by Fernholz & Finley) by suggesting that multi-layer scaling holds in compressible boundary layers. And despite the assumptions inherent to the mixing-length hypothesis, the underlying dimensional argument is sound as long as the length-scale distributions in supersonic boundary layers follow the same behavior as in subsonic flows. In fact, experimental data taken over a wide Mach-number range, with various wall-heating conditions and modest pressure gradients, and transformed via van Driest show good agreement with incompressible data correlations (for example, Kemp & Owen, 1972, Laderman & Demetriades, 1974, Owen *et al.*, 1975, Watson, 1977). The systematic discussion given by Fernholz & Finley (1980) is particularly persuasive.

It is important to note what the limits of applicability appear to be, however. Other than strong pressure gradients, the primary constraint is imposed by the dependence of similarity on large values of the Reynolds number, implying universality and independence from upstream history. Fernholz & Finley (1980) observe that the low-Reynolds-number region that begins to dominate the inner layer at high Mach number may eventually cause the failure of the velocity scaling laws that the transformed data follow. Hopkins *et al.* (1972) attribute the poor performance of van Driest at $M_e = 7.7$ to the low Reynolds number of the flow, $Re_\theta \approx 5,000$. This can be compared to a successful application of van Driest at $M_e = 9.4$ and $Re_\theta \approx 37,000$ by Laderman & Demetriades. It seems reasonable, however,that the transformation suggested by Fernholz & Finley offers a slightly more accurate variation of van Driest, since the temperature distribution is based on a Prandtl number assumption ($0.7 \leq Pr_M \leq 1.0$) that is more realistic than van Driest's assumption of $Pr_t = Pr = 1$.

In the outer region, the similarity of the velocity profile can be verified by plotting the velocity defect $\left(U_e^* - \overline{U^*}\right)/u_\tau$ versus y/δ' where the transformation of the velocities U_e^*, $\overline{U^*}$ and the characteristic length δ' have yet to be determined. Since the mean velocity approaches the velocity U_e asymptotically the boundary layer thickness is an ill-defined quantity, and it is sensible to use instead an integral length Δ as suggested by Rotta (1950) for incompressible boundary layers, where

$$\Delta = \int_0^\infty \frac{U_e - \overline{U}}{u_\tau} dy = \delta^* \sqrt{\frac{2}{C_f}}. \tag{27}$$

The only difficulty in using the reference length Δ is that both the velocity profile and the skin friction must be known which, unfortunately, is not always the case for the published measurements. If both are available then the velocity defect distribution and the integral length scale can be transformed and applied to compressible turbulent boundary layers. It is then hoped that the dimensionless velocity defect will be described by a function

$$\frac{U_e^* - \overline{U^*}}{u_\tau} = f\left(\frac{y}{\Delta^*}\right) \tag{28}$$

(for zero pressure gradients), where

$$\frac{\Delta^*}{\delta} = \int_0^1 \frac{U_e^* - \overline{U^*}}{u_\tau} d\left(\frac{y}{\delta}\right) \tag{29}$$

There is no justification for the simple relationship of equation 28 other than verification by experiment. However, an evaluation of a large number of experiments in zero-pressure gradient boundary layers, mainly along adiabatic walls appears to support this particular scaling scheme. The data suggest the following semi-empirical relation (Fernholz, 1971):

$$\frac{U_e^* - \overline{U^*}}{u_\tau} = -M \ln \frac{y}{\Delta^*} - N \tag{30}$$

with $M = 4.70$ and $N = 6.74$ ($1.5 \times 10^3 \leq Re_\theta \leq 4 \times 10^4$).

More elaborate semi-empirical relationships of the type:

$$\frac{U_e^+ - \overline{U^+}}{u_\tau} = -\frac{1}{\kappa} \ln \frac{y}{\delta} + \kappa g\left(\frac{y}{\delta}\right) \tag{31}$$

were suggested by Coles (1953), by Stalmach (1958) and by Maise & McDonald (1968), the latter two authors using van Driest's velocity transformation, that is, with Prandtl number one. Due to the different methods applied in specifying the boundary layer thickness δ, the authors of the semi-empirical relations mentioned above

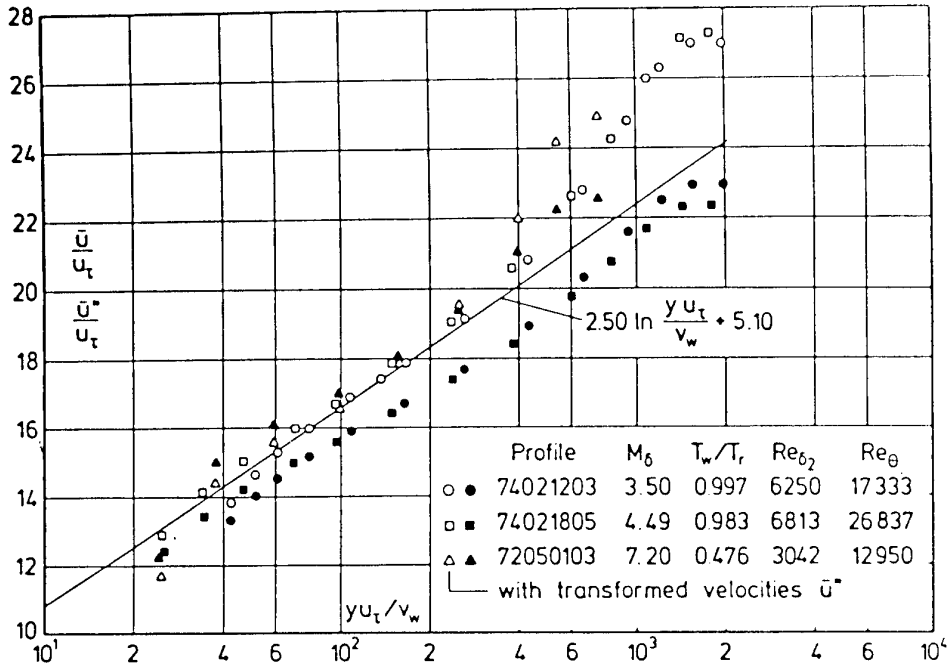

Figure 4: Log-linear plots of the velocity profile for a compressible turbulent boundary layer. Natural and transformed velocities ($\bar{U}^*$). From Fernholz & Finley (1980), where catalog numbers are referenced.

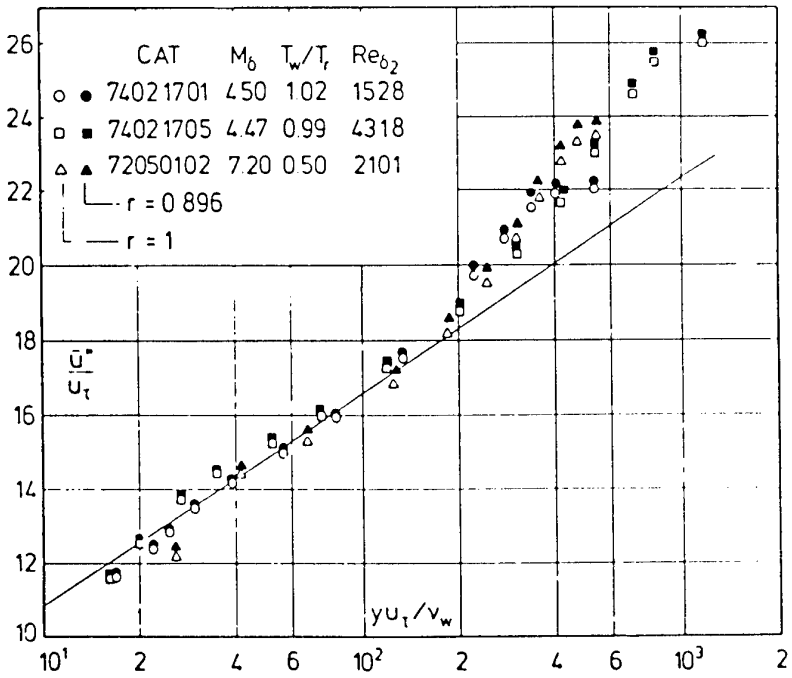

Figure 5: Comparison of velocity profiles transformed by using recovery factors of 1 and 0.896 (Mabey *et al.*, 1974, Horstman & Owen, 1972). From Fernholz & Finley (1980), where catalog numbers are referenced.

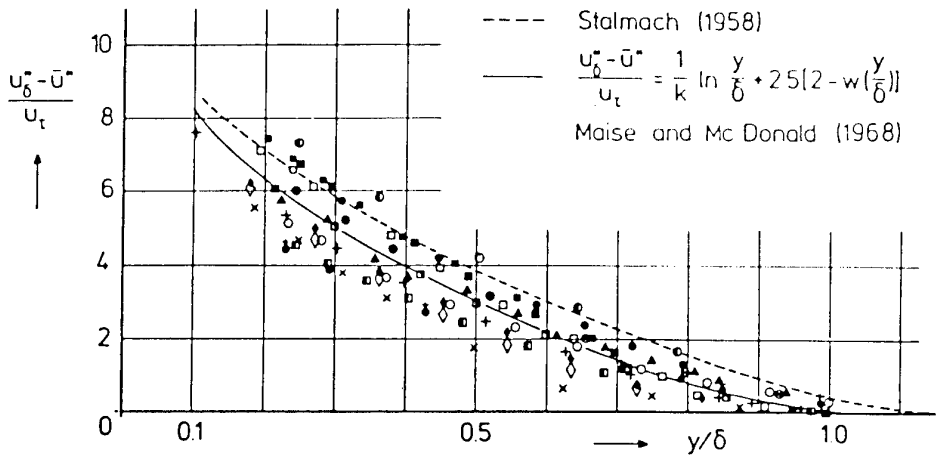

Figure 6: Mean velocity profiles in outer-layer scaling for zero pressure gradient compressible turbulent boundary layers . From Fernholz & Finley (1980). The key to the data is given in Fernholz (1969).

do not agree with each other nor do they agree with measurements if these are plotted using values as given by the experimentalists.

Figure 6 shows this comparison. Since the figure is meant only to illustrate the problem, the reader is referred to Fernholz (1969) for the identification of the experimental data.

Finally, it should be pointed out that the similarity scaling of the compressible boundary layer mean velocity profile is most usefully expressed in terms of the scaling for the mean velocity gradient $\partial U/\partial y$. That is, $\partial U/\partial y$ in the near-wall region scales with a length scale ν_w/u_τ and a velocity scale $u_\tau\,(T_w/T)^{\omega/2}$. In the outer region the length scale is δ, and the velocity scale is $u_\tau\sqrt{(T/T_w)}$. In the overlap region, the length scale becomes y, but the velocity scale is still $u_\tau\sqrt{(T/T_w)}$. So we see that the mean velocity profile in a compressible boundary layer scales with the same length scales used in scaling incompressible flows, but the velocity scale is modified by the variation in mean temperature.

3.3 Skin friction

Skin-friction measurements are more difficult to make and to interpret in supersonic flows (Fernholz & Finley, 1980, Smith *et al.*, 1992). Floating-element gauges are susceptible to inaccuracies stemming from leakage, local variations in heat transfer, flushness, and moments applied by streamwise pressure gradients. Preston-tube data can be analyzed using a variety of calibration schemes, leading to considerable uncertainty in the results. Most schemes for reducing Preston-tube data rely on boundary-layer edge conditions (for example, Hopkins & Keener, 1966), and this can introduce additional errors, particularly in perturbed flows where the edge properties are often unrelated to the flow behavior near the wall. As Finley (1994) points out, calibration equations which involve an empirical "intermediate temperature", and/or freestream properties are functionally incorrect, since the Preston tube pressure should depend on wall variables only. He adds that as long as they are used in flows with small or negligible normal pressure gradients, this is not crucial. However, in many compressible flows there are significant normal pressure gradients and the calibration equations should be expressed in terms of wall variables. The only calibration which does so is that by Bradshaw & Unsworth (1974). Here, for adiabatic flows and for $u_\tau d/\nu_w > 100$:

$$\frac{\Delta p}{\tau_w} = 96 + 60\log_{10}\left(\frac{u_\tau d}{50\nu_w}\right) + 23.7\log_{10}^2\left(\frac{u_\tau d}{50\nu_w}\right) - 10^4 M_\tau^2\left[\left(\frac{u_\tau d}{\nu_w}\right)^{0.26} - 2.0\right] \qquad (32)$$

which reduces to a very good fit to the calibration data of Patel (1965) for incompressible flows as $M_\tau \to 0$.

Allen (1977) suggested that the constants used by Bradshaw & Unsworth were incorrect and proposed that the last term should read:

$$-10^4 M_\tau^2\left[\left(\frac{u_\tau d}{\nu_w}\right)^{0.3} - 2.38\right].$$

However, Finley (1994) concluded that these corrections were based on unreliable balance data, and on the basis of a detailed analysis of the available data recommended that the original constants as given in equation 32 are more accurate than those given by Allen (1977). It should also be noted that Finley introduced a reduction procedure originally due to Gaudet (1993, private communication), in wall variables, which depends on the van Driest (1951) transformation, and not directly on balance measurements.

The Clauser method (Clauser, 1954) can also be used as long as a logarithmic region can be found, but the results obviously depend on the validity of the particular compressibility transformation used. In perturbed-flows, the compressibility transformation of Carvin *et al.* (1988) should be more reliable than that of van Driest because it does not have the additional requirement of a self-preserving boundary layer. In practice, for a wide variety

of flows, including flows with strong pressure gradients and shock wave boundary layer interactions, the differences between the Clauser-chart results obtained using the two transformations seem to be within about ±15% of the Preston-tube results (Smith *et al.*, 1992). The laser interferometer skin friction meter (LISF) is a promising new technique that does not require assumptions about the character of the wall region to deduce the wall shear stress, and can thus provide direct measurement of the skin friction in a perturbed flow. Kim *et al.* (1991) compared LISF results to Preston tube measurements in a three-dimensional shock-wave boundary-layer interaction and found encouraging agreement.

As a result of the increased viscous dissipation in compressible boundary layers is a decrease in the skin-friction coefficient with increasing Mach number (at fixed Re). The low density of the fluid near the wall indirectly results in a decrease in the slope of the non-dimensionalized velocity profile relative to that for an equivalent-Reynolds-number incompressible boundary layer. Since density has a stronger dependence on temperature than viscosity does, the skin-friction coefficient decreases with Mach number (although the dimensional wall shear increases due to the increase in velocity). The general trends for hot and cold walls can be predicted from these considerations, with heated walls leading to lower C_f (Hinze, 1975, Fernholz, 1971, Fernholz & Finley, 1980).

In fact, a variety of experimental correlations, transformations, and finite-difference solutions exist. Bradshaw (1977) critically reviewed the most widely-used skin-friction formulas and found that a variation of "van Driest II" (van Driest, 1956) exhibited the best agreement with reliable zero-pressure-gradient data, with less than 10% error for $0.2 \leq T_w/T_{aw} \leq 1$. Of course, the success of van Driest II is mainly due to the fact that for air the molecular and turbulent Prandtl numbers are close to unity.

3.4 Scales for turbulent transport

In the analysis of the mean velocity distributions in supersonic boundary layers it was assumed that the mixing length distribution was the same as in subsonic flows. This comprises essentially a variable fluid property assumption, that is, the mechanisms governing turbulent transport are the same as at low speed, and the variations of density are taken in account by scaling the local stress. This hypothesis is quite successful, since, as we have seen, experimental evidence supports that the log law is observed on the van Driest transformed velocity, with the same constant as in at low speed. Therefore it may be expected that the typical size of the energetic eddies producing turbulent transport obeys the same laws as in subsonic flows. Note that this scale is built on the shear stress $-\overline{uv}$, and that it is a scale related to turbulent diffusion.

The following discussion has been adapted from the recent work by Dussauge & Smits (1995). Consider the characteristic time scales of the turbulent and mean motions. The turbulent time scale t_t can be expressed as a function of mean time scale, flow parameters such as the Reynolds and Mach numbers R and M, the position y and the length scale L. That is:

$$t_t = g\left(t_m, R, M, y, L, ...\right).$$

We know that the energetic structures and the mean motion have characteristic scales of the same order. This suggests that the previous relationship can be rewritten as

$$t_t = t_m g\left(R, M, y, L, ...\right) \tag{33}$$

where the function g is of order 1. If we assume Morkovin's hypothesis, then for weak compressibility effects, for example in boundary layers at moderate Mach numbers, the relation between the scales is the same as at low speeds. Equation 33 reduces to:

$$t_t = t_m g\left(R, y, L, ...\right). \tag{34}$$

The turbulent time scale is defined as usual by k/ε. The mean time scale is chosen as $(\partial U/\partial y)^{-1}$, the turnover time of the mean motion, as in low speed flows. This choice can be justified as follows. The main role of the mean inhomogeneity is to amplify turbulence through linear mechanisms described, for example, by rapid distortion theories. In general, a fluctuation subjected to mean shear obeys an equation of the form:

$$\frac{Du'}{Dt} + u'\frac{\partial U}{\partial y} = f.$$

In this equation, f represents the pressure, non-linear and viscous terms. It appears from the linear left hand side that the amplification of u' by linear mechanisms occurs with a time constant of order of $(\partial U/\partial y)^{-1}$ (for incompressible turbulence, the role of the pressure terms in f is to reduce $u'\partial U/\partial y$, but the order of magnitude remains unchanged). The mean time scale can therefore be interpreted as a response time of fluctuations to mean homogeneity, and it must therefore be of order $(\partial U/\partial y)^{-1}$. If we evaluate f in the zone where the shear is constant, and where production and dissipation are equal:

$$-\overline{\rho u'v'} \approx -\bar{\rho}\overline{u'v'} = \rho_w u_\tau^2 .$$

Moreover, in this region, we assume that similarity of the profile is achieved by using either a viscous length scale, or an external length scale. We denote L the scale, whatever the choice. Equation 34 can then be rewritten as:

$$\frac{\bar{\rho}k}{\rho_w u_\tau^2} = g\left(\frac{y}{L}, R, ...\right) \tag{35}$$

We recognize in equation 35 the scaling proposed by Morkovin for the similarity of the Reynolds stresses: similarity is achieved if the local velocity scale in the constant stress region is now $\sqrt{(\rho_w/\rho)}u_\tau$ instead of u_τ. We can now define a length scale in the particular case when production is balanced by dissipation. The turbulent time scale is defined as Λ/u', where u' is a characteristic scale for velocity fluctuations, for example $\sqrt{k}$. Equating this time to k/ε, and setting ε equal to production gives the relation:

$$\frac{\Lambda}{u'} = \frac{\bar{\rho}k}{\rho_w u_\tau^2 \partial U/\partial y}$$

or, according to equation 35,

$$\Lambda = g\left(\frac{y}{L}, R, ...\right)\frac{u'}{\partial U/\partial y} \ . \qquad (36)$$

From equation 36, it can be deduced that the length scale is the same in subsonic and supersonic flows when the ratio $u'/(\partial U/\partial y)$ is unchanged. This implies that the scaling for density effects should be the same for u' and $\partial U/\partial y$. We know from experiment (and from equation 35) that in supersonic layers, u' varies like $\rho^{-1/2}$. We also know that $\partial U/\partial y$ varies as $\rho^{-1/2}$ since the van Driest transformed velocity obeys the same log-law as in subsonic flows. Therefore the characteristic length scales governing turbulent transport should not change in the supersonic regime.

To conclude these scaling considerations on turbulent transport, it should be emphasized that the presence of a logarithmic region in the mean velocity profile is a necessary condition, and that we have only considered a single velocity scale and a single length scale. This was applied to turbulent stresses, which are represented by a tensor. Therefore, it is likely that the results we obtained are related mainly to a single component or to the turbulent kinetic energy, but not to all of the components. Finally, equations 33 and 35 may give some insight into the influence of compressible turbulence on the high speed boundary layers, and indicate some possible ways to investigate departures from Morkovin's hypothesis in these flows. In equation 33, an acoustic time scale (or a Mach number) may be introduced, while the equilibrium condition should be modified by balancing the dissipation rate by the sum of production and pressure divergence terms, and by modifying equation 35.

3.5 Mean turbulence behavior

Sandborn (1974) and Fernholz & Finley (1981) both critically reviewed turbulence measurements in supersonic boundary layers. While many data sets were acquired in the period between the two reviews, their conclusions were similar and they continue to be relevant. In particular, accurate, repeatable measurements of the Reynolds-stress tensor are still needed over a wide Mach-number range. The most well-documented component is the longitudinal normal stress, which has been widely measured and properly scaled. But there have been so few systematic investigations of the effects of Reynolds number and wall heat transfer in supersonic flow that their influence on the turbulence field is not well known. The reason for the scarcity of measurements and their generally poor quality is simple: the measurement of turbulence quantities in supersonic boundary layers is exceedingly difficult, with the level of difficulty increasing with flow complexity and Mach number. But furthermore, there are significant measurement and data-reduction errors associated with every technique designed to measure fluctuating velocities in supersonic flow: thermal anemometry (see Smits & Dussauge, 1989), laser-Doppler velocimetry (Johnson, 1989), and advanced laser-based techniques such as laser-induced fluorescence (Logan, 1987, Miles & Nosenchuck, 1989).

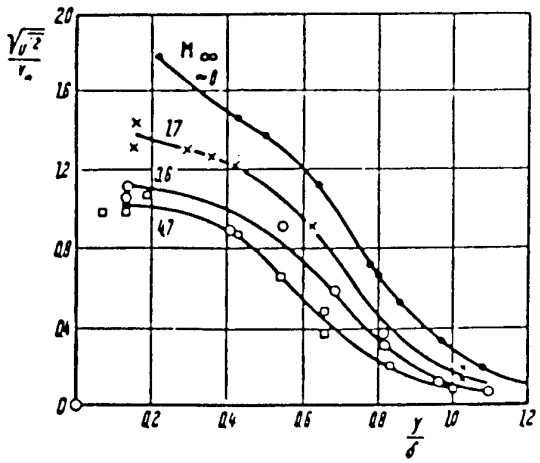

Figure 7: Distribution of turbulent velocity fluctuations in boundary layers. Measurements are from Kistler (1959) and Klebanoff (1955). Figure from Schlichting (1979).

Despite these uncertainties in the measurements, certain trends can be distinguished. For example, when the longitudinal velocity fluctuations are normalized by the shear velocity, $\overline{u'^2}/u_\tau^2$, there is a clear decrease in fluctuation level with increasing Mach number (see Kistler, 1959, Fernholz & Finley, 1981). This is shown in figure 7. However, when the streamwise normal stress is normalized by the wall shear stress, the data exhibit some degree of similarity (as suggested in section 3.4), particularly in the outer layer (see figure 8). This formulation of the velocity fluctuations indicates the success of the scaling suggested by Morkovin (1962) to account for the mean-density variation, and provides some support for the discussion given in section 3.4. In fairness, it should be mentioned that Fernholz & Finley (1981), in considering an earlier set of data, concluded that the streamwise Reynolds stress did not show a similar behavior in the outer region, no matter which velocity scale was used in the non-dimensionalization. It appears that the later data shown in figure 8 displays a more regular behavior. The streamwise normal stress distribution for supersonic flows is in fair agreement with the incompressible results of Klebanoff (1955), except near the wall where reduced accuracy affects the supersonic measurements. Morkovin's scaling appears to be appropriate to at least Mach 5. Measurements by Owen *et al.* (1975) at $M_e = 6.7$ and Laderman & Demetriades (1974) at $M_e = 9.4$ exhibit damped turbulent fluctuations, particularly near the wall. Since both of the hypersonic data sets are for cold-wall conditions, this may simply indicate the stabilizing effect of cooling.

Cross-wire measurements of both streamwise and wall-normal components of velocity have suggested additional apparent differences between Mach 3 and incompressible boundary-layer structure (Smits *et al.*, 1989). Measurements of $\overline{v'^2}$ and $\overline{w'^2}$ are less common than those of $\overline{u'^2}$, the data exhibit more scatter, and the conclusions are therefore less certain. In contrast to the streamwise turbulence intensity, both distributions appear to increase slightly with increasing Mach number (Fernholz & Fin-

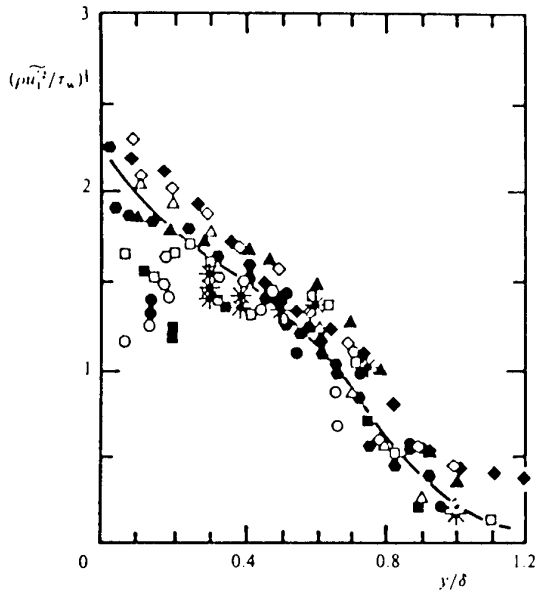

Figure 8: Velocity fluctuation intensity in supersonic boundary layers: *, Dussauge & Gaviglio (1987); , $M = 1.72$; ○, $M = 3.56$; ○, $M = 4.67$, Kistler (1959); △, hot wire; ◇, laser, $M = 2.9$, Johnson & Rose (1975); , $M = 2.9$, Smits *et al.* (1989); ■, $M = 2.32$, Eléna & Lacharme (1988); □, $M = 2.3$, Debiève (1983); , $M = 2.32$, Eléna & Gaviglio (1993); ◇, $M = 3$, Yanta & Crapo (1976). Figure taken from Dussauge & Gaviglio (1987).

ley, 1981). In this case, Morkovin's scaling does not collapse the data, and $\overline{\rho v'^2}/\tau_w$ and $\overline{\rho w'^2}/\tau_w$ show no real trend toward similarity. Konrad (1993) using hot-wire anemometry found that $\overline{w'^2}$ and $\overline{v'^2}$ in a Mach 2.9 boundary layer were approximately equal throughout the layer (see figure 9). In contrast, the measurements by Eléna & Lacharme (1988) in a Mach 2.3 boundary layer using laser Doppler anemometry indicate that the behavior of $\overline{v'^2}/u_\tau$ is almost identical to that found in subsonic flows (see figure 10). The behavior of the anisotropy parameter is therefore not clear: the measurements by Eléna & Lacharme (1988) indicate that $\sqrt{\overline{v'^2}}/\sqrt{\overline{u'^2}}$ is almost the same as in subsonic flows, whereas the hot-wire measurements by Fernando & Smits (1990) and Konrad (1993) indicate that this ratio increases with Mach number (Reynolds number effects were shown to be negligibly small in Dussauge *et al.* (1996)). The limited nature of the data precludes any conclusions regarding the effects of compressibility on this structure parameter.

Sandborn (1974) reviewed direct measurements and indirect evaluations of the zero-pressure-gradient Reynolds shear stress, $-\overline{\rho u'v'}$ (a later, more comprehensive study was provided by Fernholz & Finley, 1981). Sandborn constructed a 'best fit' of normalized shear stress profiles (τ/τ_w) from integrated mean-flow data taken by a variety of researchers over a wide Mach-number range, $2.5 < M_\infty < 7.2$ (extended to Mach 10 by Watson (1978) for adiabatic and cold walls). The data indicate a near-universal shear-stress profile that agrees well with the incompressible measurements of Klebanoff (1955) (see fig-

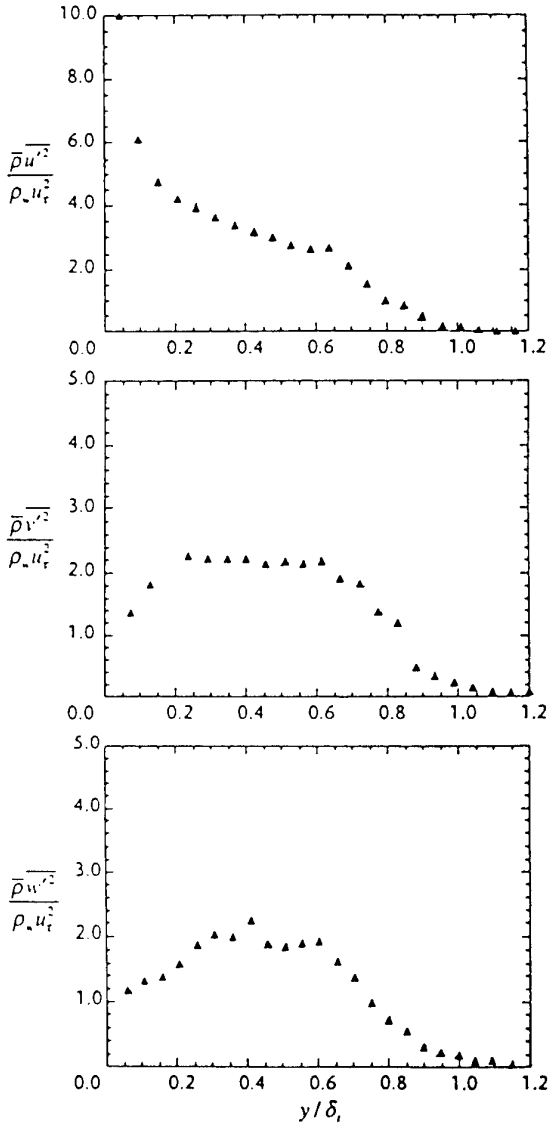

Figure 9: Turbulence distributions in a Mach 2.9 boundary layer, measured using hot-wire probes ($Re_\theta = 65,000$). Adapted from Konrad (1993).

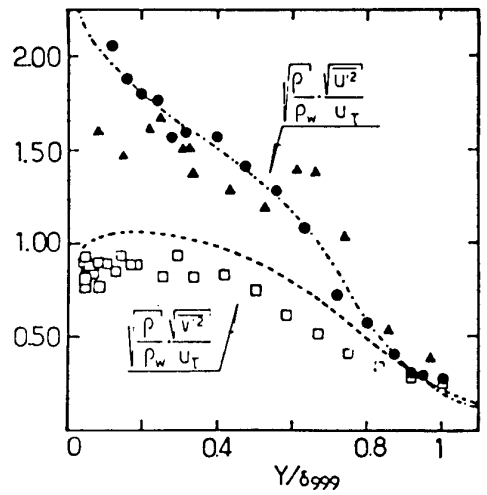

Figure 10: Turbulence distributions in a Mach 2.3 boundary layer, measured using LDV ($Re_\theta = 5,650$). Figure from Eléna & Lacharme (1988).

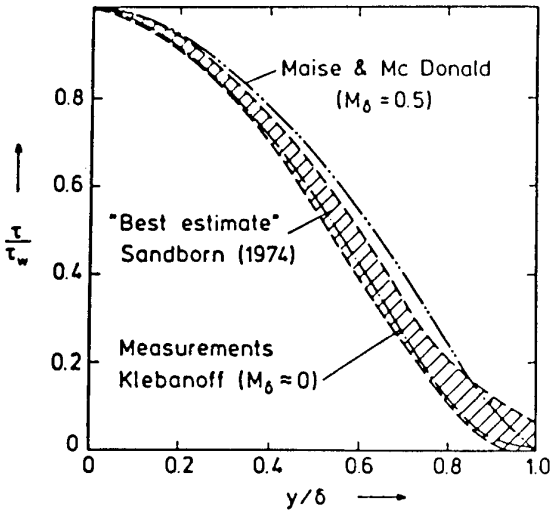

Figure 11: Distribution of turbulence shear stress in boundary layers at supersonic speed. Figure from Sandborn (1974).

ure 11). As Sandborn pointed out, the universality of τ/τ_w over such a wide Mach-number range is not surprising in light of the fixed constraints on the values of the shear stress at the wall and in the freestream. Even so, the only Reynolds shear stress measurements to agree with the 'best fit' in 1974, and then only in the outer layer, were the LDV data of Rose & Johnson (1975). Subsequent Reynolds shear stress measurements by Mikulla & Horstman (1975), Kussoy *et al.* (1978), Robinson (1983), Smits & Muck (1984), and Donovan *et al.* (1994) (all using hot wires except Robinson) have exhibited modest agreement with Sandborn's best fit and the incompressible distribution. The agreement is limited to the outer layer, with great scatter in the inner layer and most profiles not tending toward $\tau/\tau_w = 1$ near the wall. The data in the inner layer do not scale with yu_τ/ν_w, almost certainly because of the difficulties with the measurements.

The behavior of the shear correlation coefficient R_{uv} is affected strongly by the level of $\overline{v'^2}$. In the measurements by, for example, Fernando & Smits (1990) at Mach 2.9, R_{uv} decreases significantly with distance from the wall, from a value of about 0.45 near the wall to about 0.2 near the boundary layer edge (see figure 12). This is in contrast to most subsonic flows where the correlation coefficient is nearly constant at a value of about 0.45 in the region between 0.1δ and 0.8δ. As can be seen in the figure, the data by Eléna & Lacharme (1988) at Mach 2.3 follow the subsonic distribution closely, and it is difficult to say what the effect of compressibility is on the level of R_{uv} without further experiments. However, the subsonic data showed that the maximum value of $\overline{v'^2}$ increases significantly with Reynolds number (Dussauge *et al.*, 1996), and considering that there is about a factor of 15 difference in the Reynolds numbers between the results of Fernando & Smits (1990) and Eléna & Lacharme (1988), the differences seen in the distribution of R_{uv} may well indicate the effects of Reynolds number. Joint probability density distributions of the two velocity (or mass-flux) components may also be somewhat different between subsonic and supersonic flows, with the supersonic case fa-

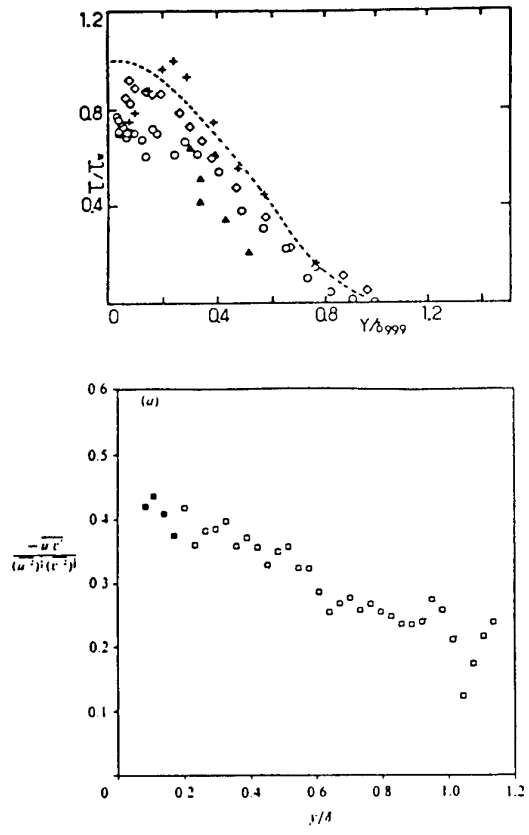

Figure 12: Distribution of R_{uv} in subsonic and supersonic boundary layer: (a) Data from Eléna & Lacharme (1988): the dotted line corresponds to the subsonic data of Klebanoff (1955). (b) Data from Fernando & Smits (1990): the filled-in symbols are subject to errors due to transonic effects.

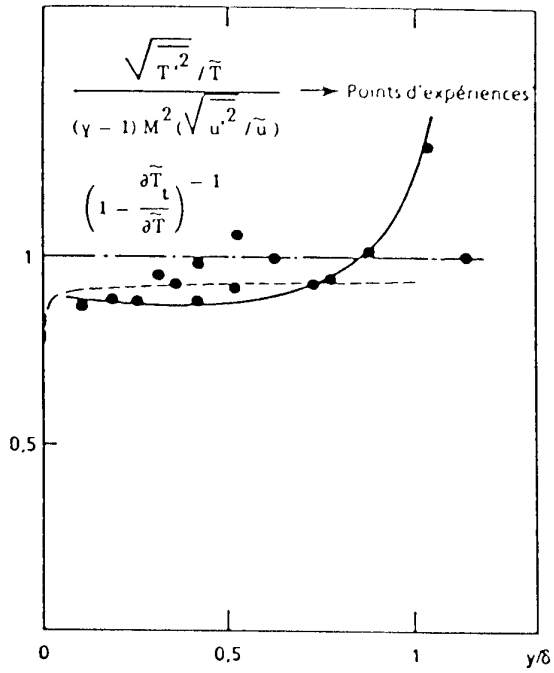

Figure 13: Test of the Strong Reynolds Analogy in a supersonic boundary layer ($M_e = 2.32$, $Re_\theta = 5,650$). Data from Debiève (1983).

voring vertical fluctuations in the mid-layer slightly more than the subsonic case (for further details see Fernando & Smits, 1990), but again the evidence is not conclusive.

In section 2.3 the Strong Reynolds Analogy was discussed. Some measurements designed to test the validity of this analogy in adiabatic flows are presented in figures 13 and 14. The results indicate that the SRA is closely followed in supersonic boundary layers, and the correlation coefficient R_{uT} is close to the value of 0.8 throughout the layer (note that for $y/\delta > 0.8$, the assumptions used in the data reduction are probably invalid). This value is considerably higher than that found in slightly heated subsonic flows, as seen in figure 14, and the reason is not entirely clear. However, the SRA can be a very useful tool in describing the behavior of supersonic turbulent boundary layers, especially in formulating turbulence models. The SRA can also be extended to non-adiabatic flows, as discussed by Gaviglio (1987).

At hypersonic Mach numbers, it is possible that the triple correlation $\overline{\rho' u' v'}$ may become comparable to the 'incompressible' Reynolds shear stress, $\overline{\rho} \overline{u'v'}$, since $\rho'/\overline{\rho} \sim M^2 u'/U$. Owen (1990) evaluated the various contributions to the 'compressible' Reynolds shear stress at Mach 6 through simultaneous use of two-component LDV and a normal hot wire. His results indicate that $\overline{\rho' u' v'}$ is negligible compared to $\overline{\rho} \overline{u'v'}$. Even though density fluctuations increase with the square of the Mach number, it should be remembered that the main contribution to the Reynolds shear stress occurs in the region where the local Mach number is small compared to the freestream value, so this 'hypersonic effect' should only be important at very high freestream Mach number.

The stagnation-temperature fluctuation must be known to evaluate the turbulent heat-flux correlation, $-c_p \overline{\rho} \overline{v' T'}$.

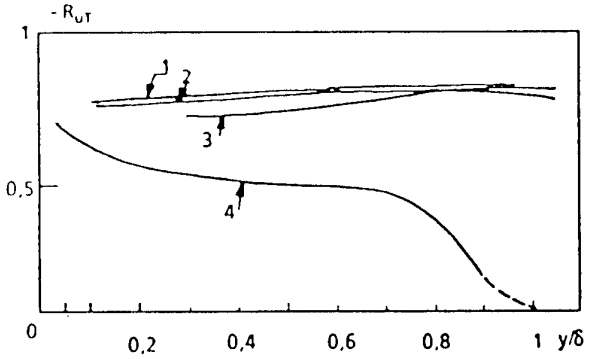

Figure 14: Distribution of R_{uT} in boundary layers. Curve 1: $M_e = 2.32$, $Re_\theta = 5,650$, from Debiève (1983). Curves 2 and 3: $M_e = 1.73$, $Re_\theta = 5,700$, from Dussauge (1981). Curve 4: $M_e << 1$, $Re_\theta = 5,000$, from Fulachier (1972). Figure from Eléna & Gaviglio (1993).

Kistler (1959) observed that $T'_{0_{rms}}/\overline{T_0}$ increased with Mach number, with maxima of 0.02 at $M_\infty = 1.72$ and 0.048 at $M_\infty = 4.67$. If Kistler's data is alternately nondimensionalized by either T_w (Fernholz & Finley, 1981) or $T_r - T_e$ (Sandborn, 1974), the Mach-number dependence appears to be eliminated, but similarity of the stagnation-temperature distributions is not achieved. Similar conclusions are reached from measurements by Morkovin & Phinney (1958) and Horstman & Owen (1972). The maximum level of stagnation-temperature fluctuations is about 6% (for $M < 7$). Further analysis of these data shows that $T'_{0_{rms}}$ scales according to either $T_{0e} - T_w$ or $T_{0e} - T_r$. The fluctuations in total temperature appear to be produced by the difference in stagnation temperature between the wall and the freestream, and not, for example, by the unsteadiness in pressure, through the term $\partial p/\partial t$ in the total enthalpy equation. In these experiments, the maximum of $T_{0_{rms}}/(T_{0e} - T_r)$ is about 0.5, regardless of the Mach number, a rather satisfactory result since it shows that the total temperature fluctuations are of the order of (but less than) the total temperature difference across the boundary layer. Finally, $T'_{0_{rms}}$ is less than that of u'_{rms} and T'_{rms}, but not low enough to satisfy the strict Strong Reynolds Analogy (see Gaviglio, 1987). In fact, the SRA can be used to estimate that $T'_{0_{rms}}$ is about 60% of T'_{rms} at Mach 3 (Smits & Dussauge, 1989).

3.5.1 Outer-layer structure

There is also considerable controversy regarding the nature of the outer-layer structure. Nevertheless, a general picture has emerged. A specific characteristic component of the outer layer is believed to be the large scale turbulent "bulge", also referred to as a "large scale motion" (LSM). The large scale motions evolve and decay slowly as they convect downstream, and, on average, they are inclined to the wall at an acute angle, leaning in the downstream direction. Between neighboring bulges, the flow is irrotational, resulting in the intermittent character of the outer layer. Figure 15 shows several LSM's. The structures are seen to vary greatly in size and inclination angle. The

Figure 15: Flow visualization by Falco (1977), of a boundary layer at $Re_\theta \approx 4,000$, obtained by seeding the flow with a fog of oil droplets, and illuminating the flow with a planar laser sheet. Flow is from left to right. Figure from Van Dyke (1982).

properties of the large scale motions, such as length scales, time scales, convection velocity, and stucture angle, as well their internal structure, such as velocity, vorticity, and pressure fields, remain the subject of controversy and active research. Furthermore, the Reynolds number and Mach number dependence of the LSM's, if any, is not well understood.

Part of the difficulty in experimental studies of the outer-layer structure, as it is in studies of the inner-layer structure, is finding an unambiguous criterion for ensemble-averaging. One method is based on discriminating between "turbulent" and "non-turbulent" fluid, and using the intermittency function (a box-car logic function) to sort the data. The most basic output is the intermittency itself, γ, which is the fraction of the time the flow is judged to be turbulent. One definition of γ is $3/F$, where the flatness $F = \overline{u'^4} \Big/ \overline{(u'^2)^2}$. The distribution of F is shown in figure 16 for a number of different freestream Mach numbers. The results imply that the intermittency in the outer part of the layer decreases with Mach number. Another method uses the VITA technique originally developed by Blackwelder & Kaplan (1976) for studies of the near-wall bursting process. A variety of similar techniques have been developed (for example, VISA by Kim & Spalart (1987), WAG by Antonia *et al.* (1990a), Antonia *et al.* (1990b)), but they are all subject to ambiguities related to the uncertainties in setting threshold levels. Nevertheless, they may still give useful insights if carefully used.

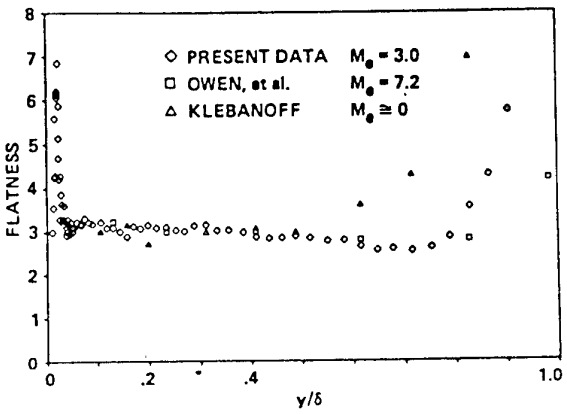

Figure 16: Comparison of flatness distributions: □, Owen *et al.* (1975) ($Re_\theta = 8,500$, $M = 7$), based on mass flux; ◇, Robinson (1986) ($Re_\theta = 15,000$, $M = 3.0$, based on mass flow; △, Klebanoff (1955) ($Re_\theta = 7,100$, $M \approx 0$), based on velocity. Figure from Robinson (1986).

Another useful method for investigating the large scale structure is multiple-point measurements of one or more flow variables, typically velocity, density, wall pressure, and wall shear stress. The data are then analysed in the context of space-time correlations. The correlation of two variables measured at two points in the flow field is given by

$$R_{ab}(\xi_x, \xi_y, \xi_z, \tau) =$$

$$\frac{\overline{a(x,y,z,t)b(x+\xi_x,y+\xi_y,z+\xi_z,t+\tau)}}{a_{rms}b_{rms}} \quad (37)$$

where a and b are the two flow variables being correlated, ξ_x, ξ_y, and ξ_z are the separations between the two points in the three coordinate directions x, y, and z, respectively, and τ is the time delay applied to the signal of variable b. For the case when both a and b are velocities, R_{ab} is typically denoted by R_{ij}, where i and j are the indices of the velocity components ($R_{11} = R_{uu}$, $R_{12} = R_{uv}$, etc...). When any of ξ_i are nonzero in equation 37, R_{ab} is called a space-time correlation. Space-time correlations generally have a single well-defined peak, which occurs at $\tau = \tau_{max}$, the optimum time delay, which may be nonzero.

Figure 17: Rayleigh scattering image of a turbulent boundary layer in a Mach 8 flow at $Re_\theta = 3,200$. Flow is from left to right. Figure from Baumgartner *et al.* (1997).

3.6 Boundary-layer structure

The eddy-structure and internal dynamics of compressible turbulent boundary layers play an important role in many aerospace engineering applications. These include turbulent mixing for high-speed propulsion systems, tripping of hypersonic laminar boundary layers (for inlet efficiency), acoustic noise generation and propagation from high-speed engines, surface heat-transfer on high-speed vehicles, performance optimization for low-observable configurations, and unsteadiness in shock/turbulent boundary layer interactions. The following review was adapted from the paper by Spina *et al.* , where further details may be found.

The current state of knowledge concerning compressible boundary layer structure is limited to large-scale motions in the outer-region, and is derived largely from recent studies by Spina *et al.* (1991a), Spina *et al.* (1991b), Smits *et al.* (1989), Spina & Smits (1987), Fernando & Smits (1990), Donovan *et al.* (1994), and Robinson (1986) of flat-plate layers with free-stream Mach numbers of approximately 3.0. These studies were preceded by a pioneering investigation by Owen & Horstman (1972), who made extensive two-point cross-correlation measurements with hot-wires in a Mach 7.2 boundary layer. Most of the results available in the literature were obtained using hot-wire anemometry (with its attendant limitations), with some degree of corroboration by high-speed flow visualization techniques (Cogne *et al.*, 1993, Smith & Smits, 1988).

For moderate Mach numbers, the outer region of the boundary layer (beyond the logarithmic region) is dominated by the entrainment process rather than by turbulence production. Thus the available studies of supersonic turbulent boundary layer structure are primarily relevant to the processes by which the boundary layer grows. In contrast, for subsonic turbulent boundary layers, most of the attention has focused upon the near-wall turbulence production processes. In addition, while most structure measurements in supersonic flow have been conducted at very high Reynolds number, the majority of studies in subsonic flow has been at quite low Reynolds number. These mismatches in emphases between subsonic and supersonic investigations sometimes make comparisons inconclusive, at least for isolating effects of compressibility on turbulence physics. To avoid the additional uncertainties due to measurement difficulties, it seems best to study quantities which are largely independent of calibration and measurement errors, such as the intermittency, ratios of Reynolds stresses, space-time correlations and structure angles.

The intermittency is one measure of the wallward extent of the entrainment process. The intermittency profile is often estimated with measurements of u' flatness. The measured flatness profile displays an apparent Mach-number dependence (see figure 16), wherein the onset of intermittency (corresponding to the rise in flatness factor) occurs nearer the boundary-layer edge as the Mach number increases. Since the cone of influence of a flow disturbance is inversely proportional to Mach number, the intermittent zone could become thinner as the Mach number increases. This interpretation is not fully supported by high-speed flow visualizations, however, so the data remain provocative. For example, Rayleigh-scattering flow visualization by Baumgartner *et al.* (1997) show deep potential incursions into the turbulent eddies of a Mach 8 boundary layer (figure 17) in patterns that are strikingly similar to visualizations of low-speed boundary layers. Estimates of the intermittency distribution from such images indicate very good agreement with the subsonic data by Klebanoff (1955), suggesting that the earlier results may be flawed in some way.

For both incompressible low Reynolds number boundary layers, and compressible high Reynolds number boundary layers, the most identifiable feature of the outer-region is a downstream-sloping shear-layer interface between upstream high-speed fluid and downstream low-speed fluid. (Unfortunately, these structures have been labeled both "fronts" and "backs" in the literature.) These interfaces are three-dimensional shear layers which are believed to form the upstream side of the largest of the boundary-layer eddies, and remain coherent long enough to convect several boundary-layer thicknesses downstream. They are not inert, however, since Spina *et al.* (1991a) have shown that 40% of the outer-layer Reynolds shear stress can be found in the neighborhood of these sloping interfaces (causality is not implied.) The intense turbulence production processes near the wall in the Mach 3 layer have not been investigated, but incompressible experience suggests that the large-scale sloping interfaces are not closely affiliated with near-wall regions of high Reynolds shear stress.

Sloping interfaces are easily detected with dual hot-wires separated in y, using either traditional space-time correlations, or a variety of conditional sampling techniques.

For Mach 3 turbulent boundary layers, the effect of compressibility on the large-scale outer structures has been found to be generally small, which may be expected since the fluctuating Mach number in the outer regions is unlikely to approach unity (figure 3). However, differences between subsonic and supersonic large-scale motions have been observed, and some of these results were mentioned in earlier sections. The main results can be summarized as follows.

The average "structure angle" at which delta-scale interfaces lean downstream in a Mach 3 turbulent boundary layer ranges from 45° to 60° (standard deviation $\approx$ 20°) across most of the boundary layer, with a decrease near the wall and an increase near the boundary layer edge. The measured value of the structure angle is strongly dependent on measurement technique, although one method in current favor employs two hot-wires, separated by a fixed distance in y of 0.1δ to 0.3δ, with both traversed across the layer. Structure angles measured using this technique in subsonic, low-Reynolds-number turbulent boundary layers are somewhat lower than those for Mach 3, high-Reynolds-number layers (Alving *et al.*, 1990b). As indicated in section 3.7, it seems likely that increasing Reynolds number decreases the structure angle, while increasing Mach number increases the structure angle.

Hot-wire and flow visualizations show that the sloping delta-scale structures convect downstream at approximately 90% of the freestream velocity (slightly greater than for similar structures in low Reynolds number, incompressible turbulent boundary layers), and persist for at least 4 boundary-layer thicknesses (and probably much farther) downstream (Spina *et al.*, 1991b).

Space-time correlation measurements by Smith (1994) at Reynolds numbers in the range $4,600 \leq Re_\theta \leq 13,200$ showed that the broad-band convection velocity and the decay of the large scales with increasing time delay scaled on outer-layer variables (specifically U_e and δ) were only weakly dependent on Reynolds number. However, isocorrelation contours indicated that the streamwise length scales increased with Reynolds number, in agreement with the results by Liu *et al.* in a fully-developed channel flow. Furthermore, space-time correlations in the wall-normal direction revealed that the broadband structure angle *decreased* by about 10° over the same range in Re_θ.

Isocorrelation contour maps (figures 18 and 19) showed an *increase* of between 30 and 60% in the streamwise length scale over the same Reynolds number range, and this behavior may be related to the decrease in the structure angle. The spanwise length scale showed comparatively little variation.

These subsonic results provide an interesting contrast to the results obtained by Spina *et al.* (1991a) in a Mach 3 boundary layer with Re_θ = 80,000 (see figures 20 and 21). In the supersonic flow, the streamwise length scales were two to three times *smaller* than in the subsonic flow, and the structure angles were about 10° *larger*. The spanwise scales were almost independent of the Mach number. Now, the smaller streamwise scales correlate well with the increased structure angle, but the trend with Reynolds number seen in the subsonic data does not seem to hold for the supersonic flow. Therefore it seems that

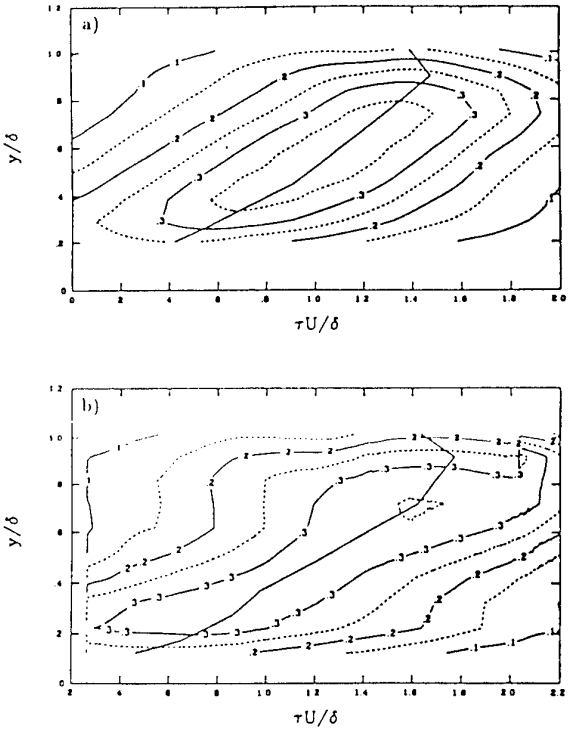

Figure 18: Isocorrelation contour maps in the x-y plane in a turbulent boundary layer at $Re_\theta = 4,981$ (top) and 13,052 (bottom) using different wall-normal probe separations: a) $\xi_y/\delta \approx 0.1$. Figure from Smith (1994).

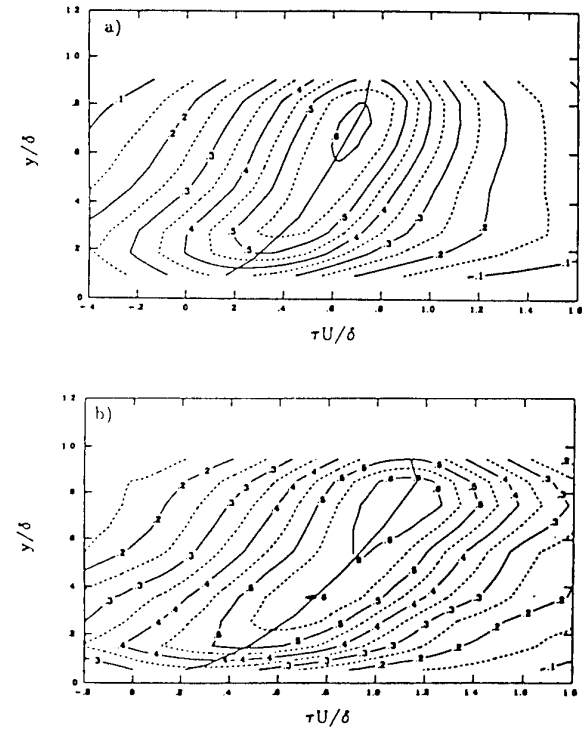

Figure 18 (cont.) b) $\xi_y/\delta \approx 0.2$.

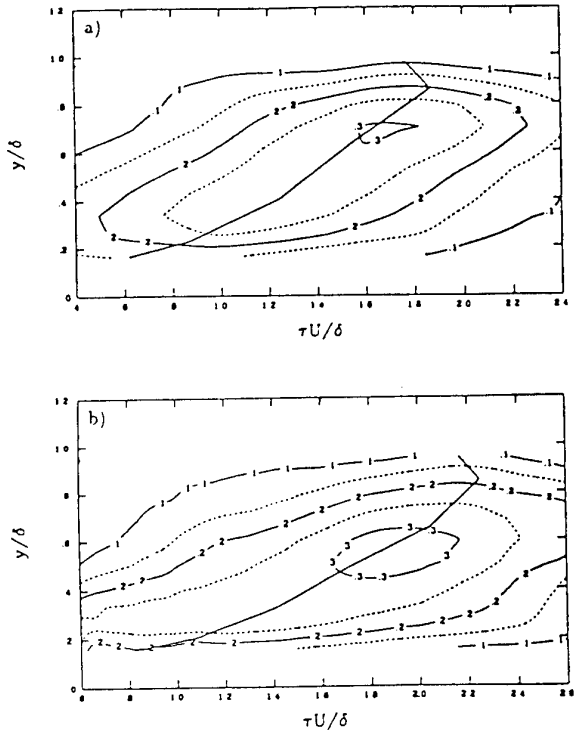

Figure 18 (cont.) c) $\xi_y/\delta \approx 0.3$.

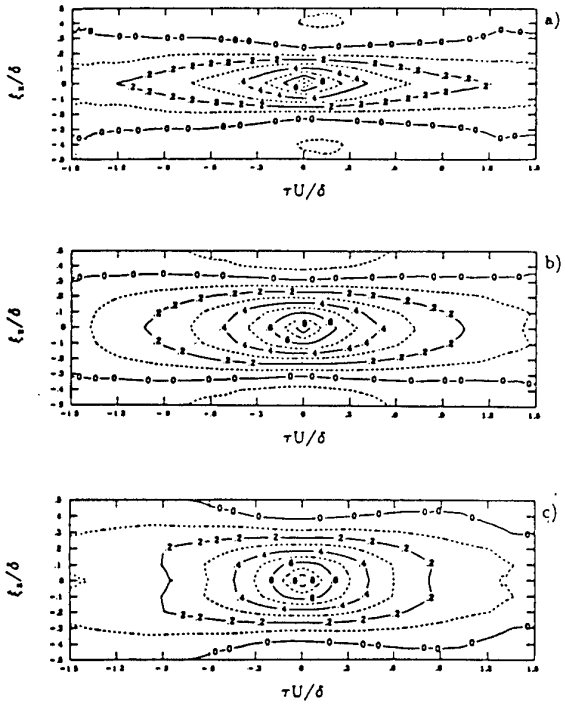

Figure 19 (cont.) (b) $Re_\theta \approx 13,200$.

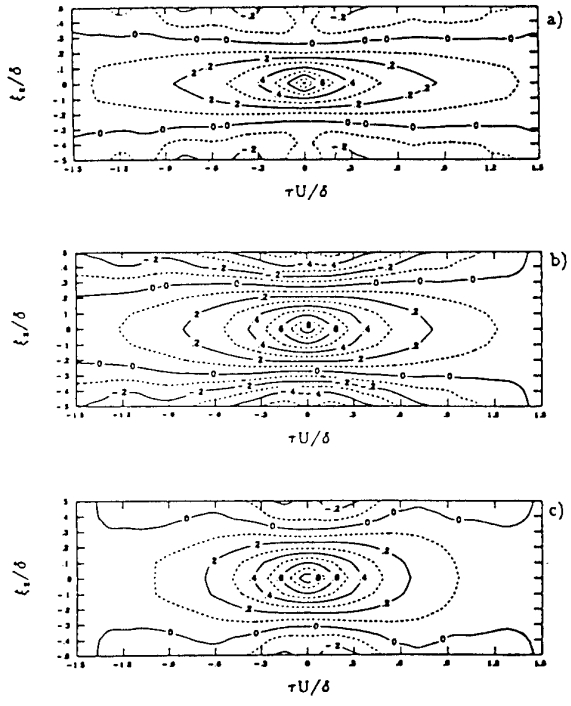

Figure 19: Isocorrelation contour maps in the x-z plane in a turbulent boundary layer at $y/\delta = 0.09$ (top),0.42 (middle), 0.80 (bottom). (a) $Re_\theta \approx 4,600$. Figure from Smith (1994).

the streamwise length scale and the structure angle depend on the Mach number and the Reynolds number. These observations have important implications for developing turbulence models for high speed flows, where it is commonly assumed that length scales follow the same scaling as in subsonic flow, and only fluid proerty variations are important. The fact that some characteristics of the turbulence depend on Mach number in a more subtle way, even at supersonic speeds where these assumptions work reasonably well, indicate that at higher Mach numbers the scaling will need to include compressibility effects directly.

3.7 Spectral data

Experimentally, the integral scales are deduced mainly from one point hot-wire measurements, so that the spatial scales are deduced using Taylor's hypothesis. Even when measurements of two-point correlations are available (see, for example, Spina & Smits, 1987, Robinson, 1986), it is often difficult to determine integral scales from the data. The types of data which are available also depend on the measurement technique. For instance, when constant current anemometers (CCA) are used, time histories are generally not measured. Spectral data for u' and T' can be obtained directly by processing the signal with the fluctuation diagram technique to separate the contributions of u' and T' (see Fulachier, 1972, Bestion, 1982, Debiève, 1982, Debiève, 1983, Bestion *et al.*, 1983, Audiffren, 1993). Bestion (1982), and Audiffren (1993) showed that for an adiabatic flat-plate boundary layer at a Mach numbers of 2.3 the shapes of the spectra of $(\rho u)'$

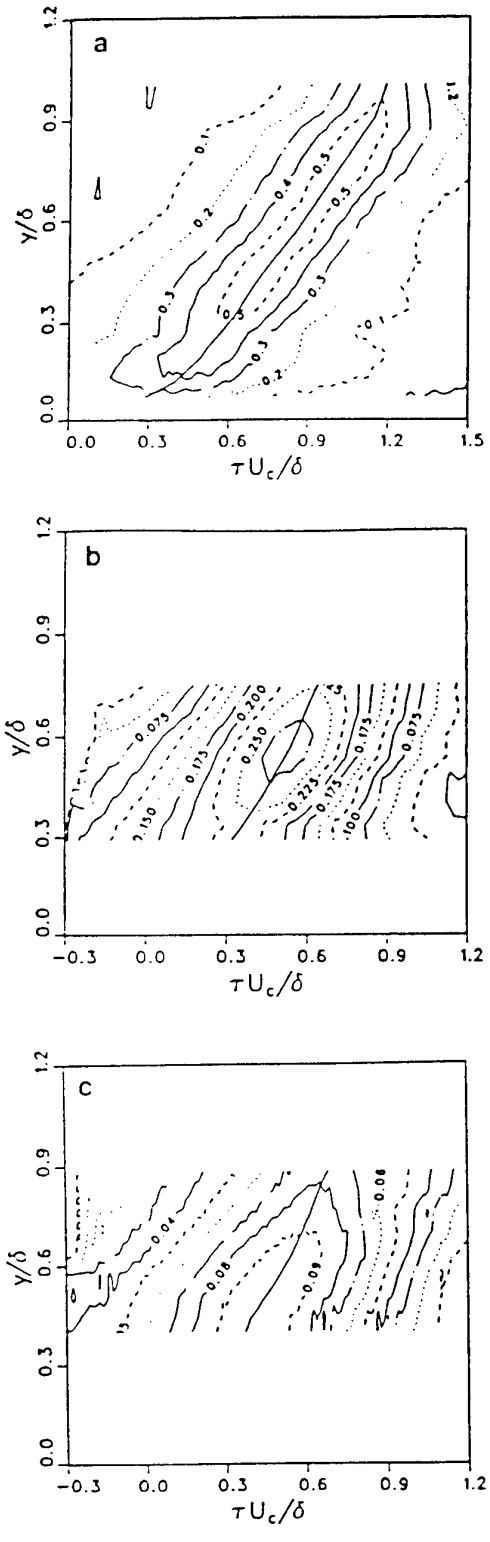

Figure 20: Isocorrelation contour maps in the x-y plane in a turbulent boundary layer at $Re_\theta = 81,000$ and $M = 2.9$ using different wall-normal probe separations: a) $\xi_y/\delta = 0.09$; b) $\xi_y/\delta = 0.30$; c) $\xi_y/\delta = 0.51$. Figure from Spina (1988).

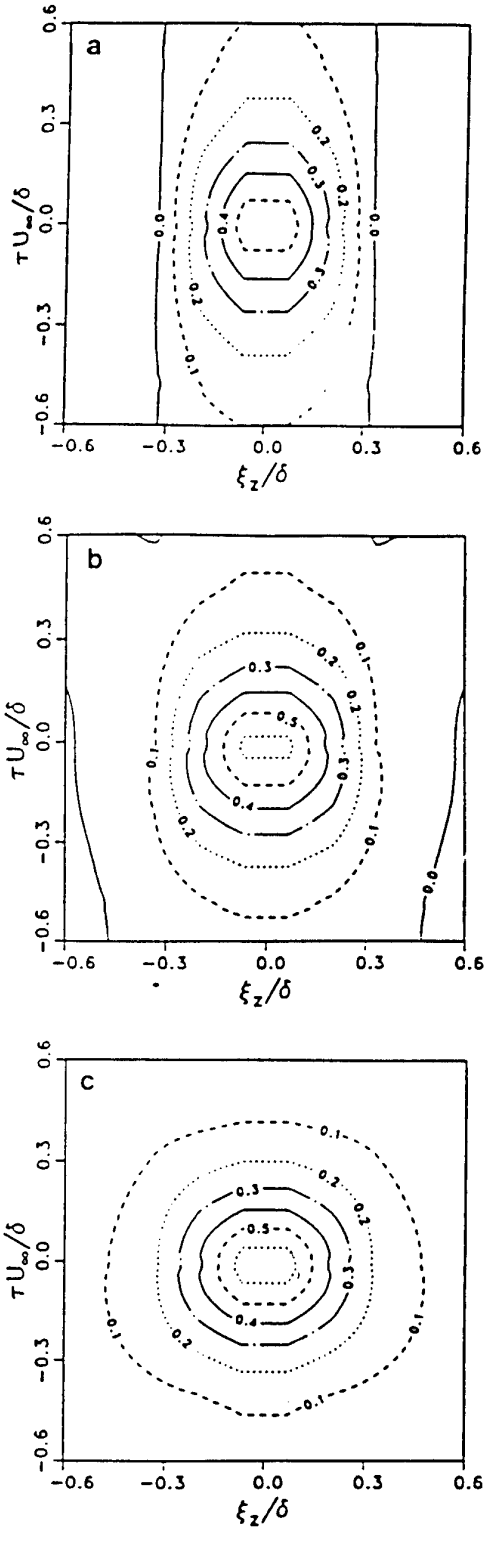

Figure 21: Isocorrelation contour maps in the x-z plane in a turbulent boundary layer at $Re_\theta = 81,000$ and $M = 2.9$ at three positions in the boundary layer: a) $y/\delta = 0.20$; b) $y/\delta = 0.51$; c) $y/\delta = 0.82$. Figure from Spina (1988).

and u' are practically the same, but differ considerably from the spectrum of total temperature T_0'. Therefore, when anemometers are operated with a single overheat, a sufficiently high value of the resistance should be chosen to minimize the contribution of T_0' and to obtain a signal practically proportional to $(\rho u)'$. When constant temperature hot-wire anemometers (CTA) are used at a high overheat ratio, the measured signal is practically proportional to $(\rho u)'$, which in turn gives spectral information on u'. Such data can be inaccurate at low wave numbers. The spectral measurements of velocity and temperature performed with a CCA in adiabatic boundary layers by Morkovin (1962), Bestion (1982), Audiffren (1993) show that the ratio $(u'/U)/(T'/T)$ at low frequencies is not a constant, and that the spectral correlation coefficient $R_{uT}(f)$ increases to unity at zero frequency. This may be the cause for the differences in the shapes of the spectra for u' and $(\rho u)'$ at low frequencies, depending on the Mach number. For higher frequencies, the ratio $(u'/U)/(T'/T)$ and the correlation coefficient are approximately constant, and the spectra are nearly proportional to each other.

Now, the classical integral scale can be determined from one-point measurements by integrating the autocorrelation coefficient of u'. It is then necessary to define the domain of integration, since the autocorrelation can become negative. When using hot-wire anemometry in supersonic flows, this question can be complicated by possible "strain-gauge" effects. These effects can cause peaks in the spectrum, which may be acceptable for measurements of the overall stress or the turbulence energy, but which can cause spurious oscillations in the autocorrelations, and make the estimates of the integral scale inaccurate.

To avoid this effect, the integral scale can be determined by finding the value of the energy spectrum at zero frequency. However, since the signal is usually filtered with a high-pass filter, it has zero mean and its spectrum has a zero value at zero frequency. The integral scale must then be found by extrapolating the spectrum to zero frequency. In practice, the value at a frequency slightly larger than the limit of the high-pass filter is taken as the best estimate. Moreover, it may be difficult to measure the low frequencies, because they can be affected by noise of the power supply, and by the peculiarities of each wind tunnel such as acoustic resonances. For CTA measurements, it has also been shown that, the spectra of u' and of $(\rho u)'$ may be different at very low frequencies.

For these reasons, an additional scale has also been used. Since we expect that the spectra have a region of k_1^{-1} dependence in the logarithmic zone, $E(k_1)$ varies as k_1^{-1}, and $k_1 E(k_1)$ is constant or presents a maximum. Here we have chosen the wave number for which this maximum occurs as the (inverse of the) characteristic space scale.

This probably has a clearer physical meaning than the integral scale, since for the incompressible part of the fluctuating motion it characterizes the eddies extracting energy from the mean field. As indicated earlier, experimentalists usually measure frequency spectra, so that a characteristic frequency is measured, and then a length scale is deduced using Taylor's hypothesis. There is usually a considerable amount of scatter because the location of the maximum is not always well defined. For the data considered here, a maximum was generally found in the external layer, but in the logarithmic zone of the subsonic boundary layer the spectra were frequently "double-humped" and the maximum was difficult to determine. Such shapes were also mentioned by Perry *et al.* (1986) who interpreted them to mean that Taylor's hypothesis failed for low frequencies. Uddin (1994) noted that the bump at low wavenumber became more prominent at higher Reynolds numbers (see also Smith, 1994). These double-humped profiles led to some difficulty in determining the length scale, and it was necessary to discard some points in the log-law region of the subsonic boundary layer data. However, the typical situation was that the higher frequency bump corresponds to scales comparable to the scales of the outer layer, and the other maximum occurs at frequencies an order of magnitude lower, corresponding to length scales five to ten times larger than the outer layer scales.

Authors	M	R_θ - $R_{\delta 2}$	Measurement method	Remarks
Klebanoff (1954)	0.044	7000	CCA	
Fulachier (1972)	0.035	4750	CCA	
Fernholz et al. 1994	0.06 and 0.17	20000 and 60000	CTA	
Spina & Smits (1986)	2.89	80 000- 40 000	CTA	Scales estimated from spectra of $(\rho u)'$
Bestion 1982 Debiève 1983	2.3	4200 - 2900	CCA	Spectra of u'. (fluctuation diagram technique)
Bestion et al. 1983	1.8	5000- 3500	CCA	Spectra of u'. (fluctuation diagram technique)
Audiffren 1993 Audiffren, Debiève 1995	2.2	6300- 3800	CCA	Spectra of u'. (fluctuation diagram technique)
McGinley et al. 1994	11	12 400- 1115 6500-633	CTA	Spectra of $(\rho u)'$

Table 2: Sources for spectral data. Table from Dussauge & Smits (1995).

For supersonic boundary layers, there is another source of uncertainty. Generally, the point where the slope is -1 occurs at frequencies beyond the natural cut-off of the wire; this means that it occurs in a range where the shape of the spectrum depends on the system used to extend the system frequency response beyond the wire thermal lag (a feed-back loop is used for the CTA, and a compensation circuit is used for the CCA). In such conditions, it can be misleading to rely on one series of experiments. The data from supersonic flows, however, were obtained in different laboratories using different techniques (CTA and CCA). In the CCA data, two different generations of anemometers were used, where the compensation of the wire was performed in completely different ways. With such sets of independent measurements, it is believed that firm conclusions can be drawn from the results.

The characteristics of the boundary layers considered in the analysis of spectra are given in table 2. As noted in the Introduction, Re_θ and $R_{\delta 2}$ are Reynolds numbers based on momentum thickness. Re_θ is defined in the usual way $(R_\theta = \rho_e U_e \theta / \mu_e)$, whereas $R_{\delta 2} = \rho_e U_e \theta / \mu_w$.

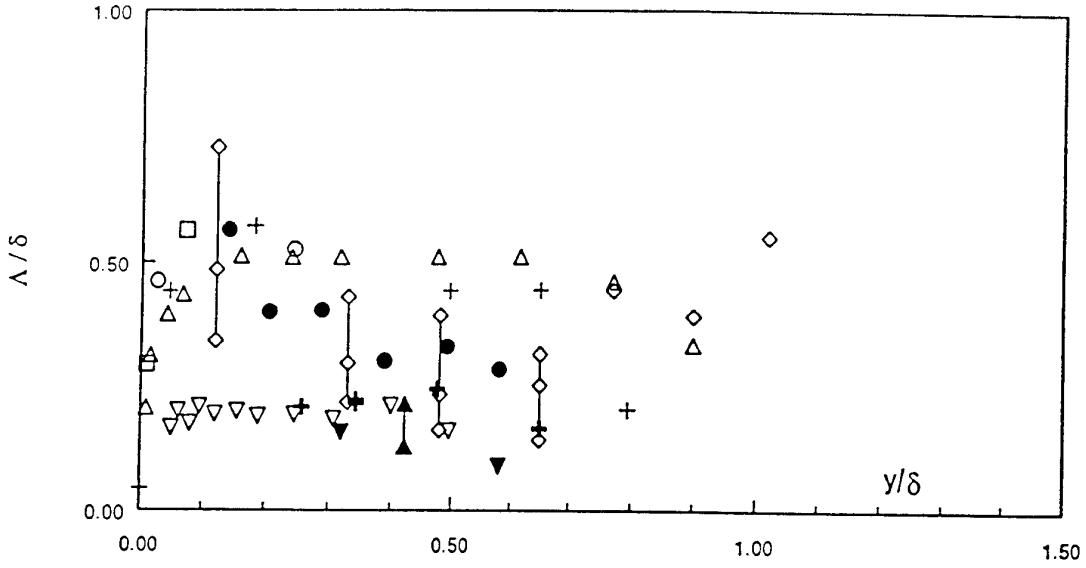

Figure 22: Integral scales in turbulent boundary layers. *Subsonic data*: +, Klebanoff (1955); △, Fulachier (1972); ○ $R_{\delta 2} = 20,900$, Fernholz *et al.* (1995); □ $R_{\delta 2} = 57,720$, Fernholz *et al.* (1995). *Supersonic data*: +, Debiève (1983); △, Bestion *et al.* (1983); ○, Spina & Smits (1987); ▽, Audiffren (1993); ◇ $R_{\delta 2} = 633$, McGinley *et al.* (1994); ▽ $R_{\delta 2} = 1,115$, McGinley *et al.* (1994). Figure from Dussauge & Smits (1995).

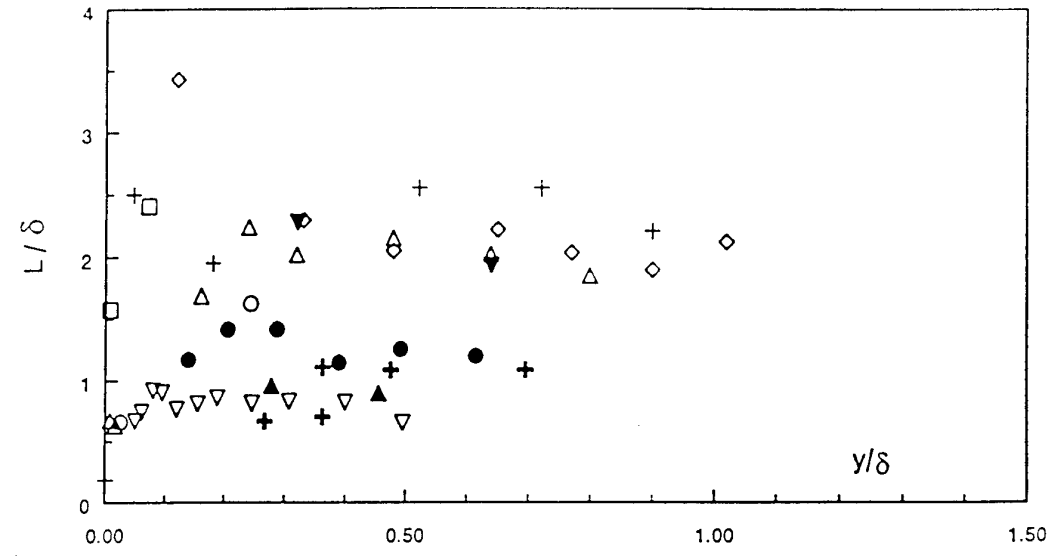

Figure 23: Production scales in turbulent boundary layers. Symbols as in figure 22. Figure from Dussauge & Smits (1995).

The results on the integral scale Λ are given in figure 22. The outer-layer scaling was used, since most of the data were obtained outside the inner layer. Plotting the data in inner-layer variables does not alter the conclusions. The data points from Smits & Dussauge (1989) were deduced from autocorrelations in a way which may underestimate the integral scale, due to a lack of experimental points for large time delays. The results in figure 22 were obtained by defining the boundary-layer thickness from the profiles of total pressure. This was recommended by Fernholz & Finley (1980) since the usual definition based on the velocity is probably not appropriate at high Mach numbers because variations of velocity near the edge of the layer are weak whereas the temperature or Mach number still vary significantly. Choosing a boundary-layer thickness based on $0.99U_e$ would make some difference in the magnitude of Λ/δ at Mach 3: in this experiment, the integral scale would be a little closer to its subsonic value. It would also significantly increase Λ/δ for the hypersonic experiment by McGinley *et al.* (1994), but in this case, the mean profiles indicate that the traditional choice based on $0.99U_e$ would be rather unphysical. In any case, a first result appears very clearly: the subsonic data indicate that in the external layer, Λ is about 0.5δ in subsonic flows, but is only about half that value in supersonic layers. The hypersonic data of McGinley *et al.* (1994) indicate a very low value, about 0.2δ, for $R_{\delta 2} = 1,115$, but larger values at the lower Reynolds number. In this case, the spectra at low frequency reveal peaks and bumps which precludes an accurate estimate of the integral scale. The uncertainty on Λ has been evaluated and is indicated in figure 22 by error bars. In fact, the lower limit of the error bar overlaps the other high speed data. This could be due to the remnants of transition, as speculated formerly. In the data by Spina & Smits, the point at at $y/\delta = 0.1$ has an integral scale nearly equal to the subsonic value. This is due to the significant slope in the spectrum, observed at low frequency, where the spectra of u' and $(\rho u)'$ are perhaps not proportional, as discussed above. In spite of this trend, the integral scales at Mach 2.9 in the middle of the layer are significantly below the subsonic results. Note that Demetriades & Martindale (1983) in a boundary layer on a flat plate at Mach 3 report measuring an integral scale of 0.28δ, also considerably smaller than that found in subsonic flows. Within the experimental accuracy the results are independent of Reynolds number.

The production scales L are given in figure 23. The Reynolds numbers in the subsonic and supersonic cases cover comparable ranges, except perhaps for the hypersonic data. It is clear that the production range is shifted to higher frequencies in supersonic flows. It should be emphasized that the limited spatial resolution of the wires probably precludes any accurate determination of the $-5/3$ law in the supersonic data, and it tends to shift the maximum of $fE(f)$ to lower frequencies, and therefore if such systematic errors are significant the values measured in high-speed flows are probably overestimated, reinforcing the notion that the scales are reduced with increasing Mach number.

It appears that the production scale L follows the same trends as Λ, and $L \approx 2\Lambda$. That is, L is about 2δ for low speed boundary layers, and about δ in high speed boundary layers. Note that the measurements of Morkovin & Phinney, quoted in Morkovin (1962) and not shown here, suggested the same trend for the production scales. Again, plotting these data in inner layer variables does not change the differences between the subsonic and supersonic data. The only discrepancy is found in the Mach 11 boundary layer, but several reasons can be found for this departure. First, the boundary layer is probably not fully turbulent, at least at the lower Reynolds number. Second, it is not clear that the velocity and mass flux spectra are proportional to each other at this Mach number. Third, the conclusions drawn from the power law analysis are probably not valid if strong compressibility effects are present. Fourth, the change in the shape of the spectra may indicate a modification of the turbulence structure. In hypersonic boundary layers, most of the mass flux occurs near the external edge of the layer, and the mean mass flux profiles have an inflexion point. This suggests that the external layer can behave more like a mixing layer than like a classical boundary layer. Such free shear flows are known for containing turbulent structure of large spatial extent, with production scales several layer thicknesses in size. This would be consistent with the surprisingly high level of energy observed at low frequencies in the present Mach 11 experiments.

So it seems that the apparent size of the energetic eddies in the longitudinal direction, deduced from u' or $(\rho u)'$ measurements in zero pressure gradient boundary layers, decreases with increasing Mach number, whatever the experimental method. This trend can also be illustrated by using another representation. If we assume that the friction Mach number can be used to characterize compressibility in turbulent boundary layers is the friction Mach number M_τ. Since $M_\tau^2 = C_f M_e^2/2$, this parameter depends on Mach and Reynolds number. The average value of L/δ in the outer layer is shown as a function of M_τ in figure 24. The results obtained for $M_e = 2$ by Bestion, Debiève, Dussauge and Audiffren have practically the same values of M_τ and L/δ, and the results obtained by Smits *et al.* , although at $M_e = 2.89$, have a comparable value of M_τ. All these results agree on the average value of L/δ in supersonic flows. The hypersonic results by McGinley *et al.* have a value of M_τ only a little larger than 0.1, but they indicate a further decrease in the production scale.

This change in typical frequencies or time scales can be attributed either to variations in the convection velocity or variations in the spatial scales. Measurements of convection velocity by Spina & Smits (1987) in a high Reynolds number boundary layer at Mach 2.9 showed that this quantity is not very sensitive to compressibility. This implies that smaller space scales are found in supersonic flows. In contrast, the transverse scales related to turbulent diffusion remain unchanged, while the longitudinal scales determined from u' decrease. Now Spina & Smits (1987) showed that the direction of the maximum space-time correlation in their boundary layer at Mach 2.9 is steeper than at low speeds (see figure 25). If the boundary layer is thought of as a forest of hairpin vortices, it can be imagined that the cross-section of the vortices is unchanged, but their inclination is changed. In fact, Uddin (1994) suggested that at high Reynolds numbers, the cross-section of the vortices reduces. This purely geometric explanation is not sufficient to explain all the evolution

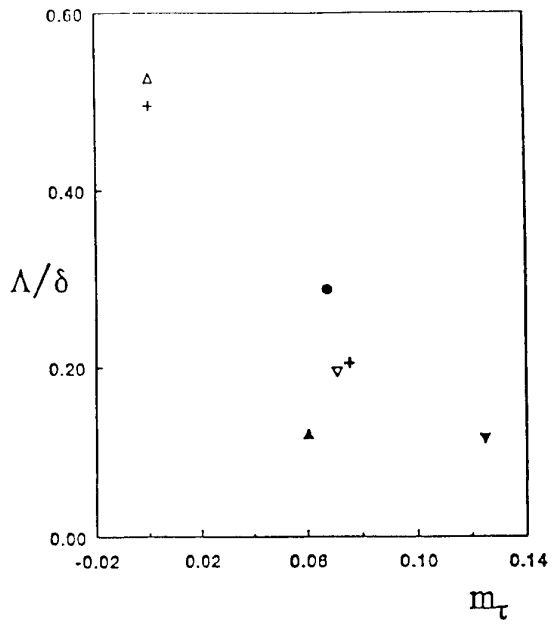

Figure 24: Evolution of the integral scale as a function of the friction Mach number. Symbols as in figure 23. Figure from Dussauge & Smits (1995).

observed seen in figure 24 since it would not be consistent either with the rather high values of v' measured in the same boundary layer.

It is expected that the observed modifications in the flow structure and scales are due to compressibility. Therefore, a possible interpretation can be found in the changes in the potential field induced in the external flow by the boundary layer, and in the generation of acoustic noise by supersonic boundary layers. Can they create smaller scales, and modify the orientation of the lines of maximum correlations? The variation of the angle has been interpreted in the previous paragraph as a change in the direction of vortical structures. In fact, the two-point measurements by Spina & Smits did not use conditional statistics, and therefore did not discriminate between the vortical and potential contributions in the intermittent zone. In supersonic flows, the induced pressure field can depend on local condition (the pressure perturbation induced by a large scale structure, for instance), but also by the noise radiated by Mach waves (see for example, Laufer, 1961). These waves can have low levels of $(\rho u)'$, but they are generally more conservative than ordinary turbulence, and could modify the space-time correlations for large separation distances. The formation of these Mach waves necessitates the velocity difference between the sources and the external flow to be supersonic. In a boundary-layer, this condition is always fulfilled, but at moderate supersonic Mach numbers the part of the layer able to radiate Mach waves is very thin and generally confined to the viscous sublayer or the logarithmic zone. In this case, the behaviour will be Reynolds and Mach number dependent. The orientation of the Mach waves will depend on this Mach number difference. For example, transonic perturbations would be very steep, and would contribute to make the maximum space-time correlation locus more vertical. Another element, as noted by Laufer (1961), is an increase of the radiated field near Mach 3, which could be interpreted as follows. If the convection velocity of the large eddies in the external layer is typically $0.8U_e$, as at low speeds, the velocity difference with respect to the external flow is $0.2U_e$. Now, it may be expected that these large eddies will start forming eddy shocklets when this relative Mach number is larger than, say, 0.6. This corresponds to an external Mach number of 3, and this criterion would be independent of the Reynolds number since the convection velocity of the large structures appears to be independent of Reynolds number. The measurements taken at a Mach number of 2.9 would then be at the onset of a new regime, and represent the first manifestation, in boundary layers, of compressible turbulence phenomena as observed in mixing layers. Of course, the previous interpretation is very approximate, because it depends critically on the value of the instantaneous convection velocities which are not known very accurately, so that the value of the Mach number for which such effects are important remains poorly determined. Such an interpretation, although speculative in many respects, is tempting because it can explain changes in the structure of u', as long as the radiated noise does not affect significantly the shear stress. To conclude, the spectral data show that there are modifications to the motions which contribute to the energy scales but not to the turbulent transport. This implies that the primary action of compressibility is to alter inactive motions. As these motions are related to the irrotational part of the fluctuations and to the pressure fluctuations induced by the layer, this explanation may be correct, but a full assessment would require a more complete knowledge of the two-point correlations, and of conditional statistics of turbulence in these flows.

3.8 Overview of structural features

Outer-region space-time correlations and spectral data suggest that the average spanwise extent of the largest eddies in the Mach 3 turbulent boundary layer is similar to that of subsonic turbulent boundary layers: approximately $1/2\delta$ in the outer layer, decreasing near the wall. (Although mean and instantaneous results for the sloping interface structure are in good agreement, the average cross-correlations used to deduce spanwise extent probably suffer from 'jitter' averaging, and the instantaneous extents may be larger.) The average streamwise scales of the largest eddies in the high Reynolds number, Mach 3 turbulent boundary layer are about two to three times those of low Reynolds number, subsonic turbulent boundary layers (see figures 18, 19, 20 and 21). This seems to be the most significant structural difference between the two flows yet found, and as indicated earlier Reynolds number and compressibility appear to be important. Increasing Reynolds number will increase the streamwise scales, whereas increasing Mach number will decrease them. Otherwise, the structural model for the large-scale motions in a supersonic is very similar to that derived from studies of subsonic flows, as can be seen from figure 26.

Since the influence of compressibility on the large-scale

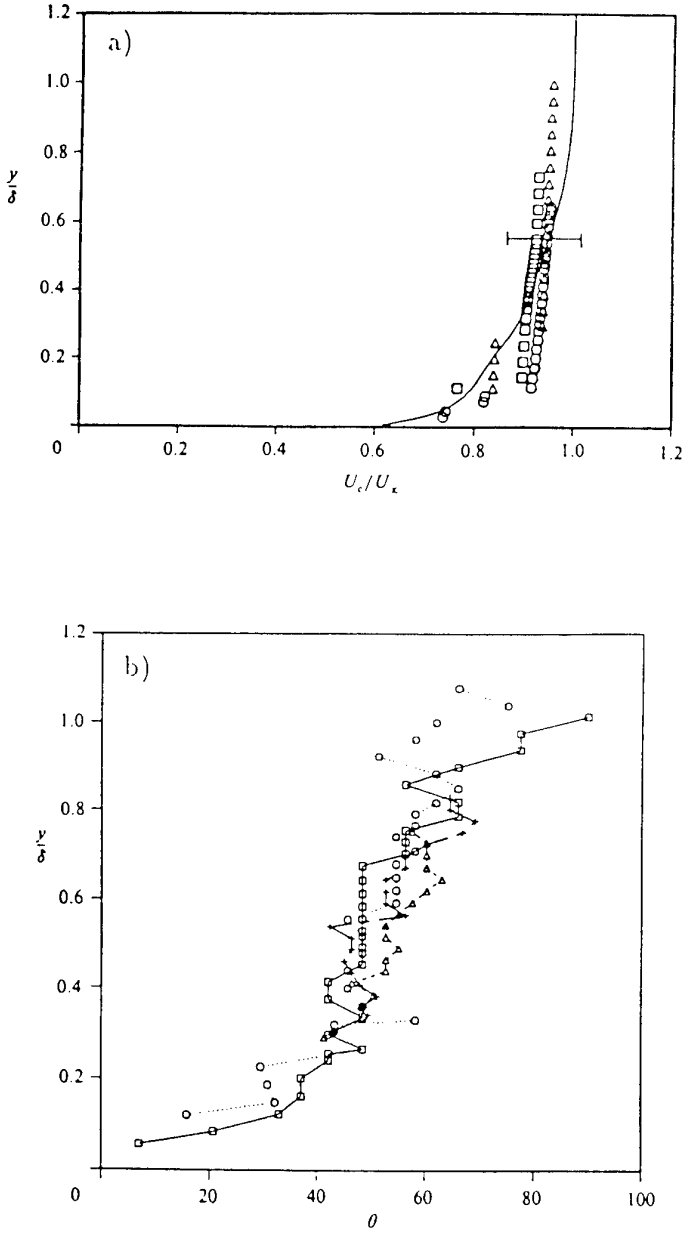

Figure 25: Characteristics of the large scale structure, as measured by Spina *et al.* (1991a), in a turbulent boundary layer at $Re_\theta = 81,000$ and $M = 2.9$. a) Broadband convection velocity based on measurements with three different streamwise probe separations. $\xi_x/\delta = 0.11$ □ ; 0.16 ○; 0.18 △. b) Broadband structure angle based on different wall-normal probe separations. $\xi_y/\delta = 0.09$ ——————□; 0.21 ----------○, 0.30 - - - - - - - - -△; 0.40 ——-——-+. Figure from Spina *et al.* (1991a).

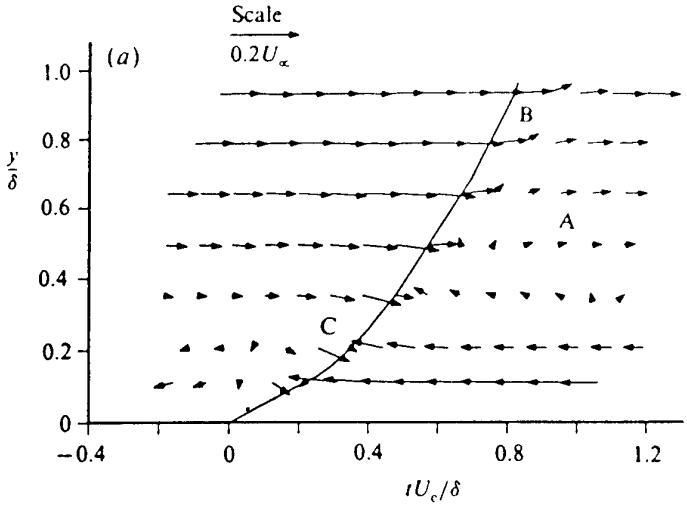

Figure 26: Ensemble-averaged view of the large-scale motions in a Mach 2.9 boundary layer. Figure from Spina *et al.* (1991a).

turbulent boundary layer motions seems to be subtle, explanations for the observed differences between low- and high-speed boundary layer structure are mostly speculative. Density-gradient effects are known to play a significant role in turbulent shear layers, but these effects are most likely to influence the near-wall region of the wall-layer, out of reach of standard measurement techniques. Parallels have also been drawn between the 45-degree slope of the interfacial structures in supersonic boundary layers and that of the hairpin-vortex structure observed in incompressible boundary layers. Insufficient evidence exists to support either side of this comparison, however. More conclusive results concerning compressibility effects on large-scale structure require higher Mach number investigations.

For boundary layers with freestream Mach numbers above 5, the near-wall region is more likely to show significant departures from known incompressible structure. The viscous sublayer for hypersonic boundary layers is likely to be much more quiescent than for incompressible flows (although pressure fluctuations will be imposed from above), and may not display the familar streaky structure. Since the mass-flux near the wall is very low for high Mach numbers, the buffer region may not be the dominant region for turbulence production, as in subsonic boundary layers (note that hypersonic laminar boundary layers undergo transition by disturbances spreading inward from the outer layer). Further investigation will depend on the development and application of non-intrusive measurement techniques to the near-wall regions of hypersonic boundary layers.

Finally, we note that the rate of decay of the large scale motions, as measured by the rate at which the peak in the space-time correlation decays with distance, appears to decrease significantly with Mach number. For example, the distance over which the peak decreased to half its original level differs by an order of magnitude in the experiments by Favre *et al.* (1957), Favre *et al.* (1958) at Mach 0.04 and Owen & Horstman (1972) at Mach 7 when scaled by δ. A better scaling for the rate of decay may be the time scale of the energy-containing eddies, Λ/u'. Λ and u' both decrease with Mach number, so that their ratio seems to remain approximately constant. This result may in turn suggest that the decrease in the streamwise length scales with Mach number simply reflects the fact that the time scale of the large eddies remains constant as the absolute fluctuation level decreases. The more complex scaling arguments presented by Smith & Smits (1991)b to explain the experimental observations may therefore not be necessary.

4 Perturbed Boundary Layers

So far we have considered boundary layers on a smooth flat plate. These studies help to improve our fundamental understanding, but such flows are rarely encountered in practice. For the aerodynamic design of high-speed vehicles, for example, it is necessary to understand the behavior of turbulence in more complex geometries, and it is not surprising that a considerable amount of experimental work has been performed to study the effects of perturbations or distortions on the behavior of turbulent boundary layers in supersonic flows, including the effects of pressure gradients, extra strain-rates such as streamline curvature, divergence and dilatation, and the interaction with shock waves. Reviews of this work were given by Fernholz & Finley (1980), Fernholz & Finley (1981), Smits & Wood (1985), Fernholz *et al.* (1989) and Spina *et al.* (1994). The general features of the mean flow behavior have been documented in detail, but there are only a few studies where extensive turbulence measurements have been made, most of them quite recently. As we indicated earlier, reliable and accurate turbulence measurements are difficult to make in any supersonic flow, and the difficulties are usually more extreme in the presence of flow distortions. For example, hot-wire measurements can suffer from many errors in flows with strong pressure gradients. In adverse pressure gradients, transonic

effects may become important in large regions of the flow and the flow may separate, whereas in favorable pressure-gradients the signal-to-noise ratio degrades because the turbulence intensities are greatly reduced. In a shock-wave boundary-layer interaction, the unsteady shock motion can impose severe loadings on the probe body, greatly increasing the possibility of breaking the hot-wire. In all cases, particular care must be exercised to produce repeatable and reliable measurements, and (as usual) the measurement errors must be taken into account when interpreting the results.

The experiments have covered a broad range of model geometries and flow conditions. To help understand the implications of the results it is useful to classify the existing work according to the particular perturbation or set of multiple perturbations that were applied to the flow. One of the major contributions made by Bradshaw (1973) in this area was to provide a classification scheme for the effects of different kinds of *extra* strain-rates e, that is, strain rates additional to the principal shear $\partial U/\partial y$. By identifying the particular extra strain-rates associated with streamline curvature ($\partial V/\partial x$), convergence and divergence ($\partial W/\partial z$), and compression and dilatation ($\nabla \cdot \mathbf{V}$), he formulated a general framework for the understanding of such complex flows. Bradshaw included pressure gradients in this classification scheme, in the sense that dp/dx is simply related to dU_e/dx for incompressible thin shear-layers.

Smits & Wood (1985) and Spina *et al.* (1994) extended this concept to include a wider variety of flows. One of the complications encountered in classifying compressible flows is that it becomes difficult to uncouple the effects due to pressure gradient, streamline curvature and bulk dilatation. This coupling occurs in all flows, but in a subsonic flow with streamline curvature, for example, dilatational effects are negligible by definition, and mean radial pressure gradients simply balance the centripetal acceleration, without straining fluid elements. In flows with streamwise pressure gradients there will always be a measure of streamline curvature as well, but for two-dimensional subsonic flows the ratio of $\partial V/\partial x$ to $\partial U/\partial x$ will be of order V/U, and therefore it is always small. In a supersonic flow, a coupling also exists between streamline curvature (that is, radial pressure gradient) and longitudinal pressure gradient, and the degree of coupling depends on the geometry. In simple wave flows, as in the flow over a compression surface, the streamline curvature and pressure gradient are directly coupled through the angle of turn and the Mach number. In reflected wave flows, where the pressure gradients are imposed on the boundary layer by an external wave generator, the streamline curvature is (approximately) coupled to the streamwise pressure gradient. This is similar to the case in subsonic flows, but for a given pressure rise the degree of curvature will depend on the decrease in streamtube area, which increases with Mach number. Curvature effects, pressure gradients and mean dilatational effects are always strongly coupled, regardless of how the pressure gradient is applied.

As seen in section 3, many of the differences observed between boundary layers on adiabatic walls in subsonic and supersonic flow can be explained in terms of the fluid property variations that occur as a result of the cross-stream temperature gradients that exist at supersonic Mach numbers. We will see that this approach continues to hold when the wall temperature suddenly increases. However, perturbations such as the sudden imposition of a pressure gradient, or longitudinal streamline curvature, or the interaction with a shock wave, produce a boundary layer response that does not have an equivalent subsonic counterpart, and which cannot be explained in terms of fluid-property variations. Vorticity can be produced through baroclinic torques. Longitudinal pressure gradients will lead to the compression or dilatation of vortex tubes, enhancing or reducing turbulent velocity and pressure fluctuations. Separation can occur when shock waves are present, if the shock is strong enough (a phenomenon that can be understood from subsonic experience), but even in the absence of separation there exists a strong coupling between the shock and the turbulence, which leads to unsteady shock motion and distortions of the shock sheet. Understanding the shock motion and the resultant unsteady heat-transfer and pressure-loading is of great importance in many aerodynamic flows. Since the shock motion seems closely connected with the incoming turbulence field and the separation unsteadiness, there is a clear need to understand the nature of the organized motions in the incoming boundary layer, particularly the large scales. Unfortunately, studies of the instantaneous or ensemble-averaged turbulent motions in supersonic flows are uncommon, and very few studies have been made in perturbed supersonic flows to try to describe the distortion of the large-scale structure.

The perturbation may originate in a number of different ways. It may be the result of a step change in the flow conditions where, for instance, the wall curvature changes suddenly. Alternatively, the distortion may be produced by an impulsive change, where the impulse consists of two step-changes of opposite character, separated by a short streamwise distance. An example of this case would be the flow which develops on a flat plate, passes over a short region of concave curvature, and then relaxes further downstream over a second flat surface. At some point away from the wall, the compression waves generated by the concave surface curvature will form a shock. For large radii of curvature, the shock will form outside the boundary layer, but for small radii it forms inside the layer. For compression corners, where the radius of curvature is essentially zero, a shock forms immediately outside the sonic layer, and multiple shocks form when the flow separates. The perturbations may also occur successively, as in the case where the surface curvature or the pressure gradient changes sign in the streamwise direction. For example, as the flow passes over a forward-facing step the surface curvature changes sign from concave to convex, and the pressure first rises and then falls.

Here we will try to use the extra strain-rate classification as a basis for discussing the response of a supersonic turbulent boundary layer to a sudden change in wall temperature, pressure gradient, streamline curvature or bulk dilatation, despite the anticipated difficulties. Flows where an additional degree of complexity is introduced by the application of successive perturbations will also be considered. At some points in this treatment, it will be useful to compare the response to these kinds of perturbations to the strong perturbations produced when a turbulent boundary layer interacts with a shock wave, although a

fuller discussion will be given in section 5.

4.1 Perturbation strength

The strength of a perturbation can be difficult to define in supersonic boundary layer flows. The simplest cases may be where the wall boundary condition is changing. For instance, when the wall-roughness changes suddenly, the ratio of the upstream and downstream equivalent roughness heights is a reasonably obvious parameter to characterize the strength of the perturbation (Smits & Wood, 1985). For a flow where the wall-temperature changes suddenly, the ratio of the wall temperatures upstream and downstream serves a similar function (Debiève *et al.*, 1996). The strength of a perturbation in pressure gradient is more difficult to define. In subsonic flows the strength of a pressure gradient distortion may be defined in terms of the parameter, $\beta \equiv \delta^*/\tau_w dp/dx$, as suggested by Clauser (1954). In a supersonic flow where streamwise pressure gradients can be accompanied by significant pressure gradients normal to the wall, additional parameters will be necessary to define the perturbation fully. For instance, it is possible to obtain the same boundary layer wall-pressure distribution in two different ways: one by using a curved wall so that the curvature generates the pressure gradient, the other on a flat plate by using a contoured ceiling to generate a reflected wave system (see figure 27). Clearly, the gradients normal to the wall in these two flows will be different. To make this more quantitative, at least for disturbances which are approximately isentropic such as simple wave flows, the ratio of the normal and streamwise pressure-gradients is given approximately by $1/(\tan \alpha_M)$, where α_M is the local Mach angle. This ratio is equal to 1.7 at Mach 2, and 5.9 at Mach 6, so that the effects of the cross-stream pressure gradient increase quickly at higher Mach numbers. For reflected wave flows, the analysis is more complicated, but the the normal gradients take their maximum values in simple flow regions (in the non-simple region, where the incident wave system crosses the reflected system, the normal pressure gradients are generally small), so that the simple-wave estimate can be taken as an upper bound. This issue is discussed more fully by Finley (1977) and Fernholz & Finley (1980).

As indicated earlier, differences between simple and reflected wave-systems also appear in the resulting streamline curvature. For a simple wave-system, the curvature can be convex or concave, and for a given overall streamline deflection the pressure rise is fixed by the incoming Mach number. A linearized analysis gives:

$$\Delta\theta = \frac{\Delta p}{p}\frac{\sqrt{M^2-1}}{\gamma M^2}.$$

In terms of the radius of curvature R_c and the initial boundary layer thickness δ_0,

$$\frac{\delta_0}{R_c} = \frac{\delta_0}{p}\frac{\partial p}{\partial x}\frac{\sqrt{M^2-1}}{\gamma M^2}.$$

Consequently it is not usually possible to discriminate between the individual contributions due to curvature, compression and pressure gradient to the distortion of the boundary layer without performing the same experiment over a range of Mach numbers, which can in turn introduce additional effects. However, for a reflected wave system with a rising pressure, the curvature is initially convex and then concave, and the overall streamline deflection and pressure rise are independent. For example, in a reflected wave flow such as that shown in figure 27 the overall streamline deflection is zero even though the overall pressure rise is not.

To help resolve these issues of discrimination, and to determine the strength of the disturbance in a complex supersonic flow, all perturbations need to be quantified separately, and their interactions need to be determined. For flows where extra strain-rates are important, one useful measure is the ratio of each extra strain-rate, e, to the principal strain-rate, $\partial U/\partial y$ (Bradshaw, 1973, 1974). A distortion is generally classified as weak if $e/(\partial U/\partial y) \approx 0.01$, and strong if $e/(\partial U/\partial y) \approx 0.1$. The final response of some structure parameter to the prolonged application of a constant, small extra strain-rate e can be expressed in a linearized and dimensionless form by an amplification factor $1 + \alpha_o eL/(\partial U/\partial y)$, where α_0 is an empirical constant of order 10 for several types of extra strain-rate, and $(\partial U/\partial y)$ can be taken as a measure of the typical *rms* eddy strain-rate (following Bradshaw, a better estimate may be given by $\sqrt{-\overline{u'v'}}\Big/ L_\varepsilon$, where L_ε is the dissipation length-scale). This amplification factor depends only on the local rate of strain rather than the rate-of-strain history. If the extra strain-rate is applied over a time comparable to the eddy lifetime, then it might be better to replace $\alpha_0 e$ with an "effective" value I, given by the integral of the extra strain-rate over the time which it is applied ($= \int e\,dt$). For example, a measure of the strength of the impulsive perturbation due to a short region of bulk compression (I_p) is given by $(1/\gamma)\log(p_2/p_1)$ (Hayakawa *et al.*, 1983), where p_2/p_1 is the pressure ratio across the compression, and for an impulse in curvature the strength (I_θ) is given by the angle through which the flow has been turned (Smits *et al.*, 1979b). It is implied that for an impulsive perturbation the overall distortion is the more important parameter, and not the rate at which it is applied.

In the assessment of perturbation strength, it is implicitly assumed that the perturbations are sufficiently small for a linear analysis to be meaningful. That is, the response of the boundary layer can be described in terms of a simple first-order lag equation. When more than one strain-rate acts, as in the case of a deflected supersonic flow where streamline curvature and bulk compression act in addition to longitudinal and normal pressure gradients, the linear addition of different perturbation strengths to arrive at some overall measure is unlikely to hold in any quantitative sense. Nevertheless, the linear analysis can still serve as a crude guide for making comparisons among different flow cases, as we hope to show here. For stronger perturbations, we know that Rapid Distortion Approximations (RDA) can give quantitatively useful results. For concavely-curved flows this was shown by Jayaram *et al.* (1989) and Donovan (1989), but the analysis will be valid only for times short compared to the (local) eddy response time.

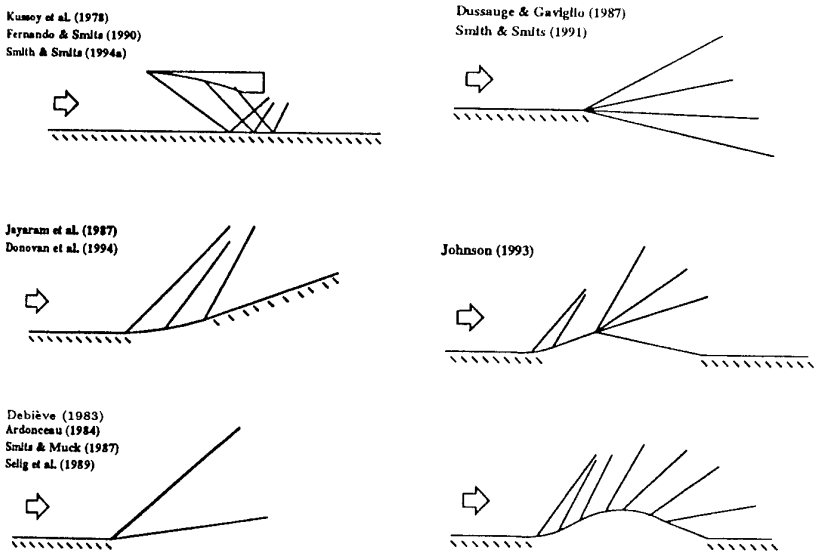

Figure 27: Boundary layer flow distortions. Left: adverse pressure gradients. Right: favorable pressure gradients. From Smith & Smits (1994).

4.2 A step change in wall temperature

The response of turbulent boundary layers to step changes in boundary conditions has been widely studied in subsonic flows (for a review see Smits & Wood, 1985). The step change may be caused by a sudden change in wall roughness, surface curvature, pressure gradient, suction/blowing, or heat transfer. The response to the change depends on how the step change is applied, but if the step is caused by a change in the wall boundary-condition, such as a sudden change in wall-temperature, the boundary layer adjusts to the new boundary condition first at the wall, and then progressively further from the wall as turbulent diffusion begins to affect the rest of the flow. From a fundamental viewpoint, the initial response of the boundary layer and its subsequent relaxation to the new boundary conditions provides useful information on the time and length scales of turbulent diffusion.

The relaxation process downstream of the step change is often described in terms of the growth of an internal boundary layer, which is the region near the wall where the flow scales with variables based upon the new wall condition (for example, the friction velocity and temperature based on the new level of heat transfer), whereas the rest of the boundary layer continues to scale on the variables based upon the wall conditions that apply in the flow upstream of the step change. Typically, the internal layer grows at a rate similar to that of an undisturbed turbulent boundary layer, that is, at a rate approximately proportional to $x^{0.8}$. The relaxation rate, therefore, decreases with downstream distance, and in some instances the asymptotic state may not be reached for distances of the order of 100 initial boundary layer thicknesses (δ_o), if at all (see, for example, the slow relaxation downstream of a prolonged region of convex curvature studied by Alving *et al.*, 1990b).

The response of boundary layers in supersonic flow to step changes in boundary conditions has not been studied so extensively, but a number of interesting experiments have been performed. For example, Kubota & Berg (1977) studied the effects of sudden changes in wall roughness (smooth-to-rough and rough-to-smooth) in a Mach 6 turbulent boundary layer. For a step change from smooth-to-rough, the boundary layer attained a self-preserving state in the mean flow at a distance of about $20\delta_o$, and in the fluctuation profiles at about $30\delta_o$. The relaxation following a step change from rough-to-smooth was somewhat slower with the mean flow relaxing over $28\delta_o$ and the turbulent field over $40-50\delta_o$. In essence, their results were not significantly different from similar work in subsonic flow (Antonia & Luxton, 1971, 1972).

Another interesting case is the boundary layer response to sudden changes in heat transfer. Despite the practical significance of such flows, the extensive reviews by Fernholz & Finley (1980, 1981) list only a few experiments where heat transfer was important, and these cases were confined to uniformly cooled walls (Voisinet & Lee, 1972, Laderman & Demetriades, 1974). However, Debiève *et al.* (1996) studied a Mach 2.3 fully-developed turbulent boundary layer experiencing different step increases in wall temperature, and we will consider this experiment in some detail. The ratio of wall temperature to recovery temperature, T_w/T_r, varied from 1.0, to 1.5, to 2.0. To capture the relaxation process, the response was studied over a distance of approximately $50\delta_o$, and many detailed mean flow and turbulence measurements were made.

We expect the step change in heat transfer to be somewhat different to a step change in wall roughness. First, two internal layers will form: one for the temperature

field, and the other for the velocity field (since we expect the friction velocity to be affected by the heating). The two internal layers are not coincident since the Prandtl number is not unity. Second, the step change is applied in the temperature field, and we expect to see, at least initially, some differences appearing in the usual relationships between temperature and velocity, that is, Crocco's relation for the mean field, and the Strong Reynolds Analogy for the fluctuations.

In section 3.1, we showed that in a self-preserving flow a relationship between velocity and temperature may be derived under the conditions that the mixed Prandtl number, P_m [$\equiv (\tau\partial h/\partial y)/(q\partial U/\partial y)$], is constant and $0.7 < P_m < 1.0$ (van Driest, 1955, Walz, 1959). The result is known as the modified Crocco relationship, or sometimes Walz's solution (equation 13). If we consider only the flow in the region where molecular transport processes can be neglected ($y \gg y_v$) and where the stress is constant, dimensional analysis or mixing length arguments give, for zero pressure gradient (Rotta, 1960, Bradshaw, 1977):

$$U_i^* = \int_{U_v^+}^{U^+} \sqrt{\frac{T_w}{T}}\, dU^+ = \frac{1}{\kappa}\log y^+ + C_1. \qquad (38)$$

If the temperature variation is known, either by measurement or by assuming the validity of Crocco's Law, the integral in equation 38 may be evaluated. Furthermore, since the appropriate velocity scale for the inner and outer regions of the boundary layer is $(\tau_w/\rho)^{1/2}$, we expect from previous considerations that the mean (and fluctuating) velocities scale with this variable if the flow is self-preserving. For an adiabatic, zero pressure-gradient boundary layer, the variation in density is due to the Mach number gradient. For a heated wall, the density variation is also affected by the level of heating.

The time scale for the adjustment of the velocity field to a given perturbation varies approximately as the turbulent kinetic energy divided by the rate of its production (Townsend, 1976). That is, the relaxation time varies approximately as $(\partial U/\partial y)^{-1}$. The flow near the wall, therefore, adjusts relatively quickly, and a limited region of self-preserving flow may occur (it is assumed here that, since P_t is close to one, an approximately self-preserving state can occur). A similar argument can be made for the relaxation rate of the temperature field[1], bearing in mind that the Prandtl number is not unity so that the physical extents of the velocity and temperature layers are not identical. Within this self-preserving part of the boundary layer (the internal layer) the velocity and temperature fields may display a logarithmic variation, and the total stress is then expected to be approximately constant over the same region.

When the mixed Prandtl number is constant, it is possible to obtain for $y < y_s$, where y_s lies in the constant stress region, a temperature-velocity relationship for perturbed flows of the form:

$$\frac{T}{T_s} = \frac{T_w}{T_s} + \frac{T_r - T_s}{T_s}\left(\frac{U}{U_s}\right) - P_m\frac{(\gamma-1)}{2}M_s^2\left(\frac{U}{U_s}\right)^2 \qquad (39)$$

[1]For the velocity field, $\tau_U = \overline{q^2}/(-\overline{u'v'}\partial U/\partial y)$, and by analogy for the temperature field, $\tau_T = \overline{T'^2}/(-\overline{v'T'}\partial T/\partial y)$.

where $M_s = U_s/\sqrt{\gamma R T_s}$, and:

$$\frac{T_r - T_w}{T_s} = 1 + P_m\frac{(\gamma-1)}{2}M_s^2 - \frac{T_w}{T_s} = -\frac{q_w U_s P}{C_p \tau_w T_s} \qquad (40)$$

(for details, see Carvin *et al.*, 1988). Equation 39 can be applied to perturbed flows that display a constant-stress region. Furthermore, in the region where molecular transport processes can be neglected ($y \gg y_v$) and where the stress is constant, equation 38 still applies as long as the scaling is based on the local wall values. Equations 38 and 39 then completely define the mean velocity and temperature fields for $y_v \ll y < y_s$.

If we assume that the presence of a logarithmic velocity profile indicates the presence of a constant stress region (this does not necessarily follow, but for the present purpose it may be a reasonable approximation), then equation 39 may be used to determine the heat transfer at the wall by fitting it to the data in the region $y_v \ll y < y_s$. This method for finding the friction temperature $T_\tau (\equiv q_w/\rho_w C_p u_\tau)$ is similar to the Clauser method for finding the friction velocity from the measured velocity profile. The skin-friction and heat-transfer coefficients can then be found from the experimental profiles by an iterative solution of equations 38 and 39. In principle, it should also be possible to find P_m using this procedure but the estimates of T_τ and C_h are rather insensitive to the value of P_m, and it difficult to find P_m accurately from the data.

To express the temperature profile in a similar logarithmic form, we note that equation 39 may be rewritten using a *turbulent total temperature*, T_i. This leads to

$$T_i^* = \int_{T_1^+}^{T_i^+} \sqrt{\frac{T_w}{T}}\, dT_i^+ = \frac{1}{\kappa}\log y^+ + C_T \qquad (41)$$

where $T_i^+ = -T_i/(T_\tau P_m)$, and C_T depends on the inner limits of the logarithmic region. It will also depend on the Prandtl number and the ratio of the wall temperature to the recovery temperature T_w/T_r (Carvin *et al.*, 1988).

Some results from the experiments by Debiève *et al.* (1996) are shown in figures 28–30. From figure 28 we see that the internal thermal layer grows relatively rapidly: at $x = 8\,cm$ it fills about half the boundary layer, and by $x = 46\,cm$ the temperature and the velocity layers are almost coincident. A comparison with Crocco's relation (equation 39) indicated that the boundary layer at $x = 8\,cm$ is strongly perturbed by the heating, and by $x = 46\,cm$ has not yet reached equilibrium. In contrast, the velocity profiles demonstrate that the temperature field has only a mild effect on the velocity distribution far from the wall.

To find the variations of wall friction and heat transfer along the plate, the experimental data were fitted to the logarithmic relationships 38 and 41. Figures 29 and 30 show the transformed velocity and static temperature data in logarithmic form. In these transformed coordinates, there appears to be little effect of heating. In other words, the variation in density due to the combined effect of compressibility and heating simply alters the velocity scale for the velocity profile without introducing any explicit effects due to the strong heating. The relaxation of

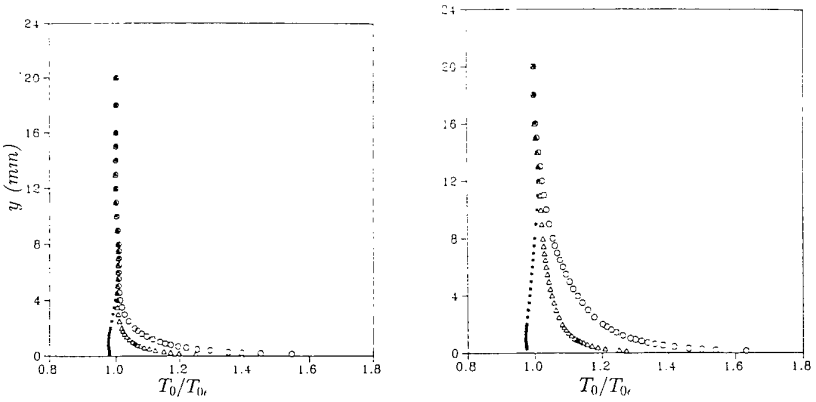

Figure 28: Total temperature profiles for step change in wall temperature. Left: $x = 8\,cm$; Right: $x = 46\,cm$ (x is the distance measured from the beginning of the heated wall; the boundary layer thickness at $x = 8cm$ is $10\,mm$). *, $T_w/T_r = 1.0$; Δ, $T_w/T_r = 1.5$; o, $T_w/T_r = 2.0$. From Debiève *et al.* (1996).

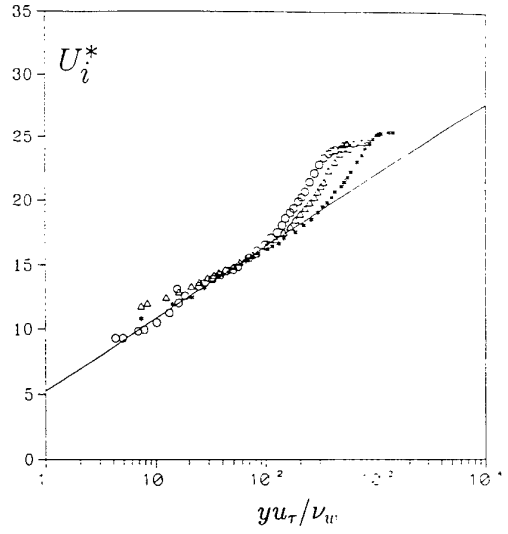

Figure 29: Semi-logarithmic representation of transformed velocity profiles at $x = 32\,cm$ for step change in wall-temperature, with u_τ adjusted to give the best fit to equation 38. Symbols as in figure 28. Figure from Debiève *et al.* (1996).

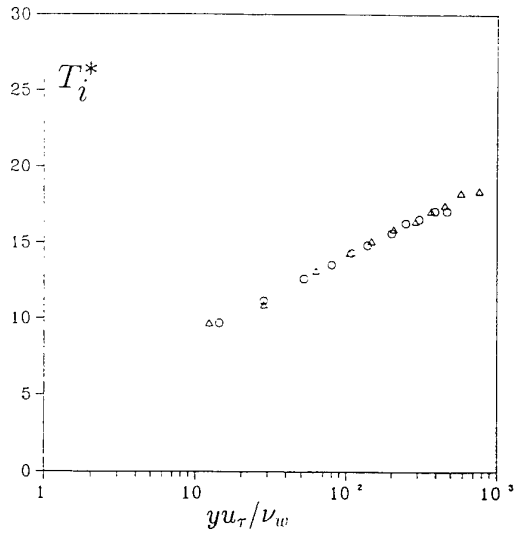

Figure 30: Semi-logarithmic representation of temperature profiles $x = 32\,cm$ for step change in wall temperature, with T_τ adjusted to give the best fit to equation 41. Symbols as in figure 28. From Debiève *et al.* (1996).

the temperature profile and the large extent of the logarithmic region are clearly evident in figure 30. For this flow, the constant C_T is approximately equal to 3.0, which is a little lower than the value of 3.6 found by Michel *et al.* (1969).

The coefficients of skin friction, C_f ($= 2\tau_w/\rho_e U_e^2$), and heat transfer, C_h ($= q_w/\rho_e U_e C_p(T_r - T_w)$) are shown in figure 31. Although the accuracy of these data is difficult to judge in the absence of an independent measure of τ_w and q_w, the effect of heating appears to reduce the skin-friction and heat-transfer coefficients significantly, regardless of the streamwise location. If we assume that the skin-friction coefficient follows the same relation as that found for adiabatic flows, provided that the density and viscosity are evaluated at the wall conditions, we find that most of the differences in C_f observed due to heating are due simply to the change in fluid properties. The argument is similar to that advanced by Hinze (1975) to explain the decrease in C_f with Mach number for adiabatic flows. A corresponding argument can also be made for the heat transfer coefficient. However, we can see that the Reynolds Analogy factor s ($= 2C_h/C_f$) appears to be strongly out of equilibrium, approaching a value of about 1.5 near the end of the test section, still well above its equilibrium value of about 1.24.

As for the longitudinal turbulence intensity, Debiève *et al.* (1996) found that Morkovin's representation appears to take into account the effects of wall heating. That is, the data can be collapsed using a scaling based solely on fluid property variations (within the experimental error). Not unexpectedly the intensity of the total temperature fluctuations increases with heating. For the turbulent heat transfer, we are more interested in the behavior of the transverse heat flux $\overline{(\rho v)'T'}$. This is a difficult quantity to measure directly, but some indication can be given by examining the behavior of the longitudinal heat flux $\overline{(\rho u)'T'}$. Debiève *et al.* (1996) found that the correlation coefficient $-R_{uT}$ is not significantly affected by the heating, and it remains almost unchanged from its adiabatic value in a supersonic flow of 0.8 – 0.9 (a typical value in a heated subsonic flow is 0.4 – 0.5). This high degree of correlation between the velocity and temperature (even though the flow is heated) suggests that the instantaneous scales of u' and T' are connected by a relationship such as $T' = f(u')$. In an adiabatic flow, we have the Strong Reynolds Analogy, but in heated flows where the total temperature fluctuations are significant an alternative analysis is required.

When the distributions $\overline{T}(y)$ and $\overline{U}(y)$ are known, a linearization for small fluctuations can obtained with the aid of a mixing-length argument, $\sqrt{\overline{u'^2}} = l_U \partial\overline{U}/\partial y$ and $\sqrt{\overline{T'^2}} = l_T \partial\overline{T}/\partial y$, or by a direct linearization of the mean relationship $\overline{T} = g(\overline{U})$. In the case of $l_U(y/\delta) = l_T(y/\delta)$, that is to say when the Prandtl number defined in terms of $\overline{u'^2}$ and $\overline{T'^2}$ is equal to unity, the two methods lead to the same result — the SRA (Gaviglio, 1987). For a direct linearization of the mean relationship $\overline{T} = g(\overline{U})$, similar mixing-length arguments are necessary.

To evaluate the influence of wall heating on the SRA, Debiève *et al.* (1996) linearized Walz's temperature-velocity relationship (equation ??) which explicitly includes the heating parameter, T_w/T_r:

$$\frac{(\gamma-1)M^2\,u'/U}{T'/T} = -\left[r + \left(\frac{T_w}{T_r}-1\right)\left(\frac{1+rM_e^2(\gamma-1)/2}{M_e^2(\gamma-1)}\right)\left(\frac{1}{\overline{U/U_e}}\right)\right]^{-1} \quad (42)$$

(a similar approach was followed by Cebeci & Smith, 1974, who assumed $r = 1$). Here, the second term on the right-hand side introduces the influence of heating. This term also depends on y/δ through the velocity profile, U/U_e, which depends only slightly on the heating. In adiabatic flows, the factor in the square brackets reduces to the recovery factor, $r = 0.89$. In the case where $T_w/T_r = 2$, we can expect that, for a point located in the middle of the layer, the right-hand side of equation 42 will be reduced by a factor of about two with respect to the adiabatic value. The data given by Debiève *et al.* (1996) show this decrease from the adiabatic value, but their data are probably not accurate enough to verify the exact form of equation 42.

To summarize, we see the growth of an internal layer in the temperature profile, but the transformed velocity field is relatively unaffected by the wall heating. Near the wall, that is, in the internal layer, logarithmic variations in the mean velocity and temperature profiles were found when the scaling arguments took into account the new values of density and friction velocity. Similarly, the change in fluid properties at the heated wall can explain the observed decrease in the skin-friction and wall heat-transfer coefficients. As for the turbulence, Morkovin's scaling collapses the streamwise Reynolds stress profiles, and the correlation between velocity and temperature fluctuations appeared unaffected by the heating at the wall. However, the relationship between the temperature and velocity fluctuations in the SRA is strongly affected by the heating.

In general, the observed changes in the boundary layer due to the heating can be explained in terms of variations in fluid properties and the new boundary conditions at the wall.

4.3 Adverse pressure gradients

The extra strain-rate due to streamline curvature, $(\partial V/\partial x)$ has a profound effect on the turbulence in incompressible flows. When the sense of curvature is concave, the effect on the turbulence in the boundary layer is destabilizing, leading to an increase in wall-friction, heat-transfer, and the Reynolds stresses. In addition, Taylor-Görtler-like vortices have often been observed to form on concavely-curved walls. Convex curvature is stabilizing, and the wall-friction, heat-transfer, and Reynolds stresses all decrease, and the Taylor-Görtler instability is absent. Von Kármán (1934) considered the equilibrium of a fluid element moving along a curved streamline, and demonstrated that a boundary layer over a curved wall was unstable if the curvature was concave, and stable if it was convex. When the flow is compressible, the stability argument must take into account the effects of density gradients, and the analysis by Bradshaw (1973) suggests that for an adiabatic wall the density gradient will enhance

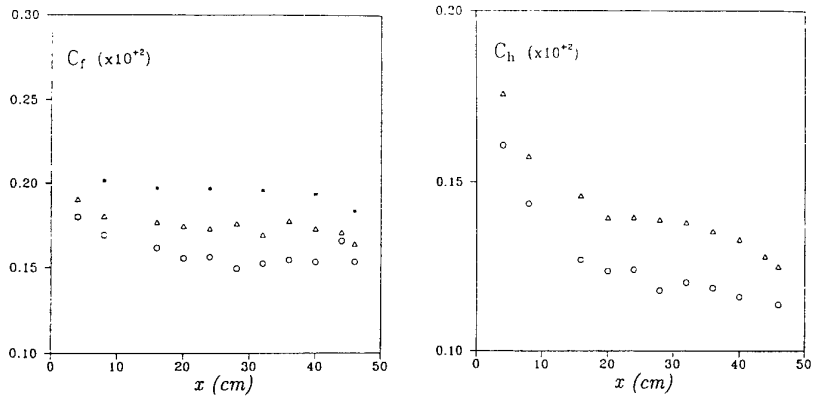

Figure 31: Distribution of skin-friction coefficients (left), and heat-transfer coefficients (right) for step change in wall-temperature. Symbols as in figure 28. From Debiève *et al.* (1996).

the effect of curvature. In a strongly cooled flow, however, the density gradient changes sign near the wall, and it is possible, at least in principle, for a boundary layer to be unstable in the outer layer and unstable in the inner layer, and vice versa.

These arguments provide qualitative descriptions of the flow stability, but experiment shows that the effects on the properties of the flow are at least an order-of-magnitude greater than the analysis would indicate. As may be expected, the effects of streamline curvature in compressible flow are more difficult to determine because, as we discussed earlier, curvature in a supersonic flow is always accompanied by pressure gradients and either compression or expansion, and the significance of each individual perturbation can only be found by comparing different experiments where the balance between these effects is changing.

A group of such experiments for impulsive perturbations were performed by Jayaram *et al.* (1987), Smits & Muck (1987) and Donovan *et al.* (1994). Two different angles of turning were investigated, 8° (Group One) and 16° (Group Two), and the non-dimensional radius of curvature, R_c/δ_o, varied from 0, to $10-12$ (*Models I* and *IV*), to 50 (*Model II*). The incoming Mach number was fixed at a value of about 2.9. The flow configurations are shown schematically in figure 27, and the estimated strengths of the corresponding impulses of extra strain-rates are given in tables 3 and 4. Here, δ_0 is the boundary layer thickness of the flow just upstream of the start of the disturbance, and the length of the impulse is L_i.

4.4 Flow over concavely-curved walls

The experiment by Donovan *et al.* (1994) illustrates many aspects of flows over concavely-curved walls in supersonic flow. The flow conditions are summarized in table 4, under *Model IV, Curved Wall*. The total turning angle was 20°. As the flow passed through the region of surface curvature, the wall pressure rose by a factor of 2.9, the Mach number decreased from 2.86 to 2.10, the density increased by a factor of 2.1 and the velocity decreased by a factor of 0.88. At the same time, the absolute wall shear-stress increased by about 125 percent, and the skin friction coefficient increased by about 77 percent. This increase is counter to that observed in subsonic flows, where an adverse-pressure gradient causes the wall shear-stress to decrease. Another example of this phenomenon is the Fernando & Smits experiment shown in figure 27. In these flows the sonic layers are very thin, and as the pressure rises the boundary layer thickness decreases. Since the turbulent mixing is strong, the net effect of a thinner layer is to increase the wall stress. The skin friction continued to increase well after the region of wall curvature had ended, and continued to increase even after the pressure gradient had ended.

Figure 32 shows the mean velocity profiles in inner-layer scaling. The undisturbed boundary-layer profile exhibits an extensive logarithmic region (the discrepancies near the wall are due to uncertainties in probe position). By the end of the curved region, the profile begins to dip below the logarithmic law near the point where $y^+ = 2000$. The dip grows in size and extends farther into the logarithmic region with increasing streamwise distance. A dip in the logarithmic region is a common feature of flows with concave curvature, and it may indicate that the length-scales of the turbulence increase faster with distance from the wall than in the unperturbed boundary layer (Bradshaw, 1973, Smits *et al.*, 1979b, Jayaram *et al.*, 1987, Smits *et al.*, 1989). The dip does not become significant until after the curved region ends, suggesting that the inner region of the boundary layer is either exhibiting a delayed response to the curvature, or it is responding relatively quickly to the removal of curvature.

In these measurements, a constant-temperature hot-wire anemometer was operated at high overheat ratio to measure the local mass-flux fluctuations, $\overline{(\rho U)'^2}\Big/\bar{\rho}^2\bar{U}^2$. The streamwise stress was obtained by using the SRA, accord-

	Group One				
	Smits & Muck	Jayaram *et al.*		Fernando & Smits	Kussoy *et al.*
	Compression Corner	Model I Curved Wall	Model II Curved Wall	Flat wall	Flat wall
M_e	2.9	2.9	2.9	2.9	2.3
R_c	0	$10\delta_o$	$50\delta_o$	∞	∞
L_i	0	$1.4\delta_o$	$7\delta_o$	$7\delta_o$	$1.5\delta_o$
I_θ	0.14	0.14	0.14	< 0.05	—
I_p	0.41	0.46	0.46	0.46	0.40
$\overline{\rho u'^2}$	+350%	+240%	+320%	+200%	+370%
$-\overline{\rho u'v'}$	+390%	+390%	+200%	+220%	+160%
θ	$+8^o$	$+8^o$	$+8^o$	0	0

Table 3: Impulses in adverse pressure-gradient cases, Group One. The "Flat Wall" cases are reflected wave flows. Adapted from Smith & Smits (1994).

	Group Two		
	Smits & Muck	Donovan *et al.* Model IV	Smith & Smits (1991)
	Compression Corner	Curved Wall	Flat wall
M_e	2.9	2.9	2.9
R_c	0	$12\delta_o$	∞
L_i	0	$3.5\delta_o$	$3.5\delta_o$
I_θ	0.28	0.28	< 0.09
I_p	0.76	0.78	0.78
$\overline{\rho u'^2}$	+1700%	+900%	+600%
$-\overline{\rho u'v'}$	+650%	+700%	—
θ	$+16^o$	$+16^o$	0

Table 4: Impulses in adverse pressure-gradient cases, Group Two. The "Flat Wall" cases are reflected wave flows. Adapted from Smith & Smits (1994).

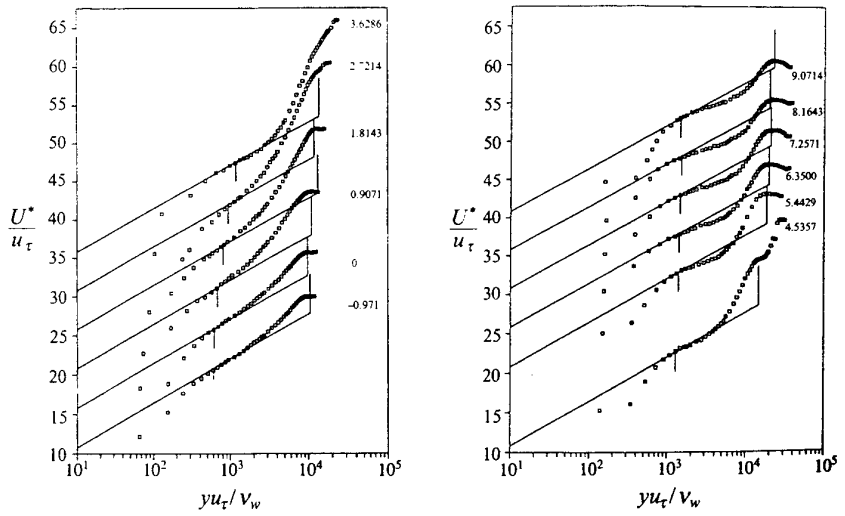

Figure 32: van Driest-transformed mean velocity profiles for the Model IV curved-wall impulse experiment (see table 4). The vertical line near 10,000 indicates the boundary layer edge. The x/δ_0 values are indicated to the right of the profiles, where δ_0 is the boundary layer thickness for the incoming boundary layer, and x is measured from the start of the curved wall (the curvature finishes at $x = 3.5\delta_0$). From Donovan *et al.* (1994).

ing to:

$$\frac{(\rho U)'}{\bar{\rho}\bar{U}} = \frac{\rho'}{\bar{\rho}} + \frac{u'}{\bar{U}}.$$

$$\text{That is,} \quad \overline{\rho u'^2} = \overline{(\rho U)'^2} \Big/ \bar{\rho}\left(1 + (\gamma - 1)\, M^2\right)^2 \quad (43)$$

The overall increase in the local mass-flux fluctuations through the perturbation is only about 60 percent, but the level of the Reynolds streamwise-stress increases considerably more through the perturbation: for instance, at $y/\delta = 0.4$ the level increases by a maximum factor of 6.8. From equation 43, it is clear that the difference in the amplification levels is primarily due to the strong role played by the mean density in the definition of the stress term. The first signs of amplification occur at points close to the wall, where the time-scales are small. By the last streamwise station, at $x = 9.1\delta_0$, the relaxation process had begun at points below 0.6δ, but the fluctuations were still growing in the outer 20 percent of the layer.

As the boundary layer exits from the curved region, the profile of the angular momentum, $\rho\,(\partial U/\partial y)$, develops an inflection point away from the wall. A generalized inflection point is defined by two conditions:

$$\left(\frac{\partial}{\partial y}\left(\rho\frac{\partial U}{\partial y}\right)\right)_{y_i} = 0 \qquad \text{and} \qquad \left(\frac{U}{U_e}\right)_{y_i} > 1 - \frac{1}{M_e}.$$

In a laminar boundary layer, a generalized inflection point can make the layer unstable to small disturbances (Morkovin, 1992). In the present case, the inflection point is first seen at $x = 4.54\delta_0$, where it is located at about $y = 0.2\delta$. Downstream, it becomes more exaggerated, and its position moves slowly away from the wall so that at $x = 8.16\delta_0$, it is at about $y = 0.3\delta$. The Mach numbers at these locations satisfy the second condition, and it seems possible that instabilities associated with the inflectional angular-momentum profile contribute to the turbulence amplification downstream of the curved wall region.

The Reynolds shear-stress distributions are shown in figure 33. The amplification of the shear stress is largest at $y = 0.4\delta$, where the level has increased by a factor of 5.3, although the shear stress relaxes considerably faster than the streamwise stress. The normal component of the stress, $\rho\overline{v'^2}$, also increased significantly, by a maximum factor of 6.0 in the middle of the layer. Somewhat surprisingly, the anisotropy ratio u_{rms}/v_{rms} showed little change through the distortion, but the correlation coefficient R_{uv} increased by more than 60 percent, suggesting that the organized motions have been altered significantly.

Two-point hot-wire measurements were also made to study the behavior of the large-scale motions directly. The convection velocity had decreased by about 5 percent relative to the local mean velocity at $x = 5.4\delta_0$, and the mean structure angle had increased by about 5°. Further downstream, the structure angle continued to increase, so that at $x = 9.1\delta_0$ it had increased to about 10° over the undisturbed value.

The schlieren visualization of the boundary layer indicates that the density fronts rapidly change their inclination in the region of curvature (see figure 34). In the beginning stages of the compression, the inclination is considerably less than the upstream value (which is about 50° in the

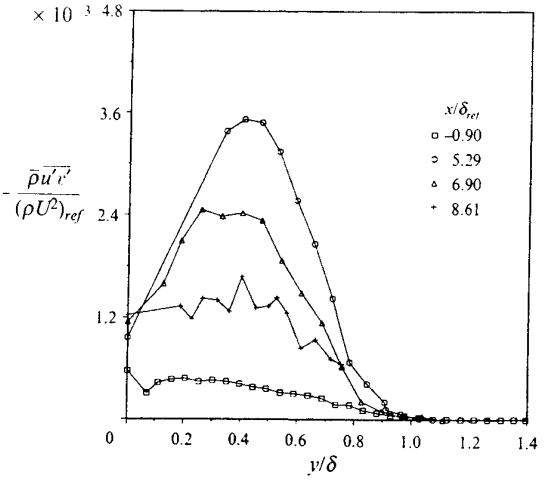

Figure 33: Streamwise variation of the Reynolds shear-stress profiles for the Model IV curved-wall impulse experiment (see table 4). The values plotted at $y = 0$ correspond to τ_w. From Donovan *et al.* (1994).

middle of the layer, see figure 25b), but the angles quickly increase so that at $x = 8.9\delta_0$ they had increased to about 15° over the undisturbed value, in reasonable agreement with the hot-wire data. Donovan *et al.* suggested that this behavior may be explained by considering the effect of the compression on the vorticity contained by the large-scale motions. We should note that the distortion is approximately isentropic, at least as far as the initial response is concerned, and baroclinic torques will therefore not generate significant levels of vorticity. A simple calculation based on the magnitude of the compression in the plane of curvature (assuming the perturbation to be rapid) suggests that the angle should decrease, not increase. If we assume the incoming large-scale motions have a vertical scale given by δ, and the overall streamwise extent is given by $\eta\delta$, then $\eta = 1.1$ for most of the central part of the upstream layer since the structure angle is about 50° (see figure 25). Furthermore, if we assume that the vertical scale downstream is still given by the local boundary-layer thickness, then the downstream value of δ can be found from the velocity ratio across the compression, as long as the viscous terms are negligible for this short time. This would imply that the downstream angle is close to 20°, primarily because of the reduction in boundary-layer thickness. If the organized motion were some type of vortical structure, then considerable stretching would be required to rotate it to an angle of 20° and still have it span the boundary layer (this leads to an increase in length of about 90 percent). If the structure is assumed to be a large-scale horseshoe vortex, then stretching would cause the legs of the vortex to move closer while their circulation remains constant (primarily because of the influence of the image vortex). Using a Biot-Savart-type argument (assuming the gradients of the sound speed are not large in the outer 80 percent of the boundary layer), the induced velocity will increase, tending to increase the angle of inclination. The schlieren photographs suggest an

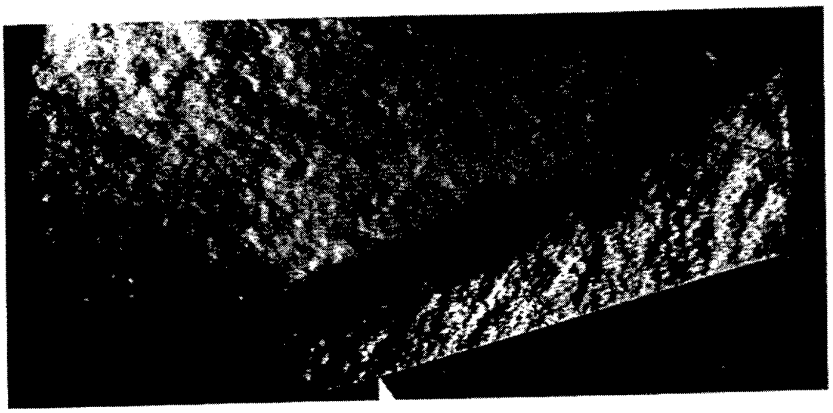

Figure 34: Schlieren photograph of a Mach 2.9 boundary layer passing over a short region of concave surface-curvature (Model IV in table 4). The flow is from right to left. The first pointer marks the end of curvature and the second marks the $x = 5.4\delta_0$ location. The dark band at the edge of the boundary layer is the compression fan/shock structure. Note the change in the inclination angle of the large-scale structures. From Donovan *et al.* (1994).

over-recovery of the structure angle in the region after curvature.

In incompressible flows, some investigators (for example, Head & Bandyopadhyay, 1981) have discussed the possibility that the angles of inclination of hairpin vortices and bulge interfaces are related to the principal axis of the rate-of-strain tensor. In any zero pressure-gradient boundary layer the inclination of the principal axis is very close to 45°. Donovan (1989) used a rotational method of characteristics to calculate the variation of the rate-of-strain tensor on *Model IV*. This procedure is valid for rapidly distorted flows where the turbulence has a negligible effect on the mean flow, a condition satisfied reasonably well by the flow for $x = 5.4\delta_0$. The smallest inclination of the principal axis was calculated to be about 40° before relaxing back to its upstream value, which to some extent reflects the behavior observed in the schlieren visualization. However, the causal relation between the principal axis of the mean strain rate and the inclination of the organized motions remains unclear.

Further information on the spatial extent of the outer-layer structures was found using two vertically-separated wires. By shifting the peak in the space-time correlations along a line corresponding to the mean structure-angle, the qualitative picture shown in figure 35 was obtained. This view may be compared to the similar view shown in figure 20a ($\xi_y/\delta = 0.09$) for the undisturbed boundary layer. Both plots illustrate the spatial nature of the organized motions in side-view when the horizontal axis is taken as the streamwise direction (using Taylor's Hypothesis). The increase in structure angle at $x = 5.4\delta_0$ is evident, as well as the stretched length of the large scales, and the increase in the streamwise correlation length-scale. This last observation is somewhat unexpected, but it may indicate that the compression enhances the correlated motions more than the uncorrelated parts.

Finally, by conditionally sampling the fluctuating streamwise and normal velocity signals simultaneously, an ap-

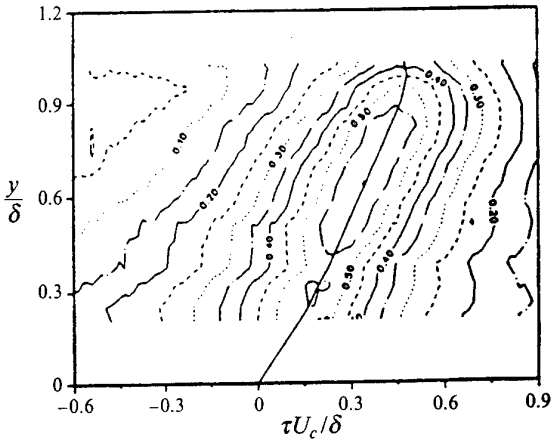

Figure 35: Model IV curved-wall impulse experiment (see table 4): correlation contours from hot wires separated by 0.1δ in a direction normal to the wall at a position $x = 5.4\delta_0$ downstream of the start of curvature. This view may be compared with the corresponding view of the undisturbed boundary layer shown in figure 20a. From Donovan *et al.* (1994).

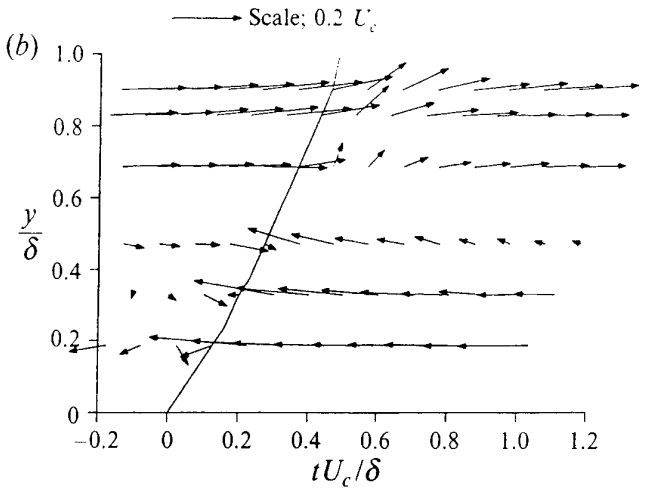

Figure 36: Model IV curved-wall impulse experiment (see table 4): average flow field in the region of instantaneous positive mass-flux gradient as seen in a reference frame moving at the convection velocity of the large-scale motions at $x = 5.4\delta_0$ downstream of the start of curvature. This view may be compared with the corresponding view of the undisturbed boundary layer shown in figure 26. From Donovan *et al.* (1994).

proximate view of the average large-scale motion can be derived. The VITA technique developed by Blackwelder & Kaplan (1976) was used to identify positive mass-flux fronts, and the ensemble-averaged flowfields around these fronts are shown in figure 36 (the corresponding view for the upstream boundary layer was shown in figure 26). The clockwise rotation within the large scales is clearly seen, as is the counter-clockwise rotation in the region behind the mass-flux front (that is, the back of the large-scale structure), and the presence of a stagnation point on the mass-flux front itself. Downstream, the rotating motion of the fluid downstream of the back of the structure is not as well defined, and the upward velocity just in front of the back is much larger than in the upstream boundary layer. Throughout the flow, the steeper angle of most of the velocity vectors reflect the amplification of the normal velocity component by the perturbation.

Having described the results of one particular study in some detail, we can now summarize the overall behavior of the curved-wall flows listed in tables 3 and 4. In all cases, the Reynolds stresses were found to be amplified downstream of the curvature. The level of amplification depended on the pressure gradient, and the largest amplification was observed in the compression-corner flows where the strongest pressure gradients are found. That is, the more rapid the perturbation, the greater the amplification of the turbulence. Changes in the turbulence structure seem to depend therefore on the strength and the rate of application of the perturbation. For the weakest distortion ($R_c/\delta_o = 50$) no changes in the structure were observed indicating that the boundary layer was near equilibrium throughout the distortion. For the more rapid distortions at 8° of turning ($R_c/\delta_o = 0$ and 10), weak changes in the turbulence structure parameters were observed.

In compression ramp interactions, Debiève (1983), Ardonceau (1984), Kuntz *et al.* (1987), Smits & Muck (1987) and Selig *et al.* (1989) found that the amplification of the turbulence increased with the ramp angle, that is, the shock strength. Ardonceau observed that the Reynolds shear-stress responded more quickly to the distortions than the streamwise and normal components. For the flow downstream of the interaction, he suggested that the turbulent motions begin to lose their coherence before beginning to dissipate energy. In the experiments by Smits & Muck, the turning of the flow was the same as the turning in the curved wall studies of *Models I, II* and *IV*. A greater amplification of the streamwise Reynolds stress was found when a shock wave was present, but the same trend was not observed in the shear stress, and in the case of an 8° ramp, the boundary layer response was the same with or without the shock wave. As the strength of the perturbation increased from 8° to 16°, the shock wave began to have an influence. For instance, Smits & Muck (1987) found a change in the anisotropy ratio downstream of a 16° shock wave interaction, but as we saw above, there is little change in the anisotropy ratio in the flow over a 16° curved wall. Initially, it was believed that there was a coupling between the unsteady shock motion and the turbulence which served to amplify the turbulence intensity without directly affecting the shear stress. However, the measurements made by Selig *et al.* using conditional sampling demonstrated that the shock motion had little effect on the amplification of the turbulence intensity. In contrast, there appears to be a strong link between the large-scale motions in the incoming boundary layer and the unsteady motion of the shock wave, at least for attached flows (Gramann & Dolling, 1992, Cogne *et al.*, 1993).

4.5 Reflected-wave flows

To study the effects of adverse pressure-gradients in the boundary layer with a minimum amount of distortion due to curvature, the pressure gradient can be imposed through a system of reflected waves (see figure 27). The response of the turbulence to this type of perturbation was studied by Kussoy *et al.* (1978) at Mach 2.3, and by Fernando & Smits (1990) and Smith & Smits (1996) at Mach 2.9. In the first two studies, the rise in pressure was approximately equal (in other words, the respective impulses due pressure changes were nearly the same); however, the pressure gradient occurred over a shorter distance in the first study ($1.5\delta_o$) than in the second ($7\delta_o$). The strengths of the perturbations were weaker than the perturbation imposed by Smith & Smits in the third study, where the distortion was stronger and more rapid (see tables 3 and 4), but in all three flows the Reynolds stresses were strongly amplified. Fernando & Smits found that the turbulence stress ratios varied less than the stresses themselves, indicating that the structure of the turbulence remained largely unchanged in their flow. This conclusion was confirmed by measurements of the space-time correlations which were essentially unchanged from the correlations in the undisturbed boundary layer. These observations were not unexpected since the distortion was comparatively weak and relatively slow. However, a frequency shift was observed in the energy spectra of the turbulence, suggesting an increase in the turbulence length-scale. This change was more obvious in the velocity profiles which exhibited the dip below the logarithmic law characteristic of subsonic flows experiencing concave streamline curvature, and it may indicate the effect of the small but perhaps significant amount of streamline curvature found in the reflected wave flows of Fernando & Smits (and Smith & Smits). Of course, if we assume that the concept of an impulsive perturbation holds in this case, $I_\theta = 0$ since the incoming and outgoing flow directions are the same. However, the region over which the pressure rises is rather long (of the order of the large-eddy turnover-distance $\approx 10\delta_0$) and the appearance of curvature-related effects may signal the limit of the impulse approximation. In that case, the approximation will also break down for the flow over *Model II* where $R_c = 50\delta_0$.

The pressure gradients in the flat plate studies by Fernando & Smits and Smith & Smits were designed to match the pressure gradients on curved walls with 8° and 16° of turning, respectively, where the non-dimensional radius of curvature was $R_c/\delta_o = 50$, and 10 – 12 (Jayaram *et al.*, 1987, Donovan *et al.*, 1994). For 8° of turning, the presence of curvature was found to enhance the increase in the streamwise Reynolds stress, and although it did not change the total amplification in the shear stress, the rate at which the shear stress changed was faster for the flow with curvature. For 16° of turning, a similar behavior in the streamwise stress was observed. Structural changes in the turbulence appear to be directly linked to the presence of substantial amounts of streamline curvature and the rate at which the perturbation is applied. For example, changes in the turbulence structure were noted by Jayaram *et al.* on an 8° curved wall, but Fernando & Smits found no structural changes in a flow with the same adverse pressure-gradient on a flat wall. The more rapid the distortion, the greater the change observed in the turbulence structure, suggesting that these changes may be described using the total strain-rate while the slower distortions should be described using local strain-rates.

4.6 Taylor-Görtler vortices

In subsonic turbulent boundary layers, concave curvature in the streamwise direction introduces longitudinal vortices according to a mechanism similar to that responsible for producing Taylor-Görtler vortices in laminar flows (Tani, 1962). These longitudinal roll-cells tend to be spaced in the spanwise direction with a reasonably regular spacing of one to two boundary layer thicknesses, and once established they are very stable in location and strength. Although they are generally weak, in that their tangential velocity is at least an order-of-magnitude smaller than the freestream velocity, they can have strong effects on the turbulence. For example, Smits *et al.* (1979b) found that downstream of an impulse in concave curvature the shear stress differed by up to a factor of two in the spanwise direction, where the low level was found in the region where the secondary flow was towards the wall (that is, a "crest" in the spanwise C_f distribution), and the high level was found where it was away from the wall (a "trough" in the C_f distribution). The corresponding C_f values differed by about 20 percent from the crest to the trough.

In some particular flows with concave curvature, Taylor-Görtler vortices have not been observed. In the study by Smits *et al.* (1979a), where the flow developed on a cylindrical forebody before diverging on a cone, the boundary layer experienced the combined effects of concave curvature and divergence. Steady vortices were not detected. It is possible that unsteady vortices were formed, without a preferred spanwise position, or that the vortices originated intermittently at different spatial locations. The measurements were not designed to detect such unsteady motions, and so we can only speculate. It is also possible that the roll-cells did not form at all because of a nonlinear interaction between concave curvature (which amplifies longitudinal vorticity) and divergence (which amplifies spanwise vorticity).

In separated supersonic flows, surface oil flow visualizations in the region of reattachment suggest that steady Taylor-Görtler vortices also occur in compressible flows (Roshko & Thomke, 1966). Visualizations of the separation and reattachment lines in compression-corner flows similarly suggest the existence of longitudinal vortices, with a spanwise spacing similar to that seen in incompressible flows (see figure 37), and Selig *et al.* (1989) suggested that longitudinal vortices could be the cause for a bimodal *pdf* in the mass-flux fluctuations downstream of a 24° compression corner, since they are an effective mechanism for sweeping low-momentum fluid up from the near-wall regions.

However, no evidence of steady Taylor-Görtler-like vortices was found in any of the attached flows listed in tables 3 – 5. It is again possible that nonlinear effects may have prevented their appearance. For example, it was suggested by Green (see Bradshaw, 1973, Smits *et al.*, 1979a) that bulk compression acts in many respects similarly to

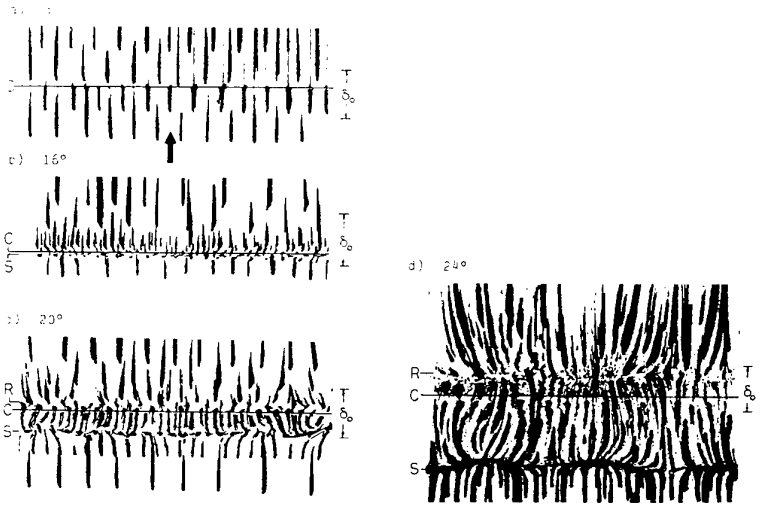

Figure 37: Surface streak patterns for compression-corner flows at Mach 2.9 (the line S indicates the mean separation line, line R the mean reattachment line and line C the position of the corner). The flow is from top to bottom, and the incoming boundary layer thickness is shown for comparison. From Settles *et al.* (1979a).

lateral divergence. If it is true that Taylor-Görtler vortices do not form in subsonic boundary layer flows when concave curvature and divergence act together, then by extension it may not be surprising that when concave curvature and dilatation occur together, Taylor-Görtler vortices again appear to be absent.

A criterion for the onset of steady Taylor-Görtler vortices in compressible flows with concave curvature may be developed as follows. According to Schlichting (1979), Taylor-Görtler vortices first appear in a laminar, incompressible boundary layer on a concavely-curved wall when the characteristic parameter, the Görtler number G_T,

$$G_T = \frac{U_e \theta}{\nu} \sqrt{\frac{\theta}{R}},$$

exceeds a certain value. Stability calculations give the neutral curve as a function of Görtler number and nondimensional wavelength.

Tani (1962) suggested that this criterion could be applied to turbulent flows by using the same characteristic length scale, θ, and simply replacing the molecular viscosity by the eddy viscosity. If we assume that the eddy viscosity in the outer layer is given by

$$\nu_t = 0.018 U_e \delta^* \tag{44}$$

(Clauser, 1956), then

$$G_T = \frac{\theta}{0.018 \delta^*} \sqrt{\frac{\theta}{R}}, \tag{45}$$

which indicates that the appearance of longitudinal vortices in a turbulent flow is a weak function of Reynolds number since the shape factor varies somewhat with Reynolds number (Coles, 1962). Bradshaw (1973) pointed out that the direct use of the neutral curve for the Blasius profile is not realistic, but Tani's measurements agreed reasonably well with this simple proposal. Note that the Görtler number for turbulent flow can also be written as

$$G_T = \frac{(\theta/\delta)^{1.5}}{0.018\,(\delta^*/\delta)} \sqrt{\frac{\delta}{R}}. \tag{46}$$

We can extend the analysis to compressible flow by assuming that the length scale remains unchanged and that the eddy viscosity is still given by equation 44. In other words, the Görtler number for a compressible turbulent flow is given by equation 46, where we recognize that the momentum and displacement thicknesses are a strong function of Mach number (Smits & Dussauge, 1996). Some typical values may then be found for the lower limit on δ/R where we expect to find longitudinal vortices, corresponding to the neutral curve calculated by Smith (1955) and a fixed wavelength of 2δ. For the present purpose, we will ignore the weak dependence of the Görtler number on Reynolds number. As the freestream Mach number increases from 0, to 1, to 3, to 5, we find $(\delta/R)_s$ increases from 0.003, to 0.005, to 0.03, to 0.11. That is, the analysis predicts a strong increase in stability with increasing Mach number. Most of the Mach 3 curved-wall cases listed in tables 3 and 4 exceed this rather crude criterion, but not by very much, and it seems likely that the absence of Taylor-Görtler vortices in these attached flows is at least partly due to the stabilizing influence of Mach number. For the separated flows, the distortion of the mean velocity profile will influence the stability calculation, and the appearance of an inflection point will obviously make the layer more unstable in every sense.

4.7 Favorable pressure gradients

When the sense of the curvature is convex, the effect on the boundary layer turbulence is stabilizing, and the wall-friction, heat-transfer and the Reynolds stresses are ex-

	Group Three			
	Dussauge & Gaviglio	Smith & Smits (1991)	Johnson	
	Expansion corner	Expansion corner	Expansion corner	Curved Wall
M_e	1.76	2.9	2.5	2.5
R_c	0	0	0	$15\delta_0$
I_i	$0-1\delta_0$	$0-6\delta_0$	$0-3\delta_0$	$3\delta_0$
I_θ	−0.21	−0.35	−0.26	−0.26
I_p	−0.50	−1.02	−0.78	−0.78
$\overline{\rho u'^2}$	−78%	−85%	−72%	−72%
$-\overline{\rho u'v'}$	—	—	—	—
θ	-12°	-20°	-15°	-15°

Table 5: Impulses in favorable pressure-gradient cases, Group Three. Adapted from Smith & Smits (1994).

pected to decrease. If the flow is supersonic, then the convex curvature will generally be accompanied by a favorable pressure-gradient which will enhance the stabilizing effect. With the exception of Morkovin (1955) and Johnson (1993), all of the studies in supersonic flows of convex curvature effects have been made in expansion-corner flows ($R_c = 0$) where the curvature and pressure gradient are stabilizing (see figure 27). Turbulence measurements in expansion corners by Dussauge & Gaviglio (1987) at Mach 1.76, and Smith & Smits (1991)a at Mach 2.9, show a substantial reduction in the streamwise Reynolds stress downstream of the corner (see Group Three, table 5).

The usefulness of RDA for rapidly expanded flows was indicated in section 4.1. The strong stabilizing influence of expansion can be seen in figure 38. The good agreement between the measured and calculated stress profiles suggests that the evolution of the mean flow field was essentially independent of the turbulence field, and that the turbulence field evolved in direct response to the changes in the mean velocity gradients. Smith & Smits also found that 90 percent of the reduction in the streamwise stress was due to the effect of bulk dilatation, that is, the change in mean density. Curvature appeared to play a very small role even though the flow was turned through a relatively large angle of 20°.

If the favorable pressure gradient is strong enough, it seems possible that the boundary layer will *relaminarize*, as in subsonic flow, although it might be more accurate to say that pressure forces can become large enough to dominate the nearly frozen Reynolds stresses, and over a large part of the boundary layer the Reynolds stresses then have little influence on the mean flow. That is, the turbulent fluctuations may not be absent, but they no longer contribute appreciably to the momentum or energy transport. Johnson (1993) made turbulence measurements downstream of a convex wall to study the possibilities for relaminarization. In his experiments, the non-dimensional radius of curvature of the wall, R_c/δ_0, was varied from 0 to 15 while the overall turning angle remained at 15° (see table 5). The incoming flow was recovering from the distortion presented by a 10° concavely-curved wall placed some distance upstream, but the incoming flow was the same for each case so that the effect of varying R_c could still be determined to some degree. Johnson found a strong suppression of the longitudinal velocity fluctuations with the suppression being remarkably similar in all four cases, suggesting that in his flow the dominating influence was the overall pressure rise (or, equivalently, the total turning angle) rather than

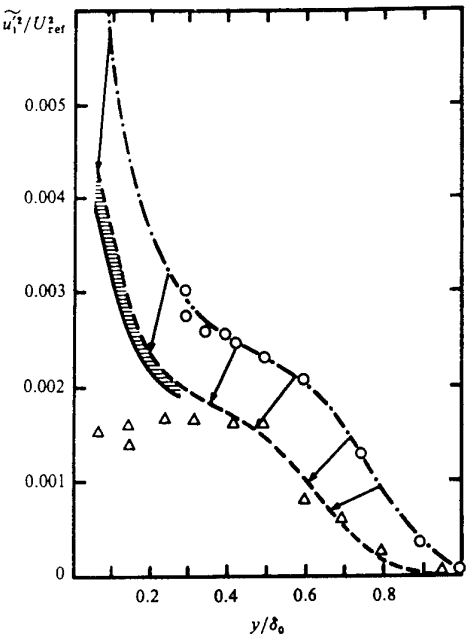

Figure 38: Velocity fluctuations in a 12° expansion corner at Mach 1.76. ○, upstream profile; △, along the last Mach wave in the expansion; - - - -, dilatation effect; shaded zone, dissipation effect. Arrows indicate streamline correspondence. From Dussauge & Gaviglio (1987).

	Group Four					
	Zheltovodov *et al.*		Smith & Smits (1993b)			
	Comp. Corner	Exp. Corner	Comp. Corner	Exp. Corner	Curved Comp.	Curved Exp.
M_e	2.9	2.9	2.9	2.9	2.9	2.9
R_c	0	0	0	0	$15\delta_o$	$15\delta_o$
L_i	$0 - 10\delta_o$	—	$0 - 6.5\delta_o$	—	$0 - 12\delta_o$	—
I_θ	+0.44	−0.44	+0.35	−0.35	+0.35	−0.35
I_p	+1.1	−1.1	+0.92	−0.92	+0.92	−0.92
θ	+25°	−25°	+20°	−20°	+20°	−20°

Table 6: Impulses in successive-distortion cases, Group Four. Here, δ_0 is the boundary layer thickness of the flow just upstream of the start of the disturbance. Adapted from Smith & Smits (1994).

the strength of the pressure gradient. Here again, the distortions were rapid, with the slowest distortion occurring over $4\delta_o$.

Unfortunately, the limitations of wind tunnel testing usually prevent the study of the full relaxation behavior in expansion-corner flows, simply because it is difficult to follow the flow far downstream in a wind tunnel of fixed geometry. For example, the measurement region downstream of the expansion corner in the study by Dussauge & Gaviglio was $11\delta_o$ long, and in the experiment by Smith & Smits it was only just over $5\delta_o$ in length. Since these flows have large and rapid decreases in pressure, it is clear that only the initial response of the boundary layer to the pressure distortion could be observed before the end of the measurement section was reached.

4.8 Successive distortions

Studies of boundary layers experiencing successive distortions can give new insight into the relaxation of a distorted boundary layer. In the investigations by Zheltovodov *et al.* (1990) and Smith & Smits (1993b), the boundary layer experienced successive impulses in curvature of opposite sign such that the direction of the flow upstream and downstream of the curved-wall regions was the same (see figure 39, and Group Four, table 6). In a study by Zheltovodov *et al.* the flow passed over a 25° forward facing step, and a remarkable relaxation behavior was found in the streamwise turbulence intensity. After the second impulse, that is, on the flat plate downstream of the step, the turbulence intensity levels initially returned to the upstream levels, but further downstream the stress levels in the middle of the boundary layer continued to decrease. Unfortunately, the limited spatial resolution of the probes in this experiment makes it difficult to gauge the response quantitatively.

In the study by Smith (1993) and Smith & Smits (1993b), two different flows over forward-facing ramps were studied, each with 20° of turning. In the first case (*Model A*), the turning was produced by sharp corners as in the Zheltovodov flow, but in the second case (*Model B*) the turning was produced by curved walls. As the flow passed over these steps, the boundary layer was subjected first to an adverse pressure gradient combined with concave streamline-curvature and bulk compression, followed by a favorable pressure gradient combined with convex streamline-curvature and bulk dilatation. On *Model A*, the initial turning at the compression corner resulted in a shock-wave boundary-layer interaction, and the subsequent expansion occurred through a centered expansion fan. On *Model B*, the concave and convex streamline-curvatures were distributed over longer streamwise distances than on *Model A*, and therefore the pressure gradients were less severe. In particular, the shock associated with the concave curvature did not form until well outside the boundary layer, and within the boundary layer the compression occurred through a compression fan rather than a shock-wave boundary-layer interaction. On *Models A* and *B*, however, there was no net change in flow direction across the successive distortions and therefore the upstream and downstream freestream-conditions were effectively the same except for a small shock loss on *Model A*.

The overall response corresponded closely to that seen by Zheltovodov. The streamwise Reynolds stress profiles first show a strong amplification downstream of the compression surface (a factor of 10 for *Model A*), followed by a large decrease just downstream of the expansion (see figure 40: the large, initial amplification downstream of the compression corner is not shown in this figure, only the relaxation behavior on the flat plate downstream of the expansion). In the profiles further downstream, this region of reduced stress grows in size and the shape of the stress profile suggests the presence of an internal layer. There is no detectable relaxation toward a self-preserving state, in agreement with the results obtained by Johnson (1993) in a similar flow configuration at Mach 2.45.

Over most of the boundary layer immediately downstream of the distortions, the shear stress appeared to change sign. A subsequent recovery of the shear stress was observed in the lower 60 percent of the boundary layer, but in the remaining part of the layer the shear stress remained at very low values.

Despite the differences between *Models A* and *B* — different distortion lengths, and the presence of a shock wave in the first case compared to an isentropic compression in the second case — the general response of the boundary layer was very similar. In both cases, the distortions occurred rapidly, suggesting that the perturbation rate was not important and that the distortion can be described qualitatively using the appropriate impulse levels (see table 6). However, it is not suggested that the overall response of the boundary layer can be described as a linear sum of the two successive impulses: this would indicate that the overall perturbation is zero (assuming that α_o is the same for all perturbations). Remarkably, the stress levels at the exit from the second perturbation were al-

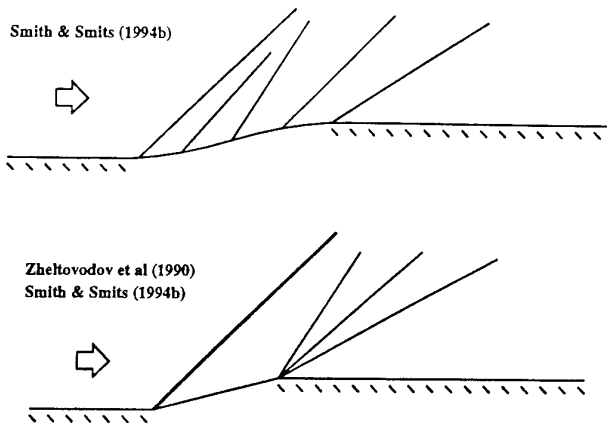

Figure 39: Successive distortion flow geometries. From Smith & Smits (1994).

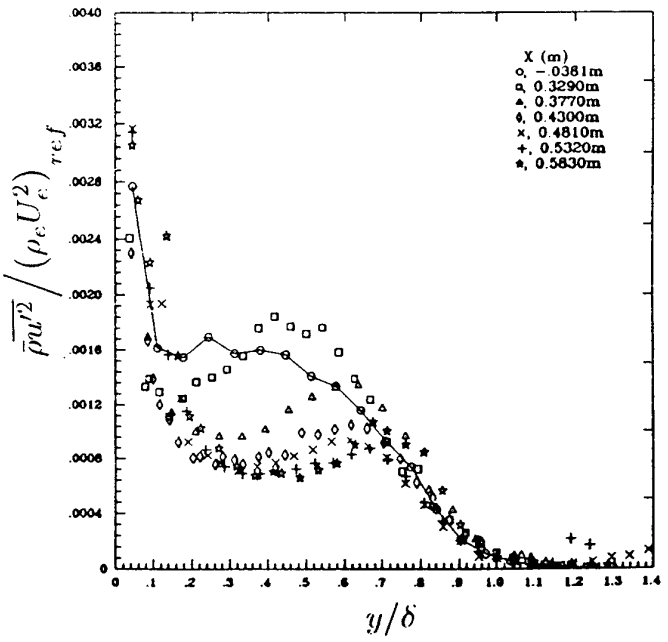

Figure 40: Longitudinal Reynolds stress profiles for the flow over a compression corner followed by an expansion corner (*Model A* in table 6). The distance x is measured from the start of the compression ramp, and the ramp is $149\,mm$ long (about $4\delta_0$). Only the profiles upstream of the compression corner and downstream of the expansion corner are shown. From Smith & Smits (1993b).

most unchanged from their upstream values, but further downstream the undershoot in the turbulence levels suggests a second-order response of an underdamped system. The turbulence is strongly out of equilibrium, and the production, dissipation and anisotropy are out of balance.

An RDA Reynolds stress calculation similar to the ones discussed earlier was used to help understand the response of the turbulence over *Model A*. In the expansion, estimates of the production terms in the Reynolds stress equations revealed that negative production can occur and this may be largely responsible for the change of sign in the shear stress, and the complex nature of the relaxation process. Not unexpectedly, this indicates that the conventional eddy viscosity approaches to turbulence modeling have severe limitations for these strongly perturbed flows. A number of factors combined to inhibit the turbulence production mechanisms in the relaxing boundary layer. These factors included a fuller velocity profile, a decay of the streamwise stress, and a collapse of the shear stress in the expansion fan. As a result, a long recovery period may be expected. Qualitatively, it appeared that the streamline curvature in the second impulse combined with the amplified streamwise Reynolds stress on the ramp to exaggerate the stabilizing effect of the expansion corner. In the flows over a simple expansion corner (Group Three), the dominant effect is that of bulk dilatation; while in the flows where a compression precedes the expansion (Group Four), curvature plays a more important role within the expansion.

The shape of the streamwise Reynolds stress profiles suggested three zones of response: a recovery region near the wall where the turbulence recovered quickly from the perturbations; a zone of strong response in the middle of the boundary layer where the turbulence eventually undershot the equilibrium distribution sharply in response to the combined effects of the perturbations (second-order response); and a zone of advection near the edge of the boundary layer where the turbulence appeared unaffected by the overall effects of the perturbations (linear response). This latter observation further supported the conclusion of Selig & Smits (1991) that at this Mach number shock-wave oscillation does not contribute appreciably to turbulence amplification in shock-wave boundary-layer interactions.

4.9 Overview of response to distortions

For the cases with both adverse pressure-gradients and concave streamline-curvature, the changes in the turbulence structure (as inferred from the trends in the Reynolds shear-stress) appear to be strongly tied to the magnitude of the impulses due to curvature. This holds true for the weak and strong distortions considered here. If the radius of curvature of the turning was small enough, a shock wave forms in the boundary layer, and the streamwise stress increased with increasing shock strength. If the pressure gradients were not strong enough to separate the layer, the shock wave seemed to exert no additional effect on the shear stress over and above the changes that could be attributed to streamline curvature (or the equivalent compression).

In the flows with rapid, favorable pressure-gradients and convex curvature, it appears that the initial response of the boundary layer turbulence is dominated by the effects of the bulk dilatation, and the effects of convex curvature are always small. That is, the turbulence initially changes in response to the pressure gradient as would be expected using the conservation of circulation (we can largely ignore the effects of compressibility on relative motions because the Mach number gradients in the outer layer are usually small). The effect of bulk dilatation on the turbulence (expressed as an impulse) is not a strong function of the pressure gradient, indicating that it is the overall pressure change which is important. In contrast, the relaxation behavior appeared to be largely controlled by the streamline curvature history. However, these observations were made in a boundary layer downstream of two successive distortions where the effect of curvature appeared to be greatly augmented by the amplification of the stresses downstream of the first distortion. The relaxation behavior is similar to the second-order response seen by Smits *et al.* (1979b) in an incompressible turbulent boundary layer downstream of an impulse of curvature. In addition, the behavior of the shear stress was similar to that observed by So & Mellor (1973) in a boundary layer developing over a surface with prolonged surface curvature in incompressible flow. What has not been explained is the observation that in the outermost part of the boundary layer there was no change in the streamwise stress from its undisturbed profile even though it is in this region where the principal strain-rate $\partial U/\partial y$ is small and that the effect of the extra strain-rates should be felt most strongly.

Overall, it appears that the boundary layer response to curvature in a supersonic flow is similar to the response in subsonic flow, even to the appearance of a dip below the log-law in the mean velocity profile as a response to any significant amount of concave streamline curvature. More specifically, in the case of a single impulse of curvature, we expect to observe the same counter-intuitive trends in the Reynolds stress behavior as observed by Smits *et al.* in subsonic flow, where a stabilizing distortion (an impulse in convex curvature) caused an increase in turbulence activity and a destabilizing distortion (an impulse in concave curvature) caused a decrease.

Compressibility effects on the turbulence appear to be small, at least at supersonic speeds. In flows with concave or convex streamline curvature, Reynolds stress calculations using subsonic turbulence models by Degani & Smits (1990) were found to give reasonable predictions of Reynolds stress behavior, at least for distortions where the boundary layer did not depart too far from equilibrium. For these flows, the limitations of the calculation are probably due to the turbulence modeling, rather than any specific influence of compressibility, and the observations tend to support the turbulence structure similarity suggested by Morkovin's Hypothesis. For strong distortions, our predictive capability is confined to the initial response where linear theories such as RDA become useful.

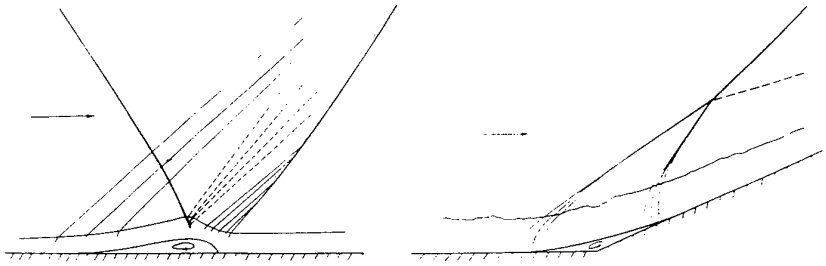

Figure 41: Typical interactions between shock waves and boundary layers: (a) incident oblique shock; (b) compression-corner interaction. From Adamson & Messiter (1980).

5 Shock Wave Boundary Layer Interactions

Shock-turbulence interactions are a common occurrence in supersonic flow since compression and flow deflection are almost always accompanied by the formation of a shock. The characteristics of the interaction depend on the Mach number, the scale and frequency content of the turbulence, the nature of the incoming flow, the shock angle, the source of the shock, and the flow geometry. The shock may interact with freestream turbulence, with a free shear layer, or with a boundary layer (figure 41). The earliest experiments concentrated on transonic interactions, to make possible flight at supersonic speeds (Liepmann, 1946, Ackeret *et al.*, 1946, Liepmann *et al.*, 1951). Once the sound barrier was broken, attention shifted to supersonic and hypersonic interactions, and to date a large number of experiments have been performed. Green (1970), Stanewski (1973), Sirieix (1975), Adamson & Messiter (1980), Délery (1985) and Viswanath (1988) give detailed surveys of interactions which are two-dimensional in the mean, and Green (1970), Korkegi (1971), Peake & Tobak (1980), Settles & Dolling (1990), Dolling (1990), Settles & Dolling (1992) and Dolling (1993) provide a similarly comprehensive treatment for three-dimensional interactions. Rather than attempting to summarize these reviews, we will instead focus on some of the salient features of shock-wave turbulence interactions, with an emphasis on the underlying mechanisms controlling the scaling of the interaction, the possibility of flowfield separation, modifications to the incoming turbulence, and the unsteadiness of the shock.

Shock-wave interactions are usually classified according to how the shock is generated. For shock-wave boundary-layer interactions, the shock may impinge on the layer from an external source (an *incident shock interaction*), or the shock may be generated by the same surface that generated the boundary layer (a compression surface or *compression-corner interaction*). In most practical flows the interaction is three-dimensional, in that the shock sheet is swept at some angle to the boundary layer (which in itself may be two- or three-dimensional). Some of the more common configurations used to study two- and three-dimensional shock wave boundary layer interactions in the laboratory are illustrated in figure 42. In three-dimensional interactions, the shock may be generated by a sharp fin placed at an angle-of-attack to the incoming flow, by a blunt fin where the leading edge has a finite radius of curvature, or by a cone or other protrusion rising from the surface. The fins may also be swept in the streamwise direction, so that the shock sheet in the freestream is angled in two directions with respect to the upstream flow. The geometries of these interactions have many degrees of freedom, and they can become quite complex. In addition, the Mach number plays a crucial role in governing the inviscid flow field. For example, as the Mach number increases for a given shock generator configuration, the inviscid shock may change from being detached to being attached, producing large changes in the near-field. Even if the inviscid shock is attached, the reduced Mach number within the boundary layer may cause detachment at some point, and this can change the entire flow pattern. Variations in Reynolds number will also play a role, but for fully-turbulent flows its influence appears to be relatively minor since most interactions are pressure-dominated.

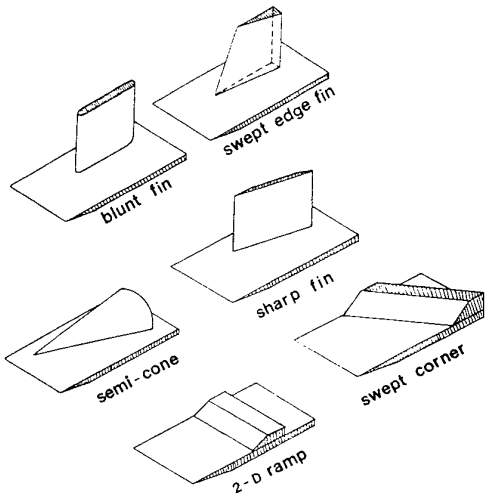

Figure 42: Examples of two- and three-dimensional shock-wave boundary-layer interaction geometries studied in the laboratory. From Tran (1987).

We consider only compression-corner flows, and not consider incident-shock interactions in detail. Incident-shock interactions for supersonic flows were studied by (see, Law, 1975, Délery, 1992, Audiffren, 1993, Deleuze & Eléna, 1995), but the data base is much smaller than for compression-corner flows. Fortunately, most of the generic effects of compressibility in two-dimensional interactions can be understood from an examination of compression-corner flows. Although shock-wave boundary-layer interactions are more complicated than interactions away from the wall, the boundary conditions are better defined. Three-dimensional interactions and more complicated flows produced by multiple shock interactions will not be considered here, and the reader is referred to the references given earlier, and the monograph by Smits & Dussauge (1996).

Two-dimensional compression ramp flows have been extensively studied (Settles *et al.*, 1979a, Debiève, 1983, Ardonceau, 1984, Smits & Muck, 1987, Dolling & Murphy, 1983, Selig *et al.*, 1989, Evans & Smits, 1996). The experiments at Mach 2.9 by Settles *et al.* and Smits & Muck are particularly revealing since they cover a wide range of turning angles, and detailed mean flow and turbulence data are available. As an illustration, we consider the 24° case (see figure 43). In this flow, the incoming boundary layer is turbulent. The 24° corner produces a shock wave with an initial turning of about 10°. The rest of the deflection is produced more gradually downstream through a series of unsteady compression waves. The pressure rise is strong enough to separate the layer, and there is a considerable increase in the turbulence level across the interaction. The velocity fluctuations are amplified by passing through the shock, and vorticity is generated by interaction between entropy spots and the shock, in agreement with the second-order modes theory discussed by Kovasznay (1953).

The whole flow is unsteady: the shock moves over a significant distance, its motion is three-dimensional and it occurs at low frequencies. It seems that the shock unsteadiness by itself makes a negligible contribution to the turbulence amplification (Selig & Smits, 1991). However, the separated zone is the source of large-scale fluctuations which are convected downstream, and these large-scale structures are probably related to low-frequency mechanisms. If the flow over the separated zone has features in common with mixing layers, we can expect this part of the flow to be very sensitive to compressibility effects, as free shear flows are. These aspects of the flow properties can be at the heart of couplings in the interaction, since they impose unsteady outlet conditions on the shock and can make it move. Since the incoming turbulence imposes an unsteady inlet condition, coupling with the incoming flow can also occur.

In terms of an extra strain rate terminology, the boundary layer experiences the combined effects of an adverse pressure gradient, concave streamline curvature, bulk compression, shock unsteadiness, and if the pressure rise is strong enough, flow separation. The wall stress typically decreases sharply near the start of the interaction, but quickly recovers as the boundary layer thins in response to the overall compression, overshooting the upstream level before eventually recovering to its undisturbed level appropriate to the new Reynolds number on the ramp. At the same time, the turbulence levels increase dramatically through the interaction and appear to relax only slowly. The shear stress is generally affected less than the normal stresses, and as a result structure parameters, such as $a_1 \equiv -\overline{u'v'}/q^2$, are strongly distorted. Because the flow responds to the combined effects of many distortions, it is difficult to conclude from the available data what the specific contributions are of, say, concave streamline curvature and bulk compression. It was apparent from section 4 that when the flow is compressed rapidly on a curved wall with a short radius of curvature, the boundary layer turbulence is amplified to a significantly larger degree than when the compression occurs more slowly, regardless of the curvature of the surface.

In the following discussion, we will try to infer the phenomena controlling the evolution of turbulence in shock-wave boundary-layer interactions by reviewing these different elements.

5.1 Skin friction distribution

For the compression-corner interaction shown in figure 43, the mean pressure distributions begin to develop a *plateau* region for turning angles greater than 16°, which indicates the onset of mean flow separation: the condition at 16° is called *incipient* separation (Settles *et al.*, 1979a). The terms *weak* and *strong* are sometimes used to describe attached and separated interactions, respectively, but these terms can mean different things in different contexts, and they will be avoided here. The instantaneous flow will show signs of reversal at smaller turning angles, but at 16° the mean skin friction becomes zero at some point (see figure 44). Both the 20° and 24° corners exhibit regions of separated flow. We noted earlier (section 4.4) that adverse pressure gradients in a compressible boundary layer flow can cause the skin friction to increase because of the thinning of the layer. Here we see that if the pressure gradients are strong enough, the skin friction can decrease suddenly, and the flow can separate. Downstream, however, the overall increase in pressure can still cause the skin friction to rise above its usual value at the same Reynolds number, again because of the thinning of the layer.

5.2 Separation

An important aspect of shock-wave boundary-layer interactions is the prediction of the onset of separation. We need to distinguish between mean flow separation, and instantaneous flow separation, especially for these inherently unsteady flows. There is evidence to indicate that the motion of the instantaneous separation point is closely tied to the instantaneous position of the shock (Gramann & Dolling, 1988), so that the probability that the flow is separated at any position is similar to the probability that the shock is located upstream of that location. Mean flow separation can then be defined as the point where the flow is separated for 50 percent of the time Simpson (1981). This location is often found using surface flow visualization such as the kerosene-graphite technique (Settles & Teng, 1984), but it should be noted that the line of accumulation seen in the visualization is located typically

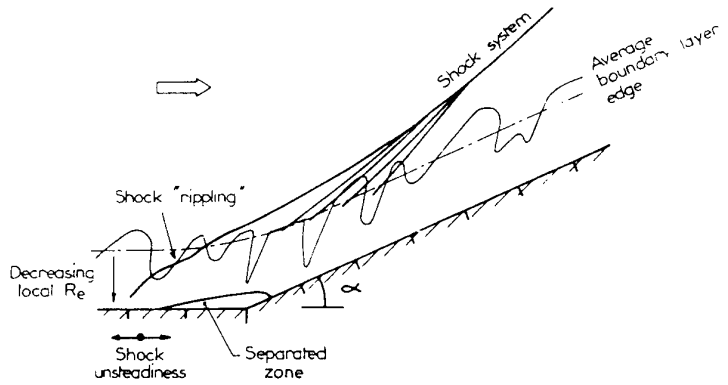

Figure 43: Sketch of the Mach 2.9, 24° compression ramp flow. From Dussauge *et al.* (1989).

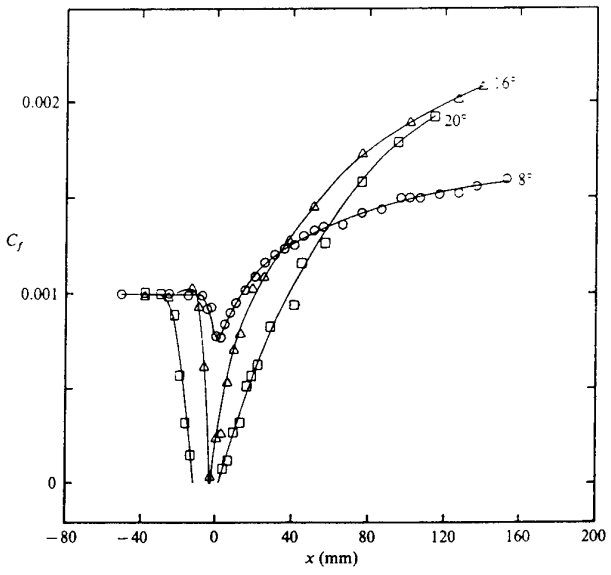

Figure 44: Distributions of C_f in compression-corner interactions at Mach 2.9. The wall stress is non-dimensionalized using "effective" edge conditions based on tunnel stagnation and local static pressures. Figure adapted from Smits & Muck (1987), showing data by Settles *et al.* (1979a).

downstream of the line of separation, since the mixture accumulates by the action of the wall shear-stress which is higher upstream of the instantaneous separation point than it is downstream, so that the flow visualization results are biased toward a position downstream of the mean separation location (Gramann & Dolling, 1988).

Chapman *et al.* (1957) used order-of-magnitude arguments to describe the similarity of the mean pressure distribution for separated flows. From an extensive series of experiments in laminar and turbulent flow, they argued that if the separated zone is large enough, the interaction in the vicinity of separation was local, independent of the underlying cause of separation. That is, the pressure rise to the point of separation, for example, should be similar for compression ramps and forward-facing steps, and it should scale with the Mach number and the incoming boundary layer characteristics. This *free-interaction* concept seems to hold well for laminar flows, but for turbulent flows the collapse of the data is not impressive, indicating a more significant dependence of the pressure distribution on the downstream boundary conditions. A mean flow concept such as free interaction theory does not take into account the unsteady motion of the shock. However, since the pressure distribution is a result of the averaging due to the unsteady shock motion, the breakdown of this criterion can be taken as further evidence to indicate that the unsteadiness depends to some extent on the downstream flow conditions, at least for separated flows.

5.3 Upstream influence

Figure ?? demonstrates that the wall pressure does not rise sharply in the region of separation. Instead, it rises gradually, levels off somewhat in the fully-separated zone (the "pressure plateau"), and then starts to rise again in the region of reattachment, eventually reaching its maximum value some distance downstream of the mean reattachment line. The region of *upstream influence* is defined as the distance from the corner to the point where a straight line drawn to fit the slope of the initial pressure rise intersects the pressure level corresponding to the incoming boundary layer. Now, even in a perfectly steady (laminar) interaction, we expect there to be an upstream influence. The pressure rise generated by the flow deflection can propagate upstream through the subsonic part of the flow near the wall. This will cause the streamtubes below the sonic line to thicken, and cause a flow deflection upstream of the corner. However, the upstream propagation distance depends on the thickness of the subsonic layer (Schneider, 1974), and the sonic line rapidly approaches the wall as the Mach number increases. For the case shown in figure 44, the sonic line for the incoming boundary layer is located at a distance less than 0.01δ from the wall, and the steady upstream propagation distance is expected to be very short. Indeed, measurements of the instantaneous wall pressure show that the shock appears as a very rapid rise in the pressure signature: there is no sign of an instantaneous upstream propagation of pressure. However, the unsteady motion of the shock occurs over a much greater distance than the steady upstream propagation distance. The unsteady motion of the shock causes the mean pressure $\bar{p}_w$ to rise at points well ahead of the average shock position, and it is this unsteady motion that is primarily responsible for the upstream influence seen in the wall pressure distributions. The mechanism is illustrated in figure 45. Within the region of shock motion, the wall pressure signal is intermittent, as seen in the figure. The values of pressure upstream and downstream of the shock are consistent with the pressure rise through the mean shock at its foot. The local mean wall pressure at a given location is simply the result of the pressure rise across the shock foot, weighted by the time the shock is upstream of that location.

5.4 Shock motion

Shadowgraphs of the instantaneous flowfields show qualitatively that the turbulent mixing appears to be considerably enhanced across the shock and the trend is more pronounced as the shock strength increases (Smits & Muck, 1987). The distortion of the shock front is also clearly evident. Visualizations using Rayleigh scattering in a 24° compression ramp flow at $M = 3$ confirmed that large scale eddies are energetic enough to distort the shock (Smith *et al.*, 1989). Recent double-pulsed Rayleigh images show how the large-scale motions in the boundary layer interact with the shock, and how they are subsequently distorted by the compression (figure 46). A detailed description of the shock motion near the wall was obtained from wall-pressure fluctuation measurements in compression ramp flows by Dolling & Murphy (1983), Muck *et al.* (1988), Bonnet (1988) and Selig *et al.* (1989) (for a review, see Dolling & Dussauge, 1989). Around the mean position of the shock, low frequency wall pressure fluctuations of large amplitude are present. The spatial extent of these oscillations is a function of the strength of the shock, as shown in figure 47. Muck *et al.* (1985) and Debiève & Lacharme (1985) used these observations to propose a reasonable approximation for the maximum *rms* value of the pressure fluctuation level across an oscillating shock from simple intermittency considerations: the maximum level is obtained when the intermittency coefficient is 0.5, and the maximum *rms* pressure p' is given by the simple relation $p'/\Delta p = 0.5$, where Δp is the mean pressure rise through the shock. This relation works well when the upstream and downstream levels of pressure fluctuations are not too high.

At Mach 2.9, the incipient separation occurs for a ramp angle α of 16°. For lower values of the wall deflection, the part of the flow involved by shock oscillation is limited and varies very slowly with α. In this case, it may be inferred that the shock moves mainly under the action of incoming turbulence. There is a significant increase when $\alpha > 16°$, suggesting that the wall pressure fluctuations are now influenced by the unsteadiness of the separation bubble. It is clear that the shock motion in this flow case has an amplitude of the order of the boundary layer thickness, but its mean frequency is an order-of-magnitude below the characteristic frequency of the boundary layer U_1/δ. This indicates that the average value of the shock speed u'_s is given by $u'_s/U_1 \approx 0.1$.

When a shock passes over a transducer it detects a rapid pressure rise, corresponding to sharp fronts in the pressure signal. The signals obtained simultaneously using a spanwise row of pressure transducers revealed that the shock

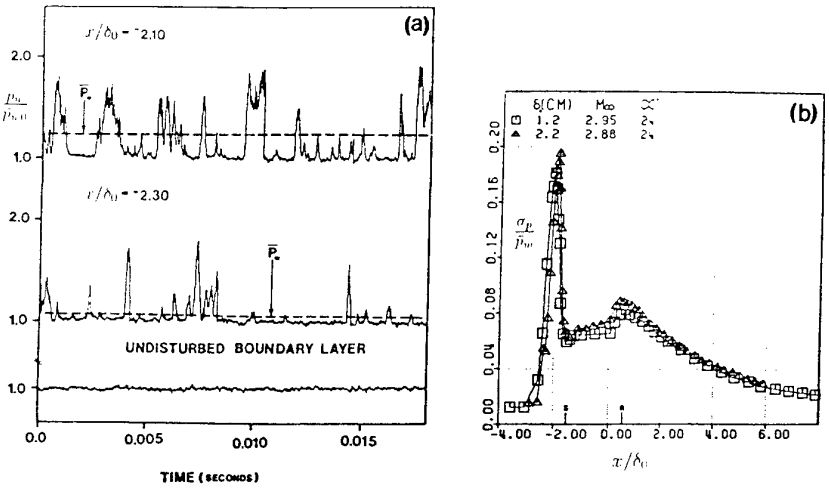

Figure 45: (a) Wall-pressure time-histories, and (b) *rms* wall pressure levels, in a 24° compression ramp at Mach 3. The lines of mean separation and reattachment are marked by S and R, respectively. The pressures were non-dimensionalized using the upstream mean wall pressure, $\bar{p}_{w0}$; σ_p is the *rms* wall-pressure level. From Dolling & Murphy (1983).

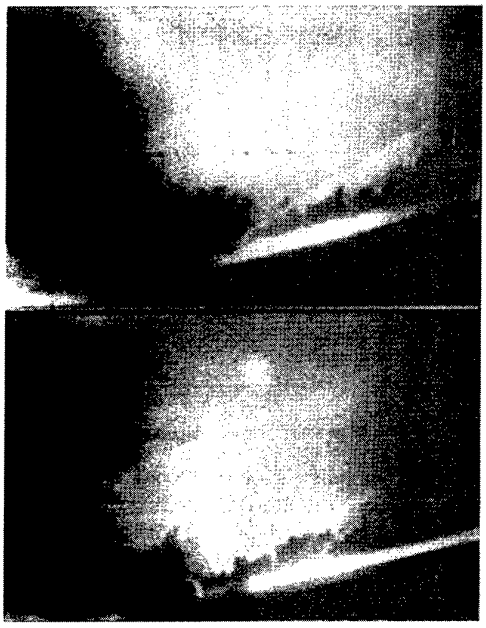

Figure 46: Double-pulsed Rayleigh images of a 16° Mach 2.9 compression-corner interaction. The time delay is $40\mu s$ between the top and the bottom images. Note the large-scale motion (outlined) passing through the shock. The flow is from left to right. From Forkey *et al.* (1993).

has spanwise ripples, since some perturbations were not measured by all the transducers. This three-dimensional structure shows that the shock not only translates back and forth, but also experiences large-scale spanwise perturbations.

5.5 Turbulence amplification

Rose (1973) and Kussoy & Horstman (1975) were the first to measure the strong amplification of turbulence levels in shock-wave boundary-layer interactions. Both investigations were peformed in incident shock interactions. Compression corner studies confirmed that interactions produce a large increase in turbulence activity: for a 20° deflection at Mach 2.9, Smits & Muck (1987) found that the maximum level of $\overline{u'^2}$ increased by a factor of about 12. The unsteady shock motion smears the region over which the amplification occurs, and it sometimes produces a local peak in the intensity profiles. The results given in figure 48 show this behavior clearly. It appears that the region directly affected by the shock has a thickness of about 0.1δ for the 8° case, and 0.2δ for the 16° case. The extent of the unsteady shock motion at the wall measures approximately 0.15δ and 0.3δ for these two cases, respectively, as indicated in figure 47. Clearly, the shock motion extends throughout the layer, and the amplitude of the motion is approximately constant with distance from the wall.

The level of turbulence intensity in the separated zone takes a maximum away from the wall, near the edge of the separation bubble. Selig *et al.* found that this level matches the high levels of turbulence found in mixing layers. Therefore, it seems possible that the separated zone can produce large-scale perturbations which are convected downstream. Such structures have been found from computations in laminar flows at low and

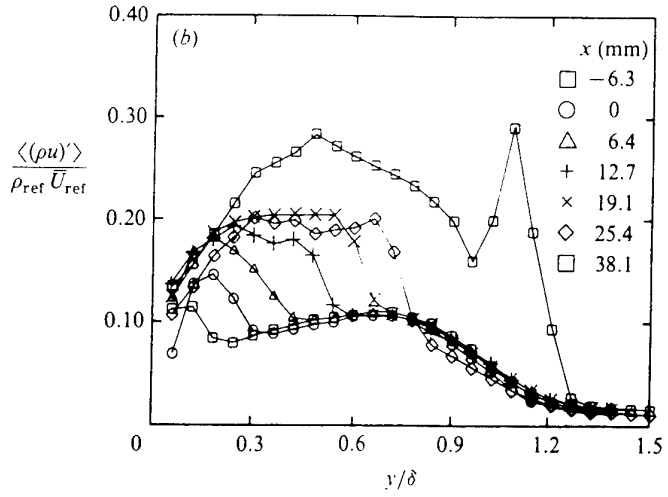

Figure 47: Distributions of $(\rho u)'$ in 16° compression-corner interaction, in the region near the corner. From Smits & Muck (1987).

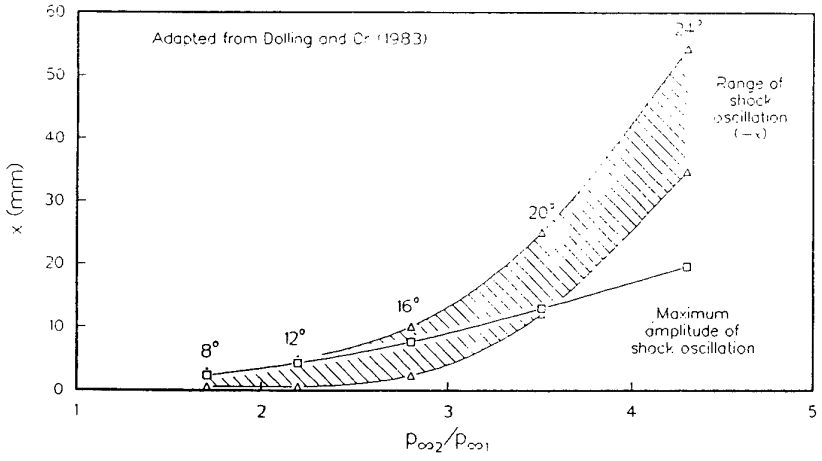

Figure 48: Range and amplitude of the shock oscillation for the Mach 2.9 compression-corner interactions examined by Dolling & Murphy (1983). From Selig *et al.* (1989).

high speeds (Daghsstani, 1993, Ripley & Pauley, 1993), and have some features in common with the perturbations seen in mixing layers. In particular, they involve low frequencies, or at least frequencies much lower than the characteristic frequency of a boundary layer of the same thickness. Other experimental evidence favors this picture also. For example, measurements of turbulence downstream of the reattachment have show a strongly perturbed outer-layer intermittency, and schlieren images triggered by a hot wire detecting the occurrence sharp fronts in the mass-flux signal very clearly showed the presence of radiation by Mach waves (Smith, 1989). Again, these visualizations are perhaps among the few which suggest the emission of shocklets in a distorted boundary layer at supersonic speeds. In recent unpublished work at Princeton, shocklets have been seen emanating from the large-scale motions in a Mach 8 boundary layer, but the evidence for their presence in wall-bounded flows at lower Mach numbers is scarce. Since the space-time characteristics of equilibrium boundary layers indicate that the large-scale structures in this flow produce only weak Mach waves at supersonic speeds, we have to suppose that there are eddies with large velocity fluctuations which are convected at a speed that is supersonic with respect to the external flow. This is consistent with the conjecture that large-scale perturbations are produced in the mixing zone over the separated bubble (see also Selig & Smits, 1991). The low frequency unsteadiness which they produce is the downstream condition imposed on the shock and thereby makes it move. This could explain why the shock motion occurs at frequencies typically an order-of-magnitude below the characteristic frequency of the boundary layer. Selig & Smits have also supposed that Taylor-Görtler vortices produced by the concave streamline contribute to the perturbation. Ünalmis & Dolling (1996) in a Mach 5 blunt-fin interaction found a significant level of correlation between the shock foot position and the ensemble-averaged total pressure well upstream of the interaction. The frequency of these events was lower than the typical frequency content of the large-scale motions, and suggest some long-term variations in the incoming boundary layer. They proposed that these variations are consistent with the presence of unsteady Taylor-Görtler vortices, possibly produced by the concave curvature in the nozzle, since the measurements were made in the nozzle wall boundary layer. The last conclusion is that the return to equilibrium of the boundary layer downstream of reattachment probably depends on the way that the perturbations shed by the separated bubble into the wall layer lose their identity, through the process by which they lose energy through acoustic losses and interact with the new structures generated near the wall.

To study the reattachment region more closely, Settles *et al.* (1982), Haya-kawa *et al.* (1984), Poggie *et al.* (1992), Shen *et al.* (1993) and Poggie (1995) conducted experiments in a backward-facing step flow where the separation point was fixed, and a relatively large recirculation zone was formed. The freestream Mach number was 2.9. The reattachment occurred on a 20° ramp, and the ramp was adjusted so that the upstream boundary layer separated without deflection. The pressure fluctuations on the ramp reached very high levels, and a peak value equal to about 11 percent of the local mean wall pressure was found just downstream of the mean reattachment line. Multiple shocks were observed in this region, interacting in complex patterns. Shocks typically formed at the upstream edges of the large-scale structures in the reattaching shear layer and redeveloping boundary layer. Double-pulsed Rayleigh scattering images showed the formation and progressive strengthening of these shocks as the structures convected through the reattachment zone (figure 49). The spectra of the wall-pressure did not display the low-frequency peak commonly observed in compression-corner interactions, supporting the notion that it is the expansion and contraction of the separation bubble that is responsible for low-frequency shock motion in those flows. In the case of the reattaching shear layer, it is the incoming turbulence that is the primary cause for the shock motion and the intense levels of fluctuating pressure that occur near the mean reattachment line.

Finally, measurements of the heat transfer in a 16° compression-corner interaction at Mach 2.84 demonstrate that the Reynolds analogy factor s, the ratio of the Stanton number to the skin friction coefficient, strongly deviates from a constant value in the region downstream of the interaction. Evans & Smits (1996) found that s initially increased by a factor of about three, relaxed quickly to a value equal to twice its upstream value at a distance $3\delta_0$ from of the corner, and then showed no obvious signs of further relaxation further downstream.

6 Summary

These notes have attempted to summarize the current literature on turbulent boundary-layer behavior at supersonic speed. The emphasis has been on Reynolds-number effects and Mach-number effects. A major drawback of the current understanding of these effects is that the data have been collected from many different flows, using different data acquisition and analysis procedures. These differences have resulted in large variations among the published results. Nevertheless, some definite conclusions can be made.

From the review of flat plate turbulent boundary layers in supersonic flows with moderate Mach number, it appears that the direct effects of compressibility on wall turbulence are rather small: the most notable differences between subsonic and supersonic boundary layers may be attributed to the variation in fluid properties across the layer. Under the assumption that the length scales are not affected by compressibility, the mean velocity profile can be transformed into an "equivalent" incompressible profile, and the agreement with the incompressible scaling appears to hold over very wide Reynolds number and Mach number ranges. Furthermore, the turbulent stresses in the outer region scale on the wall stress, as first suggested by Morkovin (1962), as far as we can tell from the available data. This result is not surprising in some ways since the fluctuating Mach number ($M' = M - \overline{M}$) for moderately supersonic flows is considerably less than one, as illustrated in figure 3. However, a more detailed inspection of the turbulence properties reveals certain characteristics that cannot be collapsed by a simple density scaling. For example, there are suggestions that the shear correlation coefficient R_{uv} decreases with distance from the wall instead of remaining approximately constant as in the

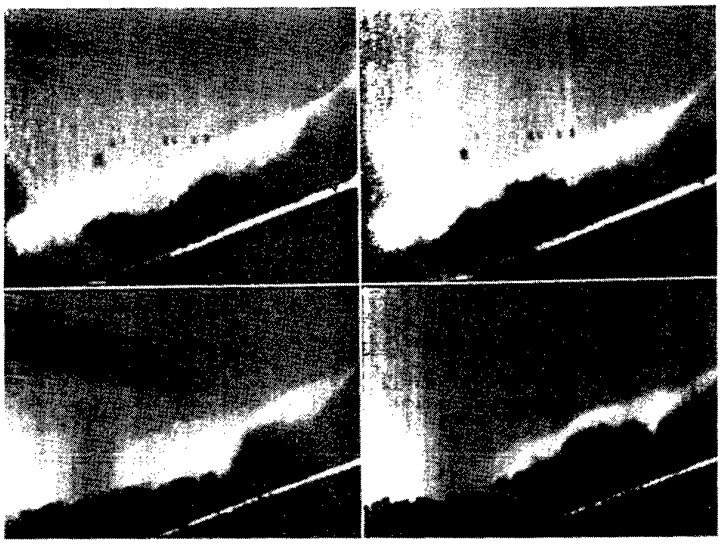

Figure 49: Rayleigh scattering flow visualization of a reattaching shear layer. The incoming flow is a free shear layer formed by a backward-facing step, with a freestream Mach number of 2.9. The visualization is just downstream of attachment which takes place on a 20° ramp. The flow is along the ramp, from left to right. The shocklets are visible as bright fronts, shrouding the darker large-scale features in the boundary layer. From Poggie (1995).

subsonic case. There are other results, however, which indicate that R_{uv} follows the incompressible trend, and there is the possibility that the differences may be caused by a Reynolds-number rather than a Mach-number dependence. Similarly, earlier data indicated a Mach number dependence of the intermittency distribution but recent measurements by Baumgartner *et al.* (1997) based on Rayleigh scattering images of a Mach 8 boundary layer (as shown in figure 17) indicate very good agreement with the subsonic intermittency distribution measured by Klebanoff (1955), suggesting that the earlier results may be flawed in some way. Unfortunately the data base is very sparse, and considerable effort needs to be spent before these issues can be laid to rest.

With respect to the streamwise and spanwise length scales of the large-scale motions, and their average inclination to the wall, there exists strong evidence to indicate the effect of Mach number. The streamwise length scales are reduced significantly by increasing Mach number, and the angle of inclination is increased, although in coming to these conclusions we have implicitly assumed that Mach and Reynolds number effects are independent. It is necessary to make this assumption since the data do not overlap to any significant extent, and we are forced to compare experiments in supersonic flow with the results obtained in subsonic flow, usually at a different Reynolds number. In fact, the actual Reynolds number to be used in such a comparison is controversial, since the temperature varies significantly across the layer, and there is usually a major difference between the values of Re_θ and $R_{\delta 2}$. Finally, there is an order-of-magnitude decrease in the rate of decay of the large-scale motions as the Mach number increases from low-subsonic to high supersonic values (Smits *et al.*, 1989). Even if we account for the change in time scale of the energy-containing eddies Λ/u', we see that the lateral correlations are almost unaffected by changes in Mach and Reynolds number.

For the cases with both adverse pressure-gradients and concave streamline-curvature, the changes in the turbulence structure (as inferred from the trends in the Reynolds shear-stress) appear to be strongly tied to the magnitude of the impulses due to curvature. This holds true for the weak and strong distortions considered here. If the radius of curvature of the turning was small enough, a shock wave forms in the boundary layer, and the streamwise stress increased with increasing shock strength. If the pressure gradients were not strong enough to separate the layer, the shock wave seemed to exert no additional effect on the shear stress over and above the changes that could be attributed to streamline curvature (or the equivalent compression).

In the flows with rapid, favorable pressure-gradients and convex curvature, it appears that the initial response of the boundary layer turbulence is dominated by the effects of the bulk dilatation, and the effects of convex curvature are always small. That is, the turbulence initially changes in response to the pressure gradient as would be expected using the conservation of circulation (we can largely ignore the effects of compressibility on relative motions because the Mach number gradients in the outer layer are usually small). The effect of bulk dilatation on the turbulence (expressed as an impulse) is not a strong function of the pressure gradient, indicating that it is the overall pressure change which is important. In contrast, the relaxation behavior appeared to be largely controlled by the

streamline curvature history. However, these observations were made in a boundary layer downstream of two successive distortions where the effect of curvature appeared to be greatly augmented by the amplification of the stresses downstream of the first distortion. The relaxation behavior is similar to the second-order response seen by Smits *et al.* (1979b) in an incompressible turbulent boundary layer downstream of an impulse of curvature. In addition, the behavior of the shear stress was similar to that observed by So & Mellor (1973) in a boundary layer developing over a surface with prolonged surface curvature in incompressible flow. What has not been explained is the observation that in the outermost part of the boundary layer there was no change in the streamwise stress from its undisturbed profile even though it is in this region where the principal strain-rate $\partial U/\partial y$ is small and that the effect of the extra strain-rates should be felt most strongly.

Overall, it appears that the boundary layer response to curvature in a supersonic flow is similar to the response in subsonic flow, even to the appearance of a dip below the log-law in the mean velocity profile as a response to any significant amount of concave streamline curvature. More specifically, in the case of a single impulse of curvature, we expect to observe the same counter-intuitive trends in the Reynolds stress behavior as observed by Smits *et al.* in subsonic flow, where a stabilizing distortion (an impulse in convex curvature) caused an increase in turbulence activity and a destabilizing distortion (an impulse in concave curvature) caused a decrease.

Compressibility effects on the turbulence appear to be small, at least at supersonic speeds. In flows with concave or convex streamline curvature, Reynolds stress calculations using subsonic turbulence models by Degani & Smits (1990) were found to give reasonable predictions of Reynolds stress behavior, at least for distortions where the boundary layer did not depart too far from equilibrium. For these flows, the limitations of the calculation are probably due to the turbulence modeling, rather than any specific influence of compressibility, and the observations tend to support the turbulence structure similarity suggested by Morkovin's Hypothesis. For strong distortions, our predictive capability is confined to the initial response where linear theories such as RDA become useful.

For compression corner interactions we noted the unsteady shock motion, the appearance of separated flow regions, the presence of strong wall-pressure fluctuations, and strongly amplified turbulence levels.

By way of a final comment, we can make some remarks on the mechanism of the flowfield unsteadiness. As discussed earlier, the large-scale motions in the incoming boundary layer provide an unsteady upstream boundary condition on the separation shock. Conversely, the unsteady separated flow provides an unsteady downstream boundary condition. The wall pressure signal has low- and high-frequency content. As suggested by Brusniak & Dolling (1994), the incoming turbulence appears to be responsible for shock distortion and some small flapping motion, but it is not on a large scale. Its effect is most clearly seen in the wall-pressure signals and the instantaneous flow visualizations of unseparated compression-corner flows. When the flow is separated, the separation bubble unsteadiness can lead to larger excursions in the shock position, and the extent of the upstream influence seen in the mean pressure distribution grows considerably. There is still some question regarding the mechanism that drives the unsteadiness of the bubble. The free shear layer forming the edge of the bubble is undoubtedly very sensitive to external disturbances. These disturbances could come from, for instance, outer-layer turbulence which may provide a trigger for a flow-field instability similar to that seen in the supersonic flow over a spiked body. It may also be possible that the low-frequency oscillations of the separation bubble are tunnel-specific, in that they are related to meandering Taylor-Görtler-like vortices formed in the the upstream flow, convecting into the interaction, as suggested by Ünalmis & Dolling (1996). Further work will be necessary before more definite proposals can be made.

Acknowledgements

The support of the NATO Advisory Group for Aerospace Research and Development is gratefully acknowledged. The support received from the Air Force Office of Scientific Research, monitored by Drs. J. McMichael, L. Sakell and J. Tishkoff (F49620-89-0420, F49620-90-0217, F49620-93-1-0476, F49620-93-0064, F49620-93-1-0427 and F49620-93-1-0478) made this research possible.

References

Ackeret, J., Feldman, F. & Rott, N. 1946. Investigations of compression shocks and boundary layers in gases moving at high speed. *NASA TM 1113.*

Adamson, T.C. & Messiter, A.F. 1980. Analysis of two-dimensional interactions between shock waves and boundary layers. *Annual Review of Fluid Mechanics*, **12**, 103–138.

Allen, J.M. 1977. Reevaluation of compressible flow Preston tube calibrations. *NASA TM X-3488.*

Alving, A.E., Smits, A.J. & Watmuff, J.H. 1990b. Turbulent boundary layer relaxation from convex curvature. *Journal of Fluid Mechanics*, **211**, 529–556.

Antonia, R.A. & Luxton, R.E. 1971. The response of a boundary layer to a step change in surface roughness. Part 1 – Smooth to rough. *Journal of Fluid Mechanics*, **48**, 721–761.

Antonia, R.A. & Luxton, R.E. 1972. The response of a boundary layer to a step change in surface roughness. Part 2 – Rough to smooth. *Journal of Fluid Mechanics*, **53**, 737–757.

Antonia, R.A., Bisset, D.K. & Browne, L.W.B. 1990a. Effect of Reynolds number on the topology of the organized motion in a turbulent boundary layer. *Journal of Fluid Mechanics*, **213**, 267–286.

Antonia, R.A., Browne, L.W.B. & Bisset, D.K. 1990b. Effect of Reynolds number on the organized motion in a turbulent boundary layer. *In:* Kline, S.J. & Afgan, N.H. (eds), *Near Wall Turbulence.* Hemisphere.

Ardonceau, P.L. 1984. The structure of turbulence in a supersonic shock-wave/boundary-layer interaction. *AIAA Journal*, **22**, 1254–1262.

Audiffren, N. 1993. *Turbulence d'une couche limite soumise à une variation de densité due à une onde de choc ou à un chauffage pariétal.* Thèse d'Université, Université d'Aix-Marseille II.

Baumgartner, M.L., Erbland, P.J., Etz, M.R., Yalin, A., Muzas, B., Smits, A.J., Lempert, W. & Miles, R.B. 1997. Structure of a Mach 8 turbulent boundary layer. *AIAA Paper 97-0765.*

Beckwith, I.E. 1970. Recent advances in research on compressible turbulent boundary layers. *NASA SP-228, 355–416.*

Bertram, M.H. & Neal, L. 1965. Recent experiments in hypersonic turbulent boundary layers. *NASA TM X-56335.*

Bestion, D. 1982. *Méthodes anémomètriques par fil chaud: Application à l'étude d'interactions turbulence-gradient de pression élevé en couches limites à vitesse supersonique.* Thèse de Docteur-Ingénieur, Université d'Aix-Marseille II.

Bestion, D., Debiève, J.F. & Dussauge, J.P. 1983. Two rapid distortions in supersonic flows: Turbulence/shock wave and turbulence/expansion. *In:* Dumas, R. & Fulachier, L. (eds), *Structure of Complex Turbulent Shear Flow.* Springer Verlag.

Blackwelder, R.F. & Kaplan, R.E. 1976. On the wall structure of the turbulent boundary layer. *Journal of Fluid Mechanics*, **76**, 89.

Bonnet, J.P. 1988. Space-time correlations of wall-pressure fluctuations in shock-induced separated flows. *Physics of Fluids A*, **31**, 2821–2833.

Bradshaw, P. 1973. Effects of streamline curvature on turbulent flow. *AGARDograph 169.*

Bradshaw, P. 1974. The effect of mean compression or dilatation on the turbulence structure of supersonic boundary layers. *Journal of Fluid Mechanics*, **63**, 449–464.

Bradshaw, P. 1977. Compressible turbulent shear layers. *Annual Review of Fluid Mechanics*, **9**, 33–54.

Bradshaw, P. & Unsworth, K. 1974. Comment on "Evaluation of Preston tube calibration equations in supersonic flow". *AIAA Journal*, **12**, 1293–1296.

Brusniak, L. & Dolling, D.S. 1994. Physics of unsteady blunt-fin-induced shock wave/turbulent boundary layer interactions. *Journal of Fluid Mechanics*, **273**, 375–409.

Bushnell, D.M., Johnson, C.B., Harvey, W.D. & Feller, W.V. 1969. Comparison of prediction methods and studies of relaxation in hypersonic turbulent nozzle-wall boundary layers. *NASA TN D-5433.*

Bushnell, D.M., Cary, Jr., A.M. & Harris, J.E. 1976. Calculation methods for compressible turbulent boundary layers. State of the art. *NASA SP-422.*

Carvin, C., Debiève, J.F. & Smits, A.J. 1988. The near-wall temperature profile of turbulent boundary layers. *AIAA Paper 88-0136.*

Cebeci, T. & Smith, A.M.O. 1974. *Analysis of Turbulent Boundary Layers.* Academic Press.

Chapman, D.R., Kuehn, D.M. & Larson, H.K. 1957. Investigation of separated flows in supersonic and subsonic streams with emphasis on the effect of transition. *NASA TN 3869.* Also NACA Rep. 1356, 1958.

Clauser, F.H. 1954. Turbulent boundary layers in adverse pressure gradients. *Journal of the Aeronautical Sciences*, **21**, 91–108.

Clauser, F.H. 1956. The turbulent boundary layer. *In: Advances in Applied Mechanics*, vol. IV. Academic Press.

Cogne, S., Forkey, J., Miles, R.B. & Smits, A.J. 1993. The evolution of large-scale structures in a supersonic turbulent boundary layer. *In: Proc. of the Symposium on Transitional and Turbulent Compressible Flows.* ASME Fluids Engineering Division.

Coles, D. 1953. Measurements in the boundary layer on a smooth flat plate in supersonic flow. *J.P.L. CalTech. Reports 20-69, 20-70, 20-71.*

Coles, D. 1962. The turbulent boundary layer in a compressible fluid. *Report R-403-PR, The Rand Corporation, Santa Monica, California.*

Daghsstani, K. 1993. *Rôle des fluctuations de pression dans les interactions onde de choc/couche-limite.* Thèse de Doctorat, Université de Poitiers.

Debiève, J.F. 1982. Turbulent behaviour through a shock-wave. Turbulent macroscale evolution. *Arch. Mech., Warszawa*, **34**, 581–592.

Debiève, J.F. 1983. *Étude d'une interaction turbulence/onde de choc.* Thèse de Doctorat d'État, Université d'Aix-Marseille II.

Debiève, J.F. & Lacharme, J.P. 1985. A shock wave/free turbulence interaction. *In:* Délery, J. (ed), *Turbulent Shear-Layer/Shock-Wave Interactions.* Springer Verlag.

Debiève, J.F., Dupont, P., Smith, D.R. & Smits, A.J. 1996. The response of a supersonic turbulent boundary layer to a step change in wall temperature. *AIAA Journal.* To appear.

Degani, D. & Smits, A.J. 1990. Effect of short regions of surface curvature on compressible turbulent boundary layers. *AIAA Journal*, **28**, 113–119.

Délery, J.M. 1985. Shock wave/turbulent boundary-layer interaction and its control. *Progress in Aerospace Sciences*, **22**, 209–280.

Délery, J.M. 1992. Étude expérimentale de la réflexion d'une onde de choc sur une paroi chauffée en présence d'une couche limite turbulente. *La Recherche Aérospatiale*, **1**, 1–23.

Deleuze, J. & Eléna, M. 1995. Quelques caractéristiques de la turbulence en aval d'une interaction onde de choc couche limite. *12ème Congrès Français de Mécanique, Strasbourg, France.*

Demetriades, A. & Martindale, W.R. 1983. Determination of one dimensional spectra in high speed boundary layers. *The Physics of Fluids*, **26**, 397–403.

Dolling, D.S. 1990. Unsteady phenomena in shock wave/boundary layer interaction. *Pages 4.1-4.46 of: Special Course on Shock Wave/Boundary Layer Interactions in Supersonic and Hypersonic Flows.* AGARD Report 792.

Dolling, D.S. 1993. Fluctuating loads in shock wave/turbulent boundary layer interaction: Tutorial and update. *AIAA Paper 93-0284.*

Dolling, D.S. & Dussauge, J.P. 1989. Fluctuating wall pressure measurements. *Chapter 8, AGARDograph 315.*

Dolling, D.S. & Murphy, M.T. 1983. Unsteadiness of the separation shock wave structure in a supersonic com-

pressible ramp flowfield. *AIAA Journal*, **21**, 1628–1634.

Donovan, J.F. 1989. *The structure of supersonic turbulent boundary layers subjected to concave surface curvature.* Ph.D. Thesis, Princeton University, Princeton, NJ.

Donovan, J.F., Spina, E.F. & Smits, A.J. 1994. The structure of a supersonic turbulent boundary layer subjected to concave surface curvature. *Journal of Fluid Mechanics*, **259**, 1–24.

Dussauge, J.P. 1981. *Évolution de transferts turbulents dans une détente rapide, en écoulement supersonique.* Thèse de Doctorat d'État, Université d'Aix Marseille.

Dussauge, J.P. & Gaviglio, J. 1987. The rapid expansion of a supersonic turbulent flow: Role of bulk dilatation. *Journal of Fluid Mechanics*, **174**, 81–112.

Dussauge, J.P. & Smits, A.J. 1995. Characteristic scales for energetic eddies in turbulent supersonic boundary layers. *In: Proceedings of the Tenth Symposium on Turbulent Shear Flows.* Pennsylvania State University.

Dussauge, J.P., Debiève, J.F. & Smits, A.J. 1989. Rapidly distorted compressible boundary-layers. *Chapter 2, AGARDograph 315.*

Dussauge, J.P., Fernholz, H., Finley, P.J., Smith, R.W., Smits, A.J. & Spina, E.F. 1996. Turbulent boundary layers in subsonic and supersonic flow. *AGARDograph 335.*

Eléna, M. & Gaviglio, J. 1993. La couche limite turbulente compressible: Méthodes D'étude et Résultats, synthèse. *La Recherche Aérospatiale*, 1–21.

Eléna, M. & Lacharme, J.P. 1988. Experimental study of a supersonic turbulent boundary layer using a laser Doppler anemometer. *Journal Mécanique Théorique et Appliquée*, **7**, 175–190.

Evans, T.T. & Smits, A.J. 1996. Measurements of the mean heat transfer in a shock wave-turbulent boundary layer interaction. *Experimental Thermal and Fluid Science*, **12**, 87–97.

Falco, R.E. 1977. Coherent motions in the outer region of turbulent boundary layers. *The Physics of Fluids*, **20**, S124–S132.

Favre, A. 1965. Equations des gaz turbulents compressibles. *Journal de Mécanique*, **4**, 361–421.

Favre, A.J., Gaviglio, J.J. & Dumas, R.J. 1957. Space-time double correlations and spectra in a turbulent boundary layer. *Journal of Fluid Mechanics*, **2**, 313–342.

Favre, A.J., Gaviglio, J.J. & Dumas, R.J. 1958. Further space-time correlations of velocity in a turbulent boundary layer. *Journal of Fluid Mechanics*, **3**, 344–356.

Feller, W.V. 1973. Effects of upstream wall temperatures on hypersonic tunnel wall boundary-layer profile measurements. *AIAA Journal*, **11**, 556–558.

Fernando, E.M. & Smits, A.J. 1990. A supersonic turbulent boundary layer in an adverse pressure gradient. *Journal of Fluid Mechanics*, **211**, 285–307.

Fernholz, H.H. 1969. Geschwindigkeitsprofile, Temperaturprofile und halbempirische Gesetze in kompressiblen turbulenten Grenzschichten bei konstantem Druck. *Ing. Archiv*, **38**, 311–328.

Fernholz, H.H. 1971. Ein halbempirisches Gesetz für die Wandreibung in kompressiblen turbulenten Grenzschichten bei isothermer und adiabater Wand. *ZAMM*, **51**, T148–T149.

Fernholz, H.H. & Finley, P.J. 1976. A critical compilation of compressible turbulent boundary layer data. *AGARDograph 223.*

Fernholz, H.H. & Finley, P.J. 1980. A critical commentary on mean flow data for two-dimensional compressible turbulent boundary layers. *AGARDograph 253.*

Fernholz, H.H. & Finley, P.J. 1981. A further compilation of compressible turbulent boundary layer data with a survey of turbulence data. *AGARDograph 263.*

Fernholz, H.H., Smits, A.J., Dussauge, J.P. & Finley, P.J. 1989. A survey of measurements and measuring techniques in rapidly distorted compressible turbulent boundary layers. *AGARDograph 315.*

Fernholz, H.H., Krause, E., Nockemann, N. & Schober, M. 1995. Comparative measurements in the canonical boundary layer at $Re_{\delta_2} \leq 6x10^4$ on the wall of the German-Dutch windtunnel. *The Physics of Fluids*, **7**, 1275–1281.

Finley, P.J. 1977. Static pressure in hypersonic nozzle boundary layers. *AIAA Journal*, **15**, 878–881.

Finley, P.J. 1994. The Preston tube in adiabatic compressible flow. *Report 94-02, Imperial College of Science and Technology, Department of Aeronautics.*

Forkey, J.N., Cogne, S., Smits, A.J., Bogdonoff, S.M., Lempert, W.R. & Miles, R.B. 1993. Time-sequenced and spectrally filtered Rayleigh imaging of shock wave and boundary layer structure for inlet characterization. *AIAA Paper 93-2300.*

Fulachier, L. 1972. *Contribution à l'étude des analogies des champs dynamiques et thermiques dans une couche limite turbulente. Effet de l'aspiration.* Thèse de Doctorat ès Sciences Physiques, Université de Provence, Aix-Marseille.

Gaviglio, J. 1987. Reynolds analogies and experimental study of heat transfer in the supersonic boundary layer. *International Journal of Heat and Mass Transfer*, **30**, 911–926.

Gramann, R.A. & Dolling, D.S. 1988. Detection of turbulent boundary layer separation using fluctuating wall pressure signals. *AIAA Paper 88-4676.*

Gramann, R.A. & Dolling, D.S. 1992. A preliminary study of turbulent structures associated with unsteady separation shock motion in a Mach 5 compression ramp interaction. *AIAA Paper 92-0744.*

Green, J.E. 1970. Interaction between shock waves and turbulent boundary layers. *Progress in Aerospace Sciences*, **11**, 235–340.

Hayakawa, K., Smits, A.J. & Bogdonoff, S.M. 1983. Turbulence measurements in two shock-wave/shear-layer interactions. *In:* Dumas, R. & Fulachier, L. (eds), *Structure of Complex Turbulent Shear Flow.* Springer Verlag.

Hayakawa, K., Smits, A.J. & Bogdonoff, S.M. 1984. Turbulence measurements in a compressible reattaching shear layer. *AIAA Journal*, **22**, 889–895.

Head, M.R. & Bandyopadhyay, P.R. 1981. New aspects of turbulent boundary-layer structure. *Journal of Fluid Mechanics*, **107**, 297–338.

Hinze, J.O. 1975. *Turbulence.* 2 edn. McGraw-Hill.

Hopkins, E.J. & Keener, E.R. 1966. Study of surface Pitots for measuring turbulent skin friction at su-

personic Mach numbers — Adiabatic wall. *NASA TN D-3478.*

Hopkins, E.J. & Keener, E.R. 1972. Pressure-gradient effects on hypersonic turbulent skin-friction and boundary-layer profiles. *AIAA Journal*, **10**, 1141–1142.

Hopkins, E.J., Keener, E.R., Polek, T.E. & Dwyer, H.A. 1972. Hypersonic turbulent skin-friction and boundary-layer profiles on nonadiabatic flat plates. *AIAA Journal*, **10**, 40–48.

Horstman, C.C. & Owen, F.K. 1972. Turbulent properties of a compressible boundary layer. *AIAA Journal*, **10**, 1418–1424.

Howarth, L. (ed). 1953. *Modern Developments in Fluid Dynamics, High Speed Flow.* Oxford Clarendon Press.

Jayaram, M., Taylor, M.W. & Smits, A.J. 1987. The response of a compressible turbulent boundary layer to short regions of concave surface curvature. *Journal of Fluid Mechanics*, **175**, 343–362.

Jayaram, M., Donovan, J.F., Dussauge, J.-P. & Smits, A.J. 1989. Analysis of a rapidly distorted, supersonic turbulent boundary layer. *Physics of Fluids A*, **1**, 1855–1864.

Johnson, A.W. 1993. *Laminarization and retransition of turbulent boundary layers in supersonic flow.* Ph.D. Thesis, Yale University, New Haven, CT.

Johnson, D.A. 1989. Laser Doppler anemometry. *Chapter 6, AGARDograph 315.*

Johnson, D.A. & Rose, W.C. 1975. Laser velocimeter and hot-wire anemometer comparison in a supersonic boundary layer. *AIAA Journal*, **13**, 512–515.

Kemp, J.H. & Owen, F.K. 1972. Nozzle wall boundary layers at Mach numbers 20 to 47. *AIAA Journal*, **10**, 872–879.

Kim, J. & Spalart, P.R. 1987. Scaling of the bursting frequency in turbulent boundary layers at low Reynolds numbers. *Physics of Fluids*, **30**.

Kim, K.S., Lee, Y. & Settles, G.S. 1991. Laser interferometry/Preston tube skin-friction comparison in a shock/boundary layer interaction. *AIAA Journal*, **29**, 1007–1009.

Kistler, A.L. 1959. Fluctuation measurements in a supersonic turbulent boundary layer. *Physics of Fluids*, **2**, 290–296.

Klebanoff, P.S. 1955. Characteristics of turbulence in a boundary layer with zero pressure gradient. *NACA Report 1247.*

Konrad, W. 1993. *A three-dimensional supersonic turbulent boundary layer generated by an isentropic compression.* Ph.D. Thesis, Princeton University, Princeton, NJ.

Korkegi, R.H. 1971. Survey of viscous interactions associated with high Mach number flight. *AIAA Journal*, **9**, 771–784.

Kovasznay, L.S.G. 1953. Turbulence in supersonic flow. *Journal of the Aeronautical Sciences*, **20**, 657–674 (cont. 682).

Kubota, T. & Berg, D.E. 1977. Surface roughness effects on the hypersonic turbulent boundary layer. *Report AD A 042141, California Institute of Technology, Pasadena, California.*

Kuntz, D.W., Amatucci, V.A. & Addy, A.L. 1987. Turbulent boundary-layer properties downstream of the shock-wave/boundary-layer interaction. *AIAA Journal*, **25**, 668–675.

Kussoy, M.I. & Horstman, C.C. 1975. An experimental documentation of a hypersonic shock-wave/turbulent boundary layer interaction flow — with and without separation. *NASA TMX-62412.*

Kussoy, M.I., Horstman, C.C. & Acharya, M. 1978. An experimental documentation of pressure gradient and Reynolds number effects on compressible turbulent boundary layers. *NASA TM 78488.*

Laderman, A.J. & Demetriades, A. 1974. Mean and fluctuating flow measurements in the hypersonic boundary layer over a cooled wall. *Journal of Fluid Mechanics*, **63**, 121–144.

Laufer, J. 1961. Aerodynamic noise in supersonic wind tunnels. *Journal of the Aerospace Sciences*, **28**, 685–692.

Law, C.H. 1975. Two-dimensional compression corner and planar shock wave interactions with a supersonic, turbulent boundary layer. *Rep. ARL 75-0157, Aerospace Research Laboratories, Wright-Patterson AFB.*

Lele, S.K. 1994. Compressibility effects on turbulence. *Annual Review of Fluid Mechanics*, **26**, 211–254.

Liepmann, H.W. 1946. The interaction between boundary layer and shock waves in transonic flow. *Journal of the Aeronautical Sciences*, **13**, 623–637.

Liepmann, H.W., Roshko, A. & Dhawan, S. 1951. On reflection of shock waves from boundary layers. *NACA TN 2334.* Also NACA Report 1100, 1952.

Logan, P. 1987. *Studies of supersonic turbulence and hot wire response using laser-induced fluorescence.* Ph.D. Thesis, Stanford University. 154 pp.

Mabey, D.G., Meier, H.U. & Sawyer, W.G. 1974. Experimental and theoretical studies of the boundary layer on a flat plate at Mach numbers from 2.5 to 4.5. *RAE TR 74127.*

Maise, G. & McDonald, H. 1968. Mixing length and kinematic eddy viscosity in a compressible boundary layer. *AIAA Journal*, **6**, 73–80.

Mathews, D.C., Childs, M.E. & Paynter, G.C. 1970. Use of Coles' universal wake function for compressible turbulent boundary layers. *Journal of Aircraft*, **7**, 137–140.

McGinley, C.B., Spina, E.F. & Sheplak, M. 1994. Turbulence measurements in a Mach 11 helium boundary layer. *AIAA Paper 94-2364.*

Meier, H.U. & Rotta, J.C. 1971. Temperature distributions in supersonic turbulent boundary layers. *AIAA Journal*, **9**, 2149–2156.

Michel, R., Quemard, C. & Durand, R. 1969. Application d'un schéma de longueur de mélange à l'étude des couches limites turbulentes d'équilibre. *ONERA NT.154.*

Mikulla, V. & Horstman, C.C. 1975. Turbulence stress measurements in a non-adiabatic hypersonic boundary layer. *AIAA Journal*, **13**, 1607–1613.

Miles, R.B. & Nosenchuck, D.M. 1989. Three-dimensional quantitative flow diagnostics. *Pages 33–107 of:* Gad-el-Hak, M. (ed), *Lecture Notes in Engineering, Advances in Fluid Mechanics Measurements*, vol. 45. Springer-Verlag.

Morkovin, M.V. 1955. Effects of high acceleration on a turbulent supersonic shear layer. *In: Proceedings of*

the 1955 Heat Transfer and Fluid Mechanics Institute. Stanford University Press.

Morkovin, M.V. 1962. Effects of compressibility on turbulent flows. *Pages 367–380 of:* Favre, A.J. (ed), *Mécanique de la Turbulence.* CNRS.

Morkovin, M.V. 1992. Mach number effects on free and wall turbulent structures in light of instability flow interactions. *Pages 269–284 of:* Gatski, T.B., Sarkar, S. & Speziale, C.G. (eds), *Studies in Turbulence.* Springer Verlag.

Morkovin, M.V. & Phinney, R.E. 1958. Extended applications of hot wire anemometry to high-speed turbulent boundary layers. *Johns Hopkins University, Baltimore, MD, Report AFOSR TN-58-469.*

Muck, K.C., Dussauge, J.P. & Bogdonoff, S.M. 1985. Structure of the wall pressure fluctuations in a shock-induced separated turbulent flow. *AIAA Paper 85-0179.*

Muck, K.C., Andreopoulos, J. & Dussauge, J.P. 1988. Unsteady nature of shock wave/turbulent boundary layer interaction. *AIAA Journal*, **26**, 179–197.

Owen, F.K. 1990. Turbulence and shear stress measurements in hypersonic flow. *AIAA Paper 90-1394.*

Owen, F.K. & Horstman, C.C. 1972. On the structure of hypersonic turbulent boundary layers. *Journal of Fluid Mechanics*, **53**, 611–636.

Owen, F.K., Horstman, C.C. & Kussoy, M.I. 1975. Mean and fluctuating flow measurements of a fully-developed, non-adiabatic, hypersonic boundary layer. *Journal of Fluid Mechanics*, **70**, 393–413.

Patel, V.C. 1965. Calibration of the Preston tube and limitations on its use in pressure gradients. *Journal of Fluid Mechanics*, **23**, 185–208.

Peake, D.J. & Tobak, M. 1980. Three-dimensional interactions and vortical flows with emphasis on high speeds. *NASA TM 81169.*

Perry, A.E., Henbest, S. & Chong, M.S. 1986. A theoretical and experimental study of wall turbulence. *Journal of Fluid Mechanics*, **165**, 163–199.

Poggie, J. 1995. *On the control of a compressible, reattaching shear layer.* Ph.D. Thesis, Princeton University.

Poggie, J., Smits, A.J. & Glezer, A. 1992. The dynamics and control of fluctuating pressure loads in the reattachment region of a supersonic free shear layer. *AIAA Paper 92-0178.*

Ripley, M.D. & Pauley, L.L. 1993. The unsteady structure of two-dimensional steady laminar separation. *Physics of Fluids A*, **5**, 3099–3106.

Robinson, S.K. 1983. Hot-wire and laser Doppler anemometer measurements in a supersonic boundary layer. *AIAA Paper 83-1723.*

Robinson, S.K. 1986. Space-time correlation measurements in a compressible turbulent boundary layer. *AIAA Paper 86-1130.*

Rose, W.C. 1973. The behavior of a compressible turbulent boundary layer in a shock wave induced adverse pressure gradient. *NASA TN D-7092.*

Rose, W.C. & Johnson, D.A. 1975. Turbulence in a shock-wave boundary-layer interaction. *AIAA Journal*, **13**, 884–889.

Roshko, A. & Thomke, G.J. 1966. Observations of turbulent reattachment behind an axisymmetric downstream-facing step in supersonic flow. *AIAA Journal*, **4**, 975–980.

Rotta, J.C. 1950. Über die Theorie der turbulenten Grenzschichten. *Mitteilung Max Planck Institut für Strömungs Forschung, No. 1.* English translation NACA TM 1344.

Rotta, J.C. 1960. Turbulent boundary layers with heat transfer in compressible flow. *NATO AGARD 281.*

Rubesin, M.W. & Rose, W.C. 1973. The turbulent mean-flow, Reynolds-stress, and heat-flux equations in mass- averaged dependent variables. *NASA TM X-62248.*

Sandborn, V.A. 1974. A review of turbulence measurements in compressible flow. *NASA TR X-62337.*

Schlichting, H. 1979. *Boundary-Layer Theory.* 7th edn. McGraw-Hill.

Schneider, W. 1974. Upstream propagation of unsteady disturbances in supersonic boundary layers. *Journal of Fluid Mechanics*, **63**, 465–485.

Schubauer, G.B. & Tchen, C.M. 1959. Turbulent flow. *Pages 75–195 of:* Lin, C.C. (ed), *Turbulent Flows and Heat Transfer.* High-Speed Aerodynamics and Jet Propulsion, vol. V. Princeton University Press.

Selig, M.S. & Smits, A.J. 1991. Effect of periodic blowing on attached and separated supersonic turbulent boundary layers. *AIAA Journal*, **29**, 1651–1658.

Selig, M.S., Andreopoulos, J., Muck, K.C., Dussauge, J.P. & Smits, A.J. 1989. Turbulence structure in a shock wave/turbulent boundary-layer interaction. *AIAA Journal*, **27**, 862–869.

Settles, G.S. & Dolling, D.S. 1990. Swept shock/boundary layer interactions — Tutorial and update. *AIAA Paper 90-0375.*

Settles, G.S. & Dolling, D.S. 1992. Swept shock wave boundary layer interaction. *AIAA Progress Series: Volume on Tactical Missile Aerodynamics*, **141**, 505–74.

Settles, G.S. & Teng, H.Y. 1984. Cylindrical and conical upstream influence regimes of three-dimensional shock/turbulent boundary layer interactions. *AIAA Journal*, **22**, 194–200.

Settles, G.S., Fitzpatrick, T.J. & Bogdonoff, S.M. 1979a. Detailed study of attached and separated compression corner flowfields in high Reynolds number supersonic flow. *AIAA Journal*, **17**, 579–585.

Settles, G.S., Baca, B.K., Williams, D.R. & Bogdonoff, S.M. 1982. Reattachment of a compressible turbulent shear layer. *AIAA Journal*, **20**, 60–67.

Shen, Z.H., Smith, D.R. & Smits, A.J. 1993. Wall pressure fluctuations in the reattachment region of a supersonic free shear layer. *Experiments in Fluids*, **14**, 10–16.

Simpson, R.L. 1981. A review of some phenomena in turbulent flow separation. *Journal of Fluids Engineering*, **102**, 520–533.

Sirieix, M. 1975. Décollement turbulent en 'ecoulement bidimensionnel. *In: Flow Separation.* AGARD CP-168, Paper 12.

Smith, A.M.O. 1955. On the growth of Taylor-Görtler vortices along highly concave walls. *Quarterly Journal of Applied Mathematics*, **13**, 233–262.

Smith, D.R. 1993. *The effects of successive distortions on a turbulent boundary layer in a supersonic flow.* Ph.D. Thesis, Princeton University.

Smith, D.R. & Smits, A.J. 1991a. The rapid expansion

of a turbulent boundary layer in a supersonic flow. *Theoretical and Computational Fluid Dynamics*, **2**, 319–328.

Smith, D.R. & Smits, A.J. 1993a. The simultaneous measurement of velocity and temperature fluctuations in the boundary layer of a supersonic flow. *Experimental Thermal and Fluid Science*, **7**, 221–229.

Smith, D.R. & Smits, A.J. 1993b. Multiple distortions of a supersonic turbulent boundary layer. *Applied Scientific Research*, **51**, 223–229.

Smith, D.R. & Smits, A.J. 1994. The effects of streamline curvature and pressure gradient on the behavior of turbulent boundary layers in supersonic flow. *AIAA Paper 94-2227.*

Smith, D.R. & Smits, A.J. 1996. A study of the effects of curvature and compression on the behavior of a supersonic turbulent boundary layer. *Experiments in Fluids.* To appear.

Smith, D.R., Fernando, E.M., Donovan, J.F. & Smits, A.J. 1992. Conventional skin friction measurement techniques for strongly perturbed supersonic turbulent boundary layers. *European Journal of Mechanics, B/Fluids*, **11**, 719–740.

Smith, M.W. 1989. *Flow visualization in supersonic turbulent boundary layers.* Ph.D. Thesis, Princeton University.

Smith, M.W. & Smits, A.J. 1988. Cinematic visualization of coherent density structures in a supersonic turbulent boundary layer. *AIAA Paper 88-0500.*

Smith, M.W., Smits, A.J. & Miles, R.B. 1989. Compressible boundary-layer density cross sections by UV Rayleigh scattering. *Optics Letters*, **14**, 916–918.

Smith, R.W. 1994. *Effect of Reynolds number on the structure of turbulent boundary layers.* Ph.D. Thesis, Princeton University.

Smith, R.W. & Smits, A.J. 1991b. Effect of Reynolds number on the large structure of turbulent boundary layers. *AIAA Paper 91-0526.*

Smits, A.J. & Dussauge, J.-P. 1989. Hot-wire anemometry in supersonic flow. *Chapter 5, AGARDograph 315.*

Smits, A.J. & Dussauge, J.P. 1996. *Turbulent Shear Layers in Supersonic Flow.* AIP Press.

Smits, A.J. & Muck, K.-C. 1984. Constant-temperature hot-wire anemometer practice in supersonic flows. Part 2: The inclined wire. *Experiments in Fluids*, **2**, 33–41.

Smits, A.J. & Muck, K.-C. 1987. Experimental study of three shock wave/turbulent boundary layer interactions. *Journal of Fluid Mechanics*, **182**, 291–314.

Smits, A.J. & Wood, D.H. 1985. The response of turbulent boundary layers to sudden perturbations. *Annual Review of Fluid Mechanics*, **17**, 321–358.

Smits, A.J., Eaton, J.A. & Bradshaw, P. 1979a. The response of a turbulent boundary layer to lateral divergence. *Journal of Fluid Mechanics*, **94**, 243–268.

Smits, A.J., Young, S.T.B. & Bradshaw, P. 1979b. The effect of short regions of high surface curvature on turbulent boundary layers. *Journal of Fluid Mechanics*, **94**, 209–242.

Smits, A.J., Spina, E.F., Alving, A.E., Smith., R.W., Fernando, E.M. & Donovan, J.F. 1989. A comparison of the turbulence structure of subsonic and supersonic boundary layers. *Physics of Fluids A*, **1**, 1865–1875.

So, R.M.C. & Mellor, G.L. 1973. Experiment on convex curvature effects in turbulent boundary layers. *Journal of Fluid Mechanics*, **60**, 43–62.

Spina, E.F. 1988. *Organized structures in a supersonic turbulent boundary layer.* Ph.D. Thesis, Princeton University.

Spina, E.F. & Smits, A.J. 1987. Organized structures in a compressible turbulent boundary layer. *Journal of Fluid Mechanics*, **182**, 85–109.

Spina, E.F., Donovan, J.F. & Smits, A.J. 1991a. On the structure of high-Reynolds-number supersonic turbulent boundary layers. *Journal of Fluid Mechanics*, **222**, 293–327.

Spina, E.F., Donovan, J.F. & Smits, A.J. 1991b. Convection velocity in supersonic turbulent boundary layers. *Physics of Fluids A*, **3**, 3124–3126.

Spina, E.F., Smits, A.J. & Robinson, S.K. 1994. The physics of supersonic turbulent boundary layers. *Annual Review of Fluid Mechanics*, **26**, 287–319.

Stalmach, C.J. 1958. Experimental investigation of the surface impact probe method of measuring local skin friction at supersonic speed. *Univ. of Texas Report DRL-410, CF 2675.*

Stanewski, E. 1973. Shock-boundary layer interaction in transonic and supersonic flow. *In: Transonic Flows in Turbomachinery.* Von Kármán Institute, Rhodes-Saint-Genèse, Belgium, Lecture Series 59.

Tani, I. 1962. Production of longitudinal vortices in the boundary layer along a concave wall. *Journal of Geophysical Research*, **67**, 3075.

Townsend, A.A. 1976. *The Structure of Turbulent Shear Flow.* 2 edn. Cambridge University Press.

Tran, T.T. 1987. *An experimental investigation of unsteadiness in swept shock wave/turbulent boundary layer interactions.* Ph.D. Thesis, Princeton University.

Uddin, A.K.M. 1994. *The structure of a turbulent boundary layer.* Ph.D. Thesis, University of Melbourne.

Ünalmis, Ö.H. & Dolling, D.S. 1996. On the possible relationship between low frequency unsteadiness of shock-induced separated flow and Görtler vortices. *27th AIAA Fluid Dynamics Conference.* To be presented.

van Driest, E.R. 1951. Turbulent boundary layer in compressible fluids. *Journal of the Aeronautical Sciences*, **18**, 145–160.

van Driest, E.R. 1955. The turbulent boundary layer with variable fluid properties. *In: Meeting. of the Heat Transfer and Fluid Mechanics Institute.*

van Driest, E.R. 1956. On turbulent flow near a wall. *Journal of the Aeronautical Sciences*, **23**, 1007–1011 and 1036.

Van Dyke, M. 1982. *An Album of Fluid Motion.* Parabolic Press.

Viswanath, P.R. 1988. Shock-wave-turbulent-boundary-layer interaction and its control: A survey of recent developments. *Sādhanā, Indian Academy of Sciences, Proceedings in Engineering Sciences*, **12**, 45–104.

Voisinet, R.L.P. & Lee, R.E. 1972. Measurements of a Mach 4.9 zero pressure gradient boundary layer with heat transfer. *Nav. Ord. Lab. TR 72-232.*

von Kármán, T. 1934. Turbulence and skin friction. *Journal of the Aeronautical Sciences*, **1**, 1.

Wallace, J.E. 1969. Hypersonic turbulent boundary-layer

measurements using an electron beam. *AIAA Journal*, **7**, 757–759.

Walz, A. 1959. Compressible turbulent boundary layers with heat transfer and pressure gradient in flow direction. *Research Journal, National Bureau of Standards*, **63 B**, 53.

Walz, A. 1966. *Strömungs- und Temperaturgrenzschichten.* Braun Verlag, Karlsruhe. English translation *Boundary Layers of Flow and Temperature*, MIT Press, 1969.

Watson, R.D. 1977. Wall cooling effects on hypersonic transitional/turbulent boundary layers at high Reynolds numbers. *AIAA Journal*, **15**, 1455–1461.

Watson, R.D. 1978. Characteristics of Mach 10 transitional and turbulent boundary layers. *NASA TP-1243.*

Watson, R.D., Harris, J.E. & Anders, J.B. 1973. Measurements in a transitional/ turbulent Mach 10 boundary layer at high Reynolds number. *AIAA Paper 73-165.*

Yanta, W.J. & Crapo, B.J. 1976. Applications of the laser Doppler velocimeter to measure subsonic and supersonic flows. *AGARD CP No. 193.*

Young, A.D. 1951. The equations of motion and energy and the velocity profile of a turbulent boundary layer in a compressible fluid. *Report No. 42, College of Aeronautics, Cranfield.*

Zheltovodov, A.A., Trofimov, V.M., Shilein, E.H. & V.N., Yakovlev. 1990. An experimental documentation of supersonic turbulent flows in the vicinity of sloping forward and back facing steps. *TPM Report 2013, Institute of Theoretical and Applied Mechanics, Siberian Division of the USSR Academy of Sciences, Novosibirsk, USSR.*

Compressible Turbulent Free Shear Layers

J. Craig Dutton
Department of Mechanical and Industrial Engineering
University of Illinois at Urbana-Champaign
Urbana, Illinois 61801 USA

1. ABSTRACT

Recent experimental work in the area of compressible turbulent free shear layers is reviewed. Results for the canonical two-stream, constant-pressure shear layer are given first. Emphasis is placed on growth rate, turbulence statistical quantities, large-scale turbulent structure, and growth rate enhancement. Compressible free shear layers present in high-speed separated flows are also considered. Here, results on mean flow, turbulence statistics, and large turbulent structures are discussed. Additional effects in these separated flows, such as the expansion that may occur at separation and the bulk compression, streamline curvature, and lateral streamline convergence that may occur at reattachment, are discussed. In order to develop a sound physical understanding of these compressible turbulent flows, particular attention is given to single-frame and multi-frame planar imaging studies.

2. INTRODUCTION AND MOTIVATION

Compressible free shear layers occur in a number of practical physical devices ranging from supersonic ejectors to gas dynamic and chemical lasers to the high-speed jets that are used for deposition of thermal spray coatings. However, the primary motivation for studying this flow in the last 10 years or so has been its importance for mixing the gaseous fuel and oxidant streams in supersonic combustors. Indeed, the major source of research funding for this problem in the U.S., especially during the mid- to late-1980s, was motivated by the desire to develop a scramjet-powered, single stage-to-orbit vehicle, such as the National AeroSpace Plane (NASP). However, since the demise of the NASP program, the volume of work addressing problems in this area has declined precipitously (at least in the U.S.). The timing of this AGARD/VKI Special Course on "Turbulence in Compressible Flows" therefore seems quite appropriate, as a review of progress made during the recent period of intense activity.

Compressible shear layers, although seemingly simple flows, are subject to quite complex fluid physics. The complications are partially due to the large Reynolds numbers, and consequent wide range of turbulent scales, that generally occur for gas flows under high-speed conditions. In addition, as will be shown abundantly below, compressibility itself has fundamental effects on turbulence that are not observed in low-speed flows. Nevertheless, considerable progress has been made in understanding compressible free shear layers in recent years. This progress has been facilitated both by the availability of vastly improved computational resources for numerical investigations and also by the development of non-intrusive laser-based diagnostic techniques for detailed experimental studies of this fundamental flow.

As might be expected, it would be impossible to thoroughly discuss all the recent accomplishments in the area of compressible free shear layers within the length constraints of this paper. Therefore, our primary objective is to review the physical understanding that has been developed through recent *experimental* studies of the *fluid dynamic* aspects of compressible shear layers. Reviews of numerical studies and topics such as scalar transport, mixing, and combustion are the subjects of other lectures in this Special Course. See also the recent review of Lele (1994) for a discussion of compressibility effects on turbulence with emphasis on analytical considerations and numerical results. The material presented here is certainly biased by our interests and experience at the University of Illinois in this general area. Therefore, we apologize in advance to any who might feel that their work has in any way been slighted or overlooked. Any errors of omission or commission are wholly the responsibility of the author.

3. CONSTANT-PRESSURE, TWO-STREAM, COMPRESSIBLE FREE SHEAR LAYERS

3.1 Dimensionless Parameters

Figure 1(a) is a schematic of a planar, matched-pressure, two-stream shear layer that is formed at the trailing edge of a splitter plate that separates the two streams. The subscript "1" will be used throughout to denote conditions of the higher speed stream, while subscript "2" refers to the lower speed stream. Thus, in the laboratory coordinates shown, the velocities of the freestreams are U_1 and U_2, their densities are ρ_1 and ρ_2, their speeds of sound are a_1 and a_2, their specific heat ratios are γ_1 and γ_2, and the static pressures at

Paper presented at the AGARD FDP Special Course on "Turbulence in Compressible Flows", held at the von Kármán Institute for Fluid Dynamics (VKI) in Rhode-Saint-Genèse, Belgium, 2-6 June 1997, and in Newport News, Virginia, USA, 20-24 October 1997, and published in R-819.

separation from the splitter plate are equal, $P_1 = P_2$. In the large body of work on *incompressible* mixing layers (*e.g.*, Brown and Roshko, 1974; Brown, 1978), it has been shown that the structure and behavior of the layer depend primarily on the freestream velocity ratio, $r = U_2/U_1$ [or, equivalently, the velocity parameter, $\lambda = (1-r)/(1+r)$], and the freestream density ratio, $s = \rho_2/\rho_1$.

To quantify the effects of *compressibility* on shear layers, Bogdanoff (1983) and Papamoschou and Roshko (1988) introduced the *convective Mach number*, M_c, which is the Mach number of the two freestreams relative to the large-scale structures in the mixing layer. To derive an expression for M_c, the layer is viewed in the reference frame that convects with the structures, Fig. 1(b). Assuming that the static pressures of the two streams are equal and that their (isentropically determined) total pressures are also equal at the stagnation point between structures in this frame, the following expression may be solved for the large-structure convection velocity, U_c

$$\left(1+\frac{\gamma_1-1}{2}\left(\frac{U_1-U_c}{a_1}\right)^2\right)^{\gamma_1/(\gamma_1-1)} = \left(1+\frac{\gamma_2-1}{2}\left(\frac{U_c-U_2}{a_2}\right)^2\right)^{\gamma_2/(\gamma_2-1)} \quad (1)$$

If $\gamma_1 = \gamma_2$, as is often the case in experimental studies, U_c is then given by

$$U_c = \frac{a_2U_1 + a_1U_2}{a_1 + a_2} \quad (2)$$

Using the definition of the convective Mach numbers of the two streams as their relative velocities with respect to the large structures divided by their speeds of sound gives

$$M_{c1} \equiv \frac{U_1 - U_c}{a_1} \quad \text{and} \quad M_{c2} \equiv \frac{U_c - U_2}{a_2} \quad (3)$$

If $\gamma_1 = \gamma_2$, the two convective Mach numbers are equal and can be written as

$$M_c = \frac{U_1 - U_2}{a_1 + a_2} \quad (4)$$

As mentioned above, this is the parameter that has been used overwhelmingly to quantify the effects of compressibility in mixing layers. It is often tacitly assumed that *all* the effects of compressibility are embodied in the magnitude of the convective Mach number. However, we must mention that there is evidence (*e.g.*, Sandham and Reynolds, 1989; Viegas and Rubesin, 1991) that the convective Mach number may be only a first-order measure of compressibility, *i.e.* that the effects of velocity ratio, density ratio, and/or other parameters may be different for compressible shear layers as compared to the incompressible case. In addition to r, s, and M_c, other "secondary" parameters that may influence the behavior of compressible mixing layers include: Reynolds number, state of the initial boundary layers, freestream turbulence, pressure gradients, and the compression and expansion waves that are virtually unavoidable in supersonic flow experiments.

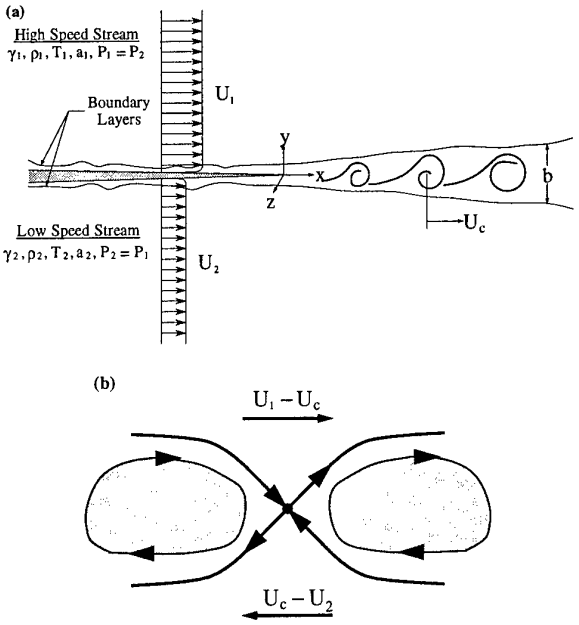

Fig. 1 Schematic of a two-stream mixing layer in (a) laboratory frame and (b) convective frame

3.2 Growth Rate

Perhaps the most well-known effect of compressibility on shear layers is the reduced growth rate that occurs as compared to that of incompressible mixing layers at the same velocity and density ratios. This is also an extremely important result in many applications, as mass *entrainment* from the freestreams into the layer, which results in its growth, is the first step in *mixing* the two streams (eventually at the molecular level so that chemical reactions can occur). Originally, the reduced growth rate effect was thought to be due to the density difference between the streams that occurs under compressible (versus incompressible) flow conditions. However, in their classic work on the subject, Brown and Roshko (1974) showed that the density effect was

small and that the growth rate reduction must be due to a separate and stronger compressibility effect.

In determining the growth rate of a shear layer, it is important that it be found only from the *fully-developed* or *self-similar* region. Goebel and Dutton (1991) studied the development of compressible mixing layers using the definition of Mehta and Westphal (1986) for fully-developed conditions: (1) linear growth rate with respect to downstream distance; (2) similarity of the mean velocity profiles when scaled by the local layer thickness; and (3) similarity of all turbulence quantity profiles when scaled by the local thickness, with peak turbulence quantities constant. Goebel and Dutton (1991) found that the mean velocity profiles required the least streamwise distance to become self-similar, followed by the streamwise turbulence intensity, transverse turbulence intensity, and Reynolds shear stress. By transforming Bradshaw's (1966) criterion for fully-developed single-stream shear layers to a criterion appropriate for two-stream layers, and by examining their experimental results for seven compressible mixing layer cases, Goebel and Dutton (1991) concluded that the following *approximate* local Reynolds number requirement must be met for full development

$$Re_b \equiv \frac{\overline{\rho}(\Delta U)b}{\overline{\mu}} \cong 1x10^5 \qquad (5)$$

where $\Delta U=U_1-U_2$ is the freestream velocity difference, b is the mixing layer thickness (defined below), and $\overline{\rho}$ and $\overline{\mu}$ are the average freestream density and viscosity, respectively. Note that Karasso and Mungal (1996) have recently found that the value of a "pairing parameter" better describes the development state of liquid plane shear layers, as compared to the local Reynolds number, although this result has not yet been extended to the compressible case.

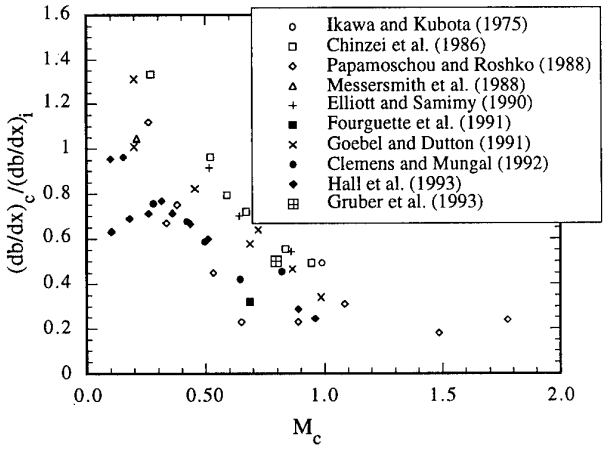

Fig. 2 Normalized growth rates of compressible mixing layers (from Gruber, 1992)

Figure 2 (from Gruber, 1992) shows the compressible mixing layer growth rate normalized by the incompressible growth rate at the same velocity and density ratios from some of the many studies that report this quantity. The incompressible growth rate for each case is determined from

$$\left(\frac{db}{dx}\right)_i = 0.165\lambda_s = 0.165\frac{(1-r)\left(1+s^{1/2}\right)}{2\left(1+rs^{1/2}\right)} \qquad (6)$$

where the constant has been suggested by Birch and Eggers (1972). It must be noted that many different definitions of the shear layer thickness are used in the literature. These include the 10%ΔU thickness, the vorticity thickness, the visual thickness, and the pitot thickness. We will usually use the 10%ΔU thickness, b, which is defined as the distance between transverse (y) locations where $U=U_1-0.1(\Delta U)$ and $U=U_2+0.1(\Delta U)$, see Fig. 1. All data presented in Fig. 2 have been transformed (assuming an error function mean velocity profile) to this common thickness definition.

As can be seen in Fig. 2, the normalized shear layer growth rate is indeed reduced as the compressibility of the layer, quantified by the convective Mach number, increases. In addition, these normalized data collapse moderately well when plotted against M_c. Possible reasons for the scatter in the data include differences in experimental techniques used to determine growth rate, lack of achievement of fully-developed conditions, differences in the thickness definition used and/or uncertainty in transforming to the "b" definition, and the possibility mentioned above that M_c provides only a first-order measure of compressibility. A few of the anomalous points in the figure deserve special mention. For example the high normalized growth rate reported at M_c=0.20 by Goebel and Dutton (1991) is due to "disturbed," high freestream turbulence conditions, which lead to an expected large growth rate. The low normalized growth rates reported by Hall *et al.* (1993) at low M_c are speculated by these authors to be due to poorly understood effects of very low density ratios coupled with a supersonic high-speed stream. In fact, the density ratios of these latter cases are lower than for any in the incompressible shear layer database, so that Eq. 6 may not accurately predict the growth rate used for normalization of these cases.

3.3 Turbulence Statistics

Because of the difficulties involved with making accurate, instantaneous velocity measurements in supersonic flows, few investigators have obtained

turbulence measurements in compressible shear layers. Elliott and Samimy (1990) studied three cases, Goebel and Dutton (1991) investigated seven cases, and Gruber *et al.* (1993) reported results for a single case. All of these measurements were obtained using laser Doppler velocimetry (LDV), where Elliott and Samimy (1990) and Goebel and Dutton (1991) presented two-component data and Gruber *et al.* (1993) obtained three-component results. Barre *et al.* (1994) have also presented one-component hot-wire anemometry (HWA) measurements for a compressible shear layer at M_c=0.62.

As discussed above in regard to the growth rate determination, it is critical that the turbulence measurements be reported from the fully-developed region, as the development of the layer immediately after separation from the splitter plate can depend strongly on the freestream and initial boundary layer conditions. This is especially true for the turbulence quantities, which have been found to develop more slowly than the mean velocity.

Figures 3-5 show averaged profiles from the fully-developed regions for five of the cases investigated by Goebel and Dutton (1991). The quantities plotted are the streamwise turbulence intensity, $\sigma_u/\Delta U$, the transverse turbulence intensity, $\sigma_v/\Delta U$, and the normalized kinematic Reynolds shear stress, $\langle u'v' \rangle/(\Delta U)^2$, respectively. (The symbol σ is used throughout to denote the rms fluctuation of the subscripted velocity component, and the angled brackets are used for ensemble-averaged quantities.) As expected, these turbulence quantities peak near the center of the shear layer and fall off to small values in the freestreams. In examining the effects of compressibility, increasing convective Mach number is seen to have a strong effect on reducing the magnitude of the transverse turbulence intensity and the Reynolds shear stress. We should note that the lowest compressibility case shown, M_c=0.20, may not have been fully developed, so that its profiles may be high in each case. With this caveat, the data shown in Fig. 3 indicate little effect of compressibility on streamwise turbulence intensity. Taken together, the trends for σ_u and σ_v, as measured by Goebel and Dutton (1991), suggest that the normal stress anisotropy, σ_u^2/σ_v^2, increases with increasing compressibility.

The effects of compressibility on the turbulence statistical quantities are more easily seen in Figs. 6-8, where the peak turbulence quantities from each of the four studies mentioned above have been plotted as a function of convective Mach number. In each case, the turbulence quantities have been normalized with respect to typical values measured for incompressible shear layers: $(\sigma_u/\Delta U)_i$=0.18, $(\sigma_v/\Delta U)_i$=0.13, and

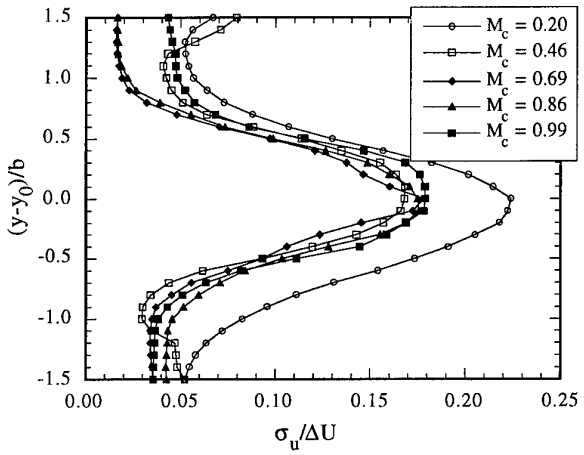

Fig. 3 Similarity profiles of streamwise turbulence intensity (from Goebel and Dutton, 1991)

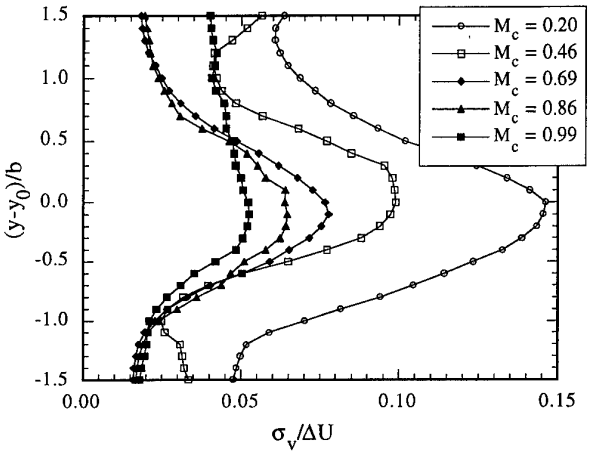

Fig. 4 Similarity profiles of transverse turbulence intensity (from Goebel and Dutton, 1991)

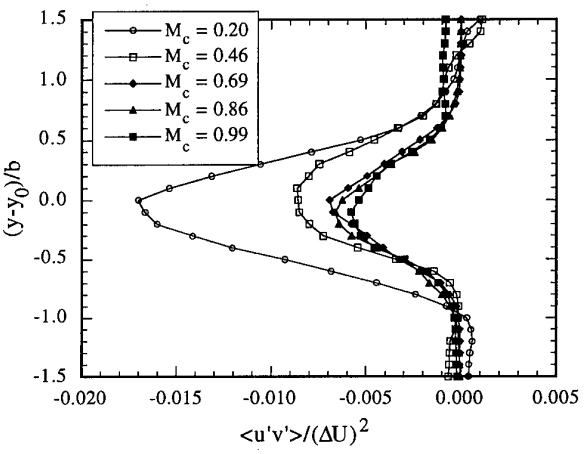

Fig. 5 Similarity profiles of normalized kinematic Reynolds stress (from Goebel and Dutton, 1991)

$(-\langle u'v'\rangle/(\Delta U)^2)_i=0.013$. The trends just mentioned from Goebel and Dutton (1991) are apparent: strongly reduced $\sigma_v/\Delta U$ and $-\langle u'v'\rangle/(\Delta U)^2$ and approximate constancy of $\sigma_u/\Delta U$ with increasing M_c. In addition, the data from all investigators for the peak transverse turbulence intensity and Reynolds shear stress collapse extremely well when plotted against convective Mach number. However, the data from Elliott and Samimy (1990) and Goebel and Dutton (1991) show some disagreement in the trends for the streamwise turbulence intensity. Instead of relatively constant values of $\sigma_u/\Delta U$ with increasing M_c, Elliott and Samimy (1990) found that this quantity also decreased, leading to a relatively constant normal stress anisotropy. In addition, these investigators found that the lateral (transverse direction) extent of the turbulence fluctuations within the shear layer is reduced as compressibility increases. Goebel and Dutton (1991), on the other hand, found no apparent reduction of the lateral extent of the turbulence fluctuations.

Gruber *et al.* (1993) reported three-component turbulence measurements for $M_c=0.80$. Their results for the streamwise and transverse turbulence intensities are in close agreement with Goebel and Dutton's (1991), which were obtained in the same facility. Gruber *et al.* (1993) found that the lateral extent of the turbulence profiles was reduced only on the high-speed side of the shear layer and that the peak spanwise turbulence intensity, $\sigma_w/\Delta U$, was about the same as for the incompressible case. Taken together with the reduced transverse turbulence intensity, the latter result implies that an effect of compressibility on the mixing layer is a tendency toward a more three-dimensional structure with enhanced spanwise, as compared to transverse, velocity fluctuations.

All three of the LDV studies consistently show that the shear stress correlation coefficient, $-\langle u'v'\rangle/(\sigma_u\sigma_v)$, is approximately constant, at a value between 0.4 and 0.5, both spatially within the shear layer and as a function of compressibility. This result provides an interesting turbulence model closure idea, which indeed has been utilized by Burr (1991). In addition, all of the LDV studies have shown that higher-order velocity moments, such as triple products, skewness, and flatness factors, are strongly reduced with increasing compressibility at the shear layer edges. This suggests that intermittency at the edges, due to excursions of large turbulent structures into the freestreams and, conversely, intrusions of inviscid freestream fluid into the shear layer, is also reduced.

We must emphasize that the discrepancies noted above for the streamwise turbulence intensity and lateral extent of the velocity fluctuations could be due to any

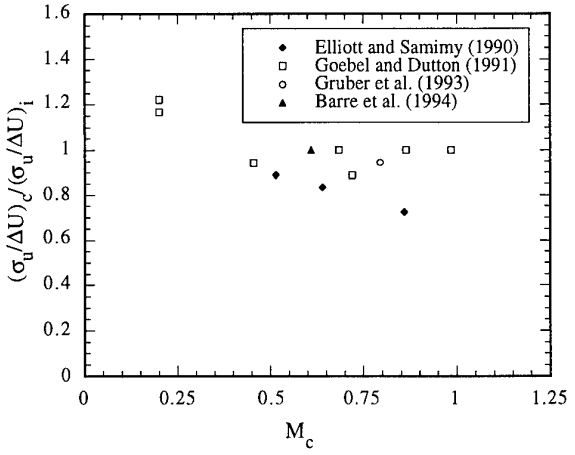

Fig. 6 Peak streamwise turbulence intensities from recent investigations (from Gruber *et al.*, 1993)

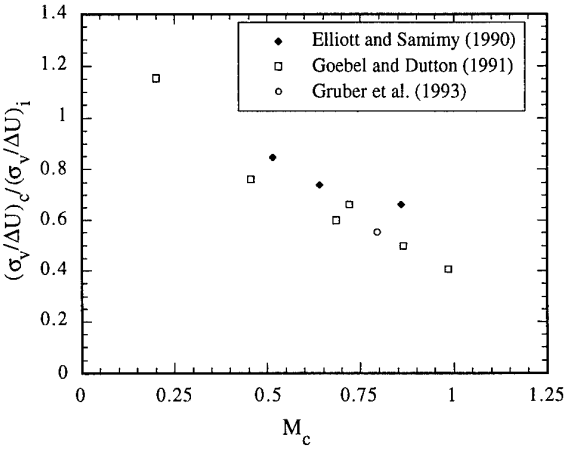

Fig. 7 Peak transverse turbulence intensities from recent investigations (from Gruber *et al.*, 1993)

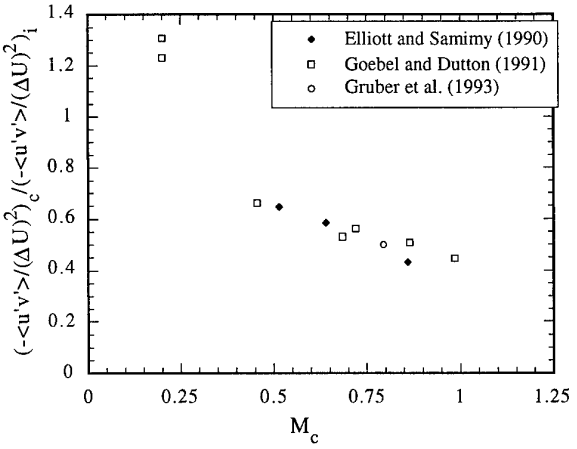

Fig. 8 Peak normalized primary Reynolds shear stresses from recent LDV investigations (from Gruber *et al.*, 1993)

of the secondary factors listed earlier or because the convective Mach number is not a complete descriptor of compressibility effects. Additional turbulence data, particularly at convective Mach numbers above about 0.8, are needed to clarify these issues. It is clear from the data presented that a primary effect of compressibility is a strong reduction of transverse velocity fluctuations and a trend toward a more three-dimensional turbulence structure, effects that will be reinforced by planar visualizations to be presented in the next section. In addition, inspection of Figs. 6-8 as a whole suggests better collapse of the normalized peak turbulence quantities when plotted against convective Mach number than for the normalized growth rate, Fig. 2, which is a surprising result.

3.4 Large-Scale Turbulent Structures

3.4.1 *Incompressible Shear Layer Structure*

As a prelude to discussing the large-scale organization of compressible shear layers, it is useful to first briefly review the structure of incompressible mixing layers. One of the landmark studies in this regard is that of Brown and Roshko (1974). In addition to investigating density ratio effects on shear layer growth rate, the shadowgraph visualizations of these authors clearly showed the dominant spanwise-oriented structures that exist in low-speed mixing layers, Fig. 9. These rolled-up structures develop from the fundamental Kelvin-Helmholtz instability of the flow. Since the time of Brown and Roshko's (1974) work, large-scale structures in turbulent shear flows have been the subject of a great deal of research. It has been found that these structures may pair, tear, and that they are stable, dominant features of low-speed shear layers even at high Reynolds numbers or in the presence of highly exothermic chemical reactions or other severe disturbances (Winant and Browand, 1974; Dimotakis and Brown, 1976; Wygnanski *et al.*, 1979). These structures have also been shown to be critically important in entrainment of the freestream fluids into the shear layer and to the cascade of turbulent scales that eventually results in mixing of the fluids at the molecular level (Dimotakis, 1986; Broadwell and Breidenthal, 1982; Broadwell and Mungal, 1988).

In addition to these spanwise structures, streamwise-oriented counter-rotating vortex pairs have been found to develop from the strain field induced by the spanwise rollers (Bernal and Roshko, 1986). These streamwise vortices, or ribs, are found in the braid region between the rollers with their ends wrapping around successive spanwise vortices; see Fig. 10 for an idealized schematic. The streamwise counter-rotating vortices induce fluid motion between them, either up or down, thus creating mushroom-shaped structures when viewed from the end (y-z plane, Fig. 1). The circulation of the streamwise ribs is found to be of the same order of magnitude as that of the spanwise rollers, suggesting that the interaction of the streamwise and spanwise vortices convolutes the layer interface and is responsible for significant entrainment and mixing between the two streams (Jimenez *et al.*, 1985).

3.4.2 *Schlieren and Shadowgraph Studies*

Against this backdrop for incompressible shear layers, it was only natural that early compressible mixing layer studies used schlieren and shadowgraph methods to investigate the existence of similar large-scale organization. This was done by several workers, *e.g.* Papamoschou and Roshko (1988), Elliott and Samimy (1990), Goebel and Dutton (1991), Clemens and Mungal (1992), and Hall *et al.* (1993). Figure 11 shows an example composite schlieren photograph of a compressible mixing layer at M_c=0.75 from the experiments of Messersmith (1992). As has been generally found in all other schlieren/shadowgraph studies, this figure shows, at best, only a slight hint of braided structure toward the downstream end, but certainly *not* the dominant, rounded, large-scale structures seen under incompressible conditions, Fig. 9. However, in drawing conclusions from these flow visualizations, we must remember that the schlieren and shadowgraph methods integrate effects along the line-of-sight, so that three-dimensionality (in the spanwise direction) of the turbulence structure will be smeared in the resulting photos.

3.4.3 *Probe-Based Structure Studies*

Time-series analyses of fluctuating pressure and hot-wire measurements have been used to investigate the structure and organization of compressible shear layers. Samimy *et al.* (1992) studied mixing layers at M_c=0.51 and 0.86 using fast-response pressure transducers. At the lower compressibility level, the measurements suggested that the large structures were similar to the incompressible case, with a predominantly two-dimensional spanwise orientation, although their spatial organization was poorer than for low-speed shear layers. At the higher compressibility, the structures were found to be highly three-dimensional in nature, with good spatial, but poor temporal organization. Figure 12, taken from this work, shows how much more strongly the streamwise coherence of the pressure fluctuations is reduced with increasing

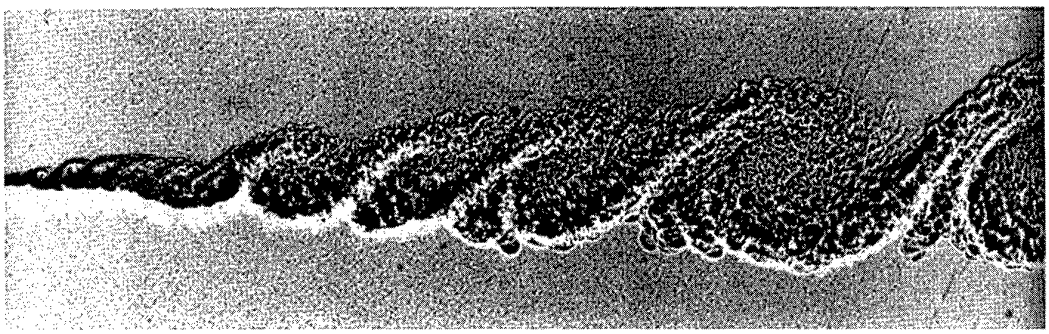

Fig. 9 Large-scale structure in an incompressible shear layer (from Brown and Roshko, 1974; as reproduced in Van Dyke, 1982)

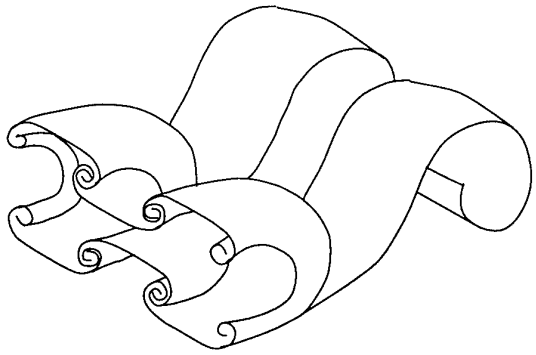

Fig. 10 Schematic of large-scale structure in an incompressible mixing layer: spanwise rollers and streamwise ribs (from Gruber, 1992)

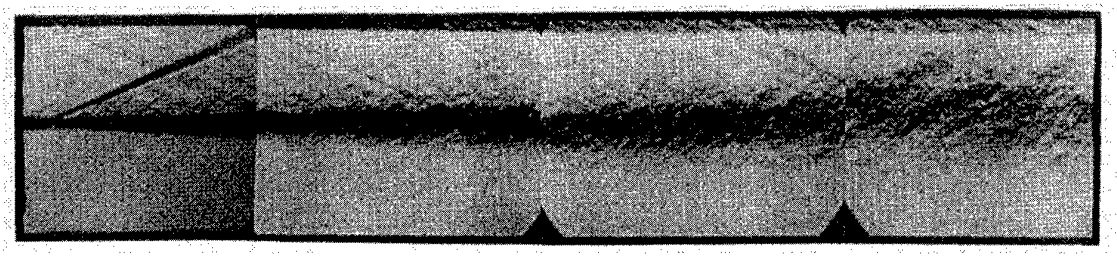

Fig. 11 Schlieren photograph of a compressible shear layer at M_c=0.75 (from Messersmith, 1992)

normalized probe separation distance, dx/δ_ω (where $\delta_\omega \approx b$), for M_c=0.86 than for M_c=0.51. This demonstrates a very strong effect of compressibility on the streamwise evolution of the structures. Spanwise correlation measurements were also suggestive of the existence of horseshoe-type vortices for the M_c=0.86 case.

Shau *et al.* (1993) and Petullo and Dolling (1993) used pressure fluctuation and dual normal hot-wire measurements, respectively, to investigate an M_c=0.28 shear layer formed between a Mach 5 and a Mach 3 stream. These measurements showed that the shear layer large structures were better organized than in the upstream boundary layer and that their organization increased with downstream distance, a finding that is in agreement with results of Samimy *et al.* (1992). Large-structure inclination angles of 35° to 55° to the streamwise direction were measured. All of the probe-based studies discussed here measured a broad range of structure angles for a given case, which is in agreement with the instantaneous planar images to be discussed below.

3.4.4 *Single-Frame Planar Imaging Results*

With the advent of laser diagnostic techniques, the line-of-sight integration limitation of the schlieren and shadowgraph methods could be removed, since thin laser sheets, generally of the order of a few hundred microns thickness, could be used to illuminate the flow. Techniques including Mie or Rayleigh scattering and planar laser-induced fluorescence (PLIF) were used in several studies of the turbulence structure of compressible shear layers (Clemens and Mungal, 1992, 1995; Elliott *et al.*, 1992; Bonnet *et al.*, 1993; Messersmith and Dutton, 1996; Poggie and Smits, 1996). Since pulsed lasers are used for these methods, the temporal resolution is also excellent, typically on the order of 10 ns, so that essentially "frozen" or "instantaneous" visualizations are obtained.

Example side-view (x-y plane, Fig. 1) Mie scattering images from the work of Clemens and Mungal (1995) are shown in Fig. 13 for a shear layer at M_c=0.28. These images utilize "product formation" seeding, in which ethanol vapor that is carried in the low-speed stream condenses into droplets only when molecularly mixed with cold fluid from the high-speed stream. This Mie scattering method therefore emphasizes large-structure cores where molecular mixing is expected to be most complete. The low compressibility case in Fig. 13 shows the existence of Brown-Roshko roller-like structures with connecting braids. The large structures and braids are most clearly seen in the downstream region of the images. Smaller-scale turbulence riding on the large-scale structures is also apparent, as might be expected for the large Reynolds number of this flow. Plan views (x-z plane, Fig. 1) of this same case are shown in Fig. 14. Here, the large structures are seen to be predominantly oriented in the spanwise direction and often span the entire field-of-view. However, skewing and bending with respect to the spanwise direction also occur frequently. Smaller streamwise-oriented structures connecting the spanwise rollers can also be observed.

Figures 15 and 16 show similar side and plan views of a compressible shear layer at M_c=0.62. The large structures visualized in the side view appear less well organized and are more jagged and irregularly spaced than those at lower compressibility. Clearly identifiable braids between large structures also appear to occur less frequently. The plan views show greatly

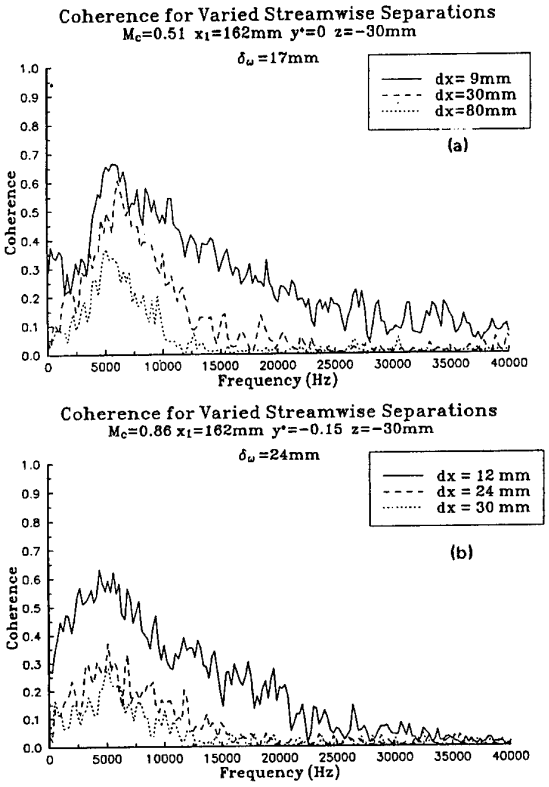

Fig. 12 Streamwise coherence for various probe separation distances for compressible shear layers at (a) M_c=0.51 and (b) M_c=0.86 (from Samimy *et al.*, 1992)

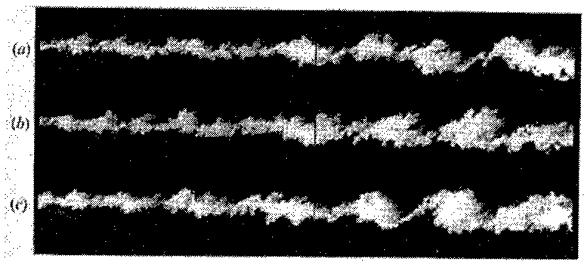

Fig. 13 Side-view planar images of a compressible shear layer at M_c=0.28 (from Clemens and Mungal, 1995)

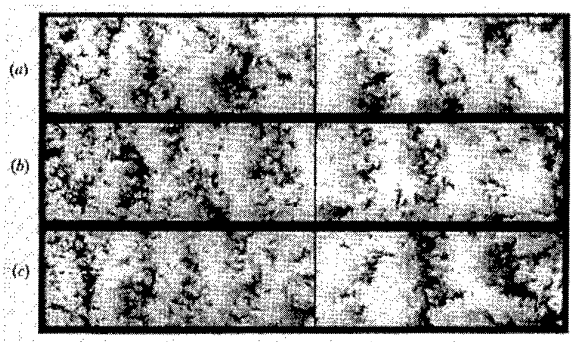

Fig. 14 Plan-view planar images of a compressible shear layer at M_c=0.28 (from Clemens and Mungal, 1995)

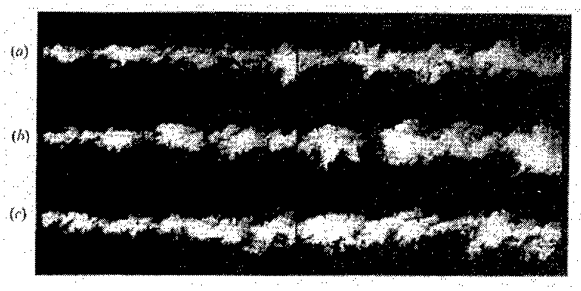

Fig. 15 Side-view planar images of a compressible shear layer at M_c=0.62 (from Clemens and Mungal, 1995)

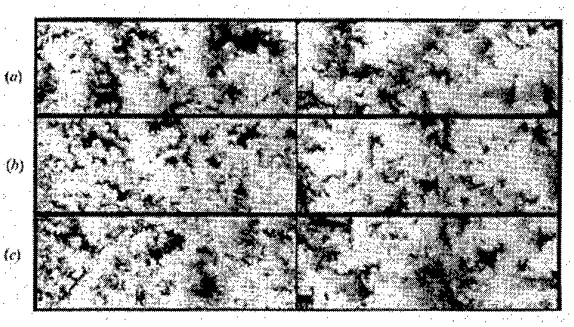

Fig. 16 Plan-view planar images of a compressible shear layer at M_c=0.62 (from Clemens and Mungal, 1995)

reduced spanwise organization of the large structures, although obliquely-oriented structures are sometimes seen to span the field-of-view, particularly in the upstream region.

Side- and plan-view product formation images are shown in Fig. 17 for an M_c=0.79 mixing layer. The jagged large structures seen in the side view are generally similar to those at M_c=0.62, although, perhaps, the large structures and intervening braids are even less easily identified here than at the lower compressibility. The structures shown in the plan views are now highly three-dimensional in nature with no apparent preferred orientation in the spanwise or streamwise directions.

Although not shown here, end views (y-z plane, Fig. 1) from Clemens and Mungal's (1995) study demonstrate that with increasing compressibility, the instantaneous shear layer cross-section becomes more convoluted with more realizations of "mushroom-shaped" structures. This is suggestive of the increased dominance of obliquely- and/or streamwise-oriented vortex structures at higher convective Mach number, as was noted in the plan views.

Messersmith and Dutton (1996) used a Mie scattering method similar to Clemens and Mungal's (1995), but obtained and statistically analyzed large image ensembles (256 images) for each of three compressibility levels. Since a broad range of structural features are observed in the images of a given ensemble, the statistical analysis was done to quantify, in an objective manner, the influence of compressibility on the characteristic features of the large structures. Figure 18 shows a comparison of instantaneous images obtained for an M_c=0.32 shear layer and ensemble-averaged spatial covariance fields, where the contour lines are drawn in increments of 0.125 about the central peak, which is normalized to unity. Side views are shown at the left, while oblique, quasi-end views are shown on the right. The images utilize "passive scalar" seeding for which ethanol vapor was seeded into the high-speed stream that condensed into droplets upon expansion to supersonic conditions. The ensemble-averaged covariance fields are not expected to reproduce exactly the features of the structures in any given instantaneous image, but rather they give the features of the "average" structure for that condition. Nevertheless, the similarity between the visualizations and spatial

covariances in Fig. 18 is unmistakable. In Messersmith and Dutton's (1996) work, the 0.5 covariance contour was used to define the normalized structure size (ratio of major axis-to-local layer thickness), eccentricity (unity minus the ratio of major-to-minor axes), and angular orientation of the major axis to the horizontal flow direction.

Similar spatial covariance fields for the side and quasi-end views are shown in Figs. 19 and 20 for M_c=0.49 and 0.75, respectively. Table 1 presents the results of the statistical analysis performed to determine the large structure characteristic features for each view and convective Mach number. From the analysis of the side views, it is clear that the large structures increase in dimensionless size with increasing compressibility, and that their angular orientation decreases substantially from about 26° at the two lower compressibility levels to 16° at M_c=0.75. Note that these structure angles are smaller than those found in the probe-based studies of Shau *et al.* (1993) and Petullo and Dolling (1993) at lower compressibility. The flattened, more downward-tilted nature of the structures at the highest compressibility investigated by Messersmith and Dutton (1996) results in a dimensionless structure size greater than unity. The downward rotation and lengthening of the structures also seem quite consistent with the LDV measurements discussed earlier, which showed a strong reduction in the transverse turbulence intensity with increasing compressibility. Less mass induction area between structures is available for this tilted, elongated configuration, which is also in agreement with the decreased normalized layer growth rate for increased convective Mach number. The eccentricity of the structures seen in the side views shows no strong trend, remaining relatively constant at about 0.5 as M_c increases. Clemens and Mungal (1995) noted that the large structures visualized in their side views underwent a shape change from rounded or elliptical at low compressibility to a squarer or more polygonal shape at high compressibility. The side-view spatial covariance fields of Figs. 18-20 show definite rounded, elliptical shapes at the two lower convective Mach numbers with, perhaps, a hint of a more polygonal shape in the outer covariance contours at the highest compressibility.

The effects of compressibility on the large structure characteristics visualized in the oblique, quasi-end views are given in the lower portion of Table 1. The results show that, for the lowest compressibility, the dimensionless structure size is approximately 0.5, while for the two more compressible cases, the normalized size increases substantially to about 0.75. The eccentricity of the obliquely-viewed structures is also

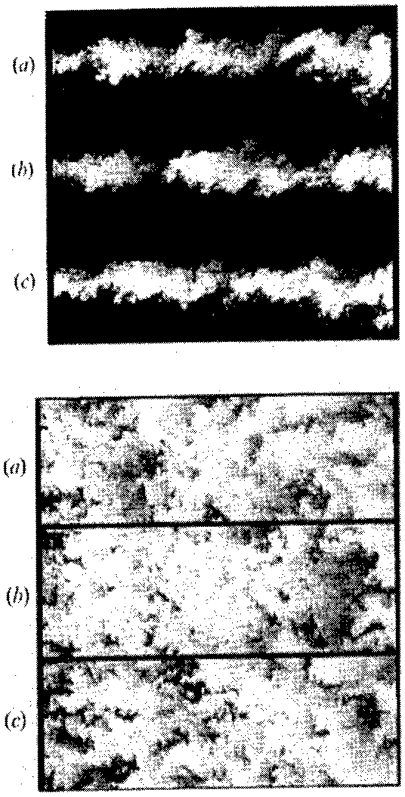

Fig. 17 Side-view and plan-view planar images of a compressible shear layer at M_c=0.79 (from Clemens and Mungal, 1995)

strongly reduced with increasing compressibility. This finding results from the increased three-dimensionality of the turbulence structure at higher convective Mach number, which causes a greater randomness in the orientation and size of the structures viewed in this plane. Comparing the dimensionless size and eccentricity of the structures in the side and oblique views at the same compressibility level shows that the oblique plane structures are always smaller and less eccentric than their side-view counterparts. These results from the statistical analysis are all quite consistent with instantaneous images obtained by Elliott *et al.* (1992), Clemens and Mungal (1992, 1995), and others.

These trends of a transition from a predominantly two-dimensional spanwise orientation of rollers at low compressibility, to obliquely-oriented spanwise structures at intermediate convective Mach numbers,

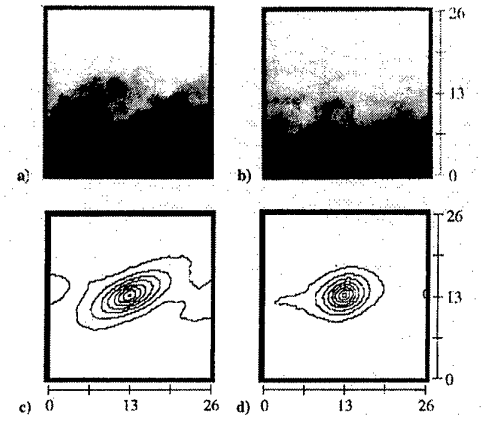

Fig. 18 Side-view and oblique-view planar images and spatial covariance fields for a compressible shear layer at M_c=0.32; dimensions given in mm (from Messersmith and Dutton, 1996)

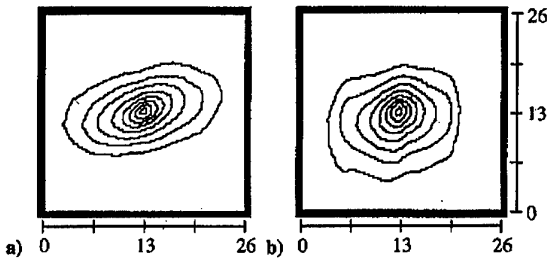

Fig. 19 Side-view and oblique-view spatial covariance fields for a compressible shear layer at M_c=0.49; dimensions given in mm (from Messersmith and Dutton, 1996)

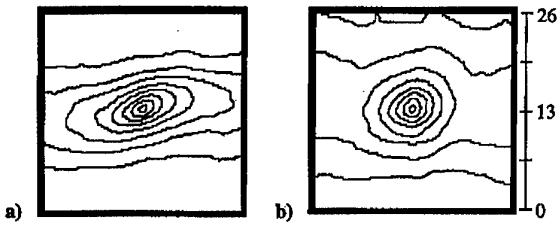

Fig. 20 Side-view and oblique-view spatial covariance fields for a compressible shear layer at M_c=0.75; dimensions given in mm (from Messersmith and Dutton, 1996)

Table 1 Large-structure features from the two-dimensional spatial covariance fields of Messersmith and Dutton (1996)

View	M_c	Normalized Size	Eccentricity	Angular Orientation
Side	0.32	0.69	0.52	26°
Side	0.49	0.85	0.45	25°
Side	0.75	1.03	0.58	16°
Oblique	0.32	0.48	0.30	----
Oblique	0.49	0.77	0.14	----
Oblique	0.75	0.71	0.10	----

and, finally, to a breakdown to a highly three-dimensional turbulence structure at large M_c are in good qualitative agreement with linear stability analyses of compressible mixing layers (Ragab and Wu, 1989; Sandham and Reynolds, 1990, 1991). These analyses show the stability of the compressible mixing layer to be characterized by three regimes: (1) $0<M_c<0.6$, in which the two-dimensional, spanwise instability is the most rapidly amplified; (2) $0.6<M_c<1.0$, for which the oblique wave is the most amplified, although the two-dimensional wave is still amplified and may have an effect; and (3) $M_c>1.0$, in which the two-dimensional wave is considerably less amplified than the most unstable oblique wave.

3.4.5 *Multi-Frame Planar Imaging Results*

Time-correlated image pairs or sequences have also been obtained to investigate the large-structure temporal evolution and convection velocity. McIntyre and Settles (1991) used high-speed schlieren cinematography and optical deflectometry to investigate axisymmetric shear layers at convective Mach numbers ranging from 0.08 to 1.5. They found that the large-scale structures were poorly organized for the more compressible cases and that they evolved rapidly as they convected downstream. Two-point spatial correlation data gave no indication of a consistent wavelength for the structures, implying that they were irregularly spaced. Mahadevan and Loth (1994) used high-speed schlieren and laser sheet cinematography to study a shear layer at $M_c=0.76$. Four-frame (or more in some cases) sequences were obtained that showed the dominant evolution characteristic to be stretching and tilting of the large structures down toward the streamwise direction as they convect; see feature B in Fig. 21. Recently, Poggie and Smits (1996) performed double-pulsed Rayleigh scattering experiments for a mixing layer at $M_c=1.1$. These visualizations clearly show the growth of small-scale structures on the periphery of large structures, which is a mechanism also observed in compressible turbulent boundary layers.

Elliott *et al.* (1995) obtained double-pulsed Rayleigh scattering images of compressible shear layers at convective Mach numbers of 0.51 and 0.86. In the near-field close to the splitter plate, the structures for the lower compressibility case were seen to roll up from instability waves of the Kelvin-Helmholtz type, Fig. 22(a). (Note that the flow direction in Figs. 22-24 is from right-to-left.) Little evidence of this roll-up mechanism was found for $M_c=0.86$, Fig. 22(b), however. In the fully-developed far-field region for $M_c=0.51$, eddy evolution mechanisms typical of incompressible shear layers, including pairing, were observed; see features 7b' and 7b" in Fig. 23. At

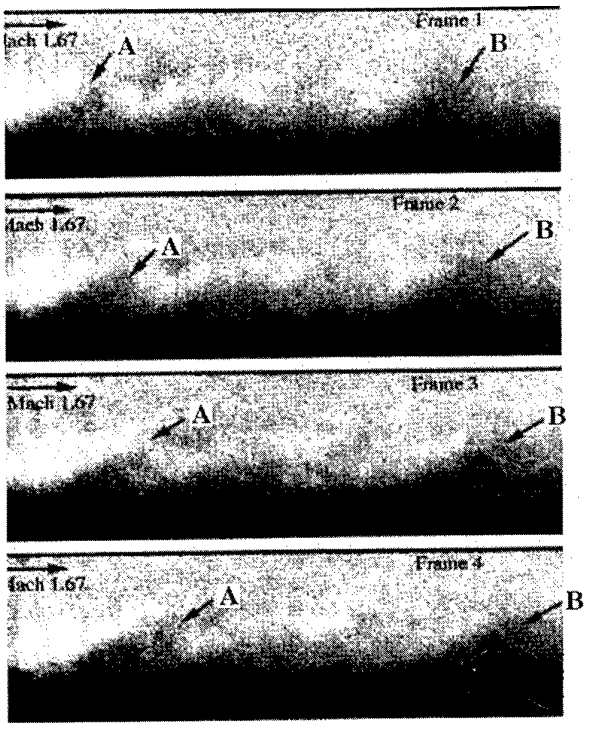

Fig. 21 Four-frame planar imaging sequence of a compressible shear layer at $M_c=0.76$ (from Mahadevan and Loth, 1994)

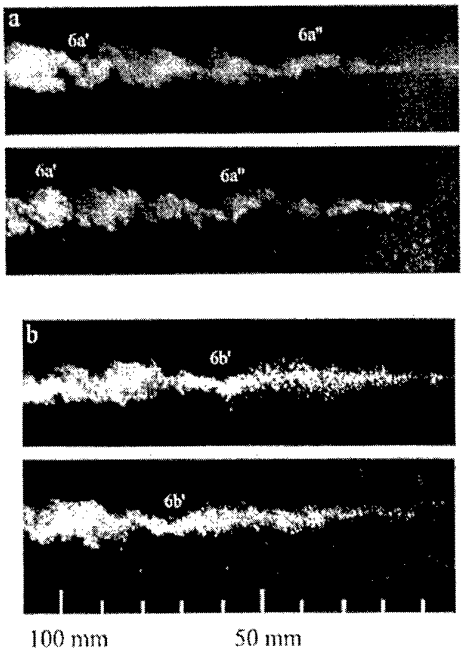

Fig. 22 **Double-pulsed planar images in the developing region of a compressible shear layer at (a) M_c=0.51 and (b) M_c=0.86 (from Elliott *et al.*, 1995)**

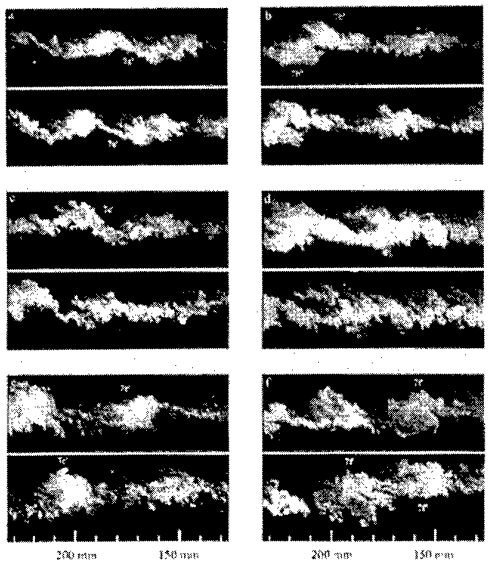

Fig. 23 **Double-pulsed planar images in the fully-developed region of a compressible shear layer at M_c=0.51 (from Elliott *et al.*, 1995)**

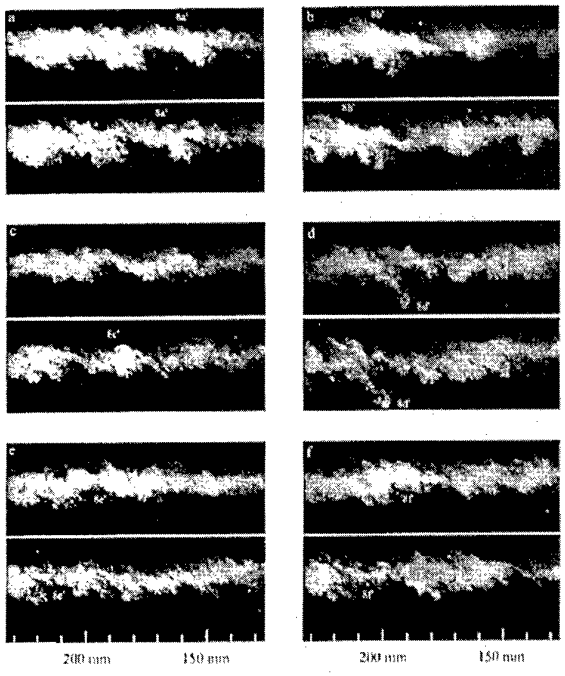

Fig. 24 Double-pulsed planar images in the fully-developed region of a compressible shear layer at M_c=0.86 (from Elliott *et al.*, 1995)

M_c=0.86 stretching or tearing of structures was commonly seen, as shown by features 8a' and 8b' in Fig. 24. However, pairing was not observed. The cinematography results of Mahadevan and Loth (1994) suggest a modified merging mechanism in compressible shear layers called "slapping" in which the two structures coalesce with little transverse displacement and rotation of the structures about each other, as occur in the incompressible case (Winant and Browand, 1974).

The multi-frame imaging techniques described above have also been used to determine the convection velocity of the large structures in compressible mixing layers. This quantity is of importance, first, because it enters the definition of the convective Mach number, Eq. 3, which is the fundamental parameter used to quantify the level of compressibility of a shear layer. Secondly, the convective velocity is used in many phenomenological models of entrainment and mixing, *e.g.* Dimotakis' (1986) entrainment model for low-speed shear layers.

The convective velocity measurements for compressible mixing layers have produced quite striking results. For low convective Mach numbers, the measured convective velocity has been found to agree closely with the isentropic theoretical value given in Eq. 2. However, for higher levels of compressibility (M_c>0.3), the structures' velocity has generally been found to be closer to that of one or the other of the freestreams, depending on whether both streams are supersonic or one is supersonic and the other is subsonic (Papamoschou, 1989, 1991; McIntyre and Settles, 1991; Bunyajitradulya and Papamoschou, 1994; Mahadevan and Loth, 1994; Papamoschou and Bunyajitradulya, 1995; Poggie and Smits, 1996). This "stream selection rule" (Dimotakis, 1991) states that U_c is closer to the velocity of the high-speed stream for supersonic/subsonic freestream combinations and is closer to that of the low-speed stream for supersonic/supersonic shear layers. Exceptions can be found, *e.g.* one of Papamoschou's (1989) and Elliott *et al.*'s (1995) two cases, but this "rule" is indeed followed in most circumstances. Figure 25 shows a plot of M_{c1} vs. M_{c2} from the work of Papamoschou (1991), where the filled-in symbols use the experimentally measured values of the convective velocity in the expressions for M_{c1} and M_{c2}, Eq. 3, and the open circles use the isentropic theoretical value, Eq. 2. The deviation between M_{c1} and M_{c2} (and, therefore, of the measured versus theoretical convective velocity) under highly compressible conditions is apparent.

A ramification of this disagreement between the theoretical and measured values of the large-structure convection velocity is that use of the convective Mach number as a measure of compressibility may not be well founded. This has led some investigators (*e.g.*, Goebel and Dutton, 1991; Gruber *et al.*, 1993; Messersmith and Dutton, 1996) to characterize compressibility level with the *relative* Mach number, M_r. This parameter is defined as the relative velocity of the high-speed stream with respect to the low-speed stream normalized by the average speed of sound,

$$M_r \equiv \frac{2(U_1 - U_2)}{a_1 + a_2}, \qquad (7)$$

and, therefore, does not use the large-structure convection velocity. However, for the case in which the two streams have equal specific heat ratios, the relative and convective Mach number definitions differ by just a constant factor of two (compare Eqs. 4 and 7). Thus, the convective Mach number may be an effective compressibility correlation parameter even though the model of flow stagnation in the braid region between well-organized, spanwise two-dimensional, large structures, Fig. 1(b), is phenomenologically incorrect under highly compressible conditions.

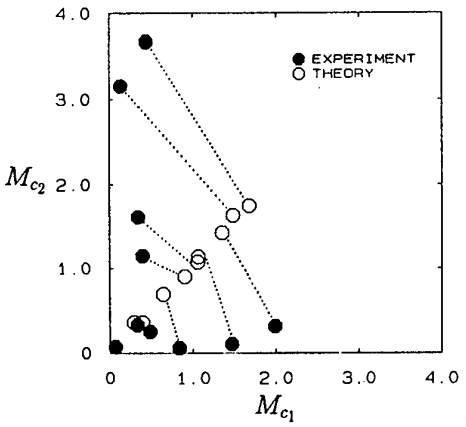

Fig. 25 Experimental and theoretical results for M_{c1} and M_{c2} for several compressible shear layers (from Papamoschou, 1991)

Some disagreement about the transverse variation of the convective velocity also exists. Bunyajitradulya and Papamoschou (1994), Papamoschou and Bunyajitradulya (1995), and Poggie and Smits (1996) found U_c to be constant or to vary only mildly across the layer. Samimy *et al.* (1992), using fluctuating pressure measurements, and Elliott *et al.* (1995), on the other hand, found the convective velocity to be equal to the isentropic theoretical value at the center of the layer, but higher toward the high-speed side and lower toward the low-speed side. It appears, therefore, that the use of different measurement methods by various investigators may be responsible for the lack of consistency in the convective velocity data. Also, note that the pressure probe measurements of Samimy *et al.* (1992) indicated a wide range of measured structure convective velocities in compressible shear layers at M_c=0.51 and 0.86.

One possibility that has been proposed for the disagreement between the measured and theoretical values of the large-structure convection velocity for highly compressible mixing layers is the asymmetric occurrence of shocklets on the structures. The presence of these shocklets, in turn, would cause asymmetric and non-isentropic deceleration of the two freestreams at the stagnation point between structures, thereby altering the convective velocity from the value predicted by Eq. 2. Two recent convective velocity models have been proposed (Dimotakis, 1991; Barre, 1994) that incorporate the dissipative effects of shocklets and have been found to effectively predict U_c for compressible shear layers. Two-dimensional numerical simulations show the existence of shocklets starting at about M_c=0.7 (*e.g.*, Lele, 1989; Burr, 1991). However, since it is known that oblique instability modes are dominant at this level of compressibility, two-dimensional simulations are not appropriate here. Three-dimensional simulations do *not* show strong evidence of eddy shocklets under highly-compressible conditions, at least up to M_c=1.2, presumably due to the swept and/or three-dimensional nature of the large structures (Sandham and Reynolds, 1990, 1991; Leep *et al.*, 1993). Experimental evidence of the existence of eddy shocklets is also sparse. The most convincing data on this point appear to be the schlieren and shadowgraph photos of Hall (1991) for two convective Mach numbers near unity. Mach waves are clearly observed in the *subsonic* stream for these cases, Fig. 26, which can only be due to the supersonic convection of structures in the shear layer with respect to this stream. However, because of the line-of-sight integrating nature of these visualization methods, the origination of the waves at specific structures in the layer was not irrefutably shown. Also note that Papamoschou (1995) has reported the occurrence of shocklets in an M_c=2.0 counterflow shear layer, although the question of whether impingement of the two streams occurs in this counterflow arrangement, thereby causing the shocklets, is problematic.

3.5 Growth Rate Enhancement

The well-known reduction in growth rate of compressible mixing layers with respect to their incompressible counterparts has led to many attempts at enhancing growth by various means. The motivation for this, of course, is that the performance of most devices that contain compressible shear layers as important flow features can be improved if the entrainment of the freestream fluids into the layer can be increased. The brief discussion here will be limited to growth rate enhancement of planar compressible mixing layers and will exclude the large body of work on round jets and other more complex geometries that have been studied as means to achieve improved mixing under supersonic conditions. The recent review article of Gutmark *et al.* (1995) provides a thorough review of these and related topics.

A widely studied method for achieving growth rate enhancement involves mounting various devices on the upstream splitter plate. The purpose of these devices is to perturb the stable structure of the compressible mixing layer, for example by introducing increased streamwise vorticity. Papamoschou (1989) investigated triangular vortex generators, slanted trip wires, and sawtooth extensions attached at the splitter plate trailing

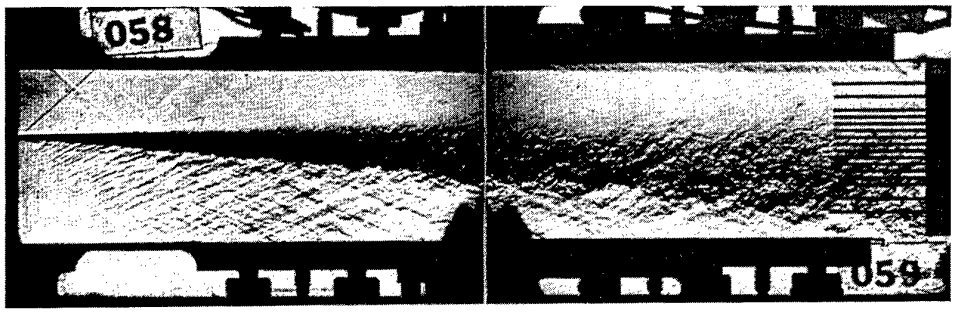

Fig. 26 Schlieren photograph of a compressible shear layer at $M_{c1}^{(i)}$=0.96 showing Mach waves in the subsonic stream (from Hall, 1991)

edge for an M_c=0.65 shear layer. However, none of the devices enhanced the growth rate by more than 5%. Dolling *et al.* (1992) placed cylindrical and wedge-shaped (corrugated plate) vortex generators in the turbulent boundary layer upstream of the splitter plate tip of an M_c=0.38 mixing layer. While both generators produced thicker layers at a given downstream location relative to the undisturbed case, this result was primarily due to a thicker boundary layer at separation and not to an enhanced shear layer growth rate. In fact, the corrugated plate generator showed no effect or even decreased the growth rate, Fig. 27(a). The cylindrical generators did provide an enhanced growth rate, Fig. 27(b), but the effect was relatively small (about 30%) and was obtained at the expense of substantial total pressure losses. Island *et al.* (1997) recently performed a parametric study of the effects of shape, spacing, and thickness of geometric disturbances placed within the supersonic side boundary layer of an M_c=0.63 shear layer. The disturbances in this case were quite thin, being from 5 to 50% of the local boundary layer thickness. In agreement with the results of Dolling *et al.* (1992), Island *et al.* (1997) found that the far-field growth rate was unaffected by the disturbances and that the enhanced thickness at a given streamwise location was due to alterations in the initial conditions. These investigators further found that triangular-shaped disturbances placed at the splitter tip, and not upstream, were the most effective and that, for equivalent flow area blockage, these discrete three-dimensional geometries were more effective than two-dimensional disturbances (*i.e.*, spanwise strips).

Fernando and Menon (1993) studied growth rate enhancement using a tapered sawtooth geometry at the trailing edge of the splitter plate. Two mixing layer conditions at M_c=0.29 and 0.47 were investigated. Unlike the studies discussed above, the results showed a significant effect on growth rate, with a 380% increase, and a doubling of the actual thickness at a given streamwise location in the optimum case. In addition, most of the increased thickness occurred on the low-speed side of the layer. The authors speculated that their results may have been affected by the recirculation region enclosed below the low-speed stream in their experiments.

The use of shock waves has also been studied as a method for achieving growth rate enhancement. Shau and Dolling (1989) impinged an oblique shock generated by a 10° wedge both on the upstream boundary layer and on a shear layer at M_c=0.32. The results showed that, when the shock was incident on the shear layer, no measurable effect on the local thickness or growth rate was detected. However, when the shock was impinged on the boundary layer, a large increase in the near-field spreading rate was measured, although it rapidly returned to the undisturbed value further downstream. Samimy *et al.* (1989) immersed round and square cylinders in compressible mixing layers at M_c=0.51 and 0.86 in order to generate bow shock interactions with the layers. For the M_c=0.51 case, the bow shock interaction was not found to affect the growth rate appreciably. However, at M_c=0.86 some enhancement of the growth rate was achieved, particularly when the cylinders were placed in the near-field developing region of the shear layer.

Both Hall *et al.* (1993) and Ramaswamy *et al.* (1996) investigated the effects of mismatching the static pressure of the two freestreams at the splitter plate tip. This generates compression or expansion waves that are reflected from the test section walls (and from the shear layer for a subsonic low-speed stream) and interact with the mixing layer. Neither of these studies found a significant effect of the waves on the layer growth rate, although Hall *et al.* (1993) noted increased large-structure organization in some cases for pressure-mismatched conditions.

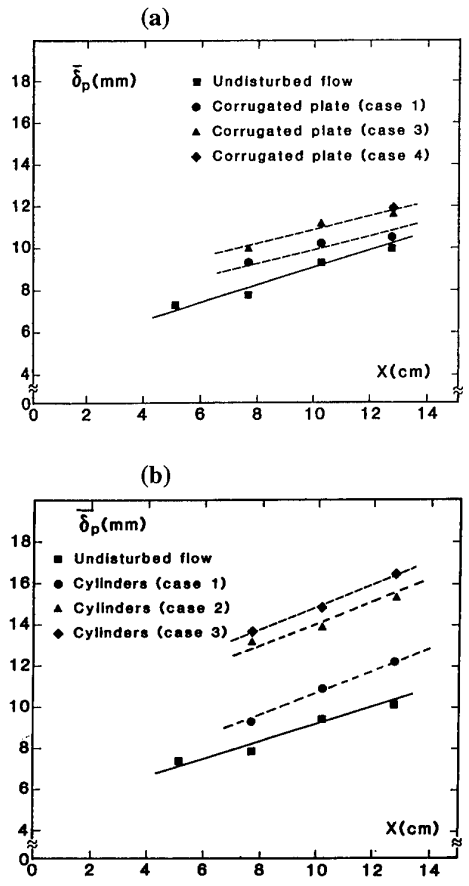

Fig. 27 **Growth rates of a compressible shear layer at M_c=0.38 with (a) corrugated plate vortex generators and (b) cylindrical vortex generators (from Dolling *et al.*, 1992)**

Martens *et al.* (1994, 1996) excited low Reynolds number mixing layers at M_C=0.50 and 0.64 using a glow discharge system. Spanwise two-dimensional forcing and oblique forcing at various angles to the spanwise direction were studied. At both convective Mach numbers, two-dimensional excitation resulted in instability waves that remained two-dimensional. On the other hand, three-dimensional forcing resulted in oblique instability waves that assumed the angle of the preferred mode, regardless of the excitation angle or value of M_C. For both levels of compressibility, the shear layer thickness in the near-field transitional region was increased compared to the undisturbed case. However, downstream in the fully-turbulent region, the growth rates of the excited shear layers returned to those of the natural cases.

Martens and McLaughlin (1995) also studied the effects of spanwise two-dimensional hemispherical arc disturbances attached to the upper and lower walls for the same two compressibility levels just discussed. These disturbances caused impingement of spatially periodic Mach waves on the shear layers. The additional effects of temporal excitation of the two-dimensional Kelvin-Helmholtz mode were also investigated using glow discharge excitation. The results showed little effect of the disturbances on growth rate for the more compressible case. However, at M_C=0.50 the optimized wall disturbance geometry showed a 50% increase in the growth rate and, when glow discharge forcing at 20 kHz was added, the growth rate enhancement was 100%; see Fig. 28.

Ramaswamy and Loth (1996) used passive acoustic excitation to enhance the growth rate of a confined, single-stream (r=0) shear layer at M_C=0.74. This study showed that two acoustically reflective surfaces were required to achieve this resonance excitation: one below and one downstream of the shear layer. In addition, an upstream reflective surface further enhanced the growth rate; note that none of the surfaces was inserted directly into the shear layer. In the optimum case, a growth rate enhancement of approximately 100% was achieved, Fig. 29. The authors concluded that a combination of streamwise and transverse modes may be responsible for the excitation.

The number of these enhancement studies that have achieved either no or only modest improvements in the growth rate attest to the inherent stability of compressible mixing layers. However, the recent studies of Martens and McLaughlin (1995) and Ramaswamy and Loth (1996), for which significant enhancement was achieved, offer hope that increased growth rates are, in fact, possible. It is likely, however, that to effect substantial growth enhancement will require that the instability modes and turbulent structure of compressible mixing layers be more clearly understood, including the influences of velocity ratio, density ratio, compressibility, wall confinement, Reynolds number, upstream history, and the like.

4. COMPRESSIBLE FREE SHEAR LAYERS IN HIGH-SPEED SEPARATED FLOWS

4.1 Flowfield Structure

Figure 30 presents a schematic diagram of a generic separated flow region embedded in a high-speed stream. For the case shown, a supersonic freestream and its associated boundary layer approach the sharp base corner of an axisymmetric or planar symmetric body where they separate geometrically through a centered expansion. A free shear layer is formed that encloses a recirculating region whose pressure is lower than that of

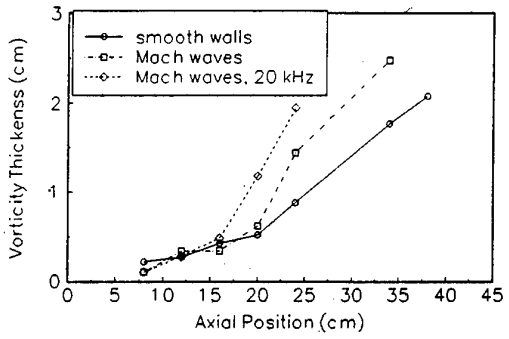

Fig. 28 **Growth rates of a compressible shear layer at M_c=0.50 with wall disturbances (Mach waves) and glow discharge excitation (20 kHz) (from Martens and McLaughlin, 1995)**

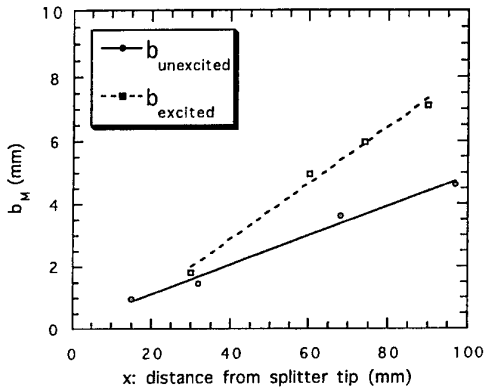

Fig. 29 **Growth rates of a compressible shear layer at M_c=0.74 with and without passive acoustic excitation (from Ramaswamy and Loth, 1996)**

the approaching stream. The shear layer and freestream are then recompressed through an oblique shock system as they are constrained to turn along the axis of symmetry near the rear stagnation (or reattachment) point. Development of the trailing wake then occurs in the downstream region.

The free shear layer is the key component in this separated flow, since it controls the entrainment and mixing of freestream and recirculating region fluids, which, in turn, determine important parameters such as the base pressure. However, the development of this shear layer is influenced by factors not present for the two-stream, constant-pressure layer described at length above. One such factor is the centered expansion that occurs at separation. This expansion alters the initial mean flow and turbulence structure of the mixing layer

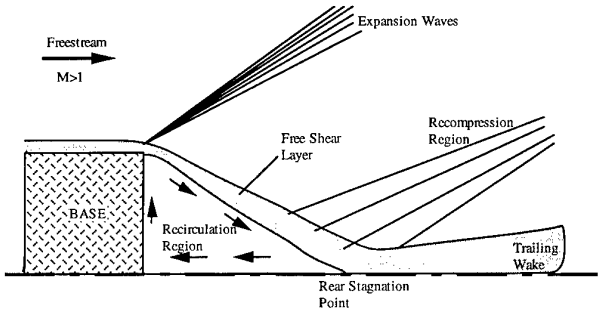

Fig. 30 **Schematic diagram of the separated flow region downstream of a body in supersonic flow (from Herrin, 1993)**

and, hence, its development. In addition, only the initial two-thirds or so of the shear layer near the base is at approximately constant pressure before encountering the adverse pressure gradient caused by the recompression waves near the reattachment point. The enclosed recirculating region also imposes an energetic and nonuniform reverse velocity at the inner edge of the shear layer. Finally, near the rear stagnation point the effects of streamline curvature and, for the axisymmteric case, lateral streamline convergence also play a role in the structure of the shear layer and on the initial development of the trailing wake.

The effects of these additional factors on compressible free shears layer present in high-speed separated flows will be described in the following sections.

4.2 Mean Flow and Turbulence Statistics

4.2.1 *Effects of Expansion at Separation*

Herrin (1993) and Herrin and Dutton (1994a,b) have made detailed three-component LDV measurements of the mean velocity and turbulence fields in the near-wakes of both cylindrical and boattailed afterbodies immersed in a Mach 2.5 freestream flow; see Fig. 30. The boattail consisted of a conical 5° convergence of the afterbody over the last 0.5 caliber (*i.e.*, diameter) of its length. The approach boundary layer on the boattailed afterbody (Case 1 below) separated through a relatively weak centered expansion, with a mean turning angle of about 2°. The rapid expansion at the corner of the cylindrical afterbody (Case 2) was considerably stronger, with a mean turning angle of approximately 9°. Herrin and Dutton (1995a) utilized these two flows to analyze the effects of expansion strength on the initial structure of the developing free shear layer. For the velocity statistics presented below, the data have been rotated such that the mean U and V components are, respectively, parallel and perpendicular to the average shear layer direction. While the flows investigated here are axisymmetric, the

ratio of the boundary layer thickness to the afterbody radius in the neighborhood of separation is of the order of only 10%, so that the results below should also apply to the planar case.

Figure 31 presents the nondimensional mean streamwise velocity, U/U_1, immediately adjacent to the separation point, where U_1 is the mean freestream velocity approaching separation for each case. The axial and radial coordinates have been nondimensionalized by the radius of the base at separation, R_0. The magnitude of the plotted variable is shown by the scale at the upper left of the figure. In addition, dotted lines denoting the approximate inner and outer edges of the shear layer are shown. The transition from a turbulent boundary layer velocity profile upstream of separation to an error function-type shear layer profile just downstream occurs smoothly and rapidly for the mildly expanded Case 1. However, immediately downstream of separation for the strong expansion of Case 2, the velocity profile develops a "kink" with an essentially piecewise linear profile and a discontinuity in velocity gradient at point A. This discontinuity is similar to that found in rapidly expanded boundary layers in supersonic flow (Hampton and White, 1986; Dussauge and Gaviglio, 1987) and likely represents the interface between two layers: an overexpanded viscous sublayer and an outer boundary layer remnant that has reduced turbulence activity due to the rapid expansion (see below).

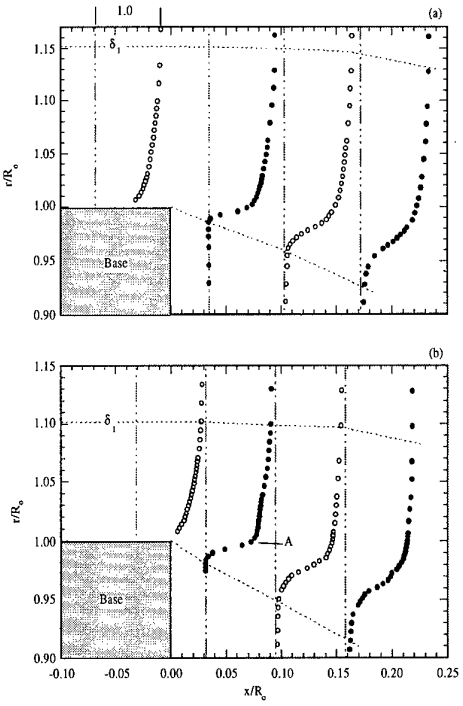

Fig. 31 Mean streamwise velocity profiles near separation, U/U_1, for (a) Case 1 and (b) Case 2 (from Herrin and Dutton, 1995a)

Profiles of the streamwise Reynolds normal stress, σ_u^2/U_1^2, adjacent to the separation point for both cases are shown in Fig. 32. One effect of the separation process, which is more obvious for the stronger expansion of Case 2, is the decrease in the streamwise velocity fluctuations over the middle portion of the shear layer relative to that of the upstream boundary layer. Recent work on rapidly expanded boundary layers (Dussauge and Gaviglio, 1987; Smith and Smits, 1991) suggests that this Reynolds stress reduction is due to the bulk dilatation and stabilizing convex streamline curvature associated with the expansion. A second, even more noticeable effect of separation shown in Fig. 32 is the large increase in turbulence level at the inner edge of the shear layer. This increased turbulence is most likely due to the impingement of recirculating region fluid on the shear layer as it is entrained by turbulent structures along the inner edge of the layer. The mean velocity vector field presented in Fig. 33 shows this entrainment of recirculation region fluid into the shear layer near the separation point for Case 1. In Fig. 32 note that the majority of the streamwise evolution of the normal stress profile occurs in the sharply-peaked region with the turbulence in the outer portion of the profile simply convecting in a frozen manner. The sharp peak in the longitudinal normal stress profile is in sharp contrast to similar measurements for rapidly expanded boundary layers, which show a reduction in normal stress across the entire thickness (Dussauge and Gaviglio, 1987; Smith and Smits, 1991). However, this difference is easily explained by the compliant fluid dynamic boundary and mass entrainment that occur along the inner edge of the expanded free shear layer as contrasted to the solid wall present for an expanded boundary layer.

Similar profiles of the transverse normal stress, σ_v^2/U_1^2 (not presented) also show a decrease in magnitude in the middle portion of the shear layer as compared to the upstream boundary layer. A peak in the transverse stress occurs near the inner shear layer edge as for the streamwise stress, although its magnitude is similar to that in the upstream boundary layer. This suggests that the expansion is on a short enough time scale that redistribution of turbulence energy from the streamwise component (primary extractor of turbulence energy from the mean flow) to the transverse component does not occur. The relative constancy of the peak transverse stress through the

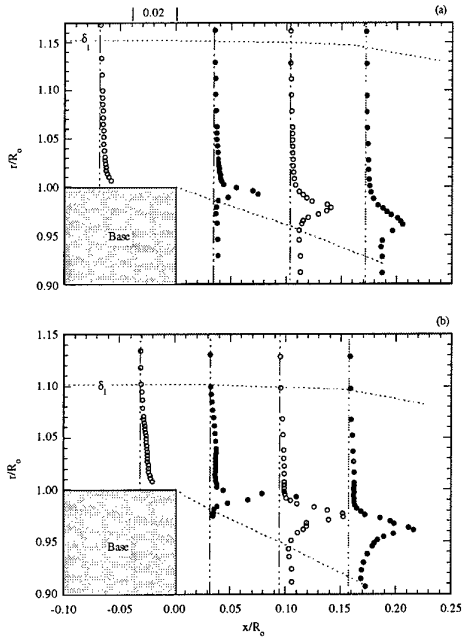

Fig. 32 Streamwise Reynolds normal stress profiles near separation, $(\sigma_u/U_1)^2$, for (a) Case 1 and (b) Case 2 (from Herrin and Dutton, 1995a)

expansion and the increase in the peak streamwise stress shown in Fig. 32 imply that the normal stress anisotropy, σ_u^2/σ_v^2, increases both across the expansion and with expansion strength. These results clearly show the nonequilibrium nature of the post-expansion turbulence field and its dependence on the strength of the expansion.

Profiles of the normalized Reynolds shear stress, $-\langle u'v'\rangle/U_1^2$, (also not shown) are similar to those for the streamwise normal stress plotted in Fig. 32, with a reduction in magnitude over the outer portion of the mixing layer and with a strong peak near the inner edge that increases with increasing expansion strength. A difference, however, is that the shear stress in the outer part of the expanded boundary layer is not only reduced, but essentially vanishes. This implies that there is essentially no turbulence production and that the large-scale structures are frozen in the outer part of the expanded boundary layer. The shear stress peak at the inner edge of the layer, on the other hand, implies the existence of large turbulent structures that actively entrain low-speed fluid, with this effect being enhanced with increased expansion strength. This increased mass entrainment from the separated region for the more

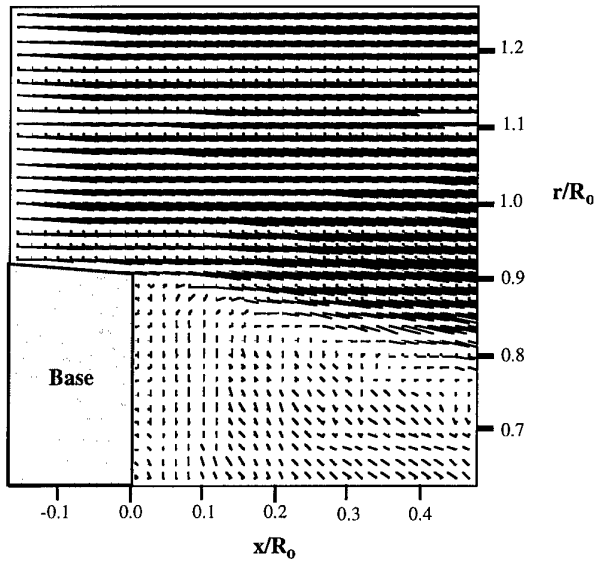

Fig. 33 Mean velocity vector field near separation for Case 1 (from Herrin, 1993)

strongly expanded cylindrical afterbody case is consistent with its lower base pressure as compared to the more weakly expanded boattailed afterbody. The location of the shear stress peak approximately corresponds to that of the peak mean velocity gradient shown in Fig. 31, so that the production of turbulent kinetic energy (proportional to the product of the two) is maximized in this region. In addition, the peak shear stress magnitude is also enhanced with increased strength of the expansion. As a result, higher downstream turbulence levels will occur for the more strongly expanded Case 2.

To further analyze the structure of the turbulence field in the neighborhood of separation, Herrin and Dutton (1995a) performed a quadrant decomposition of the instantaneous velocity realizations at each spatial location. The instantaneous u' and v' fluctuations, normalized by the local streamwise rms velocity fluctuation σ_u, are plotted against each other in Fig. 34 at three locations: upstream of separation for Case 1 (Case 2 results are similar) and immediately downstream of separation for Cases 1 and 2. The radial locations for each plot correspond to those of the peak shear stress at the given streamwise station. The quadrant decomposition in the upstream boundary layer, Fig. 34(a), displays a wide array of velocity fluctuations, with a slight preference for quadrant 2 and 4 events, but with no strongly preferred orientation. In contrast, the quadrant decomposition plots immediately downstream of separation for Cases 1 and 2, Figs. 34(b) and (c), show that the velocity fluctuations are more

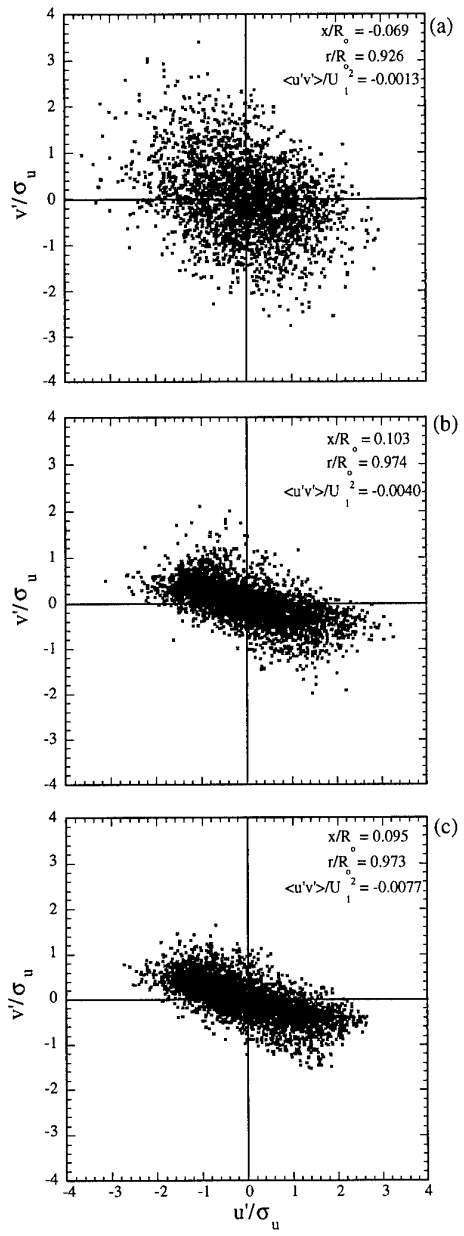

Fig. 34 **Velocity fluctuation quadrant decomposition near separation for (a) approach boundary layer of Case 1; (b) downstream of separation for Case 1; and (c) downstream of separation for Case 2 (from Herrin and Dutton, 1995a)**

organized and strongly aligned along a preferred stress direction in quadrants 2 and 4. Since large-scale turbulent structures are the most significant contributor to the Reynolds shear stress (*i.e.*, <u'v'> correlation), it follows from these results that the large structures in the initial portion of the shear layer are better organized than those in the approaching boundary layer. This result is in agreement with the fluctuating pressure probe and hot-wire studies of Shau *et al.* (1993) and Petullo and Dolling (1993), respectively, discussed above for matched-pressure, two-stream shear layers. Arnette *et al.* (1993) and Dawson and Samimy (1994) also found that rapid expansions increase large-structure organization for attached boundary layers in supersonic flow. Comparing the results for Cases 1 and 2, Figs. 34(b) and (c), shows that increasing the strength of the expansion causes a slight increase in the structure organization, although the separation process itself, and the consequent formation of the free shear layer, appears to be the more dominant factor.

Herrin and Dutton (1995a) further investigated the effects of expansion on shear layer turbulence structure by computing the instantaneous shear angle, $\psi=\tan^{-1}(v'/u')$, for each velocity realization and sorting the ensembles into histograms (probability density functions). Note that velocity fluctuations in quadrants 1 and 3 will have $\psi>0$, while quadrant 2 and 4 events will have $\psi<0$. The histograms generated in this manner for the three data locations of Fig. 34 are given in Fig. 35. The velocity fluctuations in the approach boundary layer, Fig. 35(a), show no strongly dominant shear stress orientation, although realizations in quadrants 2 and 4 ($\psi<0$) occur somewhat more frequently than in the other quadrants. Immediately downstream of separation for the more weakly expanded Case 1, Fig. 35(b), the shear stress has a strong preferential orientation about an angle of approximately -12° from the mean flow direction. This provides additional quantitative evidence of the increased organization of the turbulent structures in the separated free shear layer as compared to the upstream boundary layer. As the expansion strength is increased to Case 2, Fig. 35(c), the magnitude of the preferred shear stress angle increases slightly to -16°, although the general shape of the shear angle distribution is relatively unchanged from that of Case 1. The increase in the preferred shear angle with increased expansion strength may result from an increase in the average large-structure orientation angle with respect to the mean flow direction. The results of Arnette *et al.* (1993) for rapidly expanded, attached, supersonic boundary layers provide some support for this hypothesis.

We should note that we are unaware of any previous comparable work on the effects of separation through *compression* waves, although the current efforts of Palko (1997) are addressing this issue.

4.2.2 *Shear Layer Development*

Herrin (1993) and Herrin and Dutton (1995a) have also analyzed the development of the free shear layers contained in the near-wake regions of the boattailed and cylindrical afterbodies, Cases 1 and 2, discussed above (Fig. 30). The velocity data shown here are again rotated such that the U and V mean components are, respectively, parallel and perpendicular to the average shear layer direction. Data are presented from the $x/R_0=0$ base plane to about $x/R_0=2.5$, just before the rear stagnation point. The initial portion of this domain is at approximately constant pressure. However, the effects of the adverse pressure gradient caused by the recompression waves (see Fig. 30) are experienced by the shear layers over the last one-third or so of this region. In addition, as these shear layers approach the centerline, their thicknesses and radial locations relative to the axis will be of the same order of magnitude, so that the effects of axisymmetry will become important.

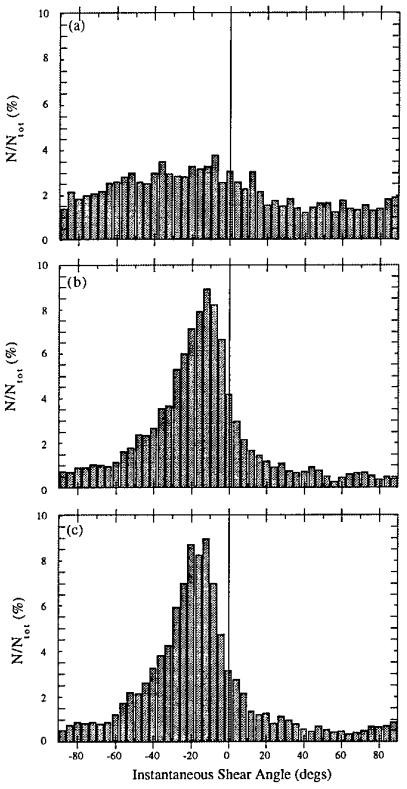

Fig. 35 Histograms of instantaneous shear angle for (a) approach boundary layer of Case 1; (b) downstream of separation for Case 1; and (c) downstream of separation for Case 2 (from Herrin and Dutton, 1995a)

As a result, it is expected that the results presented below will be qualitatively similar to planar symmetric separated flows, although precise quantitative magnitudes may differ between the two geometries.

Although the freestream velocities on either side of the shear layers contained in these separated flows vary somewhat with distance from the base corner, an average convective Mach number can be estimated (see Eq. 4). The result for both the boattailed and cylindrical afterbodies (Cases 1 and 2, respectively) is, $M_c \approx 1.3$, which indicates that these mixing layers are strongly affected by compressibility.

Figure 36 is a plot of the mean streamwise velocity profiles of the shear layers for Cases 1 and 2 in similarity coordinates (r_{mid} is the radial midpoint between the 10% and 90%ΔU locations and U_2 is the *local* mean velocity at the inner edge of the mixing layer). The two profiles plotted for each case are relatively far from separation, and the good collapse of the data demonstrates that the mean velocity field has become self-similar in this region. In addition, the agreement of the profiles for the two cases suggests that the stronger expansion that occurs at separation for Case 2, which distorted the *initial* mean velocity profile, Fig. 31(b), has little effect on the velocity profile farther downstream. All four profiles shown in Fig. 36 also have a relatively sharper corner at the outer, high-speed edge, which may be due to the reduced intermittency and altered large-scale structure in this region, as compared to that at the inner edge. Similar results have been obtained for matched-pressure, two-stream, compressible mixing layers (*e.g.*, Gruber *et al.*, 1993), although the rounding effect on the low-speed side may be accentuated for the current cases due to the nature of the recirculating flow on the shear layer inner edge.

In order to examine the growth of the shear layer in this separated flow, the loci of the 10%, 50%, and 90%ΔU lines for Case 1 are plotted in Fig. 37. It can be seen that the growth rate is initially very rapid with an overwhelming majority of it occurring on the inner edge, as shown by the divergence of the 10% and 50% velocity lines. As previously noted, this is the location where mass entrainment from the recirculation region is large. This result also clearly shows the importance of the initial shear layer development region on the overall mixing layer growth. Further downstream in Fig. 37, a region of reduced growth rate can be observed that extends to the rear stagnation point (marked with an "S").

To further investigate the growth rate characteristics of the shear layers, the dimensionless velocity thicknesses for both cases are plotted against

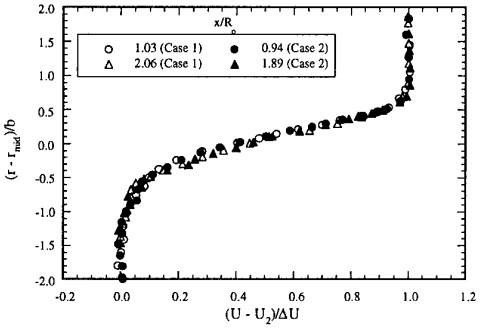

Fig. 36 Mean streamwise velocity profiles of the compressible shear layers for Cases 1 and 2 in similarity coordinates (from Herrin and Dutton, 1995a)

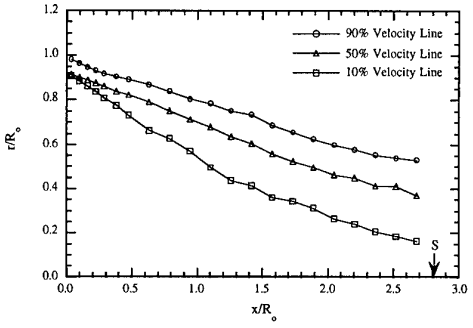

Fig. 37 Shear layer development for Case 1 (from Herrin, 1993)

distance from the separation point in Fig. 38. In both instances two regions of distinctly different growth rates (as just discussed) are apparent: a region of rapid linear growth almost immediately downstream of separation and a second region of reduced linear growth after the shear layer mean velocity profile becomes self-similar. By fitting least-squares lines to the thickness data of Fig. 38, the growth rates in the self-similar regions are found to be db/dx=0.032 and 0.090 for Cases 1 and 2, respectively. Since the convective Mach numbers for the two shear layers are essentially identical, the near tripling of the asymptotic growth rate of Case 2 relative to Case 1 cannot be a compressibility effect and is clear evidence of the sensitivity of this feature of shear layer behavior to initial conditions (*i.e.*, expansion strength at separation). The larger growth rate of Case 2 is also consistent with the higher levels of turbulence in this shear layer, both initially after separation (Fig. 32), and further downstream, as discussed next.

Using the Mehta and Westphal (1986) definition of a *fully-developed* shear layer discussed previously, not only must the growth rate be linear and the mean velocity profiles be self-similar, but the profiles of all turbulence quantities must also be self-similar with constant peak values. As an example of the approach of the shear layers in the current separated flows toward fully-developed conditions, Fig. 39 shows streamwise Reynolds normal stress profiles at several axial locations for Case 2. The comparable peak values shown for the last two measurement stations, x/R_0=1.57 and 1.89, suggest that this quantity is approaching self-similarity, although additional distance is needed for complete development. Comparable profiles of the transverse Reynolds normal stress and the Reynolds shear stress for Case 2 show an even slower approach toward self-similar conditions for these quantities. Plots of the same turbulent stress profiles for the more weakly expanded Case 1 demonstrate the same qualitative behavior with respect to attainment of the fully-developed state. However, in each case, the peak turbulent stress magnitudes for Case 1 are lower than those for Case 2. Thus, the far-field effect of increasing expansion strength at the shear layer origin is enhanced overall turbulence levels further downstream, with a concomitant increased growth rate.

Figure 40 further emphasizes this latter effect by plotting the peak streamwise and transverse normal stresses along the length of the shear layers for Cases 1 and 2. The peak streamwise normal stress distributions for the two cases, Fig. 40(a), are very comparable in shape, with a maximum immediately after separation, followed by a decrease to a local minimum, and then an increase to the end of the shear layer. However, the magnitudes for Case 2 everywhere exceed those for Case 1, especially near boundary layer separation, where the effects of expansion strength are dominant. Likewise, the peak transverse normal stress distributions for the two cases, Fig. 40(b), start with relatively small and comparable magnitudes immediately after separation, but then increase monotonically with increasing distance from the shear layer origin. In the downstream region, the peak stress values for the more strongly expanded Case 2 again are larger than those for Case 1. Comparing the two peak stress distributions, it appears that the far-field turbulence structure, in terms of the distribution of turbulence energy among the Reynolds stress components, is relatively unaffected by the strength of the initial expansion. However, the magnitudes of the individual stress components themselves increase with increasing expansion strength.

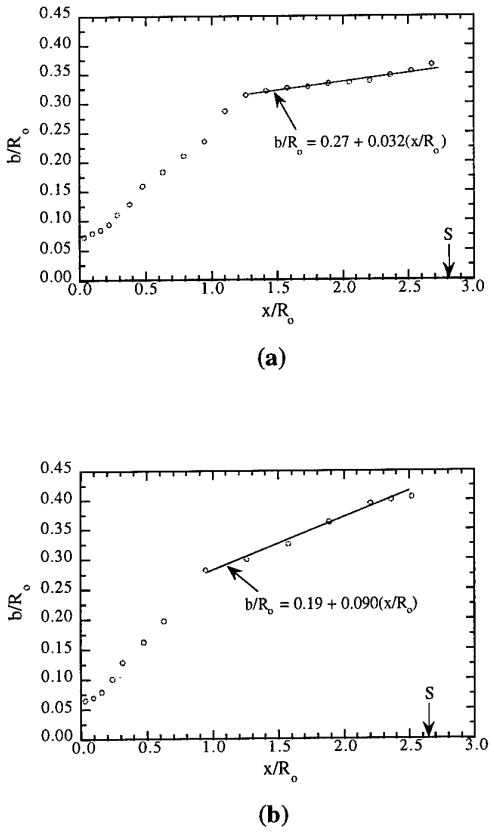

Fig. 38 **Shear layer growth rates for (a) Case 1 and (b) Case 2 (from Herrin, 1993)**

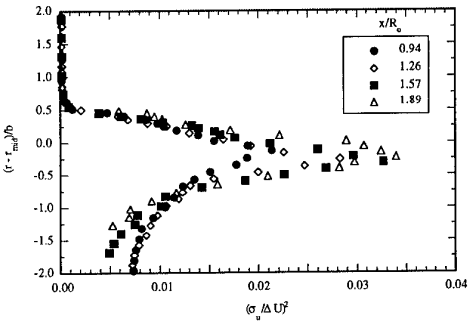

Fig. 39 **Streamwise Reynolds normal stress profiles of the compressible shear layer for Case 2 in similarity coordinates (from Herrin and Dutton, 1995a)**

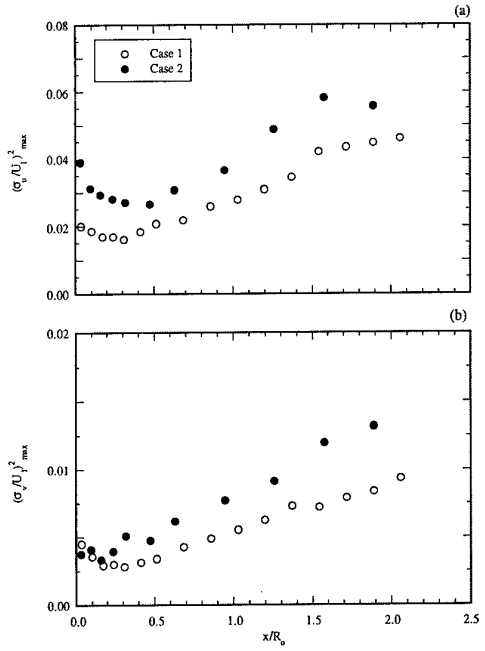

Fig. 40 **Comparison of peak Reynolds normal stress distributions for Cases 1 and 2: (a) streamwise normal stress and (b) transverse normal stress (from Herrin and Dutton, 1995a)**

4.2.3 *Effects of Recompression and Reattachment*

Herrin and Dutton (1995b) have studied the behavior of a compressible shear layer in a separated flow as it recompresses and reattaches near the rear stagnation point, see Fig. 30. The velocity measurements presented and discussed here are in standard cylindrical coordinate form, such that U and V are the axial and radial mean velocity components, respectively. Furthermore, axial distances from the base plane are nondimensionalized with respect to the reattachment length, x_R, where x_R/R_o=2.81 for the Case 1 (boattailed afterbody) measurements shown. The location of the onset of the adverse pressure gradient associated with the recompression waves has been estimated from the sidewall pressure data of Amatucci (1990) and is marked with the symbol "x_P" on the results plots. In each case at least one profile is shown upstream of recompression so that the properties of the highly compressible free shear layer (M_c≈1.3) are documented prior to the beginning of the adverse pressure gradient and reattachment processes. With the shear layer immediately adjacent to the centerline during recompression and reattachment, the effects of

axisymmetry are strong, and fundamental differences are found between the behavior of planar and axisymmetric flows in this region, as will be discussed below.

Profiles of the axial Reynolds normal stress through the reattachment region are shown in Fig. 41. The sharp peak in the first profile (upstream of recompression) is characteristic of compressible free shear layers, see Fig. 3. As the shear layer approaches the rear stagnation point, the peak values away from the axis decrease in magnitude while the centerline values reach a local maximum due to turbulence interaction effects across the axis. The net result is a less peaked, more radially uniform normal stress profile. Also, as the flow proceeds into the wake development region, the general level of the turbulent stresses is reduced because of the decreased mean strain rates in the wake as compared to those in the approaching shear layer. Qualitatively, the behavior of the radial Reynolds normal stress and primary shear stress profiles (not shown) through this region is similar. The transition from a sharply peaked, shear layer-type profile to a more rounded profile of reduced magnitude in the developing wake is, perhaps, most pronounced for the shear stress, since this quantity vanishes along the centerline by symmetry.

Figure 42 presents the peak magnitudes of the three Reynolds normal stresses and the primary shear stress as a function of axial distance near the rear stagnation point. All four of these peak turbulent stresses generally decrease in magnitude throughout the reattachment and initial wake development regions. The reduction in the peak magnitudes of the axial normal stress and the primary shear stress begin essentially immediately at the onset of recompression, while the decrease in the radial and tangential normal stresses is somewhat delayed. This delay is most likely due to the finite time required to redistribute turbulence energy from the axial normal stress, which extracts energy from the mean flow, to the radial and tangential components.

To explain the behavior of the turbulent stresses in this region, it is helpful to consider the "extra rates of strain" that are present in addition to the simple shear strain rate, $\partial U/\partial r$ (Bradshaw, 1974; Smits *et al.*, 1979a,b). In this regard, bulk compression due to the recompression waves and concave streamline curvature resulting from realignment of the flow along the axis should act to destabilize (increase) the Reynolds stresses in the reattaching shear layer. On the other hand, the effect of lateral streamline convergence as this axisymmetric shear layer approaches the centerline and reattaches on itself should stabilize (decrease) the

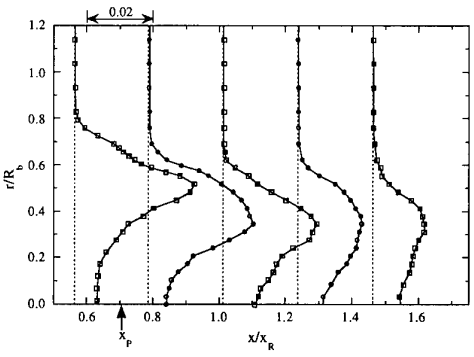

Fig. 41 Axial Reynolds normal stress profiles near reattachment, $\left(\sigma_u/U_{ref}\right)^2$ for Case 1 (from Herrin and Dutton, 1995b)

Reynolds stress magnitudes. Thus, the overall decrease in the level of the turbulent stresses through recompression and reattachment indicates the dominant influence of the lateral streamline convergence effect for this axisymmetric flow. In a similar vein, the turbulence measurements of Amatucci *et al.* (1992) show that, for a similar *two-dimensional* compliant boundary reattachment, the axial and radial turbulence intensities and the shear stress *increase* through recompression and peak at or just downstream of the reattachment point, Fig. 43. Since lateral convergence effects are not present in this two-dimensional flow, the increases in the Reynolds stresses up to the reattachment point can be explained by the destabilizing influences of bulk compression and concave streamline curvature. For both the axisymmetric and two-dimensional cases, as the shear layer realignment process is gradually completed, all of the extra strain rates vanish. Consequently, the turbulent stress magnitudes are reduced in the developing wake as the shear strain rate decreases.

In addition to investigating the magnitudes of the Reynolds stresses in the reattachment region, it is also instructive to examine the turbulence *structural* changes that result from application and removal of the extra strain rates. One such structure parameter is the anisotropy of the Reynolds normal stresses. Figure 44 presents a primary-to-secondary normal stress ratio, $(\sigma_u/\sigma_v)^2$, and a secondary-to-secondary stress ratio, $(\sigma_w/\sigma_v)^2$, plotted at the peak shear stress location through the reattachment region. During the early stages of recompression and reattachment, a significant shift in the relative magnitudes of the normal stresses is indicated by the decreasing value of $(\sigma_u/\sigma_v)^2$. This decay in normal stress anisotropy continues up to reattachment, where it appears to reach a new

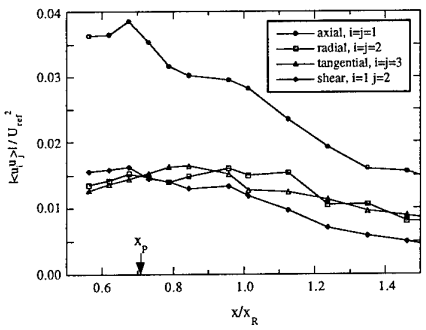

Fig. 42 Peak Reynolds stress distributions through reattachment for Case 1 (from Herrin and Dutton, 1995b)

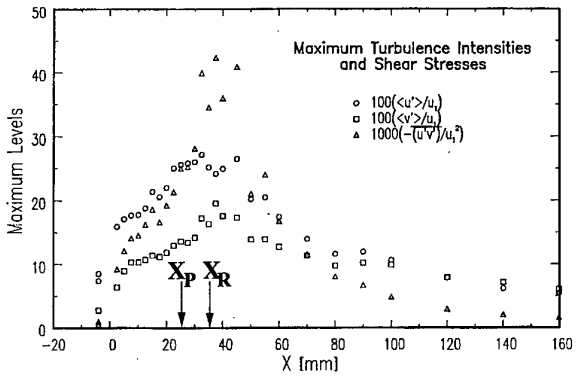

Fig. 43 Peak turbulence intensity and Reynolds shear stress distributions through reattachment for a two-dimensional, supersonic, separated flow (from Amatucci *et al.*, 1992)

equilibrium state with only small variations in the developing wake. Throughout the entire reattachment region, the $(\sigma_W/\sigma_V)^2$ secondary-to-secondary normal stress ratio remains approximately constant at a value of unity. This suggests little effect of the extra strain rates on the distribution of turbulence energy among these secondary normal stress components. Therefore, the recompression and reattachment processes generally increase the isotropy of the turbulence field as compared to that of the incoming shear layer, although the axial normal stress is still clearly the dominant component.

Herrin and Dutton (1995b) also investigated the behavior of two turbulence structure parameters: $-\langle u'v'\rangle/k$ and the shear stress correlation coefficient, R_{uv}, in the shear layer reattachment region. Both parameters were found to decrease monotonically

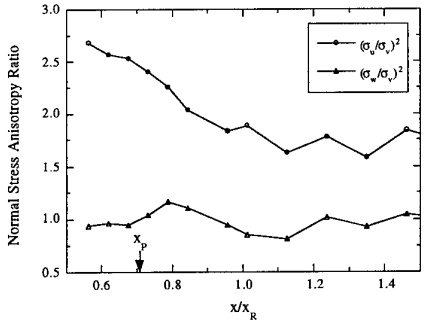

Fig. 44 Normal stress anisotropy ratios through reattachment for Case 1 (from Herrin and Dutton, 1995b)

through the region and to approach values (0.3 and 0.4-0.5, respectively) that are often used in turbulence closures. The decrease in the shear stress correlation coefficient is also indicative of a loss in organization of the large-scale turbulent structures as they negotiate the recompression and reattachment processes. This effect will be discussed further below.

Probability density functions of the instantaneous shear angle, $\psi=\tan^{-1}(v'/u')$, also discussed above in regard to the effects of expansion at separation, are presented in Fig. 45. The histograms correspond to three locations in the reattachment region: in the free shear layer just upstream of the start of recompression, very near the mean reattachment point, and downstream in the developing wake. The shear angle pdf in the approaching free shear layer exhibits a well-defined peak at a negative value of ψ, which indicates the predominance of quadrant 2 ($u'<0$, $v'>0$) and quadrant 4 ($u'>0$, $v'<0$) events. The organization of the shear layer turbulence field approaching reattachment is consistent with previous visualizations of large-scale turbulent structures in compressible mixing layers (*e.g.*, Messersmith and Dutton, 1996), and also is in agreement with shear angle pdfs constructed near the shear layer origin in the present flowfield, Fig. 35. The histograms shown here at reattachment and in the initial part of the wake retain the same general shape as that for the incoming mixing layer, although the peak at negative angles is no longer as dominant. This result suggests that, while quadrant 2 and 4 events are still the most frequent, the organization of the turbulence field decreases through reattachment. This reduction in large-structure organization is also consistent with the decrease in the magnitudes of the Reynolds shear stress and shear stress correlation coefficient in this region. It therefore appears that the large-scale structures

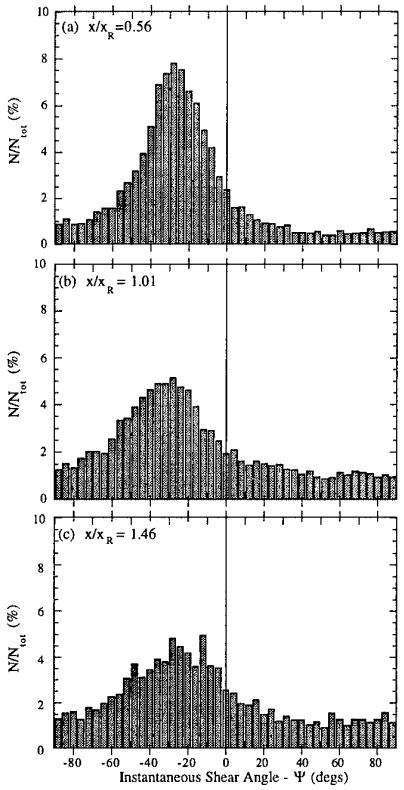

Fig. 45 Histograms of instantaneous shear angle through reattachment for Case 1: (a) x/x_R=0.56; (b) x/x_R=1.01; and (c) x/x_R=1.46 (from Herrin and Dutton, 1995b)

contained in the incoming shear layer can successfully negotiate the adverse pressure gradient and reattachment processes, but that they lose strength and organization as they do so. More evidence of this will be given below in discussions of planar visualizations of compressible separated flows.

4.3 Large-Scale Turbulent Structure

4.3.1 *Single-Frame Planar Imaging Results*

Smith (1996) and Smith and Dutton (1996) have conducted planar imaging studies in the same two-dimensional, supersonic, separated flow for which Amatucci *et al.* (1992) reported mean flow and turbulence measurements. Figure 46(a) presents a schematic of this flow, including the imaging locations that will be discussed below. The upper stream approaches the 25.4 mm thick base at M_1=2.5, while the lower stream is at M_2=2.0 before separating at the base corner. The upper stream boundary layer just before separation is about 2.3 times thicker than that of the lower stream (intentional mismatch to model a power-on missile flow). Since both flows originate from the same stagnation conditions, the static pressure of the lower-speed stream at separation is higher than that of the upper stream, P_2/P_1=2.14. Also, because both flows separate and expand to a common base pressure, the Mach 2.0 stream experiences a much stronger expansion and turning angle, 21.6°, as compared to the Mach 2.5 stream, which turns about 10.7°. After the separation and acceleration processes, the freestream flows adjacent to the recirculation region are both at approximately Mach 3.0. The two free shear layers that form after separation are recompressed and realigned to a common flow direction near the rear stagnation point. Since the lower stream static pressure at separation exceeds that of the upper stream, the flow direction of the developing wake is inclined upward at an angle of approximately 11.2°.

Figure 46(b) presents a global Mie scattering image of the entire near-wake region. Vaporized ethanol that is seeded into both flows far upstream of the test section condenses when expanded to supersonic velocities. The relatively lower-speed, and therefore warmer, fluid in the recirculation region promotes re-evaporation of the ethanol. Thus, the high-intensity regions in the image are in the supersonic freestreams, the low-intensity regions delineate recirculating region fluid, and the boundary between the two marks the turbulent structure of the shear layers and developing wake. Inspection of this global image suggests the existence of stringy large-scale structures in the shear layers that are particularly noticeable as the rear stagnation point is approached and also in the wake. Individual weak oblique shock waves that coalesce into the main recompression shocks are also easily visualized since the number density of the scattering droplets increases across the shocks. Other features are difficult to discern in this low-magnification view.

To examine in detail the structure of this separated flow, large ensembles of high-magnification images were obtained at each of the ten locations sketched in Fig. 46(a). Both side-view and end-view images were acquired and analyzed at each position. The choice of these locations was made based on the pressure gradient environment in the near-wake, as determined from the mean pressure measurements of Amatucci (1990). Positions A and B are in the constant-pressure, initial shear layer formation region. Position C is centered in the adverse pressure gradient (*i.e.*, recompression) region approaching the rear stagnation point. Position

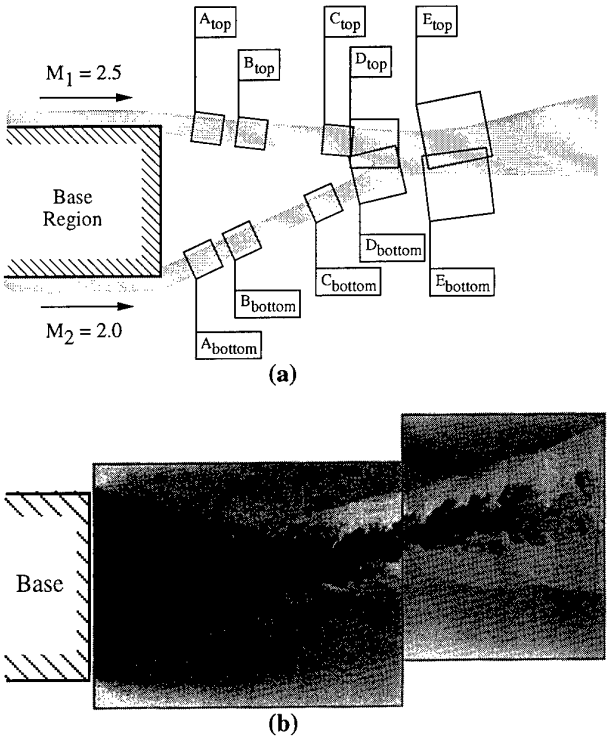

Fig. 46 Two-dimensional, supersonic, separated flow of Smith and Dutton (1996): (a) imaging locations and (b) global planar image of entire near-wake region

D is centered on the mean reattachment point, while Position E is located in the initial portion of the trailing wake. In each case the camera field-of-view was rotated so that the mean flow direction is horizontal and left-to-right across the images. Table 2 gives the imaging locations, inclination angles, and shear layer thicknesses at the five image positions in the upper shear layer, which will be discussed in detail below. Also included in Table 2 is an estimate of the convective Mach number at each location that was developed using the velocity data of Amatucci *et al.* (1992). For the first three positions before reattachment, the convective Mach number is fairly constant at a value of about 1.3. This value is similar to that of the shear layers in the axisymmetric separated flows analyzed by Herrin and Dutton (1995a,b) and indicates substantial compressibility effects. However, at reattachment, and especially as the trailing wake develops, the level of compressibility drops markedly.

The characteristics of the turbulent structures visualized at Positions A_{top} and B_{top} in the constant-pressure shear layer region are qualitatively similar, so that results only at the latter location will be shown. Figure 47 presents four time-uncorrelated instantaneous images from Position B_{top}. The mean thickness and location of the shear layer are indicated adjacent to the images. Large turbulent structures are clearly visible at this location, which, together with those visualized at Position A_{top}, demonstrate that such large structures exist even at this very early stage of shear layer development. However, the structures are not rounded, Brown-Roshko (1974) rollers, but rather are more elliptical in shape and inclined to the mean flow direction, with long filament-like braids connecting highly-strained structure cores. The structures sometimes exhibit a polygonal shape, which is similar to the observation made by Clemens and Mungal (1995) for two-stream compressible shear layers at high compressibility. The coherence and spatial periodicity of the structures at these locations are greatly reduced as compared to those of shear layers at low convective Mach number (*e.g.*, Fig. 9). This result can be attributed to the dominance of three-dimensional instability modes under the highly compressible conditions of this shear layer (Ragab and Wu, 1989; Sandham and Reynolds, 1990, 1991). The lower right image of Fig. 47 shows an excellent example of recirculation region fluid that has been surrounded by freestream fluid by means of some type of vortical motion. This engulfment-type of mass entrainment will act to reduce the base pressure and is the first step in mixing the recirculation region and freestream fluids at the molecular level (Broadwell and Breidenthal, 1982; Broadwell and Mungal, 1988).

Four instantaneous images from position C_{top}, in the adverse pressure gradient region, are shown in Fig. 48. At this location the eddies exhibit a greater diversity in size and shape than at the two earlier stations. For example, the upper right image has little well-defined large structure, while there are at least two distinct large structures and an intervening braid in the lower right image. Small-scale structures residing on larger structures are often observed at this location, as in the upper left image. A similar observation of small structures has been made for constant-pressure, two-stream, compressible mixing layers by Elliott *et al.* (1992). The compression waves that form the base of the main recompression shock are also sometimes seen in the images at this position (upper right image).

Figure 49 presents instantaneous images at the mean reattachment location, D_{top}. The large-scale structures that were seen at earlier locations have now grown and become dominant features of the flowfield; see also the global view, Fig. 46(b). Freestream fluid often makes deep excursions into the recirculation region and *vice versa*. The size and orientation of the

Table 2 Imaging locations and flowfield parameters for top shear layer (from Smith and Dutton, 1996)

Imaging position	Distance from base corner along shear layer, mm	Field-of-view inclination,[a] deg	Convective Mach number, M_c	Shear layer width, δ_{local}, mm
A_{top}	7.5	-10.7	1.27	1.65
B_{top}	15.0	-9.6	1.37	1.95
C_{top}	30.0	-5.6	1.25	2.35
D_{top}	35.0	0.0	1.12	2.77
E_{top}	50.0	11.2	0.74	3.98[b]

[a] Measured with respect to test section floor. Positive angles denote an upward inclination.
[b] An estimate for the half-wake width is used.

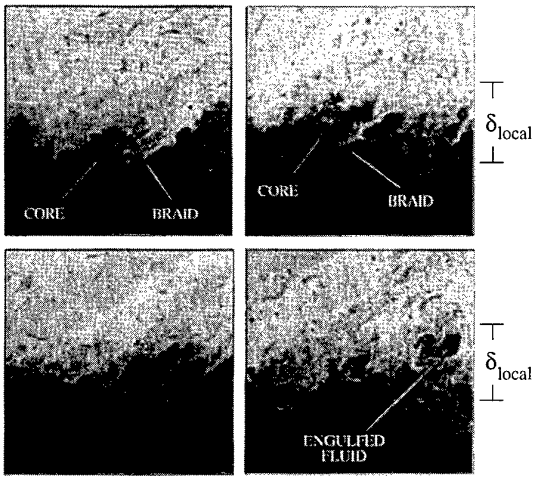

Fig. 47 Side-view planar images at Position B_{top} (from Smith and Dutton, 1996)

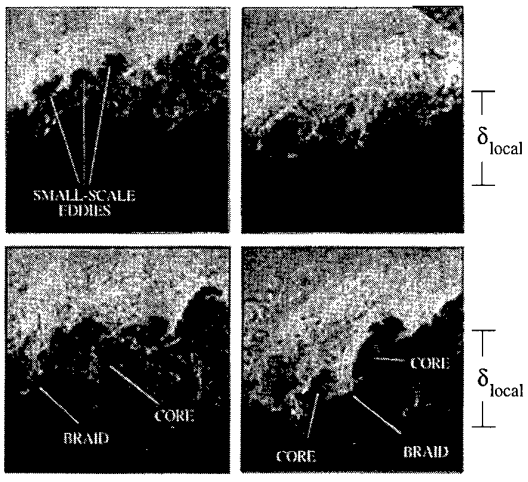

Fig. 48 Side-view planar images at Position C_{top} (from Smith and Dutton, 1996)

structures vary from image to image (compare the two images on the left), but nearly every one contains some degree of easily identifiable large-scale organization. Weak shock waves that emanate from within the shear layer are observed even more frequently than at the previous location in the adverse pressure gradient region. These shocks appear to originate from the lee side of large structures. However, whether or not the shocks are caused by the interference of large structures with the supersonic outer flow and, therefore, move with the structures, cannot be determined from these single-frame images. This subject will be addressed further in the discussion below of double-pulsed imaging results.

Images taken at Position E_{top} in the trailing wake are shown in Fig. 50. A variety of large and small structures is evident at this location. In some instances, the structure spacing is nearly periodic, as in the upper left image, while in other cases it appears to be random, as in the lower left image. At this location the structures appear to be a bit more rounded and less jagged than at earlier positions. Clear visualizations of shock origination from large structures are quite common, as is coalescence of these individual shocks into the global recompression shock.

Figure 51 presents two instantaneous end-view images at each of the four positions, B_{top}-E_{top}, at which side-view images were just shown and discussed. Compared to the side view, the quality and spatial resolution of the end-view images are somewhat reduced, since an oblique viewing angle was required in the latter case. Nevertheless, the major structural characteristics in this plane are readily discernible. The most common features at all four positions are rounded structures of freestream fluid projecting downward into the recirculation region and *vice versa*. Consequently, the shear layer has a corrugated appearance in the end views. It is expected that streamwise or obliquely-

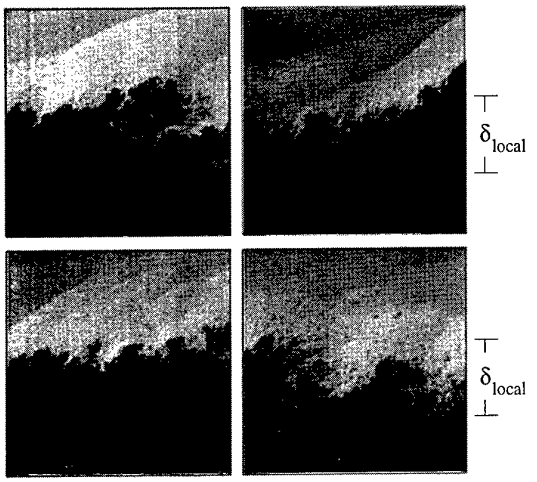

Fig. 49 Side-view planar images at Position D_{top} (from Smith and Dutton, 1996)

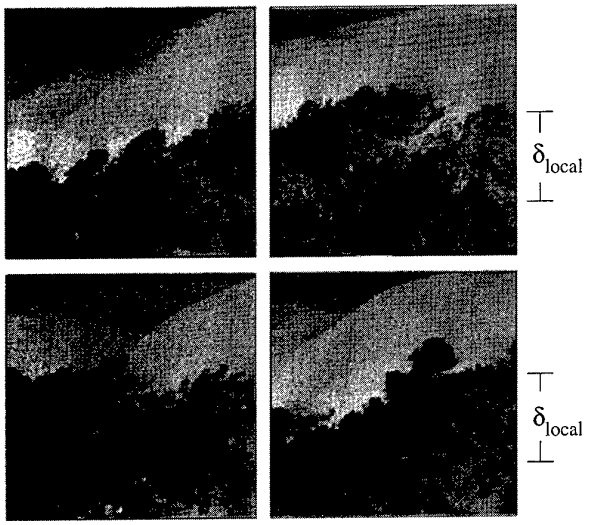

Fig. 50 Side-view planar images at Position E_{top} (from Smith and Dutton, 1996)

oriented vorticity is responsible for this trough-like structure and that this vorticity would participate strongly in entraining mass into the shear layer. Clemens and Mungal (1995) and Messersmith and Dutton (1996) have observed similar evidence of cross-stream fluid ejections in end-view images of two-stream, compressible shear layers. The general tilting of the rounded structures away from the vertical in Fig. 51 is also suggestive of obliquely-oriented large structures. This observation is consistent with the dominance of oblique instability modes at the large convective Mach number of this shear layer. Another less obvious feature that is commonly observed at the recompression, reattachment, and initial wake positions (C_{top}-E_{top}) is a high intensity "halo" that surrounds projections of recirculation region fluid into the shear layer. This may be due to shock waves that are caused by blockage of the supersonic outer flow by the structures.

In addition to obtaining time-resolved images, Smith and Dutton (1996) have computed spatial correlation fields for the image ensembles at each location A_{top}-E_{top}. This was done in order to analyze the large structure features in a statistically objective manner, much as was done by Messersmith and Dutton (1996) for two-stream, compressible mixing layers (Figs. 18-20). The ensemble-averaged spatial correlation fields for the side views at all five positions are shown in Fig. 52. In all cases the local mean flow direction corresponds to horizontal in the figure. In addition, the central correlation peak has a value of unity by definition, and the contours are drawn in increments of 0.1. The structure size and inclination are determined at the 0.5 correlation contour. The ensemble-averaged dimensionless size, eccentricity, and angular orientation at each position are summarized in Table 3.

Inspection of Fig. 52 shows that, on average, the structures at each of the five locations are elliptical in shape. As the shear layer progresses from Position A_{top} to B_{top} in the constant-pressure region, the structures seem to evolve only by growing, with little change in eccentricity or angular inclination (Table 3). The structure angles of approximately 40° at these two locations are larger than those measured by Messersmith and Dutton (1996) for two-stream, constant-pressure mixing layers at lower compressibility. In the current separated flow, however, the shear layer has been strongly expanded at its origin and a recirculating flow exists on its inner edge. These factors may account for the differences in structure angle between the two studies. In the recompression and reattachment regions, C_{top} and D_{top}, the dimensionless size increases substantially, the inclination angle is significantly decreased, while the eccentricity is increased modestly. As a result, the average structure at reattachment is highly elongated and tilted down toward the streamwise direction, Fig. 52. At position E_{top} in the initial wake, the normalized structure size is significantly reduced, the structure angle increases slightly, and the eccentricity decreases substantially with respect to the values at reattachment. The latter result is consistent with the more rounded structures visualized at this location, Fig. 50, and is most likely due to the reduced convective Mach number here.

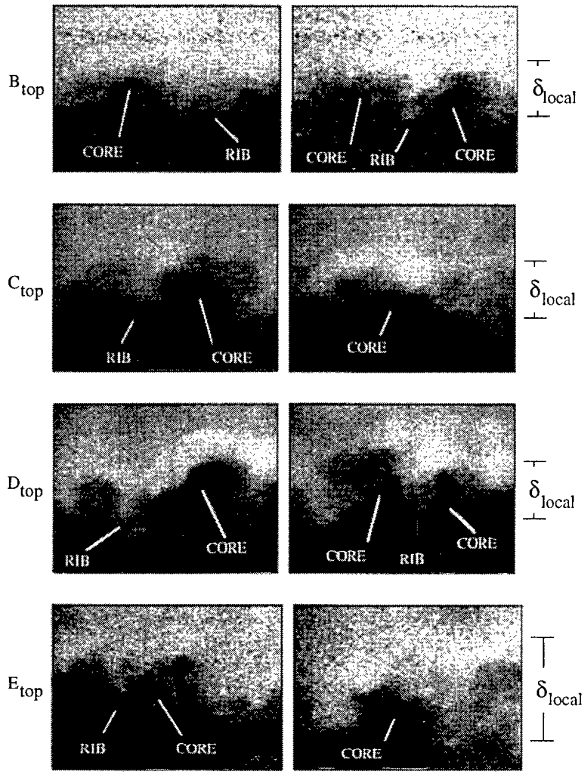

Fig. 51 End-view planar images at Position $B_{top} - E_{top}$ (from Smith and Dutton, 1996)

Messersmith and Dutton (1996) found that the structure inclination angle decreased with increasing compressibility for two-stream shear layers, Table 1. However, in the separated flow studied by Smith and Dutton (1996), the structure angle decreases from the values in the constant-pressure region as the recompression and reattachment processes are negotiated, even though the convective Mach number is roughly constant. Thus, the downward tilting in the latter case most likely results from the structures' response to the adverse pressure gradient and shear layer realignment processes. This hypothesis is supported by the two-point fluctuating pitot pressure measurements of Shau *et al.* (1993). When these investigators impinged a shear layer at M_c=0.28 with an oblique shock wave, the large structures were found to react by tilting downward. In the separated flow of Smith and Dutton (1996), the adverse pressure gradient in the recompression and reattachment regions is qualitatively similar to that caused by a shock.

A careful examination of the correlation contours at Positions C_{top} and D_{top} in the recompression and reattachment regions, Fig. 52, shows that they are not all aligned along a common axis as they are in the constant-pressure region at Positions A_{top} and B_{top}. This contour rotation is especially pronounced at the reattachment location, where the orientations of the 0.9 and 0.5 contours differ by approximately 25°. The central contours at levels from 0.7-0.9 do, however, maintain a consistent orientation from Positions A_{top} to D_{top}. These results suggest that the large-structure cores maintain their coherence, while the structure peripheries are more susceptible to the effects of the adverse pressure gradient and other localized influences (extra strain rates) in the neighborhood of the rear stagnation point. The recompression and reattachment processes therefore appear to degrade the spatial coherence of the large-scale structures present in the incoming shear layer. This conclusion is in agreement with the velocity measurements of Herrin and Dutton (1995b), made for an axisymmetric reattaching shear layer. Note that the contours for Position E_{top} in the initial wake are better aligned than at the two preceding locations, perhaps due to the reduced convective Mach number and strain rates at this position.

The end-view spatial correlation fields (not shown) at all five locations are qualitatively similar to each other and consist, essentially, of concentric circles. The spanwise symmetry of these correlations confirms that the mean flowfield is nominally two-dimensional. Table 4 presents the relevant statistical results. Since the correlation contours are nearly circular in this view, the eccentricity is very small, particularly at the later stations. The nondimensional structure size increases through the constant-pressure and recompression regions, before decreasing at reattachment and in the wake. The last column in Table 4 gives the ratio of the end-view major axis to the side-view major axis. At the first two locations, in the constant-pressure region, the large structures are slightly longer in the spanwise direction than in the streamwise. However, in the recompression region, a crossover occurs such that at the last three stations the structures exhibit a greater coherence in the streamwise direction. The large shear strain rate experienced by the layer may be responsible for stretching the structures in the streamwise direction, while the large convective Mach number is responsible for the onset of oblique instability modes that act to reduce the spanwise correlation length.

Time-resolved imaging and spatial correlation analyses have also been performed at the five locations in the bottom shear layer sketched in Fig. 46(a). In general, the results for this shear layer are quite similar to those just discussed for the upper layer. However, some distinct differences were also observed, which are thought to be due primarily to the differing expansion strengths experienced at the separation points. A detailed comparison of the top and bottom shear layer single-pulse imaging results can be found in Smith (1996).

4.3.2 *Dual-Frame Planar Imaging Results*

In addition to the single-frame planar imaging experiments described above, Smith (1996) also obtained double-pulsed images for the same high-speed separated flow shown in Fig. 46. These experiments allowed the temporal evolution and convective velocity of the turbulent structures to be examined. To accomplish this, large side-view image ensembles were obtained at Positions B-E in both the upper and lower shear layers. The cameras in this two-laser, two-camera technique were again rotated so that the horizontal direction in the images corresponds to the local streamwise direction.

Four different time delays were used at each location to investigate structure evolution over increasing pulse separations. The magnitude of these delays, τ, was chosen based on consideration of the dimensionless delay parameter, $\bar{\tau} = U_c \tau / \delta_{local}$, which relates the time delay to the local shear layer integral scales. Note that when $\bar{\tau}$ equals unity, a structure will convect a streamwise distance equal to one shear layer thickness. The four time delays for the imaging experiments at each location correspond to $\bar{\tau}$ values of approximately 0.5, 1.0, 1.5, and 2.0.

Since the structure evolution characteristics in the upper and lower shear layers at comparable locations are similar, dual-frame images will be presented only for the upper layer. At Position B_{top} in the constant-pressure region, image pairs at the shortest time delay, $\bar{\tau} = 0.43$, show that the inclined, elliptical (or sometimes polygonal) structures convect in a frozen manner with little rotation or deformation. Features in the initial images are easily detected in the delayed images, indicating that the structures retain their spatial coherence over this short time interval. In contrast, Fig. 53 shows two image pairs with $\bar{\tau} = 0.81$. In this case, the dominant evolution characteristic is rotation in a clockwise sense with an accompanying increase in size and eccentricity; see the marked structure core in Fig. 53(b). This elongation and rotation down toward the streamwise direction are consistent with other multi-frame imaging studies of two-stream compressible mixing layers (Mahadevan and Loth, 1994; Elliott *et al.*, 1995; Ramaswamy *et al.*, 1996). While clockwise rotation was observed most often, occasionally structures imaged at this location rotated counter-clockwise, thereby increasing their structure angle with respect to the local mean flow direction.

Side-view image pairs obtained at Position B_{top} and dimensionless time delays of $\bar{\tau} = 1.21$ and 1.61 show the limited temporal coherence of the structures under these conditions. In many cases, structures identified in the initial image are not easily seen in the second image. For example, the braid indicated in the delayed image of Fig. 54 at $\bar{\tau} = 1.61$ does not appear to be present in the initial image. This rapid breakdown with increasing time delay indicates that the structures

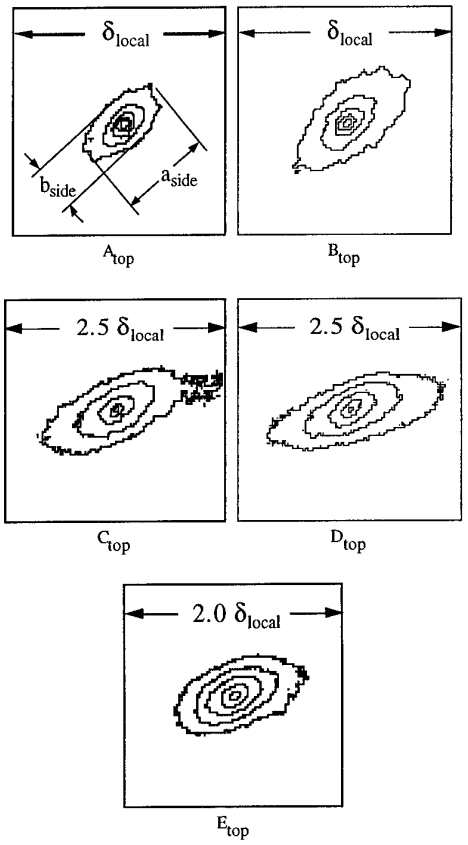

Fig. 52 **Side-view spatial correlation fields for top shear layer (from Smith and Dutton, 1996)**

Table 3 Side-view correlation results for top shear layer (from Smith and Dutton, 1996)

Position	Major axis dimension, a_{side},[a] mm	Nondimensional structure size,[a] a_{side}/δ_{local}	Eccentricity,[a] $\varepsilon=1-b_{side}/a_{side}$	Structure angle,[b] deg
A_{top}	0.71	0.43	0.50	41.2
B_{top}	1.24	0.64	0.54	40.1
C_{top}	3.96	1.69	0.61	24.6
D_{top}	5.56	2.01	0.65	17.4
E_{top}	4.57	1.15	0.46	19.8

[a] See Fig. 52 for definition of a_{side} and b_{side}.

[b] Measured with respect to local mean streamwise direction.

Table 4 End-view correlation results for top shear layer (from Smith and Dutton, 1996)

Position	Major axis dimension, a_{end}, mm	Nondimensional structure size, a_{end}/δ_{local}	Eccentricity, $\varepsilon=1-b_{end}/a_{end}$	a_{end}/a_{side}
A_{top}	0.90	0.55	0.08	1.27
B_{top}	1.45	0.75	0.02	1.17
C_{top}	2.30	0.98	0.01	0.58
D_{top}	2.30	0.83	0.00	0.41
E_{top}	3.07	0.77	0.00	0.67

at this location have a temporal coherence of order δ_{local}/U_c (*i.e.*, $\bar{\tau} \approx 1$). Using a similar two-frame imaging technique, Elliott *et al.* (1995) found greatly reduced temporal coherence of structures in their two-stream shear layer experiments when the compressibility was increased from M_c=0.51 to 0.86. Thus, the current results, which show rapid structural breakdown for the highly compressible conditions at B_{top} ($M_c \approx 1.3$), are not surprising.

At this early stage of shear layer development (Position B_{top}), no evidence of structure formation from the roll-up of instability waves was seen. As discussed earlier, this is similar to Elliott *et al.*'s (1995) results for a two-stream layer at M_c=0.86, but differs from their results at lower compressibility, M_c=0.51, where structure roll-up from Kelvin-Helmholtz waves was observed. Also, in the current separated flow, no instances of rotational pairing, as occur at small M_c, were observed for any time delay at Position B_{top}, or at any other position. The lack of pairing events in the shear layers of the present study is most likely related to their high compressibility level, $M_c \approx 1.3$. Papamoschou (1990) has suggested that a supersonic convective Mach number environment should severely limit the ability of a trailing structure to communicate with or interact with a leading structure, which would reduce the likelihood of pairing. However, it may be that other structure interactions, which are either complex or difficult to visualize, are present in the current high-speed separated flow.

Moving to Position C_{top} in the recompression region, image pairs obtained at a short time delay, $\bar{\tau} = 0.42$, are characterized primarily by convection of large-scale structures without appreciable deformation. Small-scale structures that are observed at the edges of the large structures do exhibit significant temporal evolution at this short delay, however. Two image pairs at this location at a larger pulse separation, $\bar{\tau} = 0.96$, are shown in Fig. 55. In this case, a pronounced clockwise rotation of the marked structure in the upper pair can be seen. In addition, this structure flattens noticeably and appears to lose organization during the pulse interval. In contrast, the large structures in Fig. 55(b) seem to simply convect with little alteration, although the associated smaller-scale structure is seen to evolve considerably.

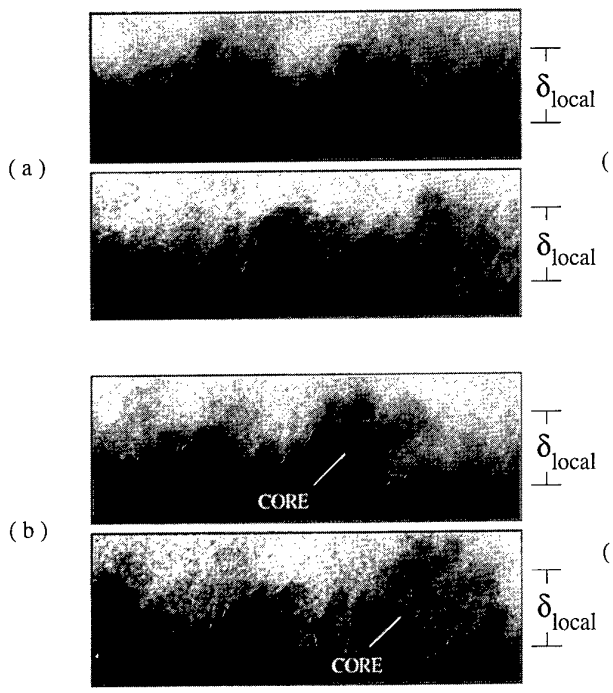

Fig. 53 Double-pulsed planar images at Position B_{top}; $\bar{\tau} = 0.81$ (from Smith, 1996)

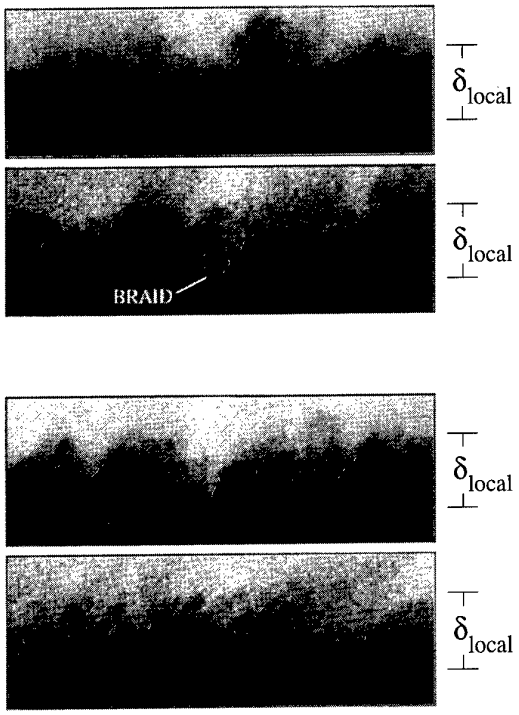

Fig. 54 Double-pulsed planar images at Position B_{top}; $\bar{\tau} = 1.61$ (from Smith, 1996)

Figure 56 presents image pairs obtained at the mean reattachment point, Position D_{top}, at the short temporal separation of $\bar{\tau} = 0.49$. As at earlier stations, the dominant mechanism here is large-structure translation, although the smaller structure on the left side of Fig. 56(b) does appear to rotate and elongate. In addition, the thin braid that separates this structure from the larger structure just to its right appears to degrade during the pulse interval. This may be a realization of the "slapping" structure interaction discussed above for compressible shear layers (Mahadevan and Loth, 1994). At a longer time delay of $\bar{\tau} = 1.03$, the previously observed large-structure evolution history of translation with a significant amount of rotation and elongation is again found. Substantial growth of smaller-scale structures along the peripheries of structure cores and braids is also seen.

Additional interesting features in both image pairs of Fig. 56 are the bright regions seen on the upstream sides of the large structures. *If* these regions are caused by the weak shocks that were seen emanating from within the shear layers in the single-frame images (see Fig. 49), then the fact that these regions maintain their position on the windward side of the large structures suggests that the shocks move with the structures. This, in turn, suggests that these shocklets are indeed caused by the structures' interference with the outer supersonic flow and are not simply stationary waves resulting from the mean recompression of the flow near the rear stagnation point. Although not absolutely conclusive, these image pairs at least suggest the existence of eddy shocklets (Dimotakis, 1991; Papamoschou, 1995) in this highly-compressible separated flow.

Two-frame time-correlated images in the initial wake region, Position E_{top}, differ quite substantially from those at the upstream locations. In this case, image pairs obtained not only at the shortest time delay, $\bar{\tau} = 0.41$, but also at the increased delay of $\bar{\tau} = 0.87$, Fig. 57, are characterized essentially exclusively by large-structure translation with little temporal evolution. Even at $\bar{\tau} = 1.30$, Fig. 58, simple structure convection seems to prevail, although some degree of rotation and elongation can be observed. In contrast, time delays of this magnitude at the upstream positions resulted in considerable structural evolution and, in some cases, an almost complete loss of temporal coherence. This result at E_{top} may be partially due to the wake-like nature of the flowfield at this location, which makes estimates of the convection velocity and local layer thickness difficult. Thus, the values of $\bar{\tau}$ given here may not be perfectly consistent with those given at the earlier stations. However, a more likely explanation for the persistence of structure identity at this location is

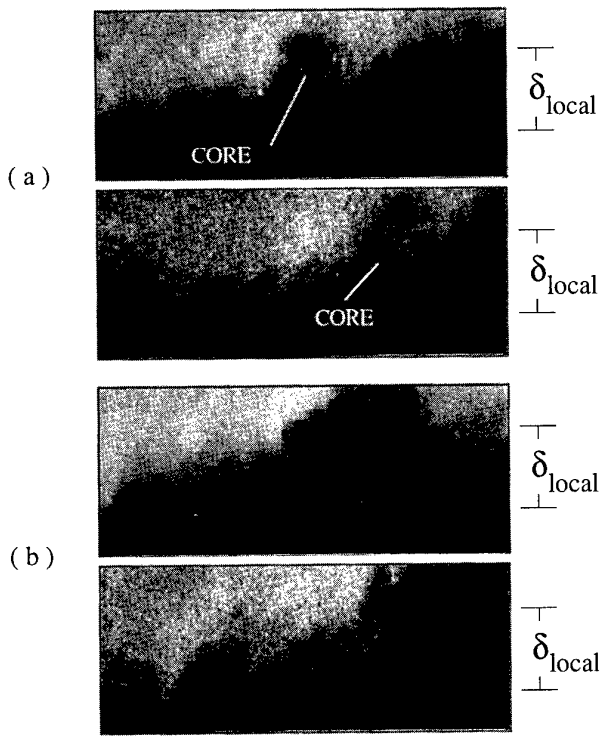

Fig. 55 Double-pulsed planar images at Position C_{top}; $\bar{\tau} = 0.96$ (from Smith, 1996)

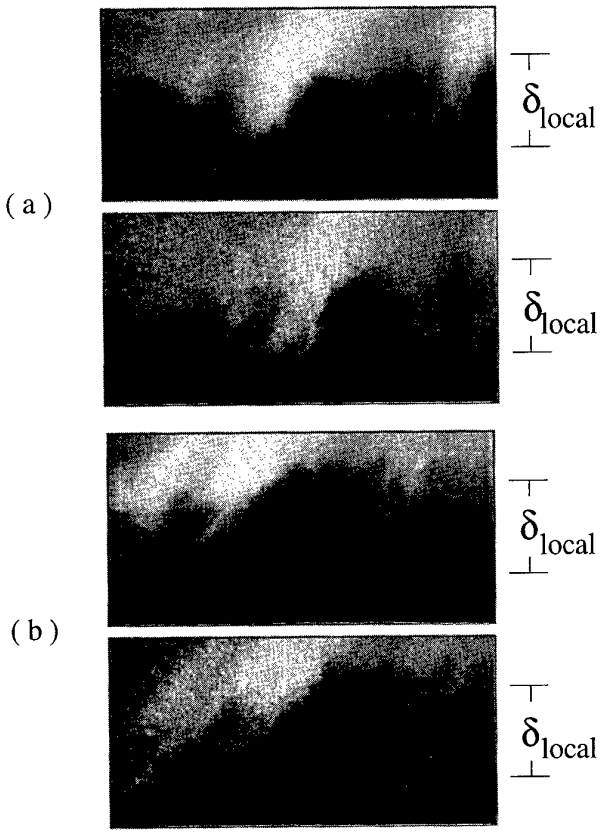

Fig. 56 Double-pulsed planar images at Position D_{top}; $\bar{\tau} = 0.49$ (from Smith, 1996)

that its compressibility is significantly reduced, M_c=0.74 (Table 2), as compared to that at the upstream locations, $M_c \approx 1.3$. This observation of increased temporal coherence with reduced compressibility is in agreement with the fluctuating pitot pressure measurements of Samimy *et al.* (1992) and the double-pulsed planar imaging study of Elliott *et al.* (1995) for two-stream compressible shear layers.

Smith (1996) has used these ensembles of time-correlated, dual-frame images to compute structure convection velocities in this separated flow. As discussed earlier in regard to two-stream shear layers, the convection velocity is an important parameter for estimating growth rates, entrainment ratios, mixing rates, and noise characteristics. Smith (1996) obtained results at Positions B_{top}-E_{top} to characterize structure velocities in the constant-pressure, recompression, reattachment, and initial wake development regions, respectively. Convection velocities were also determined at Positions B_{bottom} and C_{bottom} to study the effects of the differing expansion strengths in the initial portions of the two shear layers.

Table 5 presents the convection velocity results for the six imaging positions. The subscript "i" is used to denote the isentropic theoretical values for the convection velocity (Eq. 2) and convective Mach number (Eq. 4), while the "exp" subscript indicates experimental measurements of the same parameters. In the upper shear layer, the experimentally determined convection velocity decreases substantially as the structures leave the constant-pressure region (B_{top}) and enter the adverse pressure gradient (C_{top}) and reattachment (D_{top}) regions. Then, as the mean flow accelerates in the initial wake region (E_{top}), the structure convection velocity also increases significantly. The bottom shear layer measurements show a similar but smaller decrease in structure convection velocity from the constant-pressure (B_{bottom}) to the recompression (C_{bottom}) regions. Considering the mean pressure and velocity fields in the entire near-wake region, these general trends for the large-structure convection velocity are physically reasonable.

The measurements of U_c at the initial constant-pressure shear layer locations, B_{top} and B_{bottom}, are nearly identical. Therefore, the structure translation rate appears to be unaffected by the strength of the initial expansion at the shear layer origin. This result may not be surprising, though, since the velocity of the

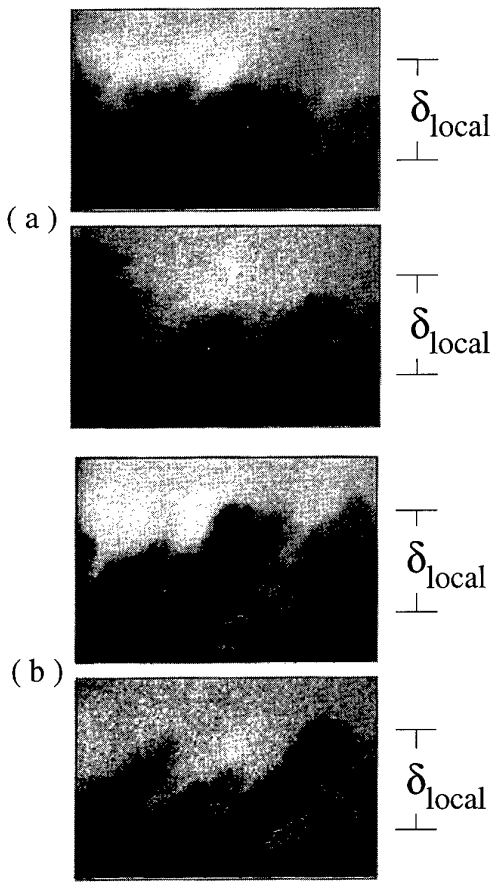

Fig. 57 **Double-pulsed planar images at Position E_{top}; $\bar{\tau} = 0.87$ (from Smith, 1996)**

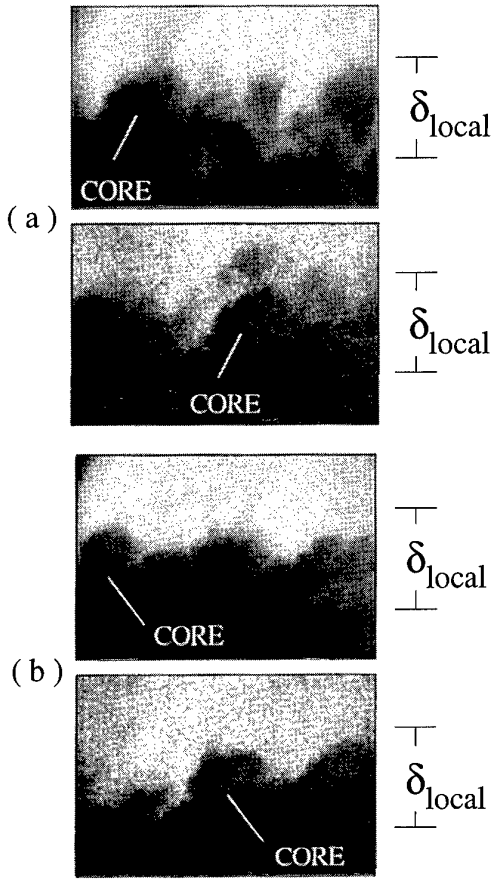

Fig. 58 **Double-pulsed planar images at Position E_{top}; $\bar{\tau} = 1.30$ (from Smith, 1996)**

freestreams immediately adjacent to the two shear layers are identical (M≈3.0). In contrast, as the structures enter the adverse pressure gradient region (C), those in the upper layer decelerate significantly more than in the lower layer. This result may again be explained by consideration of the mean pressure field, since the top shear layer experiences an adverse pressure gradient that is approximately 25% stronger than that of the bottom layer (Amatucci, 1990).

Another point that is clear from an examination of Table 5 is that the standard deviation of the U_c measurement ensembles, $\sigma_{Uc,exp}$, is quite large. As was also found for two-stream compressible shear layers, a wide range of convection velocities is therefore experienced at each of these locations. The reduced value of $\sigma_{Uc,exp}$ in the initial wake region, Position E_{top}, may be another manifestation of the better spatial and temporal coherence of the large structures for the lower convective Mach number conditions here.

Comparison of the convection velocity measurements with the isentropic theoretical values in Table 5 shows that at Positions B_{top} and B_{bottom}, in the constant-pressure portions of the shear layers, the measured values exceed the theoretical estimates. This trend is in agreement with the "stream selection rule" (Dimotakis, 1991) discussed earlier in regard to two-stream compressible mixing layers. This rule states that for supersonic/subsonic shear layers (which is the case at all positions in the current separated flow), the structure convection velocity will tend toward the velocity of the supersonic stream. As a result, the value of M_{c2} will exceed that of M_{c1} under these conditions. This result is emphasized in the M_{c1}-M_{c2} plot of Fig. 59, where the convection velocity data from other supersonic/subsonic, two-stream, constant-pressure shear layer investigations are included. For all cases (including B_{top} and B_{bottom}), except for the two cases of Elliott *et al.* (1995), $M_{c2}>M_{c1}$, in agreement with the selection rule. However, as the shear layer progresses

Table 5 Isentropic predictions and experimental results for convection velocity (from Smith, 1996)

Imaging Position	$U_{c,i}$ m/s	$U_{c,exp}$ m/s	$\sigma_{U_{c,exp}}$ m/s	$M_{c,i}$	$M_{c1,exp}$	$M_{c2,exp}$
B_{top}	335	399	112	1.37	1.06	1.55
C_{top}	360	334	120	1.25	1.37	1.17
D_{top}	387	298	123	1.12	1.55	0.86
E_{top}	466	352	93	0.74	1.29	0.40
B_{bottom}	335	392	135	1.37	1.10	1.53
C_{bottom}	360	372	135	1.25	1.19	1.28

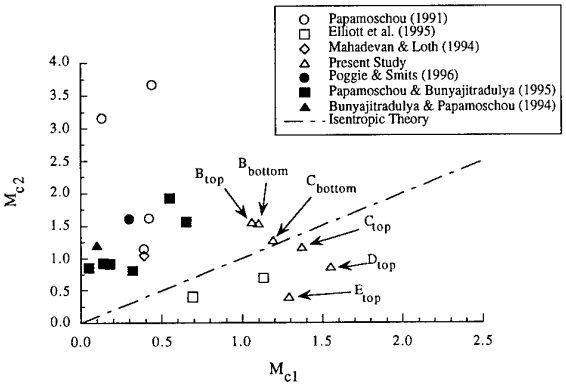

Fig. 59 Experimental results for M_{c1} and M_{c2} for several two-stream compressible shear layers and the separated flow of Smith (1996)

into the recompression (C_{top}), reattachment (D_{top}), and wake development (E_{top}) regions, the measured value of U_c drops below, in some cases quite significantly, the theoretical value; see Table 5. As a result, M_{c2} is less than M_{c1} at these positions, Fig. 59. However, this should not be considered a violation of the stream selection rule, since these four positions involve non-zero pressure gradients. As a result, the selection rule is not expected to be a good predictor of convection velocity at these locations. Note that at Position C_{bottom} the experimental and theoretical values of U_c are approximately equal so that the values of M_{c1} and M_{c2} are nearly equal here. This is most likely due to the fortuitous cancellation of the usual $M_{c2}>M_{c1}$ behavior by the effects of the adverse pressure gradient.

Another point of interest in Table 5 is the large value of M_{c1} measured at Position D_{top}. This value, $M_{c1}=1.55$, indicates that the outer flow moves supersonically with respect to the shear layer large structures, indicating the possibility of eddy shocklets at this location. Evidence of the existence of eddy shocklets at D_{top} was presented and discussed in relation to Fig. 56.

5. SUMMARY

Recent experimental efforts aimed at achieving a better understanding of the physical flow mechanisms in compressible turbulent free shear layers have been reviewed. Both two-stream, constant-pressure layers, as well as the shear layers that occur in high-speed separated flows, have been considered. While it is difficult, and perhaps a bit presumptuous, to attempt a concise summary of a broad area of research, the following observations are offered.

5.1 Two-Stream, Constant-Pressure Shear Layers

- Compressible shear layer growth rate is reduced compared to that of an incompressible layer at the same velocity and density ratios. The convective Mach number (M_c) correlates the growth rate data moderately well.
- The peak transverse Reynolds normal stress and Reynolds shear stress are strongly reduced with increasing M_c, while the peak spanwise normal stress is approximately constant. There is some disagreement about the trend of the streamwise normal stress and, therefore, the normal stress anisotropy. In general, the reduction of peak turbulence quantities with increasing compressibility is well correlated by M_c.
- A shift in the large-scale turbulent structure occurs from spanwise rollers to obliquely-oriented structures to a highly three-dimensional turbulence structure as M_c increases.
- Although the large structures of compressible shear layers are generally poorly organized, they are better organized than in the approach boundary layer, and this organization increases with downstream distance.

- As M_c increases, the large structures (side view) become more jagged and/or polygonal. The normalized size increases and the structure inclination angle decreases with increasing compressibility. End views show a more convoluted interface at large M_c.
- The large structures of compressible shear layers have limited temporal coherence. The dominant evolution characteristics are elongation, rotation down toward the streamwise direction, with attendant growth of small-scale structures.
- There is no evidence of structure roll-up from instability waves at large M_c, nor has rotational pairing been observed. A modified merging mechanism, termed "slapping," has been reported.
- At large M_c the structures do not convect at the isentropic theoretical convection velocity, but rather at a velocity closer to that of one freestream or the other ("stream selection rule").
- There is only limited experimental evidence of eddy shocklets for shear layers at large M_c.
- Efforts at growth rate enhancement have generally met with limited success. However, periodic Mach wave, glow discharge, and passive acoustic excitation methods have achieved significantly increased growth.

5.2 Compressible Shear Layers in High-Speed Separated Flows

- In the neighborhood of separation and expansion, compressible shear layers exhibit a two-layer character with a kink in the mean velocity profile. In the outer layer, turbulence levels are reduced, while in the inner layer, they are greatly enhanced. These effects are magnified with increasing expansion strength.
- Large structures in the initial portion of the shear layer are better organized than in the upstream boundary layer. Increasing expansion strength increases organization slightly.
- Shear layer growth occurs in two distinct regions: rapid initial growth immediately after separation, which is predominantly on the inner edge, and slower growth further downstream as the mean velocity profile becomes self-similar. Growth rates and turbulence levels are higher for increasing expansion strength.
- For *two-dimensional* reattaching shear layers, turbulence quantities peak at or just downstream from reattachment due to concave streamline curvature and bulk compression. For the *axisymmetric* case, these quantities decrease through the recompression and reattachment regions because of the dominant influence of lateral streamline convergence.
- The large structures in a highly compressible separated shear layer are elliptical or polygonal (side view) with long braids and highly strained cores. The structure dimensionless size increases, the inclination angle decreases, and the eccentricity increases moderately between the separation and reattachment points. End views in this region show a corrugated interface with fluid projections up and down into the shear layer.
- In the initial wake the normalized structure size is reduced, the inclination increases slightly, and the eccentricity decreases substantially compared to locations upstream. These observations are consistent with the lower M_c at this location.
- The recompression and reattachment processes cause a degradation in the spatial organization of the large structures, which results in increased turbulence isotropy.
- In the constant-pressure, recompression, and reattachment regions, the large structures have a limited temporal coherence of order δ/U_c. In the wake the temporal coherence is increased due to the lower convective Mach number in this region.
- The dominant temporal behavior of large structures is similar to that for two-stream layers: elongation, rotation toward the streamwise direction, and growth of small-scale turbulence. No instances of rotational pairing have been observed. Time-correlated images suggest the existence of eddy shocklets in the reattachment zone.
- In the constant-pressure shear layer region, the structure convective velocities follow the stream selection rule with the experimental value exceeding the theoretical. In the recompression, reattachment, and initial wake regions, the measured convective velocity is (in some cases significantly) less than the theoretical value. This is expected given the mean velocity and pressure fields in these regions.

6. ACKNOWLEDGMENTS

I have had the good fortune to work with a number of very talented individuals in the general area of compressible separated and free shear flows. We have learned a great deal together, and I thank them for their outstanding efforts in this regard. These individuals, whose work has been heavily cited herein, are: Vince Amatucci, Ron Burr, Steve Goebel, Mark Gruber, Jeff

Herrin, Laurine Leep, Eric Loth, Nate Messersmith, Mahadevan Ramaswamy, and Ken Smith.

I would also like to acknowledge the efforts of Mark Woodmansee in helping with the figures included in this document. Professors Greg Elliott (Rutgers University) and Mo Samimy (Ohio State University) were gracious enough to provide originals of some of their double-pulsed planar images for inclusion.

Finally, for the work in this area performed here at the University of Illinois, I gratefully acknowledge the financial support of the U.S. Army Research Office, with Dr. Tom Doligalski as monitor, and the Office of Naval Research, with Dr. Gabriel Roy as monitor, each under several contracts. Financial support was also provided by AGARD for the preparation of this manuscript.

7. REFERENCES

Amatucci, V.A. (1990), "An Experimental Investigation of the Two-Stream, Supersonic, Near-Wake Flowfield Behind a Finite-Thickness Base," Ph.D. Thesis, University of Illinois at Urbana-Champaign.

Amatucci, V.A., Dutton, J.C., Kuntz, D.W., and Addy, A.L. (1992), "Two-Stream, Supersonic, Wake Flowfield Behind a Thick Base, Part 1: General Features," *AIAA Journal*, Vol. 30, No. 8, pp. 2039-2046.

Arnette, S.A., Samimy, M., and Elliott, G.S. (1993), "The Effect of Expansion on the Large Scale Structure of a Compressible Turbulent Boundary Layer," AIAA Paper 93-2991.

Barre, S. (1994), "Estimate of Convective Velocity in a Supersonic Turbulent Mixing Layer," *AIAA Journal*, Vol. 32, No. 1, pp. 211-213.

Barre, S., Quine, C., and Dussauge, J.P. (1994), "Compressibility Effects on the Structure of Supersonic Mixing Layers: Experimental Results," *Journal of Fluid Mechanics*, Vol. 259, pp. 47-78.

Bernal, L.P. and Roshko, A. (1986), "Streamwise Vortex Structure in Plane Mixing Layers," *Journal of Fluid Mechanics*, Vol. 170, pp. 499-525.

Birch, S.F. and Eggers, J.M. (1972), "A Critical Review of the Experimental Data for Developed Free Shear Layers," NASA SP-321, pp. 11-40.

Bogdanoff, D.W. (1983), "Compressibility Effects in Turbulent Shear Layers," *AIAA Journal*, Vol. 21, No. 6, pp. 926-927.

Bonnet, J.P., Debisschop, J.R., and Chambers, O. (1993), "Experimental Studies of the Turbulent Structure of Supersonic Mixing Layers," AIAA Paper 93-0217.

Bradshaw, P. (1966), "The Effects of Initial Conditions on the Development of a Free Shear Layer," *Journal of Fluid Mechanics*, Vol. 26, pp. 225-236.

Bradshaw, P. (1974), "The Effect of Mean Compression or Dilatation on the Turbulence Structure of Supersonic Boundary Layers," *Journal of Fluid Mechanics*, Vol. 63, pp. 449-464.

Broadwell, J.E. and Breidenthal, R.E. (1982), "A Simple Model of Mixing and Chemical Reaction in a Turbulent Shear Layer," *Journal of Fluid Mechanics*, Vol. 125, pp. 397-410.

Broadwell, J.E. and Mungal, M.G. (1988), "Molecular Mixing and Chemical Reactions in Turbulent Shear Layers," *Twenty-Second Symposium (International) on Combustion*, The Combustion Institute, pp. 579-587.

Brown, G.L. and Roshko, A. (1974), "On Density Effects and Large Structure in Turbulent Mixing Layers," *Journal of Fluid Mechanics*, Vol. 64, pp. 775-816.

Brown, J.L. (1978), "Heterogeneous Turbulent Mixing Layer Investigations Utilizing a 2-D 2-Color Laser Doppler Anemometer and a Concentration Probe," Ph.D. Thesis, University of Missouri-Columbia, 1978.

Bunyajitradulya, A. and Papamoschou, D. (1994), "Acetone PLIF Imaging of Turbulent Shear-Layer Structure at High Convective Mach Number," AIAA Paper 94-0617.

Burr, R.F. (1991), "Numerical Modeling and Simulation of Compressible Reacting Turbulent Shear Layers," Ph.D. Thesis, University of Illinois at Urbana-Champaign.

Chinzei, N., Masuya, G., Komura, T., Murakami, A., and Kudou, K. (1986), "Spreading of Two-Stream Supersonic Turbulent Mixing Layers," *Physics of Fluids*, Vol. 29, No. 5, pp. 1345-1347.

Clemens, N.T. and Mungal, M.G. (1992), "Two- and Three-Dimensional Effects in the Supersonic Mixing Layer," *AIAA Journal*, Vol. 30, No. 4, pp. 973-981.

Clemens, N.T. and Mungal, M.G. (1995), "Large-Scale Structure and Entrainment in the Supersonic Mixing Layer," *Journal of Fluid Mechanics*, Vol. 284, pp. 171-216.

Dawson, J.A. and Samimy, M. (1994), "The Effects of Expansion on a Supersonic Boundary Layer: Surface Pressure Measurements," AIAA Paper 94-0648.

Dimotakis, P.E. (1986), "Two-Dimensional Shear Layer Entrainment," *AIAA Journal*, Vol. 24, No. 11, pp. 1791-1796.

Dimotakis, P.E. (1991), "On the Convection Velocity of Turbulent Structures in Supersonic Shear Layers," AIAA Paper 91-1724.

Dimotakis, P.E. and Brown, G.L. (1976), "The Mixing Layer at High Reynolds Number: Large Structure Dynamics and Entrainment," *Journal of Fluid Mechanics*, Vol. 78, pp. 535-560.

Dolling, D.S, Fournier, E., and Shau, Y.R. (1992), "Effects of Vortex Generators on the Growth of a Compressible Shear Layer," *Journal of Propulsion and Power*, Vol. 8, No. 5, pp. 1049-1056.

Dussauge, J.P., and Gaviglio, J. (1987), "The Rapid Expansion of a Supersonic Turbulent Flow: Role of Bulk Dilatation," *Journal of Fluid Mechanics*, Vol. 174, pp. 81-112.

Elliott, G.S. and Samimy, M. (1990), "Compressibility Effects in Free Shear Layers," *Physics of Fluids A*, Vol. 2, No. 7, pp. 1231-1240.

Elliott, G.S., Samimy, M., and Arnette, S.A. (1992), "Study of Compressible Mixing Layers Using Filtered Rayleigh Scattering Based Visualizations," *AIAA Journal*, Vol. 30, No. 10, pp. 2567-2569.

Elliott, G.S., Samimy, M., and Arnette, S.A. (1995), "The Characteristics and Evolution of Large-Scale Structures in Compressible Mixing Layers," *Physics of Fluids*, Vol. 7, No. 4, pp. 864-876.

Fernando, E.M. and Menon, S. (1993), "Mixing Enhancement in Compressible Mixing Layers: An Experimental Study," *AIAA Journal*, Vol. 31, No. 2, pp. 278-285.

Fourguette, D.C., Mungal, M.G., Barlow, R.S., and Dibble, R.W. (1991), "Concentration Measurements in a Supersonic Shear Layer," AIAA Paper 91-0627.

Goebel, S.G. and Dutton, J.C. (1991), "Experimental Study of Compressible Turbulent Mixing Layers," *AIAA Journal*, Vol. 29, No. 4, pp. 538-546.

Gruber, M.R. (1992), "Three-Dimensional Velocity Measurements in a Turbulent, Compressible Mixing Layer," M.S. Thesis, University of Illinois at Urbana-Champaign.

Gruber, M.R., Messersmith, N.L., and Dutton, J.C. (1993), "Three-Dimensional Velocity Field in a Compressible Mixing Layer," *AIAA Journal*, Vol. 31, No. 11, pp. 2061-2067.

Gutmark, E.J., Schadow, K.C., and Yu, K.H. (1995), "Mixing Enhancement in Supersonic Free Shear Flows," *Annual Review of Fluid Mechanics*, Vol. 27, pp. 375-417.

Hall, J.L. (1991), "An Experimental Investigation of Structure, Mixing and Combustion in Compressible Turbulent Shear Layers," Ph.D. Thesis, California Institute of Technology.

Hall, J.L., Dimotakis, P.E., and Rosemann, H. (1993), "Experiments in Nonreacting Compressible Shear Layers," *AIAA Journal*, Vol. 31, No. 12, pp. 2247-2254.

Hampton, L.P., and White, R.A. (1986), "The Effect of Sudden Expansions and Compressions on Turbulent Boundary Layer Momentum Thickness in Supersonic Flow," ASME Paper 86-WA/FE-11.

Herrin, J.L. (1993), "An Experimental Investigation of Supersonic Axisymmetric Base Flow Including the Effects of Afterbody Boattailing," Ph.D. Thesis, University of Illinois at Urbana-Champaign.

Herrin, J.L. and Dutton, J.C. (1994a), "Supersonic Base Flow Experiments in the Near Wake of a Cylindrical Afterbody," *AIAA Journal*, Vol. 32, No. 1, pp. 77-83.

Herrin, J.L. and Dutton, J.C. (1994b), "Supersonic Near-Wake Afterbody Boattailing Effects on Axisymmetric Bodies," *Journal of Spacecraft and Rockets*, Vol. 31, No. 6, pp. 1021-1028.

Herrin, J.L., and Dutton, J.C. (1995a), "Effect of a Rapid Expansion on the Development of Compressible Free Shear Layers," *Physics of Fluids*, Vol. 7, No. 1, pp. 159-171.

Herrin, J.L., and Dutton, J.C. (1995b), "The Turbulence Structure of a Reattaching Axisymmetric Supersonic Free Shear Layer," AIAA Paper 95-2250.

Ikawa, H. and Kubota, T. (1975), "Investigation of Supersonic Turbulent Mixing Layer with Zero Pressure Gradient," *AIAA Journal*, Vol. 13, No. 5, pp. 566-572.

Island, T.C., Urban, W.D., and Mungal, M.G. (1997), "Small-Perturbation Mixing Enhancement in Compressible Shear Layers," AIAA Paper 97-0395.

Jimenez, J. Cogollos, M., and Bernal, L.P. (1985), "A Perspective View on Plane Mixing Layers," *Journal of Fluid Mechanics*, Vol. 152, pp. 125-143.

Karasso, P.S. and Mungal, M.G. (1996), "Scalar Mixing and Reaction in Plane Liquid Shear Layers," *Journal of Fluid Mechanics*, Vol. 323, pp. 23-63.

Leep, L.J., Dutton, J.C., and Burr, R.F. (1993), "Three-Dimensional Simulations of Compressible Mixing Layers: Visualizations and Statistical Analysis," *AIAA Journal*, Vol. 31, No. 11, pp. 2039-2046.

Lele, S.K. (1989), "Direct Numerical Simulation of Compressible Free Shear Flows," AIAA Paper 89-0374.

Lele, S.K. (1994), "Compressibility Effects on Turbulence," *Annual Reviews of Fluid Mechanics*, Vol. 26, pp. 211-254.

Mahadevan, R. and Loth, E. (1994), "High-Speed Cinematography of Compressible Mixing Layers," *Experiments in Fluids*, Vol. 17, pp. 179-189.

Martens, S., Kinzie, K.W., and McLaughlin, D.K. (1994), "Measurements of Kelvin-Helmholtz Instabilities in a Supersonic Shear Layer," *AIAA Journal*, Vol. 32, No. 8, pp. 1633-1639.

Martens, S., Kinzie, K.W., and McLaughlin, D.K. (1996), "Structure of Coherent Instabilities in a Supersonic Shear Layer," *AIAA Journal*, Vol. 34, No. 8, pp. 1555-1561.

Martens, S. and McLaughlin, D.K. (1995), "Mixing Enhancement Using Mach Wave Interaction in a Confined Supersonic Shear Layer," AIAA Paper 95-2177.

McIntyre, S.S. and Settles, G.S. (1991), "Optical Experiments on Axisymmetric Compressible Turbulent Mixing Layers," AIAA Paper 91-0623.

Mehta, R.D. and Westphal, R.V. (1986), "Near-Field Turbulence Properties of Single- and Two-Stream Plane Mixing Layers," *Experiments in Fluids*, Vol. 4, pp. 257-266.

Messersmith, N.L. (1992), "An Experimental Investigation of Organized Structure and Mixing in Compressible Turbulent Free Shear Layers," Ph.D. Thesis, University of Illinois at Urbana-Champaign.

Messersmith, N.L. and Dutton, J.C. (1996), "Characteristic Features of Large Structures in Compressible Mixing Layers," *AIAA Journal*, Vol. 34, No. 9, pp. 1814-1821.

Messersmith, N.L., Goebel, S.G., Frantz, W.H., Krammer, E.A., Renie, J.P., Dutton, J.C., and Krier, H. (1988), "Experimental and Analytical Investigations of Supersonic Mixing Layers," AIAA Paper 88-0702.

Palko, C.W. (1997), "Turbulence Measurements in a Plume-Induced Boundary Layer Separated Flowfield," Ph.D. Thesis, University of Illinois at Urbana-Champaign.

Papamoschou, D. (1989), "Structure of the Compressible Turbulent Shear Layer," AIAA Paper 89-0126.

Papamoschou, D. (1990), "Communication Paths in the Compressible Shear Layer," AIAA Paper 90-0155.

Papamoschou, D. (1991), "Structure of the Compressible Turbulent Shear Layer," *AIAA Journal*, Vol. 29, No. 5, pp. 680-681.

Papamoschou, D. (1995), "Evidence of Shocklets in a Counterflow Supersonic Shear Layer," *Physics of Fluids*, Vol. 7, No. 2, pp. 233-235.

Papamoschou, D. and Bunyajitradulya, A. (1995), "Double-Exposure PLIF Imaging of Compressible Shear Layers," AIAA Paper 95-0513.

Papamoschou, D. and Roshko, A. (1988), "The Compressible Turbulent Shear Layer: An Experimental Study," *Journal of Fluid Mechanics*, Vol. 197, pp. 453-477.

Petullo, S.P. and Dolling, D.S. (1993), "Large-Scale Orientation in a Compressible Turbulent Shear Layer," AIAA Paper 93-0545.

Poggie, J. and Smits, A.J. (1996), "Large-Scale Coherent Turbulence Structures in a Compressible Mixing Layer Flow," AIAA Paper 96-0440.

Ragab, S.A. and Wu, J.L. (1989), "Linear Instability in Two-Dimensional Compressible Mixing Layers," *Physics of Fluids A*, Vol. 1, pp. 957-966.

Ramaswamy, M. and Loth, E. (1996), "Tone Excitation of a Supersonic Bounded Shear Layer," *AIAA Journal*, Vol. 34, No. 10, pp. 1997-2004.

Ramaswamy, M., Loth, E., and Dutton, J.C. (1996), "Free Shear Layer Interaction with an Expansion-Compression Wave Pair," *AIAA Journal*, Vol. 34, No. 3, pp. 565-571.

Samimy M., Erwin, D.E., and Elliott, G.S. (1989), "Compressibility and Shock Wave Interaction Effects on Free Shear Layers," AIAA Paper 89-2460.

Samimy, M., Reeder, M.F., and Elliott, G.S. (1992), "Compressibility Effects on Large Structures in Free Shear Flows," *Physics of Fluids A*, Vol. 4, No. 6, pp. 1251-1258.

Sandham, N.D. and Reynolds, W.C. (1989), "A Numerical Investigation of the Compressible Mixing Layer," Report No. TF-45, Department of Mechanical Engineering, Stanford University.

Sandham, N.D. and Reynolds, W.C. (1990), "Compressible Mixing Layer: Linear Theory and Direct Simulation," *AIAA Journal,* Vol. 28, No. 4, pp. 618-624.

Sandham, N.D. and Reynolds, W.C. (1991), "Three-Dimensional Simulations of Large Eddies in the Compressible Mixing Layer," *Journal of Fluid Mechanics*, Vol. 224, pp. 133-158.

Shau, Y.R. and Dolling, D.S. (1989), "Experimental Study of Spreading Rate Enhancement of High Mach Number Turbulent Shear Layers," AIAA Paper 89-2458.

Shau, Y.R., Dolling, D.S., and Choi, K.Y. (1993), "Organized Structure in a Compressible Turbulent Shear Layer," *AIAA Journal*, Vol. 31, No. 8, pp. 1398-1405.

Smith, D.R. and Smits, A.J. (1991), "The Rapid Expansion of a Turbulent Boundary Layer in a Supersonic Flow," *Journal of Theoretical and Computational Fluid Dynamics*, Vol. 2, No. 5/6, pp. 319-328.

Smith, K.M. (1996), "An Experimental Investigation of Large-Scale Structures in Supersonic Reattaching Shear Flows," Ph.D. Thesis, University of Illinois at Urbana-Champaign.

Smith, K.M. and Dutton, J.C. (1996), "Investigation of Large-Scale Structures in Supersonic Planar Base Flows," *AIAA Journal*, Vol. 34, No. 6, pp. 1146-1152.

Smits, A.J., Eaton, J.A., and Bradshaw, P. (1979a), "The Response of a Turbulent Boundary Layer to Lateral Divergence," *Journal of Fluid Mechanics*, Vol. 94, pp. 243-268.

Smits, A.J., Young, S.T.B., and Bradshaw, P. (1979b), "The Effect of Short Regions of High Surface Curvature on Turbulent Boundary Layers," *Journal of Fluid Mechanics*, Vol. 94, pp. 209-242.

Van Dyke, M. (1982), "An Album of Fluid Motion," Parabolic Press, Stanford, California.

Viegas, J.R. and Rubesin, M.W. (1991), "A Comparative Study of Several Compressibility Corrections to Turbulence Models Applied to High-Speed Shear Layers," AIAA Paper 91-1783.

Winant, C.D. and Browand, F.K. (1974), "Vortex Pairing: The Mechanism of Turbulent Mixing-Layer Growth at Moderate Reynolds Number," *Journal of Fluid Mechanics*, Vol. 63, pp. 237-255.

Wygnanski, I. Oster, D., Fiedler, H., and Dziomba, B. (1979), "On the Perseverance of a Quasi-Two-Dimensional Eddy-Structure in a Turbulent Mixing Layer," *Journal of Fluid Mechanics*, Vol. 93, pp. 325-335.

Turbulent Combustion

Ken Bray,

Cambridge University, Engineering Department,
Trumpington Street, Cambridge, CB2 1PZ
U. K.

ABSTRACT

This review is concerned with turbulent combustion in high speed flows. Its aim is to assess the current state of knowledge incorporated in theoretical models and, as with most turbulent flows, these models necessarily involve averaging. Because high speed turbulent combustion involves additional phenomena which are not well understood we begin by considering combustion at low Mach numbers where a substantial body of theory exists. Our purpose is to identify the key role played by the low Mach number assumption and hence to define the particular challenge posed by high Mach number reactive flows.

Experiments concerning high speed turbulent combustion in jet flames, high speed turbulent deflagration and transition to detonation are reviewed. Finally, problems involved in modelling and prediction of high speed turbulent combustion are identified and discussed. It is concluded that convincing theoretical models are currently not available.

SYMBOLS

c	reaction progress variable
c_{pi}	specific heat of species i
$\bar{c}_p$	mean specific heat
$\mathcal{D}$	diffusion coefficient; also dilatation
D_a	Damköhler number
h	specific enthalpy
$\tilde{k}$	turbulence kinetic energy
k_{fj}, k_{bj}	forward and backward rate coefficients
K_a	Karlovitz number
ℓ_K	Kolmogorov length scale
ℓ_L^o	thickness of laminar flame
ℓ_T	turbulence length scale
L_{ei}	Lewis number of species i
M_a	Mach number
M_t	turbulence Mach number
N	number of species
p	pressure
$\tilde{P}$	probability density function
R	number of reactions
R_{eT}	turbulence Reynolds number
R_o	universal gas constant
S	see Equation (7.3)
t	time

Paper presented at the AGARD FDP Special Course on "Turbulence in Compressible Flows", held at the von Kármán Institute for Fluid Dynamics (VKI) in Rhode-Saint-Genèse, Belgium, 2-6 June 1997, and in Newport News, Virginia, USA, 20-24 October 1997, and published in R-819.

t_L^o	laminar flame time
t_T	turbulence time
T	temperature
u_T	turbulent burning velocity
v_k	velocity component
$\dot{w}_i$	mass rate of production of species i per unit volume
W_i	molecular weight of species i
x_k	spatial coordinate
Y_i	mass fraction of species i
Z	mixture fraction
β	Zel'dovich number
γ	ratio of specific heats
Δ_i	enthalpy of formation of species i
$\tilde{\epsilon}$	viscous dissipation
λ	thermal conductivity
ν	kinematic viscosity
ν'_{ij}, ν''_{ij}	stoichiometric coefficients
ρ	density
$\bar{\Sigma}$	flame surface density
$(\bar{\ })$	Reynolds mean
$(\tilde{\ })$	Favre mean
$(\ )'$	Reynolds fluctuation
$(\ )''$	Favre fluctuation

Subscripts

i, j	chemical species, reaction
k, ℓ, m	cartesian components

1. INTRODUCTION

Combustion processes in high speed turbulent flows are of technological interest because of applications in the field of propulsion, including ramjet engines (Refs. 1-4), rocket engine exhaust plumes (Refs. 5-7) and ram accelerators (Refs. 8-10). Another important application is to the assessment and mitigation of explosion hazards due to detonation (Refs. 11-14) and to high speed turbulent deflagration in the presence of obstacles (Refs. 15-18). In this Introduction we first provide a brief review of some literature concerning these applications. The Section ends with a description of the organisation of the remainder of the work. Some of this material is based on an earlier review of high speed turbulent combustion (Ref.19).

In the 1960's there was considerable interest in turbulent combustion in high speed flows motivated by ramjet propulsion for hypersonic flight, i.e., by the *scramjet*, the acronym for supersonic combustion ramjet. The basic elements of such a propulsion system, Figure 1, are an inlet which compresses the free stream air from a hypersonic Mach number to roughly one third that value, a combustor within which the air mixes and reacts with the fuel, generally gaseous hydrogen, and an exhaust nozzle which expands the combustion products back to free stream presure. Because of the length scales, flow rates and pressures of practical interest in this device the mixing of the fuel and

air and the combustion of the mixture involves turbulent flow.

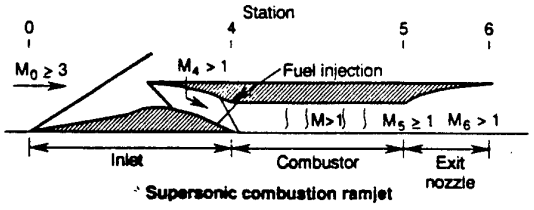

Figure 1
Scramjet engine

Although simply described, each of the components of such an engine gives rise to serious technical problems whose resolution is restricted by the basic requirement that net thrust be produced by the engine. Fundamentally, we must view the inlet as leading to a large drag and the exhaust nozzle to a large thrust with the difference in these two forces being the net thrust, i.e., the small difference of two large quantities, necessary to overcome the drag of the entire vehicle. Thus small changes in the flow in each component, in particular a change leading to a small momentum loss, can have a profound influence on engine performance. In particular shockwaves and flow separation resulting in losses in total head must be avoided if at all possible with the consequence that downstream injection of the fuel is preferred despite the reduced rates of mixing and reduced combustion efficiencies that may thereby be incurred. One circumstance necessitating such losses arises at low hypersonic Mach numbers where the static temperatures in the combustor may be so low as to require oblique or normal fuel injection to insure ignition.

The flow in a combustion chamber can involve a wide range of flow conditions as a hypersonic vehicle follows a schedule of flight Mach numbers and altitudes. An indication of conditions of interest is given by Ferri (Ref. 1) in a comparison of ramjets with subsonic versus supersonic combustion. For a flight Mach number of 12 at an altitude of 30.5 km the design Ferri considers representative of such ramjets calls for an inlet which results in a static pressure in the combustion chamber of 2.7 atmospheres, a static temperature of 1250 K and a Mach number in the airstream of 4.85. The velocity in the airstream within the combustor under these conditions is 3700 m/s. Since hydrogen is used to cool various airframe and engine components prior to being injected into the combustion chamber, its stagnation temperature is typically 1100 K and its Mach number in the range from one to two. These conditions are considered to be representative for the purpose of our discussion but others corresponding to lower flight Mach numbers at lower altitudes and higher Mach numbers at higher altitudes may be of interest. A significant design challenge is to mix and burn the fuel within the limited length of the combustion chamber while minimising shock losses. The chamber shape must be chosen so that part of the chemical energy is con-

verted into directed kinetic energy in order to avoid excessive static temperatures and associated dissociation losses.

An example of the early experimental and theoretical research on supersonic combustion is provided by Ferri (Ref. 1). In addition Libby (Ref. 2) presents an early theoretical analysis of turbulent combustion of hydrogen with equilibrium chemistry. Although widespread interest in high speed turbulent combustion waned during the decades of the 1970's and most of the 1980's, groups at the Applied Physics Laboratory of the John Hopkins University and at the Langley Research Center of NASA continued this early research on supersonic combustion for over two decades (cf. Billig, Ref. 3). A review of this work and an extensive bibliography is provided by Waltrup (Ref. 4) who *inter alia* lists research areas requiring attention for scramjet development. More recent information is contained in Ref. 20. Since, as noted earlier, it is generally considered essential to use the fuel to cool the vehicle, current research is concerned mainly with gaseous combustion and not with problems related to the combustion of liquid fuels in high speed flows (Waltrup, Ref. 4).

Because *rocket engines* often develop maximum thrust when operating fuel-rich, secondary combustion can occur in the exhaust plume. In typical rocket exhaust flames (Ref. 5), fuel-rich gases from a single nozzle or a series of nozzles at temperatures between 700 K and 2500 K mix turbulently with a moving stream of cooler air. Shock waves may occur in the flow and external combustion can take place as the excess carbon monoxide and hydrogen mix with the ambient air. A region of recirculating flow may exist behind the base wall of the rocket. Global features of these high speed reacting jet flows, such as infrared radiation emission intensity and microwave attenuation, are studied experimentally and theoretically (Refs. 6, 7). Such properties demand a detailed understanding of chemical kinetic processes and rates as influenced by turbulent mixing and flow.

The *ram accelerator* is a device proposed by Hertzberg et al. (Ref. 8) to accelerate a body flying in a tube at supersonic speed. The flying body or projectile is stabilised in the tube either by fins or by rails running along the length of the tube, Fig. 2. Acceleration is achieved by filling the launching tube with a combustible gas mixture. Shock waves attached to the flying body heat the combustible mixture and combustion is stabilized behind its bluff base. The body is continuously accelerated by the resulting high base pressure. Two alternative modes of combustion can occur, Figs. 3 and 4, depending on the flight speed relative to the CJ detonation speed. The flowfield is extremely complex. An essential parameter (Ref. 10) appears to be the specific heat release of the mixture. Below a minimum heat release, combustion decouples downstream of the pro-

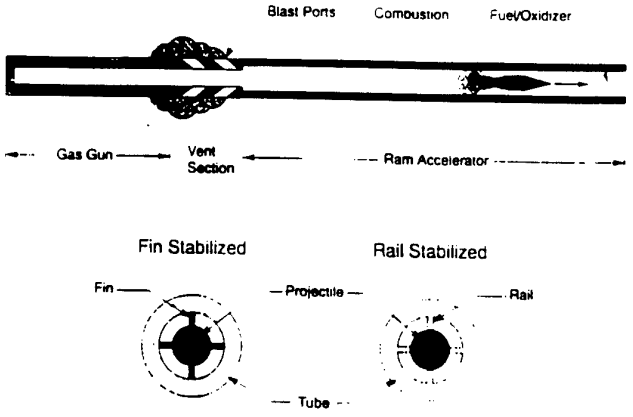

Figure 2
Schematic of a ram accelerator

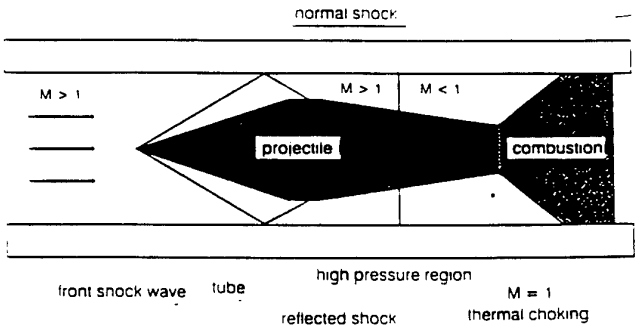

Figure 3
Flow around the projectile in the subdetonative case

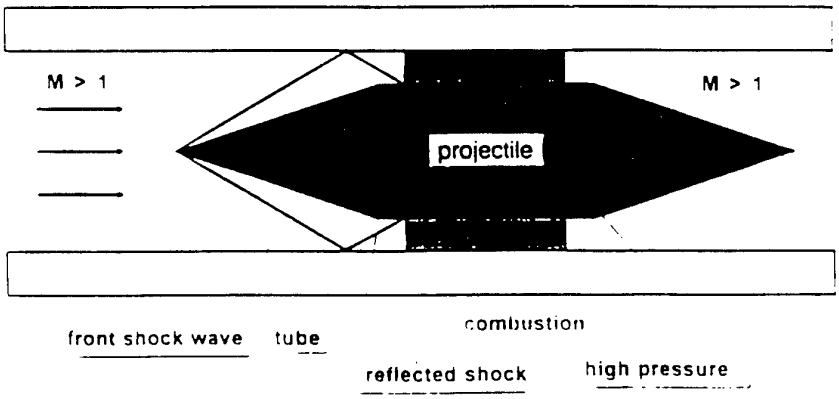

Figure 4
Flow around the projectile in the superdetonative case

jectile whereas beyond an upper limit, a detonation wave gets in front of the projectile (so-called "unstart"). Speeds up to 2600 m/s are reported (Ref. 9).

The damaging consequences of *accidental explosions* provide another motivation for the study of high speed combustion processes. The presence of obstacles such as pipes, storage tanks and other equipment can have a significant influence on the development and strength of an explosion following an accidental leakage and ignition of combustible materials in an industrial environment. Offshore oil and gas drilling operations provide examples of situations where assessments must be made of hazards due to obstructed explosions (Ref. 21). The sequence of events leading to the development and intensification of an explosion following a leakage of gaseous fuel in a space which contains obstructions may be described as follows. Mixing of fuel and air to produce a combustible mixture will occur at a rate which is determined by air motion due to ambient conditions or arising as a result of the leakage of fuel. Ignition may be caused for example by a spark, a hot surface or a pre-existing flame. The initial rate at which the flame spreads from this ignition source will probably be close to the laminar rate unless ambient conditions or the release of fuel has generated significant turbulence.

However, a strong feedback mechanism (Refs. 15-17) can convert this slowly propagating flame into a powerful explosion. Expansion of the hot products of combustion drives the unburned mixture ahead of the spreading flame. The unburned gas flows past obstacles and becomes turbulent. The flame then engulfs this turbulent gas mixture and is wrinkled by the turbulence so that its surface area and burning rate are increased. The accelerating flame drives the unburned mixture past other obstacles at higher speed generating more intense turbulence and when this turbulence is engulfed it causes further acceleration of the flame. If the flame speed becomes sufficiently high shock waves and other compressibility effects can influence the development of the explosion (Ref. 22) and it is even possible for detonation to occur (Ref. 15, 23). An illustration of the physical mechanisms involved in a transition from deflagration to detonation is given (Ref. 12) by use of stroboscopic laser Schlieren photography. In particular, the importance of turbulence on the onset of detonation is pointed out. Significant contributions to the study of transition, both experimental and numerical, can be found in the work of Oppenheim (Refs. 13, 14). Recent numerical work may be found in Refs. 24, 25.

The adverse effects of an obstructed explosion can often be reduced by the provision of appropriate venting to allow the hot combustion products to escape from the obstructed area. However, unsuitable venting can lead to the generation of excessive turbulence in the path of the flame and to an even more damaging explosion

outside the vented area (Ref. 26). In these circumstances improved theoretical models are required (Refs. 27, 28) to predict explosion hazards and to aid the design of safer industrial plants. Practical questions which should be addressed by these models include prediction of the maximum overpressure produced in a given event and the influence on this overpressure of factors such as the nature of the fuel, the manner in which the obstacles are arranged or the size and location of venting.

All of these practical high speed combustion problems, both in propulsion and in the field of industrial safety, require a deep understanding of the complex processes which control the rate of heat release through interactions between combustion and flow. Such understanding is accumulated through both theory and experiment and the resulting experience must guide the development of theoretical models. Reviews of relevant material may be found in Refs. 19, 20, 29-31.

Combustion flows may be characterized in many ways: laminar or turbulent, high or low Mach number, single or multiple phase. In this review we are mainly concerned with turbulent, high Mach number, single phase (gaseous) combustion. Another important distinction is between situations where fuel and oxidiser are fully premixed before they begin to burn and cases where fuel and oxidiser enter the combustion zone separately so that they mix as they burn. Most high Mach number propulsion systems involve non-premixed combustion but the detonation engine (Ref. 20) requires premixing of fuel and air. Also studies of accidental explosions (Refs. 11-18) generally assume premixing.

The structure of the paper is as follows. Section 2 briefly reviews relevant fundamentals of combustion thermochemistry. Although direct numerical simulation of turbulent combustion (DNS, Ref. 32) provides unique and valuable information, its application is restricted to low Reynolds numbers, idealised boundary conditions and greatly simplified chemical kinetic models. Prediction by DNS of practical engineering problems with realistic Reynolds numbers and a detailed description of hydrocarbon oxidation kinetics is not yet on the horizon. For the foreseeable future such problems will have to be addressed in terms of time or ensemble averaged equations. Averaging of the highly nonlinear chemical source terms in the transport equations poses a particularly challenging task. A formulation is presented in §3.

Because of the complexity of the interactions between combustion and high Mach number turbulent flows we continue, in §4, with a review of important processes and models for combustion at lower speeds. Chemical reaction occurs at molecular scale and is often closely coupled to molecular diffusion processes with the result that descriptions of mean reaction rates are strongly in-

fluenced by assumptions concerning the small-scale structure of a turbulent flame. Two relatively simple limiting cases have been identified. If combustion chemistry is sufficiently fast in comparison with time scales of the turbulent flow burning takes place in thin laminar flamelets (Refs. 33, 34), which retain the deterministic structure of a laminar flame, while being convected and distorted by the turbulent flow. At the other extreme where chemical time scales are sufficiently long in comparison time scales of the flow, probability density function (*pdf*, Refs. 35, 36) approaches assume a more random small scale structure. Section 4 describes these theories and reviews information from DNS and from experiment.

The limited amount of useful published experimental data concerning high speed turbulent combustion in jet flames, with application to propulsion problems, is reviewed in §5. Experimental data describing high speed turbulent deflagration and transition to detonation is described in §6. Finally §7 turns to the theoretical description of high speed turbulent reacting flows.

2. THERMOCHEMISTRY (Refs. 11, 30, 31, 37)

Consider a reactive mixture of gaseous chemical species $A_i\,(i = 1, 2 \cdots N)$. The concentration of substance i in the mixture is denoted by $[A_i]\,kg\ \ mol/m^3$. Then its mass concentration is $\rho_i = [A_i]/W_i\ kg/m^3$ where W_i is its molecular weight and its mass fraction is $Y_i = \rho_i/\rho$ where $\rho = \Sigma_{i=1}^{N}\ \rho_i$ is the mass density of the mixture. Assuming that ideal gas laws are applicable the thermal equation of state for the mixture is

$$p = \rho R_o T \sum_{i=1}^{N} Y_i/W_i = \rho \frac{R_o}{\bar{W}} T \tag{2.1}$$

where p is the pressure, T is the temperature, R_o is the universal gas constant and $\bar{W}$ is the mean molecular weight for the mixture. The calorific equation of state for the mixture is

$$h = \sum_{i=1}^{N} Y_i h_i \tag{2.2}$$

where h is the specific enthalpy and

$$h_i = \int_{T_{\text{ref}}}^{T} c_{pi}\, dT + \Delta_i \tag{2.3}$$

with Δ_i representing the enthalpy of formation of A_i at temperature T_{ref}. The specific heats c_{pi} may be approximated as polynomial functions of temperature. Alternatively, if the c_{pi} can be assumed to be constant, a mean specific heat is

$$\bar{c}_p = \sum_{i=1}^{N} c_{pi} Y_i \tag{2.4}$$

and the temperature can be expressed explicitly as

$$T = \frac{1}{\bar{c}_p}\left[h - \sum_{i=1}^{N} Y_i \Delta_i\right] \tag{2.5}$$

In a reactive gas mixture (Ref. 37) the equations of fluid flow must be supplemented by the following continuity equations for the individual species $A_i (i = 1, 2 \cdots N)$:

$$\frac{\partial}{\partial t}\rho Y_i + \frac{\partial}{\partial x_k}\rho v_k Y_i = -\frac{\partial}{\partial x_k} J_{ik} + \dot{w}_i \quad (2.6)$$

Here v_k is the velocity component in the direction of the cartesian spatial coordinate x_k. A summation convention is employed for subscripts k, l and m which are associated with these coordinates. However subscripts i and j are reserved for chemical species and reactions for which no summation is implied. Assuming Fick's law the diffusion flux J_{ik} is

$$J_{ik} = -\rho D_i \frac{\partial Y_i}{\partial x_k} \quad (2.7)$$

where D_i is a diffusion coefficient. The final term in Equation (2.6) is the chemical source term $\dot{w}_i$: the net mass rate of creation of species i per unit volume due to chemical reactions.

It is sometimes convenient to introduce local element mass fractions $\zeta_q (\underline{x}, t) (q = 1, 2 \cdots Q)$ which are defined by

$$\zeta_q = \sum_{i=1}^{N} \mu_{qi} Y_i \quad (2.8)$$

where μ_{qi} is the mass of element q in unit mass of species i. Since elements are conserved in chemical reactions we have

$$\sum_{i=1}^{N} \mu_{qi} \dot{w}_i = 0$$

and it follows that the conservation equation for element q is

$$\frac{\partial}{\partial t}\rho\zeta_q + \frac{\partial}{\partial x_k}\rho v_k \zeta_q = \frac{\partial}{\partial x_k} \sum_{i=1}^{N} \rho \, \mu_{qi} D_i \frac{\partial Y_i}{\partial x_k} \quad (2.9)$$

which obviously contains no chemical source term. If the diffusivities D_i of all species i have the same value, D, these equations are compatible with linear relationships between the element mass fractions. For nonpremixed combustion problems we may then define a local mixture fraction $Z (\underline{x}, t)$ as the local element mass fraction of an element contained in the fuel, divided by the mass fraction of the same element in pure undiluted fuel. The mixture fraction satisfies an equation similar to Equation (2.9) namely

$$\frac{\partial}{\partial t}\rho Z + \frac{\partial}{\partial x_k}\rho v_k Z = \frac{\partial}{\partial x_k}\left(\rho D \frac{\partial Z}{\partial x_k}\right) \quad (2.10)$$

and all the element mass fractions $\zeta_q (q = 1, 2 \cdots Q)$ are linearly related to Z.

If there are R elementary chemical reactions $j = 1, 2 \cdots R$ then the chemical source term in Equation (2.6) is

$$\dot{w}_i = \sum_{j=1}^{R} \dot{w}_{ij} \quad (2.11)$$

where $\dot{w}_{ij}$ is the rate of creation of A_i in reaction j. This reaction may be represented symbolically by

$$\sum_{i=1}^{N} \nu'_{ij} A_i \underset{k_{bj}}{\overset{k_{fj}}{\rightleftharpoons}} \sum_{i=1}^{N} \nu''_{ij} A_i \tag{2.12}$$

The process from left to right is the forward reaction, and is associated with the forward rate coefficient, k_{fj}, while the backward process from right to left is associated with the backward rate coefficient k_{bj}. The quantities ν'_{ij} and ν''_{ij} are the stoichiometric coefficients for the forward and backward reactions of reaction j respectively. They are small positive integers. A set of Equations (2.12) for $j = 1, 2 \cdots N$ together with all the ν'_{ij}, ν''_{ij}, k_{fj} and k_{bj} constitutes a complete reaction rate mechanism for a given gas mixture (Refs. 40, 41). A detailed description of the combustion of hydrogen in air (Ref. 42) takes into account the eight species $H_2, O_2, H_2O, O, H, OH, HO_2$ and H_2O_2 and twenty one elementary reactions. Hydrocarbon combustion (Ref. 40) can involve very large numbers of species and up to thousands of elementary reactions.

To complete the chemical kinetic formulation the net chemical source term for species i in reaction j is (Ref. 37)

$$\dot{w}_{ij} = \left(\nu''_{ij} - \nu'_{ij}\right) k_{fj} \rho^{m_{fj}} \frac{W_i}{W_j} \Pi_{i=1}^{N} Y_i^{\nu'_{ij}} \cdot \left\{1 - \frac{k_{bj}}{k_{fj}} \Pi_{i=1}^{N} (\rho Y_i)^{(m_{bj} - m_{fj})}\right\} \tag{2.13}$$

where the following definitions are used

$$m_{fj} \equiv \sum_{i=1}^{N} \nu'_{ij} \;\; ; \;\; m_{bj} \equiv \sum_{i=1}^{N} \nu''_{ij};$$

$$W_j \equiv \sum_{i=1}^{N} \nu'_{ij} W_i$$

The rate coefficients k_{fj} and k_{bj} are usually expressed in the form

$$k_{fj} = B_{fj} T^{\alpha_{fj}} exp\left(-\frac{E_{fj}}{R_o T}\right) \tag{2.14}$$

where B_{fj}, α_{fj} and E_{fj} are constants. If the temperature, pressure and chemical composition are such that reaction j is in chemical equilibrium the curly bracket term in Equation (2.13) must be zero. This requires that

$$\frac{k_{bj}}{k_{fj}} = K_j(T) \tag{2.15}$$

where $K_j(T)$ is the equilibrium constant for reaction j. Since k_{fj} and k_{bj} are functions of temperature alone, Equation (2.15) applies also when chemical equilibrium does not prevail and may be used to calculate k_{bj}.

Recalling that $\sum_{i=1}^{N} Y_i = 1$ we have N independent mass fractions to describe the mixture composition. With 3 velocity components v_k $(k = 1, 2, 3)$ and 4 thermodynamic variables $(p, \rho, T$ and $h)$ a total of $(7 + \mathrm{N})$ dependent variables have been introduced. If the $\dot{w}_i$ source terms are evaluated using Equations (2.11) and (2.13) there are N independent species equations

of the form of Equation (2.6). The remaining 7 equations are the two equations of state (Equations 2.1 and 2.2) plus the equations of fluid mechanics: continuity, energy and three equations of motion.

3. MEAN REACTION RATES : PROBLEM STATEMENT

As stated earlier, combustion DNS is not a feasible option for practical engineering problems involving high Reynolds numbers and detailed chemical kinetic processes. Under these conditions it is necessary to invoke averaged flow equations in which some of the information destroyed in the averaging process is replaced in the form of turbulence models. The chemical source terms summarized in Equations (2.13 - 2.15) are highly nonlinear and the evaluation of average values presents a particular problem. A time average may be defined in the usual way as

$$\overline{\dot{w}}_i(\underline{x}) = \frac{1}{\Delta t}\int_t^{t+\Delta t} \dot{w}_i(\underline{x},t)\,dt \tag{3.1}$$

where $\dot{w}_i(\underline{x},t) = \dot{w}_i(\rho,T,Y_j(j=1,2\cdots N-1))$. However it is not helpful to decompose ρ, T etc. into mean and fluctuating components. Instead the mean is expressed (Ref. 37) in terms of the joint probability density function (*pdf*) of these thermochemical variables so that

$$\overline{\dot{w}}_i(\underline{x}) = \int\int\cdots\int \dot{w}_i(\rho,T,Y_j\cdots)\,\bar{P}(\rho,T,Y_j\cdots;\underline{x})\,d\rho dT dY_j\cdots \tag{3.2}$$

where integration must extend over all possible values of the $(N+2)$ stochastic thermochemical variables appearing as arguments of the *pdf* $\bar{P}$. If this *pdf* is simply a delta function in the multidimensional composition space then $\bar{\dot{w}}_i = \dot{w}_i(\bar{\rho},\bar{T},\bar{Y}_j\cdots)$. On the other hand a broad *pdf* implies that $\bar{\dot{w}}_i$ is not a function of the mean thermochemical state alone.

This probability distribution depends in a complex way on the transport of energy, mass and chemical species in and out of an infinitesimal control volume, by convection and molecular diffusion, and on the progress of chemical reactions inside the control volume. Molecular diffusion and chemical reaction interact strongly. If chemical reactions are fast the rate of conversion into products is determined by the rates at which diffusion can transport reactants to the reaction zone and products away from it. We shall return to this topic later.

As will be explained later, two routes are available for estimating the unknown function $\bar{P}$. The first (Refs. 35, 36) involves modelling and solution of a *pdf* transport equation while the second more empirical approach (Refs. 43 - 45) replaces $\bar{P}$ by a simple "presumed *pdf* " expression such as a Gaussian or a beta function. However both of these approaches become impracticable unless the number of arguments of the joint *pdf* is small. Applications of these methods in the literature generally involve *pdf*'s which are func-

tions of a single stochastic variable while the largest feasible number of such variables is probably around four.

For example consider a presumed *pdf* which is to be represented in terms of four stochastic variables: a, b, c and d. A simple *pdf*, such as a Gaussian or a beta function, can be evaluated in terms of its first and second moments. Here we have 4 first moments $(\bar{a}, \bar{b}, \bar{c}$ and $\bar{d})$, 4 variances $\left(\overline{a'^2}, \overline{b'^2}, \overline{c'^2}\right.$ and $\left.\overline{d'^2}\right)$ and six covariances $\left(\overline{a'b'}, \overline{a'c'}, \overline{a'd'}, \overline{b'c'}, \overline{b'd'}\right.$ and $\left.\overline{c'd'}\right)$ - a total of 14 quantities - requiring closure and solution of 14 Reynolds averaged transport equations.

It is therefore essential to express the instantaneous rate $\dot{w}_i$ in terms of the smallest possible number of independent thermochemical variables. One way to do this is by simplifying the chemical kinetics. This can be done in a rational manner (Ref. 41) by assuming that some reactions are sufficiently fast to maintain quasi-equilibrium and/or that some species exist in sufficiently small concentrations so that a steady state approximation can be employed. The furthest this process can be taken while retaining some information about finite rates of reaction is to reduce the whole chemical kinetic mechanism to a single global reaction. Then $N = 1$ and $\dot{w}_i = \dot{w}_i(\rho, T, Y_1)$ where Y_1 is the only remaining independent mass fraction. Using the equations of state we can rewrite this functional relationship as $\dot{w}_i(p, h, Y_1)$. The corresponding joint *pdf* is $\tilde{P}(p, h, Y_1;\ \underline{x})$.

The other way to reduce the number of independent variables is to simplify the thermodynamics, as will be explained next.

4. TURBULENT COMBUSTION IN LOW MACH NUMBER FLOWS

Because the physics of turbulent combustion at high Mach numbers is not well understood we begin by considering low Mach numbers where a substantial body of theory does exist (Refs. 30 - 39). Our aim is to identify the key role played by the low Mach number assumption and hence to define the particular challenge posed by high Mach number reactive flows. Note that the terms compressible flow and incompressible flow can lead to confusion when applied to combustion where heat release can lead to density changes of a factor of six or more while the Mach number remains small.

The Section begins with the thermochemical simplifications arising from the low Mach number assumption. Regimes of low Mach number turbulent combustion are then described and theoretical models are described. Finally §4.4 contains comments on experimental validation of theoretical models.

4.1 Low Mach Number Flow Assumption

Introduce characteristic quantities: v, p, ρ, h and $a = (\gamma p/\rho)^{\frac{1}{2}}$ to represent typical values of flow velocity, pressure, density, specific enthalpy and speed of sound in a given reactive flow. The change in pressure δp associated with velocity change v may be estimated as

$$\frac{\delta p}{p} = \frac{\rho v^2}{p} = \gamma M_a^2 \tag{4.1}$$

where $M_a = v/a$ is the flow Mach number. Thus, when $M_a << 1$, pressure changes within the flow become very small. In these circumstances, local pressure variations within the flow have a negligible effect on chemical reaction rates. In evaluating the thermochemical state for this purpose we may replace the instantaneous pressure $p(\underline{x}, t)$ by its mean value $\bar{p}(\underline{x},)$ which is a deterministic rather than a stochastic variable. Thus the *pdf* $\tilde{P}(p, h, Y_1; \underline{x},)$ is reduced to $\tilde{P}(h, Y_1; \underline{x},)$.

To seek further simplification we note that the order of magnitude of the ratio of kinetic energy per unit mass to specific enthalpy is

$$\frac{\frac{1}{2}v^2}{h} = \frac{1}{2}(\gamma - 1) M_a^2 \tag{4.2}$$

showing that, when $M_a << 1$, the kinetic energy of the flow makes a negligible contribution to the total energy balance. Then the specific enthalpy equation reduces to

$$\frac{\partial}{\partial t}\rho h + \frac{\partial}{\partial x_k}\rho v_k h = \frac{\partial p}{\partial t} + \frac{\partial}{\partial x_k}\left[\frac{\lambda}{\bar{c}_p}\frac{\partial h}{\partial x_k} + \frac{\lambda}{\bar{c}_p}\sum_{i=1}^{N}\left(\frac{1}{L_{ei}} - 1\right) h_i \frac{\partial Y_i}{\partial x_k}\right] \tag{4.3}$$

where radiative heat loss is neglected, λ is the thermal conductivity of the mixture and

$$L_{ei} = \frac{\lambda}{\rho \bar{c}_p D_i} \tag{4.4}$$

is the Lewis number of species i. In statistically stationary flow at low Mach number the term $\partial p/\partial t$ is negligibly small. If additionally we assume Lewis numbers L_{ei} to be sufficiently close to unity so that the last term can be neglected Equation (2.20) finally becomes

$$\frac{\partial}{\partial t}\rho h + \frac{\partial}{\partial x_k}\rho v_k h = \frac{\partial}{\partial x_k}\left(\frac{\lambda}{\bar{c}_p}\frac{\partial h}{\partial x_k}\right) \tag{4.5}$$

Consider premixed combustion first. If the flow is adiabatic Equation (4.5) allows h to be constant everywhere. The *pdf* is then further reduced from $\tilde{P}(h, Y_i; \underline{x})$ to the desired monovariate form $\tilde{P}(Y_i; \underline{x})$. In the nonpremixed case with unity Lewis number Equations (2.10) and (4.5) are the same showing that h is a linear function of the mixture fraction Z. If in addition, the mass fractions Y_i can be expressed as functions $Y_i(Z)$ then the *pdf* reduces to $\tilde{P}(Z; \underline{x})$ as required. Both of these cases will be explained further in §4.3. First we

consider the validity of the so-called laminar flamelet approximation in which the small-scale structure of reaction zones in turbulent reacting flow is represented by the structure of a laminar flame.

4.2 Turbulent Combustion Regimes

In this Section we define key dimensionless parameters in terms of which various different regimes of low speed turbulent combustion may be defined. It is to be expected that successful models will involve such parameters and will show appropriate behaviour in the various combustion regimes. An important aim is to identify circumstances in which laminar flamelet models are valid. Confining attention to gaseous systems we first consider premixed combustion. This is the more complex situation because unlike a diffusion flame a premixed flame can propagate and so avoid some regions of the turbulence field.

If fuel and oxidiser are fully premixed the unstretched laminar flame provides characteristic chemical length and time scales which we denote by ℓ_L^o and t_L^o where $\ell_L^o/t_L^o = u_L^o$ is the laminar burning velocity. Characteristic length and time scales of the turbulent flow may be defined in terms of a characteristic turbulence kinetic energy k and its dissipation ϵ. Then we have time and length scales

$$t_T = k/\epsilon \; ; \; \ell_T = k^{3/2}/\epsilon \qquad (4.6)$$

which are associated with the most energetic scales of the turbulence spectrum. A turbulence Reynolds number may be defined as

$$R_{eT} = \frac{k^{\frac{1}{2}}\ell_T}{\nu} = \frac{k^2}{\epsilon\nu} \qquad (4.7)$$

where ν is the kinematic viscosity. The smallest scales, associated with Kolmogorov, are

$$t_K = (\nu/\epsilon)^{\frac{1}{2}} \; ; \; \ell_K = \left(\nu^3/\epsilon\right)^{\frac{1}{4}} \qquad (4.8)$$

so that

$$\frac{\ell_T}{\ell_K} = (R_{eT})^{\frac{3}{4}} \qquad (4.9)$$

Ratios of these scales may be used to define dimensionless parameters and to identify combustion regimes. Key parameters are the turbulent Damköhler number

$$Da = \frac{t_T}{t_L^o} = \frac{ku_L^o}{\epsilon\ell_L^o} \qquad (4.10)$$

and the turbulent Karlovitz number

$$Ka = \frac{t_L^o}{t_K} = \frac{\ell_L^o\epsilon^{\frac{1}{2}}}{u_L^o\nu^{\frac{1}{2}}} \qquad (4.11)$$

Equations (4.10) and (4.11) compare the laminar flame time t_L^o with the large and small characteristic times of the turbulence, t_T and t_K, respectively. Note that Ka is the reciprocal of a Damköhler number. The three parameters Da, Ka and the turbulence Reynolds number R_{eT} allow us to identify regimes of premixed turbulent combustion. Note however that

$$Ka = R_{eT}^{\frac{1}{2}}/Da \qquad (4.12)$$

so only two parameters are independent. It is sometimes convenient to replace R_{eT}, Da and Ka by the velocity and length ratios

$$\frac{k^{\frac{1}{2}}}{u_L^o} = \alpha^{\frac{1}{2}} R_{eT}^{\frac{1}{2}} / Da^{\frac{1}{2}} \; ; \; \frac{\ell_T}{\ell_L^o} = \alpha^{\frac{1}{2}} R_{eT}^{\frac{1}{2}} Da^{\frac{1}{2}} \; ;$$

$$\frac{\ell_L^o}{\ell_K} = \left(\frac{Ka}{\alpha}\right)^{\frac{1}{2}} \tag{4.13}$$

where α is the order-unity coefficient in

$$\nu = \alpha u_L^o \, \ell_L^o \tag{4.14}$$

Consider the so-called eddy break-up limit, $D_a \rightarrow \infty$, where chemical reactions are very fast and the rate of conversion of reactants is limited by a finite rate of small-scale mixing so that "mixed-is-burned". In mixing and combustion problems we are interested in scalar variables such as the mass fraction $Y_i(\underline{x}, t)$ of species $i (i = 1, 2, \cdots N)$ whose Favre mean and variance are

$$\tilde{Y}_i = \overline{\rho Y_i} / \bar{\rho} \; ; \; \widetilde{Y_i''^2} = \overline{\rho \left(Y_i - \tilde{Y}_i\right)^2} / \bar{\rho} \tag{4.15}$$

The rate at which fluctuations in $Y_i(\underline{x}, t)$ are reduced by molecular diffusion is described by the mean *scalar dissipation* function

$$\tilde{\epsilon}_{ii} = \frac{2}{\bar{\rho}} \overline{\rho \mathcal{D}_i \frac{\partial Y_i}{\partial x_k} \frac{\partial Y_i''}{\partial x_k}} \tag{4.16}$$

where $\mathcal{D}_i$ is the Fick's Law diffusion coefficient for species i; $\tilde{\epsilon}_{ii}$ has dimension (time)$^{-1}$ and provides a characteristic time for the important small scale mixing process. An instantaneous quantity closely related to $\tilde{\epsilon}_{ii}$ is $2\mathcal{D}_i \left(\partial Y_i / \partial x_k\right)^2$ which is the reciprocal of a local diffusion time. High activation energy analysis of both laminar premixed flames and laminar diffusion flames shows that this diffusion time, evaluated at the reaction surface, is equal to the local chemical time scale of the reaction surface. We shall see later that both turbulent premixed flames and turbulent diffusion flames behave in an analogous manner in the fast-chemistry limit. In both cases the mean reaction rate is proportional to the mean scalar dissipation.

In 1940 Damköhler(Ref. 46) argued that if $\ell_L^o << \ell_K$ turbulence has the effect of wrinkling the laminar flame increasing its area and hence the burning rate. Locally in the laminar flame reaction and molecular diffusion are in balance. However at the other extreme where $\ell_L^o >> \ell_T$ it is turbulent transport which must balance the rate of reaction. In further development of these ideas the following combustion regimes may be displayed diagrammatically with either Da and R_{eT}(Ref. 47) or $k^{\frac{1}{2}}/u_L^o$ and ℓ_T/ℓ_L^o(Ref. 48, 49) as independent variables. The second of these options is chosen in Figure 5. The following regimes may be identified (Ref. 39):

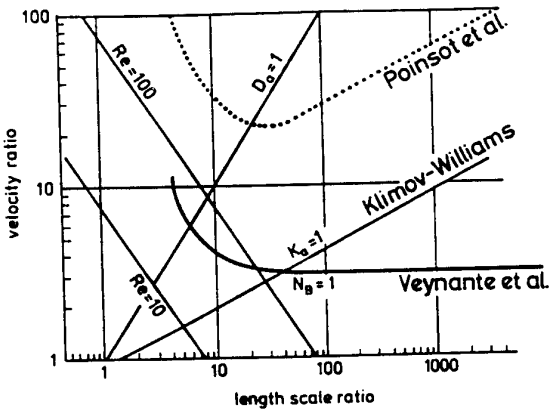

Figure 5
Turbulent burning regimes

$R_{eT} < 1$. Essentially *laminar flow* behaviour is to be expected.

$Ka < 1, R_{eT} > 1$. This is the regime of *laminar flamelet* combustion in which the laminar flame time scale t_L^o is smaller than the shortest time scale t_K of the turbulent flow. Burning is expected to occur in thin laminar flames, which are stretched and curved by the turbulent flow, but chemical reaction remains fast and turbulence cannot extinguish the laminar flames.

$Ka > 1, Da > 1, R_{eT} > 1$. In this intermediate regime $t_K < t_L^o < t_T$ so small scale turbulent motions can dominate the flame structure quenching laminar flamelets and producing *distributed reaction zones.* However, because of the intermittency of intense small scale motion in high Reynolds number turbulent flow, local regions of laminar flamelet burning may also survive as discussed later.

$Da < 1, R_{eT} > 1$. This is the *well stirred reactor* regime in which t_L^o is greater than the largest turbulence time scale so chemistry is relatively slow.

The situation is less clear in cases where fuel and oxidiser are not premixed. Some authors(Ref. 49, 50) argue that, since the laminar diffusion flame does not possess a unique thickness or propagation speed, the stoichiometric premixed laminar flame provides the most appropriate chemical scales. It may then be concluded that the four regimes identified above are also applicable to all types of nonpremixed and partially premixed combustion. An alternative perspective(Ref. 34) identifies the flamelet regime for nonpremixed combustion in terms of the mixture fraction $Z(\underline{x}, t)$. In a two-stream combustion process with all species diffusivities assumed equal $Z(\underline{x}, t)$ is the mass fraction of all material at $(\underline{x}, t)$ which originated in the fuel stream. Burning regimes are described in terms of the laminar flame reaction zone thickness ΔZ_L in *mixture fraction* space: separated laminar flamelets can exist if $\Delta Z_L < \left(\widetilde{Z''^2}\right)^{\frac{1}{2}}$, otherwise connected reaction zones will occur. A second requirement for the laminar flamelets is that a time scale ratio t_K/t_c must be greater than unity where t_K is the Kolmogorov time and t_c is a characteristic chemical time for the laminar diffusion flame. This

is defined as $t_c = 1/a_q$ where a_q is the strain rate which is just sufficiently large to extinguish the laminar flame. Note that t_K/t_c is the reciprocal of a turbulent Karlovitz number so the flamelet criterion $t_K/t_c > 1$ is similar to the requirement $K_a < 1$.

The question of the validity of these criteria for laminar flamelet combustion has received much attention. It is important to recognise that the arguments summarized above are concerned with orders of magnitude and describe asymptotic behaviour. The transition between laminar flamelets and well stirred reactor combustion may be sudden or gradual and is likely to be influenced by other factors in addition to these which have been identified. Significant uncertainties are associated with the choice of characteristic quantities such as ν which is a strong function of temperature.

The classical criterion $Ka < 1$ for laminar flamelet combustion requires the chemical time t_L^o to be smaller than the Kolmogorov time scale t_K which is associated with the smallest dissipative eddies. In these circumstances burning is supposed to occur exclusively in laminar reaction zones. However, numerical calculations by Poinsot et al.(Ref. 51), who studied the two-dimensional interaction between a laminar premixed flame and a vortex pair, show that these small eddies decay before they can have a strong influence on the flame. Eddies of intermediate scale are found to be much more important. Experiments by Roberts and Driscoll(Ref. 52) support these findings. Applying their results to a turbulent spectrum of eddy scales Poinsot et al.(Ref. 51) conclude that the laminar flamelet regime, defined in terms of the absence of local flame quenching rather than as the presence of a laminar reaction zone, extends about an order of magnitude beyond the limit $Ka = 1$ as shown in Figure 5 if Ka is calculated in terms of conditions in unburned reactants.

Despite these observations the Kolmogorov time remains an important characteristic time scale in turbulent reactive flows. Results from combustion DNS show(Ref. 53) that the mean tangential strain on the flame surface due to turbulence is correlated by B/t_K where $B = 0.28$ in the limit where $u_L^o << \ell_K/t_K$ while $B = 0$ if $u_L^o >> \ell_K/t_K$. Also the experimentally observed extinction of turbulent flames near stagnation points can be correlated with laminar flame extinction data, for both premixed(Ref. 54) and non-premixed(Ref. 55) flames, by modelling the turbulent flame stretch as the sum of the bulk strain and the reciprocal of the Kolmogorov time.

In the case of premixed combustion results of DNS with one-step chemistry (see review by Poinsot et al.(Ref. 32) and references cited there) clearly show the ability of thin reaction zones with structures similar to that of a laminar flame to sur-

vive when $Ka > 1$. However the instantaneous propagation speeds of these structures do not correlate well with those of steady strained laminar flames. Curvature effects are also found to be important. On the average the central portions of local reaction zones are found (Ref. 56) to be indistinguishable from unstretched laminar flames in terms of magnitude of gradient, reaction rate and relative velocity of iso-surface. At the edges of the reaction zones all these conditional mean properties deviate from the properties of an unstretched laminar flame due, presumable, both to the combined effects of flame curvature and strain and to the influence of small eddies which can enter the relatively thick preheat zone of the laminar flame. The deviations from laminar flame distributions do not appear large as may be seen from Figure 6. However these out-of-flamelet regions have a much larger probability of occurrence in the turbulent flame than the thin laminar flame structures, so they can make an important contribution to mean properties(Ref. 44). This contribution, which involves the characteristic scales of the turbulent flow rather than those of the laminar flame, is present even in the limit $Da >> 1$. We conclude that the transition from laminar flamelets to distributed reaction zones is gradual and sensitive to definitions.

Computational costs currently limit predictions from DNS with even simplified multi-step reaction schemes to a two-dimensional computational domain.

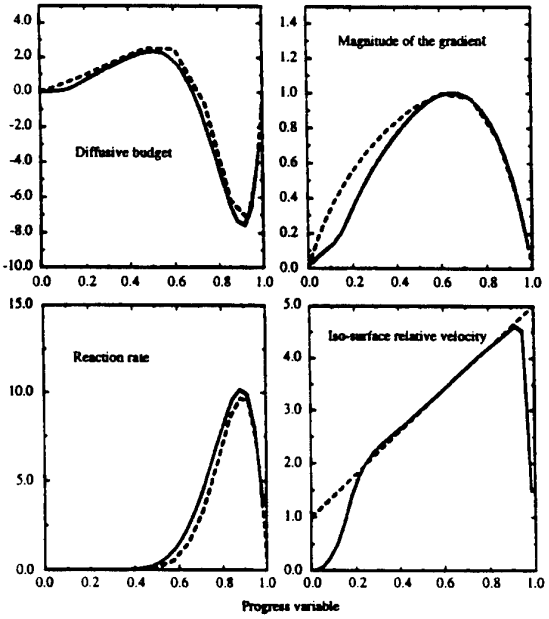

Figure 6
Data from DNS of premixed turbulent combustion compared with laminar flame profiles (Ref. 56).

Such calculations do however allow differential diffusion effects to be studied(Ref. 57). Because of their large diffusivities H and H_2 are strongly influenced by flamelet curvature whereas CO which reacts slowly is more sensitive to tangential strain. This complex behaviour is not easily described in terms of a simple laminar flame speed. Calculations with detailed chemistry(Ref. 58) also show an enhanced sensitivity of the reaction surface to strain. Direct experimental determination of any deviation from laminar flamelet behaviour is difficult because of the three-dimensionality of the

thin wrinkled surface which must be studied. However measurements(Refs. 59, 60) do confirm the existence of such a surface at large Karlovitz numbers while indicating local variations in its thickness.

We now turn to nonpremixed turbulent combustion. At high enough values of Da instantaneous point measurements of say temperature and mixture fraction lie close to a single theoretical curve for a weakly strained laminar diffusion flame.(Ref. 58) At smaller values of Da experiments provide scatter plots(Ref. 58) in which the data is more widely dispersed. If local extinction and reignition occur these scatter plots are sufficiently widely distributed to include points which correspond to nonreactive mixing between fuel and air and others which represent combustion going to completion(Ref. 61). Three dimensional DNS by Mahalingam et al.(Ref. 62) employ both a single-step global reaction model and a two-step model to provide data which is compared with predictions for a steady laminar diffusion flame. At Damköhler numbers of order unity the DNS data is widely dispersed and does not correspond well to the laminar flame prediction. Burning is observed to occur in the turbulent flow under conditions which completely extinguish the steady laminar flame. Time-dependent strain rates in the turbulent flow may provide an explanation(Refs. 62 , 63). More recent two-dimensional DNS by Chen et al.(Ref. 64) also identify a strong influence of iso-surface curvature in nonpremixed combustion. If partial premixing is allowed DNS(Ref. 65) predicts that triple flames(Ref. 66) can play a significant role during autoignition.

We must conclude from both DNS and experimental evidence that conditions of interest exist in nonpremixed and partially premixed combustion where a steady laminar flamelet assumption is *not* valid. However this data does yet not appear to allow a clear judgement to be made as to whether laminar flamelet burning will occur in circumstances corresponding to the flamelet regimes defined by Borghi(Ref. 49) or by Bray and Peters(Ref. 34).

4.3 Theoretical Models

The set of equations, to be found in Libby and Williams (Ref. 37), comprises the equations of continuity, motion, energy and species balance, supplemented by equations of state, chemical kinetic data and molecular transport models. These low Mach number flow equations are to be averaged either in the form of a time average, Equation (3.1), or as an ensemble average. In combustion flows, where large changes in density occur as a result of heat release, it is usual to employ a mass-weighted or Favre average. For any variable $\phi(\underline{x},t)$ we have a Favre mean

$$\tilde{\phi}(\underline{x}) = \frac{1}{\Delta t}\int_t^{t+\Delta t} \frac{\rho(\underline{x},t)}{\bar{\rho}(\underline{x})}\phi(\underline{x},t)\,dt \tag{4.17}$$

and Favre fluctuation

$$\phi''(\underline{x},t) = \phi(\underline{x},t) - \tilde{\phi}(\underline{x}) \ . \tag{4.18}$$

This notation greatly simplifies the averaged equations by suppressing many density fluctuation terms which occur in the mean equations if they are averaged without mass weighting. For example

$$\begin{aligned}\overline{\rho v_k v_\ell} &= \bar{\rho}\tilde{v}_k\tilde{v}_\ell + \overline{\rho v_k'' v_\ell''} \\ &= \bar{\rho}\tilde{v}_k\tilde{v}_\ell + \bar{\rho}\overline{v_k' v_\ell'} + \bar{v}_k\overline{\rho' v_\ell'} \\ &+\bar{v}_\ell\overline{\rho' v_k'} + \overline{\rho' v_k' v_\ell'}\end{aligned} \tag{4.19}$$

It is often assumed that, because the mass weighted average converts the flow equations into a form similar to that of constant density flow, it somehow captures all the additional physics associated with large changes in density. Thus constant density models of turbulent transport are widely used with little or no modification to allow for effects of combustion. This assumption is naive and can sometimes be grossly in error (Ref. 39). The starting point for development of mean flow models must be the hierarchy of nonreactive flow models (Ref. 39):

- large eddy simulation (LES),
- probability density function (*pdf*) models,
- second moment or Reynolds stress models,
- $k-\epsilon$ models.

Reactive turbulent flow models in all these categories may be found in the literature. However it is necessary to review and revise the nonreactive flow closures in each of these models to take into account the possibility of interactions between combustion and flow, Figure 7.

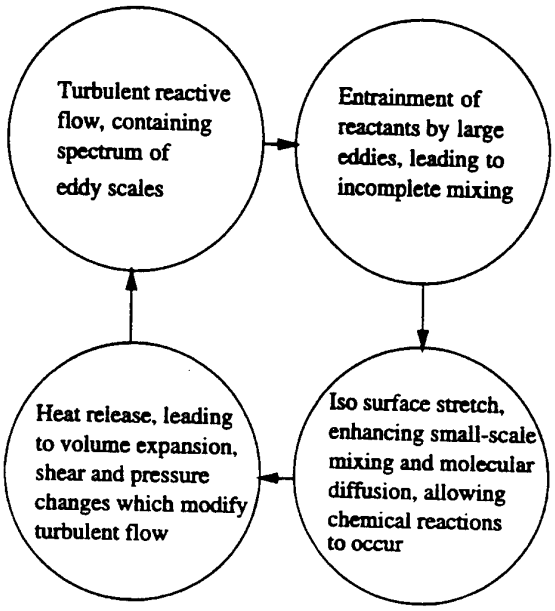

Figure 7
Interaction between turbulent flow and combustion (Ref. 39).

Some relevant phenomena may be identified (Ref. 39) as follows:

- Instabilities of the laminar flame can modify the flow field and introduce additional length and time scales which are unrelated to turbulence scales ahead of the flame (Ref. 67).
- Both large and small scale features of the flow are modified as a result of

dilatation due to heat release. Dilatation dissipation (Refs. 68-70) is a contribution to the viscous dissipation of turbulence energy which is proportional to the mean square dilatation. It can be important in reactive flows (Refs. 69,70) as in high speed flows (Ref. 68).

- The combination of a pressure field and a spatially varying density field leads to vorticity generation due to baroclinic torque (Ref. 38) and also to related phenomena of pressure gradient transport (Ref. 71) and turbulence generation (Ref. 71). According to one study (Ref. 72) self-generated pressure gradient transport leads to countergradient turbulent diffusion of combustion products if

$$N_B \equiv \frac{\tau u_L^o}{2\alpha u'} \geq 1 \tag{4.20}$$

where $(1+\tau)$ is the ratio of adiabatic flame temperature to ambient temperature and α is a function of ℓ_T/ℓ_L^o. See Figure 5.

- Pressure fluctuation terms are known (Ref. 73) to play a key role in flow turbulence models with closure at Reynolds stress or equivalent *pdf* level. Turbulent combustion provides a strong monopole acoustic source so the use of nonreactive flow models to predict pressure fluctuation terms in combustion flows must be viewed with suspicion (Ref. 38).

The accurate prediction of mean reaction rates represents the central problem and challenge of turbulent combustion modelling. The instantaneous reaction rate is influenced by local molecular diffusion fluxes linked to small scale mixing. Indeed in the eddy break-up limit when chemistry is fast it is these fluxes which control the net rate of reaction. Consequently mean reaction rate predictions can be strongly influenced by underlying assumptions concerning small-scale flame structure. Two different starting points may be identified in theoretical approaches to these problems. The first is a probabilistic approach, typically involving the use of stochastic models to describe small-scale mixing. Simple models of mixing as a random process become suspect at large Damköhler numbers where laminar flamelet burning implies the existence of deterministic mixing rate expressions. The alternative starting point, restricted to situations where $Da >> 1$ so that reaction is restricted to sheets of vanishingly small thickness, is introduced later. Much effort is directed to the problem of bridging the gap between these two approaches whose origins lie at opposite ends of the Damköhler number range.

The starting point for *pdf* models is the exact but unclosed transport equation for the joint *pdf* of the relevant set of scalar variables (Refs. 74-76). As explained earlier, low Mach number assumptions are used to reduce as far as possible the number of independent thermochemical vari-

ables. It is possible to add the velocity to this list of variables (Ref. 74) but we illustrate the *pdf* approach by considering only scalar variables $\phi_i(\underline{x},t)(i=1,2\cdots)$ for which the equation is

$$\bar{\rho}\frac{\partial \tilde{P}}{\partial t}+\bar{\rho}\tilde{u}_k\frac{\partial \tilde{P}}{\partial x_k}= -\frac{\partial}{\partial x_k}\left[\bar{\rho}<u_k''\mid \phi(\underline{x},t)=\varphi>\tilde{P}\right] -\bar{\rho}\frac{\partial}{\partial \varphi_i}\left[\dot{w}_i(\varphi)\tilde{P}\right]-\frac{1}{2}\bar{\rho}\frac{\partial^2}{\partial\varphi_i\partial\varphi_j} \left[<\epsilon_{ij}\mid \phi(\underline{x},t)=\varphi>\tilde{P}\right] \quad (4.21)$$

where $\varphi = \varphi_i(i=1,2\cdots)$ is a set of independent variables corresponding to the physical variables $\phi_i(\underline{x},t)$ $(i=1,2\cdots)$ and $\tilde{P}=\tilde{P}(\varphi;\underline{x},t)$ is the Favre joint *pdf*. This is related to the conventional joint *pdf* $\bar{P}(\varphi;\underline{x},t)$ by $\tilde{P}=\bar{P}\rho(\varphi)/\bar{\rho}$ where $\rho(\varphi)$ is the density evaluated at the state $\varphi_i,(i=1,2\cdots)$. The notation $<\epsilon_{ij}\mid \phi(\underline{x},t)=\varphi>$ represents the conditional mean of $\epsilon_{ij}(\underline{x},t)$ subject to the constraint $\phi(\underline{x},t)=\varphi$ where

$$\epsilon_{ij} = 2\mathcal{D}\frac{\partial\phi_i}{\partial x_k}\frac{\partial\phi_j}{\partial x_k} \quad (4.22)$$

is an instantaneous scalar dissipation, the inverse of a diffusion time, evaluated with the assumption of equal mass diffusivities for all species. Equation (4.21) is valid at high Reynolds numbers and the summation convention applies not only to spatial coordinates $x_k\,(k=1,2,3)$ but also in composition space $\varphi_i\,(i=1,2\cdots)$. From left to right terms in Equation (4.21) represent, respectively, accumulation of probability, its advection in physical space by the mean velocity, $\tilde{u}_k$, its turbulent transport in physical space, transport of probability in composition space by chemical reaction rate $\dot{w}_i$ and its transport in composition space by molecular diffusion. Equations of state and other information must be used to reduce as far as possible the number of independent scalar variables φ_i which might for example represent temperature and several species mass fractions. The *pdf* equation must be closed and then solved in conjunction with a turbulent flow model which provides all necessary information about the mean velocity and turbulence. Mean values of the scalar variables are found by integration of the *pdf* in the scalar space.

An important advantage is that the reaction rate term in Equation (4.21) is automatically closed because the rate $\dot{\omega}_i$ is expressed in terms of the chosen set of scalars. Two types of model are however required in order to close the equation. These are deterministic and/or stochastic models which are selected with the aim of causing the *pdf* to evolve in a desired manner. The first is a model of the transport of probability in physical space due to turbulent motion. A gradient transport approximation is sometimes introduced (Ref. 76) such as

$$< u_k'' \mid \phi = \varphi > \tilde{P} \;=\; -C_c \frac{\tilde{k}}{\tilde{\epsilon}} \widetilde{u_k'' u_m''} \frac{\partial \tilde{P}}{\partial x_m} \tag{4.23}$$

where C_c is a model constant. On the other hand the premixed combustion DNS (Refs. 56, 72, 77) show that if $Da >> 1$ the conditional mean velocity on the isosurface $c(\underline{x}, t) = c^*$ varies linearly with c^* (see Figure 6) so that

$$< u_k \mid c(x,t) = c^* >$$

$$= \bar{u}_{rk}(\underline{x}) + c^* [\bar{u}_{pk}(\underline{x}) - \bar{u}_{rk}(x)] \tag{4.24}$$

It can be shown (Ref. 39) that

$$< u_k'' \mid c = c^* >= (c^* - \tilde{c}) \frac{\widetilde{u_k'' c''}}{\tilde{c}(1-\tilde{c})}$$

$$= (c^* - \tilde{c}) \left[\tau u_L^o - 2\alpha u' - \frac{b\tau \ell_T^2}{\rho_r \nu_r} \frac{\partial \bar{p}}{\partial x_k} \right] \tag{4.25}$$

where $c(\underline{x}, t)$ is the progress variable corresponding to $\phi(\underline{x}, t)$ in Equation (4.21) and c^* is the isosurface value corresponding to φ. The first version of Equation (4.25) corresponds precisely to the "linear mean-square estimate" model of Dopazo[115]. In general Equations (4.23) and (4.25) predict qualitatively different behaviour indicating that the gradient transport expression, Equation (4.23), is inappropriate when $Da >> 1$. The necessity to model this turbulent transport term is avoided if $\tilde{P}$ is defined as the joint *pdf* of velocity and scalar variables (Ref. 78). However this gain must be paid for in terms of greater computational complexity and the need to model unknown and combustion-sensitive pressure fluctuation terms.

The second type of model provides an approximation to the conditional dissipation term in Equation (4.21). This important term describes transport of probability in the space of the scalar variables through molecular diffusion influenced by small-scale turbulent mixing. Experimental measurements have been reported of the conditional dissipation or of closely related quantities (Refs. 79, 80). Relevant DNS data is also available (Refs. 56, 81) together with reviews of models (Refs. 74-76) It is often represented by stochastic models which cause the *pdf* to evolve towards a Gaussian shape and which do not allow for deterministic correlations between scalars and their gradients. Differential diffusion effects are not represented. Equation (4.21), supplemented by these turbulent transport and small-scale mixing models, is generally solved by means of a Monte Carlo simulation (Ref. 74). At this level of description the mean turbulent flow equations must be solved separately by conventional means. The two calculations are coupled through the mean density which is given by

$$\frac{1}{\bar{\rho}(\underline{x}, t)} \;=\; \int_o^1 \frac{1}{\rho(\varphi)} \tilde{P}(\varphi; \underline{x}, t)\, d\varphi \;. \tag{4.26}$$

In the limit $Da >> 1$ chemical reaction is fast in comparison with convection in

physical space so the reaction rate term in Equation (4.21) must essentially be balanced by the small-scale mixing term. This is the *pdf* version of the eddy break-up limit where "mixed-is-burned". However as we have noted laminar flame structures are often to be expected in these circumstances. In a laminar flame scalar gradients are deterministically related to each other and to scalar variables so existing models of the small-scale mixing term are not applicable. This question - how to take into account the influence of fast chemical reactions on the small scale mixing term - raises a fundamental issue which must be solved if *pdf* methods are to be universally applicable. One relatively simple approach (Ref. 78) is to represent it as the sum of two independent terms. The first of these is derived from the known scalar gradient in a premixed laminar flame and so requires no modelling. The second term is a stochastic model representing nonreactive small-scale mixing due to turbulence. With $Da >> 1$ it is small in comparison with the first term except near $c^* = 0, 1$ where the laminar flame scalar gradient approaches zero, see Figure 6, so that turbulent mixing controls the rate of entry to the fast flamelet combustion process (Ref. 82). Data from DNS (Ref. 56) tends to confirm this picture with the conditional mean gradient agreeing well with the flamelet value everywhere except near the edges of the flamelet where turbulent mixing predominates. A more rigourous way to deal with this problem in the framework of a *pdf* model is to consider the joint *pdf* of a scalar c and its gradient $|\nabla c|$. However a price must be paid in terms of new closure assumptions and in the solution of an equation with a larger number of independent variables.

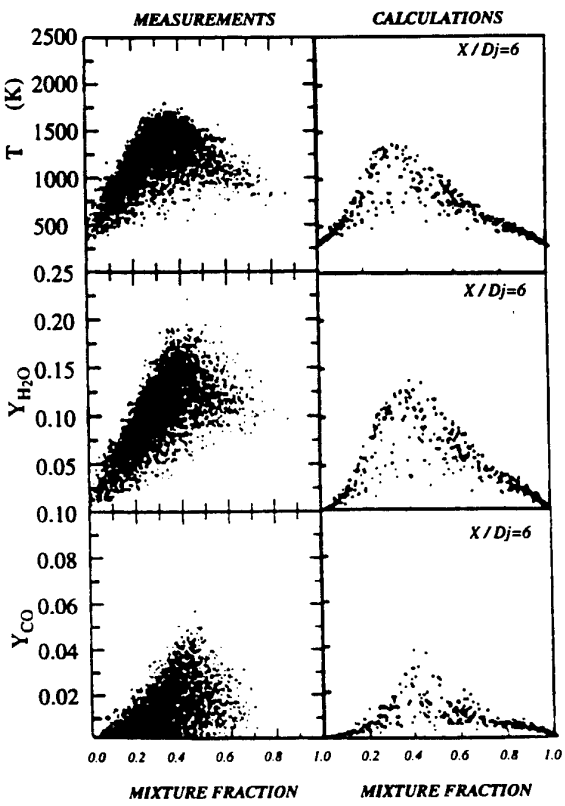

Figure 8
Jet diffusion flame experiments (Ref. 84) and *pdf* calculations (Ref. 83).

The scatter plots reproduced in Figure 8 illustrate what can be achieved by the transported *pdf* method. The calculations which are shown on the right are by Taing et al. (Ref. 83). They compute the joint *pdf* for velocity and four scalar variables using a reduced kinetic mechanism whose

rates are stored in a look-up table. The predictions are compared with measurements by Masri et al. (Ref. 84) in a pilot-stabilised $H_2/CO_2/$ air jet diffusion flame. Agreement is seen to be reasonably good. Deviations in flames close to extinction are attributed to finite rate kinetic effects and the blow-off limit is underpredicted by about 20 %.

Presumed pdf methods (Refs. 44, 45, 48, 85) provide a more simple and empirical way to estimate the shape of the scalar *pdf*. Equation (4.21) is replaced by a *pdf* of assumed form, typically a beta function, clipped Gaussian or other simple shape which can be specified in terms of its first two moments.

We take nonpremixed turbulent combustion as an example. At low Mach numbers the pressure is thermochemically constant as explained earlier. Assuming a single diffusion coefficient and a Lewis number of unity we define a mixture fraction Z such that

$$Z = \frac{h - h_2}{h_1 - h_2} = \frac{\zeta_F - \zeta_{F2}}{\zeta_{F1} - \zeta_{F2}} \quad (4.27)$$

where subscripts 1 and 2 refer to fuel and oxidiser streams respectively and ζ_F is the mass fraction of an element in the fuel. Hence $0 \leq Z \leq 1$ with $Z = 0$ in the oxidiser stream and $Z = 1$ in fuel. It is further assumed that the combustion chemistry is infinitely fast so $D_a \rightarrow \infty$ and the reaction zone shrinks to a flame sheet. Outside this sheet the mixture is inert. Equation (2.6) for $Y_i(\underline{x}, t)$ is similar in form to Equation (2.10) for $Z(\underline{x}, t)$ and so Y_i varies linearly with Z. The relationship is illustrated in Figure 9 where

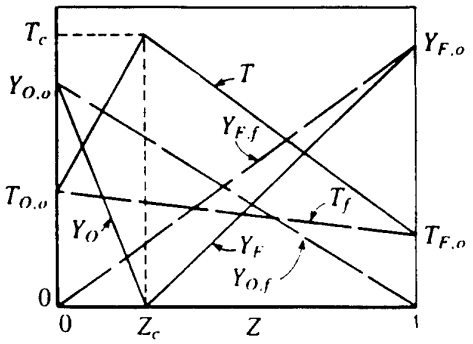

Figure 9
Flame sheet approximation (Ref. 31).

it may be seen that discontinuities of shape occur at the stoichiometric mixture fraction where $Z = Z_s$. Fuel and oxidiser concentrations are zero at this point.

This simple thermochemical model is averaged using a beta function for the presumed Favre *pdf* $\tilde{P}(Z^*\,;\,\underline{x})$ which is related to $\bar{P}(Z^*\,;\underline{x})$ by

$$\tilde{P}(Z^*;\underline{x}) = \frac{\rho(\underline{x}, t)}{\bar{\rho}(\underline{x})} \bar{P}(Z^*;\underline{x}) \quad (4.28)$$

For the beta function we have

$$\tilde{P}_\beta(Z^*;\underline{x}) = \frac{Z^{*r-1}(1 - Z^*)^{s-1}}{\int_o^1 Z^{r-1}(1 - Z)^{s-1}\, dZ} \quad (4.29)$$

where the exponents r and s are related to the first and second Favre moments of Z by

$$r = \tilde{Z}\left\{\frac{\tilde{Z}\left(1-\tilde{Z}\right)}{\widetilde{Z''^2}} - 1\right\} \tag{4.30}$$

$$s = \frac{1-\tilde{Z}}{\tilde{Z}} r \tag{4.31}$$

and $\widetilde{Z''^2} = \overline{\rho Z''^2}/\bar{\rho}$. It follows from Equations (4.29), (4.30) and (4.31) that

$$\tilde{P}_\beta\left(Z^*;\underline{x}\right) = \tilde{P}_\beta\left(Z^*;\tilde{Z}\left(\underline{x}\right),\widetilde{Z''^2}\left(\underline{x}\right)\right) \tag{4.32}$$

so the *pdf* can be evaluated in terms of its first two moments.

Because Z is related to elemental mass fractions Equation (2.10) has no troublesome chemical source terms to be averaged. Its first and second moments satisfy

$$\frac{\partial}{\partial x_k}\bar{\rho}\tilde{v}_k\tilde{Z} = \frac{\partial}{\partial x_k}\left(\overline{\rho\mathcal{D}\frac{\partial Z}{\partial x_k}} - \overline{\rho v_k'' Z''}\right) \tag{4.33}$$

$$\frac{\partial}{\partial x_k}\bar{\rho}\tilde{v}_k\widetilde{Z''^2} = 2\overline{\rho v_k'' Z''}\frac{\partial\tilde{Z}}{\partial x_k} - \frac{\partial}{\partial x_k}\overline{\rho v_k'' Z''^2} - \bar{\rho}\tilde{\epsilon}_{ZZ} \tag{4.34}$$

At this level of description the flow and the thermochemistry influence each other only through the mean density $\bar{\rho}\left(\underline{x}\right)$.

In order to solve Equations (4.33) and (4.34) we must determine $\bar{\rho}\left(\underline{x}\right)$ from Equation (4.26). Other mean properties are also obtainable from the *pdf*, for example

$$\tilde{Y}_i\left(\underline{x}\right) = \int_o^{\prime} Y_{i,eq}\left(Z^*\right)\tilde{P}_\beta\left(Z^*;\underline{x}\right)dZ^* \tag{4.35}$$

The subscript eq attached to $Y_{i,eq}\left(Z^*\right)$ indicates that these are the linear functions which are appropriate for our equilibrium thermochemical model with $D_a \to \infty$.

If D_a is large but finite the flame sheet at $Z = Z_s$ is replaced by a reaction zone of small but finite thickness centred on $Z = Z_s$. As explained in §4.2 this has the structure of a strained laminar diffusion flame. Neglecting unsteady effects a laminar diffusion flame satisfies the equation (Ref. 34)

$$\dot{w}_i = \frac{1}{2}\rho\epsilon_{ZZ}\frac{\partial^2 Y_{i,L}}{\partial Z^2} \tag{4.36}$$

where $\epsilon_{ZZ} = 2\mathcal{D}\left(\partial Z/\partial x_t\right)^2$ is the scalar dissipation. Choosing a typical value of this in a given turbulent flow Equation (4.37) may be solved to give $Y_i = Y_{i,L}\left(Z^*\right)$. The presumed *pdf* model, as described above, may then be employed (Refs. 33, 34, 43, 48, 86) with these laminar flame properties replacing $\rho_{eq}\left(Z^*\right)$ and $Y_{i,eq}\left(Z^*\right)$. The mean reaction rate, obtained from Equation (4.26), may be approximated as

$$\bar{\dot{w}}_i = \frac{1}{2}\bar{\rho}\tilde{\epsilon}_{ZZ}\left(\frac{\partial^2 Y_{i,L}}{\partial Z^2}\right)_s \bar{P}_\beta\left(Z_s\right) \tag{4.37}$$

where subscript s denotes stoichiometric conditions. The mean rate is predicted to be proportional to the scalar dissipation and to the probability of a stoichiometric mixture.

Similar mean reaction rate models are available for premixed turbulent combustion. Here it is convenient to define a reaction progress variable $c(\underline{x},t)$ as the mass fraction of a major combustion product species divided by the value of this mass fraction in fully burned products. Then $0 \leq c \leq 1$ with $c = 0$ in reactants and $c = 1$ in fully burned products. See Ref. 78 for a transported *pdf* model and Refs. 44, 45, 85 for presumed *pdf* models. The transport equation for the Favre mean of $c(\underline{x},t)$ in high Reynolds number flow is

$$\frac{\partial}{\partial x_k}\bar{\rho}\tilde{v}_k\tilde{c} = -\frac{\partial}{\partial x_k}\overline{\rho v_k'' c''} + \bar{\dot{w}}_c \tag{4.38}$$

If $D_a >> 1$, reaction zones are thin, and the *pdf* of this progress variable may be partitioned into contributions from unburned mixture, fully burned product and mixture undergoing reaction, so that

$$\tilde{P}(c^*;\underline{x},t) = \alpha(\underline{x},t)\,\delta(c^*) + \beta(\underline{x},t)\,\delta(1-c^*) + \gamma(\underline{x},t)\,\tilde{P}_F(c^*;\underline{x},t) \tag{4.39}$$

where $\alpha(\underline{x},t)$, $\beta(\underline{x},t)$, and $\gamma(\underline{x},t)$, are, respectively, the probabilities of observing unburned mixture, fully burned products and partially reacted mixture at $(\underline{x},t)$, while $\tilde{P}_F(c^*\underline{x},t)$, is the *pdf* of this partially reacted mixture. If the chemistry is sufficiently fast reaction zones become thin sheet-like regions which separate pockets of reactant from pockets of product. Then the reaction zone probability is $\gamma(\underline{x},t) = 0(1/D_a) << 1$. The *pdf* $\tilde{P}(c^*;\underline{x},t)$ is strongly bimodal with spikes at $c^* = 0$ and $c^* = 1$ representing reactants and products, respectively. Mean properties derived from this *pdf* are a weighted average of reactant and product properties plus a small, $0(\gamma)$, contribution from the reaction zone.

At these high Damköhler numbers the reaction zone approaches a thin wrinkled sheet. The area per unit volume or surface density of this flame sheet is denoted by $\bar{\Sigma}(\underline{x})$. It is related (Ref. 87) to $\tilde{P}(c^*;\underline{x})$ by

$$\bar{\Sigma}(\underline{x}) = \\ < |\nabla c| \,|\, c(\underline{x},t) = c^* > \tilde{P}(c^*;\underline{x}) \tag{4.40}$$

and the mean chemical source term in Equation (4.38) is related to $\bar{\Sigma}(\underline{x})$ by

$$\bar{\dot{w}}_c = \rho_o u_L^o I_o \bar{\Sigma} \tag{4.41}$$

The factor $\rho_r u_L^o I_o$ is the rate of creation of reaction products per unit flame area: ρ_r is the reactant density, u_L^o is the burning velocity of an unstretched laminar flame and $I_o = \bar{u}_L/u_L^o$ is a factor to allow for the influence of flame stretch. Both transport equation models (Refs. 88, 89) and algebraic models (Ref. 90) have been proposed for the prediction of $\bar{\Sigma}(\underline{x})$. For example Bray (Ref. 91) suggests the eddy

break-up expression

$$\bar{\Sigma} = 12.2 \frac{(1+\tau)\,\tilde{c}(1-\tilde{c})}{(1+\tau\tilde{c})^2} \frac{\tilde{\epsilon}}{u_L^o \tilde{k}} \quad (4.42)$$

Descriptions of other models may be found in Refs. 34, 37, 39 and 44.

4.4 Comments on Experimental Validation

Turbulent reactive flows involve complex processes. The theoretical models describe above necessarily incorporate many restrictive assumptions about turbulent flow, combustion chemistry and the interactions between them. In these circumstances it is essential that model predictions must be tested by comparison with experimental data. For such comparisons in low Mach number combustion see for example Ref. 37.

The conclusions to be drawn from a comparison between model predictions and experiment depend on the purpose of the predictions. If only global properties such as flame length are of interest a simple experiment allows straightforward conclusions to be drawn. In contrast to industrially orientated experiments which, for example, allow predictions of the performance and pollutant emissions of engines and furnaces to be tested, fundamental model development needs experiments in simple flow configurations. A generic flow geometry such as, for example, the jet flame (Refs. 59, 92), expanding spherical flame (Refs. 93, 94) or stagnation point flame (Refs. 95-98) combines this simplicity with the ability to control particular features of the flow, namely: turbulent shear, turbulence intensity and residence time, respectively, in these three examples. An ideal experimental configuration can be addressed, with different simplifying assumptions, by theory, by averaged flow models, by LES and by DNS. It allows unobstructed access for optical measurements and all initial and boundary conditions are accurately determined. Important parameters such as Reynolds numbers and time scale ratios should be varied over a wide range. This ideal specification is of course difficult to meet in every respect.

What should be measured in an ideal experiment? The most important requirement is that the data should be sufficiently complete to define experimental conditions so that quantitative interpretation and numerical simulation can be performed without ambiguity. Turbulent combustion models are concerned with correlations so simultaneous measurements are particularly valuable, e.g.: several scalars at the same point in space and time (Ref. 84), joint velocity-scalar measurements (Refs. 99, 100), field measurements of one or more variables (Refs. 52, 101, 102). Such measurements are possible only because of developments in the use of lasers (Ref. 103). Data will be useful only if valid average values can be formed from it. The present review emphasizes the importance of small-scale

turbulent flame structure. Measurements of small scale flame structure (Ref. 79), instantaneous reaction zone thicknesses (Refs. 59, 60, 104) and flame surface density (Refs. 104, 105-107) are urgently required but pose problems in terms of requirements for space-time resolution and the three-dimensional nature of the phenomena.

Sections 5 and 6 review experimental data in high speed turbulent combustion where, as we shall see, such detailed information is very scarce.

5. EXPERIMENTS ON SUPERSONIC JET FLAMES

These experiments can be separated into two categories. The first is concerned with jet flames in ducted supersonic flows which aim to simulate combustion in a particular high enthalpy propulsion system such as the scramjet. Global properties including wall static pressure distribution and scramjet nozzle thrust are measured; see, for example, a review by Billig (Ref. 108). In the second category may be found more generic experiments on high speed jet flames whose primary aim is to study the controlling physical and chemical processes, but which do not simulate the high enthalpies of hypersonic flight. A good example is provided by the experiments of Cheng et al. (Ref. 109) who used laser techniques to explore mixing and chemical reaction in a supersonic hydrogen jet flame. We shall review this experiment in detail at the end of this Section.

	air	fuel
Mach number	4.85	1 - 2
static pressure, atm.	2.7	2.7
static temperature, K	1250	916-611
stagnation pressure, atm	1200	5.1 - 23.1
stagnation temperature, K	7140	1100 K

Table 5.1 Estimated air and fuel combustor entry flow conditions for a Mach 12 scramjet at an altitude of 30.5 km.

A fundamental problem, which is particularly serious for experiments attempting to represent specific propulsion systems, but is also relevant to more generic experiments, is that hypersonic flight conditions are very difficult to simulate in the laboratory. Taking as an example the representative scramjet flow (Ferri, Ref. 1) quoted in §1, with a flight Mach number of 12 at an altitude of 30.5 km, combustor air and hydrogen entry stagnation pressures and temperatures may be estimated from ideal gas equations, as shown in Table 5.1. It is clear that the air supply stagnation conditions are very difficult to achieve.

Short duration shock tunnel or expansion tube facilities are required to generate the necessary high enthalpy flow. Free piston driven, reflected shock tunnels exist in the U.S.A. at the Graduate Aeronautical

Laboratories, California Institute of Technology (GALCIT, Ref. 110) and at the Arnold Engineering Development Center (AEDC, Ref. 111).

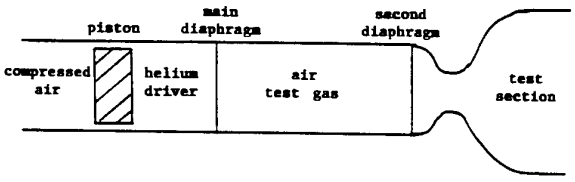

Figure 10
Free piston shock tunnel

In these facilities (Figure 10) compressed air drives a free piston which compresses and heats the helium driver gas of the shock tunnel, breaking the main diaphragm. A normal shock wave then compresses the air which forms the test gas in the driven tube. On reflection from the closed end of the driven tube the shock wave brings the test gas to rest and further heats it while causing a secondary diaphragm to burst. The test gas then expands and accelerates through a convergent-divergent nozzle into the test section. Test times of 1-2 ms are obtained. The T5 Tunnel at GALCIT reaches a stagnation temperature of nearly 9000 K and a stagnation pressure of 700 atm. (Ref. 110). Under such conditions the air upstream of the expansion nozzle is partly dissociated and the expansion process is too rapid to allow atomic recombination to reach equilibrium in the test section (Ref. 112) so the test gas is not fully representative of flight conditions.

This problem is less serious in expansion tubes such as the NASA HYPULSE facility at General Applied Science Laboratory (GASL) Inc. (Ref. 113). This uses an unsteady expansion in a constant-area tube to generate high enthalpy, high velocity flow with a lower level of dissociation than in a shock tunnel. However, the test time is small ($\sim$ 0.5 ms: Ref. 112), so only short models can be tested.

It appears to be impossible to fully simulate in the laboratory the scramjet combustor air entry properties and combustion processes which will occur over the full range of a plausible flight Mach number and altitude corridor. Reliance must be placed on theoretical models to fill in the gaps where experiment is not possible. Models must be validated by comparison with experiment. However, if used injudiciously, experiments conducted under near-ambient conditions can potentially be misleading, because they may study a combustion regime which is not representative of conditions in flight.

Krishnamurthy et al. (Ref. 112) report results of a comparison between experiments in the high enthalpy GALCIT T5 shock tunnel facility and predictions from the NASA GASP code (Ref. 114). Predicted (Ref. 112) wall static pressure distributions agree well with the experimental data.

In the experiments air at a Mach number of 5.17, stagnation temperature 8100 K, stagnation pressure 85 MPa, flows into a combustion chamber of constant cross-section with a velocity of 4805 m/s. Hydrogen fuel is injected from one wall into the chamber at an angle of 15° to the chamber axis. Its injection velocity is 3980 m/s, stagnation temperature 1500 K. The disturbance caused by this fuel injection leads to the formation of an oblique bow shock wave which reflects back from the opposite wall of the combustor. In comparison with inert flow tests, combustion causes the bow shock wave to move further upstream. However, the wall pressure distribution is generally similar for cases with and without combustion. It is concluded (Ref. 112) that, because of the high static temperature (2340 K) of the air in these tests, dissociation predominates over formation of combustion products. Direct heat release due to combustion is then small. To generate thrust dissociation energy must be recovered due to atomic recombination as the hot gases are accelerated and cooled in an expansion nozzle.

Other experiments referenced here do not achieve the high enthalpies which are required for simulation of high Mach number propulsion devices. Early scramjet experiments are reviewed in Refs. 1, 3 and 4 and also by Libby (Ref. 115). Reviews of more recent work may be found in Ref. 20.

Evans et al. (Ref. 116) studied combustion of a supersonic hydrogen jet discharged co-axially with a supersonic air flow and used sampling techniques to determine mean composition profiles of stable species.

Mixing between fuel and air strongly influences the length of a jet flame because combustion cannot begin until a nearly stoichiometric mixture has been produced. Driscoll et al. (Ref. 117) studied the visible lengths of hydrogen jet flames in co-flowing subsonic and supersonic air streams. The supersonic flames were found to be significantly shorter than corresponding subsonic flames (typically half as long), providing that both the velocity and density ratio are matched for the two cases. The authors suggest that the difference may be due to transverse velocities caused by compression and expansion waves in the supersonic flow. The supersonic air flow Mach number was 2.2. Increasing the air stagnation temperature from 294 K to 600 K caused a substantial further reduction in the length of the supersonic flames.

In a related series of experiments Huh and Driscoll (Ref. 118) studied the influence of shock waves on jet mixing and the length of supersonic hydrogen jet flames. The air flow Mach number was 2.5 and the oblique shock waves were generated by two 10° wedges which were placed downstream of the fuel injector. The shock waves were found to have a strong effect on the flame shape. Under optimum con-

ditions the flame length was reduced by 30 % by shock wave interactions.

Sato et al. (Ref. 119) report results of experiments to establish conditions for autoignition of hydrogen injected into high speed air flows. Srikrishnan et al. (Ref. 120) and Anil and Damodaran (Ref. 121) explore the use of lobed nozzles to enhance the rates of mixing and combustion when a high speed jet discharges axially in a supersonic air flow. Substantial effects are observed.

Finally, an important paper by Cheng et al. (Ref. 109) gives the first quantitative indication of the extent of incomplete mixing in a supersonic jet flame. In their laser spectroscopic experiments a sonic jet of hydrogen is discharged coaxially with an annular Mach 2 jet of vitiated air and an unconfined, lifted, supersonic hydrogen-air diffusion flame is stabilised above the jet exit. The vitiated air is produced by burning hydrogen with oxygen-enriched air in a pre-chamber. Its stagnation pressure and temperature at 0.107 MPa and 1250 K. The apparatus (Figure 11) is small: air nozzle internal diameter 17.78 mm, fuel nozzle internal diameter 2.36 mm. The flame generates a noise level in excess of 135 db. A lifted flame sits at about 25 fuel nozzle diameters downstream of the nozzle exit and the authors speculate that it may be stabilised on a weak shock wave.

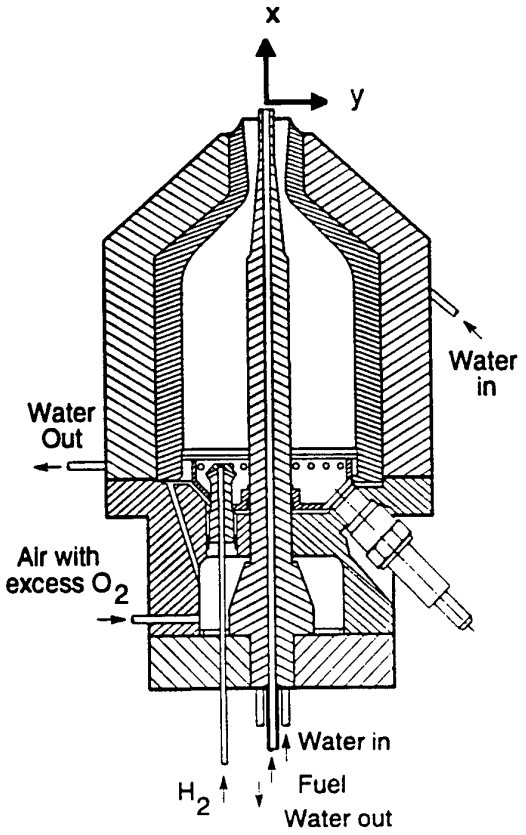

Figure 11
Supersonic jet flame burner of Cheng et al. (Ref. 109).

Point measurements are made (Ref. 109) using ultraviolet spontaneous vibrational Raman scattering and laser-induced predissociative fluorescence from a pulsed excimer laser. Temperature is obtained by vibrational Raman scattering of nitrogen assuming nitrogen molecules to be vibrationally equilibrated. Simultaneous concentration measurements of major species $H_2, 0_2, N_2$ and H_2O are also obtained from the Raman spectra. The OH concentra-

tion is found from laser-induced predissociative fluorescence and is insensitive to collisional quenching.

Questions of spatial and temporal resolution are discussed in detail by Cheng et al. (Ref. 109). Typical Kolmogorov time and length scales in the flame are estimated to be of order 0.7 μs and 0.02 mm respectively. The laser pulse duration is very short, 20 μs, but vibrational relaxation of nitrogen is identified as being important for the temperature measurements. In the presence of H_2O a relaxation time of 1.7 μs is estimated and is judged to be sufficiently close to Kolmogorov time. Spatial resolution is less satisfactory. The laser probe volume is 0.75 mm long and 0.25 mm in diameter and 0.4 mm of this volume is viewed by the spectrometer. Although these dimensions are larger than the Kolmogorov length of 0.02 mm the authors conclude that their measurements will capture at least 90 % of the scalar variance in this flow.

Figure 12 shows typical results (Ref. 109) in the form of scatter plots. Lines representing adiabatic equilibrium and nonreactive mixing are also shown. The authors conclude that this supersonic flame has higher levels of fluctuation of temperature and species concentrations in comparison with subsonic flames. Note that, if incomplete spatial resolution does influence this data, the true level of fluctuations will be even higher.

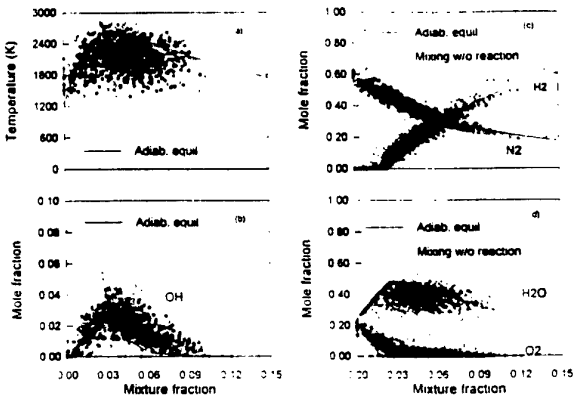

Figure 12
Scatter plots from experiments of Cheng et al. (Ref. 109).

The following conclusions are drawn from this review of experimental data.

1. In view of the immense difficulty of simulating the high specific enthalpies typical of combustion in high Mach number propulsion systems we should not be surprised at the shortage of detailed measurements in such flames. There are no detailed measurements at sufficiently high combustor Mach numbers for compressibility effects to become dominant.

2. Even without realistic high enthalpy simulation small spatial scales are difficult to resolve and incomplete resolution can lead to underestimation of scalar fluctuation levels.

3. If the high scalar fluctuation levels measured by Cheng et al. (Ref. 109)

are typical of real systems then the neglect of these fluctuations in calculations of mean reaction rates will lead to gross errors. The evaluation of these rates in terms of a *pdf* (see Equation 3.2) must be recognised as essential.

4. Shock waves play a major role in many of these flames: the bow shock and its reflection in the GALCIT shock tunnel experiments (Ref. 112), the observed reduction in flame length due to imposed oblique shock waves (Ref. 118) and the possible stabilisation of the Cheng et al. lifted flame (Ref. 109) by a weak shock wave. The incorporation of shock wave processes in high speed turbulent combustion models presents an additional challenge.

6. EXPERIMENTS ON DEFLAGRATION AND TRANSITION TO DETONATION

In contrast to §5 the experiments reviewed here concern situations where the gaseous fuel and oxidiser are fully premixed. The distinction between deflagration and detonation waves may be understood by referring to Figure 13 (Williams, Ref. 31), which is a plot of final pressures, p, and specific volumes, v, in combustion waves. The initial state, ahead of the wave, is represented by the point (1, 1). In Figure 13, the locus of all possible final states is an intersection between the Hugoniot curve (states satisfying conservation of momentum and energy) and a Rayleigh line (a straight line, of negative slope, on which conservation of mass and

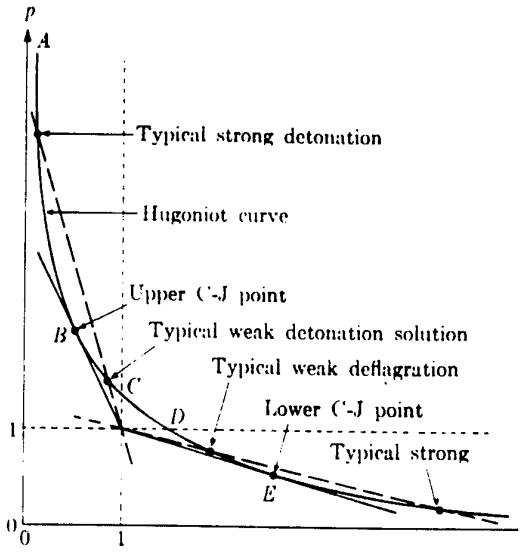

Figure 13
Hugoniot curve in terms of presure and specific volume (Ref. 31).

momentum is satisfied). At the so-called Chapman-Jouget (C J) points the burned gas velocity is sonic. Detonation waves involve an increase in pressure which is usually large. Propagation speeds are measured in km / s. The pressure falls in a deflagration wave. Although a laminar deflagration propagates at around 1 m/s and is almost isobaric, high speed deflagrations also occur and, as we shall see, turbulence plays an essential role.

In the case of a transient phenomenon such as an explosion, the averaged turbulent flow equations must be generated

from an ensemble averaging process rather than from the more familiar time average. Apart from the addition of a time-derivative term, the resulting equations are identical in form to those obtained by time averaging. However their meaning is not necessarily the same. Consider various velocities $\underline{u}(\underline{x},t)$, all observed at a fixed location $\underline{x}$ and elapsed time t, but in different realisations of the explosion. Variations within this set of instantaneous velocities arise partly from the existence at $(\underline{x},t)$, of the vortical motions, which are characteristic of turbulence, but also partly from other causes. For example $\underline{u}(\underline{x},t)$, may be influenced by the initial rate of flame spread from the ignition source which can vary from one realisation to another. Similar processes can cause the ensemble-averaged turbulent flame brush thickness to be greater than the spatially averaged brush thickness in a single realisation. It is unlikely that the non-turbulent property fluctuations associated with these phenomena will be well described by conventional turbulent flow models. Similar difficulties arise in describing turbulence and combustion in reciprocating engines, where up to about one half of the observed velocity variation may be attributable (Refs. 122, 123) to cycle-to-cycle variability rather than to turbulence. Also the ensemble-averaged flame brush thickness is observed (Ref. 124) to be several times greater than its thickness in a single cycle. It is rare for sufficient data to be available to allow accurate ensemble averages to be formed.

In the absence of strong confinement spark-ignited, turbulent hydrocarbon-air mixtures burn in relatively low speed deflagrations. The turbulent burning velocity, u_T, defined as the mean speed of propagation into a stationary unburned mixture, is usually of the same order of magnitude as the *rms* turbulence velocity u'. If the burned gas is brought to rest then volume expansion due to heat release ensures that the unburned gas is driven ahead of the flame which then travels, typically, about six times faster. In both cases these velocities are usually very small in comparison with the speed of sound. Figure 14 shows a correlation of turbulent burning velocity data of Bradley et al. (Refs. 85, 93, 125).

As explained in §1, a deflagration wave travelling past obstacles tends to accelerate as a result of a positive feedback mechanism. Unburned gas, ahead of the flame, is forced to flow past these obstacles and becomes turbulent. When the flame catches up with and burns this turbulent mixture, it accelerates, and causes the remaining unburned mixture to flow more rapidly past further obstacles, generating more intense turbulence. This process has been studied in a spherical geometry (Ref. 126) but most laboratory experiments involve straight tubes or channels with repeated baffles or other obstacles (Refs. 16, 17, 22, 127-130). Measurements include static pressure, as a function of position and time, flame position as a function of time and, in some cases, flame photographs.

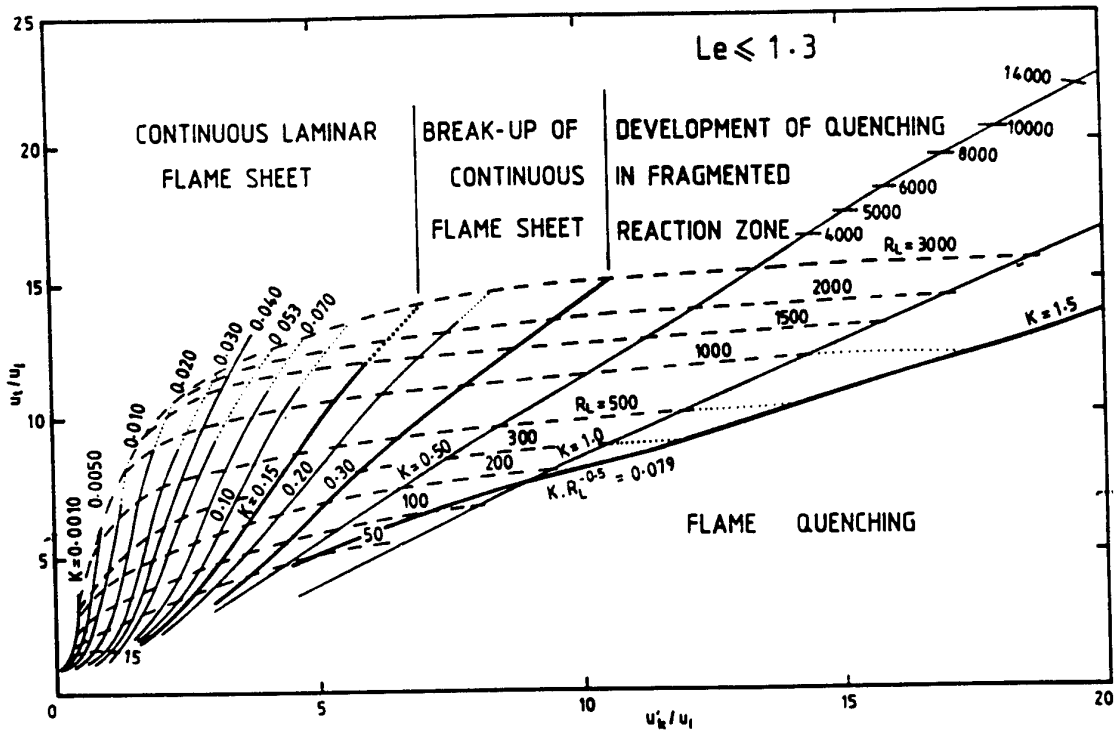

Figure 14
Correlation of turbulent burning velocities (Ref. 125).

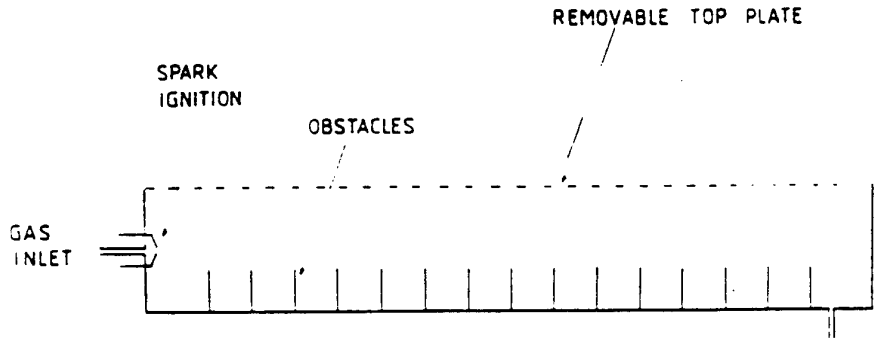

Figure 15
Flame acceleration by obstacles: experiment of Chan et al. (Ref. 129).

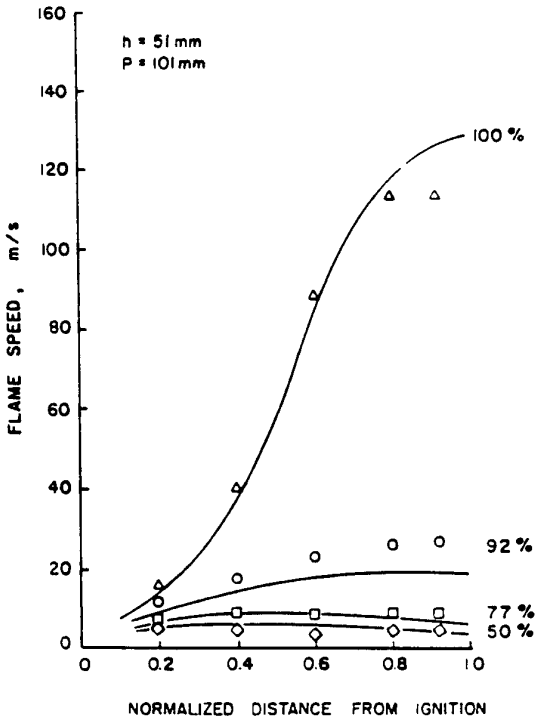

Figure 16
Effect of confinement on flame speed (Chan et al., Ref. 129).

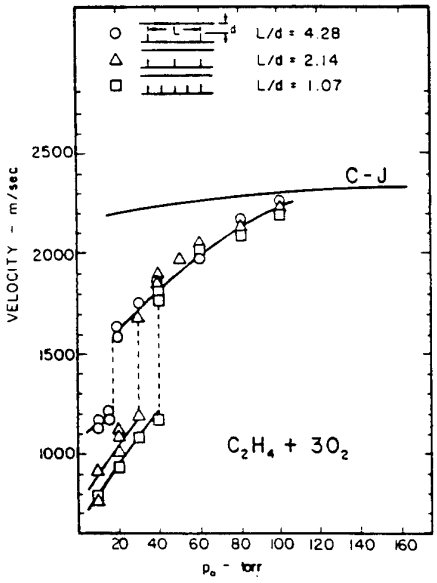

Figure 17 **Steady state propagation velocity as a function of mixture sensitivity (Teodorczyk et al. Ref. 131).**

Figure 15 is a sketch of the rectangular explosion channel used in one such series of tests by Chan et al. (Ref. 129). It is 1.22 m in length and 127 mm by 203 mm in cross section with glass sides and a set of removable top plates of different opening areas to confine the explosion. A solid top plate provides complete confinement and tests without any top plate are regarded as unconfined. A set of vertical baffle plates act as obstacles within the explosion channel. The stoichiometric methane-air mixture is spark-ignited at the closed left hand end of the channel. The right hand end is then open. High speed Schlieren movies show that pockets of unburned gas, in the cavities between pairs of obstacles, burn rapidly in the turbulent flame and cause the process to accelerate.

An important conclusion from this experiment (Ref. 129) is that the flame acceleration is very sensitive to the degree of confinement from the top plate of the explosion channel as illustrated in Figure 16. The highest flame speeds (up to 110 m/s in this case) occur in the fully confined channel with a solid roof. But if the confinement is reduced to 77 % (top plate with 23 % open area) the flame barely accelerates at all.

Higher flame speeds, and hence stronger explosions, are favoured by a more strongly reactive mixture (e.g. by raising the initial pressure and/or by use of oxygen in place of air) and by stronger turbulence generation through a higher degree of confinement, through more rows of obstacles or with obstacles presenting a higher percentage blockage of the channel. Turbulent flame speeds of the order of 1000 m/s are obtainable (Teodorczyk et al., Refs. 22, 131), before a sudden transition occurs to a quasi-detonation, whose velocity is significantly less than the CJ velocity, as illustrated in Figure 17. Both modes of propagation are accompanied by shock waves travelling laterally as well as axially, see Figure 18. In the case of the high speed turbulent flame the leading shock wave is well separated from the reaction zone whereas in the quasi-detonation it is not.

The phenomenon of transition to detonation is often seen to be triggered by a so-called explosion within an explosion: a sudden, highly localised release of energy which generates a strong shock wave out of which the detonation quickly develops. In sufficiently reactive mixtures the transition will occur in a smooth tube without obstacles and the explosion within an explosion can then be identified as shown by Meyer et al. (Ref. 132) whose photographs are reproduced in Figure 19. The process involves a localised spatial gradient of induction time in the unburned mixture (Ref. 25). Under these conditions the flow structure appears to be dominated by gas dynamic waves and their interactions with combustion. Molecular diffusion processes cannot make a large contribution and inviscid reactive flow calculations (Ref. 133) provide a good descrip-

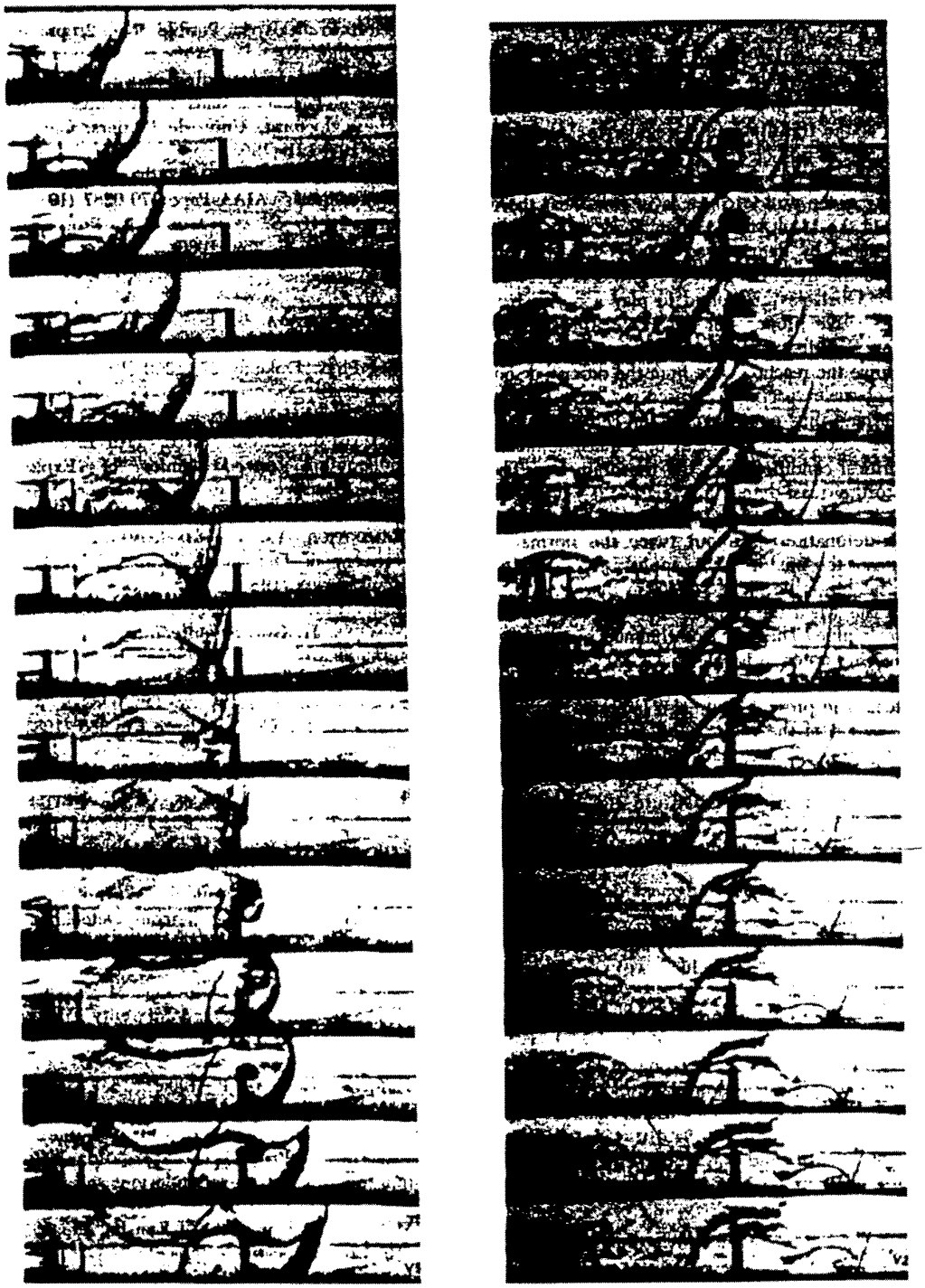

Figure 18 Propagation of quasi-detonation (left) and high speed turbulent flame (right) from (Teodorczyk et al. Ref. 131).

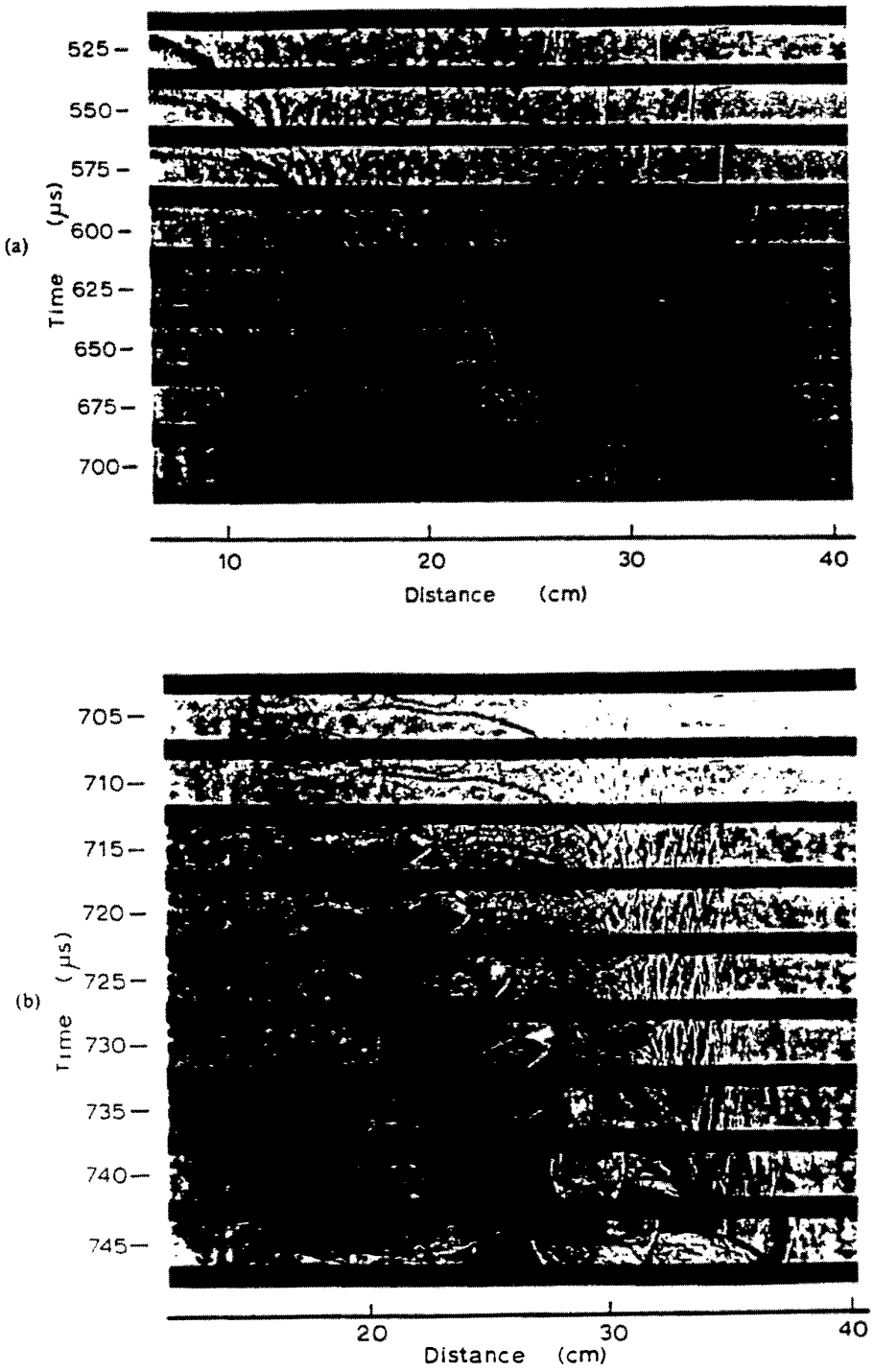

Figure 19 Stroboscopic laser-schlieren images of transition to detonation (Meyer et al. Ref. 132).

tion. A recent theory for the transition to detonation in unconfined flames is presented in Ref. 134.

Very recent experiments by Thomas et al. (Ref. 135) illustrate the important role of shock waves. A spherical laminar flame is created by spark ignition in a shock tube. The flame bubble is toroidally distorted and convected by a weak incident shock wave which then reflects from the end wall and meets the flame bubble for a second time. The flame now becomes intensely turbulent and couples with the initially weak reflected shock which accelerates rapidly. It achieves detonation just beyond the viewing window, having trebled its velocity in a distance of only 150 mm. No explanation for this rapid acceleration has yet been confirmed.

The following conclusions are drawn:

1. Many of these transient flows are geometrically complex with regions of separated flow and trapped pockets of unburned reactants.

2. Pressure waves play an increasingly important role as flame speeds increase.

3. Available experimental data either give global quantities such as flame speed and wall pressure or are in the form of photographs describing shock wave and flame geometries.

4. No experimental information has been found concerning regimes of turbulent combustion. Is the variance of, say, temperature fluctuations negligibly small so that turbulent fluctuations can be neglected in calculations of mean reaction rates? Or is this variance large as in, for example, laminar flamelet models for $D_a >> 1$? Are molecular diffusion processes important in a given flow?

7. MODELS FOR HIGH SPEED TURBULENT REACTIVE FLOWS

We begin this Section by identifying some features of high speed reactive flows which make them particularly difficult to describe in terms of averaged flow equations. In contrast to the low speed flows described in §4 their kinetic energy per unit mass is no longer negligible in comparison with their specific enthalpy. Fluctuations in velocity now lead directly to fluctuations in specific enthalpy because of coupling between the equations of motion and energy. Consequently, localised changes in thermodynamic state due, for example, to intense viscous dissipation or the presence of an eddy shocklet, must be taken into account when evaluating the local rates of reaction. The number of stochastic variables in a *pdf* description of the mean reaction rate, Equation (3.2), should be increased to allow for these processes.

Numerical simulations of autoignition in supersonic laminar mixing layers (De-

shaies et al., Ref. 136, Nishioka and Law, Ref. 137) show that accurate predictions must take into account the influence of temperature-dependent transport properties on viscous heating. Detailed chemical kinetic information is also required and, in many cases, the distance to autoignition becomes impracticably large. It is likely that many industrially relevant high Mach number turbulent combustion flows will also be sensitive to details of combustion chemistry.

Under conditions of locally supersonic flow the pressure fluctuations at a given spatial location depend on the velocity field in the forward Mach cone from that point, i.e., on a limited portion of the flow, while in low speed cases that dependence results from the velocity field over the entire fluid space. As a consequence of these fundamental differences the modelling of the important pressure-velocity and pressure-rate-of-strain terms in the second moment equations of turbulence must be expected to require alteration in high speed flows without and with combustion. Density inhomogeneities due to heat release exist in both high and low speed combustion while those due to compressibility arise only in high speed flows. However, it is worth noting that as the speed of the flow increases the mean kinetic energy per unit mass $v^2/2$ dominates the static enthalpy per unit mass h so that heat release due to combustion adds relatively smaller amounts of energy as the mean Mach number increases. Therefore the influence of combustion on the flow becomes less important as that Mach number increases.

The experiments reviewed in §5 and §6 led us to conclude that shock waves often occur in high speed reactive flows of practical interest and that their presence can have a strong influence on the development of the flame. Numerical codes based on combustion and flow models for such applications must therefore be capable of "capturing" shock waves and of predicting their location and strength. Numerical simulations of interactions between shock waves and isolated vortices (Guichard et al., Ref. 138), shock waves and homogeneous turbulent mixing (Réveillon and Vervisch, Ref. 139) and shock waves with two-dimensional turbulent mixing layers (Stoukov, Ref. 140) all illustrate the complex nature of these interactions. Turbulence and mixing rates are modified by the presence of the shock wave. Localised, transient hot spots are formed due to shock wave curvature. Models are required to incorporate these processes in averaged turbulent flow equations.

7.1 Parameters and Regimes of High Speed Turbulent Combustion (Ref. 19)

Our exposition is facilitated if we consider a premixed system although the concepts apply without significant modification for all other systems. As noted above, the essential difference between low and

high speed combustion relates to the relative magnitudes of the kinetic energy per unit mass and the chemical energy associated with the adiabatic temperature rise in the chemical conversion from reactants to products. In low speed flows the kinetic energy is negligible so that fluctuations in velocity do not alter chemical kinetic behaviour. As the velocity of reactants increases their kinetic energy becomes increasingly significant relative to their chemical energy such that in due course the latter becomes negligible. In this limit fluctuations in velocity result in large changes in static temperature and thus in chemical kinetic rates although the absence or presence of chemical reaction has a small influence on the state of the gas. We know from compressible flow theory that it is the Mach number which characterizes the relative magnitude of the kinetic energy and the internal energy of a gas. Therefore, it is to be expected that our discussion of compressibility effects centres on a mean Mach number $\bar{M}$ considered to be representative in the sense that it can be explicitly related to all other Mach numbers.

The nondimensional parameters, e.g., of turbulent Reynolds and Damköhler numbers, discussed in §4.2 delineate the regimes of low speed turbulent combustion, remain relevant for high speed flows but must now be augmented by $\bar{M}$. To define $\bar{M}$ it is necessary to select a representative velocity U and a reference static temperature T_{ref} which defines a representative speed of sound a_{ref}. The obvious definition

$$\bar{M} \equiv \frac{U}{a_{ref}} \tag{7.1}$$

becomes useful only when the two quantitites appearing therein are known. For example, in low speed flows sometimes a mean velocity is relevant for U while in other situations the square root of the turbulent kinetic energy is most important. Similarly, in examining ignition phenomena a relatively low initial temperature may provide the most relevant T_{ref} while in examining other phenomena the much higher adiabatic flame temperature is more appropriate.

To advance our discussion in the light of our earlier observations about the importance of the relative magnitudes of kinetic and chemical energies to define $\bar{M}$ we select a mean velocity and a mean static temperature, both measured in a laboratory frame of reference, i.e., with respect to coordinates fixed, e.g., on the walls of the combustor. As a result $\bar{M}$ is typically about ten times the turbulent Mach number $M_t = (2k)^{\frac{1}{2}}/a$ if $k^{\frac{1}{2}}/U$ is 10^{-1}, a reasonable value for purposes of estimation.

In a one-step approximation to the kinetics of the chemical system under consideration the sensitivity of the reaction rate to temperature is measured by the Zel'dovich number

$$\beta = \frac{\Delta T_c}{T_{ref}} \frac{T_a}{T_{ref}} \tag{7.2}$$

where T_a is the activation temperature and ΔT_c the temperature rise in the adiabatic combustion of the reactants at constant pressure, a rise as noted earlier associated with the chemical energy. The typical values of $\beta >> 1$ lead to the special features of low speed turbulent combustion in the reaction sheet regime, features which are expected to persist in high speed flows, until the kinetic energy is comparable with ΔT_c. It is therefore relevant (Ref. 19) to introduce the parameter

$$S \equiv \frac{\Delta T_s}{\Delta T_c} \tag{7.3}$$

where ΔT_s is a measure of the temperature rise associated with kinetic energy, a rise we take equal to the stagnation temperature of a chemically frozen stream, i.e.

$$\Delta T_s \approx \frac{1}{2}(\gamma - 1)\bar{M}^2 T_{ref} \tag{7.4}$$

We thus have

$$S = \frac{1}{2}(\gamma - 1)\bar{M}^2 \frac{T_{ref}}{\Delta T_c} \tag{7.5}$$

It may be seen that in low Mach number flows $S << 1$ and the kinetic energy is negligible compared withthe chemical energy. When $S \approx 1$ the two energies are about equal but when $S >> 1$, the kinetic energy in the reactants dominates. Since $\Delta T_c/T_{ref}$ lies typically between one and ten in applications, Equation (7.5) indicates that S exceeds unity when $\bar{M}$ exceeds a value ranging from two to ten. The coupling between *compressibility and chemical kinetic behaviour* thus become an important feature of turbulent combustion when $\bar{M}$ exceeds a critical value dependent on this temperature ratio.

These observations suggest that the plane of the Damköhler number D_a and Reynolds number R_{eT} of Figure 5 be extended in a third dimension having S as its coordinate. For $S << 1$ the regimes of turbulent combustion are as described in §4.2 but for $S >> 1$ chemical behaviour becomes dominated by compressibility effects and the previous identification of reaction-sheet and distributed reaction limits, although perhaps applicable, become less well founded. Both flamelets and shocklets may occur at sufficiently large values of D_a and S.

The manner in which velocity fluctuations influence chemical kinetic behaviour at high enough values of $\bar{M}$ may be deduced from Equation (2.14). Since T_a/T_c is large in combustion applications, small changes in $T - T_c$ influence greatly the rates of chemical reaction. Thus the argument of the exponential function in Equation (2.14) indicating the temperature changes produced by velocity changes produced by velocity changes becomes βS. This result shows that if $\beta S << 1$, velocity changes have only a small influence on chemical reaction rates but that if this inequality is not satisfied, there is coupling between velocity fluctuations and those rates. Compressiblity may thus begin to influence such rates well before the regime

$S \approx 1$ is reached. Rather it is necessary only that $S > \beta^{-1}$ for that influence to become significant. Compressibility effects may thus dominate ignition and extinction in high speed turbulent flows.

From these results it is possible to summarize the effects of compressibility on turbulent reacting flows by considering different Mach number ranges:

1. $\bar{M} << [2/(\gamma-1)(T_{ref}/T_a)]^{\frac{1}{2}}$: Temperature changes from compressibility have negligible effect on chemical kinetic behaviour because $\beta S << 1$.
2. $[2/(\gamma-1)(T_{ref}/T_a)]^{\frac{1}{2}} < \bar{M} < 1$: Temperature changes from compressibility may influence chemical kinetic behaviour but shocklets do not occur.
3. $1 < \bar{M} < [2/(\gamma-1)(\Delta T_c\, T_{ref})]^{\frac{1}{2}}$: Shocklets and expansion waves form when flow deflections occur but the temperature changes and therefore reaction rate changes produced by compressibility remain less than those resulting from heat release.
4. $[2/(\gamma-1)(\Delta T_c/T_{ref})]^{\frac{1}{2}} < \bar{M} < 0.6\bar{M}/M_t$: Temperature changes associated with compressibility are larger than those stemming from heat release and eddy shocklets are relatively unimportant because $M_t < 0.6$.
5. $\bar{M} > 0.6\bar{M}/M_t$: Eddy shocklets become increasingly important in influencing mean viscous dissipation while compressibility remains the largest contributor to temperature changes.

Although involving restrictions on $\gamma, T_a/T_{ref}$ and $\Delta T_c/T_{ref}$ and thus quantitative uncertainties the sequence of Mach number regimes described here appears to be representative of the most realistic situations and suggests the variety of phenomena arising in turbulent combustion as the Mach number increases.

7.2 Direct Numerical Simulations

In contrast to subsonic flows, turbulence can readily be convected into the computational domain of a numerical simulation for supersonic flow (van Kalmthout et al., Refs. 141, 142), paving the way for quasi-steady high speed reactive DNS. The two simulations reviewed here are both two-dimensional.

In the work of van Kalmthout et al. (Refs. 141, 142) the injected turbulence is homogeneous and isotropic, the Mach number is 1.3 and the two-dimensional fuel-air mixing layer is set up without shear. Acoustic waves and flow compressibility are fully accounted for but heat release due to combustion is set to zero. The aim of the calculations is to derive statistical data in order to develop a theoretical model of nonpremixed turbulent combustion: in this case, a flame surface density model. The benefit of combustion DNS for

this purpose is clearly demonstrated, (Ref. 141).

Stoukov (Ref. 140) also considers a two-dimensional supersonic mixing layer. Entry conditions are shown in Table 7.1.

Flow	Velocity m/s	Mach No.	Reynolds No.
H_2	3000	1.29	1.6×10^4
Air	1780	2.94	1.05×10^5

Table 7.1 Entry conditions (Ref. 140)

These entry conditions are perturbed in such a way that transition to turbulent flow is predicted. A detailed hydrogen-air reaction scheme is used including 37 elementary reactions and 9 chemical species. Four types of flow are calculated: inert and reactive mixing layers, with and without oblique shock waves. A shock wave is generated by placing a wedge at the bottom of the computational domain.

Figure 20 illustrates the regular vortical structure of the inert mixing layer without a shock wave (Ref. 140). Regions of high pressure occur in the braids between these vortices and are associated with a local temperature rise of 20K. The convective Mach number is 0.416. The corresponding inert mixing layer, with a shock wave generated by a 5° wedge, is shown in Figure 21. The shock is wrinkled and large fluctuations in pressure and temperature occur behind it. In a reactive flow, Figure 22, the location of autoignition fluctuates in response to the varying upstream conditions. Figure 23 presents scatter plots illustrating the wide range of instantaneous conditions occurring in the established flame. Recall that, in a steady laminar flame, each of these plots would reduce to a single data point. The computed fluctuation level is clearly very high. Finally the interaction between a reactive shear layer and the shock wave generated by a 5° wedge is illustrated in Figure 24. Very strong reaction behind the shock wave causes the shock wave to move upstream during the time interval between these two sets of images.

These simulations illustrate the complexity of the interaction between turbulent mixing, chemical reaction, supersonic flow and shock waves. Although it is not yet possible to carry out three dimensional DNS with detailed chemistry the results provide valuable insight as well as unique statistical information for model development.

7.3 Selection of a Model

It is first necessary to identify the purpose of a model calculation. Is the aim to estimate global trends or are detailed and accurate flow field and combustion predictions required? The purpose of the work often dictates features of the model which is selected. For example, if distances to autoignition are to be predicted, the model must be capable of including sufficient detail of the ignition chemistry.

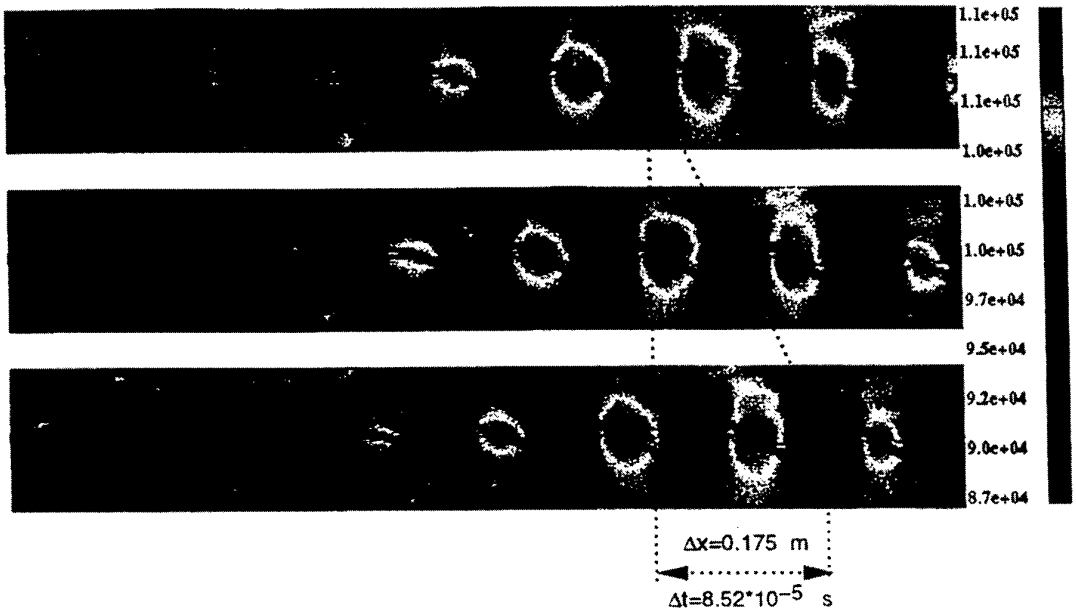

Figure 20
Inert mixing (lines) and pressure field (shades of grey) in 2D mixing layer (Stoukov Ref. 140).

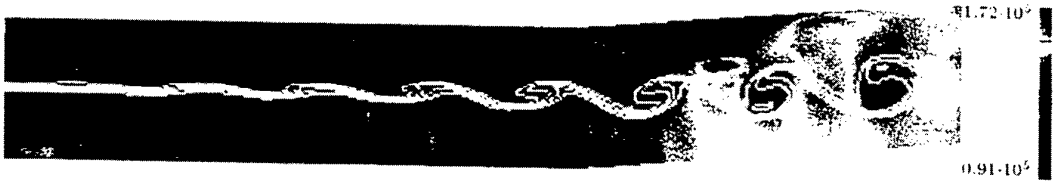

Figure 21
Effect of shock wave on inert mixing (lines) and pressure (shades of grey), Stoukov (Ref. 140).

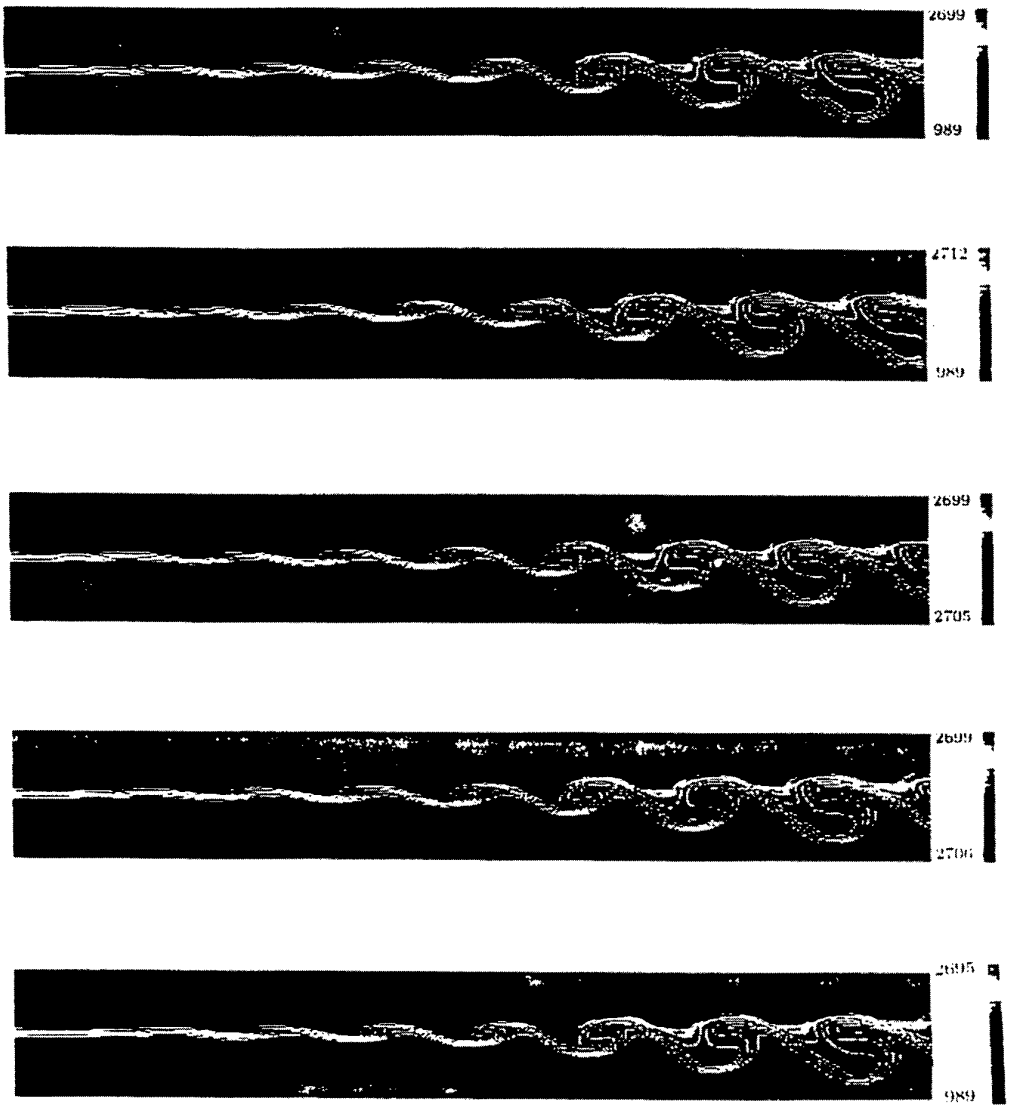

Figure 22
Autoignition in a mixing layer, Stoukov (Ref. 140).

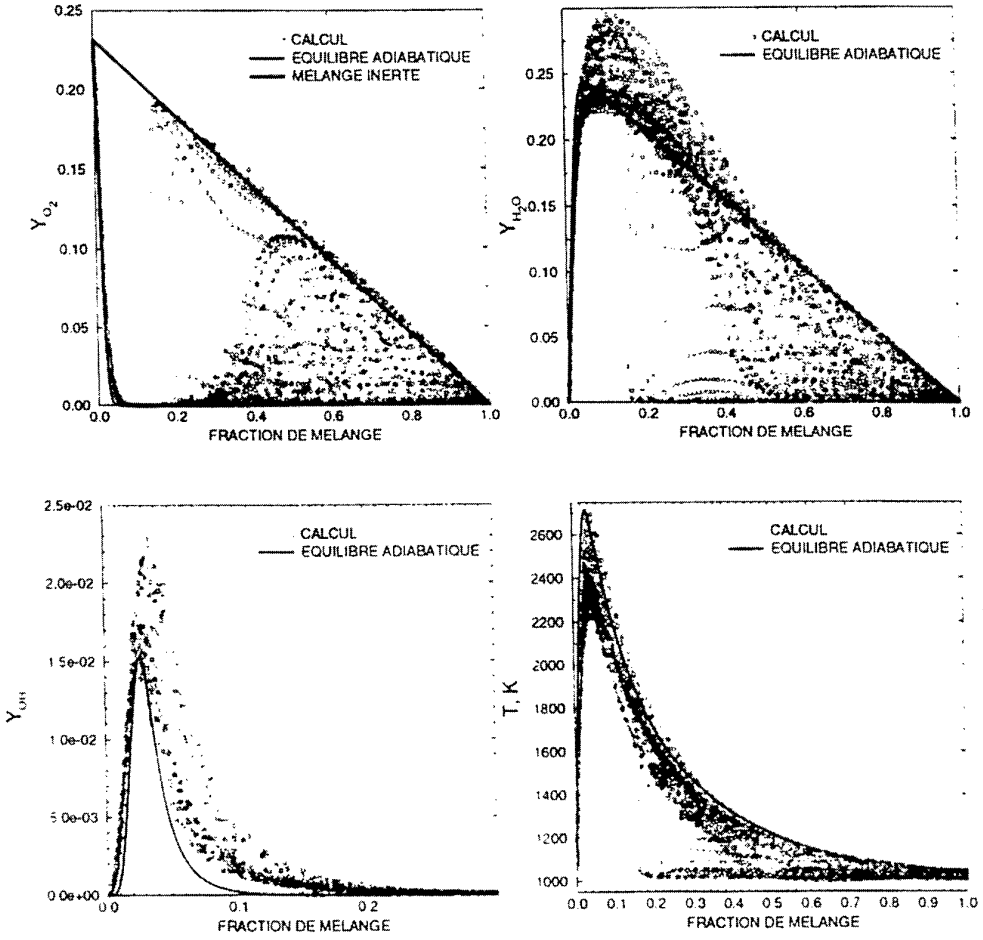

Figure 23
Reactive mixing layer, scatter plots (Ref. 140).

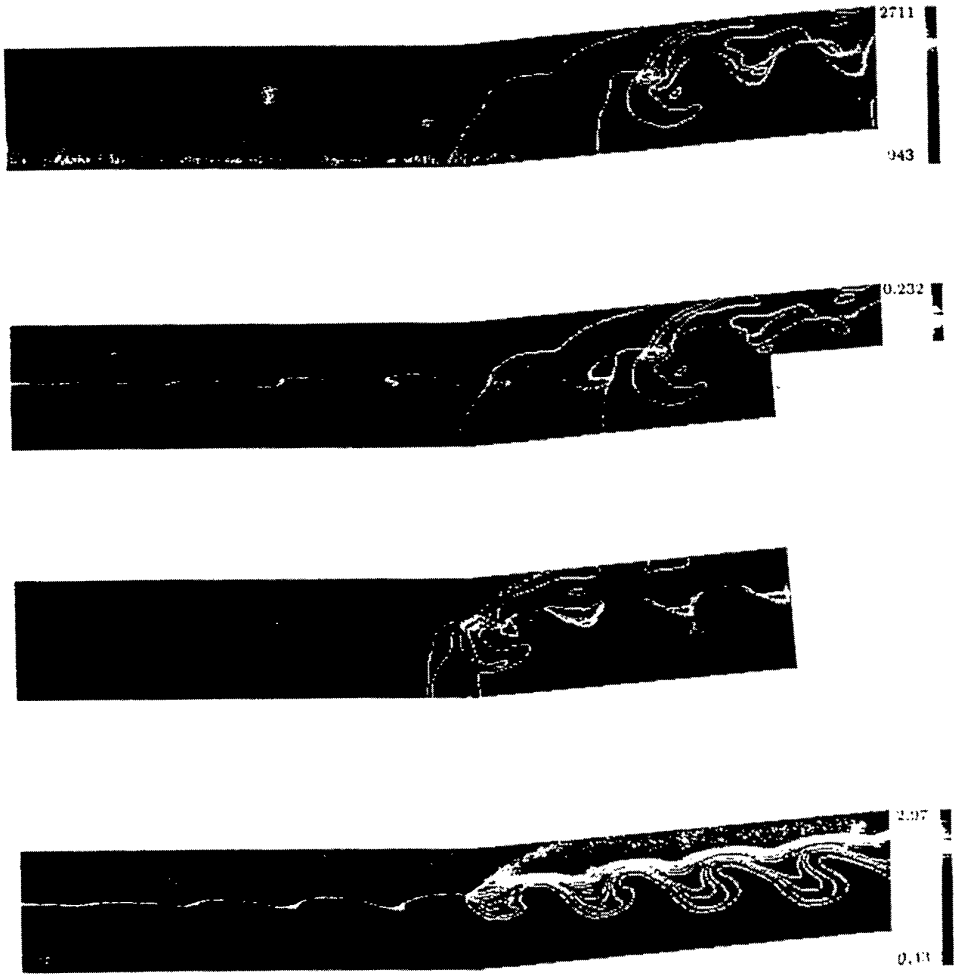

Figure 24
Effect of shock wave on reactive mixing layer. Grey scales represent temperature (upper figure) and Mach number (lower figure). Stoukov (Ref. 140).

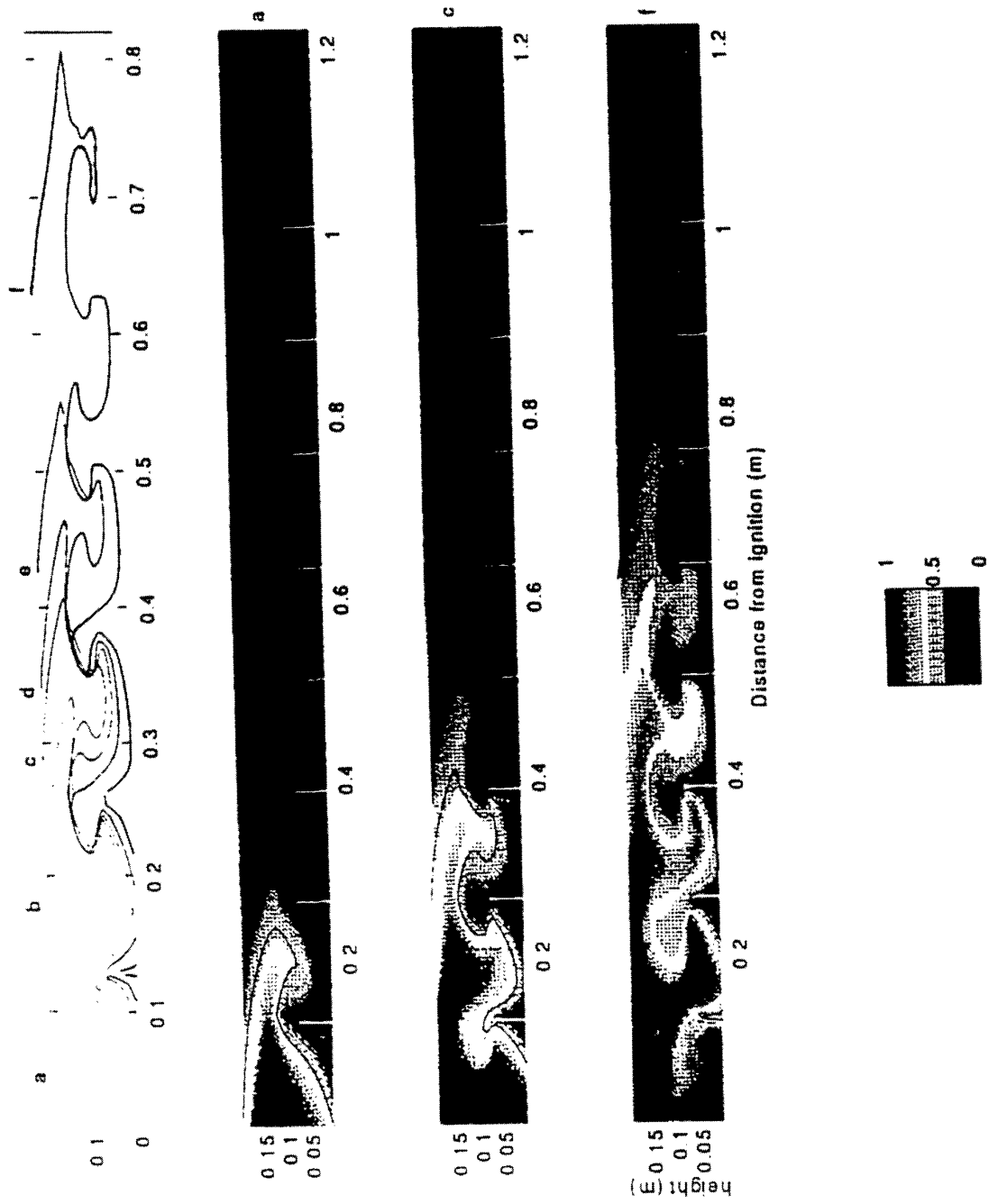

Figure 25
Flames passing obstacles: Simulation (Ref. 143) of experiment (Ref. 129).

Important decisions must then be made about the expected combustion and flow regimes. Are large fluctuations of thermochemical state to be expected? Can it be assumed that burning takes place in the laminar flamelet regime? Will Mach numbers be so high that fluctuations in pressure and enthalpy due to compressibility cannot be neglected? Will shock waves occur?

In the light of these decisions, three types of model must be selected:

Turbulence : The choice is likely to be between a $k - \epsilon$ model and a second moment (Reynolds stress, Reynolds flux) model. In either case closure of each term must be reviewed to allow for effects due to both compressibility and combustion (Refs. 38, 39, 44).

Chemistry : Is a detailed reaction scheme essential or will either a reduced scheme (Refs. 40, 41) or a global scheme be adequate?

Mean reaction rates : Assuming that scalar fluctuations are not negligibly small the choice here is between transported *pdf* (Refs. 35, 36), presumed *pdf* (Refs. 43-45) and laminar flamelet models (Refs. 33, 34, 69). Application of these models to high Mach number of flows, even with simple chemistry, presents severe problems.

If Mach numbers are not too high, so that thermochemical state fluctuations can be neglected, and shock waves do not occur, these choices can be made in terms of conventional models. We now identify a few examples of cases where such assumptions are made. Barsanti et al. (Refs. 18, 143) use a second moment, laminar flamelet model to calculate the development of confined explosions and compare their predictions with available experimental data, see Figures 25 and 26. A feature of this work is that the

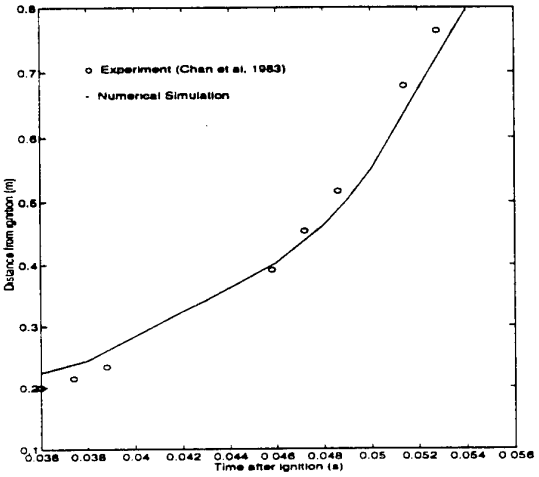

Figure 26
Speed of flame passing obstacles: Simulation (Ref. 143) and experiment (Ref. 129).

validity of the laminar flamelet combustion model in which high Mach number effects are neglected is checked *a posteriori* by calculating characteristic values of the Karlovitz number, Equation 4.11, and the Mach number. It is noteworthy

that agreement with experiment is not obtained (Ref. 143) in cases where this test is failed.

Model calculations by Baurle et al. (Ref. 144) predict the high speed jet flame experiments of Cheng et al. (Ref. 109). They employ a one-equation turbulence model, solve Favre averaged mean flow equations and represent hydrogen-oxygen chemistry through seven reactions between six reactive species plus inert nitrogen. A presumed joint *pdf* of temperature and mass fractions is modelled by assuming that temperature and composition fluctuations are uncorrelated. The temperature *pdf* is a Gaussian and the mass fractions are represented as a multivariate beta function. Comparison with the experiments is only qualitative because Favre means are predicted while Reynolds means are obtained from the experiments. However it is clear that the predicted scalar variances become far too small because of the large negative value of the chemical source term in the variance transport equation. This may either be because the shape of the presumed *pdf* is inappropriate - for example, the lack of correlation between temperature and composition fluctuations seems counter intuitive - or for some other reason.

7.4 Methods Based on the Probability Density Function (Ref. 19).

As described in §4 methods based on solution of a transport equation for a suitably chosen single point, joint probability density function (*jpdf*) possess the important property that the chemical source term which in moment methods leads to grave difficulties appears in closed form. This section explores the extension of *pdf* methods to nonpremixed turbulent combustion in high speed flows. As elsewhere in this chapter uncertainties and unresolved difficulties are identified.

The first step in the derivation of a *pdf* model is to choose the set of stochastic variables which together with the spatial location form the independent variables in the (*jpdf*) transport equation. Established methods (Pope Ref. 35), Kollmann Ref. 75) allow this equation to be derived from the time dependent conservation equations for the selected variables. Some of the terms in the resulting transport equation are unclosed and the next step is to devise suitable closure expressions. There are strong incentives to keep the number of independent variables as small as possible within the constraint of respecting physical reality both to limit the extent of this modelling and also to minimize the complexity and computational cost of the numerical solutions. Finally, the resulting equation must be solved by appropriate numerical means.

In flows involving high speed turbulent combustion inhomogeneities of density arise from the heat release due to combustion *and* from both viscous heating and

local compressions and expansions associated with the high speeds. The quantity which distinguishes these flows from the constant density turbulence treated extensively for a century is the dilatation

$$\mathcal{D} \equiv \frac{\partial u_k}{\partial x_k} \tag{7.6}$$

which from conservation of mass can be seen to be directly related to the change in density. Although not explicitly incorporated in the current phenomenology of low speed turbulent combustion, it has been proposed by Eifler and Kollman (Ref. 145) as a primary variable describing the mechanical and thermochemical state of the gas in high speed turbulent combustion. Clearly such a proposal is physically appealing. The time resolved equation for the dilatation is obtained by appropriate differentiation and addition of the momentum equation. There results

$$\begin{aligned} &\frac{\partial}{\partial t}\rho\mathcal{D} + \frac{\partial}{\partial x_k}\rho u_k \mathcal{D} \\ &= -\frac{\partial^2 p}{\partial x_k \partial x_k} + \frac{\partial^2 \tau_{ik}}{\partial x_k \partial x_l} - \rho \frac{\partial u_k}{\partial x_l}\frac{\partial u_l}{\partial x_k} \\ &\quad + \left[\frac{\partial}{\partial x_k}\left(-p\delta_{lk} + \tau_{lk}\right)\right]\frac{1}{\rho}\frac{\partial \rho}{\partial x_l} \end{aligned} \tag{7.7}$$

If the dilatation is identically zero and hence the density is constant, this becomes the Poisson equation for the calculation of the pressure given the velocity field at a particular time. In low speed turbulent combustion the influence of the pressure and the velocity held on the dilatation can be neglected; under these circumstances the dilatation is due only to heat release. However, in high speed combustion all of these influences play a role.

Following Kollman (Ref. 146), we first discuss the high speed turbulent flow of a single component nonreactive gas. Two variables are required to specify the thermodynamic state of such a gas but as indicated at several points in our discussion in high speed flows it is no longer possible to neglect changes in static pressure and enthalpy with the consequence that an extended definition of *state* is required. The *mechanical and thermodynamic state* of the gas is completely specified, for example, by the instantaneous values of the velocity $\underline{v}$, the density p and the internal energy e. However, there are considerable advantages of adding to this list the dilatation $\mathcal{D}$ as discussed in connection with Equation (7.7) (Kollmann Ref. 146 and Eifler and Kollman Ref. 145). In particular the pressure-work term which appears in the energy equation written in terms of the internal energy is closed. Closure of the dilatation equation and the dilatation terms in the transport equation for the solenoidal dissipation, $\tilde{\epsilon}_x$ is straightforward. Finally and perhaps most importantly, inclusion of the inverse time scale associated with $\mathcal{D}$ in the list of stochastic variables results in a conventional evolution equation for the *jpdf* in place of the hyperbolic equation which would otherwise results (Kollman Ref. 146).

Similar arguments apply to high speed reactive flows but it is now necessary to augment the list of independent stochastic variables to account for the more complex thermochemical state of the gas. The simplest case is one with fast chemical kinetics so that chemical equilibrium prevails everywhere. If in addition all chemical species are assumed to have a common molecular diffusivity, as assumption frequently used in studies of turbulent combustion, then the conserved scalar $Z(\boldsymbol{x},t)$ again provides all the necessary thermochemical information. Thus Z is added to our earlier set of defining variables.

With the set of variables identified earlier application of the *jpdf* equation to a three dimensional, unsteady flow involves 11 independent variables: three from the space coordinates, three from the velocity components, one each from time, density, internal energy, dilatation and conserved scalar.

Phenomena which are described by such an equation without further assumptions or modelling include turbulent transport in physical space (Pope Ref. 35) and in velocity space by body forces such as gravity and by mean pressure gradients. The coupling between the velocity field and the thermochemical state of the mixture is fully taken into account in this approach. However, the equation contains unknown terms which must be modelled and which present severe challenges. As a result of molecular diffusion the rate at which reaction proceeds in a flow in chemical equilibrium is determined by transport in the space of the conserved scalar. This term appears in the application of *pdf* methods to simple low speed, nonreactive flows and as a consequence has been studied for many years. Various models therefore are available (see §4, Pope Ref. 35 and Kollman Ref. 146) but unfortunately these fail in the laminar flamelet limit, i.e., as reaction is confined to thin sheets (Pope Ref. 147). Models are also available to describe transport in velocity space due to viscous stresses and pressure gradient fluctuations (Pope Ref. 35). However, the need to describe transport in the spaces of the internal energy and dilatation raises new problems.

The work of Kollman (Ref. 146) and Eifler and Kollmann (Ref. 145) represents the most comprehensive treatment of high speed flows involving chemical reaction to date. Their formulation encompasses important features of the interaction among turbulence, compressibility and combustion. The present restrictive assumption of chemical equilibrium can be removed by the addition of one or more additional scalar variables contributing to the determination of the thermochemical state of the gas. It is here that reduced chemical kinetic mechanisms (Ref. 41) may beneficially impact on these *pdf* methods. Relative diffusion, e.g. of highly mobile molecules such as hydrogen, cannot presently be taken into account without significant increases in the dimensions of

the set of stochastic variables.

Formidable problems remain to be solved and numerical predictions have yet to be reported using this analysis for either nonreactive or reactive high speed flows. However, Eifler and Kollmann (Ref. 145) present numerical solutions to a simpler problem in which the *jpdf* transport equation sketched earlier is integrated over the three velocity components so as to yield a transport equation for four scalar variables: the density ρ, the internal energy e, the dilatation $\mathcal{D}$ and the conserved scalar Z. This procedure requires that the statistical properties of the velocity field be determined separately, e.g. by a second moment theory. The mean density is the variable coupling the two calculations together. With the velocity component excluded from the list of stochastic variables additional empiricism must be incorporated to achieve closure in the *pdf* transport equation.

As shown by Pope (Ref. 35) single point *pdf* equations can be simulated under certain conditions by an ensemble of notional particles whose behaviour is described by stochastic differential equations. Eifler and Kollman (Ref. 145) adopt this approach in which the *jpdf* transport equation is replaced by a suitably large number of mixed Eulerian-Lagrangian equations obtained from the basic conservation equations. To these deterministic equations are added terms characterizing the random processes, both continuous and discrete, which the particles can experience in turbulent flow. There results an approximate treatment of the behaviour of notional particles in the turbulent field. This behaviour in a collective sense is equivalent to solving the *jpdf* transport equation. Details of this procedure are beyond the scope of our discussion. The contributions of Pope (Ref. 35) and Eifler and Kollman (Ref. 145) should be consulted for details. Several of the models introduced in the implementation of these ideas, including those describing the random processes, must be regarded as tentative.

Eifler and Kollmann (Ref. 145) use their model to predict the development of a supersonic nonpremied flame burning hydrogen and air. They compare their results with the experimental data of Evans et al. (Ref. 116), the same data used by Zheng and Bray (Refs. 70, 148, 149) for the purpose of evaluating their presumed *pdf* theory. Both sets of authors conclude that the experimental data is too limited for firm conclusions to be drawn. However, despite the inconclusiveness of the existing evaluation the generality of the *jpdf* transport approach and its potential to encompass a variety of the processes arising in high speed combustion argue for continued development.

7.5 Presumed *pdf* Methods (Ref. 19, 70, 148, 149).

Because, as suggested earlier, there is

coupling between the temperature and velocity in high speed flows, the presumed *pdf* analysis of §4 can no longer be used to relate the enthalpy and thus the temperature to Z, so that the calculation of the important variable $\bar{p}(\underline{x})$, which is responsible for the interaction between the fluid mechanical and chemical features of the flow, calls for a further set of sweeping assumptions. An important difference between the treatment of low and high speed flows relates to the desirability of expressing the conservation of energy in terms of the stagnation enthalpy

$$h_s = h + \frac{1}{2} v_k v_k$$

rather than the static enthalpy h or internal energy e. For high speed reactive flows h_s obeys the following equation

$$\frac{\partial}{\partial t}\rho h_s + \frac{\partial}{\partial x_k}\rho v_k h_s = \frac{\partial p}{\partial t}$$

$$+\frac{\partial}{\partial x_k}\left[\frac{\lambda}{\bar{c}_p}\frac{\partial h_s}{\partial x_k} + \frac{\lambda}{\bar{c}_p}\sum_{i=1}^{N}\left(\frac{1}{L_{ei}} - 1\right) h_i \frac{\partial Y_i}{\partial x_k}\right.$$

$$\left. +\mu\left(1 - \frac{1}{P_R}\right)\frac{\partial}{\partial x_k}\frac{1}{2} v_k v_k\right] \qquad (7.8)$$

where $P_R = \bar{c}_p \mu/\lambda$ is the Prandtl number. The question arises as to the availability of an algebraic relationship between the stagnation enthalpy and the conserved scalar, Z, i.e., a relation analogous to that of Equation (4.27). We now show that with some serious assumptions such a connection does exist. To proceed we first note that an approximate form of Equation (7.8) is

$$\frac{\partial}{\partial t}\rho h_s + \frac{\partial}{\partial x_k}\rho u_k h_s = \frac{\partial}{\partial x_k}\rho \mathcal{D}\frac{\partial h_s}{\partial x_k} \qquad (7.9)$$

Comparison of this form with that for the time resolved equation for $Z(x,t)$, Equation (2.10), indicates that there does indeed exist a connection $h_s = h_s(Z)$. The assumptions necessary to achieve Equation (7.9) are as follows. Firstly, the Lewis number based on the single diffusion coefficient $\mathcal{D}$ and the mixture Prandtl number are both set to unity. In connection with the combustion of hydrogen the mobility of the atoms and molecules of this fuel makes the validity of this assumption suspect. Secondly, the pressure term $\partial p/\partial t$ is neglected, an assumption which as discussed earlier is inappropriate in high speed flows.

With these serious assumptions adopted and with various restrictions concerning the initial and boundary conditions we are led to the linear relation

$$h_s(\underline{x},t) = h_{s2} + Z(\underline{x},t)(h_{s1} - h_{s2}) \qquad (7.10)$$

where h_{s1} and h_{s2} are the stagnation enthalpies of the fuel and oxidizer streams respectively. Because Equation (7.10) is linear it provides a simple connection between the mean stagnation enthalpy $\tilde{h}_s(x)$ and the mean $\tilde{Z}(x)$ and between the intensities $\overline{\rho h_s''^2}$ and $\overline{\rho Z''^2}$. Thus the restrictions in this approach result in the simplification permitting the energy equation to be

replaced by the algebraic equation Equation (7.10). Accordingly, provided we can calculate the mean density $\bar{\rho}(\underline{x})$ standard second moment methods can be applied to calculate the mean velocities, the mean and the intensity of the conserved scalar, the various Reynolds stresses and fluxes which arise in these equations and finally the mean viscous dissipation. The equation for the latter variable should include the effects associated with high speed, e.g., the contribution of dilatation, (Ref. 70).

We now turn our attention to the evaluation of the mean density. Our analysis (Bray et al., Ref. 19) is based on the presumed *pdf* method discussed in §4. The most convenient form for $\tilde{P}(Z;\underline{x})$ is the beta function with its exponents determined by $\tilde{Z}(\underline{x})$ and $\left(\overline{\rho Z''^2}/\bar{\rho}\right)(\underline{x})$ but other forms dependent on these two variables can be adopted. The precise form of the *pdf* need not be prescribed within the context of our discussion. For low speed flows in chemical equilibrium a crucial function needed in the *pdf* analysis is $\rho(Z)$, i.e., the density as a function of the conserved scalar independent of the spatial location. However, in high speed flows the coupling between the velocity and energy implies the corresponding function must be thought of as $\rho(Z;\underline{x})$ i.e., the instantaneous density depends on the conserved scalar and on space. Given this situation we must think in terms of approximation methods such that an initial estimate for $\rho(Z;\underline{x})$ can be improved systematically, an estimate which permits the mean density $\bar{\rho}(\underline{x})$ and thus all of the other dependent variables $\tilde{v}_x(\underline{x}), \tilde{Z}(\underline{x})$ et al. to be calculated from appropriate conservation equations.

The starting point is provided by the equations of state

$$p = \rho R_o T \sum_{i=1}^{N} \frac{Y_i}{w_i} \qquad h = c_p T + \Sigma_{i=1}^{N} Y_i \Delta_i \tag{7.11}$$

Here $N = 4$ corresponding to fuel, oxidizer, product and a diluent, generally nitrogen. These two equations plus the connection between the two enthalpies can be rearranged into

$$\rho h_s - \frac{1}{2}\rho v_k v_k - \rho \Sigma_{i=1}^{N} Y_i \Delta_i = \frac{\bar{c}_p}{\bar{R}} p \tag{7.12}$$

where $\bar{c}_p$ and $\bar{R}$ are the mixture coefficient of specific heat at constant pressure and the mixture gas constant respectively. In Equation (7.12) the quantities $h_s, Y_i, \bar{c}_p$ and $\bar{R}$ are known functions of the conserved scalar Z but v_k and p are functions of space and time. If they were known, then Equation (7.12) would yield $\rho(Z;\underline{x},t)$. In a statistically stationary flow this would lead to the desired quantity $\rho(Z;\underline{x})$. This equation exposes the connection between the velocity and state fields emphasized in this review.

In order to progress it is clearly now necessary to make further assumptions, in particular that pressure fluctuations

are thermochemically unimportant, an assumption consistent with our earlier neglect of the $\partial p/\partial t$-term in Equation (7.9) and as in the earlier instance progressively less defensible as the Mach number of the flow increases. With that assumption $p(\underline{x})$ in Equation (7.12) is replaced by $\bar{p}(\underline{x})$ and we obtain (Ref.) by averaging

$$\bar{\rho}\left[\tilde{h}_s - \frac{1}{2}\tilde{v}_k\tilde{v}_k - \tilde{k} - \Sigma_{i=1}^{N}\tilde{Y}_i\Delta_i\right]$$

$$= \bar{p}(\underline{x})\int_o^{\prime}\frac{c_p(Z)}{R(Z)}\tilde{P}(Z;x)\,dZ \qquad (7.13)$$

where $\tilde{k}$ is the Favre averaged turbulent kinetic energy and where $\tilde{P}(Z;\underline{x})$ is the probability distribution function for the conserved scalar.

Now suppose, as suggested earlier, an estimate for $\bar{\rho}(\underline{x})$ is available. Then the Favre averaged continuity equation and equations of motion with Equation (7.10) and supplemented appropriately are solved *inter alia* for $\tilde{v}_k(\underline{x}), \bar{p}(\underline{x}), \tilde{k}(\underline{x}), \tilde{h}_s(\underline{x}), \tilde{Z}(\underline{x})$ and $\overline{\rho Z''^2}/\bar{\rho}(\underline{x})$. The final two variables permit the parameters for the *pdf* $\tilde{P}(Z;x)$ to be determined. These results when substituted into Equation (7.13) enable an improved estimate of $\bar{\rho}(\underline{x})$ to be made.

The proposed linear relationship between mixture fraction $Z(\underline{x},t)$ and stagnation enthalpy $h_s(\underline{x},t)$, namely, Equation (7.10), has been tested in a nonreactive, supersonic DNS by Luo et al. (Ref. 150). In this simulation, with maximum mesh

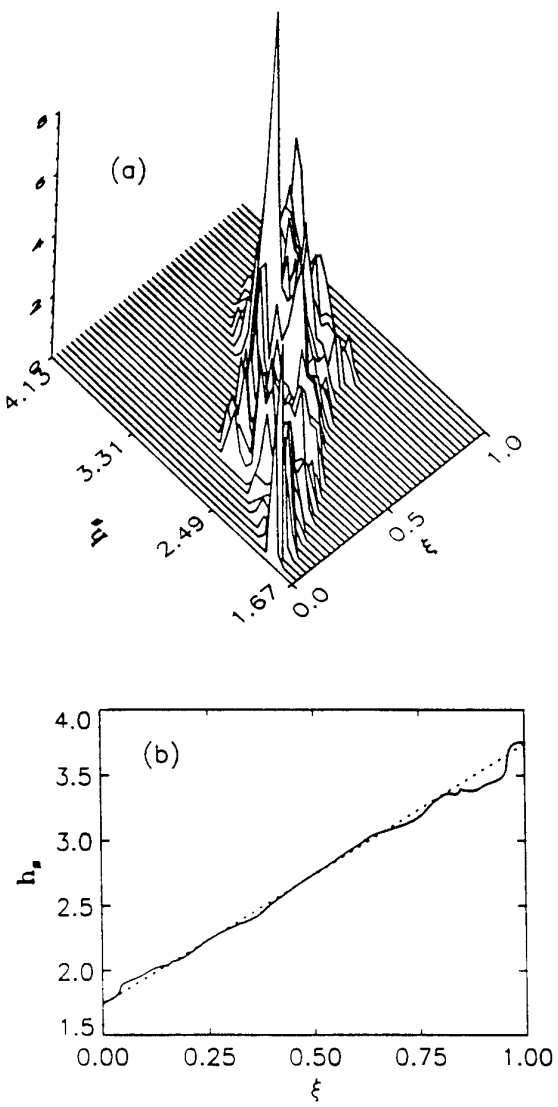

Figure 27
(a) Joint *pdf* of stagnation enthalpy and mixture fraction (b) mean stagnation enthalpy vs. mixture fraction (Ref. 150).

size 96 × 301 × 96, the initial condition is a laminar mixing layer of two streams,

each of Mach number 1.2, moving in opposite directions (convective Mach number 1.2). The initial flow field is seeded with disturbances deduced from linear stability analysis. The Lewis and Prandtl numbers are both unity and the Reynolds number based on vorticity thickness and fuel stream velocity reaches 1000 at the end of the simulation. Figure 27, which shows the joint *pdf* of h_s and Z and the conditional mesh of h_s versus Z, is consistent with the proposed linear relationship. This implies that the $\partial p/\partial t$ term in Equation (7.8) has a negligible effect under the conditions of this simulation.

Zheng and Bray (Refs. 70, 148, 149) report results of presumed *pdf* calculations of supersonic jet flames in which they assume the validity of this linear relationship between Z and h_s. A laminar flamelet approach is adopted, analogous to that described in §4, and use is made of a "libary" of strained laminar hydrogen-air diffusion flame solutions compiled by Balakrishnan (Ref. 151). Research by Balakrishnan and Williams (Ref. 152) indicates that laminar flamelet models are applicable to a significant portion of the anticipated flight trajectory of proposed scramjet engines.

The fluid flow model used by Zheng and Bray (Refs. 70, 148, 149) involves Favre averaged equations of continuity, fluid motion and chemical species together with an algebraic stress turbulence model for Reynolds stress and Reynolds flux components.

The Balakrishnan laminar flame solutions (Ref. 151), which are based on detailed chemical kinetics, specify fuel and oxidiser mass fractions and static temperature as functions of mixture fraction Z and strain rate a, as shown in Figure 28. Zheng and Bray (Refs. 70, 148, 149) assume that Z and a are statistically independent. They represent the *pdf* $\bar{P}(Z)$ as a beta function, Equation (4.29), and $\bar{P}(a)$ as a Gaussian. In order to calculate the mean density $\bar{\rho}(\underline{x})$ they apply an adjustment to the temperature $T^{(1)}(Z,a)$ in this data set from Ref. (151) which is referred to as Library I. The adjusted temperature is

$$T(Z,a,\tilde{u}) = T^{(1)}(Z,a) - \frac{\tilde{u}^2}{2\bar{c}_p}$$

$$+\frac{u_f^2}{2\bar{c}_p}\left[Y_f^{(1)}(Z,a) + \frac{Y_p^{(1)}(Z,a)}{s+1}\right]$$

$$+\frac{u_o^2}{2\bar{c}_p}\left[Y_o^{(1)}(Z,a) + \frac{sY_p^{(1)}(Z,a)}{s+1}\right] \qquad (7.14)$$

where $\tilde{u}$ is the local axial mean velocity, subscripts f, o and p correspond to fuel, oxidiser and product, respectively, the stoichiometric mass ratio of the reaction is s and superscript (1) denotes Library I.

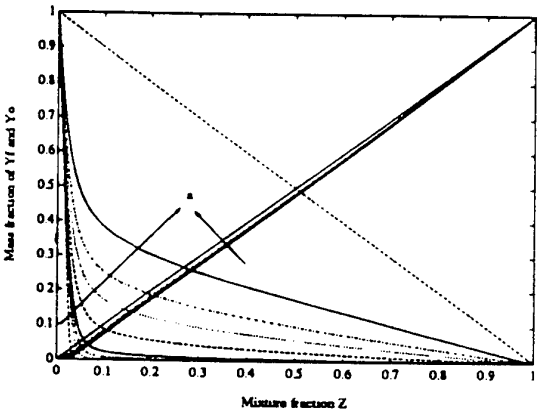

(a)

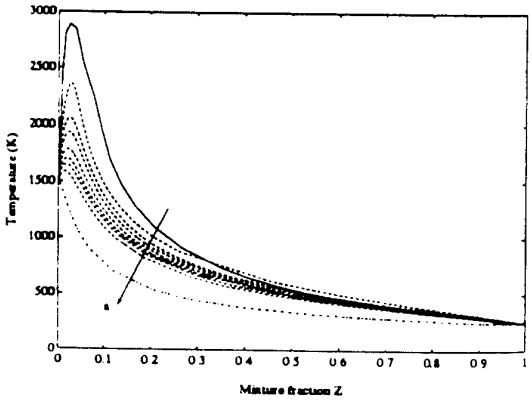

(b)

Figure 28
Flamelet Library I: H_2/air laminar diffusion flames at strain rates of 60 to 210815 s^{-1}
(Ref. 149 from Ref. 151).

Sabel'nikov et al. (Ref. 153) propose a more detailed description of the interaction between scalar and velocity fields. They compare their predicted static temperatures with Equation (7.14) and find similar results.

Zheng and Bray (Refs. 70, 148, 149) compare their predictions with the hydrogen-air jet flame experiments of Evans et al. (Ref. 116) in which the initial velocities of the fuel and oxidiser streams, which appear in Equation (7.14) are

$$u_f = 2432m/s \text{ and } u_o = 1510m/s \ ,$$

respectively. Figure 29 (Ref. 148)

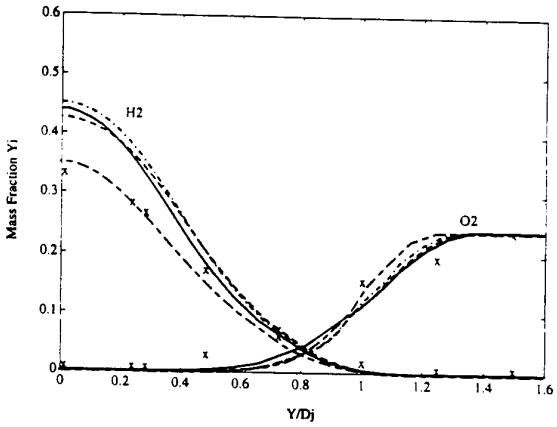

Figure 29
Composition profiles from experiment (Ref. 116) and from model predictions (Ref. 148). The long dashed curves are predictions from model based on strained laminar flamelets.

compares radial composition profiles from these experiments (symbol X) with four different predictions from the model. Cases 1, 2 and 3 are for $D_a \rightarrow \infty$ when the laminar flamelet reduces to a flame sheet. Case 1 uses the basic model. Case 2 includes a model for dilatation dissipation due to both compressibility and heat release (Ref. 70). Case 3 uses this

model plus a representation of the correlation between fluctuations in pressure and dilatation (Ref. 70). It will be seen from Figure 29 that these three versions all give similar predictions. Case 4, the long dashed lines in Figure 29, uses the adjusted flamelet library from Equation (7.14) as well as the models for dilatation dissipation and pressure-dilatation correlation. Agreement with experiment is improved. It is concluded that finite reaction rate effects, as contained in the flamelet library, play a significant role under the conditions of this experiment. However the Mach number of this flow is too low to provide a challenging test of high Mach number combustion models.

8. CONCLUSIONS

1. The most serious hindrance to a fuller understanding of turbulent combustion in supersonic flows is the lack of suitable experimental data. Detailed, well characterised experiments are needed, particularly at sufficiently high Mach numbers for compressibility effects to be significant and with good space and time resolution so that small scale mixing can be studied.

2. Direct numerical simulation (DNS) is beginning to contribute both to understanding of supersonic reactive flows and to the development of averaged flow models. This trend can be expected to continue and DNS must be used to fill the gaps in knowledge where experiment is impracticable or where models are not available. Examples include small scale mixing in high Mach number reactive turbulent flows and reactive turbulent flows containing shock waves.

3. There is scope for large eddy simulation (LES) of supersonic reactive turbulent flows.

4. A need will remain for averaged models of high speed turbulent flow with combustion. The present review leads to the conclusion that convincing theoretical models are currently not available. The specification for such a model includes the ability to incorporate effects of

   - a detailed description of the chemical kinetic mechanism and rates,
   - molecular transport processes characterised by Lewis and Prandtl numbers different from unity,
   - incomplete small scale mixing
   - coupling between the local thermochemical state and the mean and fluctuating kinetic energy of the flow,
   - the presence of shock waves in the reactive turbulent flow.

REFERENCES

1. Ferri, A., "Review of Problems in Application of Supersonic Combustion", J. R. Aero. Soc. 68, 1964, 575.

2. Libby, P.A., "Theoretical Analysis of Turbulent Mixing of Reactive Gases with Application to Supersonic Combustion of Hydrogen", Am. Rocket Soc. J. 32, 1962, 388.

3. Billig, F.S., "Ramjets with Supersonic Combustion". AGARD-NATO Lecture Series No. 136, "Ramjet and Ramrocket Propulsion Systems for Missiles", 1984.

4. Waltrup, P.J., "Liquid Fuelled Supersonic Ramjets: a Research Perspective of the Past, Present and Future". AIAA Paper 86-0158, 1986.

5. Kalghatgi, G.T., Cousins, J.M. and Bray, K.N.C., "Crossed Beam Correlation Measurements and Model Predictions in a Rocket Exhaust Plume", Combustion and Flame 43, 1981, pp.51-67.

6. Jensen, D.E. and Wilson, A.S., "Predictions of Rocket Exhaust Flame Properties", Combustion and Flame 25, 1975, pp. 43-55.

7. Jensen, D.E., Spalding, D.B., Tatchell, D.G. and Wilson, A.S., "Computation of Structures of Flames with Recirculating Flow and Radial Pressure Gradients", Combustion and Flame 34, 1979, 309-326.

8. Hertzberg, A.P., Bruckner, A.P., Bogdanoff, D.W., "Ram Accelerator: A New Chemical Method of Achieving Ultra-high Velocities" 37th ARA Meeting, Quebec, 1986.

9. Knowlen, C., Hinkey, J.B., Dunmore, B., "University of Washington Ram Acceleration Facility", 42nd ARA Meeting, Adelaide, 1991.

10. Smeets, G.: "The Ram Accelerator: Perspectives and Experimental Results Already Achieved" *in* "IUTAM Symposium on Combustion in Supersonic Flows" (Eds. M. Champion and B. Deshaies) Kluwer Ac. Publishers, 1997, pp. 219-236.

11. Strehlow, R., "Combustion Fundamentals", McGraw-Hill, New York, 1984.

12. Urtiew, P. and Oppenheim, A.K., "Experimental Observations of the Transition to Detonation in an Explosive Gas", Proc. R. Soc. Lond. A. 295, 1966, pp. 13-28.

13. Oppenheim, A.K. and Stern, R.A., "On the Development of Gaseous Detonation-analysis of Wave Phenomena", 7th Symp. (Int.) on Combustion, Butterworths, 1959, pp.837-850.

14. Kurylo, J., Dwyer, H.A. and Oppenheim, A.K., "Numerical Analysis

of Flow Fields Generated by Accelerating Flames", AIAA Paper No. 79-0290, Presented at AIAA 17th Aerospace Sciences Meeting, New Orleans, 1979.

15. Knystautas, R., Lee, J.H., Moen, I. and Wagner, H. Gg., "Direct Initiation of Spherical Detonation by a Hot Turbulent Gas Jet". 17th Symp. (Int.) on Combustion, The Combustion Inst., 1979, pp. 1235-1245.

16. Lee, J.H., Knystautas, R. and Chan, C.K., "Turbulent Flame Propagation in Obstacle-filled Tubes", 20th Symp. (Int.) on Combustion, The Combustion Inst., 1984, pp. 1663-1672.

17. Harrison, A.J. and Eyre, J.A., "The Effect of Obstacle Arrays on the Combustion of Large Premixed Air Clouds", Combust. Sci. and Tech. 52, 1987, pp.121-137.

18. Barsanti, P.S., Bray, K.N.C. and Cant, R.S., "Modelling of Confined Turbulent Explosions" *in* "Dynamics of Exothermicity - in honour of Antoni Kazimierz Oppenheim" (Ed. J. Ray Bowen) Gordon and Breach, 1996, pp.13-52.

19. Bray, K.N.C., P.A. Libby and F.A. Williams, "High Speed Turbulent Combustion" *in* "Turbulent Reacting Flows" (Eds. P.A. Libby and F.A. Williams) Academic Press, 1994, pp.609-638.

20. Champion, M. and Deshaies, B. (Eds.), "IUTAM Symposium on Combustion in Supersonic Flows", Kluwer Ac. Publishers, 1997.

21. Cullen, The Hon. Lord, "The Public Enquiry into the Piper Alpha Disaster", U.K. Dept. of Energy, H.M.S.O., London, 1990.

22. Teodorczyk, A., Lee, J.H.S. and Knystautas, R., "The Structure of Fast Turbulent Flames in very Rough Obstacle-filled Channels", 23rd Symp. (Int.) on Combustion, The Combustion Inst. (1990), pp.735-741.

23. Moen, I.O., Bjerketvedt, D., Engebretsen, T., Jenssen, A., Hjertager, B.H. and Bakke, J.R., "Transition to Detonation in a Jet Flame", Combust. and Flame 75, 1989, pp.297-308.

24. Oran, E.S., "The Structure of Detonation Waves" *in* "Dynamics of exothermicity, in honour of Antoni Kazimierz Oppenheim" (Ed. J. Ray Bowen), Gordon and Breach, 1996, pp.253-290.

25. Nikiforakis, N. and Clarke, J.F., "Quasi-steady Structures in the Two-dimensional Initiation of Detonations", Proc. R. Soc. Lond. A 452, 1996, pp.2023-2042.

26. Harrison, A.J. and Eyre, J.A., "External Explosions as a Result of Explosion Venting", Combust. Sci. and Tech. 52, 1987, pp.91-106.

27. British Gas, "Review of the Applicability of Predictive Methods to Gas Explosions in Offshore Models". Offshore Technology Report OTH 89 312, U.K. HMSO, (1990).

28. Hjertager, B.H., Trans. I. Chem. E., Part B 69, No. B2, 1991, pp.59-66.

29. Bowen, J.R. (Ed.), "Dynamics of Exothermicity, in honour of Antoni Kazimierz Oppenheim, Gordon and Breach, 1996.

30. Borghi, R. and Destriau, M., "La Combustion et les Flammes", Éditions Technip, Paris, 1995.

31. Williams, F.A., "Combustion Theory", Benjamin/Cummings Publishing Co., Menlo Park, Cal., 1985.

32. Poinsot, T., Candel, S. and Trouvé, A., "Applications of Direct Numerical Simulation to Premixed Turbulent Combustion", Prog. Energy and Combust. Sci. 21, 1995, pp.531-576.

33. Peters, N. "Laminar Diffusion Flamelet Models in Non-premixed Turbulent Combustion", Prog. Energy and Combust. Sci. 10, 1984, pp.319-339.

34. Bray, K.N.C. and Peters, N., "Laminar Flamelets in Turbulent Flames" *in* "Turbulent reacting flows" (Eds. P.A. Libby and F.A. Williams), Academic Press, 1994, pp.63-113.

35. Pope, S.B., "*Pdf* Methods for Turbulent Reactive Flows", Prog. Energy and Combust. Sci. 11, 1985, pp.119-192.

36. Dopazo, C., "Recent Developments in *pdf* Methods" *in* "Turbulent Reacting Flows" (Eds. P.A. Libby and F.A. Williams), Academic Press, 1994, pp.375-474.

37. Libby, P.A. and Williams, F.A. (Eds.), "Turbulent Reacting Flows", Academic Press, 1994.

38. Bray, K.N.C., "Turbulent Transport in Flames", Proc. R. Soc. Lond. A 451, 1995, pp.231-256.

39. Bray, K.N.C., "The Challenge of Turbulent Combustion", Hottel Plenary Lecture, 26th Symp. (Int.) on Combustion, the Combustion Inst., 1996.

40. Warnatz, J., "Resolution of Gas Phase and Surface Combustion into Elementary Reactions", 24th Symp. (Int.) on Combustion, The Combustion Inst., 1992, pp.553-579.

41. Peters, N. and Rogg, B., "Reduced Kinetic Mechanisms for Applications in Combustion Systems", Springer-Verlag, Berlin, 1993.

42. Dixon-Lewis, G., "Structure of Laminar Flames", 23rd Symp. (Int.) on Combustion, The Combustion Inst., 1990, pp.305-324.

43. Bilger, R.W., "Turbulent Jet Diffusion Flames", Prog. Energy Combust. Sci. 1, 1976, pp.87-109.

44. Borghi, R., "Turbulent Combustion Modelling", Prog. Energy Combust. Sci. 14, 1989, pp.245-292.

45. Bray, K.N.C., "The Interaction Between Turbulence and Combustion" 17th Symp. (Int.) on Combustion, The Combustion Inst., 1979, pp.223-233.

46. Damköhler, G. Z. Elektrochem. 46, 1940, pp.601-626.

47. Williams, F.A. *in* "The Mathematics of Combustion" (J.D. Buckmaster, Ed.) SIAM, Philadelphia, 1985, pp.97-128.

48. Peters, N. "Laminar Flamelet Concepts in Turbulent Combustion", Twenty First Symposium (International) on Combustion. The Combustion Institute, Pittsburgh, 1986, pp.1231-1250.

49. Borghi, R. *in* Recent Advances in Aerospace Science (C. Bruno and C. Casci, Ed.), Plenum Press 1985, p.117.

50. Libby, P.A. and Williams, F.A., "Fundamentals and a Review". In Reference 37, pp.1-61.

51. Poinsot, T.J., Veynante, D. and Candel, S. "Quenching Processes and Premixed Turbulent Combustion Diagrams", J. Fluid Mech. 228, 1991, pp.561-606.

52. Roberts, W.L. and Driscoll, J.F., "A Laminar Vortex Interacting with a Premixed Flame: Measured Formation of Pockets of Reactants", Combustion and Flame 87, 1991, pp.245-256.

53. Yeung, P.K., Girimaji, S.S. and Pope, S.B., "Straining and Scalar Dissipation on Material Surfaces in Turbulence: Implications for Flamelets", Combustion and Flame 79, 1990, pp.340-365.

54. Yoshida, A., Kakinuma, H. and Kotani, Y., "Extinction of Turbulent Premixed Flames by Small Scale Turbulence at Kolmogorov Microscale", Twenty Sixth Symposium (International) on Combustion, The Combustion Institute, Pittsburgh, 1996.

55. Tsuji, H., Yoshida, A. and Endo, N. "Effect of Turbulence on Extinction of Counterflow Diffusion Flame", Twenty Fifth Symposium (International) on Combustion, The Combustion Intitute, Pittsburgh, 1994, pp.1191-1197.

56. Vervisch, L., Kollmann, W., Bray, K.N.C. and Mantel, T. "*Pdf* Modelling for Premixed Turbulent Combustion Based on the Properties of Iso-concentration Surfaces". Proc. Summer Prog. 1994, Center for Turbulence Research, Stanford University, 1994, pp.125-150.

57. Echekki, T. and Chen, J.H., "Unsteady Strain Rate and Curvature Effects in Turbulent Premixed Methane-air Flames", Combustion and Flame 106, 1996, pp.184-202.

58. Magre, P. and Dibble, R.W. "Finite Chemical Kinetic Effects in a Subsonic Turbulent Hydrogen Flame", Combustion and Flame 73, 1988, pp.195-206.

59. Chen, Y.-C., Peters, N., Schneemann, G.A., Wruck, N., Renz, U. and Mansour, M.S. "Detailed Flame Structure of Stretched Turbulent Premixed Methane Flames". Submitted, 1995.

60. Buschmann, A., Dinkelacker, F., Schafer, T., Schafer, M. and Wolfrum, J., "Measurement of the Instantaneous Detailed Flame Structure in Turbulent Premixed Combustion", Twenty Sixth Symposium (International) on Combustion, The Combustion Institute, Pittsburgh, 1996.

61. Dibble, R.W., Masri, A.R. and Bilger, R.W., "The Spontaneous Raman Scattering Technique Applied to Nonpremixed Flames of Methane", Combustion and Flame 67, 1987, p.189.

62. Mahalingam, S., Chen, J.H. and Vervisch, L., "Finite Rate Chemistry and Transient Effects in Direct Numerical Simulations of Turbulent Nonpremixed Flames", Combustion and Flame 102, 1995, pp.285-297.

63. Mauss, F., Keller, D. and Peters, N., "A Lagrangian Simulation of Flamelet Extinction and Re-ignition in Turbulent Jet Diffusion Flames", Twenty Third Symposium (International) on Combustion, The Combustion Institute, Pittsburgh, 1990, pp.693-698.

64. Chen, J.H., Mahalingam, S. and Card, J.M., "Curvature, Ignition and Extinction Dynamics of Turbulent Nonpremixed Methane-air Flames. Submitted, 1995.

65. Domingo, P. and Vervisch, L., "Triple Flame and Partially Premixed Combustion in Autoignition of Nonpremixed Turbulent Mixtures", Twenty Sixth Symposium (International) on Combustion, The Combustion Institute, Pittsburgh, 1996.

66. Kioni, P.N., Rogg, B., Bray, K.N.C. and Liñán, A., "Flame Spread in Laminar Mixing Layers: The Triple Flame", Combustion and Flame 95, 1993, pp.276-290.

67. Paul, R.N. and Bray, K.N.C., "Study of Premixed Turbulent Combustion including Landau-Darrieus Instability Effects", Twenty Sixth Symposium (Int.) on Combustion, The Combustion Institute, Pittsburgh, 1996.

68. Zeman, O., "Dilatation Dissipation: The Concept and Application in Modelling Compressible Mixing Layers", Phys. Fluids, A2, 1990, p.178.

69. Libby, P.A. and Bray, K.N.C., "Implications of the Laminar Flamelet Model in Premixed Turbulent Combustion", Combustion and Flame 39, 1980, pp.33-41.

70. Zheng, L.L. and Bray, K.N.C., "Effects of Dilatation Dissipation on Turbulent Shear Layer Combustion in High Speed Flow", 24th Symposium (Int.) on Combustion, The Combustion Institute, 1992, pp.405-411.

71. Bray, K.N.C., Libby, P.A., Masuya, G. and Moss, J.B., "Turbulence Production in Premixed Turbulent Flames", Combust. Sc. and Tech. 25, 1981, pp.127-140.

72. Veynante, D., Trouvé, A., Bray, K.N.C. and Mantel, T. "Gradient and Countergradient Scalar Transport in Turbulent Premixed Flames". J. Fluid Mech., 332, 1997, pp.263-293.

73. Launder, B.E., "Second-moment Closure: Present ··· and Future?" Int. J. Heat and Fluid Flow 10, 1989, p.282-300.

74. Pope, S.B., "*Pdf* Methods for Turbulent Reactive Flows", Prog. Energy Combust. Sci., 11, 1985, pp.119-192.

75. Kollmann, W., "The *pdf* Approach to Turbulent Flow", Theor. Comput. Fluid Dyn. 1, 1990, p.249.

76. Dopazo, C., "Recent Developments in *pdf* Methods". In Reference 37, pp.375-474.

77. Trouvé, A., Veynante, D., Bray, K.N.C. and Mantel, T., "The Coupling Between Flame Surface Dynamics and Species Mass Conservation in Premixed Turbulent Combustion", Center for Turbulence Research, Proc. Summer Prog., 1994, Stanford University, pp.95-124.

78. Anand, M.S. and Pope, S.B., "Calculations of Premixed Turbulent Flames by *pdf* Methods", Combustion and Flame 67, 1987, pp.127-142.

79. Stårner, S.H., Bilger, R.W., Lyons, K.M., Frank, J.H. and Long, M.B., "Conserved Scalar Measurements in Turbulent Diffusion Flames by a Raman and Rayleight Ribbon Image Method", Combustion and Flame, 99, 1994, pp.347-354.

80. Nandula, S.P., Brown, T.M. and Pitz, R.W., "Measurements of Scalar Dissipation in the Reaction Zones of Turbulent Nonpremixed H_2-air Flames", Combustion and Flame, 99, 1994, pp.775-783.

81. Rutland, C.J. and Cant, R.S., "Turbulent Transport in Premixed Flames", Proc. Summer Prog.,

1994, Center for Turbulence Research, Stanford University, 1994, pp.75-94.

82. Hulek, T. "Modelling Turbulent Combustion using Transported Probability Density Function Methods". University of London, Ph.D. thesis, 1996.

83. Taing, S., Masri, A.R. and Pope, S.B., "*Pdf* Calculations of Turbulent Nonpremixed Flames of H_2/CO_2 Using Reduced Chemical Mechanisms", Combustion and Flame 95, 1993, pp.133-150.

84. Masri, A.R., Dibble, R.W. and Barlow, R.S., "Chemical Kinetic Effects in Nonpremixed Flames of H_2/CO_2 Fuel", Combustion and Flame 91, 1992, pp.285-309.

85. Bradley, D., "How Fast Can We Burn?", Twenty Fourth Symposium (Int.) on Combustion. The Combustion Institute, Pittsburgh, 1992, pp.247-262.

86. Liew, S.K., Bray, K.N.C. and Moss, J.B., "A Stretched Laminar Flamelet Model of Turbuent Nonpremixed Combustion", Combustion and Flame 56, 1984, pp.199-213.

87. Vervisch, L., Bidaux, E., Bray, K.N.C. and Kollmann, W., "Surface Density Function in Premixed Turbulent Combustion Modelling, Similarities Between Probability Density Function and Flame Surface Approaches", Phys. Fluids 7, 1995, pp.2496-2503.

88. Marble, F.E. and Broadwell, J.E. "The Coherent Flame Model for Turbulent Chemical Reactions", Project Squid Report, TRW-9-PU, TRW, El Segundo, 1977.

89. Wu, A.S. and Bray, K.N.C., "A Coherent Flame Model of Premixed Turbulent Combustion in a Counterflow Geometry", Combustion and Flame, to appear, 1997.

90. Bray, K.N.C. and Libby, P.A., "Recent Developments in the BML Model of Premixed Turbulent Combustion". *In* Reference 37, pp.115-151.

91. Bray, K.N.C., "Studies of the Turbulent Burning Velocity", Proc. R. Soc. Lond., A 431, 1990, 315-335.

92. Bilger, R.W., "Turbulent Diffusion Flames", Ann. Rev. Fluid Mech. 21, 1989, pp.101-135.

93. Abdel-Gayed, R.G., Bradley, D. and Lawes, M., "Turbulent Burning Velocities: a General Correlation in Terms of Straining Rates", Proc. R. Soc. Lond. A 414, 1987, pp.389-413.

94. Mouqallid, M., Lecordier, B. and Trinité, M., "High Speed Laser Tomography Analysis of Flame Propagation in a Simulated Internal Combustion Engine - Applications to Nonuniform Mixture", S.A.E. Tech. Paper No. 941990, 1994.

95. Cho, P., Law, C.K. Shepherd, I.G. and Cheng, R., "Velocity and Scalar Fields Turbulent Premixed Flames in Stagnation Flow", Twenty Second Symposium (Int.) on Combustion, The Combustion Institute, Pittsburgh, 1988, pp.739-745.

96. Kostiuk, L.W., Bray, K.N.C. and Cheng, R., "Experimental Study of Premixed Turbulent Combustion in Opposed Streams. Part II - Reacting Flow Field and Extinction." Combustion and Flame 92, 1993, pp.396-409.

97. Mastorakos, E., Taylor, A.M.K.P. and Whitelaw, J.H., "Extinction and Temperature Characteristics of Turbulent Counterflow Diffusion Flames with Partial Premixing", Combustion and Flame, 91, 1992, pp.40-54.

98. Bray, K.N.C., Champion, M. and Libby, P.A. "Flames in Stagnating Turbulence", *in* Reference 37, pp.573-607.

99. Moss, J.B., "Simultaneous Measurements of Concentration and Velocity in an Open Premixed Turbulent Flame", Combust. Sci. Tech. 22, 1980, pp.115-129.

100. Cheng, R.K. and Shepherd, I.G., "The Influence of Burner Geometry on Premixed Turbulent Flame Propagation", Combustion and Flame 85, 1991, pp.7-26.

101. Mueller, C.J., Driscoll, J.F., Reuss, D.L. and Drake, M.C. "Effects of Unsteady Stretch on the Strength of a Freely Propagating Flame Wrinkled by a Vortex". 26th Symposium (Int.) on Combustion, The Combustion Institute, Pittsburgh, 1996.

102. Stårner, S.H., Bilger, R.W., Dibble, R.W., Barlow, R.S. Fourguette, D.C. and Long, M.B., "Joint Planar CH and OH Imaging in Piloted Turbulent Jet Diffusion Flames Near Extinction", Twenty Fourth Symposium (Int.) on Combustion, The Combustion Institute, Pittsburgh, 1992, pp.341-349.

103. Taylor, A.M.K.P. Ed., Instrumentation for Flows with Combustion, Academic Press, London, 1993.

104. Ghenai, C., Chauveau, C., Gokalp, I., "Spatial and Temporal Dynamics of Flamelets in Turbulent Premixed Flames", Twenty Sixth Symposium (Int.) on Combustion, The Combustion Institute, Pittsburgh, 1996.

105. Veynante, D., Duclos, J.M. and Piana, J., *in* Direct Numerical Simulation for Turbulent Combustion (T. Poinsot, T. Baritaud and M. Baum, Eds.), Editions Technip, Paris, 1996.

106. Zhang, Y. and Bray, K.N.C., "Correlation of Temporal and Spatial Data in Turbulent Premixed Bunsen Flames", *in* Dynamics of Heterogeneous combustion and Reacting Systems (A.L. Kuhl, J.C. Leyer, A.A.

Borisov and W.A. Sirignano, Eds.), Vol. 152 of Progress in Astronautics and Aeronautics, AIAA, Washington, 1993, pp.56-69.

107. Smallwood, G.J. and Deschamps, B.M., "Flame surface density measurements with PLIF in an S.I. Engine." Submitted, 1996.

108. Billig, F.S., "Research on Supersonic Combustion", J. Propulsion and Power 9, 1993, pp.499-514.

109. Cheng, T.S., Wehrmeyer, J.A., Pitz, R.W., Jarrett, O. and Northam, G.B., "Raman Measurement of Mixing and Finite-rate Chemistry in a Supersonic Hydrogen-air Diffusion Flame", Combustion and Flame 99, pp.157-173.

110. Hornung, H.G., "Performance Data of the new Free-piston Shock Tunnel at GALCIT", AIAA Paper 92-3943, 1992.

111. Maus, J., Laster, M. and Hornung, H., "The *G*-Range Impulse Facility - a High Performance Free-Piston Shock Tunnel", AIAA Paper 92-3046, 1992.

112. Krishnamurthy, R., Rogers, R.C. and Tiwari, S.N., "Numerical Study of Hypervelocity Flows Through a Scramjet Combustor", J. Propulsion and Power 13, 1997, pp.131-141.

113. Tamagno, J., Bakos, R., Pulsonetti, M. and Erdos, J., "Hypervelocity real gas capabilities of GASL's Expansion Tube (HYPULSE) facility", AIAA Paper 90-1390, 1990.

114. Walters, R.W., Slack, D.C., Cinella, P., Applebaum, M. and Frost, C., "A User's Guide to GASP", NASA Langley Research Center, Hampton, VA, and Virginia Poly, Inst. and State University, Blacksburg, VA, 1990.

115. Libby, P.A., "Observations Concerning Supersonic Combustion". In Ref. 20, pp.1-11.

116. Evans, J.S., Schexnayder, C.J. and Beach, H.L., "Application of Two-dimensional Parabolic Computer Program to the Prediction of Turbulent Reacting Flows", NASA TP 1169, 1978.

117. Driscoll, J.F., Huh, H., Yoon, Y. and Donbar, J., "Measured Lengths of Supersonic Hydrogen-air Jet Flames - Compared to Subsonic Flame Lengths and Analysis". Combustion and Flame 107, 1996, pp.176-186.

118. Huh, H. and Driscoll, J.F., "Shock Wave Enhancement of the Mixing and the Stability Limits of Supersonic Hydrogen-air Flames", 26th Symp. (Int.) on Combustion, The Combustion Inst., 1996.

119. Sato, Y., Sayama, M., Masuya, G., Komuro, T., Kudou, K., Murakami, A., Tani, K. and Chinzei, N., "Experimental Study on Autoignition in

a Scramjet Combustor", J. Propulsion and Power, 7, 1991, pp.657-658.

120. Srikrishnan, A.R., Kurian, J. and Sriramulu, V., "An Experimental Investigation of Thermal Mixing and Combustion in Supersonic Flows", Combustion and Flame 107, 1996, pp.464-474.

121. Anil, K. and Damodaran, K.A., "Experimental Studies on Piloted Supersonic Combustion Using the Petal Nozzle", J. Propulsion and Power 13, 1997, pp.142-149.

122. Fraser, R.A. and Bracco, F.V., "Cycle-Resolved L.D.V. Integral Length Scale Measurements in an I.C. Engine", SAE-880381, 1988.

123. Glover, A.R., Hundleby, G.E. and Hadded, O., "An Investigation into Turbulence in Engines Using L.D.A.", SAE-880379, 1988.

124. Armstrong, N.W.H., "Planar Flowfield Measurements in Premixed Turbulent Combustion", Ph.D. thesis, University of Cambridge, 1992.

125. Abdel-Gayed, R.G., Bradley, D. and Lung, F.K.K., "Combustion Regimes and the Straining of Turbulent Premixed Flames", Combustion and Flame 76, 1989, pp.213-218.

126. Dörge, K.J., Pangritz, D. and Wagner, H. Gg., "Experiments on Velocity Augmentation of Spherical Flames by Grids", Acta Astr. 3, 1976, pp.1067-1076.

127. Moen, I.O., Donato, M., Knystautas, R. and Lee, J.H.S., "Flame Acceleration due to Turbulence Produced by Obstacles", Combustion and Flame 39, 1980, pp.21-32.

128. Moen, I.O., Lee, J.H.S., Hjertager, B.H., Fuhre, K. and Eckhoff, R.K., "Pressure Development due to Turbulent Flame Propagation in Large Scale Methane-air Explosions", Combustion and Flame 47, 1982, pp.31-52.

129. Chan, C., Moen, I.O. and Lee, J.H.S., "Influence of Confinement on Flame Acceleration due to Repeated Obstacles", Combustion and Flame, 49, 1983, pp.27-39.

130. Fairweather, M., Ibrahim, S.S., Jaggers, H. and Walker, D.G., "Turbulent Premixed Flame Propagation in a Cylindrical Vessel", 26th Symp. (Int.) on Combustion, The Combustion Institute, 1996.

131. Teodorczyk, T., Lee, J.H.S. and Knystautas, R., " Propagation Mechanism of Quasi-detonations", 22nd Symp. (Int.) on Combustion, The Combustion Inst., 1988, pp.1723-1731.

132. Meyer, J.W., Urtiew, P.A. and Oppenheim, A.K., "On the Inadequacy of Gasdynamic Processes for Triggering the Transition to Detonation", Combustion and Flame 14, 1970, pp.13-20.

133. Clarke, J.F., "Fast Flames, Waves and Detonation", Prog. Energy and Combust. Sci., 15, 1990, pp.241-271.

134. Khokhlov, A.M., Oran, E.S. and Wheeler, J.C., "A Theory of DDT in Unconfined Flames", Combustion and Flame, 108, 1997, pp.503-517.

135. Thomas, G.O., Sands, C.J., Bambrey, R.J. and Jones, S.A., "Experimental Observations of the Onset of Turbulent Combustion Following Shock-flame Interaction", 14th Int. Colloq. on Dynamics of Explosions and Reactive Systems, Krakow, Poland, 1997.

136. Deshaies, B., Figuera da Silva, L.F. and René-Corail, M., "Some Generic Problems Related to Combustion of Hydrogen and Air in Supersonic Flows". In Ref. 20, pp.15-42.

137. Nishioka, M. and Law, C.K., "A Numerical Study of ignition in a Supersonic Hydrogen/air Laminar Mixing Layer", Combustion and Flame 108, 1997, pp.199-219.

138. Guichard, L., Vervisch, L. and Domingo, P., "Two-dimensional Weak Shock-vortex Interaction in a Mixing Zone". AIAA J. 33, 1995, pp.1797-1802.

139. Réveillon, J. and Vervisch, L., "Dynamics of Isoconcentration Surfaces in Weak Shock Turbulent Mixing Interaction", AIAA J. 34, 1996, pp.2539-2544.

140. Stoukov, A., "Etude Numerique de la Couche de Mélange Réactive Supersonique". Doctoral thesis, Université de Rouen, 1996.

141. van Kalmthout, E., Veynante, D. and Candel, S., "Direct Numerical Simulation Analysis of Flame Surface Density in Non-premixed Combustion". *In* 26th Symp. (Int.) on Combustion, The Combustion Institute, 1996.

142. van Kalmthout, E., "Stabilisation et Modélisation des Flammes Turbulentes Non-prémélangées. Etude Théorique et Simulations Directes". Ph.D. thesis, Ecole Centrale, Paris, 1996.

143. Barsanti, P.S., "Simulations of Confined Turbulent Explosions". Ph.D. thesis, Cambridge University, 1994.

144. Baurle, R.A., Alexopoulos, G.A. and Hassan, H.A., "Assumed Joint Probability Density Function Approach for Supersonic Turbulent Combustion", J. Propulsion and Power 10, 1994, pp.473-484.

145. Eifler, P. and Kollmann, W., "*Pdf* Predictions of Supersonic Hydrogen Flames", AIAA Paper 93-0448, 31st Aerospace Sciences Meeting, Reno, NV, 1993.

146. Kollmann, W., "The *pdf* Approach to Turbulent Flow", Theor. Comput. Fluid Dyn. 1, 1990, p.249.

147. Pope, S.B., "Computations of Turbulent Combustion: Progress and Challenges", Twenty Third Symposium (Int.) on Combustion, The Combustion Institute, 1991, pp.591-612.

148. Zheng, L.L. and Bray, K.N.C., "The Application of New Combustion and Turbulence Models to H_2-air Nonpremixed Supersonic Combustion", Combustion and Flame 99, 1994, pp.440-448.

149. Zheng, L.L., "Studies of Hydrogen-air Turbulent Diffusion Flames for Subsonic and Supersonic Flows". Ph.D. thesis, Cambridge University, 1993.

150. Luo, K.H., Bray, K.N.C. and Sandham, N.D., "Relation Between Stagnation Enthalpy and Mixture Fraction in Supersonic Mixing Layers". Accepted for poster session, 16th Int. Colloq. on Dynamics of Explosions and Reactive Systems, Cracow, Poland, August, 1997.

151. Balakrishnan, G., "Studies of Hydrogen-air Diffusion Flame and of Compressibility Effects Related to High Speed Propulsion", Ph.D. thesis, University of California, San Diego, 1992.

152. Balakrishnan, G. and Williams, F.A., "Turbulent Combustion Regimes for Hypersonic Propulsion Employing Hydrogen-air Diffusion Flames", J. Propulsion and Power, 10, 1994, pp.434-436.

153. Sabel'nikov, V., Deshaies, B. and Figuera da Silva, L.F., "Revisited Flamelet Model for Nonpremixed Combustion in Supersonic Turbulent Flows". Submitted, 1996.

Large-Eddy Simulations of Compressible Turbulent Flows

M. Lesieur & P. Comte
L.E.G.I./Institut de Mécanique de Grenoble *
B.P. 53, 38041 Grenoble Cedex 09, France
Tel : (33) 04 76 82 50 19, Fax : (33) 04 76 82 52 71, E-Mail: Marcel.Lesieur@hmg.inpg.fr

ABSTRACT

In the first lecture, we describe the general framework of large-eddy simulations (LES) applied to incompressible flows, with *Smagorinsky's model* [1]. Afterwards we concentrate on LES from a spectral-space point of view. We introduce Kraichnan's spectral eddy-viscosity[2], and how it can be handled for LES purposes in isotropic turbulence, in terms of the *plateau-cusp model.* We generalize the spectral eddy viscosity to a spectral eddy diffusivity. Using the nonlocal interaction theory, we discuss the backscatter issue, and present a generalization of spectral eddy coefficients allowing to account for non-developed turbulence in the subgridscales, the *spectral-dynamic model.* Applications of this model to a channel flow will be given, with comparisons with DNS, experiments, and the classical *dynamic model.* The latter will be presented and discussed.

The second lecture will be devoted to the action of compressibility upon free-shear and separated flows. We will work in physical space. We will first present the *structure-function model* (SSF), the *filtered SSF*, and the *selective SSF*, as well as a version of the spectral-dynamic model in physical space, in terms of a combination of the structure-function model and a hyperviscosity. Afterwards, we will justify the use of an essentially incompressible subgrid-modelling for LES of compressible turbulence. Then, we will look at the effects of compressibility upon coherent vortices in mixing layers, and see in particular how helical pairing is inhibited above a convective Mach number of 0.7. We will consider also a round jet, and finally a separated flow in a configuration related to ARIANE V solid-propergol boosters.

In the third lecture, we will concentrate on LES of compressible boundary layers. First, we will look at a weakly compressible boundary layer ($M_\infty = 0.5$) spatially developing upon an adiabatic flat plate. Afterwards, we will consider a temporal boundary layer at Mach 4.5, and show how LES allow to describe the whole process of transition to turbulence. Finally, the structure of turbulence in the neighbourhood of HERMES space shuttle's rear flap at Mach 2.5 will be examined.

*Institut National Polytechnique de Grenoble (INPG), Université Joseph Fourier (UJF) et Centre National de la Recherche Scientifique (CNRS). M. Lesieur is senior member of *Institut Universitaire de France.*

Paper presented at the AGARD FDP Special Course on "Turbulence in Compressible Flows", held at the von Kármán Institute for Fluid Dynamics (VKI) in Rhode-Saint-Genèse, Belgium, 2-6 June 1997, and in Newport News, Virginia, USA, 20-24 October 1997, and published in R-819.

Chapter I:

LES formalism in physical and spectral space

1 MODELS, DNS AND LES

A direct-numerical simulation (DNS) of a turbulent flow has to take into account explicitly all scales of motion, from the largest, imposed by the existence of boundaries or the periodicities, to the smallest. The latter may be for instance the Kolmogorov dissipative scale $(\epsilon/\nu^3)^{-1/4}$ in three-dimensional isotropic turbulence, or the viscous thickness $\delta_v = \nu/v_*$ in a turbulent boundary layer. Around a wing or a fuselage for instance, and if one wants to simulate three-dimensionally all motions ranging from $\delta_v \approx 10^{-6}$ m to to 10 m, it would be necessary to put 10^{21} modes on the computer. Right now, the calculations done to the expense of not excessive computing times on the biggest machines take about 2. 10^7 grid points, which is very far from the above estimation. Even with the unprecedented improvement of scientific computers, it may take several tenths of years (if it becomes ever possible) before DNS permit to simulate situations at Reynolds numbers comparable to those encountered in natural conditions.

In front of such a situation, there are several attitudes. The first one consists in trying to develop statistical models. This is compulsory from an industrial point of view, but it is well known that models which have been validated for a given situation fail when external conditions change, under the effect for instance of pressure gradients, separation, compressibility or rotation. The second one is to work in very simple geometries at low Reynolds number and develop DNS which, as already stressed, are costly but may be very useful to study transition for instance. The third attitude consists in trying to simulate deterministically only the large scales of the flow, which, from an engineering point of view, are responsible for an important part of turbulent transfers of momentum or heat for example. This is the large-eddy simulation (LES) point of view, where the small scales are filtered out, but influence statistically the large-scale motions.

The problem of LES is a very difficult one, which poses a lot of unsolved problems and has several inconsistencies. But it is the only way to obtain spatio-temporal informations upon flows at high Reynolds. As will be seen, LES are extremely useful in particular to understand the dynamics of coherent vortices and structures in turbulence.

2 THE FORMALISM OF LES IN PHYSICAL SPACE

2.1 Filtering

In the first of these three lectures, we present the LES formalism for incompressible turbulence. This is valid for constant-density flows, and also for variable-density flows in the framework of Boussinesq approximation. In the second lecture, we will defend the point of view that, in compressible turbulence and away from the shocks, compressibility effects decrease with the scale, so that a compressible large-eddy simulation using incompressible subgrid models may be justified if the filtering scale is chosen small enough.

We mention that parts of this text will follow closely the lines of [3][4].

To begin with, let us consider a simulation of Navier-Stokes equations carried out in physical space, using finite-difference or finite-volume methods. We assume first for sake of simplification that the spatial discretization is orthogonal and cubic, Δx being the grid mesh. To the fields defined in the continuous space $\vec{x}$, one will associate filtered fields obtained through the convolution with a filter $\bar{G}_{\Delta x}$, chosen so as to eliminate fluctuations in the motions of wavelength smaller than Δx. The filtered velocity and temperature fields are:

$$\underline{\bar{u}}(\vec{x},t) = \int \vec{u}(\vec{y},t)\bar{G}_{\Delta x}(\vec{x}-\vec{y})d\vec{y} \qquad (1)$$

$$\bar{T}(\vec{x},t) = \int T(\vec{y},t)\bar{G}_{\Delta x}(\vec{x}-\vec{y})d\vec{y} \quad , \qquad (2)$$

and more generally for any quantity f (scalar or vectorial)

$$\bar{f}(\vec{x},t) = \int f(\vec{y},t)\bar{G}_{\Delta x}(\vec{x}-\vec{y})d\vec{y} = \int f(\vec{x}-\vec{y},t)\bar{G}_{\Delta x}(\vec{y})d\vec{y} \quad . \qquad (3)$$

One can easily check that such a filter commutes with temporal and spatial derivatives, so that the continuity equation for the filtered field holds. Let $\vec{u}'$ and T' be the fluctuations of the actual fields with respect to the filtered fields

$$\vec{u} = \underline{\bar{u}} + \vec{u}' \ ; \ T = \bar{T} + T' \qquad (4)$$

and more generally $f = \bar{f} + f'$. The fields "prime" concern fluctuations at scales smaller than Δx (the "grid scale"), and will then be referred to as subgrid-scale fields.

Let us write Navier-Stokes equations as

$$\frac{\partial u_i}{\partial t} + \frac{\partial}{\partial x_j}(u_i u_j) = -\frac{1}{\rho_0}\frac{\partial p}{\partial x_i} + \frac{\partial}{\partial x_j}\left\{\nu\left(\frac{\partial u_i}{\partial x_j} + \frac{\partial u_j}{\partial x_i}\right)\right\} \quad . \qquad (5)$$

After applying the filter, one gets

$$\frac{\partial \bar{u}_i}{\partial t} + \frac{\partial}{\partial x_j}(\bar{u}_i \bar{u}_j) = -\frac{1}{\rho_0}\frac{\partial \bar{p}}{\partial x_i} + \frac{\partial}{\partial x_j}\left\{\nu\left(\frac{\partial \bar{u}_i}{\partial x_j} + \frac{\partial \bar{u}_j}{\partial x_i}\right) + T_{ij}\right\} \quad . \tag{6}$$

$$T_{ij} = \bar{u}_i \bar{u}_j - \overline{u_i u_j} \tag{7}$$

is the subgridscale tensor. The filtered fields do not need to be resolved at scales smaller than Δx, since they do not contain fluctuations under this scale. Therefore, they can be properly represented by the computer, provided proper numerical schemes are used. The main problem lies in the subgridscale tensor: let us first express it in terms of fluctuations with respect to the filtered field, as

$$T_{ij} = \bar{u}_i \bar{u}_j - \overline{\bar{u}_i \bar{u}_j} - (\overline{\bar{u}_i u_j'} + \overline{\bar{u}_j u_i'}) - \overline{u_i' u_j'} \quad .$$

Here, $\bar{u}_i \bar{u}_j - \overline{\bar{u}_i \bar{u}_j}$ is called "Léonard term". It is explicit since it is expressed in terms of the filtered field, and may give some indications as to model the action of the subgridscales (see the section on the dynamic model below). The term $-(\overline{\bar{u}_i u_j'} + \overline{\bar{u}_j u_i'})$ is the "cross term", and $-\overline{u_i' u_j'}$ is the "Reynolds-stress like term", following the terminology given in [5]. These two terms are unknown. The equations of motion for the filtered field have analogies with Reynolds equations for the mean flow in non-homogeneous turbulence, but other terms than $-\overline{u_i' u_j'}$ arise in the LES. Another difference is that LES deal with fields which are rapidly varying in space and time, whereas Reynolds equations are generally time-independant, and the fields vary slowly in space. In the LES, we have to solve Navier-Stokes equations for the filtered field (large scales) modified by supplementary subgridscale terms which we do not know.

The same analysis may be held for a scalar T (not necessarily passive) of molecular diffusivity κ convected and diffused by the flow. It satisfies

$$\frac{\partial T}{\partial t} + \frac{\partial}{\partial x_j}(T u_j) = \frac{\partial}{\partial x_j}\left\{\kappa \frac{\partial T}{\partial x_j}\right\} \quad . \tag{8}$$

If the low-pass filter $\bar{G}_{\Delta x}$ is applied to this equation, one finds

$$\frac{\partial \bar{T}}{\partial t} + \frac{\partial}{\partial x_j}(\bar{T}\bar{u}_j) = \frac{\partial}{\partial x_j}\left\{\kappa \frac{\partial \bar{T}}{\partial x_j} + \bar{T}\bar{u}_j - \overline{T u_j}\right\} \quad . \tag{9}$$

Here again, the question of modelling the subgrid scalar fluxes is posed.

2.2 From micro to macro...

The problem of the subgridscale modelling is a particular case of the passage from "micro" to "macro", where the laws governing a medium are known at a certain microscopic level, and one seeks evolution laws at a macroscopic level. Navier-Stokes is already the result of such a passage: the micro corresponds here to Boltzmann equations for the molecules, and the macro to the continuous medium approximation, where the molecular viscous and conductive coefficients model the momentum and heat exchanges across the surface of the fluid parcels, due to molecular fluctuations. In LES of turbulence, the micro corresponds to the individual fluid parcel obeying Navier-Stokes equations, and the macro is the filtered field.

Such problems of passage from micro to macro can be solved when a separation between large and small scales exists. This is in particular the case for Navier-Stokes equations, valid as far as the dissipative scales are large in front of the molecular scales, which is true except in hypersonic conditions at Mach numbers larger than 15. One of the main problems of LES of turbulence is the fact that there is in general a continuous spectrum of energy between the resolved and subgridscales. We will see below how the spectral-eddy viscosity concept allows to solve this problem at an energetic level.

2.3 LES and unpredictability growth

From a mathematical viewpoint, the LES problem is not very well posed. Indeed, let us consider the time evolution of the fluid as the motion of a point in a sort of phase space of extremely large dimension (e.g. $\sim 10^{21}$ around a wing, as seen above). At some initial instant, the flow computed with LES will differ from the actual flow, due to the uncertainty contained in the subgridscales. This initial difference between the actual and the computed flow will grow, due to nonlinear effects, as in a dynamical system having a chaotic behaviour. Therefore, the two points will separate in phase space, and, as time goes on, the LES will depart from reality. However, as will be seen below, LES permit to predict the statistical characteristics of turbulence, as well as the dynamics of coherent vortices and structures.

Note that chaos in dynamical systems with a low number of degrees of freedom is generally characterized by a positive Lyapounov exponent, with exponential growth of the distance between two points initially very close in phase space. In isotropic turbulence, one introduces for predictability studies the error spectrum $E_\Delta(k,t)$, characterizing the spatial-frequency distribution associated to the energy of the difference between two random fields $\vec{u}_1$ and $\vec{u}_2$ with same statistical properties:

$$\frac{1}{4} < [\vec{u}_1^2(\vec{x},t) - \vec{u}_2^2(\vec{x},t)] > = \int_0^{+\infty} E_\Delta(k,t)\, dk \quad , \tag{10}$$

the energy spectrum $E(k,t)$ being such that

$$\frac{1}{2} < \vec{u}_1^2 > = \frac{1}{2} < \vec{u}_2^2 > = \int_0^{+\infty} E(k,t)\, dk \quad . \qquad (11)$$

The error rate

$$r(t) = \frac{\int_0^{+\infty} E_\Delta(k,t)dk}{\int_0^{+\infty} E(k,t)dk} \qquad (12)$$

is zero when the two fields are completely correlated, and one when they are totally uncorrelated. In predictability studies, one takes generally an initial state such that complete unpredictability ($E(k) = E_\Delta(k)$) holds above $k_E(0)$, while $E_\Delta(k)$ is 0 for $k < k_E(0)$. Two-point closures of the EDQNM type (see below for details) show (in three or two dimensions) an inverse cascade of error, where the wavenumber $k_E(t)$ characterizing the error front decreases (see [6]). Thus, the error rate can be approximated by

$$r(t) \approx \frac{\int_{k_E(t)}^{\infty} E(k,t)dk}{\int_0^{+\infty} E(k,t)dk} \; .$$

We assume that the turbulence is forced by external forces, so that the kinetic energy arising at the denominator of Eq. (12) is fixed. In three-dimensional turbulence, and if a $k^{-5/3}$ spectrum is assumed for $k > k_E$, the error rate will be proportional to $k_E^{-2/3}$. In fact, closures (see [6][3]) show that k_E^{-1} follows a Richardson's law ($k_E^{-1} \propto t^{3/2}$), so that the error rate grows linearly with time. This is in fact a slow increase compared with the exponential growth of chaotic dynamical systems, and quite encouraging concerning the potentialities of large-eddy simulations for three-dimensional turbulent flows. Remark that the same result ($r(t) \propto t$) has been obtained in Ref. [7], on the basis of numerical data corresponding to atmospheric wheather forecast models. On the other hand, the above analysis carried in a k^{-3} enstrophy cascade of two-dimensional isotropic turbulence yields an exponential growth of the error (see [6][3]). It seems, quite surprisingly since large-scale atmospheric motions are quasi two-dimensional, that the atmosphere behaves more as a three-dimensional turbulence. This is confirmed by the $k^{-5/3}$ kinetic energy spectra measured in the atmosphere for scales comprised between a few and 500 kilometers.

2.4 Eddy-viscosity and diffusivity

In a similar way to what was done when considering a Newtonian fluid, we are going to make an eddy-viscosity and eddy-diffusivity assumption, in order to model the subgrid terms. More specifically, we write

$$T_{ij} = 2\nu_t\, \bar{S}_{ij} + \frac{1}{3} T_{ll}\, \delta_{ij} \quad , \qquad (13)$$

where

$$\bar{S}_{ij} = \frac{1}{2}\left(\frac{\partial \bar{u}_i}{\partial x_j} + \frac{\partial \bar{u}_j}{\partial x_i}\right) \qquad (14)$$

is the deformation tensor of the filtered field. The LES momentum equation becomes

$$\frac{\partial \bar{u}_i}{\partial t} + \bar{u}_j \frac{\partial \bar{u}_i}{\partial x_j} = -\frac{1}{\rho_0}\frac{\partial \bar{P}}{\partial x_i} + 2\frac{\partial}{\partial x_j}\left\{(\nu + \nu_t)\bar{S}_{ij}\right\} \; , \qquad (15)$$

$\bar{P} = \bar{p} - (1/3)\rho_0 T_{ll}$ being a modified pressure, determined with the help of the filtered continuity equation (still valid on a regular mesh). If the grid is no more regular, one has to consider Eq. (13) as a model for all subgrid terms, in particular those arising from the irregular-grid effects.

For the scalar, one introduces an eddy diffu sivity κ_t, such that

$$\bar{T}\bar{u}_j - \overline{Tu_j} = \kappa_t \frac{\partial \bar{T}}{\partial x_j} \qquad (16)$$

to yield

$$\frac{\partial \bar{T}}{\partial t} + \bar{u}_j \frac{\partial \bar{T}}{\partial x_j} = \frac{\partial}{\partial x_j}\left\{(\kappa + \kappa_t)\frac{\partial \bar{T}}{\partial x_j}\right\} \quad . \qquad (17)$$

The eddy diffusivity is related to the eddy viscosity by the relation

$$P_r^{(t)} = \frac{\nu_t}{\kappa_t} \quad , \qquad (18)$$

$P_r^{(t)}$) being a turbulent Prandtl number which will be specified below.

The question is now to determine the eddy viscosity $\nu_t(\vec{x},t)$, as well as the turbulent Prandtl number. Notice that this eddy-viscosity assumption in physical space is rather questionable since, as stressed already, there is no spectral gap between the large and small scales. One expects, however, that the informations about the physics of turbulence derived using this unperfect concept may help to improve it.

2.5 Smagorinsky's model

The most widely used eddy-viscosity model was proposed by Smagorinsky[1]. As a meteorologist, he was studying quasi-geostrophic models of the atmosphere, and was looking for an eddy-viscosity simulating some sort of three-dimensional Kolmogorov energy cascade in the subgridscales. A local mixing-length assumption is made, in which the eddy viscosity is assumed to be proportional to the subgrid-scale characteristic length Δx, and to a characteristic turbulent velocity $v_{\Delta x} = \Delta x |\bar{S}|$. Here $|\bar{S}|$ is typical velocity gradient at Δx, determined with the aid of the second invariant of the filtered-field deformation tensor $\bar{S}_{ij}$ defined in Eq. (14). Smagorinsky's eddy viscosity writes

$$\nu_t = (C_S \Delta x)^2 |\bar{S}| \quad , \qquad (19)$$

with

$$|\bar{S}| = \sqrt{2\bar{S}_{ij}\bar{S}_{ij}} \quad .$$

If one assumes that $k_C = \pi/\Delta x$, the cutoff wavenumber in Fourier space, lies within a $k^{-5/3}$ Kolmogorov cascade, one can adjust the constant C_S so that the ensemble averaged subgrid kinetic-energy dissipation is identical to the kinetic-energy flux in the cascade ϵ. It is found:

$$C_S \approx \frac{1}{\pi}\left(\frac{3C_K}{2}\right)^{-3/4} \quad . \tag{20}$$

This yields $C_S \approx 0.18$ for a Kolmogorov constant $C_K = 1.4$. In fact, the dynamic-model ideas (see [8]) will consist in adjusting locally C_S with the aid of a double filtering, basically to reduce the eddy-viscosity in places where turbulence is not totally developed, or during transition.

We are now going to present a different point of view of LES when working in Fourier space.

3 LES IN SPECTRAL SPACE

3.1 Spectral eddy viscosity and diffusivity

The formalism of spectral eddy viscosity is due to Kraichnan ([2], see also [9] [3]) in the case of a Kolmogorov subgridscale spectrum. The spectral eddy-diffusivity was introduced in [10]. Here, we will extend these results to spectra which may not follow Kolmogorov law at the cutoff.

We assume that Navier-Stokes is written in Fourier space (which requires periodicity in the three spatial directions). Let

$$\hat{u}_i(\vec{k},t) = \left(\frac{1}{2\pi}\right)^3 \int e^{-i\vec{k}.\vec{x}} \;\; \vec{u}(\vec{x},t)d\vec{x} \tag{21}$$

and

$$\hat{T}(\vec{k},t) = \left(\frac{1}{2\pi}\right)^3 \int e^{-i\vec{k}.\vec{x}} \;\; \vec{u}(\vec{x},t)d\vec{x} \tag{22}$$

be the spatial Fourier transforms of the velocity and scalar fields. The spectral tensor $\hat{U}_{ij}(\vec{k},t)$, Fourier transform of the velocity correlation tensor

$$U_{ij}(\vec{r},t) = < u_i(\vec{x},t)u_j(\vec{x}+\vec{r},t) > \quad ,$$

is such that

$$< \hat{u}_i(\vec{k}',t)\hat{u}_j(\vec{k},t) >= \hat{U}_{ij}(\vec{k},t)\delta(\vec{k}+\vec{k}') \quad .$$

For isotropic turbulence, the kinetic energy spectrum verifies

$$E(k,t) = 2\pi k^2 \hat{U}_{ii}(\vec{k},t) \quad . \tag{23}$$

The scalar spectrum is such that

$$< \hat{T}(\vec{k}',t)\hat{T}(\vec{k},t) >= \frac{E_T(k,t)}{2\pi k^2}\delta(\vec{k}+\vec{k}') \quad . \tag{24}$$

We consider the cutoff wave number $k_C = \pi\Delta x^{-1}$ already envisaged above when discussing Smagorinsky's model. We define a sharp low-pass filter by setting equal to zero the velocity and scalar amplitudes at wave vectors whose modulus is larger than k_C. Let us first consider the kinetic-energy spectrum evolution equations given by the EDQNM theory[1] ([11][3]):

$$\left(\frac{\partial}{\partial t} + 2\nu k^2\right) E(k,t) = \iint_{\Delta_k} dp\; dq\; \theta_{kpq}(t) \frac{k}{pq} b(k,p,q) E(q,t)[k^2 E(p,t) - p^2 E(k,t)] \quad . \tag{25}$$

where the integration is carried out in the domain Δ_k of the (p,q) plane such that (k,p,q) can be the sides of a triangle. The non-dimensional coefficient

$$b(k,p,q) = \frac{p}{k}(xy + z^3)$$

is defined in terms of the cosines (x,y,z) of the interior angles of the triangle (k,p,q). The angle $\theta_{kpq}(t)$ characterizes the nonlinear relaxation of velocity triple-correlation. It is given by

$$\theta_{kpq} = \frac{1 - e^{-[\mu_{kpq} + \nu(k^2+p^2+q^2)]t}}{\mu_{kpq} + \nu(k^2+p^2+q^2)} \quad , \tag{26}$$

with

$$\mu_{kpq} = \mu_k + \mu_p + \mu_q$$

and

$$\mu_k = a_1 \left[\int_0^k p^2 E(p,t)dp\right]^{1/2} \quad . \tag{27}$$

The constant a_1 is adjusted in such a way that the kinetic-energy flux is equal to ϵ in a Kolmogorov cascade. One finds ([11][3])

$$a_1 = 0.218\; C_K^{3/2} \quad . \tag{28}$$

The EDQNM evolution equation for the passive scalar spectrum $E_T(k,t)$ is

$$\left(\frac{\partial}{\partial t} + 2\kappa k^2\right) E_T(k,t) = \iint_{\Delta_k} dp\; dq\; \theta^T_{kpq} \frac{k}{pq} (1-y^2) E(q,t)[k^2 E_T(p) - p^2 E_T(k)] \quad , \tag{29}$$

where θ^T_{kpq} is a scalar-velocity triple relaxation time, given by

$$\theta^T_{kpq} = \frac{1 - e^{-[\kappa(k^2+p^2) + \mu'(k) + \mu'(p) + \nu q^2 + \mu"(q)]t}}{\kappa(k^2+p^2) + \mu'(k) + \mu'(p) + \nu q^2 + \mu"(q)}$$

with

$$\mu'(k) = a_2 \left(\int_0^k p^2 E(p,t)dp\right)^{1/2}$$

[1] Kraichnan [2] considered the Test-Field Model (TFM) instead of the Eddy-Damped Quasi-Normal Markovian theory (EDQNM), but the transfers are the same in a Kolmogorov inertial range.

$$\mu"(k) = a_3 \left(\int_0^k p^2 E(p,t) dp \right)^{1/2} \quad .$$

The choice of the new adjustable constants a_2 and a_3 is not simple. It was shown in Ref. [12] that a given value of the Corrsin-Oboukhov constant arising in the inertial-convective range of the scalar spectrum (here taken equal to 0.67 from experimental measurements of Ref. [13]) imposes a certain one to one correspondence between a_2 and a_3. The last condition, allowing to determine a_2 and a_3, comes from considerations on the turbulent Prandtl number, in spectral space, defined below and equal to $(a_2 + a_3)/6a_1$. It is then possible to express this number in function of a_2/a_3 only, in such a way that the Corrsin-Oboukhov constant should be fixed to the value given above. This leads to a turbulent Prandtl number decreasing continuously from 0.6 to 0.325 for a_2/a_3 going from zero to infinity. Since the values of turbulent Prandtl numbers found experimentally in the boundary layer are in the range $0.6 \approx 0.8$, this could lead to the choice $a_2 = 0$ (and hence $a_3 = 1.3$, as determined in Ref. [12]). One could object that the analogy between both theoretical and experimental turbulent Prandtl numbers is not obvious. Nevertheless the choice $a_2 = 0$ has the further advantage of allowing analytical resolutions of the $EDQNM$ temperature spectral equation. It has to be stressed that the simpler choice $a_2 = a_3 = a_1$ gives the same Corrsin-Oboukhov constant and a turbulent Prandtl number of 0.35.

We come back to the subgridscale modelling problem, and assume first $k << k_C$, both modes being larger than k_i, the kinetic-energy peak. Then one can write the spectral evolution equations for the supergrid-scale velocity, $\bar{E}(k,t)$, and scalar, $\bar{E}_T(k,t)$ spectra as

$$(\frac{\partial}{\partial t} + 2\nu k^2)\bar{E}(k,t) = T_{<k_C}(k,t) + T_{sg}(k,t) \quad (30)$$

$$(\frac{\partial}{\partial t} + 2\kappa k^2)\bar{E}_T(k,t) = T^T_{<k_C}(k,t) + T^T_{sg}(k,t) \quad . \quad (31)$$

Expansions in powers of the small parameter k/k_C yield to the lowest order[2]

$$T_{sg}(k,t) = -2\nu_t^\infty \; k^2 \; \bar{E}(k,t) \quad (32)$$

$$\nu_t^\infty = \frac{1}{15} \int_{k_C}^\infty \theta_{0pp} \left[5E(p,t) + p \frac{\partial E(p,t)}{\partial p} \right] dp \quad (33)$$

$$T^T_{sg}(k,t) = -2\kappa_t^\infty \; k^2 \; \bar{E}_T(k,t) \quad (34)$$

$$\kappa_t^\infty = \frac{2}{3} \int_{k_C}^\infty \theta^T_{0pp} \; E(p,t) \; dp \quad , \quad (35)$$

The supergrid-scale transfers $T_{<k_C}(k,t)$ and $T^T_{<k_C}(k,t)$ correspond to triad interactions whose wave numbers lie in the supergrid range, and hence do not need any modelling, since they can be calculated exactly in the large-eddy simulation.

Let us start by assuming a $k^{-5/3}$ inertial range at wave numbers greater than k_C. We obtain:

$$\nu_t^\infty = 0.441 \; {C_K}^{-3/2} \left[\frac{E(k_C)}{k_C} \right]^{1/2} \quad (36)$$

$$\kappa_t^\infty = \frac{\nu_t^\infty}{P_r^{(t)}} \quad (37)$$

with

$$P_r^{(t)} = \frac{a_2 + a_3}{6a_1} \quad . \quad (38)$$

If one assumes for instance a Kolmogorov constant of 1.4 in the energy cascade, the constant in front of Eq. (36) will be 0.267.

When k is close to k_C, the above concept of spectral eddy viscosity and eddy diffusivity can be generalized for a $k^{-5/3}$ inertial range extending over wave numbers larger than k_C. It is possible, with the aid of the EDQNM approximation, to calculate the subgridscale transfers, corresponding to triadic interactions where at least one of the wave numbers p and q is greater than k_C. This allows us to define two functions $\nu_t(k|k_C)$ and $\kappa_t(k|k_C)$, respectively the eddy viscosity in spectral space ([2] and the eddy diffusivity in spectral space ([10]), such that

$$T_{sg}(k,t) = -2\nu_t(k|k_C) \; k^2 \; \bar{E}(k,t) \quad (39)$$

$$T^T_{sg}(k,t) = -2\kappa_t(k|k_C) \; k^2 \; \bar{E}(k,t) \quad . \quad (40)$$

The functions $\nu_t(k|k_C)$ and $\kappa_t(k|k_C)$ are such that

$$\nu_t(k|k_C) = K(k/k_C)\nu_t^\infty \quad (41)$$

$$\kappa_t(k|k_C) = C(k/k_C)\kappa_t^\infty \quad (42)$$

where ν_t^∞ and κ_t^∞ are the asymptotic values given by Eqs (36), (37) and (38). As shown by Kraichnan[2], $K(x)$ is approximately constant and equal to 1, except in the vicinity of $k/k_C = 1$ where it displays a strong overshoot (cusp-behaviour), due to the predominance of semi-local transfers across k_C. It was shown in [10] that $C(x)$ behaves qualitatively as $K(x)$ (plateau at 1 and positive cusp), and that the spectral turbulent Prandtl number $\nu_t(k|k_C)/\kappa_t(k|k_C)$ is approximately constant (and thus equal to 0.6 if one takes $a_2 = 0$). These three quantities (eddy-viscosity, eddy-diffusivity and turbulent Prandtl number), taken from [10], are shown on Figure 1, in function of k/k_C. On the figure, the eddy coefficients are normalized by $\sqrt{E(k_C)/k_C}$, with $C_K = 1.4$.

In fact, the function $K(x)$ can be put under the form

$$K(x) = 1 + \nu_n^* x^{2n} \quad , \quad (43)$$

[2] the relaxation times are not expanded

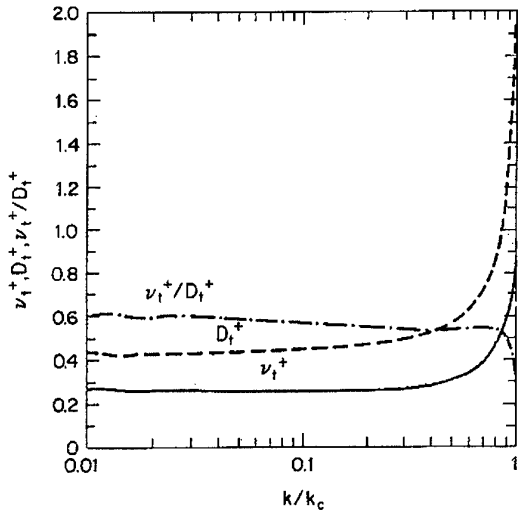

Figure 1: Eddy viscosity, eddy diffusivity and turbulent Prandtl number in spectral space, determined using the EDQNM theory (from [10])

with $2n \approx 3.7$ ([9][10]). We propose to determine ν_n^* by considering the energy balance between explicit and subgridscale transfers. This yields:

$$\int_0^{k_C} 2\nu_t k^2 E(k,t)dk = \epsilon \quad ,$$

which, in an infinite Kolmogorov inertial range, leads to

$$321 + \frac{1}{1+(3n/2)}\nu_n^* = \frac{2}{3 \times 0.441} \quad . \qquad (44)$$

We will come back to this expression below, when working in physical space in terms of generalized hyperviscosities.

Let us mention that the use of the eddy viscosities and eddy diffusivities given by Eqs (41) and (42) allow one to solve numerically the EDQNM kinetic energy and passive scalar evolution equations at zero molecular viscosity and diffusivity in the self-similar decaying regime (for $k \leq k_C$), as shown by [9][10].

3.2 LES of isotropic turbulence

Let us now come back to the evolution equations (in spectral space) of the instantaneous filtered fields (for $|\vec{k}| < k_C$)

$$(\frac{\partial}{\partial t} + \nu k^2)\bar{\hat{u}}_i(\vec{k},t) = t_{i,<k_C}(\vec{k},t) + t_{sg}(\vec{k},t) \qquad (45)$$

$$(\frac{\partial}{\partial t} + \kappa k^2)\bar{\hat{T}}(\vec{k},t) = t^T_{<k_C}(\vec{k},t) + t^T_{sg}(\vec{k},t) \quad . \qquad (46)$$

The explicit supergrid transfers are calculated by a truncation for $k,p,q \leq k_C$ of the nonlinear terms involved in Navier-Stokes and transported scalar equations in Fourier space (see [3]):

$$t_{i,<k_C}(\vec{k},t) = -ik_m\left(\delta_{ij} - \frac{k_i k_j}{k^2}\right) \int_{\vec{p}+\vec{q}=\vec{k}\ ,|\vec{p}|,|\vec{q}|<k_C} \hat{u}_j(\vec{p},t)\hat{u}_m(\vec{q},t)d\vec{p} \qquad (47)$$

$$t^T_{<k_C}(\vec{k},t) = -ik_j \int_{\vec{p}+\vec{q}=\vec{k}\ ,|\vec{p}|,|\vec{q}|<k_C} \hat{u}_j(\vec{p},t)\hat{T}(\vec{q},t)d\vec{p} \quad . \qquad (48)$$

We propose to model the unknown subgridscale transfers with the aid of $\nu_t(k|k_C)$ and $\kappa_t(k|k_C)$ introduced above, namely

$$t_{sg}(\vec{k},t) = -\nu_t(k|k_C)k^2\bar{\hat{u}}_i(\vec{k},t) \qquad (49)$$

$$t^T_{sg}(\vec{k},t) = -\kappa_t(k|k_C)k^2\bar{\hat{T}}(\vec{k},t) \quad . \qquad (50)$$

This subgridscale modelling is justified at the energetic transfer level, in the sense that, when one writes the exact evolution equations for the spectra of $\underline{\bar{u}}$ and $\bar{T}$ as they arise from Eqs (49) and (50), one obtains the EDQNM subgridscale transfers. However, the assumption of real eddy coefficients is constraining, and discards the possible phase effects arising in the neighbourhood of k_C.

As already mentioned, the cusp part of the spectral-cusp eddy viscosity takes into account the non-existence of a spectral gap at k_C, and this is a great advantage with respect to eddy-viscosities in physical space.

The results of the spectral-cusp eddy viscosity applied to LES of decaying three-dimensional isotropic turbulence are satisfactory. The first calculations of this type at a very low resolution (32^3) were done by [9][10] respectively for the momentum equation and the passive scalar. Figures 2-a and 2-b show the decaying kinetic-energy and passive scalar spectra obtained in these LES, with formation of approximate $k^{-5/3}$ inertial and inertial-convective ranges. Although we were not aware of this fact at the moment this computation was done, it is clear on the figure

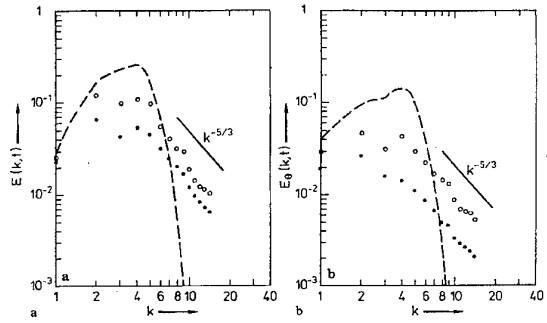

Figure 2: 3D isotropic decaying turbulence, resolution 32^3; decay of kinetic-energy (a) and passive-scalar (b) spectra, calculated from the LES of [10] using the spectral-cusp eddy viscosity

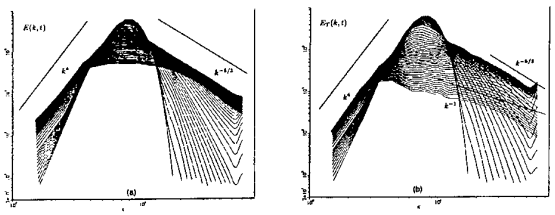

Figure 3: 3D isotropic decaying turbulence, resolution 128^3; decay of kinetic-energy (a) and passive-scalar (b) spectra, calculated from the LES of [14] using the spectral-cusp eddy viscosity

that the temperature spectrum decays much faster than the kinetic energy. Figure 3 is an analogous LES at a resolution of 128^3 Fourier modes carried out by [14] (see also [15]). The initial velocity and scalar spectra are analogous, with a Gaussian ultraviolet behaviour and a k^8 infrared spectrum. It can be checked that Kolmogorov and Corrsin-Oboukhov $k^{-5/3}$ cascades establish. Afterwards, the kinetic-energy spectrum decays self-similarly, with a slope comprised between $-5/3$ and -2. The scalar spectrum seems to have a very short inertial-convective range close to the cutoff, and a very wide range shallower than k^{-1} in the large scales. Here also the scalar decays much faster than the temperature. This anomalous range was explained by [16] as due to the quasi two-dimensional character of the scalar diffusion in the large scales, leading to large-scale intermittency of the scalar. In these LES, a direct determination of the eddy-viscosity and the eddy-diffusivity was done, by evaluating the transfers across a fictitious cutoff $k'_C = k_C/2$. The eddy viscosity thus determined has the plateau-cusp behaviour predicted by the closures. However, the eddy diffusivity is anomalous with respect to the EDQNM prediction, with a logarithmic decrease in the plateau region. This is presented on Figure 4, where only the explicit transfers involving the range $[k'_C, k_C]$ are indicated.

It was shown in Ref. [16] that the anomaly disappears when the temperature is no more passive and coupled with the velocity within the frame of Boussinesq approximation. It is possible that the same holds for compressible turbulence, which would legitimate the use of the plateau-cusp eddy diffusivity in this case.

3.3 The spectral backscatter

Let us look now at the infrared ($k \to 0$) spectra obtained in Figures 3-a and 3-b. The initial slope is k^8, as already stressed, and one sees k^4 spectra which form. These spectra had been predicted with the aid of two-point closures such as EDQNM[3] (see

[3]This is also valid for TFM, DIA (Direct-Interaction Approximation) and even Quasi-Normal theories.

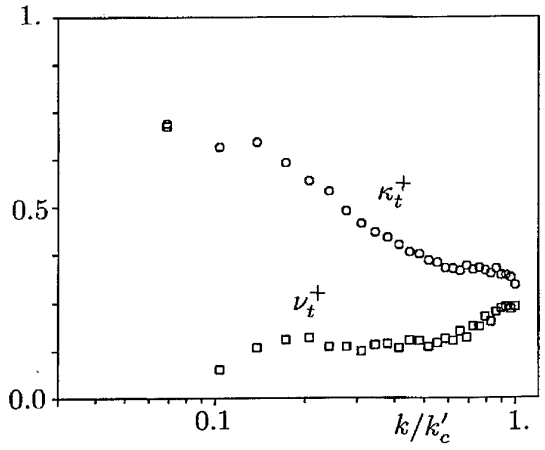

Figure 4: 3D isotropic decaying turbulence, resolution 128^3; eddy-viscosity and diffusivity calculated from the LES of of [16]

[17]) many years before they could be observed in the LES of [14] [15]. The derivation is the following: let k_i and k_i^T be respectively the peaks of the kinetic-energy and scalar spectra. The nonlocal interactions theory, where the nonlocal transfers are calculated to the leading order in terms of expansions in powers of the small parameters k/k_i (resp. k/k_i^T) permits to show that nonlocal transfers are dominant in this infrared range, and respectively equal to

$$T(k,t) \approx \frac{14}{15} k^4 \int_{k_i}^{\infty} \theta_{0pp} \frac{E(p)^2}{p^2} dp \qquad (51)$$

$$T^T(k,t) = \frac{4}{3} k^4 \int_{k_i^T}^{\infty} \theta_{0pp}^T \frac{E(p)}{p^2} E_T(p) dp \qquad (52)$$

for the velocity and the scalar. These transfers, which arise in the rhs of the evolution equations for the spectra

$$(\frac{\partial}{\partial t} + 2\nu k^2) E(k,t) = T(k,t)$$

$$(\frac{\partial}{\partial t} + 2\kappa k^2) E_T(k,t) = T^T(k,t) \quad ,$$

inject a k^4 spectrum in low wave numbers, through some kind of nonlinear resonant interaction between two modes $\approx k_i$. This spectral backscatter is responsible for the sudden appearance of k^4 infrared spectra when the initial spectra are sharply peaked, or simply $\propto k^s$ with $s > 4$. This spectral backscatter phenomenon is important, since energy is thus injected in very low wave numbers, and, to our knowledge, two-point closure theories are the only ones which permit to predict it analytically[4]. Violent backscatter phenomena occur also in the statistical unpredictability theory both in two and three dimensions, as shown by [6].

[4]In two-dimensional turbulence, a k^3 backscatter also arises (see [3])

Notice finally that, if turbulence is fed by some forcing concentrated around k_i, a stationary solution will imply an infrared balance between the backscatter and the eddy-viscous transfers, yielding a k^2 equipartition spectrum. A last remark is that the k^4 backscatter is negligible in LES where the cutoff k_C lies in the middle of a Kolmogorov range. Backscatter effects exist, which send back energy from the filtered to the subgridscales. But, from an energetic point of view, they are contained in the cusp-part of the plateau-cusp eddy viscosity considered above.

4 SPECTRAL DYNAMIC MODEL

We will present below a local generalization of the plateau-cusp spectral eddy viscosity to the physical space (structure-function model), which gives better results for isotropic turbulence as far as the Kolmogorov cascade is concerned. But let us show now an adaptation of the spectral-cusp model to kinetic-energy spectra $\propto k^{-m}$ for $k > k_C$, when the exponent m is not necessarily equal to 5/3. The eddy viscosity given by Eq. (33) is now

$$\nu_t^\infty = \frac{1}{15a_1}\,\frac{5-m}{m+1}\sqrt{3-m}\,\left[\frac{E(k_C)}{k_C}\right]^{1/2} \quad , \qquad (53)$$

for $m \leq 3$. The constant $1/(15a_1)$ is equal to $0.31\ {C_K}^{-3/2}$. This expression, derived by [16], was used by Lamballais ([18] [19]) for LES of a plane channel (see below). The associated eddy diffusivity is

$$\kappa_t^\infty = \frac{4}{3a_3}\,\frac{\sqrt{3-m}}{m+1}\,\left[\frac{E(k_C)}{k_C}\right]^{1/2} \quad , \qquad (54)$$

and the turbulent Prandtl number

$$P_r^{(t)} = \frac{5-m}{20}\,\frac{a_3}{a_1} \quad . \qquad (55)$$

Taking the value of a_3 necessary to recover $P_r^{(t)} = 0.6$ for $m = 5/3$, one finds finally

$$P_r^{(t)} = 0.18\ (5-m) \quad . \qquad (56)$$

For $m > 3$, this scaling is no more valid, and the eddy-viscosity and diffusivity coefficients will be set equal to zero. In the spectral dynamic model, the exponent m is determined through the LES with the aid of least-squares fits of the kinetic-energy spectrum close to the cutoff. The asymptotic eddy viscosity of Eq. (53) is multiplied by the plateau-cusp function $K(k/k_C)$ defined above.

4.1 Incompressible plane channel

We show now how the spectral dynamic model may be applied to an incompressible turbulent Poiseuille flow between two infinite parallel flat plates. The channel has a width $2h$, and we define the macroscopic Reynolds number by $R_e = 2hU_m/\nu$, where U_m is the bulk velocity. We assume periodicity in the streamwise and spanwise directions. Calculations are carried out at constant U_m. They are initiated by a parabolic laminar profile perturbed by a small three-dimensional random noise, and pursued up to complete statistical stationarity. When turbulence has developed, we define a microscopic Reynolds number $h^+ = v_* h/\nu$, based on the friction velocity. We use a numerical code combining pseudo-spectral methods in the streamwise and spanwise directions, and compact finite-difference schemes of sixth order in the transverse direction (see [18]), whith grid refinement close to the walls. This is a very precise code of accuracy comparable to a spectral method at equivalent resolution, for the DNS presented on Figure 5 at $h^+ = 162$. It is compared with a DNS carried out in Ref. [20] using spectral methods at $h^+ = 150$). These DNS, which use very precise numerical methods, turn out to be in very good agreement with the experiments. We see on Figure 5-a that the logarithmic range begins at $y^+ = 30$. We show on Figure 5-b the r.m.s. velocity-fluctuations profile in terms of y. It is clear that there is a strong production of u' at the wall, with a peak at $y^+ = 12$. This corresponds in fact to the low- and high-speed streaks. Figure 5-e shows the Reynolds stresses, whose peak is higher (at the bottom of the logarithmic layer), which is the signature of ejections of vorticity from the wall. The same peak is observed for the pressure fluctuations (Figure 5-d), which is certainly due to low pressure associated to high vorticity at the tip of the ejected hairpin (see below). Finally Figure 5-f shows the r.m.s. vorticity fluctuations, a quantity very difficult to measure precisely experimentally. It indicates that the maximum vorticity produced is spanwise and at the wall, in fact under the high-speed streaks (see below). The vorticity perpendicular to the wall is about 40% higher than the longitudinal vorticity in the region $5 < y^+ < 30$, which indicates only a weak longitudinal vorticity stretching by the ambient shear. We will present two LES using the spectral-dynamic model, at $R_e = 6666$ ($h^+ = 204$, case A) and $R_e = 14000$ ($h^+ = 389$, case B). They are respectively subcritical and supercritical with respect to the linear-stability analysis of the Poiseuille profile. In the two simulations there is a grid refinement close to the wall, in order to simulate accurately the viscous sublayer. The kinetic-energy spectrum allowing to determine the eddy-viscosity is calculated in each plane parallel to the walls. In fact, the original formula for the spectral-eddy viscosity considered a three-dimensional spectrum. It is possible, in the isotropic case and when spectra decrease as a power law, to relate the two-dimensional to the three-dimensional spectrum. LES of the channel seem to be insensitive to the particular spectrum chosen.

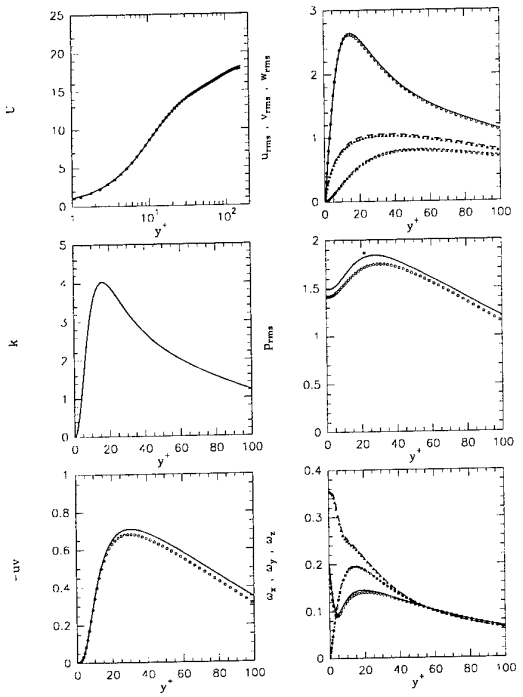

Figure 5: statistical data obtained in DNS of a turbulent channel flow by Lamballais (straight line) and Kuroda (symbols); from left to right and top to bottom, a) mean velocity, b) r.m.s. velocity fluctuations (respectively from top to bottom, longitudinal, spanwise, vertical), c) kinetic energy, d) r.m.s. pressure fluctuation, e) Reynolds stresses, f) r.m.s. vorticity (from top to bottom, spanwise, vertical, longitudinal)

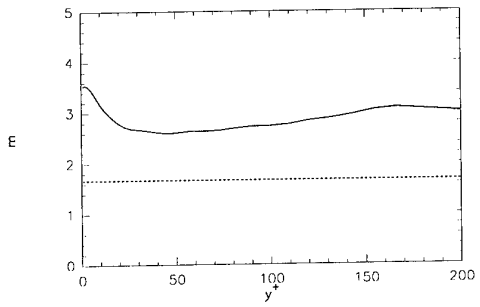

Figure 6: Spectral-dynamic LES of the channel flow (case A), exponent $m(y^+)$ of the kinetic-energy spectrum at the cutoff

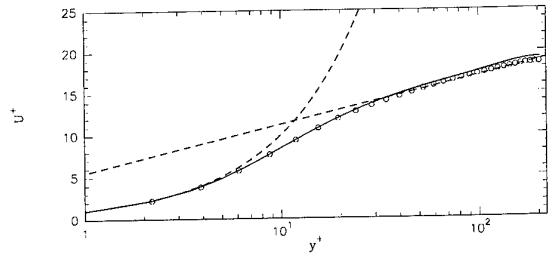

Figure 7: Same LES as Figure 6. Comparison of the mean velocity profile (solid line) versus Piomelli's [21] dynamic-model simulations (symbols)

Figure 6 shows for case A the exponent m arising in the energy spectrum at the cutoff, as a function of the distance to the wall y^+. Regions where $m > 3$ correspond to a zero eddy viscosity and hence a direct-numerical simulation. This is the case in particular close to the wall, up to $y^+ \approx 12$ where we know that longitudinal velocity fluctuations are very intense, due to the low- and high-speed streaks. Therefore, and since the first point is very close to the wall ($y^+ = 1$), our LES has the interesting property of becoming a DNS in the vicinity of the wall, which enables us to capture events which occur in this region. Figure 7 shows the mean velocity profile in case A, compared with the LES of Piomelli [21] using the dynamic model of [8]. The latter is known to agree very well with experiments at these low Reynolds numbers. Our simulation coincides, with the right value for the Karman constant. On the other hand, a LES carried out with the classical spectral-cusp model with $m = 5/3$ gives an error of 20% for the Karman constant. Figure 8 shows for case A the rms velocity fluctuations, compared with the dynamic-model predictions of [21]. The agreement is still very good, with a correct prediction of the longitudinal velocity fluctuations peak. Concerning the supercritical case, the LES of case B are in very good agreement with a DNS at $h^+ = 395$ carried out by [22], both for the mean velocity and the rms velocity components. The latter are shown on Figure 9. Notice that the LES allows to reduce the computational cost by a factor

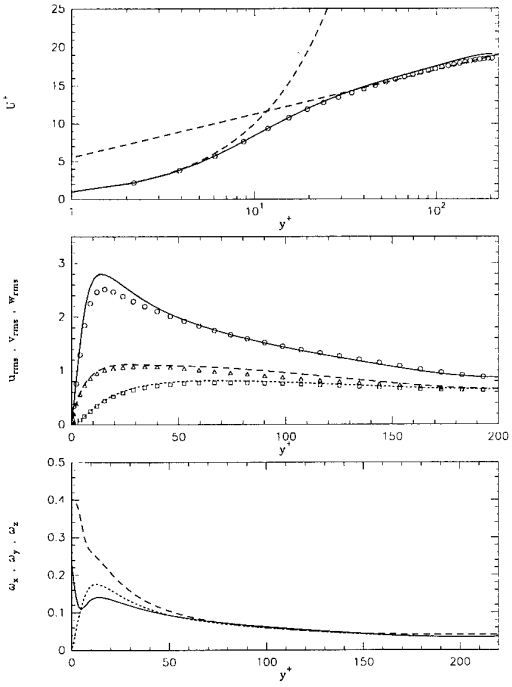

Figure 8: Same as Figure 7, but for the rms velocity fluctuations, from top to bottom longitudinal, spanwise and transverse

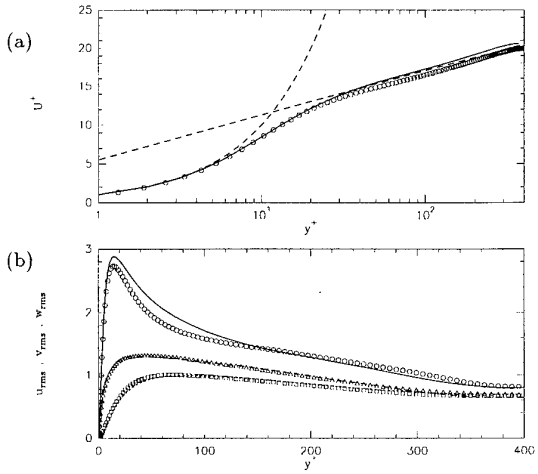

Figure 9: Turbulent channel flow, comparisons of the spectral-dynamic model (solid lines, $h^+ = 389$) with the DNS of Kim ([22], symbols, $h^+ = 395$); a) mean velocity, b) rms velocity components

of the order of 100, which is huge.

We present finally on Figure 10 a map of the vorticity modulus at the same threshold for cases A and B. The flow goes from left to right.

5 DYNAMIC MODEL

We have already noted for Kraichnan's spectral eddy viscosity that the parameters defining it could be computed from a LES with a cutoff k_C, by defining a fictitious cutoff $k'_C = k_C/2$, and explicitly calculating the transfers across k'_C (see Refs [14][16]). This is the underlying philosophy of the dynamic model in physical space [8]. The method relies on a LES using a "base" subgrid-scale model such as Smagorinsky's model[5], with a grid mesh Δx. The computed fields $\bar{f}$ are filtered by a "test filter" $\tilde{}$ of larger width $\alpha\Delta x$ (for instance $\alpha = 2$), to yield the field $\widetilde{\bar{f}}$. If one applies the double filter to the Navier-Stokes equation (with constant density), the subgrid-scale tensor of the field $\widetilde{\bar{u}}$ is readily obtained from with the replacement of the filter "bar" by the double filter "bar-tilde", that is:

$$\mathcal{T}_{ij} = \widetilde{\bar{u}}_i\widetilde{\bar{u}}_j - \widetilde{\overline{u_i u_j}} \quad . \tag{57}$$

We consider now the following resolved turbulent stress corresponding to the test-filter applied to the field $\bar{u}$:

$$\mathcal{L}_{ij} = \widetilde{\bar{u}}_i\widetilde{\bar{u}}_j - \widetilde{\bar{u}_i\bar{u}_j} \quad . \tag{58}$$

Finally we apply the filter "tilde" to Eq. (7), to yield

$$\widetilde{T_{ij}} = \widetilde{\bar{u}_i\bar{u}_j} - \widetilde{\overline{u_i u_j}} \quad . \tag{59}$$

Adding Eqs (58) and (59), using (57)

$$\mathcal{L}_{ij} = \mathcal{T}_{ij} - \widetilde{T_{ij}} \quad , \tag{60}$$

[5] But it may be used with other subgrid models.

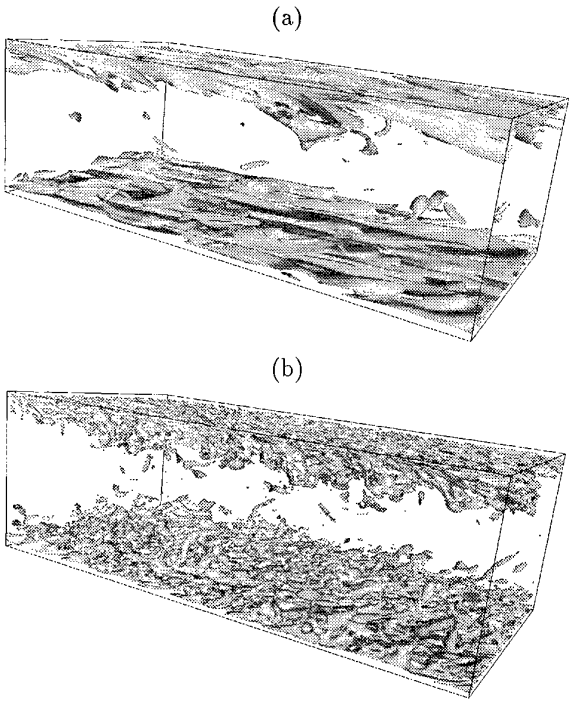

Figure 10: Turbulent plane channel, vorticity modulus; a) DNS ($h^+ = 165$), b) LES using the spectral-dynamic model ($h^+ = 389$), from [18]

called Germano's identity. In this expression, $\mathcal{T}_{ij}$ and $\widetilde{T_{ij}}$ have to be modelled, while $\mathcal{L}_{ij}$ can be explicitly calculated by applying the test filter to the base LES results. Using Smagorinsky's model, we have

$$\widetilde{T_{ij}} - \frac{1}{3}\widetilde{T_{ll}}\ \delta_{ij} = 2\widetilde{\mathcal{A}_{ij}C} \quad , \tag{61}$$

whith $C = C_S^2$ and

$$\mathcal{A}_{ij} = (\Delta x)^2\ |\bar{S}|\bar{S}_{ij} \quad .$$

Still using Smagorinsky, we have

$$\mathcal{T}_{ij} - \frac{1}{3}\mathcal{T}_{ll}\ \delta_{ij} = 2\mathcal{B}_{ij}C \ , \tag{62}$$

whith

$$\mathcal{B}_{ij} = \alpha^2(\Delta x)^2\ |\tilde{\bar{S}}|\ \tilde{\bar{S}}_{ij} \quad .$$

$|\tilde{\bar{S}}|$ and $\tilde{\bar{S}}_{ij}$ are the quantities analogous to $|\bar{S}|$ and $\bar{S}_{ij}$ built with the doubly-filtered field $\tilde{\bar{u}}$. Substracting Eq. (61) from Eq. (62) yields with the aid of Eq. (60)

$$\mathcal{L}_{ij} - \frac{1}{3}\mathcal{L}_{ll}\ \delta_{ij} = 2\mathcal{B}_{ij}C - 2\widetilde{\mathcal{A}_{ij}C} \quad .$$

In order to obtain C, many people remove it from the filtering as if it were constant, leading to

$$\mathcal{L}_{ij} - \frac{1}{3}\mathcal{L}_{ll}\ \delta_{ij} = 2CM_{ij} \quad , \tag{63}$$

with

$$M_{ij} = \mathcal{B}_{ij} - \widetilde{\mathcal{A}_{ij}} \quad .$$

Now, all the terms of Eq. (63) can be determined with the aid of $\bar{u}$. There are however five independent equations for only one variable C, and the problem is overdetermined.

Two alternatives have been proposed to deal with this undeterminacy. A first solution (Ref. [8]) is to contract Eq. (63) by $\bar{S}_{ij}$ to obtain

$$C = \frac{1}{2}\frac{\mathcal{L}_{ij}\bar{S}_{ij}}{M_{ij}\bar{S}_{ij}} \quad , \tag{64}$$

since, due to incompressibility, $\bar{S}_{ij}$ is traceless. This permits in principle to "dynamically" determine the "constant" C as a function of space and time, to be used in the LES of the base field $\bar{u}$. In tests using channel flow data obtained from direct numerical simulations, it was however shown in [8] that the denominator in Eq. (64) could locally vanish or become sufficiently small to yield computational instabilities. To get rid of this problem, Lilly [23] chose to determine the value of C which "best satisfies" the system Eq. (63) by minimizing the error using a least squares approach. It yields

$$C = \frac{1}{2}\frac{\mathcal{L}_{ij}M_{ij}}{M_{ij}^2} \quad . \tag{65}$$

This removes the undeterminacy of Eq. (63).

The analysis of DNS data revealed, however, that the C field predicted by the models (64) or (65) varies strongly in space and contains a significant fraction of negative values, with a variance which may be ten times higher than the square mean. So, the removal of C from the filtering operation is not really justified and the model exhibits some mathematical inconsistencies. The possibility of negative C is an advantage of the model since it allows a sort of backscatter in physical space, but very large negative values of the eddy viscosity is a destabilizing process in a numerical simulation, yielding a non-physical growth of the resolved scale energy. The cure which is often adopted to avoid excessively large values of C consists in averaging the numerators and denominators of (64) and (65) over space and/or time, thereby losing some of the conceptual advantages of the "dynamic" local formulation. Averaging over direction of flow homogeneity has been a popular choice, and good results have been obtained in [8] and [21], who took averages in planes parallel to the walls in their channel flow simulation. Remark that the same thing has been done, with success, when averaging the dynamic spectral eddy viscosity in the channel-flow LES presented above. It can be shown that the dynamic model gives a zero subgrid-scale stress at the wall, where L_{ij} vanishes, which is a great advantage with respect to the original Smagorinsky model; it gives also the proper asymptotic behavior near the wall. Notice again that the use of Smagorinsky's model as a base for the dynamic procedure is not compulsory, and any of the models described in the present

paper can be a candidate. As an example, Ref. [24] have applied the dynamic procedure to the structure-function model (see below) applied to a compressible boundary layer above a long cylinder.

Chapter II:

Compressible free-shear and separated flows

6 STRUCTURE-FUNCTION MODELS

Now, let us consider the EDQNM eddy viscosity (still scaling on $\sqrt{E(k_C)/k_C}$) with no cusp, and adjust the constant as proposed by [25], by balancing in the inertial range the subgridscale flux with the kinetic energy flux ϵ in the energy spectrum evolution equation[6]. This yields

$$\nu_t(k_C) = \frac{2}{3}\, C_K^{-3/2} \left[\frac{E(k_C)}{k_C}\right]^{1/2} \quad . \qquad (66)$$

The problem with such an eddy-viscosity (if the energy spectrum may be computed) is that it is uniform in space when used in physical space. Obviously, the eddy viscosity should take into account the intermittency of turbulence: there is no need for any subgridscale modelling in regions of space where the flow is laminar or transitional. On the other hand, it is essential to dissipate in the subgridscales the local bursts of turbulence if they become too intense. Considering also that turbulence in the small scales may not be too far from isotropy, it was proposed by [16] to come back to the classical formulation in the physical space, where the eddy viscosity is determined with the aid of (66). $E(k_C, \vec{x})$ is now a local kinetic energy spectrum, calculated in terms of the local second-order velocity structure function of the filtered field

$$F_2(\vec{x}, \Delta x) = \left\langle \|\overline{\vec{u}}(\vec{x}, t) - \overline{\vec{u}}(\vec{x} + \vec{r}, t)\|^2 \right\rangle_{\|\vec{r}\| = \Delta x} \qquad (67)$$

as if the turbulence is three-dimensionally isotropic, with Batchelor's formula

$$F_2(\vec{x}, \Delta x) = 4 \int_0^{k_C} E(k) \left(1 - \frac{\sin(k\Delta x)}{k\Delta x}\right) dk \quad . \qquad (68)$$

In fact, the original formula involves a k integral from 0 to ∞. But the filtered field has no energy at modes larger than k_C, which explains Eq. (68). This yields for a Kolmogorov spectrum

$$\nu_t^{SF}(\vec{x}, \Delta x) = 0.105\, C_K^{-3/2}\, \Delta x\, [F_2(\vec{x}, \Delta x)]^{1/2} \quad . \qquad (69)$$

F_2 is calculated with a local statistical average of square velocity differences between $\vec{x}$ and the six closest points surrounding $\vec{x}$ on the computational grid. In some cases, the average may be taken over four points parallel to a given plane; in a channel, for instance, the plane is parallel to the boundaries. Notice also that if the computational grid is not regular (but still orthogonal), interpolations of (69) have been proposed by [4]. Let $\Delta c = (\Delta x_1 \Delta x_2 \Delta x_3)^{1/3}$ be a (geometric) mean mesh in the three spatial directions. Remembering Kolmogorov's (1941) law in physical space, which states that the second-order velocity structure-function scales like $(\epsilon r)^{2/3}$, one can in Eq. (69) replace Δx by Δc, with (in the six-point formulation)

$$F_2(\vec{x}, \Delta c) = \frac{1}{6} \sum_{i=1}^{3} F_2^{(i)} \left(\frac{\Delta c}{\Delta x_i}\right)^{2/3} \quad ,$$

with

$$F_2^{(i)} = [\|\vec{u}(\vec{x}) - \vec{u}(\vec{x} + \Delta x_i \vec{e}_i)\|^2 + \|\vec{u}(\vec{x}) - \vec{u}(\vec{x} - \Delta x_i \vec{e}_i)\|^2] \quad ,$$

where $\vec{e}_i$ is the unit vector in direction x_i.

One can also look at the relation of Smagorinsky's and the structure-function models when the differences in the structure-function are replaced (within a first-order approximation!) by spatial derivatives. It is found for the six-point formulation, in the limit of $\Delta x \to 0$:

$$\nu_t^{SF} \approx 0.777\, (C_S \Delta x)^2 \sqrt{2\bar{S}_{ij}\bar{S}_{ij} + \bar{\omega}_i \bar{\omega}_i} \quad ,$$

where $\overline{\vec{\omega}}$ is the vorticity of the filtered field, whereas C_S is Smagorinsky's constant defined by Eq. (20).

The structure-function model (SF) works very well for decaying isotropic turbulence, where it yields a fairly good Kolmogorov spectrum ([16]), better than Smagorinsky's model (with $C_S = 0.2$) and Kraichnan's spectral-cusp model.

The SF model gives also good results for free-shear flows, where it is able to stretch secondary thin longitudinal hairpin vortices between primary vortices (see [4]). However, selective or filtered versions of it work better in this case (see below in this chapter). The SF model permits also to go beyond transition in a temporal[7] compressible boundary layer upon an adiabatic wall at Mach 4.5 (see Chapter III). But it does not work for transition in a boundary layer at low Mach (or incompressible) where, like Smagorinsky, it is too dissipative and prevents TS waves to degenerate into turbulence (see next chapters). This is still true within the four-point formulation in planes parallel to the wall, which eliminates the effect of the mean shear at the wall on the eddy viscosity. In fact, the spectrum $E_{\vec{x}}(k_C)$ determined by the isotropic formula Eq. (68) is too sensitive to the inhomogeneous low-frequency oscillations caused by the TS waves.

[6] The same was done in oder to obtain (44).

[7] periodic in the flow direction

6.1 Selective and filtered SF models

To overcome the difficulty of dissipating too much the large quasi two-dimensional vortices or transitional waves, two improved versions of the SF model have been developed: the *selective structure-function model* (SSF), and the *filtered structure-function model* (FSF). The dynamic model in physical space (see [8]) is another way of adapting the eddy viscosity to the local conditions of the flow.

The SSF model was developed by [27]. The idea is to switch off the eddy viscosity when the flow is not three-dimensional enough. The three-dimensionalization criterion is the following: one measures the angle between the vorticity at a given grid point and the average vorticity at the six closest neighbouring points (or the four closest points in the four-point formulation). If this angle exceeds 20^0, the most probable value according to simulations of isotropic turbulence at a resolution of $32^3 \sim 64^3$, the eddy viscosity is turned on. Otherwise, only the molecular dissipation is active. The constant arising in (69) is changed, and determined with the aid of LES of freely-decaying isotropic turbulence: one requires that the eddy viscosity averaged over the computational domain should be the same in a selective structure-function model and a SF model simulation. It is found that the constant in (69) has to be multiplied by 1.56.

The SSF model works very well for isotropic turbulence and free-shear flows, as well as for a compression ramp at Mach 2.5 (see [27] and next chapter). We have used it also with success in LES of a flow above a backward-facing step. The SSF model depends however upon the most probable angle of the next neighbours average vorticity, chosen above equal to 20^0. In fact, this angle is a function of the resolution of the simulation, since it should go to zero with Δx, and may be with the type of flow considered. Progresses in this model should be made by adjustment of this angle to the local grid.

The FSF model was developed by Ducros ([28]) and applied to a boundary layer at Mach 0.5 ([29] and next chapter). Here, the filtered field $\bar{u}_i$ is submitted to a high-pass filter in order to get rid of low-frequency oscillations which affect $E_{\bar{x}}(k_C)$ in the SF model. The high-pass filter is a Laplacian discretized by second-order centered finite differences and iterated three times. It was shown by Ducros that, for some 3D random or turbulent isotropic test fields, the spectrum of the high-pass filtered field is

$$\frac{\tilde{E}(k)}{E(k)} \approx 40^3 \left(\frac{k}{k_C}\right)^9 \quad . \tag{70}$$

This is different from the $(k^4)^3$ law one should expect from an iterated Laplacian, the loss being due to the finite-difference scheme[8] . On the other hand, the second-order velocity structure function of the filtered field satisfies an equation analogous to (68):

$$\tilde{F}_2(\vec{x}, \Delta x) = 4 \int_0^{k_C} \tilde{E}(k) \left(1 - \frac{\sin(k\Delta x)}{k\Delta x}\right) dk \quad . \tag{71}$$

Substituting (70) into (71), and replacing $E(k)$ by a Kolmogorov spectrum, one can determine $\tilde{F}_2(\vec{x}, \Delta x)$ in terms of a spectrum $E(k_C)$ which is no more sensitive to the low wavenumber fluctuations, which yields

$$\nu_t^{FSF}(\vec{x}, \Delta x) = 0.0014\, C_K^{-3/2}\, \Delta x\, [\tilde{F}_2(\vec{x}, \Delta x)]^{1/2} \quad . \tag{72}$$

This model will be applied below with good results to a spatially-growing incompressible mixing layer, and in the next chapter to transition in a spatially-developing boundary layer at Mach 0.5.

6.2 Generalized hyperviscosities

One of the common drawbacks of the different versions of the SF model is the absence of cusp near k_C. We go back to (43), where we take $n = 2$, which yields $2n = 4$, not far from the EDQNM 3.7 value. Then Eq. (44) yields $\nu_2^* = 2.044$, so that an equivalent of the spectral-cusp eddy viscosity in physical space is for the subgridscale dissipative operator in the filtered Navier-Stokes equation:

$$2\frac{\partial}{\partial x_j}[0.661\, \nu_t^{SF} \bar{S}_{ij}] + 1.351 \left(\frac{\Delta x}{\pi}\right)^4 \nu_t^{SF} (\nabla^2)^3 \bar{u}_i \quad , \tag{73}$$

where ν_t^{SF} has been given above. Notice that an analogous model (with Smagorinsky's model replacing the structure-function model) had been proposed in [31]. This model[9] was used by [30] in LES of a rotating stratified jet submitted to baroclinic instability. They could show developments of primary and secondary instabilities of the thermal fronts very similar to what is observed in the atmosphere.

If one wants to have now in physical space a model equivalent to the spectral-dynamic model, the dissipative operator (73) has to be multiplied by the constant:

$$\tilde{A} = \frac{\sqrt{12}}{5} \frac{5-m}{m+1} \sqrt{3-m} \quad , \tag{74}$$

where m is the slope of the kinetic-energy spectrum at the cutoff, which has to be obtained dynamically in some way. This might be possible if one periodicity direction exists at least in the flow. For a scalar, the corresponding turbulent Prandtl number is given by Eq. (56).

[8] This shows that finite-difference methods up to the fourth order cannot deal with high-order Laplacian operators.

[9] with an equivalent formulation for the density and a turbulent Prandtl number of 0.6

Such a spectral-dynamic generalized hyperviscosity model should be tested on various shear flows, such as those presented below.

7 INCOMPRESSIBLE MIXING LAYERS

We will first examine in details what DNS and LES can tell about the dynamics of incompressible mixing layers, in particular for primary and secondary coherent vortices. Later on, we will look at the compressibility effects upon these flows.

We show now three-dimensional results of the filtered structure function model applied to a plane mixing layer, respectively in the temporal and spatial cases.

7.1 Temporal mixing layer

We consider in a fluid of constant density a mixing layer periodic in the streamwise and spanwise directions, initiated by a hyperbolic-tangent velocity profile, to which is superposed a small random perturbation. We take free-slip boundary conditions on the upper and lower boundary, and use pseudo-spectral methods in the three dimensions of space. LES using the FSF model show the following results. If the perturbation is quasi two-dimensional, the mixing layer evolves into a set of big quasi two-dimensional vortices which both undergo pairing and stretch intense longitudinal hairpin vortices in the stagnation regions between them. Such a pattern is shown on Figure 11, taken from [32], and presenting a map of the vorticity modulus. This stretching of longitudinal vortices, observed experimentally for a long time (see e.g. [33] and [34]), may be explained as follows: let us consider the vorticity equation, written for a perfect fluid of uniform density as

$$\frac{D\vec{\omega}}{Dt} = \vec{\nabla}\vec{u} : \vec{\omega} = \overline{\overline{S}} : \vec{\omega} + \frac{1}{2}\vec{\omega} \times \vec{\omega} = \overline{\overline{S}} : \vec{\omega} \quad , \qquad (75)$$

where D/Dt is the substancial derivative following the flow motion, and $\overline{\overline{S}}$ the deformation tensor, already introduced in (14) for the filtered field. If one supposes that the vorticity in the stagnation region between the vortices is weak, one can assume (at least initially) that the deformation tensor will not vary while the vorticity is stretched. Since the deformation tensor is real and symmetric, it admits eigenvectors (principal axes of deformation) which are orthogonal and can form a basis. Let s_1, s_2, s_3 be the three eigenvalues. Due to incompressibility, their sum is zero, so that one at least is positive (the largest positive is called here s_1) and another one at least is negative. Let s_2 be the smallest eigenvalue, always negative. Working in the orthonormal frame

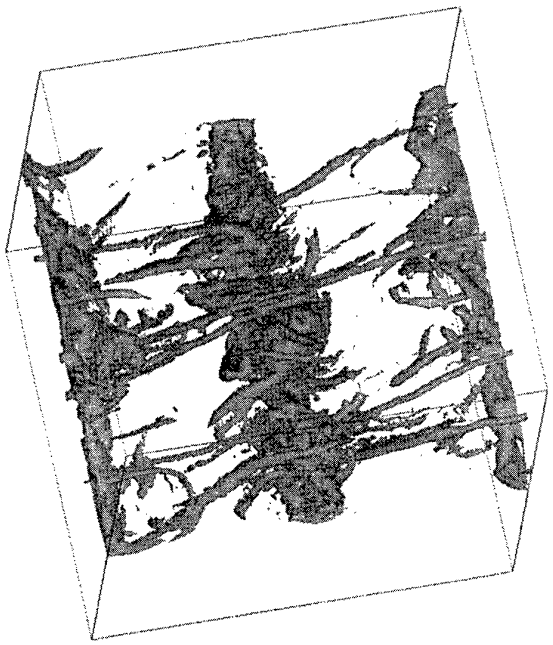

Figure 11: Vorticity field obtained in the LES of a temporal mixing layer forced quasi two-dimensionally

formed by the eigenvectors $\vec{l}, \vec{t}, \vec{s}$ respectively associated to s_1, s_2, s_3, the vorticity components $\omega_1, \omega_2, \omega_3$ satisfy the following equations

$$\begin{aligned} \frac{D\omega_1}{Dt} &= s_1\omega_1 \quad , \\ \frac{D\omega_2}{Dt} &= s_2\omega_2 \quad , \\ \frac{D\omega_3}{Dt} &= s_3\omega_3 \quad , \end{aligned} \qquad (76)$$

and the vorticity will be stretched in the direction of the first principal axis, and compressed in the direction of the second. Generally, $\overline{\overline{S}}$ is not far from a pure deformation in the stagnation region, so that, approximately, $\vec{l}$ will be inclined 45^0 with respect to the mean flow, $\vec{s}$ will be spanwise, $s_3 = 0$ and $s_2 = -s_1$. Such a derivation unifies explanations given by [36] and [37]. Intense longitudinal hairpins had also been found by [38] in temporal mixing-layer LES using the spectral-cusp eddy viscosity. An interesting feature of these simultions is to show that longitudinal vorticity stretched between the primary Kelvin-Helmholtz vortices is rolled up within the cores of the big vortices, thus producing intense longitudinal vorticity fluctuations in the cores themselves. In Figure 11, the maximum longitudinal vorticity stretched is of the order of $4\omega_i$, which might be larger than the effective values reached experimentally. Actually, the efficiency of the longitudinal stretching could depend upon the amplitude of the initial perturbation and the Reynolds number.

Experiments in a developed mixing layer ([34]) show that the spanwise wavelength of the longitudinal vor-

tices is of the order of two third of the longitudinal wavelength of the primary Kelvin-Helmholtz vortices between which they are stretched. This is precisely the most-amplified spanwise wavelength within a secondary-instability analysis of Stuart's vortices, as shown by Pierrehumbert and Widnall [35]. This instability, called the translative instability, corresponds in fact to a global in-phase oscillation of the big billows in the spanwise direction, and cannot explain the formation of the thin longitudinal hairpins. A plausible explanation could be that they do form according to the mechanisms just explained above, but with a preferred spanwise wavelength imposed by the translative instability. Numerical simulations in the temporal or spatial cases need larger domains in the spanwise direction in order to validate the value of the preferred spanwise wavelength.

In fact, the numerical resolution of the three-dimensional Orr-Sommerfeld equation at large Reynolds show that the most-amplified mode in the 3D temporal mixing layer is indeed two-dimensional. By a naive application of this result, one might have believed that two-dimensional Kelvin-Helmholtz vortices would emerge from a weak three-dimensional random isotropic perturbation superposed upon the basic shear. But this is not at all what happens numerically. Instead, Comte et al. ([39][40]), using DNS with pseudo-spectral methods at a resolution of 128^3 Fourier wave vectors and a Reynolds number $U\delta_i/\nu = 100$, displayed the evidence for helical pairing, where vortex filaments oscillate out-of-phase in the spanwise direction, and reconnect, yielding a vortex-lattice structure. We have recovered the same dislocated pattern in LES (using the FSF model) with the same forcing. Figure 12 shows the vorticity modulus obtained in such a simulation. Figure 13 shows the low-pressure field from an analogous LES using the spectral-cusp eddy viscosity. It confirms that low pressure is a very good indicator of big or intense vortices. Notice that at the end of the FSF-based LES corresponding to Figure 12, the statistical data concerning velocity, rms velocity fluctuations and Reynolds stresses, are in very good agreement with the experiments of unforced mixing layers. The simulation with a quasi two-dimensional forcing is less good from this standpoint.

The term "helical pairing" was first proposed by [41], concerning highly three-dimensional pairings in a mixing-layer experiment. Afterwards, helical pairing was documented in the experiments of Browand and coworkers [42]. In the secondary-instability analysis of [35], the subharmonic instability found is identified with the previously observed helical pairing. Surprisingly, its amplification rate is three times lower than its translative-instability counterpart. Looking at DNS or LES of helical-pairing, it turns out that this is not exactly a "secondary instability": one does not observe first the roll up of primary billows fol-

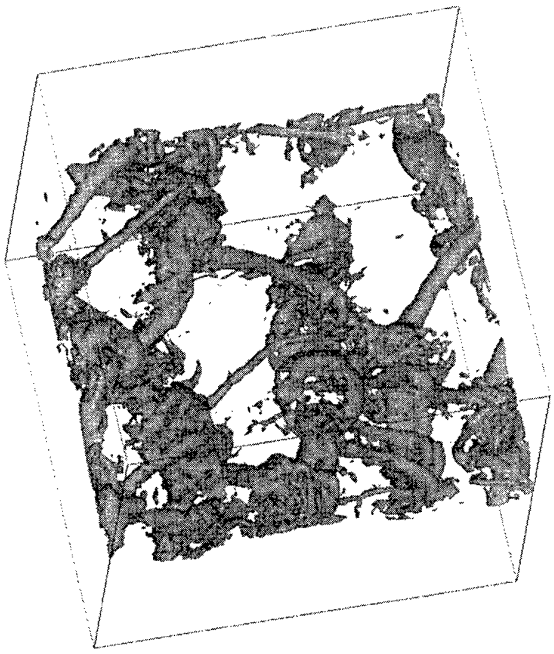

Figure 12: Vorticity field obtained in the LES of a temporal mixing layer undergoing helical pairing

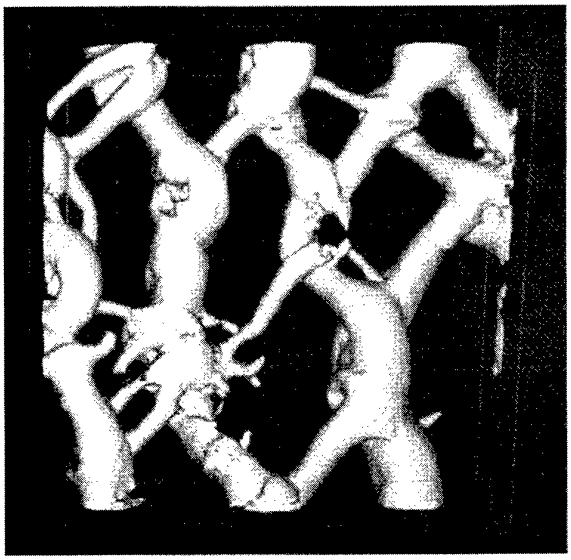

Figure 13: Low-pressure field obtained in a spectral-cusp LES in the helical-pairing case

lowed by a staggered deformation. Instead, oblique waves are seen to grow quickly, yielding directly the lattice structure of dislocated billows.

Finally, it may be interesting to look at what can be said from the point of view of a scalar gradient when a scalar is transported passively by the flow. This may be very important if the two currents in the mixing layer react chemically, such as in combustion for instance. If the scalar σ satisfies $D\sigma/Dt = 0$, its gradient follows the equation

$$\frac{D}{Dt}\vec{\nabla}\sigma = -\vec{\nabla}\vec{u}|^t : \vec{\nabla}\sigma \quad . \tag{77}$$

If we are in a stagnation region between two vortices[10], and assume that the vorticity is small in front of the deformation, (77) may be approximated by

$$\frac{D}{Dt}\vec{\nabla}\sigma = -\overline{\overline{S}} : \vec{\nabla}\sigma \quad ,$$

which yields for the three components of $\vec{\nabla}\sigma$ in the principal axes of deformation

$$\frac{D}{Dt}\frac{\partial\sigma}{\partial l} = -s_1\frac{\partial\sigma}{\partial l} \quad , \quad \frac{D}{Dt}\frac{\partial\sigma}{\partial n} = -s_2\frac{\partial\sigma}{\partial n} \quad ,$$

$$\frac{D}{Dt}\frac{\partial\sigma}{\partial s} = -s_3\frac{\partial\sigma}{\partial s} \quad .$$

This shows that the scalar gradient is compressed along the first principal axis of deformation, and stretched in the transverse direction, so that scalar gradients across the mixing-layer interface will steepen. In case of chemical reaction between the two layers, this will enhance the molecular exchanges at the interface, and favour the reaction.

7.2 Spatial mixing layers

The temporal approximation is only a crude approximation of a mixing layer spatially developing, where one works in a frame traveling with the average velocity between the two layers. We present now LES using the FSF model of a spatial mixing layer, initiated upstream by a hyperbolic-tangent velocity profile superposed on the average flow, plus a weak random forcing regenerated at each time step.

Free-slip conditions are still imposed upon the upper and lower boundaries. The outflow boundary condition is of the Orlanski's type [43]. With an upstream forcing consisting in a quasi two-dimensional random perturbation, intense longitudinal hairpins stretched between quasi 2D Kelvin-Helmholtz vortices are found again (Figure 14). An interesting feature found is that longitudinal vortices of same sign may come close together and merge, contributing thus to the global self-similarity of the mixing

[10] situation where longitudinal hairpin vortices are likely to form

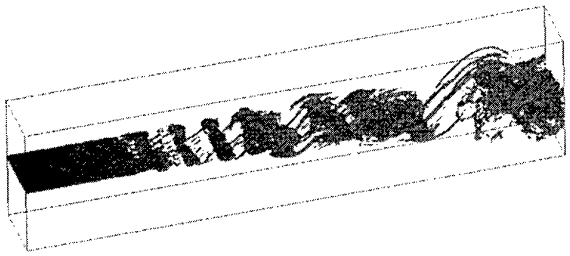

Figure 14: LES of an incompressible mixing layer forced upstream by a quasi two-dimensional random perturbation; the vorticity modulus is shown at a threshold $(2/3)\omega_i$

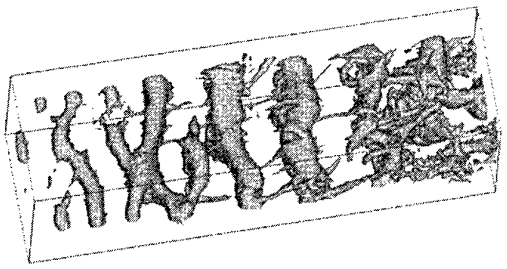

Figure 15: Same as Figure 14, but with a three-dimensional upstream white-noise forcing, low-pressure field

layer. When the forcing is a three-dimensional random white noise, helical pairing occurs upstream, as indicated by the low-pressure maps of Figure 15. But none of these simulations has reached self-similarity, since the kinetic-energy spectra in the downstream region are steeper than $k^{-5/3}$, and rms velocity fluctuations have a departure of about 20% with respect to the experiments. Thus calculations in longer domains are necessary, in order in particular to know in the helical-pairing case whether quasi two-dimensionality might not be restored further downstream.

8 COMPRESSIBLE L.E.S. FORMALISM

In Cartesian co-ordinates, the compressible Navier-Stokes equations can be cast in the so-called fast-conservation form

$$\frac{\partial U}{\partial t} + \frac{\partial F_1}{\partial x_1} + \frac{\partial F_2}{\partial x_2} + \frac{\partial F_3}{\partial x_3} = 0 \quad , \tag{78}$$

with

$$U = {}^T(\rho, \rho u_1, \rho u_2, \rho u_3, \rho e) \quad , \tag{79}$$

ρe being the total energy defined by, for an *ideal* gas,

$$\rho e = \rho\, C_v\, T + \tfrac{1}{2}\rho(u_1^2 + u_2^2 + u_3^2) \quad . \tag{80}$$

The fluxes F_i read, $\forall i \in \{1,2,3\}$,

$$F_i = \begin{pmatrix} \rho u_i \\ \rho u_i u_1 - \sigma_{i1} \\ \rho u_i u_2 - \sigma_{i2} \\ \rho u_i u_3 - \sigma_{i3} \\ \rho e u_i - u_j \sigma_{ij} - k \dfrac{\partial T}{\partial x_i} \end{pmatrix} \quad , \tag{81}$$

$k = \rho C_p \kappa$ being the thermal conductivity (and κ the thermal diffusivity).

The components σ_{ij} of the stress tensor are given by the Newton law

$$\sigma_{ij} = -p\ \delta_{ij} + \mu S_{ij} \quad , \tag{82}$$

in which

$$S_{ij} = \left[\frac{\partial u_j}{\partial x_i} + \frac{\partial u_i}{\partial x_j} - \frac{2}{3} (\boldsymbol{\nabla}.\boldsymbol{u}) \delta_{ij} \right] \tag{83}$$

denotes the deviatoric part of the strain-rate tensor. Bulk viscosity is neglected (Stokes hypothesis), as commonly accepted except in extreme thermodynamical situations. This yields

$$F_i = \begin{pmatrix} \rho u_i \\ \rho u_i u_1 + p\ \delta_{i1} - \mu S_{i1} \\ \rho u_i u_2 + p\ \delta_{i2} - \mu S_{i2} \\ \rho u_i u_3 + p\ \delta_{i3} - \mu S_{i3} \\ (\rho e + p) u_i - \mu u_j S_{ij} - k \dfrac{\partial T}{\partial x_i} \end{pmatrix} \quad . \tag{84}$$

The Sutherland empirical law

$$\begin{aligned} \mu(T) = \ & \mu(273.15) \left(\frac{T}{273.15} \right)^{1/2} \frac{1 + S/273.15}{1 + S/T} \\ & \text{with } \mu(273.15) = 1.711\ 10^{-5} Pl \\ & \text{and } S = 110.4K \quad , \end{aligned} \tag{85}$$

and its extension to temperatures lower than 120 K :

$$\mu(T) = \mu(120)\ T/120 \quad \forall\ T < 120 \quad , \tag{86}$$

are prescribed for molecular viscosity. Conductivity $k(T)$ is obtained assuming the molecular Prandtl number $Pr = C_p \mu(T)/k(T)$ constant and equal to 0.7, as in air at ambiant temperature. The equation of state

$$p = R\ \rho\ T \tag{87}$$

closes the system, with $R = C_p - C_v = \frac{\mathcal{R}}{\mathcal{M}} = 287.06\ Jkg^{-1}K^{-1}$ for air.

8.1 compressible filtering procedure

As in the incompressible regime, and whatever the numerical method used, the discretization of the above equations introduces a cut-off scale Δx which is by hypothesis larger than the Kolmogorov scale. We still account for this by a low-pass filter of width Δx, characterized by the convolution in space with a function $G_{\Delta x}(\vec{x})$. The operator $\overline{\ }$ commutes with the space and time derivatives in the case of uniform cubic meshes of side Δx. Convolution of the above equations therefore yields

$$\frac{\partial \overline{U}}{\partial t} + \frac{\partial \overline{F}_1}{\partial x_1} + \frac{\partial \overline{F}_2}{\partial x_2} + \frac{\partial \overline{F}_3}{\partial x_3} = 0 \quad , \tag{88}$$

with

$$\overline{\rho e} = \overline{\rho\ c_v\ T} + \tfrac{1}{2} \overline{\rho (u_1^2 + u_2^2 + u_3^2)} \tag{89}$$

and

$$\overline{p} = \overline{\rho\ R\ T} \tag{90}$$

At this level, it is convenient to introduce the density-weighted (or Favre [45]) filter $\widetilde{\ }$ defined, for a given variable ϕ, by

$$\widetilde{\phi} = \frac{\overline{\rho \phi}}{\overline{\rho}} \quad . \tag{91}$$

We then have

$$\overline{U} = {}^T(\overline{\rho}, \overline{\rho u_1}, \overline{\rho u_2}, \overline{\rho u_3}, \overline{\rho e}) \quad , \tag{92}$$

and the *resolved total energy*

$$\overline{\rho e} = \overline{\rho} \widetilde{e} = \overline{\rho}\ C_v\ \widetilde{T} + \tfrac{1}{2} \overline{\rho (u_1^2 + u_2^2 + u_3^2)} \quad . \tag{93}$$

The resolved fluxes $\overline{F_i}$ read

$$\overline{F_i} = \begin{pmatrix} \overline{\rho} \widetilde{u_i} \\ \overline{\rho u_i u_1} + \overline{p}\ \delta_{i1} - \overline{\mu S_{i1}} \\ \overline{\rho u_i u_2} + \overline{p}\ \delta_{i2} - \overline{\mu S_{i2}} \\ \overline{\rho u_i u_3} + \overline{p}\ \delta_{i3} - \overline{\mu S_{i3}} \\ \overline{(\rho e + p) u_i} \qquad - \overline{\mu S_{ij} u_j} - k \overline{\dfrac{\partial T}{\partial x}} \end{pmatrix} \quad , \tag{94}$$

with the filtered equation of state

$$\overline{p} = \overline{\rho} R \widetilde{T} \quad . \tag{95}$$

8.2 The simplest possible closure

The usual subgrid-stress tensor $\overline{\overline{\mathcal{T}}}$ of components

$$\mathcal{T}_{ij} = -\overline{\rho u_i u_j} + \overline{\rho} \widetilde{u}_i \widetilde{u}_j \tag{96}$$

is introduced and split into its isotropic and deviatoric parts, the latter being noted $\overline{\overline{\tau}}$:

$$\mathcal{T}_{ij} = \underbrace{\mathcal{T}_{ij} - \frac{1}{3} \mathcal{T}_{ll} \delta_{ij}}_{\tau_{ij}} + \frac{1}{3} \mathcal{T}_{ll} \delta_{ij} \quad . \tag{97}$$

Equations (94) and (93) then read

$$\overline{F_i} = \begin{pmatrix} \overline{\rho} \widetilde{u_i} \\ \overline{\rho} \widetilde{u_i} \widetilde{u_1} + (\overline{p} - \frac{1}{3} \mathcal{T}_{ll})\ \delta_{i1} - \tau_{i1} - \overline{\mu S_{i1}} \\ \overline{\rho} \widetilde{u_i} \widetilde{u_2} + (\overline{p} - \frac{1}{3} \mathcal{T}_{ll})\ \delta_{i2} - \tau_{i2} - \overline{\mu S_{i2}} \\ \overline{\rho} \widetilde{u_i} \widetilde{u_3} + (\overline{p} - \frac{1}{3} \mathcal{T}_{ll})\ \delta_{i3} - \tau_{i3} - \overline{\mu S_{i3}} \\ \overline{(\rho e + p) u_i} \qquad - \overline{\mu S_{ij} u_j} - k \overline{\dfrac{\partial T}{\partial x}} \end{pmatrix} \tag{98}$$

and

$$\overline{\rho}\widetilde{e} = \overline{\rho}\, C_v \widetilde{T} + \frac{1}{2}\overline{\rho}\,(\widetilde{u_1}^2 + \widetilde{u_2}^2 + \widetilde{u_3}^2) - \frac{1}{2}\mathcal{T}_{ll} \quad (99)$$

There are two options for the treatment of the uncomputable term $\mathcal{T}_{ll}$:

- simply neglect it, arguing as in [46] that it can be re-written as $\mathcal{T}_{ll} = \gamma M_{\rm sgs}^2 \overline{p}$, in which the *subgrid Mach number* $M_{\rm sgs}$ can be expected to be small when M_∞ is small.
- model it, as proposed by Yoshizawa [47], in a way which is consistent with the model chosen for $\overline{\overline{\tau}}$ (see *e.g.* [48]). Note that this was the initial choice of Erlebacher *et al.* [49].

We will here choose the first option, as in [50], bringing another argument: the incompressible LES formalism (see above in Chapter I), often introduces the *macro-pressure*

$$\varpi = \overline{p} - \frac{1}{3}\mathcal{T}_{ll} \quad . \quad (100)$$

It thus seems a good idea to re-write equation (99) as

$$\overline{\rho}\widetilde{e} = \overline{\rho}\, C_v \left(\widetilde{T} - \frac{1}{2C_v\overline{\rho}}\mathcal{T}_{ll}\right) + \frac{1}{2}\overline{\rho}\,(\widetilde{u_1}^2 + \widetilde{u_2}^2 + \widetilde{u_3}^2) \quad (101)$$

and introduce a *macro-temperature*

$$\vartheta = \widetilde{T} - \frac{1}{2C_v\overline{\rho}}\mathcal{T}_{ll} \quad , \quad (102)$$

computable out of $\overline{U}$ thanks to equation (101). The filtered equation of state (95) then reads

$$\begin{aligned} \varpi &= \overline{\rho} R \vartheta + \left(\frac{R}{2C_v} - \frac{1}{3}\right)\mathcal{T}_{ll} \\ &= \overline{\rho} R \vartheta + \frac{3\gamma - 5}{6}\,\mathcal{T}_{ll} \quad . \end{aligned} \quad (103)$$

Thus, for monoatomic gases like argon or helium (for which $\gamma \approx 5/3$), the contribution of $\mathcal{T}_{ll}$ to equation (103) is quite negligible whatever the Mach number, which makes ϖ computable in all cases. It is extremely tempting to generalize this to air (for which $\gamma \approx 1.4$) by assuming

$$\varpi \simeq \overline{\rho} R \vartheta \quad . \quad (104)$$

In other words, the first option amounts to assume $[(3\gamma-5)/6]\,\gamma M_{\rm sgs}^2 \ll 1$ in the equation of state only, which sounds slightly less stringent than assuming $\gamma M_{\rm sgs}^2 \ll 1$ everywhere.

Considering from now on ϖ computable, it is sensible to involve it in the definition of a subgrid heat-flux vector, noted $\boldsymbol{Q}$, of components

$$Q_i = -\overline{(\rho e + p)u_i} + (\overline{\rho}\widetilde{e} + \varpi)\widetilde{u}_i \quad . \quad (105)$$

Provided acceptable models are proposed for $\overline{\overline{T}}$ and $\boldsymbol{Q}$, the *resolved fluxes* already look more tractable:

$$\overline{F_i} = \begin{pmatrix} \overline{\rho}\widetilde{u}_i \\ \overline{\rho}\widetilde{u}_i\widetilde{u_1} + \varpi\,\delta_{i1} - \tau_{i1} - \overline{\mu S_{i1}} \\ \overline{\rho}\widetilde{u}_i\widetilde{u_2} + \varpi\,\delta_{i2} - \tau_{i2} - \overline{\mu S_{i2}} \\ \overline{\rho}\widetilde{u}_i\widetilde{u_3} + \varpi\,\delta_{i3} - \tau_{i3} - \overline{\mu S_{i3}} \\ (\overline{\rho}\widetilde{e} + \varpi)\widetilde{u}_i \quad - Q_i - \overline{\mu S_{ij} u_j} - k\overline{\dfrac{\partial T}{\partial x}} \end{pmatrix} \quad . \quad (106)$$

The remaining non-computable terms are viscous terms, which can be considered of less importance when the Reynolds number is sufficiently large. We therefore simply replace (106) by

$$\overline{F_i} \simeq \begin{pmatrix} \overline{\rho}\widetilde{u}_i \\ \overline{\rho}\widetilde{u}_i\widetilde{u_1} + \varpi\,\delta_{i1} - \tau_{i1} - \mu\widetilde{S_{i1}} \\ \overline{\rho}\widetilde{u}_i\widetilde{u_2} + \varpi\,\delta_{i2} - \tau_{i2} - \mu\widetilde{S_{i2}} \\ \overline{\rho}\widetilde{u}_i\widetilde{u_3} + \varpi\,\delta_{i3} - \tau_{i3} - \mu\widetilde{S_{i3}} \\ (\overline{\rho}\widetilde{e} + \varpi)\widetilde{u}_i \quad - Q_i - \mu\widetilde{S_{ij}}\,\widetilde{u}_j - k\dfrac{\partial \vartheta}{\partial x} \end{pmatrix} \quad , \quad (107)$$

in which μ and k are linked to ϑ through the Sutherland relation (85) and the constant Prandtl number assumption $Pr = C_p\mu(\vartheta)/k(\vartheta) = 0.7$.

The system is finally closed with the aid of variable-density eddy-viscosity and diffusivity models, in the form

$$\tau_{ij} \simeq \overline{\rho}\nu_t\widetilde{S_{ij}} \quad (108)$$

$$Q_i \simeq \overline{\rho}\,\frac{\nu_t}{Pr_t}\,\frac{\partial \vartheta}{\partial x_i} \quad , \quad (109)$$

expressions for $\nu_t(\widetilde{\boldsymbol{u}})$ and Pr_t used in the following compressible simulations correspond to the incompressible *structure-function model* and its *filtered* and *selective* extensions, with a constant turbulent Prandtl number 0.6.

9 EXTENSION TO CURVILINEAR CO-ORDINATES

When the domain is no longer cubic or parallelepipedic, it is still convenient to use body-fitted co-ordinates, that is, co-ordinates (ξ_1, ξ_2, ξ_3) such that each boundary of the domain corresponds either to constant ξ_1, ξ_2 or ξ_3. An appropriate grid generator can provide a set of vectors $\boldsymbol{\xi}$ which are the co-ordinates of the cell vertices or centres. Assume that the domain (hereafter refered to as "physical domain") can be remapped onto a cubic domain (called "computational") meshed with a uniform grid of spacing Δ as in the above sections. Let $\boldsymbol{x}$ be the co-ordinates of the cell vertices or centres of these cubic meshes. There exists a mapping function $\boldsymbol{h}$ such that

$$\boldsymbol{\xi} = \boldsymbol{h}(\boldsymbol{x}) \quad ; \quad \boldsymbol{x} = \boldsymbol{h}^{-1}(\boldsymbol{\xi}) \quad , \quad (110)$$

and characterized by its Jacobian

$$J = \det \begin{pmatrix} \frac{\partial \xi_1}{\partial x_1} & \frac{\partial \xi_1}{\partial x_2} & \frac{\partial \xi_1}{\partial x_3} \\ \frac{\partial \xi_2}{\partial x_1} & \frac{\partial \xi_2}{\partial x_2} & \frac{\partial \xi_2}{\partial x_3} \\ \frac{\partial \xi_3}{\partial x_1} & \frac{\partial \xi_3}{\partial x_2} & \frac{\partial \xi_3}{\partial x_3} \end{pmatrix} \quad , \qquad (111)$$

which satisfies

$$d\xi_1 d\xi_2 d\xi_3 = J dx_1 dx_2 dx_3 \quad . \qquad (112)$$

To each nodal variable $\phi(\boldsymbol{x})$ of the "computational" (*i.e.* cubic) domain corresponds a nodal variable $\psi(\boldsymbol{\xi})$ of "physical" domain, such that $\psi(\boldsymbol{\xi}) = \phi(\boldsymbol{x})$. Afterwards, the filter $\overline{}$ is applied onto ϕ It can then be proved that this new operator $\overline{}$, defined in the "physical" domain, commutes with the partial derivatives with respect to ξ_i up to second order (see *e.g.* Ghosal and Moin [51], who coinded the expression *Second-Order Commuting Filter*).

Straightforward application of the chain rule

$$\frac{\partial}{\partial x_i} = \frac{\partial}{\partial \xi_1}\frac{\partial \xi_1}{\partial x_i} + \frac{\partial}{\partial \xi_2}\frac{\partial \xi_2}{\partial x_i} + \frac{\partial}{\partial \xi_3}\frac{\partial \xi_3}{\partial x_i} \qquad (113)$$

to (88) yields, after some manipulations ([53], see also [54] or [55] for details),

$$\frac{\partial \hat{U}}{\partial t} + \frac{\partial \hat{F}}{\partial \xi_1} + \frac{\partial \hat{G}}{\partial \xi_2} + \frac{\partial \hat{H}}{\partial \xi_3} = 0 \quad , \qquad (114)$$

with

$$\begin{aligned} \hat{U} &= \overline{U}/J \\ \hat{F} &= \frac{1}{J}\left[\left(\frac{\partial \xi_1}{\partial x_1}\right)\overline{F_1} + \left(\frac{\partial \xi_1}{\partial x_2}\right)\overline{F_2} + \left(\frac{\partial \xi_1}{\partial x_3}\right)\overline{F_3}\right] \\ \hat{G} &= \frac{1}{J}\left[\left(\frac{\partial \xi_2}{\partial x_1}\right)\overline{F_1} + \left(\frac{\partial \xi_2}{\partial x_2}\right)\overline{F_2} + \left(\frac{\partial \xi_2}{\partial x_3}\right)\overline{F_3}\right] \\ \hat{H} &= \frac{1}{J}\left[\left(\frac{\partial \xi_3}{\partial x_1}\right)\overline{F_1} + \left(\frac{\partial \xi_3}{\partial x_2}\right)\overline{F_2} + \left(\frac{\partial \xi_3}{\partial x_3}\right)\overline{F_3}\right] \quad , \end{aligned} \qquad (115)$$

The chain rule has to be used again to express all the derivatives which arise in the fluxes $\hat{F}$, $\hat{G}$ and $\hat{H}$ (see section below). Note also that vector $\hat{U}$ is still a function of the cartesian co-ordinates x_i and time t.

10 NUMERICS

The system (114) is solved on this grid by means of a (2,4) extension of the fully-explicit McCormack scheme devised by Gottlieb and Turkel [52], in the form

$$\begin{aligned} \overline{U}^{(1)}_{i,j,k} &= \overline{U}^{n}_{i,j,k} \\ &\quad - J^{(p)}_{i,j,k} \left\{ \begin{array}{l} \frac{\Delta t}{\Delta \xi_1}\left[\frac{1}{6}\left(7\hat{F}^n_{i+1,j,k} - \hat{F}^n_{i+2,j,k}\right) - \frac{1}{6}\left(7\hat{F}^n_{i,j,k} - \hat{F}^n_{i+1,j,k}\right)\right] \\ + \frac{\Delta t}{\Delta \xi_2}\left[\frac{1}{6}\left(7\hat{G}^n_{i,j+1,k} - \hat{G}^n_{i,j+2,k}\right) - \frac{1}{6}\left(7\hat{G}^n_{i,j,k} - \hat{G}^n_{i,j+1,k}\right)\right] \\ + \frac{\Delta t}{\Delta x_3}\left[\frac{1}{6}\left(7\hat{H}^n_{i,j,k+1} - \hat{H}^n_{i,j,k+2}\right) - \frac{1}{6}\left(7\hat{H}^n_{i,j,k} - \hat{H}^n_{i,j,k+1}\right)\right] \end{array} \right\} \end{aligned} \qquad (116a)$$

$$\begin{aligned} \overline{U}^{n+1}_{i,j,k} &= \tfrac{1}{2}\left[\overline{U}^{(1)}_{i,j,k} + \overline{U}^{n}_{i,j,k}\right] \\ &\quad - \tfrac{1}{2} J^{(c)}_{i,j,k} \left\{ \begin{array}{l} \frac{\Delta t}{\Delta \xi_1}\left[\frac{1}{6}\left(7\hat{F}^{(1)}_{i,j,k} - \hat{F}^{(1)}_{i-1,j,k}\right) - \frac{1}{6}\left(7\hat{F}^{(1)}_{i-1,j,k} - \hat{F}^{(1)}_{i-2,j,k}\right)\right] \\ + \frac{\Delta t}{\Delta \xi_2}\left[\frac{1}{6}\left(7\hat{G}^{(1)}_{i,j,k} - \hat{G}^{(1)}_{i,j-1,k}\right) - \frac{1}{6}\left(7\hat{G}^{(1)}_{i,j-1,k} - \hat{G}^{(1)}_{i,j-2,k}\right)\right] \\ + \frac{\Delta t}{\Delta x_3}\left[\frac{1}{6}\left(7\hat{H}^{(1)}_{i,j,k} - \hat{H}^{(1)}_{i,j,k-1}\right) - \frac{1}{6}\left(\hat{H}^{(1)}_{i,j,k-1} - \hat{H}^{(1)}_{i,j,k-2}\right)\right] \end{array} \right\} \end{aligned} \qquad (116b)$$

As mentioned in [56] and recalled in [54], the metrics $\partial \xi_i / \partial x_j$ which arise in the fluxes and Jacobians above have to be discretized in such a way that unwanted cross-terms cancel out, otherwise the scheme is not consistent.

Firstly, they have to be expressed as analytic functions of the metrics $\partial x_\ell / \partial \xi_m$ of the inverse transform $\boldsymbol{h}^{-1}$, in order to eliminate all derivatives with respect to the x_i's. Secondly, the inverse metrics are discretized, the only 3-point stencil which works in the present case is

$$\left(\frac{\partial x_\ell}{\partial \xi_1}\right) = \left\{ \begin{array}{l} \dfrac{-\,x_{\ell_{i+2,j,k}} + 8\; x_{\ell_{i+1,j,k}} - 7\; x_{\ell_{i,j,k}}}{6\;\Delta \xi_1} \\ \text{in the predictor step (116a), and} \\ \\ \dfrac{7\; x_{\ell_{i,j,k}} - 8\; x_{\ell_{i-1,j,k}} + x_{\ell_{i-2,j,k}}}{6\;\Delta \xi_1} \\ \text{in the corrector step (116b)} \end{array} \right. \qquad (117)$$

This is only first-order accurate, and acceptable only when the grid is quasi-orthogonal (*i.e.* $\partial x_\ell / \partial \xi_m \approx \delta_{\ell m}$ almost everywhere). Otherwise, 5-point stencils at least have to be used.

In the same way, the chain rule (113) has to be applied to eliminate all derivatives with respect to x_1, x_2 and x_3 from the fluxes F_i. This introduces metrics to be evaluated as said above, together with derivatives of velocity and temperature with respect to ξ_1, ξ_2 and ξ_3. Consistency then determines the way these derivatives should be discretized.

10.1 boundary conditions

The boundary conditions are based on a decomposition into characteristics, in the spirit of Thompson ([57], [58]) and Poinsot and Lele ([59]). The Riemann invariants of outgoing characteritics are extrapolated, whereas the incoming ones are either prescribed (*e.g.* at the inflow boundary) or set to zero (*non-reflective* or *open* boundary condition). For example, going back to cartesian co-ordinates for the sake of simplicity, in the case of a boundary perpendicular to the direction x_1, the Euler equations are recast in their quasi-linear form

$$\frac{\partial V}{\partial t} + A \frac{\partial V}{\partial x_1} = 0, \text{ with } V = {}^T(\rho, \rho u_1, \rho u_2, \rho u_3, p) \quad . \tag{118}$$

The matrix A is, as per usual, diagonalized in the form $\Lambda = L^{-1}AL$. Assuming L to be locally constant and introducing the vector $W = LV$, system (118) decouples into 5 equations of the form

$$\frac{\partial w}{\partial t} + \lambda \frac{\partial w}{\partial x_1} = 0 \quad , \tag{119}$$

to be solved at the boundary point N through the semi-implicit scheme

$$\frac{w_N^{n+1} - w_N^n}{\Delta t} + \frac{\lambda_N^n + |\lambda_N^n|}{2} \left[\frac{w_N^{n+1} - w_{N-1}^{n+1}}{\Delta x_1} \right] + \frac{\lambda_N^n - |\lambda_N^n|}{2} \left[\frac{w_{N+1}^{n+1} - w_N^{n+1}}{\Delta x_1} \right] = 0 \quad . \tag{120}$$

For the outgoing characteristics ($\lambda_N^n > 0$), the values of w_N^{n+1} are obtained from that of λ_N^n, w_N^n and w_{N-1}^{n+1}, which are supposed to be known. For the incoming characteristics ($\lambda_N^n < 0$), it is necessary to prescribe w_{N+1}^{n+1} in order to pull out w_N^{n+1}. This is done by considering the nature of the boundary condition (adherence, free slip, periodicity, prescribed flow rate, non-reflectivity, inter-block matching...). V_N^{n+1} is finally deduced from W_N^{n+1} assuming simply $L_N^{n+1} = L_N^n$.

11 COMPRESSIBLE MIXING LAYERS

We quote here excerps of Ref. [3], with the permission of Kluwer academic publishers:

- Beginning of quotation:

Hypersonic-planes development have boosted research on free-shear or wall turbulent flows in supersonic or hypersonic conditions. Some of these studies might be easier numerically than experimentally. Since one-point closure modelling have some difficulties to capture the effects of Mach number on turbulence, these works should be done using direct or large-eddy numerical simulations(...).

In compressible mixing layers between two flows of parallel velocities U_1 and U_2 in unbounded domains, the relevant Mach numbers are the convective Mach numbers $M_c^{(1)}$ and $M_c^{(2)}$, built with the velocity difference of each layer with respect to U_c, the velocity of the large vortices [60], and respectively c_1 and c_2, the sound velocities in the two external flows. It can be shown, by assuming isentropy in the stagnation regions between the vortices, that

$$U_c = \frac{U_1 c_2 + U_2 c_1}{c_1 + c_2} \quad . \tag{121}$$

Then, within this assumption, the convective Mach numbers

$$M_c^{(1)} = \frac{U_1 - U_c}{c_1} \quad , \quad M_c^{(2)} = \frac{U_c - U_2}{c_2} \quad , \tag{122}$$

are both equal to

$$M_c = \frac{U_1 - U_2}{c_1 + c_2} = \frac{U}{\bar{c}} \quad , \tag{123}$$

where $2U$ is the velocity difference, and $\bar{c}$ an average speed of sound between the two layers. Note that Eq. (123) writes also as

$$U_c = U_1 \frac{1 + (U_2/U_1)\sqrt{\rho_2/\rho_1}}{1 + \sqrt{\rho_2/\rho_1}} \quad .$$

This expression allows to recover the value $U_c = (U_1 + U_2)/2$ in the incompressible uniform-density case. It may also be useful in an incompressible mixing layer with density differences, since it takes into account density effects which are not of gravitational type.

Returning to compressible mixing layers, laboratory experiments of [61] show that this hypothesis (identity of the two convective Mach numbers) is valid up to $M_c \approx 0.6$. Experiments show also a dramatic decrease of the spreading rate of the mixing layer, with respect to the incompressible value (...) between $M_c \approx 0.5$ and $M_c \approx 1$. What we call M_c is now the highest of the two convective Mach numbers. Above, it saturates at about 40% of the incompressible case (see Figure 16).

The inviscid linear-stability analysis of the compressible mixing layer in the temporal case was performed by [62][63] and [64]. The stability diagram found by the latter (for $\gamma = 1.4$) shows that the maximum-amplification rate is a decreasing function of the initial Mach number $M_c^{(i)} = U/\bar{c}$, with a drastic change in the slope at $M_c^{(i)} = 0.6$. Two-dimensional DNS of [65] show an inhibition of Kelvin-Helmholtz instability for $M_c^{(i)} > 0.6$: there is hardly any roll-up of the vortices, which remain extremely flat and merge "longitudinally", without turning around each other. On

Figure 16: experimental growth rate of the compressible mixing layer (normalized by the incompressible value) in terms of the largest convective Mach number (from Papamoschou and Roshko, 1988, courtesy J. Fluid Mech.)

the contrary, for $M_c^{(i)} \leq 0.6$, the roll-up and pairing occur qualitatively in the same fashion as in the incompressible case, although they are delayed by factors corresponding exactly to the amplification rates predicted by [64]. Another interesting characteristic feature in two dimensions is the occurrence of shocklets on the edge of the vortices at $M_c^{(i)} \approx 0.7 \sim 0.8$. (...) They are visible as discontinuities in the pressure field, and leave weak traces (may be of numerical origine) on the vorticity. They are exactly analogous to shocks arising on a transsonic wing, and due to the fact that the flow is accelerated on the side of the vortex and becomes locally supersonic. Similar results were found by [66][67] and [68]. This occurs both in the temporally and spatially-growing cases. It was however checked by [69] that at higher convective Mach number (still in 2D), these shocklets disappear, due to the very elongated character of the vortices.

A three-dimensional linear-stability analysis of the compressible temporal mixing layer was carried out by [70]. It turned out that oblique waves are more amplified than 2D waves when $M_c^{(i)}$ exceeds 0.6. Another result shown with the aid of DNS by [69] is that the helical pairing found in the incompressible case (with a 3D random forcing) is inhibitted above $M_c^{(i)} = 0.6 \approx 0.7$. The vortex structure of the mixing layer is then made of staggered Λ vortices, as shown in Figure 17-a, where the basic flow in the upper layer goes from top to bottom[11]. The corresponding pressure is displayed on Figure 17-b. It indicates a longitudinal reconnexion of pressure into tubes following the legs of the Λ's. This is an example where low pressure ceases to follow the coherent vortices.

Spatially-growing DNS of compressible mixing layers were also performed by [69]. Helical pairings was observed when the compressibility is low (upstream

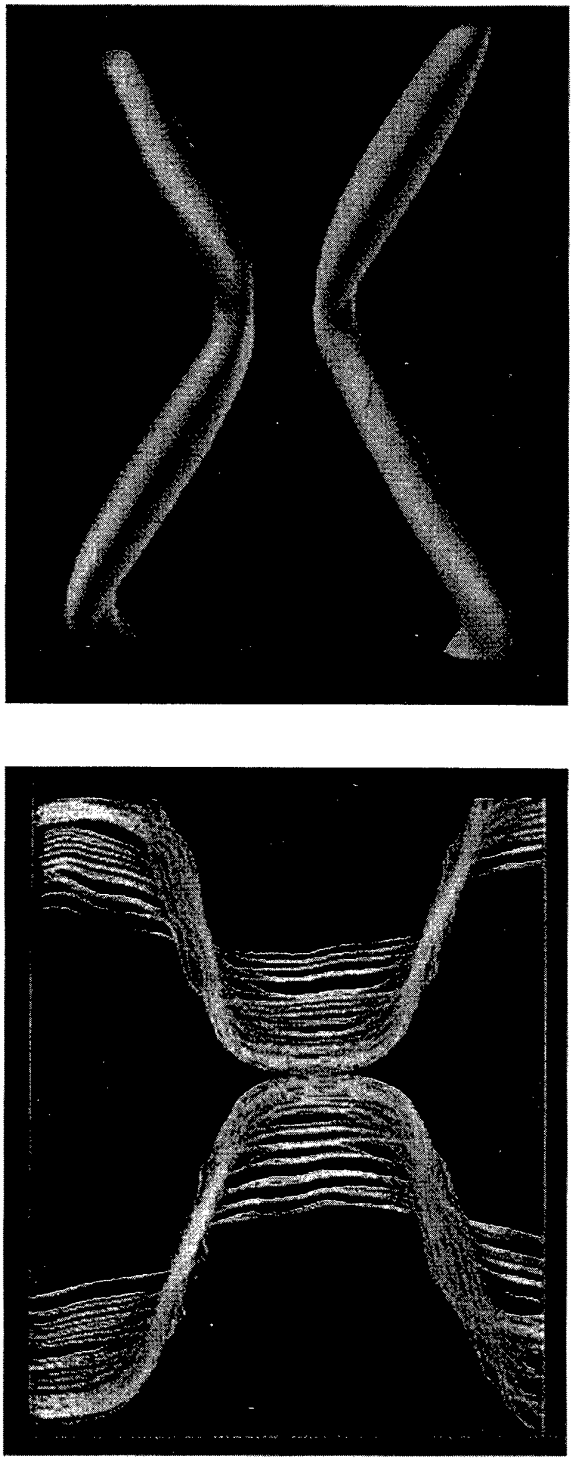

Figure 17: top view of vortex lines (a) and pressure (b) in the DNS of a compressible temporal mixing layer at convective Mach number 1 (from [69])

[11] The same structure was also found in the DNS of ([71]) with a quasi 2D initial forcing.

$M_c = 0.3$), as in the incompressible simulations presented above. At upstream $M_c = 0.7$ on the contrary, a pattern of very elongated staggered Λ vortices is obtained. The same pattern was found by [72] in a supersonic mixing layer confined between parallel planes. Notice that, to our knowledge, no compressible three-dimensional free mixing-layer simulation has ever shown shocklets at high convective Mach numbers.

The saturation in the spreading rates observed experimentally when M_c exceeds 0.6 might be due to two causes. The first one is the reflexion of Mach waves on the walls of the facility. The second is the inhibition of the Kelvin-Helmholtz instability at this cross-over convective Mach number 0.6. Such an inhibition may be physically explained as follows. We first consider an incompressible mixing-layer, where the vortex cores correspond to pressure troughs, while pressure highs are located in the stagnation regions. We assume now that compressibility is present, but is not too high so that the same type of pressure distribution is preserved. We suppose also that the fluid is a barotropic ideal gas, where p/ρ^γ is conserved with the motion. Therefore, fluid particles travelling from low to high pressures (...) will see their density increase when arriving at the stagnation points (which means convergence, that is, $D\rho/Dt > 0$ and $\vec{\nabla}.\vec{u} < 0$). Afterwards they will expand (..., $D\rho/Dt < 0$ and $\vec{\nabla}.\vec{u} > 0$). Let us now consider the vorticity equation (...), which reduces, in this compressible two-dimensional case, to

$$\frac{D}{Dt}\frac{\omega}{\rho} = \frac{1}{\rho^3}(\vec{\nabla}\rho \times \vec{\nabla}p).\vec{z} + \frac{\nu}{\rho}\nabla^2\omega \quad .$$

[68] and [69] have verified in their numerical simulations that the baroclinic and the viscous terms are negligible, so that the vorticity dynamics reduces to the conservation of the "potential vorticity" ω/ρ . Thus, the convergence and divergence zones will be respectively a source and a sink of vorticity. This will work against Kelvin-Helmholtz instability, which tends to diminish the vorticity at the stagnation points, and increase it in the low-pressure regions (...)

- Round jet:

We first recall the DNS of a weakly compressible periodic (in the flow direction) round jet done by [69] (see also[73]). The jet is initiated from a top-hat profile characteristic of the potential cone immediately downstream of the orifice. The initial Mach number based on the maximum velocity is 0.6, so that, from a mixing-layer point of view (...), the convective Mach number is approximately 0.3 and the flow is quasi-incompressible. A weak 3D random white-noise perturbation is superposed to the initial velocity. The computational grid is a rectangular mesh of resolution $64 \times 32 \times 32$. The initial Reynolds number based on the maximum velocity at the centre U_1 and the half-velocity radius R is of 2000.

The evolution of the simulation at various times is shown on Figure 18. One sees iso-surfaces of density[12] (core of the vortex) and low-pressure. At $t = 15R/U_1$, the instability is still not visible on the isopycnic surface. The isobaric surfaces are made of portions of tori of axis slightly inclined with respect to the streamwise direction. They reveal the emergence of an axisymmetric mode of vortex rings. This is compatible with the linear-stability theory which predicts that the axisymmetric mode is the most amplified in the potential cone ([74]), in good agreement with experiments ([75]). As time proceeds, the jet spreads out, and its shape factor decreases, the velocity profile becoming quasi-Gaussian. Then the low-pressure tori (or vortex rings) incline each other with respect to the axis in an alternate way, corresponding to the growth of oblique (or helical) modes in the linear-stability theory ([74]). Afterwards the tori reconnect (see Figure 18), giving rise to a double-helix structure, as one can check in particular at $t = 35R/U_1$. This is obviously the equivalent of helical pairings observed in the plane mixing layer. Then the jet breaks down very abruptly into turbulence, and one can check that the longitudinal kinetic-energy spectrum is close to the $k^{-5/3}$ Kolmogorov's law. However, the double-helix shaped coherent vortices persist. As in the mixing layer, this scenario of transition is reminiscent of the Ruelle-Takens route to turbulence, with emergence of a fundamental mode and growth of a subharmonic. Other DNS of the incompressible temporal round jet, where the white-noise perturbation is replaced by a deterministic sine oscillation in the azimuthal direction, show the formation of vortex rings, which stretch longitudinal hairpin vortex filaments between them[13]. These filaments have been very nicely visualized in laboratory experiments performed by [76]. Let us mention also the numerical simulations using vortex-filament methods done by [77][78], both in the case of azimuthal and helical perturbations. Three-dimensional LES of the incompressible spatially-growing round jet have been carried out by [79], using finite-difference volumes methods. The jet is forced upstream by a top-hat profile to which is superposed a weak 3D white noise ("natural forcing"). The Reynolds number is 2000. Figure 19 indicates the development of the same type of double-helix structure as in the above temporal case. It seems then that the preferred topology of the turbulent round jet forced "naturally" upstream is this double-helix, resulting from a sort of helical pairing of vortex rings.

- End of quotation

[12] Here, density is not a passive scalar, since the flow is compressible.

[13] This is exactly like in a plane mixing layer forced by a quasi two-dimensional perturbation

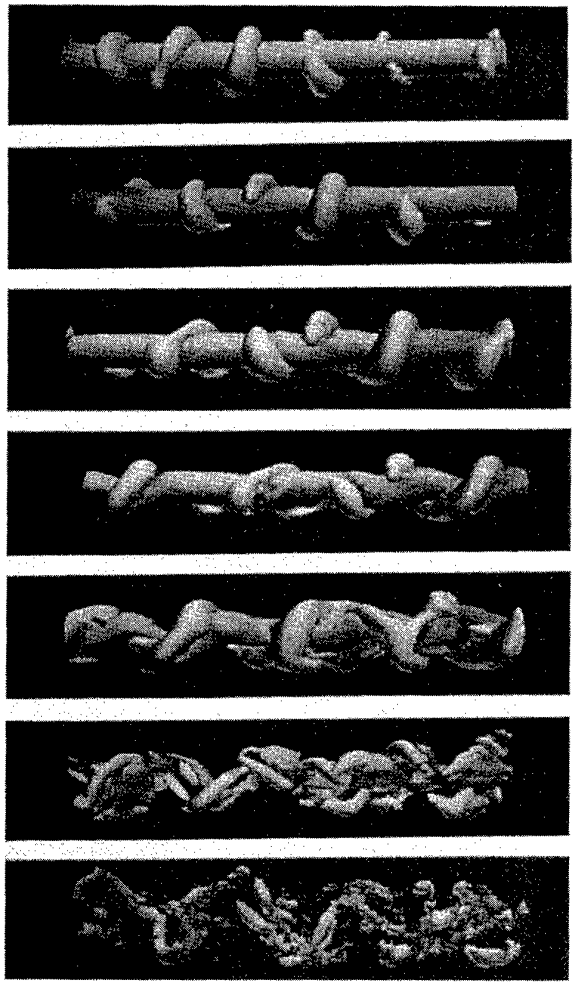

Figure 18: DNS of transition to turbulence in a weakly-compressible temporal round jet; time evolution at 15, 20, 25, 30, 35, 40 and 45 initial characteristic times R/U_1

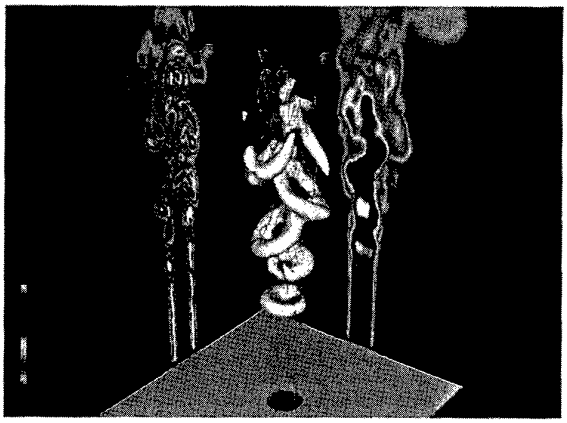

Figure 19: LES of an incompressible spatially-developing round jet forced naturally; low-pressure field (from [79])

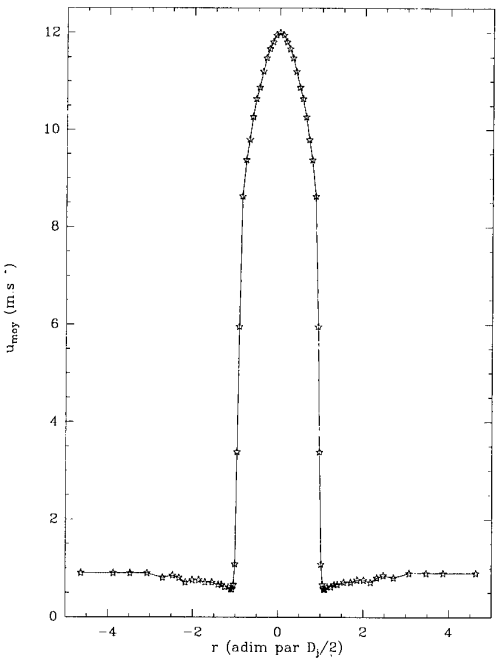

Figure 20: Experimental mean velocity profile of the incompressible round jet corresponding to figs 21 and 22. Notice the co-flow.

Using the same code as for the spatially-developing mixing layer presented in Chapter II, we have also carried out the LES of an incompressible round jet, in cartesian co-ordinates with the selective structure function model (72). Visualizations of two calculations are presented below: for Figures 21 and 22, the mean and fluctuation velocity profiles are taken from experimental results at $Re = 21000$ [80]. The fluctuations, which correspond to a fully-developed turbulent pipe flow of turbulent intensity 15%, are modeled by stochastic perturbations. Figures 23 and 24 correspond to a similar calculation, with upstream conditions akin to the "natural forcing" case in [79] which was presented earlier (p. 25). In both cases, double helices are observed, together with intense longitudinal vortices.

When the Mach number increases, it was found in the DNS of [69] that the jet rings become more and more elongated in the flow direction, and that compressibility delays strongly the various instabilities.

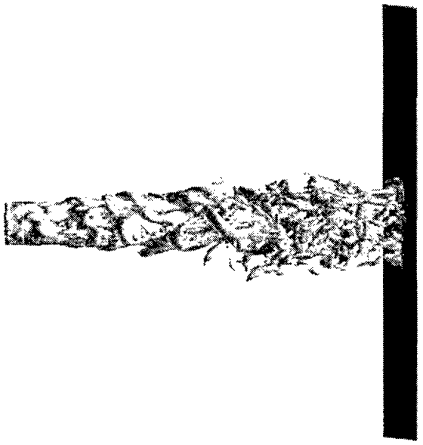

Figure 21: Incompressible round jet. Isosurface $\|\vec{\omega}\| = \omega_i/3$. The black surface showns the outlet of the computational domain.

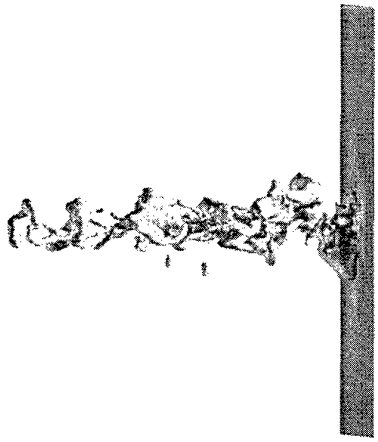

Figure 22: Isobaric surface (low pressure) corresponding to 21.

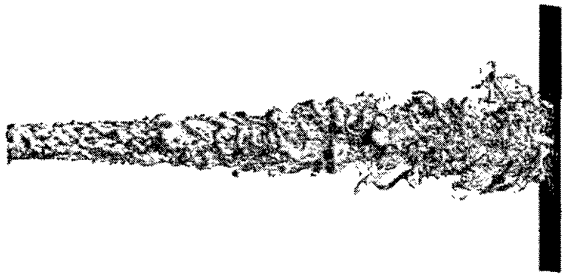

Figure 23: Weakly-perturbed counterpart of Figs.21 and 22. Isosurface $\|\vec{\omega}\| = \omega_i/2$.

Figure 24: Isobaric surface (low pressure) corresponding to 23.

12 TOWARD INDUSTRIAL APPLICATIONS : THE VORTEX SHEDDING INSIDE A SIMPLIFIED SOLID ROCKET ENGINE

We are participating in an operation set up by CNES and ONERA concerning the control of the vibrations induced by vortex shedding within the solid-propellant boosters of the European launcher ARIANE V. We show below preliminary simulations performed with the code described above, in a simplified planar test case, with the grid shown below (Fig. 25).

Figure 25: Grid of the C1 test case (length $L = 0.47m$, radius $H = 0.045m$, resolution 318×31 points

The step is made of burning propellant, at a flame temperature of 3387 K and a mass flow rate, normal to the walls, of 21.2 $kg/m^2/s$. Pressure $p = 4.66$ bar is prescribed at the upstream end. The outlet is a nozzle and the outflow boundary conditions are supersonic. The burnt gases are characterized by the following parameters: $\gamma = 1.14$, $R = 299.53$ $J/kg/K$, $\mu_{mol} = 9.\ 10^{-5}$ Pl et $Pr = 1$.

With such values, 2D simulations are not possible without flux limiters or artificial viscosities. With a viscosity 8 times as large, they become possible without such limiters, and Figure 26 shows the resulting vortices, in time evolution. In such a case, the code gives approximately the same results as the second-

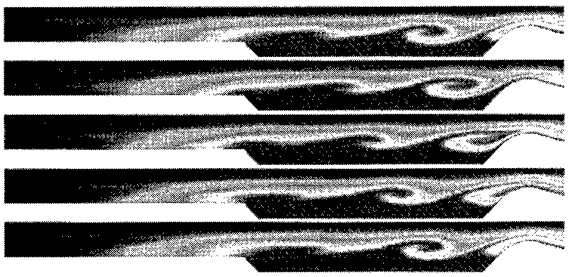

Figure 26: Contour maps of entropy at 5 equally spaced instants, in a low-Reynolds number 2D DNS.

order Mc Cormack code SIERRA of ONERA [81].

In 3D at the true viscosity and with the filtered structure function model described above, the advantages of the (2,4) scheme become evident. The following figures correspond to a LES at a spanwise resolution of 90 points equally spaced over the span $L_z = \pi\ H \approx 0.141\ m$, with periodic boundary conditions. The initial condition consists of the 2D flow shown above, taken at a given instant of the steady regime, with low-amplitude white noise (of amplitude 10^{-4} the speed of sound at the surface of the propellant) on all the components of $\vec{U}$. Without this perturbation, the flow would have remained 2D, which proves that the code is not "noisy". After having reached the steady regime, which took 50 hours of Cray 90 at 450 Mflops (corresponding to $8ms$ of real time), time series are recorded for $5ms$. Figure 27 shows an animation of an isosurface of the magnitude of the vorticity vector. Streamwise vortices are not only visible inbetween the large Kelvin-Helmholz billows, but also at the wall of the nozzle. These are likely to result from a Dean-Görtler instability of the detached boundary layer, which re-attaches in the convergent part of the nozzle (Fig. 28).

The statistics are in global agreement with the experimental data. In particular, we found kinetic energy and pressure spectra which exhibit a fundamental peak around 2500Hz, and its successive harmonics. More precisely, Figure 29 shows a comparison between the present LES and the 2D calculation just above. In the 3D case, the spectra are more developed, in particular in the low frequency, and the fundamental frequency is lower (2300Hz versus 2670). This proves that the streamwise vortices which periodically impinge the nozzle (as seen in Figure 27 affect and lower the shedding frequency of the quasi-2D Kelvin-Helmholtz billows. Although the reasons for this are not yet clear to us, this is of crucial importance for the design of the anti-vibration protections of the rocket's control systems, and illustrates the importance of taking three-dimensionality into account, even when the largest vortices are expected to be two-dimensional.

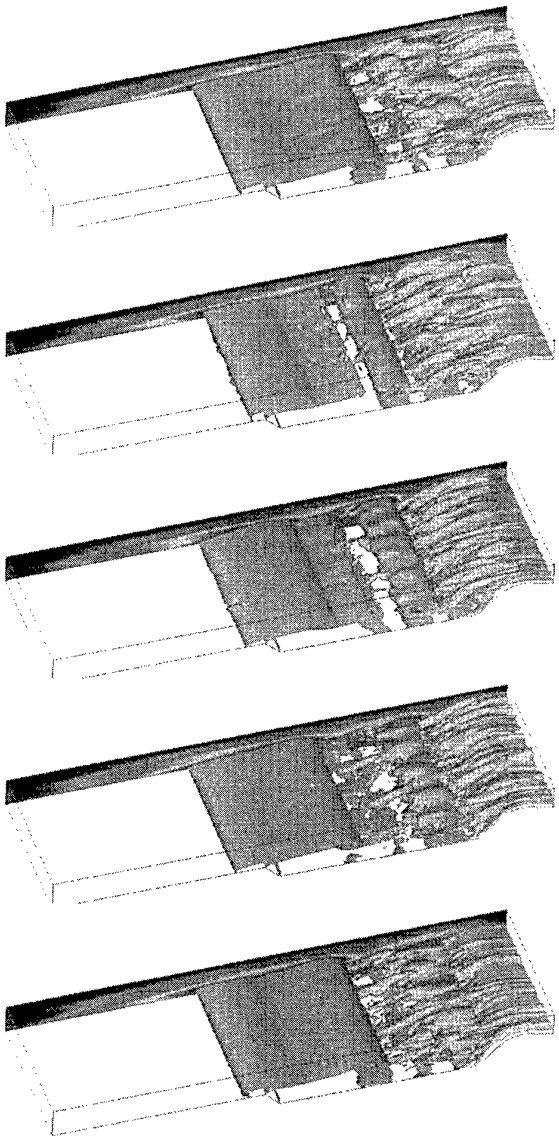

Figure 27: One period of the vortex shedding sequence in LES, in an "almost industrial" configuration.

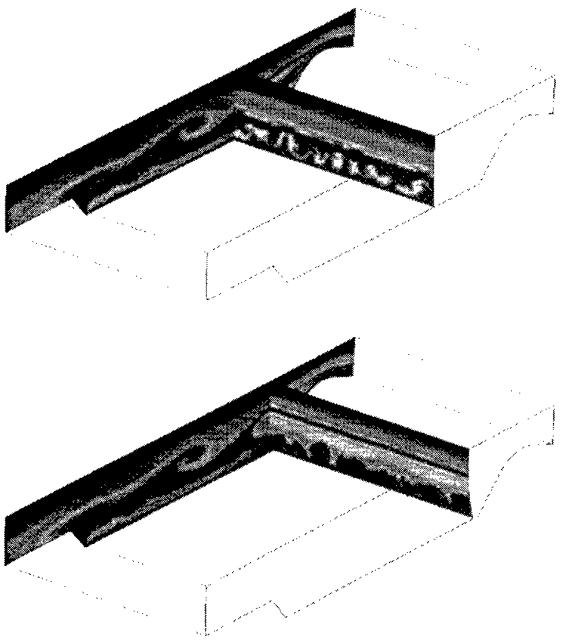

Figure 28: Maps of the entropy field. The top view shows a cross section of the Görtler vortices, the bottom one the streamwise vortices which connect the KH billows.

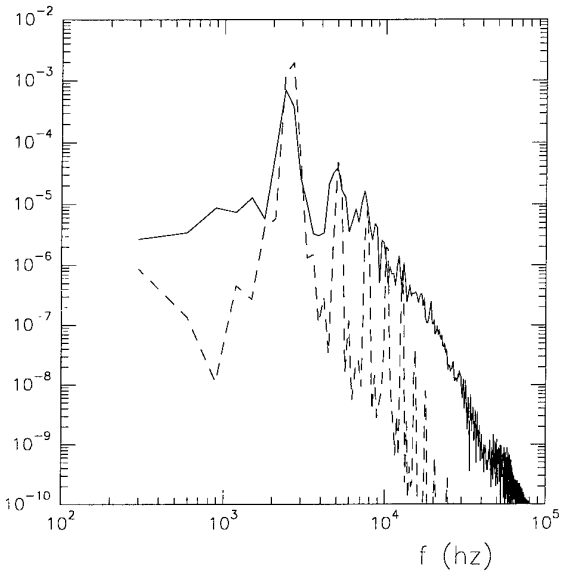

Figure 29: Temporal kinetic energy spectra recorded in the middle of the booster. The solid line corresponds to the LES and the dashed line to the 2D DNS.

Chapter III: Wall flows

13 COMPRESSIBLE BOUNDARY LAYERS ON A FLAT PLATE

13.1 LES of a spatially-developing boundary layer at Mach 0.5

A LES using the SSF model was carried out (see [29]) in a weakly-compressible case at $M_\infty = 0.5$, for an adiabatic plate. The flow upstream is the superposition of the laminar profile at this Mach, a two-dimensional pertubation forcing the most-amplified Tollmien-Schlichting mode, and a three-dimensional white noise of same amplitude. The upstream Reynolds number based on the displacement thickness is 1000. The resolution is $650 \times 32 \times 20$ in the streamwise, transverse and spanwise directions. It is seen how the TS wave generated upstream propagates downstream. First, quasi two-dimensional billows of relatively low pressure and high vorticity form, and travel with the wave velocity. A top view of the low pressure and longitudinal vorticity in the transitional region is shown on Figure 30: just before the transition, TS waves give rise to straight lower pressure quasi two-dimensional rolls. During the transition, these rolls evolve into a staggered pattern which breaks down into turbulence. Meanwhile, the longitudinal velocity seems to develop a longitudinal mode close to the wall, as shown on Figure 31. The existence of this mode might be related to the low and high-speed streaks existing in the developed region. We show now on Figure 32 an enlarged view of a hairpin ejected away from the wall above a low-speed streak, just after transition. Such hairpins have a longitudinal vorticity which is low in front of the spanwise vorticities attained at the wall under the high-speed streaks, where most of the drag comes from. Another remark is that we could never find in these calculations coherent alternate longitudinal vortices at the wall. On the contrary, there are several hairpins ejected above one single low-speed streak.

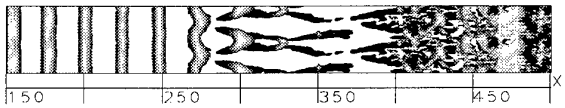

Figure 30: FSF structure-function based LES of a weakly-compressible spatially-developing boundary layer; isosurfaces of pressure ($p = 0.999p_\infty$, grey) and longitudinal vorticity ($\omega_1 = \pm 0.1 U_\infty \delta_i$, dark) are shown

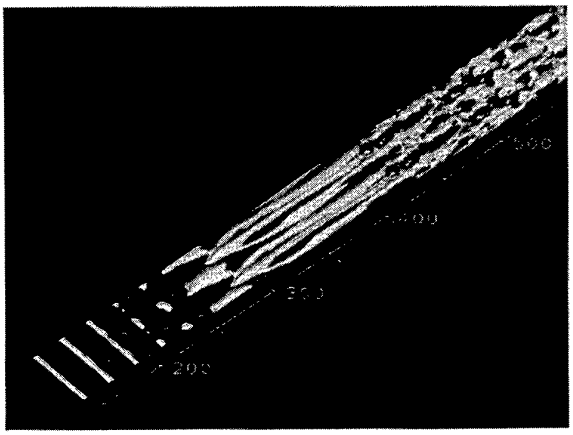

Figure 31: same calculation as Figure 30; isosurfaces of the longitudinal velocity fluctuations ($u_1' = 0.024 U_\infty$, grey)

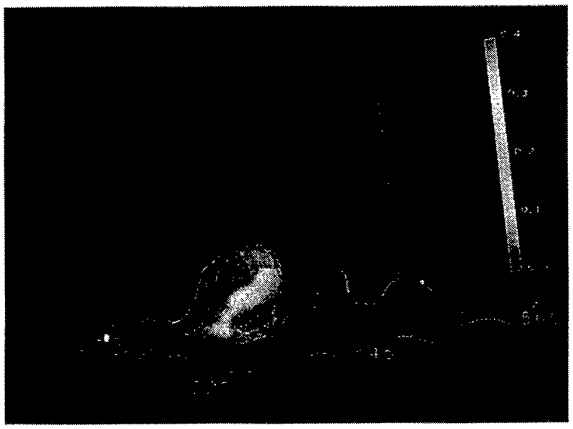

Figure 32: LES of the spatial boundary layer at Mach 0.5; vortex lines and low pressure characterizing a hairpin vortex ejected from the wall at the end of transition

Although it gives interesting informations as far as the structure of turbulence" is concerned, the FSF model is however not "perfect" for the prediction of average quantities. It overestimates in particular of about 15% the mean velocity in the logarithmic profile.

13.2 Temporal boundary layer at Mach 4.5

In odrer to advocate the straightforward closure of the compressible LES equations presented in section 8, we herefter present a temporal simulation of the transition to turbulence of a high-Mach number boundary layer over an adiabatic flat plate. The Mach and Reynolds numbers are $M_\infty = 4.5$ and $Re_{\delta_i} = 10000$ (δ_i denotes the initial displacement thickness), which matches a case which has been extensively investigated at ICASE (see *e.g.* Ng and Erlebacher [82]). For such a Mach number, the dominant instability is inviscid and two-dimensional

Figure 33: vorticity map after the growth of the second mode (the top part of the domain is not shown). The production of vorticity of both signs at the wall results from baroclinic effects induced by the reflexion of acoustic waves.

(Mack's second mode [83]), because the solution to the laminar similarity equations exhibit a generalized inflection point, *i.e.* a distance y_S to the wall where the local angular momentum $\rho\omega = \rho du/dy$ is maximum (in magnitude). Consequently, Kelvin-Helmholtz-like vortices of period $\lambda_a = 2.8\ \delta_i$ form around $y_S = 1.05\ \delta_i$, as shown below as the result of a 2D simulation initialized by the laminar similarity solution for a wall temperature $T_w = 180K$, perturbed by small-amplitude white noise. The domain's size is $L_x = 4\ \lambda_a = 11\ \delta_i$ and $L_y = 20\ \delta_i$ for a resolution $40 \times 70 \times 36$, most of the points are concentrated between the wall and y_S, the first mesh line away from the wall is at $y = 0.024\ \delta_i$.

A 3D DNS and a LES with the *structure-function model* in its four-neighbour formulation (see again [4] or [3]) are now performed, in a smaller domain $L_x = 2\ \lambda_a = 5.5\ \delta_i$, $L_y = 7.15\ \delta_i$ and $L_z = 6.28\ \delta_i$ (the preferential wavelength of the subharmonic mode of secondary instability found in [82]), with the resolution $40 \times 70 \times 36$. Both runs start from the same initial conditions: the fluctuations at the same timestep as for figure 33 are rescaled to an amplitude $A = 8\%$ of U_∞ and sprinkled with 3D white noise of amplitude $10^{-4}\ U_\infty$. The DNS blows up at $t = 390\ \delta_i/U_\infty$, but the LES continues further. We stopped it at $t = 450\ \delta_i/U_\infty$, after transition is completed. Figure 34 shows the time evolution of the prominent modes. Mack's second mode then appears as $(2,0)$ and the oblique subharmonic of [82] as $(1,1)$. Notice in particular that both the DNS and the LES give about the same growth rate for this mode, *viz.*, $\approx 1.7\ 10^{-2} U_\infty/\delta_i$, which is in acceptable agreement with Ng and Erlebacher [82] who find $2.5\ 10^{-2} U/\delta_i$ for $A = 6\%$. However, the most interesting fact is the resonance of the x-independent (*i.e.* purely spanwise) mode (0,2), which shoots up as from $200\delta_i/U_\infty$.

Until $t \approx 350\ \delta_i/U_\infty$ (the time origin is the beginning of the 3D calculations), this resonance appears essentially in the form of streks of weak vorticity normal to the wall ($\omega_y \approx \pm 0.03 U_\infty/\delta_i$, see Figure 6 of [26]), which supports its interpretation in terms of Squire modes. The vortical structure of the flow remains

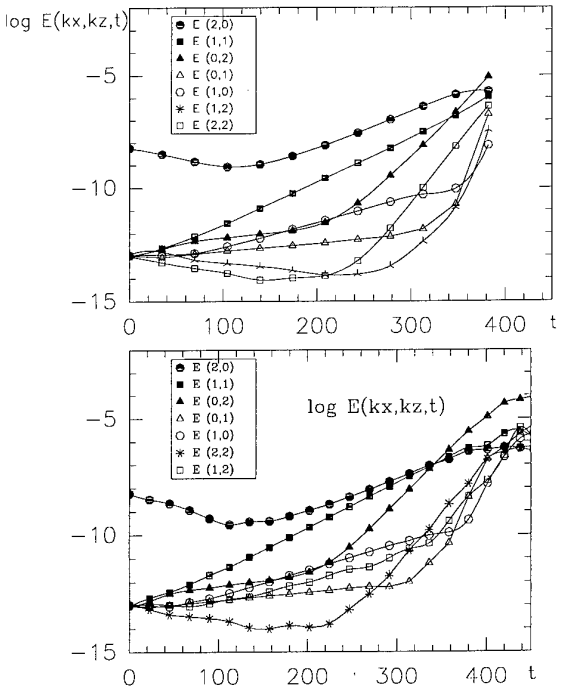

Figure 34: Energy of the prominent modes for the DNS (top) and the LES (bottom).

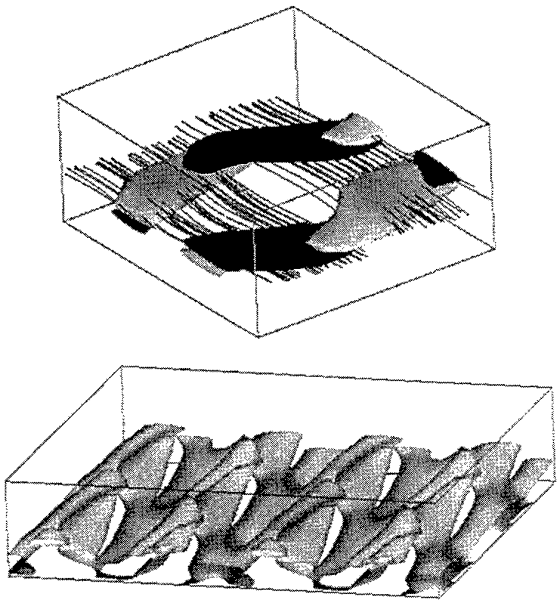

Figure 35: ***top:*** *Vortex lines at $t = 350\ \delta_i/U_\infty$, with the isosurfaces $\omega_x = 0.1 U_\infty/\delta_i$ in clear and $\omega_x = -0.1 U_\infty/\delta_i$ in dark.*
bottom: *Isosurface of spanwise vorticity $\omega_z = -U_\infty/\delta_i$, still at $t = 350\ \delta_i/U_\infty$. In order to increase the resemblance with Fig. 11 of [84], the domain is instanced twice thanks to spanwise periodicity.*

dominated by Kelvin-Helmholtz-like vortices at y_S, slowly going three-dimensional as mixing layers at $M_c \approx 1$ ([71], [73], [69]), in the form of Λ-vortices facing each other; The left plot of figure 35 shows the most intense vortex lines together with isosurfaces of streamwise vorticity ω_x. Another representation of the flow at the same instant is given in the right plot: from isosurfaces of spanwise vorticity (or vorticity norm), one can make out staggered Λ-vortices stretched into *Y-layers*, as proposed by Adams and Kleiser [84] (see also [85]). Both views show the DNS results, but the LES ones are almost identical.

This is only the beginning of the transition process: at $t = 390\ \delta_i/U_\infty$, when the DNS blows up because of the onset of small-scale turbulence, the LES shows the skin-friction coefficient lifting off (from $0.5\ 10^{-3}$ up to $3.8\ 10^{-3}$) while the shape factor H_{12} decreases from 14.5 down to 9.5, as expected from the empirical formula proposed in [86]

$$H_{12} = H_{inc} + 0.4\ M_\infty^2 + 1.222\ \frac{T_w - T_{ad}}{T_\infty} \quad , \quad (124)$$

in which $H_{inc} = 1.4$ denotes the incompressible counterpart of H_{12} and T_{ad} the adiabatic recovery temperature at the wall, equal to the wall temperature $T_w = 180K$ in our case.

After transition, the flow pattern is too messy to render properly with vortex lines in black and white. However, just at the beginning of it, *i.e.* $t \approx 400\ \delta_i/U_\infty$, a fairly well organized streaky pattern is observed at the wall (figure 36), which can be interpreted as the result of the temporary emergence of mode (0,2). Later on, some of this organization persists, with a striking resemblence with incompressible boundary layers (see *e.g.* [29]). In particular, the velocity profile after transition exhibits a logarithmic zone which is not very different from its incompressible counterpart (not shown here).

Finally, figure 37 shows the instantaneous Reynolds stress profiles $\langle\rho\rangle\langle u'u'\rangle(y,t)$ and $\langle\rho\rangle\langle u'v'\rangle(y,t)$ normalized by $\rho_\infty U_\infty^2$, in which $\langle\rangle$ denotes the streamwise and spanwise average over the box. $\langle\rho\rangle\langle u'u'\rangle$ remains about 4 times as large as $\langle\rho\rangle\langle u'v'\rangle$. During the laminar stage (*i.e.* up to $t \approx 370\ \delta_i/U_\infty$), the curves grow almost self-similarly with a peak around y_S. Between 360 and 420 δ_i/U_∞, the peak of $\langle\rho\rangle\langle u'u'\rangle$ gets more and more acute. Meanwhile, it shifts towards the wall and settles down at about $y \approx 0.2\ \delta_i \approx 10$ wall units. In contrast, the profile of $\langle\rho\rangle\langle u'v'\rangle$ flattens in time with no visible shift towards the wall.

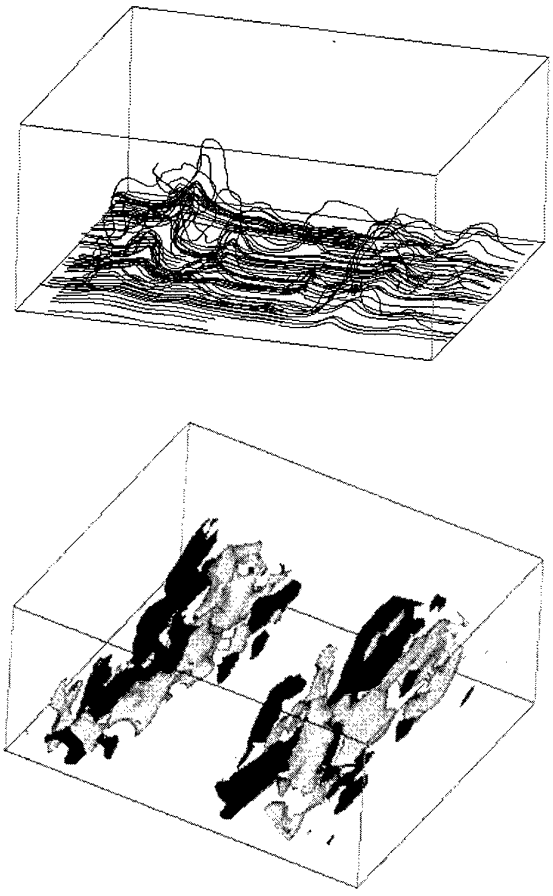

Figure 36: ***top:*** *Vortex lines at* $t = 390\ \delta_i/U_\infty$. ***bottom:*** *Corresponding isosurfaces of vorticity normal to the wall* $\omega_y = 0.7\ U_\infty/\delta_i$ *in clear and* $\omega_y = -0.7U_\infty/\delta_i$ *in dark.*

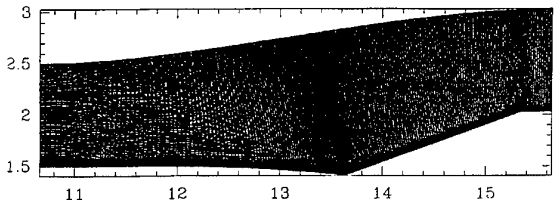

Figure 38: Transverse section of the $220 \times 140 \times 25$ *– point grid used for the simulation of the transition on a the curved ramp (angle* $20°$*). The axes are graded in metres, counted from the nose of the full-size shuttle. The spanwise size of the domain is* 4.5 *the displacement thickness* δ_i *of the boundary layer prescribed at the upstream boundary.*

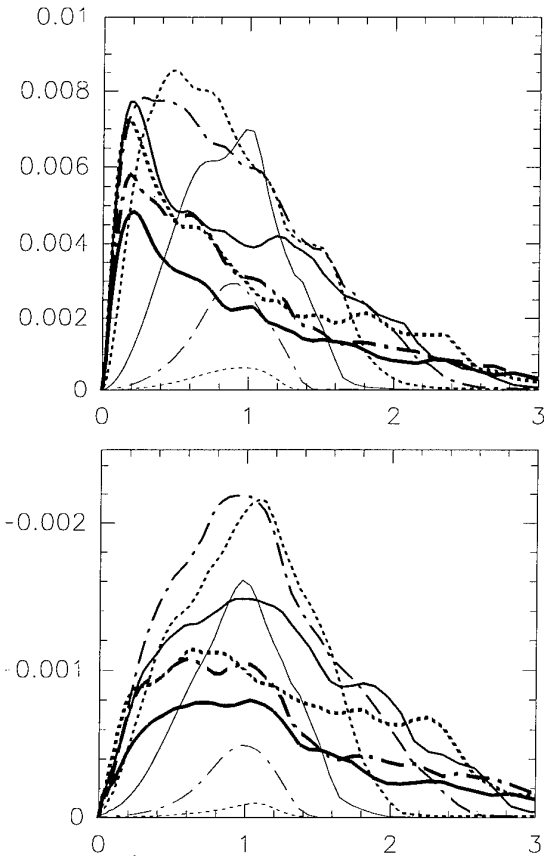

Figure 37: Time evolution of the Reynolds stress between 350 *and* 450 δ_i/U_∞*. The heavier the line the later.* ***top:*** $\langle\rho\rangle\langle u'u'\rangle(y,t)/(\rho_\infty U_\infty^2)$ ***bottom:*** $\langle\rho\rangle\langle u'v'\rangle(y,t)(\rho_\infty U_\infty^2)$.

14 GORTLER VORTICES OVER A CURVED COMPRESSION RAMP

The simulation presented above can be considered as a validation of our numerics and SGS model. It showed in particular the ability of the code to reproduce the effect of strong heating on Reynolds stresses. It thus can be considered as a suitable tool for prediction of heat fluxes in situations for which experimental data are absent or sparse. We therefore present a preliminary simulation of the detached boundary layer over a curved compression ramp at Mach 2.5 modelling the wind-side region of the body-flap of HERMES during its projected re-entry. The external Mach number relevant to the shuttle is about 10 (altitude 50 km, incidence 30°, flap extension angle $\alpha_0 = 20°$). The whole computational domain is contained within the bow shock. The grid used is shown, upside down, in 38. The resolution is $220 \times 140 \times 25 = 770\,000$ grid points. The first part of the boundary (up to $13.6m$ away from the nose) is curved. It corresponds to the wind side of the body. The ramp corresponds to the body flap, assumed to be flat. For computational reasons, it is prolonged by a fictitious horizontal surface introducing a cut-off with the lee-side of the flap and the after-body. This enables the prescription of well-posed boundary conditions at the exit of the domain.

By constrast with the wedge simulation presented before, the present simulation requires knowledge of the density, temperature and velocity profiles at the upstream boundary of the domain. Since these are not available for in-flight conditions, we simulate a well-documented 1/90 experiment performed at ONERA in the wind tunnel R3CH. Our upstream condition results from the experimental profiles plotted in Fig. 39, with white noise of amplitude $2\ 10^{-3}\ U_\infty$ superimposed onto the 3 components of the velocity at each time step.

On the model, the wall temperature is $T_w = 290K$ and the "external" (outside of the boundary layer,

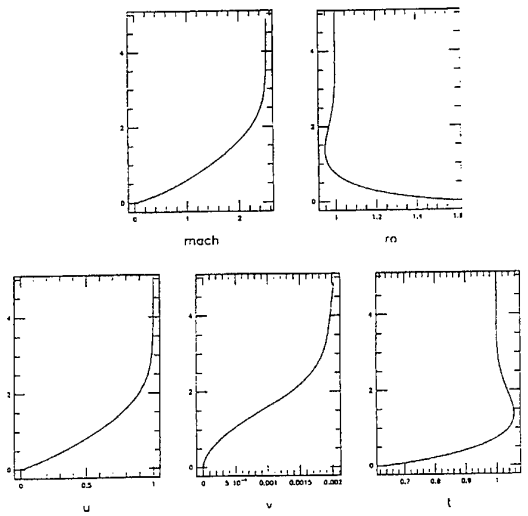

Figure 39: Profiles prescribed at the upstream boundary (Mach number and normalized density ρ/ρ_∞ on top, streamwise and transverse normalized velocity components u/U_∞, v/U_∞, and normalized temperature T/T_∞ at the bottom). For all plots, the vertical co-ordinate is ξ_2/δ_i. For the 1/90 experiment, $\rho_\infty = 7.685\ 10^{-2} kg/m^3$, $U_\infty = 1089 m/s$ and $T_\infty = 460.3K$.

but inside the bow shock) temperature is $T_\infty = 460K$. The adiabatic recovery temperature, defined by

$$T_{ad} = T_\infty \left(1 + \sqrt{Pr}\ \frac{\gamma - 1}{2}\ M_\infty^2\right) \quad , \qquad (125)$$

is $T_{ad} = 1047K$, yielding $T_w/T_{ad} = 0.277$. The ramp is therefore very cool with respect to the fluid, which models the radiative balance of the true shuttle during its re-entry.

The upstream displacement thickness of the boundary layer measured is $\delta_1 = 0.21\ 10^{-3} m$, yielding a Reynolds number $Re_{\delta_1} = 727$. This is too much for the code described here[14] The simulation is therefore performed at the maximal Reynolds number permitted by our resolution, that is $Re_{\delta_1} = 280$. For this reason, the results presented below have to be considered as qualitative only. One also have to bear in mind that the similitude between the experiment and the in-flight conditions cannot be exact (if the Mach and Stanton numbers are in similitude, it is extremely unlikely that the Reynolds numbers also are.)

Fig. 40 shows the detachment of the boundary layer and its re-attachment onto the flap obtained from a preliminary 2D simulation. One sees clearly the multiple-legged Λ-shock focalizing outside the domain. Its position fluctuates in time, due to the large vortices in the recirculation zone around the hinge.

However, the most interesting feature of the flow is

[14] Limiters have recently been implemented into this code. They seem to have solved the problem.

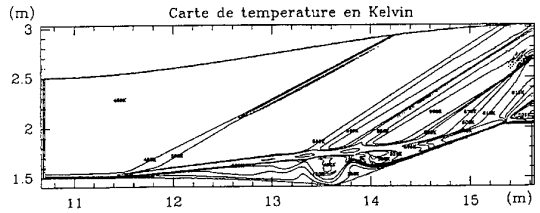

Figure 40: Instantaneous temperature map obtained from a preliminary 2D simulation of the flow over the curved ramp. Here again, the axes correspond to the full-size shuttle, whereas it is the 1/90 experiment which is actually simulated.

not reproduced in this 2D simulation: between its detachment and re-attachment, the boundary layer undergoes a certain curvature, whose radius R can be roughly estimated from Fig. 40. This yields a Görtler number

$$\mathcal{G} = Re_{\delta_i} \sqrt{\frac{\delta_i}{R}} \approx 2 - 3 \quad , \qquad (126)$$

high enough to give rise to centrifugal instability, according to the linear stability theory (see Ref. [87] for a review).

Experimental evidence of (streamwise counter-rotating) Görtler vortices in a similar case was brought in particular by [88], but the consequence of these vortices on the wall heat flux has remained an open question. Fig. 41 shows such Görtler vortices, obtained from a 3D simulation performed with the selective structure-function model in a domain of spanwise extension equal to 4.5 δ_i. One clearly sees two large structures, cross-cuts of which (Fig. 42) show that each of them corresponds to a pair of counter-rotating Görtler vortices.

The extreme values of the temperature fluctuations plotted in Fig. 42 are $\pm 90K$. They are found close to the wall, which is at $T_w = 290K$. These 30% of temperature fluctuations induce huge fluctuations of the Stanton number (Fig. 43), between $2\ 10^{-3}$ and $14\ 10^{-3}$, with an average of about $6\ 10^{-3}$. The *r.m.s.* of the Stanton-number fluctuations is thus 133%. The same trend is observed for the skin-friction coefficient C_f, which remains approximately proportional to St as predicted by the strong Reynolds analogy. An analogy factor $\bar{s} = \overline{St}/2\overline{C_f} \approx 2.9$ can be (quite roughly) estimated from the mean values of St and C_f. More precisely, The minima of C_f and St are located at $\xi_3 = 0.1 \equiv 0.5$ (owing to spanwise periodicity), with a secondary minimum at $0.3m$ (coordinates relevant to the full-size shuttle. They have to be divided by 90 to correspond to what is actually simulated, *i.e.* the model.). These minima are associated to the uplift of slow and cold fluid from the boundary which occurs in between each pair of couter-rotating vortices (as sketched in Fig. 44).

Conversely, maximal values of C_f and St are found at $\xi_3 = 0.2$ and $0.4m$, that is half-way in between the

Figure 41: Ramp flow. Zoom on the hinge and body-flap region showing an isosurface of the vorticity magnitude. This surface is coloured by temperature. This shows clearly that hot fluid in the outer part of the boundary layer is being downwashed to the wall, which brings about wall-heat-flux fluctuations.

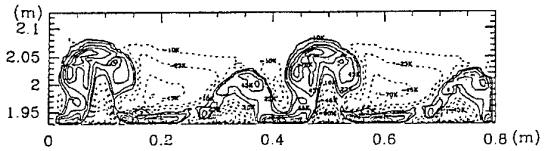

Figure 42: Ramp flow. Spanwise slice of instantaneous temperature fluctuations (with respect to the time-average). The slice is repeated twice in the spanwise directions, which is permitted by the periodic boundary conditions and makes the vortex structure easier to understand. Here again, the graduations are relevant to the full-size shuttle.

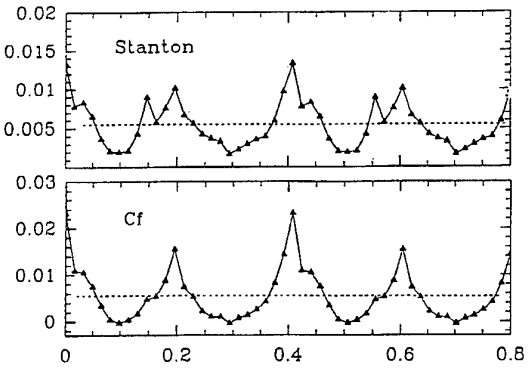

Figure 43: Instantaneous profiles of Stanton number St (top) and skin-friction coefficient C_f (bottom), to be correlated with Fig. 42.

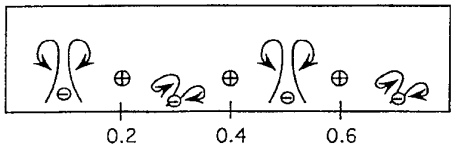

Figure 44: Sketch of the vertical motion induced by the Görtler vortices and its consequences on St and C_f, symbols $\oplus$ meaning high St and C_f because of downwashing of hot fluid. Symbols $\ominus$ represent low St and C_f because of upfilt of cool fluid.

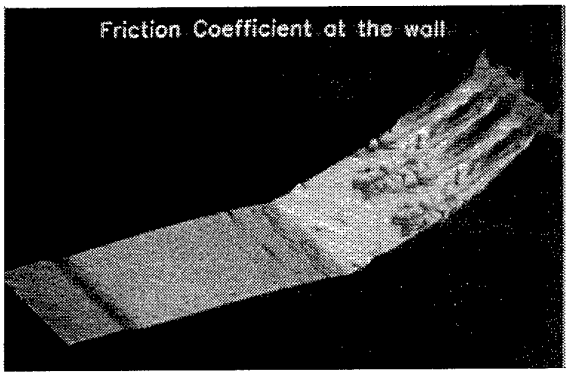

Figure 45: Ramp simulation. Instantaneous contours (with elevation) of the Stanton number St showing the streamwise alignment of the extrema. This picture is very stable in time, because the Görtler vortices are phase-locked.

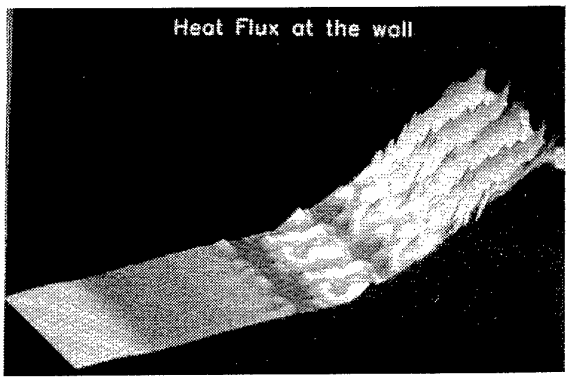

Figure 46: Counterpart of Fig. 45 for the skin-friction coefficient Cf.

two pairs, where the downwash of hot (and fast) fluid from the outer part of the layer is maximal. If one tries to work out analogy factors associated to the peak and valleys of C_f and St, one finds $s_{max} = 1.1$ and $s_{min} \longrightarrow \infty$ respectively (because C_f goes to zero). This clearly shows that the strong Reynolds analogy, although globally satisfied, cannot be relied upon to deduce local Stanton numbers out of local values of the skin-friction coefficient. Finally, the elevated contour-maps of C_f and St shown in Figs. 45 and 46 prove that the values above – recorded from an instantaneous cross-section of the flow – are almost independent of the streamwise co-ordinate ξ_1. Time-averaged plots (not shown here) also prove that the Görtler vortices are, in this simulation, fairly stable in time. This is likely to enhance considerably their destructive effects on the material of the body flap.

15 CONCLUSION

We have presented the general framework of large-eddy simulations (LES), where subgridscale motions are filtered out, their effect being represented by eddy-viscosity and eddy-diffusivity coefficients in the

supergrid-scale motions. We have discussed the unpredictability issue associated to the LES formalism, and shown that, in three dimensions, one could expect a linear growth of the error, instead of the exponential growth obtained in dynamical systems with a low number of degrees of freedom. We have described Smagorinsky's model, which is the most-widely used for engineering applications. Afterwards, we have considered a different point of view, where the filtering is a sharp low-pass filter in Fourier space. We have presented Kraichnan's spectral eddy viscosity, which permits to avoid the assumption of separation of scales done in physical space in order to justify the eddy viscosity concept. We have introduced also the spectral eddy diffusivity. We have demonstrated, using the nonlocal interaction theory applied to a stochastic model of isotropic turbulence, how a k^4 backscatter arises in three dimensions, with a k^3 equivalent in two dimensions. We have confirmed the existence of such a spectral backscatter in large-eddy simulations. We have also presented the spectral-dynamic model, which is a generalization of the spectral eddy coefficients allowing to deal with laminar and transitional situations, and more generally when the kinetic energy spectrum at the cut-off decays faster than Kolmogorov law. Returning to physical space, we have reinterpreted these models in terms of velocity-structure functions and generalized hyperviscosity models.

We have applied the spectral-dynamic model to the turbulent channel flow at a subcritical ($h^+ = 204$) and supercritical ($h^+ = 389$) wall Reynolds number. In the two cases, the results are in excellent agreement with experiments and direct-numerical simulations. Compared with the latter at same Reynolds number, the LES reduces the computational cost by a factor of the order of hundred.

We have applied the selective structure-function model to a temporal and spatially-growing mixing layer. Depending upon the quasi two-dimensional or three-dimensional character of the initial or upstream weak perturbation, whe have shown how the flow could bifurcate from a quasi two-dimensional state (where longitudinal hairpins are stretched between the Kelvin-Helmholtz vortices) to a helical-pairing configuration of dislocated vortices. In the former case, consideration of the vorticity equation permits to show how the vorticity is stretched in the direction of the first principal axis of deformation. A convected scalar gradient, on the contrary, is reduced in this direction, and intensified across the interface. Returning to the hairpin stretching, we have found in the spatially-growing case that two longitudinal vortices may merge.

We have extended the LES formalism to compressible flows in Cartesian and curvilinear co-ordinates. Despite the evident crudity of some approximations made, informative results have been obtained both in academic an applied situations. We have looked at compressible mixing layers, and shown that the helical pairing disappears above a convective Mach number of $0.6 \approx 0.7$. For a weakly compressible remporal jet, one recovers the equivalent of the helical pairing, in the form of alternate pairings of vortices. The same phenomenon is found for an incompressible spatially-developing jet. In the more applied situation of a transonic mixing layer forced by acoustic modes (the case of the planar model booster), LES have contributed to the improvement of the understanding of the mechanism of vortex shedding. We have shown in particular that quasi two-dimensional Kelvin-Helmholtz vortices stretch intense longitudinal alternate vortices. The latter seem to be amplified by Görtler instability before impinging the nozzle. This has important consequences on the pressure (and thrust) fluctuation spectra, with a lowering of the dominant spatial mode.

We have also simulated the complete transition to turbulence of a boundary layer developing above a flat plate at Mach 0.5. Interesting informations were obtained concerning the physics of high and low-speed streaks at the wall, and weak hairpin vortices ejected above the latter. Here, compressibility effects do not seem to be very important. Afterwards, we have simulated the transition to turbulence in a temporal boundary layer above a flat plate at Mach 4.5. Results are in good agreement with experimental and numerical linear stability analyses in the linear regime (growth rate and phase speed of the second mode and the dominant mode of secondary instability) and experimental results in the turbulent regime (shape factor, log law, Reynolds stresses). LES are here an economic way to go beyond transition. We have shown how the end of the transition period is dominated by the growth of the (0,2) mode at the wall. Later on, the turbulence collapes on the wall, and the structure of the resulting boundary layer is not much different from an incompressible one.

Finally, numerical evidence of phase-locked Görtler vortices on the body flap of a model HERMES has been obtained, with drastic consequences on the thermal erosion of the surface. Although the conditions of the re-entry are not fully accounted for in the simulation, it is shown that LES are able to reproduce satisfactorily, at least at a qualitative level, such complex phenomena as the interaction between an oblique shock, a recirculation zone and intense three-dimensional vortices.

16 Aknowledgements

The results presented here have been obtained by E. David [27], F. Ducros [28], E. Lamballais [18] and J.

Silvestrini [32]) during their PhD's in Grenoble. We are indebted to P. Begou for the computational support. Most of the computating time used for the 3D calculations has been freely allocated by IDRIS, the CNRS computing center. The study of the vortex shedding in the boosters of Ariane V is under the CNES/ ONERA contract $n°$ 22.492/DA/A1.CC1. That of the Görtler vortices on HERMES was sponsored by CNES/Dassault Aviation.

Marcel Lesieur is supported by IUF.

References

[1] J. Smagorinsky, General circulation experiments with the primitive equations. *Mon. Weath. Rev.* 91, 3 (1963) 99-164.

[2] R.H. Kraichnan, Eddy viscosity in two and three dimensions. *J. Atmos. Sci.* 33 (1976) 1521-1536.

[3] M. Lesieur, *Turbulence in fluids, third edition*, Kluwer Academic Publishers (1997).

[4] M. Lesieur and O. Métais,, New trends in large-eddy simulations of turbulence. *Ann. Rev. Fluid Mech.* 28 (1996) 45-82.

[5] Clark, R.A., Ferziger, J.H. and Reynolds, W.C., 1979, "Evaluation of subgrid scale models using an accurately simulated turbulent flow", J. Fluid Mech., **91** , pp 1-16.

[6] O. Métais and M. Lesieur, Statistical predictability of decaying turbulence. *J. Atmos. Sci.* 43 (1986) 857-870.

[7] Hunt, J., 1997, Methodology and philosophy of turbulence and wheather forecasting, in *Turbulence and determinism*, Presses Universitaires de Grenoble, M. Lesieur ed., to appear.

[8] Germano, M., U. Piomelli, P. Moin and W. Cabot, A dynamic subgrid-scale eddy-viscosity model. *Phys. Fluids A.* 3 (1991) 1760-1765.

[9] Chollet, J.P. and Lesieur, M., Parameterization of small scales of three-dimensional isotropic turbulence utilizing spectral closures. *J. Atmos. Sci.* 38 (1981) 2747-2757.

[10] Chollet, J.P. and Lesieur, M., Modélisation sous maille des flux de quantité de mouvement et de chaleur en turbulence tridimensionnelle isotrope. *La Météorologie* 29-30 (1982) 183-191.

[11] André, J.C. and Lesieur, M., 1977, Influence of helicity on high Reynolds number isotropic turbulence, J. Fluid Mech., **81** , pp 187-207.

[12] Herring, J.R., Schertzer, D., Lesieur, M., Newman, G.R., Chollet, J.P. and Larchevêque, M., 1982, A comparative assessment of spectral closures as applied to passive scalar diffusion, J. Fluid Mech., **124**, pp 411-437.

[13] Champagne, F.H., Friehe, C.A., LaRue, J.C., Wyngaard, J.C., 1977, Flux measurements, flux estimation techniques and fine-scale turbulence measurements in the unstable surface layer over land, J. Atmos. Sci., **34**, pp 515-530.

[14] M. Lesieur and R. Rogallo, Large-eddy simulation of passive-scalar diffusion in isotropic turbulence. *Phys. Fluids A* 1 (1989) 718-722.

[15] M. Lesieur, O. Métais and R. Rogallo, Etude de la diffusion turbulente par simulation des grandes échelles. *C.R. Acad. Sci. Paris* Ser II 308 (1989) 1395-1400.

[16] O. Métais and M. Lesieur, Spectral large-eddy simulations of isotropic and stably-stratified turbulence. *J. Fluid Mech.* 239 (1992) 157-194.

[17] Lesieur, M. and Schertzer, D., 1978, Amortissement auto similaire d'une turbulence à grand nombre de Reynolds, Journal de Mécanique, **17**, pp 609-646.

[18] E. Lamballais, Simulations numériques de la turbulence dans un canal plan tournant. Thèse de l'Institut National Polytechnique de Grenoble (1995).

[19] E. Lamballais, M. Lesieur, and O. Métais, Influence d'une rotation d'entraînement sur les tourbillons cohérents dans un canal. *C. R. Acad. Sci. Paris* Ser II 323 (1996) 95-101.

[20] Kuroda, A., 1990, Direct-numerical simulation of Couette-Poiseuille flows, PhD thesis, University of Tokyo, 1990.

[21] U. Piomelli, High Reynolds number calculations using the dynamic subgrid-scale stress model. *Phys. Fluids A* 5 (1993) 1484-1490.

[22] R. A. Antonia, M. Teitel, J. Kim, and L.W.B. Browne, Low-Reynolds-number effects in a fully developed turbulent channel flow. *J. Fluid Mech.* 236 (1992) 579–605.

[23] Lilly D.K., in Computational Fluids Dynamics, Les Houches; session *LIX*, 1993 Lesieur, Comte, Zin-Justin eds., Elsevier Sciences Publishers, B.V., 1996, p. 353.

[24] El-Hady, N. and Zang, T.A., 1995, Large-eddy simulation of nonlinear evolution and breakdown to turbulence in high-speed boundary layers, Theor. and Comp. Fluid Dynamics, **7**, pp 217-240.

[25] D.C. Leslie and G.L. Quarini, The application of turbulence theory to the formulation of subgrid modelling procedures. *J. Fluid Mech.* 91 (1979) 65-91.

[26] F. Ducros, P. Comte and M. Lesieur, Direct and large-eddy simulations of a supersonic boundary layer. In: *Turbulent Shear Flows IX.* Springer-Verlag, (1995) 283-300.

[27] E. David, Modélisation des écoulements compressibles et hypersoniques: une approche instationnaire. Thèse, Institut National Polytechnique de Grenoble (1993).

[28] F. Ducros, Simulations numériques directes et des grandes échelles de couches limites compressibles. Thèse, Institut National Polytechnique de Grenoble (1995).

[29] F. Ducros, P. Comte and M. Lesieur, Large-eddy simulation of transition to turbulence in a boundary-layer developing spatially over a flat plate. *J. Fluid Mech.* 326 (1996) 1-36.

[30] E. Garnier, O. Métais and M. Lesieur, Instabilités primaires et secondaires dans un jet barocline. *C.R. Acad. Sci. Paris* Ser II b 323 (1996) 161-168.

[31] Chollet, J.P., 1994, Two-point closure used for a subgridscale model in large-eddy simulations, in *Turbulent shear flows 4*, Springer-Verlag, L.J.S. Bradbury et al. eds, pp 62-72.

[32] J. Silvestrini, Simulation des grandes échelles des zones de mélange: application à la propulsion solide des lanceurs spatiaux. Thèse de l'Institut National Polytechnique de Grenoble (1996).

[33] J.H. Konrad, An experimental investigation of mixing in two-dimensional turbulent shear flows with applications to diffusion-limited chemical reactions. Ph.D. Thesis, California Institute of Technology (1976).

[34] L.P. Bernal and A. Roshko, Streamwise vortex structure in plane mixing layer. *J. Fluid Mech.* 170 (1986) 499-525.

[35] R.T. Pierrehumbert and S.E. Widnall, The two- and three-dimensional instabilities of a spatially periodic shear layer. *J. Fluid Mech.* 114 (1982) 59-82.

[36] G.M. Corcos and S.J. Lin, The mixing layer: deterministic models of a turbulent flow. Part 2. The origin of the three-dimensional motion. *J. Fluid Mech.* 139 (1984) 67-95.

[37] J.C. Neu, The dynamics of stretched vortices. *J. Fluid Mech.* 143 (1984) 253-276.

[38] P. Comte and M. Lesieur, Coherent structures of mixing layers in large-eddy simulation. In: H.K. Moffatt (ed.) *Topological Fluid Dynamic.* Cambridge University Press (1989) pp.649-658.

[39] P. Comte, Y. Fouillet, M.A. Gonze, M. Lesieur, O. Métais, and X. Normand, Large-eddy simulations of free-shear layers. In: O. Métais and M. Lesieur (eds.) *Turbulence and coherent structures.* Kluwer Academic Publishers (1991) pp.45-73.

[40] P. Comte, M. Lesieur, and E. Lamballais, Large and small-scale stirring of vorticity and a passive scalar in a 3D temporal mixing layer. *Phys. Fluids A* 4 (1992) 2761-2778.

[41] C. Chandrsuda, R.D. Mehta, A.D. Weir and P. Bradshaw, Effect of free-stream turbulence on large structure in turbulent mixing layers. *J. Fluid Mech.* 85 (1978) 693-704.

[42] F.K. Browand and T.R. Troutt, A note on spanwise structure in the two-dimensional mixing layer. *J. Fluid Mech.* 93 (1980) 325-336.

[43] I. Orlanski, A simple boundary condition for unbounded hyperbolic flows, *J. Comp. Phys.* 21 (1976) 251-269.

[44] Ghosal S., Lund T.S., Moin, P., Annual Research Briefs, Center for Turbulence Research, Ames Research Center and Stanford University, 1992, 3.

[45] Favre A., J. de Mécanique, 4, 1965, 361.

[46] Erlebacher G., Hussaini M.Y., Speziale C.G., Zang T.A., J. Fluid Mech., 238, 1992, 155.

[47] Yoshizawa Y., Phys. fluids, 29, 1986, 2152.

[48] Moin P., Squires K., Cabot W., Lee S., Phys. Fluids A 3, 11, 1991, 2746.

[49] Erlebacher G., Hussaini M.Y., Speziale C.G., Zang T.A., ICASE Report, 87-20, 1987.

[50] Normand X., Lesieur M., Theor. and Comp. Fluid Dyn., 3, 1992, 231.

[51] Ghosal S., Moin, P. J. Comp. Phys., 118, 1995, 24.

[52] Gottlieb D., Turkel E., Math. Comp., 30, 1976, 703.

[53] Viviand H. Rech. Aeros., 1, 1974, 65.

[54] Fletcher C.A.J. Computational techniques for fluid dynamics 2, (Springer series in Computational Physics, 1988), p. 484.

[55] Vinokur, M. J. Comp. Phys., 14, 1974, 105.

[56] Thompson J.F., Warsi Z.U.A, Mastin, Numerical grid generation, foundations and applications, North-Holland, Amsterdam, 1995.

[57] Thompson K.W., J. Comp. Phys., 68, 1987, 1.

[58] Thompson K.W., J. Comp. Phys., 89, 1990, 439.

[59] Poinsot T.J., Lele S.K., J. Comp. Phys., 101, 1992, 104.

[60] Bogdanoff, D.W., 1983, Compressibility effects in turbulent shear layers, AIAA J., **21**, pp 926-927.

[61] Papamoschou, D. and Roshko, A., 1988, The compressible turbulent shear layer: an experimental study, J. Fluid Mech., **197**, pp 453-477.

[62] Lessen , M., Fox, J.A. and Zien, H.M., 1965, On the inviscid stability of the laminar mixing of two parallel streams of a compressible fluid, J. Fluid Mech., **23**, pp 355-367.

[63] Lessen, M., Fox, J.A. and Zien, H.M., 1966, Stability of the laminar mixing of two parallel streams with respect to supersonic disturbances, J. Fluid Mech., **25**, pp 737-742.

[64] Blumen, W., 1970, Shear-layer instability of an inviscid compressible fluid, J. Fluid Mech., **40**, pp 769-781.

[65] Normand, X., 1990, Transition à la turbulence dans les écoulements cisaillés libres et pariétaux, Thèse de l'Institut National Polytechnique de Grenoble.

[66] Soetrisno, M., Eberhardt, S., Riley, J. and McMurtry, P., 1988, A study of inviscid, supersonic mixing layers using a second-order TVD scheme, AIAA/ASME/SIAM/APS 1st Nat. Fluid Dynamics Congress, Cincinnati, AIAA paper 88-3676-CP.

[67] Soetrisno, M., Greenough, J.A., Eberhardt, S. and Riley, J., 1989, Confined compressible mixing layers: part I. Three-dimensional instabilities, AIAA 20 Fluid Dynamics, Plasma Dynamics and Lasers Conference, Buffalo, pp th st Nat. Fluid Dynamics Congress, Cincinnati, AIAA paper 89-1810.

[68] Lele, S.K., 1989, Direct-numerical simulation of compressible free-shear flows, A.I.A.A. Paper, n^0 89-0374.

[69] Fouillet, Y. *Contribution à l'étude par expérimentation numérique des écoulements cisaillés libres : effets de compressibilité*, Thèse de l'Institut National Polytechnique de Grenoble, 1991.

[70] Sandham, N.D. and Reynolds, W.C., 1989, 'The compressible mixing layer: linear theory and direct simulation, AIAA Paper 89-0371.

[71] Sandham, N.D. and Reynolds, W.C., 1991, Three-dimensional simulations of large eddies in the compressible mixing layer, J. Fluid Mech., **224**, pp 133-158.

[72] Gathmann, R., Si-Ameur, M. and Mathey, F., 1993, Numerical simulation of three-dimensional natural transition in the compressible confined shear layer, Phys. Fluids A, **5**, pp 2946-2968.

[73] Comte P., Fouillet Y., Lesieur M., Revue Scientifique et Technique de la Défense, 3, 1992, 43.

[74] Michalke, A. and Hermann, G., 1982, On the inviscid instability of a circular jet with external flow, J. Fluid Mech., **114**, pp 343-359.

[75] Tso, J. and Hussain, F., 1989, Organized motions in a fully-developed turbulent axisymmetric jet, J. Fluid Mech., **203**, pp 425-448.

[76] Lasheras, J.C. and Meiburg, E., 1991, On the three-dimensional dynamics of coherent vortical structures forming in Free, shear flows, in *Turbulence and coherent structures*, O. Métais and M. Lesieur eds, Kluwer, pp 91-111.

[77] Martin, J.E. and Meiburg, E., 1991, Numerical investigation of three-dimensionally evolving jets subject to axisymmetric and azimuthal perturbations, J. Fluid Mech., **230**, pp 271-318.

[78] Martin, J.E. and Meiburg, E., 1992, Numerical investigation of three-dimensionally evolving jets under helical perturbations, J. Fluid Mech., **243**, pp 457-487.

[79] Urbin, G. and Métais, O., in *Turbulent shear flows 11*, Grenoble.

[80] Djeridane, T., 1994, Contribution à l'étude expérimentale de jets turbulents axisymétriques à densité variable *Thèse*, Université d'Aix-Marseille II.

[81] Lupoglazoff N., Vuillot F., AIAA Paper **92-0776**, 30th AIAA Aerospace Sciences Meeting Reno, USA

[82] Ng L.L., Erlebacher G., Phys. Fluids A, 4, 1992, 710.

[83] Mack L.M., Boundary-layer stability theory, Jet Propulsion Lab., Pasadena, Calif., rep. **900-277**, 1969.

[84] Adams N.A., Kleiser L., Transitional and Turbulent Compressible flows; ASME, 151, 1993, 101.

[85] Adams N.A., Kleiser L., J. Fluid Mech, 317, 1996, 301.

[86] Michel R., Couches limites - frottement et transfert de chaleur, Cours E.N.S.A.E., 1967.

[87] Jallade, 1990, Etude théorique et numérique de l'instabilité de Görtler, Thèse INPT, Toulouse.

[88] Settles, G.S., Fitzpatrick, T.J. & Bogdonoff, S.M., 1979, Detailed study of attached and separated compression corner flowfields in high-Reynolds-number supersonic flow, AIAA J., **17**, (6), 579–585.

Numerical Simulation of Compressible Turbulent Flows Using the Reynolds-Averaged Navier-Stokes Equations

Doyle D. Knight
Department of Mechanical and Aerospace Engineering
Rutgers University - The State University of New Jersey
PO Box 909 · Piscataway NJ 08855-0909
knight@jove.rutgers.edu

Abstract

The paper assesses the capability for numerical simulation of compressible turbulent flows using the Reynolds-averaged Navier-Stokes equations. The governing Favre-averaged equations are derived, and the various levels of turbulence models defined. Examples of zero, one-equation, two-equation and Reynolds Stress Equation turbulence models are presented. Specific results are discussed for boundary layer and free shear flows. Conclusions regarding future work are presented.

1 NOMENCLATURE

ROMAN

c_p	specific heat at constant pressure
c_v	specific heat at constant volume
D	Van Driest damping factor; damping term in $q-\omega$ model
e	total energy per unit mass
$\hat{k}$	molecular thermal conductivity
$\hat{k}_t$	turbulent thermal conductivity
k	turbulence kinetic energy
ℓ	length scale of turbulence
M_t	turbulence Mach number, $\sqrt{2k}/a$
n	normal distance to boundary
p	static pressure
Pr	molecular Prandtl number, $\mu c_p/\hat{k}$
Pr_t	turbulent Prandtl number, $\mu_t c_p/\hat{k}_t$
q_i	laminar heat flux vector
$\mathcal{Q}_i$	total heat flux vector
R	gas constant
RANS	Reynolds-averaged Navier-Stokes equations
s	entropy per unit mass
T	static temperature
T_o	total temperature
$\mathcal{T}_{ij}$	total stress tensor
u_i	Cartesian velocity component
u_*	shear velocity, $\sqrt{\tau_w/\rho_w}$
x_i	Cartesian coordinate

GREEK

γ	ratio of specific heats
Γ	Klebanoff intermittency factor
δ	boundary layer thickness; mixing layer thickness
δ_i^*	incompressible displacement thickness
δ^*	compressible displacement thickness
δ_{ij}	Kronecker delta
Δ	dilatation
ϵ	rate of decay of turbulence kinetic energy
η	Kolmogorov scale
κ	von Karman's constant
λ	second coefficient of molecular viscosity
μ	molecular dynamic viscosity
μ_t	turbulent dynamic viscosity
ν	molecular kinematic viscosity
ρ	density
τ_w	wall shear stress
τ_{ij}	molecular stress
υ	velocity scale of turbulence
Ω	magnitude of mean vorticity
ω	frequency scale of turbulence

SUBSCRIPTS AND SUPERSCRIPTS

e	evaluated at edge of boundary layer
m	matching location (for algebraic eddy viscosity)
o	stagnation conditions
w	evaluated at wall

Paper presented at the AGARD FDP Special Course on "Turbulence in Compressible Flows", held at the von Kármán Institute for Fluid Dynamics (VKI) in Rhode-Saint-Genèse, Belgium, 2-6 June 1997, and in Newport News, Virginia, USA, 20-24 October 1997, and published in R-819.

2 INTRODUCTION

The accurate prediction of compressible turbulent flow is an essential element of modern engineering design in many disciplines including, for example, propulsion and aerodynamics. Recent advances in the physical understanding and modeling of compressible turbulent flows, and the continued rapid rate of growth of computer performance, has enabled more accurate simulation.

The objective of this paper is to introduce the concepts and methods of prediction using the Reynolds-averaged Navier-Stokes (RANS) equations.[1] Our scope must necessarily be limited, and therefore we focus on homogeneous compressible turbulent flows without chemical reaction or real gas effects. Additionally, we consider fully turbulent flows only, and omit any discussion of transition to turbulence. The general outline of the paper is as follows. In Section 3, the compressible Navier-Stokes equations are presented. The Reynolds-averaged Navier-Stokes equations are derived in Section 4. The Reynolds-averaged equations for the Reynolds stress, turbulence kinetic energy and rate of dissipation of turbulence kinetic energy are described in Sections 5, 6 and 7, respectively. The nature of fluctuations in turbulent flow and Morkovin's hypothesis are described in Sections 8 and 9. The notation is simplified in Section 10. In Section 11, the concept of turbulent eddy viscosity is presented. A taxonomy of turbulence models developed by Reynolds [1] is described in Section 12. A selection of zero, one-equation, two-equation and Reynolds Stress Equation models are presented in Section 13. A derivation of the compressible Law of the Wall for the $k-\epsilon$ turbulence model is given in Section 14. Results for a variety of bounded and free turbulent shear flows are presented in Section 15. Section 16 offers conclusions and proposals for future work.

There are many excellent reviews on Reynolds-averaged Navier-Stokes models for incompressible and compressible turbulent flows which should be consulted for additional information. Examples include Lakshminarayana [2], Speziale [3] and Marvin[4]. Additionally, there are several experimental databases of compressible turbulent flows which provide excellent cases for evaluation of turbulence models. Examples include Fernholz and Finley [5] and Settles and Dodson [6].

[1] Oftentimes, a subset of the Reynolds-averaged Navier-Stokes equations, *e.g.*, the Reynolds-averaged boundary layer equations, may be sufficient. We shall use the term Reynolds-averaged Navier-Stokes equations to denote both the full equations and any appropriate subset.

3 COMPRESSIBLE NAVIER-STOKES EQUATIONS

The governing equations for compressible viscous flow of a perfect gas are [7]

$$\frac{\partial \rho}{\partial t} + \frac{\partial \rho u_j}{\partial x_j} = 0 \tag{1}$$

$$\frac{\partial \rho u_i}{\partial t} + \frac{\partial \rho u_i u_j}{\partial x_j} = -\frac{\partial p}{\partial x_i} + \frac{\partial \tau_{ij}}{\partial x_j} \tag{2}$$

$$\frac{\partial \rho e}{\partial t} + \frac{\partial \left(\rho e + p\right) u_j}{\partial x_j} = \frac{\partial}{\partial x_j}\left(u_i \tau_{ij} - q_j\right) \tag{3}$$

$$p = \rho R T \tag{4}$$

where ρ is the density, u_i are the components (u_1, u_2, u_3) of the velocity along the Cartesian coordinate directions (x_1, x_2, x_3), p is the static pressure and the Einstein summation convention is employed.[2] The laminar stress tensor is

$$\tau_{ij} = \lambda \frac{\partial u_k}{\partial x_k}\delta_{ij} + \mu\left(\frac{\partial u_i}{\partial x_j} + \frac{\partial u_j}{\partial x_i}\right) \tag{5}$$

where δ_{ij} is the Kronecker delta, $\lambda = -\frac{2}{3}\mu$ according to Stokes Law, and the molecular viscosity μ is typically a function of static temperature alone. For air,

$$\mu = 1.456 \times 10^{-6} \frac{T^{3/2}}{T + 110.3} \text{ Nt-sec/m}^2 \tag{6}$$

[2] The Einstein summation convention employs the appearance of a repeated index to imply summation over all values of the index. Thus,

$$\frac{\partial \rho u_j}{\partial x_j} \text{ indicates } \sum_{j=1}^{j=3} \frac{\partial \rho u_j}{\partial x_j}$$

with T is °K. The total energy per unit mass e is

$$e = c_v T + \tfrac{1}{2}\, u_i u_i \tag{7}$$

where c_v is the specific heat at constant volume ($c_v = 717.5$ J/kg°K for air). The ratio of specific heats $\gamma = c_p/c_v$ is assumed constant ($\gamma = 1.4$ for air) where c_p is the specific heat at constant pressure, and the gas constant $R = c_p - c_v$. The laminar heat flux is

$$q_i = -\hat{k}\frac{\partial T}{\partial x_i} \tag{8}$$

and the molecular Prandtl number $Pr = \mu c_p/\hat{k}$ is assumed constant. Eqs (1) to (4) are the Navier-Stokes equations.

Compressible turbulent flows are characterized by an extraordinary large range of spatial and temporal scales. Consider an F-15C fighter aircraft [8] operating at maximum cruise (Mach 2.24) at 14,600 m altitude. The boundary layer thickness at the aft end of the 19.4m aircraft fuselage is roughly[3] $\delta \approx 0.20$ m. The largest scale of the turbulence within the boundary layer is the energy-containing eddies whose size is approximately δ. The smallest scale of the turbulence is the Kolmogorov scale $\eta = (\nu^3/\epsilon)^{1/4}$ where ν is the kinematic molecular viscosity and ϵ is the rate of decay of turbulence kinetic energy per unit mass [9]. At this scale the turbulence energy is dissipated into heat. The energy dissipated at the Kolmogorov scale is supplied by the nonlinear interactions of the large scales through the turbulent energy cascade [9] and thus $\epsilon \approx k^{3/2}/\delta$ where k is the turbulence kinetic energy. From Dussauge *et al* [10], $k \approx \frac{7}{2}\,(\tau_w/\rho)$ in a flat plate supersonic turbulent boundary layer, where τ_w is the wall shear stress. Thus, the ratio of the two scales is

$$\frac{\delta}{\eta} \approx \left(\frac{U_\infty \delta}{\nu_\infty}\right)^{3/4} \left(\tfrac{7}{4}\, c_f\right)^{3/8} \approx 5 \times 10^3 \tag{9}$$

This would imply a prohibitively large number of mesh points for complete resolution (*Direct Numerical Simulation*) of the flowfield,[4] and hence approximate methods are needed based on simplified models of (1) to (4). These models, which are categorized in Section 12, are based on averaging of the Navier-Stokes equations.

4 REYNOLDS-AVERAGED EQUATIONS

The ensemble average of a function $f(x_i, t)$ is defined by

$$\bar{f}(x_i, t) = \lim_{n\to\infty} \frac{1}{n} \sum_{\nu=1}^{\nu=n} f^{(\nu)} \tag{10}$$

where $f^{(\nu)}$ are the individual realizations of $f(x_i, t)$. The effect of ensemble averaging is to remove the high frequency (*i.e.*, small scale) fluctuations, thereby reducing the range of scales in $\bar{f}$ compared to f. The ensemble average $\bar{f}$ in general remains a function of both x_i and t, although the focus of this paper will be on turbulent flows where the $\bar{f}$ is independent of t (stationary turbulent flows). For further discussion on ensemble averages of non-stationary turbulent flows, see, for example, Antonia [12].

For stationary turbulent flows, the ensemble average may be replaced by the conventional time average

$$\bar{f}(x_i) = \lim_{\mathcal{T}\to\infty} \frac{1}{\mathcal{T}} \int_0^{\mathcal{T}} f(x_i, t)dt \tag{11}$$

under certain conditions [13]. This is the typical method employed in experiment.

The function f can be decomposed as

$$f = \bar{f}(x_i, t) + f'(x_i, t) \tag{12}$$

where $\bar{f}$ and f' represent the *conventional mean* and *conventional fluctuating* parts of the turbulent motion.

The ensemble average (10) can be applied to the Navier-Stokes equations (1) to (4). Since

[3] The estimate is obtained assuming a flat plate and using the $k-\epsilon$ turbulence model.

[4] For example, to fully resolve a region of size $\delta \times \delta \times \delta$ requires roughly $\left(5 \times 10^3\right)^3 = 1.25 \times 10^{11}$ grid points (125 *billion* grid points) in this case. Resolution of the entire boundary layer on the full aircraft would require substantially more [11] grid points. Note, however, that there are engineering problems wherein the Reynolds numbers are substantially lower (*e.g.*, flow in the high temperature section of a gas turbine) and hence Direct Numerical Simulation may be feasible.

all of the flow variables (*i.e.*, ρ, u_i, e, p and T) have mean and fluctuating components according to (12), the resultant equations become very lengthy [14, 15]. Consequently, the Favre average (density-weighted average) [16], defined by

$$\tilde{f} = \frac{1}{\bar{\rho}} \lim_{n\to\infty} \frac{1}{n} \sum_{\nu=1}^{\nu=n} (\rho f)^{(\nu)} = \frac{\overline{\rho f}}{\bar{\rho}} \tag{13}$$

is typically employed, since it yields a more compact form of the averaged equations. Using the Favre average, the function f can be decomposed as

$$f = \tilde{f} + f'' \tag{14}$$

where $\tilde{f}$ and f'' are the *Favre mean* and *Favre fluctuating* parts of the turbulent motion. The Favre average also yields the following

$$\begin{aligned}
\overline{\tilde{f}} &= \tilde{f} && (15)\\
\overline{\rho f''} &= 0 && (16)\\
\overline{f''} &= -\overline{\rho' f'}/\bar{\rho} && (17)\\
\overline{\rho f g} &= \bar{\rho}\tilde{f}\tilde{g} + \overline{\rho f'' g''} && (18)
\end{aligned}$$

It is important to note that $\overline{\rho f''} = 0$ while $\overline{f''} \neq 0$. Conversely, $\overline{\rho f'} \neq 0$ while $\overline{f'} = 0$. Also, in (18), the density ρ in $\overline{\rho f'' g''}$ is the instantaneous density, not $\bar{\rho}$.

The conventional and Favre means and fluctuations are related by

$$\tilde{f} = \bar{f} + \frac{\overline{\rho' f'}}{\bar{\rho}} \tag{19}$$

$$f'' = f' - \frac{\overline{\rho' f'}}{\bar{\rho}} \tag{20}$$

The ensemble average (10) satisfies the *Reynolds Conditions* [13]. For arbitrary functions $f(x_i, t)$ and $g(x_i, t)$ and arbitrary scalar constant a,

$$\begin{aligned}
\overline{f+g} &= \bar{f} + \bar{g} && (21)\\
\overline{af} &= a\bar{f} && (22)\\
\bar{a} &= a && (23)\\
\overline{\frac{\partial f}{\partial s}} &= \frac{\partial \bar{f}}{\partial s} && (24)\\
\overline{\bar{f} g} &= \bar{f}\bar{g} && (25)
\end{aligned}$$

where $s = x_i$ or t.

Application of the ensemble average (10) to the conservation of mass (1) yields

$$\begin{aligned}
\overline{\frac{\partial \rho}{\partial t} + \frac{\partial \rho u_j}{\partial x_j}} &= 0\\
\overline{\frac{\partial \rho}{\partial t}} + \overline{\frac{\partial \rho u_j}{\partial x_j}} &= 0 \text{ using (21)}\\
\frac{\partial \bar{\rho}}{\partial t} + \frac{\partial \overline{\rho u_j}}{\partial x_j} &= 0 \text{ using (24)}\\
\frac{\partial \bar{\rho}}{\partial t} + \frac{\partial \bar{\rho}\tilde{u}_j}{\partial x_j} &= 0 \text{ using (13)} \qquad (26)
\end{aligned}$$

Similarly, application of the ensemble average to the conservation of momentum in conjunction with the Reynolds' Conditions yields

$$\begin{aligned}
\overline{\frac{\partial \rho u_i}{\partial t} + \frac{\partial \rho u_i u_j}{\partial x_j}} &= \overline{-\frac{\partial p}{\partial x_i} + \frac{\partial \tau_{ij}}{\partial x_j}}\\
\overline{\frac{\partial \rho u_i}{\partial t}} + \overline{\frac{\partial \rho u_i u_j}{\partial x_j}} &= -\frac{\partial \bar{p}}{\partial x_i} + \frac{\partial \bar{\tau}_{ij}}{\partial x_j}\\
\frac{\partial \bar{\rho}\tilde{u}_i}{\partial t} + \overline{\frac{\partial \rho u_i u_j}{\partial x_j}} &= -\frac{\partial \bar{p}}{\partial x_i} + \frac{\partial \bar{\tau}_{ij}}{\partial x_j}
\end{aligned}$$

From (18), the term $\overline{\rho u_i u_j}$ is expanded

$$\overline{\rho u_i u_j} = \bar{\rho}\tilde{u}_i\tilde{u}_j + \overline{\rho u_i'' u_j''} \tag{27}$$

The final form of the ensemble-averaged momentum equation is

$$\frac{\partial \bar{\rho}\tilde{u}_i}{\partial t} + \frac{\partial \bar{\rho}\tilde{u}_i\tilde{u}_j}{\partial x_j} = -\frac{\partial \bar{p}}{\partial x_i} + \frac{\partial}{\partial x_j}\left(-\overline{\rho u_i'' u_j''} + \bar{\tau}_{ij}\right) \tag{28}$$

where $-\overline{\rho u_i'' u_j''}$ is the *Reynolds Stress.*[5] Note that the density ρ in the Reynolds Stress is the instantaneous density, not $\bar{\rho}$.

Similarly, application of the ensemble average to the conservation of energy yields,

$$\begin{aligned}
\overline{\frac{\partial \rho e}{\partial t} + \frac{\partial (\rho e + p) u_j}{\partial x_j}} &= \overline{\frac{\partial}{\partial x_j}(u_i \tau_{ij} - q_j)}\\
\frac{\partial \overline{\rho e}}{\partial t} + \overline{\frac{\partial (\rho e + p) u_j}{\partial x_j}} &= \frac{\partial}{\partial x_j}\left(\overline{u_i \tau_{ij}} - \overline{q_j}\right)\\
\frac{\partial \bar{\rho}\tilde{e}}{\partial t} + \overline{\frac{\partial (\rho e + p) u_j}{\partial x_j}} &= \frac{\partial}{\partial x_j}\left(\overline{u_i \tau_{ij}} - \bar{q}_j\right)
\end{aligned}$$

[5] The relationship of $-\overline{\rho u_i'' u_j''}$ to $-\bar{\rho}\,\overline{u_i' u_j'}$ is discussed in Appendix B.

The term $\bar{\rho}\tilde{e}$ may be expressed as

$$\begin{aligned}\bar{\rho}\tilde{e} &= \overline{\rho c_v T} + \tfrac{1}{2}\,\overline{\rho u_i u_i} \\ &= c_v\bar{\rho}\tilde{T} + \tfrac{1}{2}\,\bar{\rho}\tilde{u}_i\tilde{u}_i + \tfrac{1}{2}\,\overline{\rho u_i'' u_i''} \\ &= c_v\bar{\rho}\tilde{T} + \tfrac{1}{2}\,\bar{\rho}\tilde{u}_i\tilde{u}_i + \bar{\rho}k \qquad (29)\end{aligned}$$

where k is the *turbulence kinetic energy*[6] per unit mass [15]

$$\bar{\rho}k = \tfrac{1}{2}\,\overline{\rho u_i'' u_i''} \qquad (30)$$

Thus

$$\tilde{e} = c_v\tilde{T} + \tfrac{1}{2}\,\tilde{u}_i\tilde{u}_i + k \qquad (31)$$

The term $\overline{(\rho e + p)\,u_j}$ may be expanded

$$\begin{aligned}\overline{(\rho e + p)\,u_j} &= \overline{\left(\rho c_v T + p + \tfrac{1}{2}\,\rho u_i u_i\right) u_j} \\ &= \overline{\left(\rho c_p T + \tfrac{1}{2}\,\rho u_i u_i\right) u_j} \\ &= c_p\overline{\rho T u_j} + \tfrac{1}{2}\,\overline{\rho u_i u_i u_j} \qquad (32)\end{aligned}$$

Now

$$\begin{aligned}\overline{\rho T u_j} &= \overline{\rho\left(\tilde{T} + T''\right)\left(\tilde{u}_j + u_j''\right)} \\ &= \overline{\rho\tilde{T}\tilde{u}_j} + \overline{\rho\tilde{T}u_j''} + \overline{\rho T''\tilde{u}_j} + \overline{\rho T'' u_j''} \\ &= \bar{\rho}\tilde{T}\tilde{u}_j + \overline{\rho T'' u_j''}\end{aligned}$$

since $\overline{\rho u_j''} = 0$ and $\overline{\rho T''} = 0$. By a similar analysis,

$$\begin{aligned}\tfrac{1}{2}\,\overline{\rho u_i u_i u_j} &= \tfrac{1}{2}\,\bar{\rho}\tilde{u}_i\tilde{u}_i\tilde{u}_j + \bar{\rho}k\tilde{u}_j + \\ &\quad \overline{\rho u_i'' u_j''}\tilde{u}_i + \tfrac{1}{2}\,\overline{\rho u_i'' u_i'' u_j''}\end{aligned}$$

Thus

$$\begin{aligned}\overline{(\rho e + p)\,u_j} &= c_p\left(\bar{\rho}\tilde{T}\tilde{u}_j + \overline{\rho T'' u_j''}\right) + \\ &\quad \tfrac{1}{2}\,\bar{\rho}\tilde{u}_i\tilde{u}_i\tilde{u}_j + \bar{\rho}k\tilde{u}_j + \\ &\quad \overline{\rho u_i'' u_j''}\tilde{u}_i + \tfrac{1}{2}\,\overline{\rho u_i'' u_i'' u_j''} \\ &= \bar{\rho}\left(c_p\tilde{T} + \tfrac{1}{2}\,\tilde{u}_i\tilde{u}_i + k\right)\tilde{u}_j + \\ &\quad c_p\overline{\rho T'' u_j''} + \overline{\rho u_i'' u_j''}\tilde{u}_i + \\ &\quad \tfrac{1}{2}\,\overline{\rho u_i'' u_i'' u_j''} \\ &= \left(\bar{\rho}\tilde{e} + \bar{p}\right)\tilde{u}_j + c_p\overline{\rho T'' u_j''} + \\ &\quad \overline{\rho u_i'' u_j''}\tilde{u}_i + \tfrac{1}{2}\,\overline{\rho u_i'' u_i'' u_j''} \qquad (33)\end{aligned}$$

using the ensemble average of the equation of state

$$\bar{p} = \bar{\rho}R\tilde{T} \qquad (34)$$

Writing

$$\begin{aligned}\overline{u_i\tau_{ij}} &= \overline{\left(\tilde{u}_i + u_i''\right)\tau_{ij}} \\ &= \tilde{u}_i\bar{\tau}_{ij} + \overline{u_i''\tau_{ij}} \qquad (35)\end{aligned}$$

The ensemble averaged energy equation thus becomes

$$\begin{aligned}&\frac{\partial\bar{\rho}\tilde{e}}{\partial t} + \frac{\partial\left(\bar{\rho}\tilde{e} + \bar{p}\right)\tilde{u}_j}{\partial x_j} = \\ &\frac{\partial}{\partial x_j}\left[\tilde{u}_i\left(-\overline{\rho u_i'' u_j''} + \bar{\tau}_{ij}\right)\right] + \\ &\quad \frac{\partial}{\partial x_j}\left(-c_p\overline{\rho T'' u_j''} - \bar{q}_j\right) + \\ &\frac{\partial}{\partial x_j}\left(-\tfrac{1}{2}\,\overline{\rho u_i'' u_i'' u_j''} + \overline{u_i''\tau_{ij}}\right) \qquad (36)\end{aligned}$$

The last term is generally negligible[7] and thus the ensemble averaged energy equation becomes

$$\begin{aligned}&\frac{\partial\bar{\rho}\tilde{e}}{\partial t} + \frac{\partial\left(\bar{\rho}\tilde{e} + \bar{p}\right)\tilde{u}_j}{\partial x_j} = \\ &\frac{\partial}{\partial x_j}\left[\tilde{u}_i\left(-\overline{\rho u_i'' u_j''} + \bar{\tau}_{ij}\right)\right] + \\ &\quad \frac{\partial}{\partial x_j}\left(-c_p\overline{\rho T'' u_j''} - \bar{q}_j\right) \qquad (37)\end{aligned}$$

Defining the *total stress tensor* $\mathcal{T}_{ij}$ and *total heat flux vector* $\mathcal{Q}_i$ by

$$\begin{aligned}\mathcal{T}_{ij} &= -\overline{\rho u_i'' u_j''} + \bar{\tau}_{ij} \\ \mathcal{Q}_i &= c_p\overline{\rho T'' u_j''} + \bar{q}_j \qquad (38)\end{aligned}$$

the ensemble averaged Navier-Stokes equations may be summarized as

$$\frac{\partial\bar{\rho}}{\partial t} + \frac{\partial\bar{\rho}\tilde{u}_j}{\partial x_j} = 0 \qquad (39)$$

[6] Note that this is not the incompressible definition of turbulence kinetic energy, *i.e.*

$$k = \tfrac{1}{2}\,\overline{u_i' u_i'}$$

[7] Compared to the first term on the right side of (36).

$$\frac{\partial \bar{\rho}\tilde{u}_i}{\partial t} + \frac{\partial \bar{\rho}\tilde{u}_i\tilde{u}_j}{\partial x_j} = -\frac{\partial \bar{p}}{\partial x_i} + \frac{\partial \mathcal{T}_{ij}}{\partial x_j} \quad (40)$$

$$\frac{\partial \bar{\rho}\tilde{e}}{\partial t} + \frac{\partial \left(\bar{\rho}\tilde{e} + \bar{p}\right)\tilde{u}_j}{\partial x_j} = \frac{\partial}{\partial x_j}\left(\tilde{u}_i\mathcal{T}_{ij} - \mathcal{Q}_j\right) \quad (41)$$

$$\bar{p} = \bar{\rho}R\tilde{T} \quad (42)$$

Eqs (39) to (41) are the *Reynolds-averaged Navier-Stokes Equations (RANS).*

The mean molecular viscous stress $\bar{\tau}_{ij}$ is typically approximated by

$$\bar{\tau}_{ij} = -\frac{2}{3}\tilde{\mu}\frac{\partial \tilde{u}_k}{\partial x_k}\delta_{ij} + \tilde{\mu}\left(\frac{\partial \tilde{u}_j}{\partial x_i} + \frac{\partial \tilde{u}_i}{\partial x_j}\right) \quad (43)$$

where $\tilde{\mu}$ is taken to be $\mu(\tilde{T})$. Similarly, the molecular heat flux is

$$\bar{q}_i = -\frac{c_p\tilde{\mu}}{Pr}\frac{\partial \tilde{T}}{\partial x_i} \quad (44)$$

The closure of the system of equations (39) to (42) requires the specification of the Reynolds stress $-\overline{\rho u_i'' u_j''}$ and the Reynolds heat flux $-c_p\overline{\rho T'' u_j''}$. This is the *turbulence modeling* problem which has been addressed at various levels of complexity as described in subsequent sections.

5 REYNOLDS STRESS EQUATION

An equation for the Reynolds stress $-\overline{\rho u_i'' u_j''}$ can be obtained from the conservation of momentum and mass by

$$\overline{u_i''[\text{momt}]_j + u_j''[\text{momt}]_i - u_i'' u_j''[\text{mass}]}$$

where $[\text{momt}]_i$ indicates the i^{th} component of the conservation of momentum. The exact equation is

$$\frac{\partial \overline{\rho u_i'' u_j''}}{\partial t} + \frac{\partial \overline{\rho u_i'' u_j''}\tilde{u}_k}{\partial x_k} = A_{ij} + B_{ij} + C_{ij} - D_{ij} \quad (45)$$

where

$$A_{ij} = -\overline{\rho u_j'' u_k''}\frac{\partial \tilde{u}_i}{\partial x_k} - \overline{\rho u_i'' u_k''}\frac{\partial \tilde{u}_j}{\partial x_k} \quad (46)$$

$$B_{ij} = \frac{\partial}{\partial x_k}\left\{-\overline{\rho u_i'' u_j'' u_k''} + \overline{u_j''\tau_{ik}} + \overline{u_i''\tau_{jk}} - \overline{p u_i''}\delta_{jk} - \overline{p u_j''}\delta_{ik}\right\} \quad (47)$$

$$C_{ij} = \overline{p\left(\frac{\partial u_i''}{\partial x_j} + \frac{\partial u_j''}{\partial x_i}\right)} \quad (48)$$

$$D_{ij} = \overline{\tau_{ik}\frac{\partial u_j''}{\partial x_k}} + \overline{\tau_{jk}\frac{\partial u_i''}{\partial x_k}} \quad (49)$$

The conventional description for each of the terms on the right side of (45) is given in Table 1. It should be noted that the grouping in (45) is not unique,[8] and furthermore that ρ, p and τ_{ij} appearing in (47), (48) and (49) are the *instantaneous* values, respectively. The first term A_{ij} represents the production of Reynolds stress by action of the mean velocity gradients. The second term B_{ij} is diffusive in character, since its volume integral is zero[9] for an unbounded flow in which the turbulence vanishes at infinity. The third term represents the correlation between the pressure and rate-of-strain[10] based on the Favre fluctuating velocity. The fourth term is quadratic in the velocity gradients and represents dissipation.

Table 1: Terms in Reynolds Stress Equation

Term	*Description*
A_{ij}	Production
B_{ij}	Diffusion
C_{ij}	Pressure Rate-of-Strain
D_{ij}	Dissipation

The Reynolds Stress Equation (45) is actually *six* equations for the six independent elements of $-\overline{\rho u_i'' u_j''}$. It is evident from (46) to (49) that the Reynolds Stress Equation introduces *additional* turbulent correlations which do not appear in the Reynolds-averaged Navier-Stokes equations, namely, $\overline{\rho u_i'' u_j'' u_k''}$, $\overline{u_i''\tau_{jk}}$, $\overline{p u_i''}$, $\overline{p\left(\partial u_i''/\partial x_j + \partial u_j''/\partial x_i\right)}$, and $\overline{\tau_{ik}\frac{\partial u_j''}{\partial x_k}} + \overline{\tau_{jk}\frac{\partial u_i''}{\partial x_k}}$. Additional equations could be derived for these correlations; however, such equations would in-

[8] For different, but equivalent, forms of (45) to (49), see, for example, Lee *et al* [17] and Speziale and Sarkar [18].

[9] By the Divergence Theorem.

[10] Actually, twice the rate-of-strain.

troduce even more correlations. Thus, the system of equations cannot be closed by taking averages of different moments of the Navier-Stokes equations, and therefore it is necessary to introduce model equations.

It is similarly possible to derive an equation for the turbulent heat flux $-c_p\overline{\rho T'' u_j''}$, which will introduce higher order correlations as well. In the interests of brevity, the equation for $-c_p\overline{\rho T'' u_j''}$ is omitted.

6 TURBULENCE KINETIC ENERGY

An equation for the turbulence kinetic energy can be obtained from (45) to (49) by summation over the indices. The result is[11]

$$\frac{\partial \bar{\rho} k}{\partial t} + \frac{\partial \bar{\rho} k \tilde{u}_i}{\partial x_i} = A + B + C - D \tag{50}$$

where

$$A = -\overline{\rho u_i'' u_j''} \frac{\partial \tilde{u}_i}{\partial x_j} \tag{51}$$

$$B = \frac{\partial}{\partial x_j} \left\{ -\tfrac{1}{2} \overline{\rho u_i'' u_i'' u_j''} + \overline{u_i'' \tau_{ij}} - \overline{p u_j''} \right\} \tag{52}$$

$$C = \overline{p \frac{\partial u_i''}{\partial x_i}} \tag{53}$$

$$D = \overline{\tau_{ij} \frac{\partial u_i''}{\partial x_j}} \tag{54}$$

The conventional description for each of the terms on the right side of (50) are given in Table 2. The production A and diffusion B terms are the contracted version of their counterparts for the Reynolds Stress equation (45). The pressure-dilatation C is unique to compressible turbulent flow[12]. Sarkar *et al* [20] showed that for high Reynolds number homogeneous turbulence the rate of dissipation of turbulence kinetic energy D can be approximated by

$$D \approx \tilde{\mu} \left(\overline{\omega_i' \omega_i'} + \tfrac{4}{3} \overline{d'^2} \right) \tag{55}$$

where ω_i' is the fluctuating vorticity and d' is the fluctuating divergence of the velocity. Thus, the dissipation of turbulence kinetic energy has both vortical and dilatational contributions. A number of models of the effect of dilatational dissipation have been developed, *e.g.*, Sarkar *et al* [20], Zeman [21], Wilcox [15]. and Ristorcelli [22].

Table 2: Terms in Turbulence Kinetic Energy Equation

Term	*Description*
A	Production
B	Diffusion
C	Pressure-Dilatation
D	Dissipation

7 DISSIPATION EQUATION

The rate of dissipation of turbulence kinetic energy by viscosity D (54) is oftentimes used as a variable in turbulence model equations. It is possible to derive an equation for D from the Navier-Stokes equations, however in its full compressible form it is rather complex. In the interests of brevity, we present the equivalent equation [3] for the incompressible dissipation $\hat{\epsilon}$ defined by[13]

$$\hat{\epsilon} = \nu \overline{\frac{\partial u_i'}{\partial x_j} \frac{\partial u_i'}{\partial x_j}} \tag{56}$$

[11] A different, though equivalent, form is presented by Rubesin [19].

[12] For incompressible turbulence, $u_i'' = u_i'$ and the ensemble average of the conservation of mass yields

$$\frac{\partial u_i'}{\partial x_i} = 0$$

and hence $C = 0$.

[13] For incompressible flow, the terms

$$\overline{\frac{\partial u_i'' \tau_{ij}}{\partial x_j}} - \overline{\tau_{ij} \frac{\partial u_i''}{\partial x_j}}$$

may be written as

$$\mu \frac{\partial^2 k}{\partial x_i^2} - \mu \overline{\frac{\partial u_i'}{\partial x_j} \frac{\partial u_i'}{\partial x_j}}$$

The second term $\mu \overline{\left(\partial u_i'/\partial x_j\right)^2}$ is $\rho\hat{\epsilon}$ [23].

which satisfies

$$\begin{aligned}\frac{\partial \hat{\epsilon}}{\partial t}+\frac{\partial \hat{\epsilon}\bar{u}_i}{\partial x_i} &= \nu\frac{\partial^2\hat{\epsilon}}{\partial x_i^2}-2\nu\overline{\frac{\partial u_i'}{\partial x_j}\frac{\partial u_k'}{\partial x_j}\frac{\partial \bar{u}_i}{\partial x_k}}\\ &-2\nu\overline{\frac{\partial u_j'}{\partial x_i}\frac{\partial u_j'}{\partial x_k}\frac{\partial \bar{u}_i}{\partial x_k}}\\ &-2\nu\overline{u_k'\frac{\partial u_i'}{\partial x_j}\frac{\partial^2\bar{u}_i}{\partial x_k\partial x_j}}\\ &-2\nu\overline{\frac{\partial u_i'}{\partial x_k}\frac{\partial u_i'}{\partial x_m}\frac{\partial u_k'}{\partial x_m}}\\ &-\nu\frac{\partial}{\partial x_k}\left(\overline{u_k'\frac{\partial u_i'}{\partial x_m}\frac{\partial u_i'}{\partial x_m}}\right)\\ &-2\nu\frac{\partial}{\partial x_k}\left(\overline{\frac{\partial p'}{\partial x_m}\frac{\partial u_k'}{\partial x_m}}\right)\\ &-2\nu^2\overline{\frac{\partial^2 u_i'}{\partial x_k\partial x_m}\frac{\partial^2 u_i'}{\partial x_k\partial x_m}} \qquad (57)\end{aligned}$$

The terms on right side of (57) can be identified as production, diffusion and destruction of $\hat{\epsilon}$; however, these terms are modeled instead using the mean flow quantities.

8 ON THE NATURE OF FLUCTUATIONS IN COMPRESSIBLE FLOW

Kovasznay [24] examined the nature of fluctuations in a compressible flow, and demonstrated on the basis of the unsteady compressible Navier-Stokes equations that there are three different types of disturbances: acoustic, entropy and vorticity. His analysis identified the effect of these different disturbances on the velocity, pressure and temperature fields. For small disturbances, the modes are independent, and can be analyzed separately (Table 3). The velocity fluctuations can be separated into solenoidal and dilatational components.[14] The solenoidal fluctuations constitute the vorticity mode, while the irrotational fluctuations contribute to the acoustic mode. The static pressure fluctuations contribute to the acoustic mode. The density and static temperature fluctuations can be separated into isentropic and nonisentropic parts, which contribute to the acoustic and entropy fluctuations, respectively.

[14] This is a general consequence of the Helmholtz [25] decomposition.

Table 3: Turbulent fluctuations

Mode	$\boldsymbol{u}_s$	$\boldsymbol{u}_d$	p	ρ_i	ρ_n	T_i	T_n
acoustic		•	•	•		•	
entropy					•		•
vorticity	•						

LEGEND

$\boldsymbol{u}_s$	solenoidal velocity
$\boldsymbol{u}_d$	dilatational velocity
p	static pressure
ρ_i	isentropic density
ρ_n	nonisentropic density
T_i	isentropic static temperature
T_n	nonisentropic static temperature

Compressible fluctuations may be equivalently categorized into acoustic, total temperature and vorticity disturbances. The total temperature T_o is defined as

$$c_pT_o = c_pT + \tfrac{1}{2}\,u_iu_i \qquad (58)$$

For a perfect gas

$$ds = c_p\frac{dT}{T} - R\frac{dp}{p} \qquad (59)$$

where s is the entropy per unit mass. Thus,

$$\begin{aligned}\frac{ds}{c_p} &= \left[1+\frac{(\gamma-1)}{2}M^2\right]\frac{dT_o}{T_o}-(\gamma-1)\,M^2\frac{dU}{U}\\ &-\frac{(\gamma-1)}{\gamma}\frac{dp}{p} \qquad (60)\end{aligned}$$

where $U = \sqrt{u_iu_i}$ and $M = U/\sqrt{\gamma RT}$ is the Mach number.

9 MORKOVIN'S HYPOTHESIS

A fundamental concept in development of turbulence models for the Reynolds-averaged Navier-Stokes Equations is *Morkovin's Hypothesis* [26]. It states that the effect of density fluctuations ρ' on the turbulence structure are unimportant if the root-mean-square density fluctuations are small compared to the mean density, *i.e.*,

$$\overline{\rho'^2} \ll \bar{\rho} \qquad (61)$$

This is generally valid for non-hypersonic (*i.e.*, $M < 5$) boundary layers at conventional rates of heat transfer and non-hypersonic wakes, and for free shear layers (*e.g.*, jets, mixing layers) at Mach numbers less than approximately one [27].

Morkovin [26] demonstrated on the basis of experimental data that, for non-hypersonic turbulent boundary layers at adiabatic or near adiabatic conditions, the acoustic and total temperature modes are negligible. From the equation of state (4),

$$\log p = \log \rho + \log R + \log T \tag{62}$$

and thus

$$\frac{dp}{p} = \frac{d\rho}{\rho} + \frac{dT}{T} \tag{63}$$

and hence to a first approximation,

$$\frac{p'}{\bar{p}} \approx \frac{\rho'}{\bar{\rho}} + \frac{T'}{\bar{T}} \tag{64}$$

Morkovin's conclusion that the acoustic mode is negligible implies

$$\frac{p'}{\bar{p}} \ll \frac{\rho'}{\bar{\rho}} \text{ and } \frac{p'}{\bar{p}} \ll \frac{T'}{\bar{T}} \tag{65}$$

and thus

$$\frac{\rho'}{\bar{\rho}} \approx -\frac{T'}{\bar{T}} \tag{66}$$

From the definition of total temperature (58),

$$c_p dT_o = c_p dT + U dU \tag{67}$$

where $U = \sqrt{u_i u_i}$. Thus, to a first approximation,

$$c_p T_o' \approx c_p T' + \bar{U} U' \tag{68}$$

Morkovin's conclusion that the total temperature mode is negligible implies

$$c_p T_o' \ll c_p T' \text{ and } c_p T_o' \ll \bar{U} U' \tag{69}$$

and thus

$$c_p T' \approx -\bar{U} U' \tag{70}$$

For a 2-D turbulent boundary layer, $U' \approx u'$ where u is the velocity component parallel to the surface. From (70), the correlation coefficient R_{Tu}, defined by

$$R_{Tu} = \frac{\overline{T' u'}}{\sqrt{\overline{T'^2}\,\overline{u'^2}}} \tag{71}$$

is $R_{Tu} = -1$. Kistler [28] showed that $R_{Tu} \approx -0.6$ to -0.8 for flat plate zero pressure gradient supersonic boundary layers.

Equations (66) and (70) are useful in comparing $-\overline{\rho u_i'' u_j''}$ with $-\bar{\rho}\,\overline{u_i' u_j'}$ as discussed in Appendix B.

Morkovin's Hypothesis provides a plausible justification for extending incompressible RANS turbulence models to compressible flow by simply allowing for a variable density ρ. Indeed, most compressible RANS turbulence models have been principally developed in this manner, notwithstanding additional modifications to specifically account for compressibility effects.

10 SIMPLIFYING THE NOTATION

We hereafter[15] drop the overbar $\bar{}$ and tilde $\tilde{}$ in the interests of simplicity of notation. For reference, the governing Reynolds-averaged Navier-Stokes equations are

$$\frac{\partial \rho}{\partial t} + \frac{\partial \rho u_j}{\partial x_j} = 0 \tag{72}$$

$$\frac{\partial \rho u_i}{\partial t} + \frac{\partial \rho u_i u_j}{\partial x_j} = -\frac{\partial p}{\partial x_i} + \frac{\partial \mathcal{T}_{ij}}{\partial x_j} \tag{73}$$

$$\frac{\partial \rho e}{\partial t} + \frac{\partial \left(\rho e + p\right) u_j}{\partial x_j} = \frac{\partial}{\partial x_j}\left(u_i \mathcal{T}_{ij} - \mathcal{Q}_j\right) \tag{74}$$

$$p = \rho R T \tag{75}$$

$$\mathcal{T}_{ij} = -\overline{\rho u_i'' u_j''} + \tau_{ij} \tag{76}$$

$$\mathcal{Q}_j = c_p \overline{\rho T'' u_j''} + q_j \tag{77}$$

[15] Except in those instances where the overbar and tilde are essential for interpretation.

$$\tau_{ij} = -\frac{2}{3}\mu \frac{\partial u_k}{\partial x_k}\delta_{ij} + \mu\left(\frac{\partial u_j}{\partial x_i} + \frac{\partial u_i}{\partial x_j}\right) \quad (78)$$

$$q_i = -\frac{c_p \mu}{Pr}\frac{\partial T}{\partial x_i} \quad (79)$$

11 THE CONCEPT OF EDDY VISCOSITY

The earliest model for the Reynolds Stress[16] is due to Boussinesq [29]. By analogy with the Newtonian description of viscous stresses in a laminar flow (5), the Reynolds Stress is assumed to be proportional to the rate-of-strain tensor

$$\begin{aligned} -\overline{\rho u_i'' u_j''} &= \mu_t \Bigg(\underbrace{\frac{\partial u_i}{\partial x_j} + \frac{\partial u_j}{\partial x_i}}_{I} - \underbrace{\tfrac{2}{3}\frac{\partial u_k}{\partial x_k}\delta_{ij}}_{II} \Bigg) \\ &\quad \underbrace{-\tfrac{2}{3}\rho k \delta_{ij}}_{III} \end{aligned} \quad (80)$$

Term I (together with μ_t) constitutes the Boussinesq hypothesis, where μ_t is the *turbulent eddy viscosity* which must be defined. Terms II and III provide the proper trace of the Reynolds Stress, *i.e.*,

$$\begin{aligned} -\overline{\rho u_i'' u_i''} &= \mu_t \left(\frac{\partial u_i}{\partial x_i} + \frac{\partial u_i}{\partial x_i} - \tfrac{2}{3}\frac{\partial u_k}{\partial x_k}\delta_{ii} \right) \\ &\quad -\tfrac{2}{3}\rho k \delta_{ii} \\ -\overline{\rho u_i'' u_i''} &= -2\rho k \end{aligned} \quad (81)$$

which is (30) using $\delta_{ii} = 3$. Oftentimes, (80) is expressed as

$$-\overline{\rho u_i'' u_j''} = 2\mu_t\left(S_{ij} - \tfrac{1}{3}\Delta\delta_{ij}\right) - \tfrac{2}{3}\rho k \delta_{ij} \quad (82)$$

where S_{ij} is the mean rate-of-strain tensor

$$S_{ij} = \tfrac{1}{2}\left(\frac{\partial u_i}{\partial x_j} + \frac{\partial u_j}{\partial x_i}\right) \quad (83)$$

and Δ is the dilatation

$$\Delta = \frac{\partial u_k}{\partial x_k} \quad (84)$$

[16] Although developed in the context of incompressible turbulent flow, the concept is extendible to compressible flow. Here we present the concept in its compressible form.

The turbulent eddy viscosity μ_t has the units

$$\mu_t \sim \text{density} \times \text{velocity} \times \text{length} \quad (85)$$

Morkovin's hypothesis suggests that the density can be taken to be the local mean density $\rho(x_i, t)$ provided that (61) is applicable. This is typically assumed. Thus, the eddy viscosity is expressed as

$$\mu_t = \rho v \ell \quad (86)$$

where v and ℓ are the velocity and length scales associated with the turbulence. By analogy with kinetic theory [30], the functions v and ℓ represent the rms fluctuating velocity and typical size, respectively, of the turbulent eddies responsible for momentum transport. These definitions are qualitative, yet nonetheless provide an understanding of the physical concepts.[17]

Similarly, the Boussinesq model for the turbulent heat flux, in analogy with the laminar heat flux (8), is

$$c_p \overline{\rho T'' u_i''} = -\hat{k}_t \frac{\partial T}{\partial x_i} \quad (87)$$

where $\hat{k}_t$ is the *turbulent thermal conductivity* and must be defined. Typically, $\hat{k}_t$ is written as

$$\hat{k}_t = \frac{\mu_t c_p}{Pr_t} \quad (88)$$

where Pr_t is the *turbulent Prandtl number*. For boundary layers, experimental data [7, 15, 31] indicates that $Pr_t \approx 0.9$, while for free shear layers $Pr_t \approx 0.5$ is more appropriate [15].

If the Boussinesq concept of a turbulent eddy viscosity μ_t and the additional assumption of a constant turbulent Prandtl number Pr_t are accepted, then the closure of the system of equations (72) to (75) is reduced[18] to determining μ_t. Turbulence models developed in this manner are denoted *eddy viscosity models.*

It should be emphasized that (80) and (87) are *assumptions* which have been found valid in

[17] Note that v and ℓ are arbitrary to the extent of a constant, *i.e.*, $\mu_t = \bar{\rho} v \ell = \bar{\rho}(v/2)(2\ell)$, etc. Thus, no unique definition of v or ℓ can be given.

[18] This statement is not rigorously correct, although in some practical applications it suffices. This is discussed in Appendix A.

some (but not all) turbulent flows. Moreover, in principle, (80) does not give an unambiguous definition for μ_t. In general, the Reynolds stress tensor $-\overline{\rho u_i'' u_j''}$ has six independent components. Since $-\overline{\rho u_i'' u_j''}$, u_i, ρ and k are in principle measurable quantities, then (80) represents six equations for one variable μ_t. This fundamental limitation can be overcome by the introduction of a tensor eddy viscosity at the cost of substantial added complexity [23].

12 TAXONOMY OF TURBULENCE MODELS

Closure of the Reynolds-averaged Navier-Stokes equations requires additional equations for the turbulent stresses $-\overline{\rho u_i'' u_j''}$ and turbulent heat flux $-\overline{c_p \rho T'' u_j''}$, collectively denoted as *turbulent correlations*. One reasonable categorization is between eddy viscosity and non-eddy viscosity models. For compressible turbulent flow, the number of turbulence models and their applications in the former category is far more numerous, although more recent work has emphasized the non-eddy viscosity approach.

12.1 Eddy Viscosity Models

Eddy viscosity models assume the forms (80) and (87) for the Reynolds Stress and turbulent heat flux, respectively. Typically, the turbulent Prandtl number is assumed constant.[19] Following Reynolds [1], a taxonomy of eddy viscosity turbulence closure models can be defined.

12.1.1 Zero Equation

The turbulent correlations are expressed in terms of an eddy viscosity which is obtained from the mean field (*i.e.*, the velocity u_k, density ρ and temperature T) and a prescribed physical length scale which depends on the specific geometry of the problem. No additional partial differential equations are employed (hence the name "zero-equation").

12.1.2 One Equation

One additional partial differential equation is specified for a turbulence quantity (*e.g.*, k). An eddy viscosity is typically employed for the turbulent correlations. A length scale is also prescribed which is geometry dependent.

12.1.3 Two Equation

Two additional partial differential equations are specified for two turbulence quantities (*e.g.*, k and the rate of dissipation of k). An eddy viscosity is typically employed for the turbulent correlations. No additional length scale is needed.

12.2 Reynolds Stress Equation

Reynolds Stress Equation models employ partial differential equations for the components of the Reynolds stress $-\overline{\rho u_i'' u_j''}$. The turbulent heat flux $-\overline{c_p \rho T'' u_j''}$ may be similarly modeled using a partial differential equation, or modeled using an turbulent eddy viscosity.[20] No additional length scale is needed. These models are known as Reynolds Stress Equation or Second Moment Closure models.

A simplified subset of the Reynolds Stress Equation model is the Algebraic Stress Equation model wherein the partial differential equations for the Reynolds stress and turbulent heat flux are replaced by algebraic equations obtained under the assumption of near equilibrium turbulence.

12.3 Other Models

In addition to models employing the Reynolds-averaged Navier Stokes equations, two additional categories need to be mentioned. Large Eddy Simulation (LES) employs a time-

[19] Shang [32] studied the effect of variable Pr_t on a hypersonic flat plate turbulent boundary layer. He found that the computed mean velocity and static temperature were insensitive to the upper and lower limits of the experimental envelope of the Pr_t data of Simpson *et al* [33], and accurately predicted by the constant value $Pr_t = 0.9$.

[20] In the latter case, the Reynolds Stress Equation model would not be strictly non-eddy-viscosity, of course.

dependent, three-dimensional computation of the large-eddy structure and a model for the small-scale turbulent motions. Direct Numerical Simulation (DNS) involves the computation of all scales in a turbulent flow. DNS calculations are currently feasible only for low Reynolds numbers due to limitations on computer resources. These approaches are discussed in a companion paper in this Special Course.

13 SPECIFIC TURBULENCE MODELS

This section presents examples of turbulence models from the taxonomy of Section 12. The presentation is not exhaustive for any specific type of model. For example, there are numerous variations of zero-equation turbulence models; however, due to limitations of space we present two commonly used models – Cebeci-Smith and Baldwin-Lomax. Moreover, the presentation is not exhaustive for the different types of models. We focus on zero-, one-equation, two-equation and Reynolds Stress Equation models which have been applied to compressible turbulent flows. There are additional models, *e.g.*, Algebraic Stress Equation models (see, for example, Pope [34], Gatski and Speziale [35], Abid *et al* [36]) and RNG-based models (see, for example, Yakhot and Orszag [37], Martinelli and Yakhot [38], Yakhot *et al* [39]), however, which are not covered here and the reader is encouraged to consult the references listed for further information.

In presentation of the turbulence models, the notation of the authors has been used wherever possible to facilitate cross reference. The constants in the turbulence models are typically determined by comparison with experimental data for simple flows. The values of the constants are cited here, and the reader is referred to the primary references for further information. All turbulence models require boundary conditions. An adequate description of the boundary conditions is beyond the scope of this paper, and the reader is referred to the references herein.

13.1 Zero Equation

The nomenclature "zero equation" turbulence model implies that no additional partial differential equations are introduced to define the eddy viscosity μ_t. Instead, algebraic equations are employed. In the following sections, we present two popular zero equation models in their original form. The variations to these models are too numerous to classify here.

13.1.1 Cebeci-Smith

The Cebeci-Smith model [40, 41, 42] is a two-layer algebraic eddy viscosity model for boundary layer flows.

$$\mu_t = \begin{cases} \rho\left(k_1 n D\right)^2 \Omega & \text{for } n \le n_m \\ \rho k_2 u_e \delta_i^* \Gamma & \text{for } n \ge n_m \end{cases} \tag{89}$$

The first expression is the *inner eddy viscosity*, where n is the normal distance to the boundary,[21] D is the Van Driest damping factor, Ω is the mean vorticity and $k_1 = 0.40$ is a constant. Oftentimes, k_1 is written instead as κ to signify that it represents von Karman's constant. The Van Driest damping factor is

$$D = 1 - \exp(-nu_*/A\nu_w) \tag{90}$$

where u_* is the *friction velocity*

$$u_* = \sqrt{\frac{\tau_w}{\rho_w}} \tag{91}$$

where τ_w is the local wall shear stress, ν_w is the local wall kinematic molecular viscosity, and $A = 26$ is a constant.[22]

The second expression in (89) is the *outer eddy viscosity* where $k_2 = 0.0168$ is a constant, u_e

[21] The normal distance n to the boundary is not always uniquely defined, *e.g.*, in the vicinity of a sharp corner. The Buleev length scale [43] is a generalization of the concept of normal distance and is commonly used.

[22] Variations in (89) and (90) abound. For example, the original model was developed for 2-D or axisymmetric boundary layers, and the velocity derivative $\partial u/\partial n$ was employed instead of Ω. It is possible to use the contraction of the mean rate of strain $\sqrt{2S_{ij}S_{ij}}$ instead of $\Omega = \nabla \times \vec{u}$. Also, the molecular viscosity ν_w in (90) may be evaluated locally. For simple boundary layers, such changes have little effect; however, for complex flows (*e.g.*, separation) there may be a significant, although localized, effect.

is the velocity at the local edge of the boundary layer, δ_i^* is the local *incompressible* displacement thickness

$$\delta_i^* = \int_0^\delta \left(1 - \frac{u}{u_e}\right) dn \tag{92}$$

and Γ is the Klebanoff intermittency factor

$$\Gamma = \left[1 + 5.5\left(\frac{n}{\delta}\right)^6\right]^{-1} \tag{93}$$

where δ is the local boundary layer thickness. The constants are summarized in Table 4.

Table 4: Cebeci-Smith Model

Constant	*Value*
A	26.0
k_1	0.40
k_2	0.0168

The physical basis for the velocity scale v and length scale ℓ in the inner eddy viscosity is the mixing length argument of Prandtl. Outside of the viscous and transition regions of the boundary layer, (*i.e.*, $nu_*/\nu_w > 100$), the VanDriest damping factor $D \approx 1$. Considering a 2-D turbulent boundary layer with y denoting the normal distance to the wall, the inner μ_t is approximately

$$\mu_{t_{\text{inner}}} \approx \rho\kappa^2 y^2 \frac{\partial u}{\partial y} \tag{94}$$

which is recognizable as the Prandtl mixing length model with $v = \kappa y\, \partial u/\partial y$ and $\ell = \kappa y$, respectively.[23]

In the outer eddy viscosity, the velocity scale is proportional to the velocity at the edge of the boundary layer $v \propto u_e$, and the length scale $\ell \propto \delta_i^*$. The intermittency factor Γ forces the eddy viscosity to zero outside the boundary layer.

The matching distance n_m is defined as the smallest value of n such that $\mu_{t_{\text{inner}}} = \mu_{t_{\text{outer}}}$. Since $\mu_{t_{\text{inner}}} = 0$ at the wall and $\mu_{t_{\text{outer}}} > 0$ there, the matching point will occur away from the boundary.

The Cebeci-Smith model has two disadvantages. First, the Van Driest factor D requires the definition of the local wall shear stress τ_w. This may be ambiguous in certain geometries, similar to the definition of the normal distance n, requiring the imposition of an *ad hoc* definition. Second, the outer eddy viscosity requires the definition of the local edge of the boundary layer (for determining u_e and δ). In both 2-D and 3-D simulations, this may prove problematic. A typical definition (*e.g.*, $u = 0.995u_e$ at $n = \delta$) may yield inaccurate and non-smooth values of δ due to small numerical errors.[24] Moreover, in complex flows (*e.g.*, flows which shock wave-turbulent boundary layer interactions) the precise definition of the edge of the boundary layer may be difficult due to the non-uniformity of the inviscid region.

13.1.2 Baldwin-Lomax Model

The Baldwin-Lomax model [44] is a two-layer algebraic model for boundary layer and free shear flows. It was developed principally as an alternative to the Cebeci-Smith model with the objective of avoiding the requirement for determining the local edge of the boundary layer.

$$\mu_t = \begin{cases} \rho\left(\kappa n D\right)^2 \Omega & \text{for } n \le n_m \\ \rho K C_{cp} F_{\text{wake}} \Gamma & \text{for } n \ge n_m \end{cases} \tag{95}$$

The inner eddy viscosity (first expression) is identical to the inner eddy viscosity in (89). The function F_{wake} is

$$F_{\text{wake}} = \min \begin{cases} n_{\max} F_{\max} \\ C_{wk} n_{\max} u_{\text{diff}}^2 / F_{\max} \end{cases} \tag{96}$$

where $n_{\max}$ is the location of the maximum of the function

$$F = n\Omega D \tag{97}$$

and $F_{\max} = \max F$. The velocity scale u_{diff} is

$$u_{\text{diff}} = \max_{\text{in shear layer}} |\vec{u}| - \min_{\text{in shear layer}} |\vec{u}| \tag{98}$$

[23] As indicated previously, the functions v and ℓ cannot be defined uniquely in a strict sense. However, for the mixing length model, $v = \ell\, \partial u/\partial y$, and thus $\ell = \kappa y$.

[24] This is particularly troublesome for Navier-Stokes simulations since the velocity gradient may be very small in the outer portion of the boundary layer, and small oscillations may be present in the numerical solution. It is not typically a problem with boundary layer codes.

where $|\vec{u}|$ is the magnitude of the velocity. The Klebanoff intermittency factor is

$$\Gamma = \left[1 + 5.5\left(\frac{C_{\text{Kleb}} n}{n_{\max}}\right)^6\right]^{-1} \tag{99}$$

The constants[25] are listed in Table 5. The matching distance is defined in the same fashion as Cebeci-Smith, *i.e.*, n_m is the smallest value of n such that $\mu_{t_{\text{inner}}} = \mu_{t_{\text{outer}}}$.

Table 5: Baldwin-Lomax Model

Constant	*Value*
A	26.0
C_{cp}	1.6
C_{Kleb}	0.3
C_{wk}	0.25
κ	0.4
K	0.0168

The physical model for the inner eddy viscosity is Prandtl's mixing length. In the outer eddy viscosity, the function F_{wake} represents $v\ell$ (modulo the constant KC_{cp}). The first definition of F_{wake} is typically employed in boundary layers.[26] For boundary layers in mild pressure gradients, the function F displays a peak in the outer region of the boundary layer,[27] thereby defining a length scale ℓ which is appropriately[28] $\mathcal{O}(\delta)$.

The Baldwin-Lomax model exhibits the first disadvantage of the Cebeci-Smith model, namely, the requirement of defining the local wall shear stress τ_w in the Van Driest factor D. It does not require the definition of the local boundary layer thickness, however, in contrast to Cebeci-Smith. However, the definition of $v\ell$ using (97) is not unique in all cases; in particular, F can exhibit two (or more) local maxima within (or near) the boundary layer [49], thereby requiring *ad hoc* modifications (*e.g.*, [49, 50, 51]).

[25] For additional discussion regarding the values of the constants, see [45].

[26] In some boundary layer computations, the second expression for F_{wake} has been ignored, *e.g.*, [46].

[27] For an incompressible flat plate zero pressure gradient turbulent boundary layer, it is straightforward [47] to show that $n_{\max} = 0.646\delta$ and $F = u_\star(1 + 1.82\Pi)/\kappa$ where $\Pi \approx 0.55$ is the wake strength parameter [48].

[28] The symbol $\mathcal{O}(\delta)$ means "on the order of δ".

13.2 One Equation

A fundamental limitation of zero equation models is the assumption that the Reynolds stress $-\overline{\rho u_i'' u_j''}$ and heat flux $-\overline{c_p \rho T'' u_j''}$ can be directly related to the local mean flow variables (*e.g.*, u_i, ρ). It is well known that turbulence does not respond instantly to changes in the mean flow,[29] but rather adjusts (relaxes) over a time scale associated with the turbulence structure. An example of an abrupt change is the embedded shock which may appear on the lifting side of a transonic airfoil. Although the mean flow (*e.g.*, mean pressure and velocity) responds virtually immediately to the shock (*e.g.*, on a time scale equal to the time interval between molecular collisions), the turbulence reacts on a finite time scale (*e.g.*, on a time scale equal to the eddy turnover time which can be estimated as ℓ/v.)

One equation[30] models attempt to incorporate this "history" effect by postulating a single partial differential equation which, combined with an explicit expression for the length scale ℓ, defines the eddy viscosity $\rho v \ell$. A detailed history of one-equation models is presented in Wilcox [15]. For compressible turbulent flows, the one equation models of Baldwin-Barth [53], Johnson-King [54] and Spalart-Allmaras [55] are commonly employed. In this section, we present the Johnson-King model.

13.2.1 Johnson-King

The Johnson-King model [54, 56] is a one-equation model[31] principally developed for a restricted class of flows, *i.e.*, transonic boundary layers with strong pressure gradients. Several small modifications were later proposed to the original model [57, 58] to improve agreement with experiment. Herein we present the version from [56].

The Johnson-King model incorporates a "his-

[29] For an extensive review of the response of turbulent boundary layers to abrupt perturbations, see Smits and Wood [52].

[30] And all higher order models, *e.g.*, two equation models, Reynolds Stress Equation models, and Large Eddy Simulation.

[31] For reasons discussed below, Johnson and King consider the model to be a hybrid Reynolds-stress / eddy viscosity model.

tory" effect in the definition of the turbulent eddy viscosity μ_t in order to emulate the physical response of turbulence to rapid changes in the mean flow. The concept of an equilibrium turbulent eddy viscosity μ_{t_e} is introduced, where μ_{t_e} is the eddy viscosity which is obtained in the absence of any abrupt changes to the flow, or, in the case of an abrupt change, the eddy viscosity which is obtained far downstream. The equilibrium eddy viscosity is a blending of "inner" and "outer" equilibrium eddy viscosities according to

$$\mu_{t_e} = \mu_{t_{oe}} \left[1 - \exp(-\mu_{t_{ie}}/\mu_{t_{oe}})\right] \tag{100}$$

where the inner and outer equilibrum turbulent eddy viscosities are[32]

$$\mu_{t_{ie}} = \rho D^2 \kappa y \sqrt{\varsigma_{e_m}} \tag{101}$$
$$\mu_{t_{oe}} = \rho k_2 u_e \delta_i^* \Gamma \tag{102}$$

where ς is the *kinematic* Reynolds shear stress

$$\varsigma = -\overline{u''v''} \tag{103}$$

and

$$\varsigma_{e_m} = \max(-\overline{u''v''}_e) \tag{104}$$

and $-\overline{u''v''}_e$ is the equilibrium (kinetic) Reynolds shear stress

$$-\rho\overline{u''v''}_e = \mu_{t_e}\left(\frac{\partial u}{\partial y} + \frac{\partial v}{\partial x}\right) \tag{105}$$

The inner equilbrium eddy viscosity (101) employs $\sqrt{\varsigma_{e_m}}$ for v and y for ℓ, with the Van Driest damping factor[33] (90). The outer equilibrium eddy viscosity is the same as Cebeci-Smith (89). In principle, given the velocities and density, the value of ς_{e_m} can be determined implicitly from (100) to (105). In practice, ς_{e_m} is determined from the x-station immediately upstream of the point of interest.

The eddy viscosity is obtained from a blending of "inner" and "outer" *non-equilibrium* eddy viscosities according to

$$\mu_t = \mu_{t_o} \left[1 - \exp(-\mu_{t_i}/\mu_{t_o})\right] \tag{106}$$

where

$$\mu_{t_i} = \rho D^2 \kappa y \sqrt{\varsigma_m} \tag{107}$$
$$\mu_{t_o} = \rho \sigma(x) k_2 u_e \delta_i^* \Gamma \tag{108}$$

The function $\sigma(x)$ is determined in the following manner. The maximum kinematic Reynolds stress ς_m is assumed to be determined by the following equation

$$\frac{dg}{dx} = \frac{a_1}{2u_m L_m}\left[\left(1 - \frac{g}{g_e}\right) + \frac{C_{\text{dif}} L_m}{a_1 \delta \left[0.7 - (y/\delta)_m\right]}\left|1 - \sqrt{\frac{\mu_{t_o}}{\mu_{t_{oe}}}}\right|\right] \tag{109}$$

where

$$g = \varsigma_m^{-1/2} \tag{110}$$
$$g_e = \varsigma_{e_m}^{-1/2} \tag{111}$$

The subscript $_m$ indicates evaluation at the location where ς is a maximum. The length scale L_m is

$$L_m = \begin{cases} 0.4 y_m & \text{if } y_m \le 0.225\delta \\ 0.09\delta & \text{if } y_m \ge 0.225\delta \end{cases} \tag{112}$$

and δ is the local boundary layer thickness. The function $\sigma(x)$ is determined by the requirement that the value of ς_m obtained from (109) match the value obtained from (106) and (80). The constants are listed in Table 6.

Table 6: Johnson-King Model [56]

Constant	*Value*
A	15
a_1	0.25
C_{dif}	0.50
k_2	0.0168

The evolution equation (109) represents a non-equilibrium model for the turbulent eddy viscosity. In regions of rapid changes to the mean flow (*e.g.*, in the vicinity of a shock wave), the terms on the right side of (109) are non-zero due to the rapid response of the equilibrium eddy viscosity μ_{t_e} to the changes in the mean flow.

[32] Here we employ the conventional notation for a 2-D turbulent boundary layer, where x and y represent the streamwise and normal directions, respectively, and u and v the corresponding velocities.

[33] However, the value of A is taken to be 15.

The eddy viscosity μ_t relaxes towards equilibrium over a length scale $\mathcal{O}(L_m)$ or $\mathcal{O}(\delta)$, depending on whether the first or second term on the right side of (109) is dominant. This reflects the behavior of the turbulence. The use of ς_m as the relaxation function is motivated by the experimental data of Perry and Schofield [59] for boundary layers in adverse pressure gradients, wherein it was observed that ς_m provided an accurate correlation of the velocity defect.

13.3 Two Equation

The inherent limitations of the zero and one equation models influenced the development of two equation turbulence models. By specifying partial differential equations for two turbulence scalars, it is possible to define the turbulent eddy viscosity without reference to a particular geometric length scale.[34] The general form of the two equations is assumed to be

$$\begin{aligned} \frac{\partial \rho f}{\partial t} + \frac{\partial \rho f u_i}{\partial x_i} &= P_f - D_f + Di_f \\ \frac{\partial \rho g}{\partial t} + \frac{\partial \rho g u_i}{\partial x_i} &= P_g - D_g + Di_g \end{aligned} \tag{113}$$

where f and g are two different turbulence scalars, and P, D and Di represent production, dissipation and diffusion, respectively. In general, once the particular choice for f and g has been made, exact equations can be obtained for f and g from appropriate moments of the instantaneous Navier-Stokes equations. However, these exact equations introduce higher order correlations (beyond $-\rho\overline{u_i'' u_j''}$ and $-c_p\rho\overline{T'' u_j''}$), and therefore cannot be employed without modification. These exact equations do *suggest* the general form of (113), *i.e.*, the fundamental processes of convection, production, dissipation and diffusion.

It is straightforward to show that any dimensionally independent pair[35] of turbulence scalar functions f and g are sufficient to define μ_t. Assume that the units of f and g are

$$\begin{aligned} f &\sim [\text{length}]^a \times [\text{time}]^b \\ g &\sim [\text{length}]^c \times [\text{time}]^d \end{aligned} \tag{114}$$

[34] This is not strictly true, since some two equation models use the normal distance from the boundary.

[35] Dimensionally independent implies $ad - bc \neq 0$.

Then

$$\begin{aligned} v &= f^{(d+c)/e}\ g^{-(a+b)/e} \\ \ell &= f^{d/e}\ g^{-b/e} \end{aligned} \tag{115}$$

where $e = ad - bc$.

A wide variety of two equation models have been developed, differing principally in the choice of the functions f and g. In the following sections, three specific models are presented. It should be emphasized that oftentimes small but nonetheless important changes to these models are made to improve the prediction of certain flows, and thus in examining the results of subsequent sections, the original reference should be cited for the exact version of the model.

13.3.1 $k-\omega$

Kolmogorov [60] developed the first two-equation model using the functions $f = k$ and $g = \omega$ where k is the turbulence kinetic energy and ω is the specific dissipation rate for turbulence, *i.e.*, $\epsilon = k\omega$ where ϵ is the rate of decay of k per unit time (at a point). Saffman [61] independent developed a two equation model using k and ω^2. Wilcox and Alber [62] extended the Saffman model to compressible flows. Subsequent extensive model development by Wilcox and his colleagues [15] led to the present form of the $k-\omega$ model.

$$\begin{aligned} \frac{\partial \rho k}{\partial t} + \frac{\partial \rho k u_i}{\partial x_i} &= -\overline{\rho u_i'' u_j''}\frac{\partial u_i}{\partial x_j} - \beta^* \rho k \omega + \\ &\quad \frac{\partial}{\partial x_j}\left[(\mu + \sigma^* \mu_t)\frac{\partial k}{\partial x_j}\right] \end{aligned} \tag{116}$$

$$\begin{aligned} \frac{\partial \rho \omega}{\partial t} + \frac{\partial \rho \omega u_i}{\partial x_i} &= -\alpha\frac{\omega}{k}\overline{\rho u_i'' u_j''}\frac{\partial u_i}{\partial x_j} - \beta \rho \omega^2 + \\ &\quad \frac{\partial}{\partial x_j}\left[(\mu + \sigma \mu_t)\frac{\partial \omega}{\partial x_j}\right] \end{aligned} \tag{117}$$

where β^* and β are functions of the turbulence Mach number

$$M_t = \frac{\sqrt{2k}}{a} \tag{118}$$

where $a = \sqrt{\gamma RT}$ is the local speed of sound. The general expressions for β^* and β are

$$\begin{aligned} \beta^*(M_t) &= \beta_o^* [1 + \xi^* F(M_t)] \\ \beta(M_t) &= \beta_o - \beta_o^* \xi^* F(M_t) \end{aligned} \quad (119)$$

where β_o, β_o^* and ξ^* are constants and $F(M_t)$ is a prescribed function. Wilcox [15] developed three different models for F, corresponding to the dilational dissipation models of Sarkar [63], Zeman [21] and Wilcox [15]. The Wilcox model is $\xi^* = 3/2$ and

$$F(M_t) = \left[M_t^2 - M_{t_o}^2\right] \mathcal{H}(M_t - M_{t_o}) \quad (120)$$

where $M_{t_o} = 1/4$ and $\mathcal{H}(x)$ is the Heaviside function.[36]

The turbulent eddy viscosity μ_t is obtained from

$$\mu_t = \rho \frac{k}{\omega} \quad (121)$$

and the constants are given in Table 7.

Table 7: $k-\omega$ Model

Constant	*Value*
α	5/9
β_o	3/40
β_o^*	9/100
σ	1/2
σ^*	1/2
ξ^*	3/2
M_{t_o}	1/4

13.3.2 $k-\epsilon$

The Jones-Launder model [64] (also known as the k–ϵ model) employs the functions $f = k$ and $g = \epsilon$ where ϵ is the rate of decay of turbulence kinetic energy. Numerous subsequent modifications have been made, *e.g.*, Launder and Sharma [65], Chien [66], Lam and Bremhorst [67] and Becht and Knight [68]. Here we present the Jones-Launder model with the Chien modifications which enable integration to a solid boundary.

[36] $\mathcal{H}(x) = 1$ for $x > 0$ and $\mathcal{H}(x) = 0$ for $x < 0$.

$$\begin{aligned} \frac{\partial \rho k}{\partial t} + \frac{\partial \rho k u_i}{\partial x_i} &= P_k - \rho\left(\epsilon + 2\nu k n^{-2}\right) \\ &\quad + \frac{\partial}{\partial x_i}\left[\left(\frac{\mu_t}{\sigma_k} + \mu\right)\frac{\partial k}{\partial x_i}\right] \end{aligned} \quad (122)$$

$$\begin{aligned} \frac{\partial \rho \epsilon}{\partial t} + \frac{\partial \rho \epsilon u_i}{\partial x_i} &= C_1 \frac{\epsilon}{k} P_k \\ &\quad - \rho \frac{\epsilon}{k}\left(C_2 f \epsilon + 2\nu k n^{-2} e^{-C_4 n^+}\right) \\ &\quad + \frac{\partial}{\partial x_i}\left[\left(\frac{\mu_t}{\sigma_\epsilon} + \mu\right)\frac{\partial \epsilon}{\partial x_i}\right] \end{aligned} \quad (123)$$

where P_k is the production of turbulence kinetic energy

$$P_k = \mu_t \left(\frac{\partial u_i}{\partial x_j} + \frac{\partial u_j}{\partial x_i}\right)\frac{\partial u_i}{\partial x_j} \quad (124)$$

and $n^+ = n u_*/\nu$ is the dimensionless normal distance. The turbulent eddy viscosity is

$$\mu_t = C_\mu \rho \frac{k^2}{\epsilon}\left(1 - e^{-C_3 n^+}\right) \quad (125)$$

where the dimensionless damping function f is

$$f = 1 - 0.22 e^{-\left(k^2/6\nu\epsilon\right)^2} \quad (126)$$

The constants are given in Table 8.

13.3.3 $q-\omega$

The Coakley model (also known as the $q-\omega$ model) employs the functions $f = \sqrt{k}$ and $g = \omega$ where ω is interpreted as the specific turbulent dissipation rate, *i.e.*, $\omega = \epsilon/k$. Several versions of the model have been developed [72, 73, 74, 75]. Here we present the version in Ref. [74].

$$\begin{aligned} \frac{\partial \rho q}{\partial t} + \frac{\partial \rho q u_i}{\partial x_i} &= \tfrac{1}{2}\left(C_\mu D \frac{S}{\omega^2} - \tfrac{2}{3}\frac{D}{\omega} - 1\right)\rho \omega q \\ &\quad + \frac{\partial}{\partial x_i}\left[\left(\frac{\mu_t}{Pr_q} + \mu\right)\frac{\partial q}{\partial x_i}\right] \end{aligned} \quad (127)$$

$$\begin{aligned} \frac{\partial \rho \omega}{\partial t} + \frac{\partial \rho \omega u_i}{\partial x_i} &= \left[C_1\left(C_\mu \frac{S}{\omega^2} - \tfrac{2}{3}\frac{D}{\omega}\right) - C_2\right]\rho \omega^2 \\ &\quad + \frac{\partial}{\partial x_i}\left[\left(\frac{\mu_t}{Pr_\omega} + \mu\right)\frac{\partial \omega}{\partial x_i}\right] \end{aligned} \quad (128)$$

Table 8: $k-\epsilon$ Model

Constant	*$k-\epsilon$ Chien*	*Thies & Tam [69]*
C_μ	0.09	0.0874
C_1	1.35	1.40
C_2	1.80	2.02
C_3	0.0115	-
C_4	0.5	-
σ_k	1.0	0.324
σ_ϵ	1.3	0.377
Pr_t	0.90	0.422

NOTES
1. Constants C_3 and C_4 are inapplicable to Thies & Tam since their computations are for free shear flows.
2. Thies & Tam have two additional terms corresponding to the corrections of Pope [70] and Sarkar [71] which add two additional constants.

where

$$S = \left(\frac{\partial u_i}{\partial x_j} + \frac{\partial u_j}{\partial x_i}\right)\frac{\partial u_i}{\partial x_j} - \frac{2}{3}\left(\frac{\partial u_i}{\partial x_i}\right)^2 \quad (129)$$

$$D = 1 - e^{-\alpha R} \quad (130)$$

and

$$R = \frac{qn}{\nu} \quad (131)$$

The constants are given in Table 9.

Table 9: $q-\omega$ Model

Constant	*Value*
C_μ	0.09
C_1	$0.5D + 0.055$
C_2	0.833
α	0.02
Pr_q	2.0
Pr_ω	2.0

13.4 Reynolds Stress Equation

Reynolds Stress Equation models are based on the second moment equation (45) for $-\overline{\rho u_i'' u_j''}$. The terms B_{ij}, C_{ij}, and D_{ij} must be modeled. The production term A_{ij} is already expressed in terms of the Reynolds stress and mean velocity, and therefore requires no further modeling. Additionally, a model for the turbulent heat flux $-c_p\overline{\rho T'' u_j''}$ must be given.

13.4.1 Zhang-So-Gatski-Speziale

The Zhang-So-Gatski-Speziale model [76] is a Reynolds Stress Equation model. The diffusion term B_{ij} is modeled as

$$B_{ij} = \frac{\partial}{\partial x_k}\left[\frac{C_s\bar{\rho}k}{\epsilon}\left(T_{im}\frac{\partial T_{jk}}{\partial x_m} + T_{jm}\frac{\partial T_{ik}}{\partial x_m} + T_{km}\frac{\partial T_{ij}}{\partial x_m}\right) - \mu\frac{\partial T_{ij}}{\partial x_k}\right] \quad (132)$$

where T_{ij} is the *kinematic* Reynolds stress[37]

$$T_{ij} = -\widetilde{u_i'' u_j''} = -\frac{\overline{\rho u_i'' u_j''}}{\bar{\rho}} \quad (133)$$

The pressure-rate of strain correlation[38] is modeled as

$$C_{ij} = \Phi_{ij} + \Phi_{ij}^R + \Phi_{ij}^w \quad (134)$$

where

$$\Phi_{ij} = -C_1\epsilon b_{ij} - \alpha_1\left(P_{ij} - \tfrac{1}{3}P_{kk}\delta_{ij}\right) - \beta_1\left(\hat{D}_{ij} - \tfrac{1}{3}P_{kk}\delta_{ij}\right) - 2\gamma_1 k\left(S_{ij} - \tfrac{1}{3}S_{kk}\delta_{ij}\right) \quad (135)$$

and

$$\Phi_{ij}^R = 2C_w k\left(S_{ij} - \tfrac{1}{3}S_{kk}\delta_{ij}\right)\left(\frac{k^{3/2}}{\epsilon x_2}\right) \quad (136)$$

and

$$\Phi_{ij}^w = f_{w1}\left[C_1\epsilon b_{ij} + \frac{\epsilon}{k}\left(T_{ik}n_j n_k + T_{jk}n_i n_k\right) + \alpha^*\left(P_{ij} - \tfrac{1}{3}P_{kk}\delta_{ij}\right)\right] \quad (137)$$

In the above expressions

$$P_{ij} = A_{ij} \text{ (production term)}$$

[37] Morrison *et al* [77] use $-T_{ij}$.

[38] Actually, the deviatoric part of the pressure-rate-of-strain

$$
\begin{aligned}
b_{ij} &= -\frac{\left(T_{ij}+\frac{2}{3}\,k\delta_{ij}\right)}{2k} \\
\hat{D}_{ij} &= -\overline{\rho u_j'' u_k''}\frac{\partial u_k}{\partial x_i} - \overline{\rho u_i'' u_k''}\frac{\partial u_k}{\partial x_j} \\
S_{ij} &= \tfrac{1}{2}\left(\frac{\partial u_i}{\partial x_j}+\frac{\partial u_j}{\partial x_i}\right)
\end{aligned}
\qquad (138)
$$

and x_2 is the normal distance to the boundary.

The dissipation term is

$$D_{ij} = \tfrac{2}{3}\,\rho\epsilon\delta_{ij} + \rho\epsilon_{ij}^{w} \qquad (139)$$

where ϵ_{ij}^{w} is a wall correction term

$$\epsilon_{ij}^{w} = f_{w1}\left[-\tfrac{2}{3}\,\epsilon\delta_{ij} - \frac{\epsilon}{k}\Upsilon_{ij}\right] \qquad (140)$$

with

$$\Upsilon_{ij} = \frac{T_{ij}+T_{ik}n_kn_j+T_{jk}n_kn_i+T_{kl}n_in_jn_kn_l}{1-\frac{3}{2}T_{kl}n_kn_l/k} \qquad (141)$$

and

$$f_{w1} = \exp\left[-\left(Re_t/150\right)^2\right] \qquad (142)$$

where $Re_t = k^2/\nu\epsilon$.

The dissipation equation is

$$\frac{\partial\rho\epsilon}{\partial t}+\frac{\partial\rho\epsilon u_k}{\partial x_k} = A_\epsilon + B_\epsilon + C_\epsilon + D_\epsilon \qquad (143)$$

where

$$
\begin{aligned}
A_\epsilon &= -\left[\tfrac{1}{3}\ + m\left(\gamma-1\right)\right]\rho\epsilon\frac{\partial u_i}{\partial x_i} \\
&\quad -C_{\epsilon 1}\frac{\epsilon}{k}\overline{\rho u_i'' u_j''}\left(\frac{\partial u_i}{\partial x_j}-\tfrac{1}{3}\frac{\partial u_k}{\partial x_k}\delta_{ij}\right) \\
B_\epsilon &= -C_{\epsilon 2}\rho\frac{\epsilon\epsilon_{w1}}{k} \\
C_\epsilon &= \frac{\partial}{\partial x_i}\left(-C_\epsilon\frac{\rho k}{\epsilon_s}T_{ij}\frac{\partial\epsilon}{\partial x_j}+\mu\frac{\partial\epsilon}{\partial x_i}\right) \\
D_\epsilon &= \rho f_{w2}\left[-2\frac{\epsilon\epsilon_{w1}}{k}+\tfrac{3}{2}\frac{\epsilon_{w2}^2}{k}\right. \\
&\quad \left.-\tfrac{3}{4}\,C_{\epsilon 1}\frac{\epsilon}{k}P_{ii}\right] \\
\epsilon_{w1} &= \epsilon-\nu\left(\frac{\partial\sqrt{k}}{\partial x_2}\right)^2 \\
\epsilon_{w2} &= \epsilon-\frac{2\nu k}{x_2^2} \\
f_{w2} &= \exp\left[-\left(Re_t/40\right)^2\right]
\end{aligned}
\qquad (144)
$$

For the model of the turbulent heat flux and closure of the mean energy equation, see [77]. The constants are listed in Table 10.

Table 10: Zhang *et al* Model

Constant	*Value*
C_s	0.11
C_1	3.0
C_2	0.4
C_w	see [77]
$C_{\epsilon 1}$	1.50
$C_{\epsilon 2}$	1.83
C_ϵ	0.10
m	0.7 (see [77])
α_1	$(8+C_2)/11$
β_1	$(8C_2-2)/11$
γ_1	$(30C_2-2)/55$

13.4.2 Knight

Knight [78] extended to compressible flow a standard incompressible Reynolds Stress Equation model. The diffusion term is modeled as

$$
\begin{aligned}
B_{ij} &= \frac{\partial}{\partial x_k}\left\{C_{d_1}\frac{k}{\rho\epsilon}\left[\overline{\rho u_i'' u_m''}\frac{\partial\overline{\rho u_j'' u_k''}}{\partial x_m}\right.\right. \\
&\quad \left.+\overline{\rho u_j'' u_m''}\frac{\partial\overline{\rho u_i'' u_k''}}{\partial x_m}+\overline{\rho u_k'' u_m''}\frac{\partial\overline{\rho u_i'' u_j''}}{\partial x_m}\right] \\
&\quad \left.+\nu\left[\frac{\partial\overline{\rho u_i'' u_j''}}{\partial x_k}+\frac{\partial\overline{\rho u_i'' u_k''}}{\partial x_j}+\frac{\partial\overline{\rho u_j'' u_k''}}{\partial x_i}\right]\right\}
\end{aligned}
\qquad (145)
$$

where C_{d_1} is a constant. This model is an extension of the incompressible flow model of Launder, Reece and Rodi [79].

The correlation of the instantaneous pressure and fluctuating rate-of-strain is modeled as

$$
\begin{aligned}
C_{ij} &= -C_{p_1}\frac{\epsilon}{k}\left(\overline{\rho u_i'' u_j''}-\frac{2}{3}\rho k\delta_{ij}\right) \\
&\quad +C_{p_2}\rho k\left(\frac{\partial u_i}{\partial x_j}+\frac{\partial u_j}{\partial x_i}\right)
\end{aligned}
\qquad (146)
$$

where C_{p_1} and C_{p_2} are constants. This is the extension of Rotta's model [80] for incompressible flow.

An isotropic dissipation model with compressibility effect is used to determine the dissipation

term,

$$D_{ij} = \frac{2}{3}\rho\epsilon\delta_{ij} \tag{147}$$

According to Sarkar *et al* [20] and Zeman [21]

$$\rho\epsilon = \rho\left(\epsilon_s + \epsilon_c\right) \tag{148}$$

where $\epsilon_c = C_k\epsilon_s M_t^2$ and the turbulence Mach number is $M_t = \sqrt{2k}/a$.

The conventional equation [64] is employed for ϵ_s,

$$\frac{\partial\rho\epsilon_s}{\partial t} + \frac{\partial\rho\epsilon_s u_k}{\partial x_k} = P_\epsilon - D_\epsilon + Di_\epsilon \tag{149}$$

where

$$P_\epsilon = -C_{\epsilon_1}\frac{\epsilon_s}{k}\overline{\rho u_i'' u_k''}\frac{\partial u_i}{\partial x_k} \tag{150}$$

$$D_\epsilon = C_{\epsilon_2}\rho\frac{\epsilon_s^2}{k} \tag{151}$$

$$Di_\epsilon = \frac{\partial}{\partial x_k}\left\{\left(C_{\epsilon_3}\rho\frac{k^2}{\epsilon} + \mu\right)\frac{\partial\epsilon_s}{\partial x_k}\right\} \tag{152}$$

where C_{ϵ_1}, C_{ϵ_2} and C_{ϵ_3} are constants.

The turbulent heat flux is modeled using a gradient diffusion hypothesis

$$-c_p\overline{\rho T'' u_i''} = c_p\,\rho\,C_h\frac{k^2}{\epsilon}\frac{\partial T}{\partial x_i} \tag{153}$$

where C_h is a constant.

The closure constants are given in Table 11. The model employs wall functions which are described in [81].

Table 11: Knight Model

Constant	*Value*
C_{d_1}	0.086
C_{p_1}	4.325
C_{p_2}	0.179
C_{ϵ_1}	1.01
C_{ϵ_2}	1.80
C_{ϵ_3}	0.10
C_k	0.0
C_h	0.0857

14 COMPRESSIBLE LAW OF THE WALL

There are certain fundamental properties of compressible turbulent flows which any acceptable turbulence model must be capable of predicting with reasonable accuracy. One specific example is the compressible Law of the Wall, first derived by Van Driest [14]. Consider a 2-D compressible turbulent boundary layer on a flat plate with zero pressure gradient. The velocity components $(u_1, u_2, u_3) = (u, v, w)$ along the coordinate directions $(x_1, x_2, x_3) = (x, y, z)$ where x is aligned with the mean flow direction and y is normal to the plate. The Reynolds shear stress is $-\overline{\rho u'' v''}$. On the basis of a simple mixing length argument for the Reynolds shear stress

$$-\overline{\rho u'' v''} = \rho l^2\left(\frac{\partial u}{\partial y}\right)^2 \tag{154}$$

Van Driest derived the relation[39]

$$u^+ = \frac{u_*}{\kappa}\log y^+ + \hat{B}u_* \tag{155}$$

where

$$u^+ = \frac{u_e}{A}\left[\sin^{-1}\left(\frac{2A^2u/u_e - B}{\sqrt{B^2+4A^2}}\right) + \sin^{-1}\left(\frac{B}{\sqrt{B^2+4A^2}}\right)\right]$$

$$A = \sqrt{\frac{\gamma-1}{2}Pr_t M_e^2\frac{T_e}{T_w}}$$

$$B = \left[1 + \sqrt{Pr_t}\frac{(\gamma-1)}{2}M_e^2\right]\frac{T_e}{T_w} - 1 \tag{156}$$

where $u_* = \sqrt{\tau_w/\rho_w}$ is the friction velocity, τ_w is the (local) wall shear stress, ρ_w is the (local) wall density, $y^+ = yu_*/\nu_w$, u_e and M_e are the velocity and Mach number at the edge of the boundary layer, T_{aw} is the adiabatic wall temperature, T_w is the (actual) wall temperature, $\kappa = 0.41$ is Von Karman's constant, and $\hat{B} = 5.0$. Note that B is also equivalent to

$$B = \frac{T_{aw}}{T_w} - 1 \tag{157}$$

[39]The expression includes the effect of non-unity turbulent Prandtl number, not originally considered by Van Driest. See, for example, Sun and Childs [82].

since

$$T_{aw} = \left(1 + \sqrt{Pr_t}\frac{(\gamma-1)}{2}M_e^2\right)T_e \qquad (158)$$

Experimental data supports this result [7, 14].

It is possible to demonstrate that (155) can be derived for most turbulence models. This was first shown by Saffman and Wilcox [83] for the two equation turbulence model developed by Saffman [61] and extended to compressible flows by Wilcox and Alber [62]. A derivation for the $k-\omega$ model is presented in [15].

We present the derivation for the $k-\epsilon$ turbulence model. Within the lower portion of the zero pressure gradient turbulent boundary layer, the total shear stress $-\overline{\rho u'' v''} + \mu \partial u/\partial y$ is approximately constant

$$0 = \frac{\partial}{\partial y}\left(-\overline{\rho u'' v''} + \tilde{\mu}\frac{\partial \tilde{u}}{\partial y}\right) \qquad (159)$$

By comparison with the streamwise momentum equation (73), this implies that convective effects are negligible in this portion of the boundary layer. It is reasonable to assume that convective effects are likewise negligible in the conservation equations for energy, k and ϵ. Thus, the equations are[40]

$$0 = \frac{\partial}{\partial y}\left(-\overline{\rho u'' v''} + \mu\frac{\partial u}{\partial y}\right) \qquad (160)$$

$$0 = \frac{\partial}{\partial y}\left[-c_p\overline{\rho T'' v''} - q_y + \left(-\overline{\rho u'' v''} + \mu\frac{\partial u}{\partial y}\right)u\right] \qquad (161)$$

$$0 = -\overline{\rho u'' v''}\frac{\partial u}{\partial y} - \rho\epsilon + \frac{\partial}{\partial y}\left(\frac{\mu_t}{\sigma_k \rho}\frac{\partial \rho k}{\partial y}\right) \qquad (162)$$

$$0 = -C_1\frac{\epsilon}{k}\overline{\rho u'' v''}\frac{\partial u}{\partial y} - C_2\rho\frac{\epsilon^2}{k} + \frac{\partial}{\partial y}\left(\frac{\mu_t}{\sigma_\epsilon}\frac{\partial \epsilon}{\partial y}\right) \qquad (163)$$

[40] A slightly different form of the k equation has been utilized wherein the diffusion term is

$$\frac{\partial}{\partial y}\left(\frac{\mu_t}{\sigma_k \rho}\frac{\partial \rho k}{\partial y}\right) \text{ instead of } \frac{\partial}{\partial y}\left(\frac{\mu_t}{\sigma_k}\frac{\partial k}{\partial y}\right)$$

to simplify the analysis.

where

$$\mu_t = \rho C_\mu \frac{k^2}{\epsilon} \qquad (164)$$

Eq (160) may be integrated and yields within the turbulent region

$$-\overline{\rho u'' v''} = \tau_w \qquad (165)$$

where τ_w is the (local) wall shear stress. Similarly, Eq (161) may be integrated and yields within the turbulent region

$$-c_p\overline{\rho T'' v''} - \overline{\rho u'' v''}u = -q_w \qquad (166)$$

where

$$q_w = -\hat{k}_w \left.\frac{\partial T}{\partial y}\right|_w \qquad (167)$$

is the heat transfer at the wall. Using (87),

$$c_p\frac{\mu_t}{Pr_t}\frac{\partial T}{\partial y} + \tau_w u = -q_w \qquad (168)$$

Assuming a Crocco-type relationship $T = T(u)$,

$$\frac{c_p}{Pr_t}\underbrace{\mu_t\frac{\partial u}{\partial y}}_{\tau_w}\frac{dT}{du} + \tau_w u = -q_w \qquad (169)$$

which may be directly integrated

$$\frac{T}{T_w} = -\frac{Pr_t}{2c_p T_w}u^2 - \frac{q_w Pr_t}{\tau_w c_p T_w}u + \text{constant} \qquad (170)$$

and since $T \to T_w$ as $u \to 0$,

$$\frac{\rho_w}{\rho} = \frac{T}{T_w} = 1 + \mathcal{B}\frac{u}{u_e} - \mathcal{A}^2\left(\frac{u}{u_e}\right)^2 \qquad (171)$$

where

$$\mathcal{A} = \sqrt{\frac{\gamma-1}{2}Pr_t M_e^2\frac{T_e}{T_w}} \qquad (172)$$

$$\mathcal{B} = -\frac{Pr_t q_w u_e}{c_p T_w \tau_w} \qquad (173)$$

Assume a solution for k of the form

$$\rho k = \alpha u_*^2 \qquad (174)$$

where α is a constant. Then (162) yields

$$\frac{\partial u}{\partial y} = \frac{\rho\epsilon}{\tau_w} \tag{175}$$

Substituting into (163) assuming $\epsilon = \epsilon(u)$,

$$\frac{d^2\epsilon}{d\mathcal{U}^2} - \mathcal{R}^2\mathcal{D}\epsilon = 0 \tag{176}$$

where

$$\mathcal{U} = \frac{u}{u_e} \tag{177}$$

$$\mathcal{R} = \sqrt{\frac{\sigma_\epsilon (C_2 - C_1)}{C_\mu \alpha^3}} \frac{u_e}{u_*} \tag{178}$$

and

$$\mathcal{D}(\mathcal{U}) = \frac{\rho}{\rho_w} = \left(1 + \mathcal{B}\mathcal{U} - \mathcal{A}^2\mathcal{U}^2\right)^{-1} \tag{179}$$

In the incompressible limit, Eqs (162) and (163) admit solutions [15]

$$k = \frac{u_*^2}{\sqrt{C_\mu}} \tag{180}$$

$$\epsilon = \frac{u_*^3}{\kappa y} \tag{181}$$

where

$$\kappa = \sqrt{(C_2 - C_1)\,\sigma_\epsilon \sqrt{C_\mu}} \tag{182}$$

and thus

$$\mathcal{R} = \kappa \frac{u_e}{u_*} \tag{183}$$

An asymptotic solution of (176) can be obtained in the limit $Re \to \infty$ where Re is the Reynolds number. Note that

$$\mathcal{R} = \kappa \sqrt{\frac{2}{c_f} \frac{T_e}{T_w}} \tag{184}$$

and the skin friction coefficient $c_f \to 0$ as $Re \to \infty$. The solution, obtained[41] by the WKBJ Method [84], is

$$\epsilon \sim E\left(1 + \mathcal{B}\mathcal{U} - \mathcal{A}^2\mathcal{U}^2\right)^{1/4} \exp\left\{-\frac{\mathcal{R}}{\mathcal{A}} \sin^{-1}\left[\frac{2\mathcal{A}^2\mathcal{U} - \mathcal{B}}{\sqrt{\mathcal{B}^2 + 4\mathcal{A}^2}}\right]\right\} \tag{185}$$

[41] Two solutions are allowed by the WKBJ Method, but only one is bounded as $y \to \infty$.

where E is a constant. Using (175) and integrating, the expression for the velocity to lowest order is

$$u^+ = \frac{u_*}{\kappa} \log y^+ + \breve{B} u_* \tag{186}$$

where

$$u^+ = \frac{u_e}{\mathcal{A}} \left\{ \sin^{-1}\left(\frac{2\mathcal{A}^2 u/u_e - \mathcal{B}}{\sqrt{\mathcal{B}^2 + 4\mathcal{A}^2}}\right) + \sin^{-1}\left(\frac{\mathcal{B}}{\sqrt{\mathcal{B}^2 + 4\mathcal{A}^2}}\right) \right\} \tag{187}$$

Comparison with (156) yields

$$\begin{aligned} \mathcal{A} &= A \\ \mathcal{B} &= B \\ \breve{B} &= \hat{B} \end{aligned} \tag{188}$$

Using (158), the second equation implies

$$\frac{2c_h}{c_f} = \frac{1}{Pr_t} \tag{189}$$

where the Stanton number c_h is

$$c_h = \frac{q_w}{\rho_e u_e c_p (T_w - T_{aw})} \tag{190}$$

where q_w is the heat transfer to the fluid (positive if heat is transferred to the fluid), T_w is the wall temperature, and T_{aw} is the adiabatic wall temperature. Eq (189) is the Reynolds analogy.

The asymptotic forms for k and ϵ are

$$\rho k \sim \frac{\rho_w u_*^2}{\sqrt{C_\mu}} \tag{191}$$

$$\epsilon \sim \left(\frac{\rho_w}{\rho}\right)^{1/4} \frac{u_*^3}{\kappa y} \tag{192}$$

Eqs (186), (191) and (192) can be used to formulate boundary conditions in the vicinity of the wall outside the viscous sublayer (wall functions) as described, for example, in Jacon and Knight [85].

15 RESULTS

We present a selection of computations using the range of turbulence models described previously. The emphasis is on compressible turbulent flows in simple geometries. The efficacy of the turbulence models is determined by comparison with experiment. Although the examples described below illustrate the typical performance of these turbulence models, the selection is by no means exhaustive.

In comparing computations and experiment, we employ terms such as "excellent", "good", "fair" and "poor". The precise definition of these terms is, in the author's opinion, impractical although there is reasonably uniform conformity amongst researchers in their use. In general, we employ the following qualitative definitions. "Excellent" agreement implies either agreement to within the experimental uncertainty or plottable accuracy.[42] "Poor" agreement implies both significant quantitative differences (*e.g.*, percentage relative differences which are several times the experimental uncertainty) and disagreement in the trends (*e.g.*, the experimental data increases with x and the computed results decrease with x). "Fair" and "good" are qualitative judgments intermediate between the two extremes of excellent and poor. An "accurate" prediction also means "good" to "excellent".

15.1 Flat Plate

The simplest configuration for a bounded compressible turbulent shear flow is a boundary layer on a flat plate with no pressure gradient. In general, all turbulence models accurately predict the mean flow properties,[43] *e.g.*, skin friction coefficient,[44] heat transfer coefficient, and mean profiles of velocity and temperature. In Fig. 1, the predicted skin friction coefficient c_f using the Cebeci-Smith model is compared at several different Mach numbers with experimental data for an adiabatic flat plate [40]. The Reynolds number Re_x based on distance x from the leading edge varies among the different experiments. In each case, the ratio of c_f at the specific Mach number to the incompressible c_f at the same Re_x is shown. Also displayed is the Spalding-Chi correlation [86]. The predicted c_f is within the experimental uncertainty indicated by the data scatter. In Fig. 2, the Cebeci-Smith model is compared with experimental data of Winkler and Cha [87] for a non-adiabatic flat plate boundary layer at Mach 5.2 and $T_w/T_e = 5.145$ for Stanton number (190) and skin friction coefficient.[45]

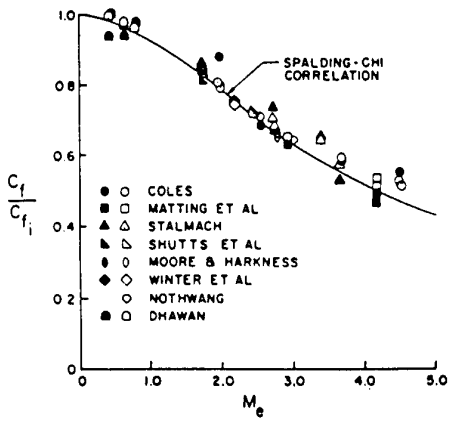

Figure 1: Skin friction coefficient *vs* Mach number on adiabatic flat plate. Open symbols are computed values using Cebeci-Smith model, and closed symbols are experimental values (from [40])

In Figs. 3 and 4, the computed skin friction and momentum thickness Reynolds number Re_θ using the Baldwin-Lomax model are compared

[42] Agreement to within plottable accuracy implies that the differences between the two results are indistinguishable on an appropriately scaled plot.

[43] Except possibly at low Reynolds numbers; see, for example, Cebeci *et al* [40].

[44] The local skin friction coefficient is defined as

$$c_f = \frac{\tau_w}{\frac{1}{2}\rho_\infty u_\infty^2} \tag{193}$$

Sometimes, the notation $\frac{1}{2}\rho_e u_e^2$ is employed to denote the dynamic pressure based on conditions at the local edge of the boundary layer, which may differ in the experiment from the freestream dynamic pressure $\frac{1}{2}\rho_\infty u_\infty^2$ upstream of the flat plate.

[45] Using the empirical formula [7]

$$T_{aw} = T_e\left[1 + \frac{(\gamma-1)}{2} r M_e^2\right] \tag{194}$$

where $r \approx Pr^{\frac{1}{3}}$, the experiment of Winkler and Cha corresponds to $T_w/T_{aw} = 0.88$. Alternately, using (158), $T_w/T_{aw} = 0.85$. This implies a *cold* wall (*i.e.*, $T_w < T_{aw}$).

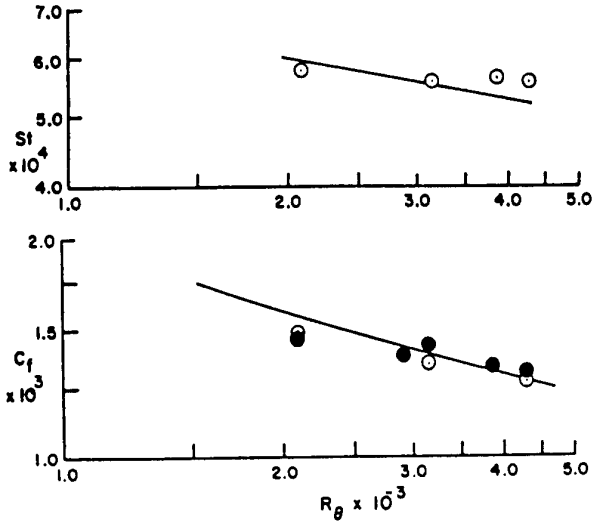

Figure 2: Stanton number St and skin friction coefficient c_f *vs* Re_θ on a flat plate. Symbols are experimental values, and solid line is computed values using Cebeci-Smith model (from [41])

with the correlation of Hopkins and Inouye [88] for an adiabatic flat plate boundary layer at $M_\infty = 1.5$ and 2.85. The comparison is good.

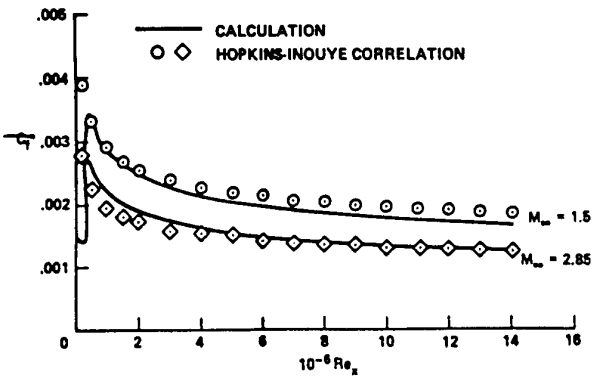

Figure 3: Skin friction coefficient *vs* Re_x on adiabatic flat plate. Open symbols are Hopkins-Inouye correlation, and solid line is computed result using Baldwin-Lomax model (from [44]).

In Fig. 5, the computed skin friction for an adiabatic flat plate boundary layer using the Wilcox k–ω model with several different compressibility corrections is compared to the Van Driest correlation [88] for Mach numbers up to five. The comparison is very good.

In Fig. 6, the computed skin friction for an adia-

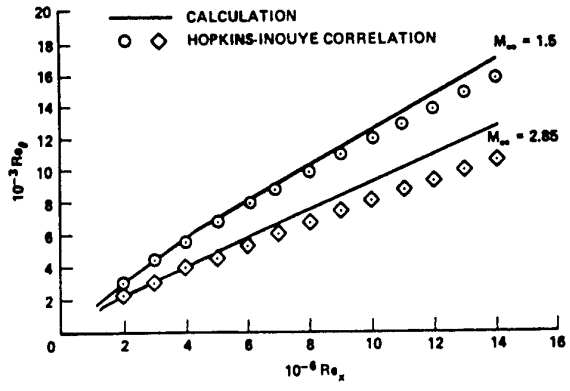

Figure 4: Re_θ *vs* Re_x on adiabatic flat plate. Open symbols are Hopkins-Inouye correlation, and solid line is computed result using Baldwin-Lomax model (from [44]).

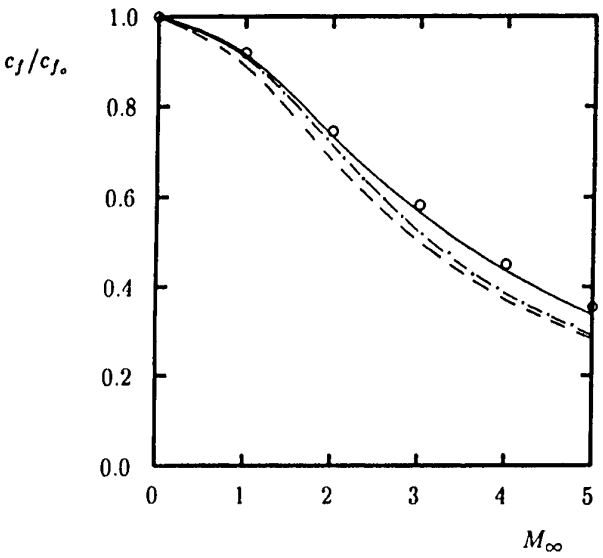

Figure 5: Skin friction coefficient *vs* Mach number on adiabatic flat plate. — k–ω with $\xi^* = 0$ and $\xi^* = 3/2$, –– Sarkar with $\xi^* = 1$, – · – Zeman with $\xi^* = 3/4$, ∘ Van Driest correlation (from [15])

batic flat plate at $Re_\theta = 10^4$ using the Speziale-Sarkar-Gatski (SSG) model is compared with the correlation of Van Driest [88]. The agreement is very good. Similar close agreement is obtained for cold wall flat plate boundary layer [18].

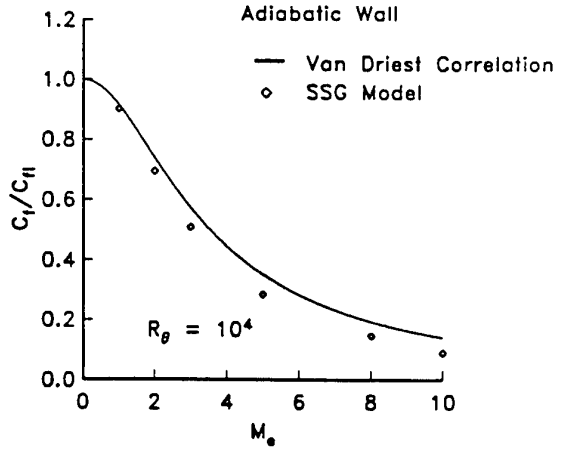

Figure 6: Skin friction coefficient *vs* Mach number on adiabatic flat plate at $Re_\theta = 10^4$. ○ Speziale-Sarkar-Gatski model, — Van Driest correlation [88] (from [18]).

15.2 Transonic Bump

An axisymmetric transonic shock wave turbulent boundary layer interaction was generated by an thin wall cylinder with a circular arc bump [89] as shown in Fig. 7. The Mach number range is $M_\infty = 0.43$ to 0.925. The Reynolds number $Re_x = 6.1 \times 10^6$ at $M_\infty = 0.875$ based on distance of the leading edge of the bump from the leading edge of the cylinder. The chord of the bump $c = 20.3$ cm and the thickness ratio is 0.0936. A strong embedded shock formed on the downstream portion of the bump causing a massive separation of the boundary layer. Computations were performed by Johnson [57] using the Johnson-King model [57], and by Horstman and Johnson [90] using both the Cebeci-Smith and Jones-Launder ($k-\epsilon$) models.

The computed and experimental surface pressure coefficient c_p is shown in Fig. 8 for $M_\infty = 0.6$ to 0.925. Results are presented for the

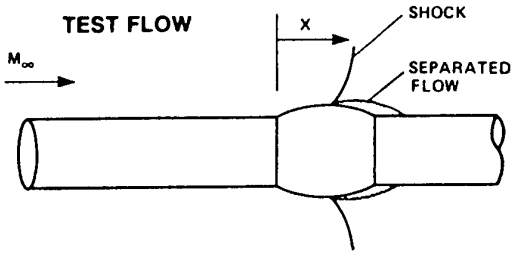

Figure 7: Transonic bump (from [57])

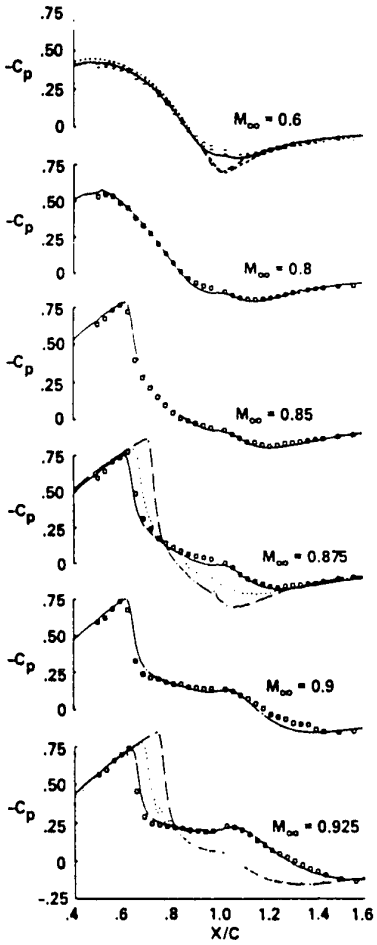

Figure 8: Surface pressure coefficient for transonic bump — Johnson-King, - - - Jones-Launder, — — Cebeci-Smith, □ experiment (from [57])

Johnson-King model at six Mach numbers, and for the Cebeci-Smith and Jones-Launder ($k-\epsilon$) models at three Mach numbers. The Johnson-King model is clearly superior. In particular, Johnson-King accurately predicts the location of the embedded shock which is indicated by the abrupt decrease in $-c_p$ (*e.g.*, at $x/c \approx 0.6$ for $M_\infty = 0.875$).

The predicted compressible boundary layer displacement thickness δ^* is displayed in Fig. 9 for $M_\infty = 0.875$. On the bump ($0 < x/c < 1$), the Johnson-King provides the most accurate prediction of δ^*. This is expected, since the displacement thickness, in combination with the surface shape, determines the pressure distribution and thus the location of the embedded shock.

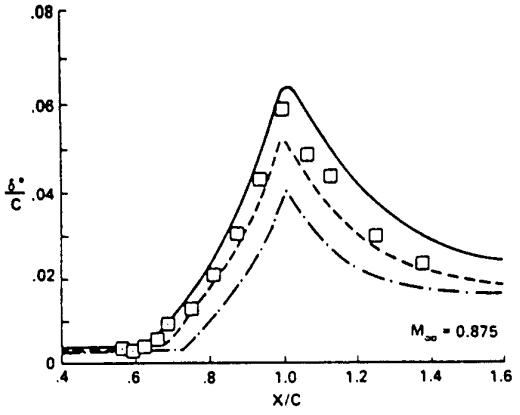

Figure 9: Displacement thickness for transonic bump — Johnson-King, - - - Jones-Launder, — · — Cebeci-Smith, □ experiment (from [57])

The velocity profile at the trailing edge of the bump ($x = c$) for $M_\infty = 0.875$ is shown in Fig. 10. The Johnson-King model is again superior, with the Cebeci-Smith model yielding the worst prediction.

The separation and reattachment locations for $0.43 < M_\infty < 0.925$ are presented in Fig. 11 for the Johnson-King and Jones-Launder models. The Johnson-King model is more accurate.

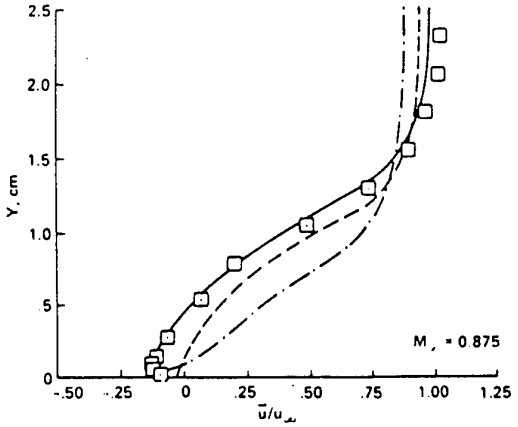

Figure 10: Velocity profile at model trailing edge for transonic bump — Johnson-King, - - - Jones-Launder, — · — Cebeci-Smith, □ experiment (from [57])

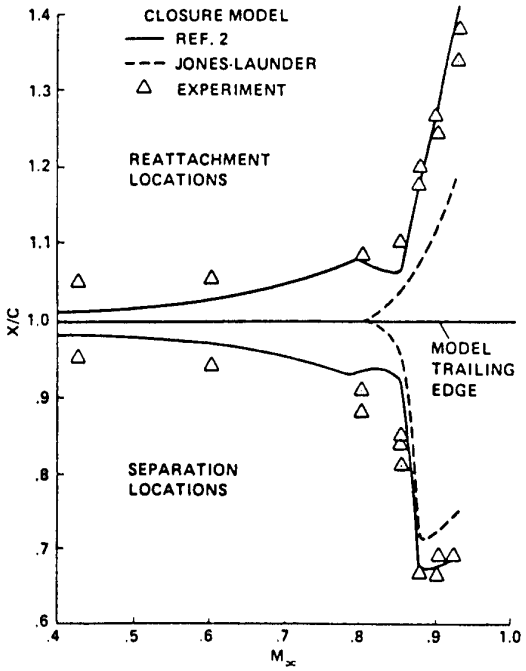

Figure 11: Separation and reattachment locations for transonic bump — Johnson-King, - - - Jones-Launder, △ experiment (from [57])

15.3 Transonic Airfoil I

A transonic shock wave turbulent boundary layer interaction was generated on an NACA 0012 airfoil [91] at angle of attack. The Mach number range is $M_\infty = 0.55$ to 1.1 and the Reynolds number $Re_c = 9 \times 10^6$ based on the chord. Computations by Coakley [92] (using the Cebeci-Smith, Baldwin-Lomax, Johnson-King and $q-\omega$ models) and King [93] (using the Baldwin-Lomax, Cebeci-Smith and Johnson-King models) are presented herein.

The computed and experimental surface pressure on the airfoil are shown in Figs. 12 and 13 for the computations by Coakley and King, respectively. The Johnson-King model is clearly superior in predicting the pressure distribution (and, in particular, the embedded shock location) on the suction surface .

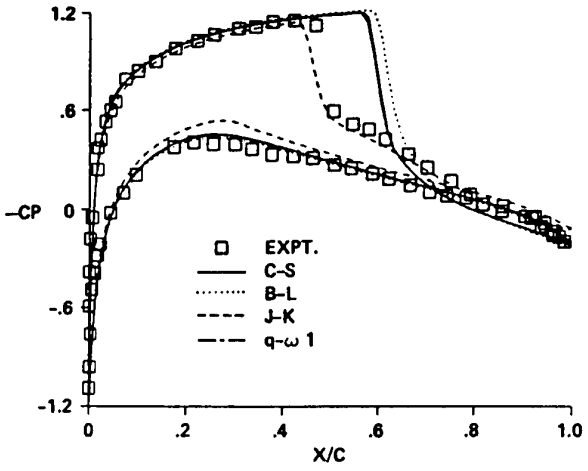

Figure 12: Surface pressure on NACA 0012. C-S Cebeci-Smith, B-L Baldwin-Lomax, J-K Johnson-King (from [92])

15.4 Transonic Airfoil II

A transonic shock wave turbulent boundary layer interaction was generated on an RAE2822 airfoil [94] at angle of attack. The Mach number is $M_\infty = 0.750$, the Reynolds number $Re_c =$

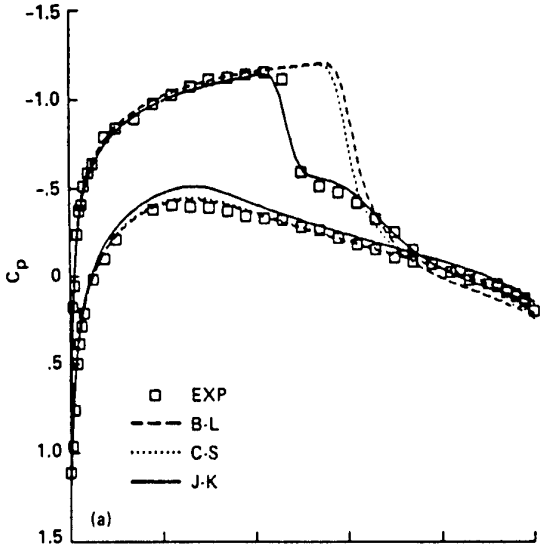

Figure 13: Surface pressure on NACA 0012. C-S Cebeci-Smith, B-L Baldwin-Lomax, J-K Johnson-King (from [93])

6.2×10^6 and angle of attack $\alpha = 3.19°$.[46] Computations were performed by Hellström *et al* [96] using the four turbulence models, namely, Baldwin-Lomax, k–ϵ, and two versions of a Reynolds Stress Equation model.

In Fig. 14, the computed and experimental surface pressure coefficient c_p is displayed. The boundary layer on the upper surface separates due to the embedded shock wave. All of the turbulence models predict separation in the vicinity of the shock. For the Baldwin-Lomax model computation, the boundary layer does not reattach on the airfoil surface. Although the Reynolds Stress Equation model provides the most accurate prediction of the shock location, it nonetheless overestimates the location of the shock by approximately $0.05c$.

In Fig. 15, the computed and experimental momentum thickness θ/c is shown. The Reynolds Stress Model displays the closest agreement with experiment.

[46] In order to compensate for blockage effects in the wind tunnel test, the computed test conditions [95] were $M_\infty = 0.754$ and $\alpha = 2.57°$. The Reynolds number was unchanged.

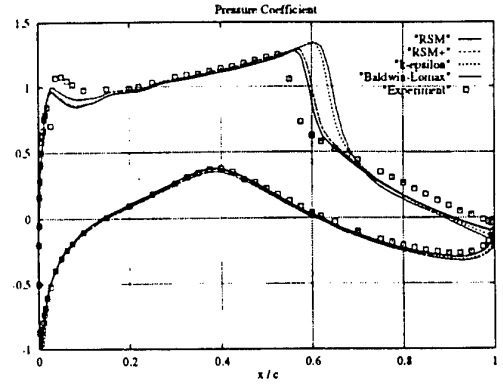

Figure 14: Pressure coefficient *vs* x/c for RAE2822 airfoil (from [96])

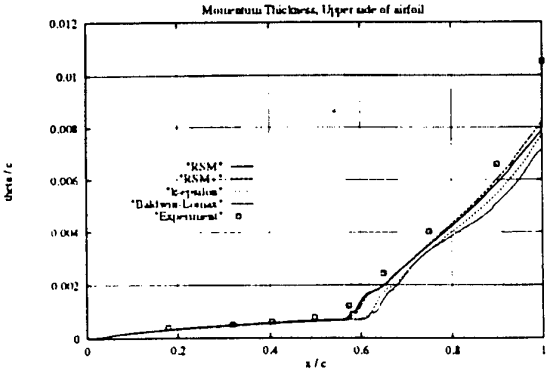

Figure 15: Momentum thickness θ/c *vs* x/c for RAE2822 airfoil (from [96])

15.5 Transonic Nozzle

A 2-D transonic shock wave turbulent boundary layer interaction was generated in a nozzle comprised of a straight upper surface and a lower wall with a bump [97]. The experimental configuration is shown[47] in Fig. 16. The inflow Mach number $M_\infty = 0.63$, and the Reynolds number based on the momentum thickness $Re_\theta = 3.8 \times 10^3$. The second throat controls the downstream pressure to enable a normal shock to be fixed in the vicinity of the trailing edge of the bump. The flow structure is shown in Fig. 17. Computations were performed by Degrez *et al* [98] using the Baldwin-Lomax and $k-\epsilon$ models.

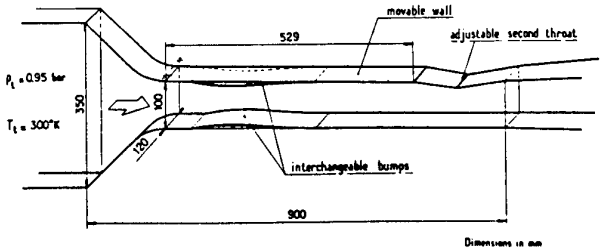

Figure 16: Transonic nozzle (from [97])

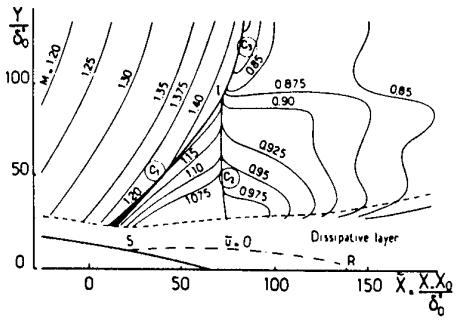

Figure 17: Flow structure for transonic nozzle (from [97])

In Fig. 18, the computed and experimental surface pressure is displayed. The agreement upstream of the shock is excellent. In the vicin-

[47] The upper bump was removed in the experiment.

ity of the shock wave boundary layer interaction, the Baldwin-Lomax model more accurately predicts the location of the initial pressure rise, while the $k-\epsilon$ model provides a more accurate prediction of the plateau pressure.[48]

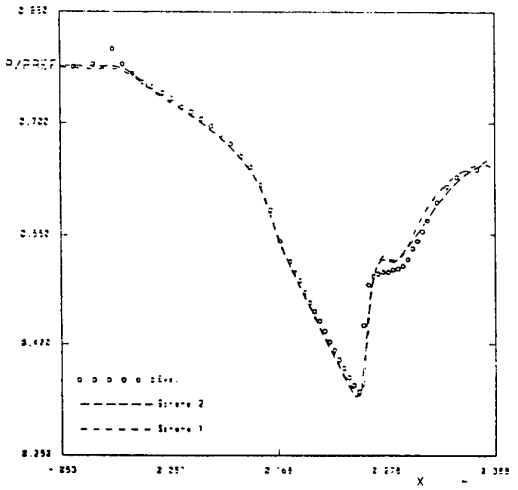

Figure 18: Surface pressure for transonic nozzle — — $k-\epsilon$, - - - Baldwin-Lomax, ○ experiment (from [98])

In Fig. 19, the computed and experimental mean velocity profiles at four successive x locations are shown. The $k-\epsilon$ model predictions are in close agreement with experiment and superior to the Baldwin-Lomax model.

The definition of the Baldwin-Lomax outer function (96) can lead to pathological behavior for $n_{\max}$ in shock wave turbulent boundary layer interactions. In Fig. 20, the computed distribution of $n_{\max}$ *vs* x is displayed.[49] An abrupt and unphysical rise in $n_{\max}$ is observed at $x = 3.0$ due to the large value of vorticity in the vicinity in the quasi-normal shock wave in the nozzle. This behavior can be eliminated by *ad hoc* restriction of allowable values of $n_{\max}$ as described, for example, in Degrez *et al* [98], Visbal and Knight [49], and Degani and Schiff [50].

[48] For 2-D separated flows, the surface pressure is approximately constant in the separation region (see, for example, Green [99]).

[49] The distribution of $n_{\max}$ is based on the converged solution obtained with the modified Baldwin-Lomax model (see [98] for details).

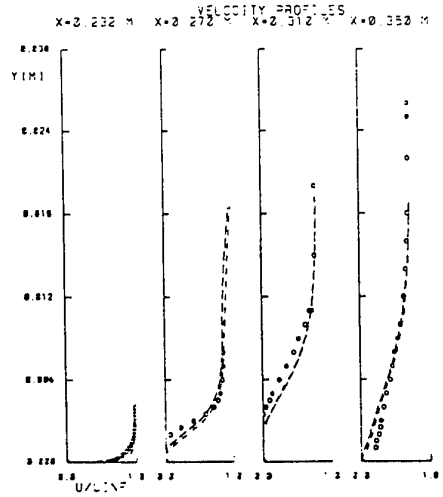

Figure 19: Velocity profiles for transonic nozzle — — $k-\epsilon$, - - - Baldwin-Lomax, ○ experiment (from [98])

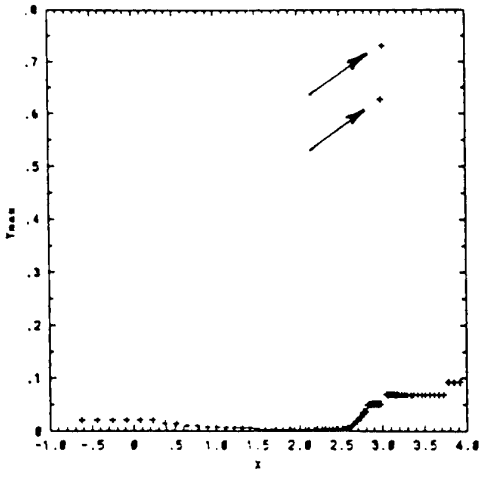

Figure 20: Behavior of $n_{\max}$ for transonic nozzle (from [98])

15.6 Wall Jet

A wall jet generates a complex viscous-inviscid interaction. Aso *et al* [100] performed a series of experiments for a 2-D sonic nitrogen wall jet injected into a supersonic airstream. The experimental configuration is shown in Fig. 21. The freestream Mach number $M_\infty = 3.71$, the Reynolds number based on the distance l from the leading edge to the injection slot is $Re_l = 2.07 \times 10^7$, and the ratio of total pressure in the wall jet to the freestream airstream is 0.31. The jet causes a strong shock to form upstream which separates the incoming boundary layer. Computations were performed by Gerlinger *et al* [101] using several versions of the q–ω model.

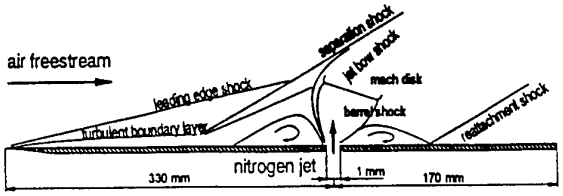

Figure 21: Wall jet (from [101])

The computed and experimental surface pressure is shown in Fig. 22. The different versions of the $q-\omega$ model display small variations in the surface pressure, with the closest agreement achieved with the length scale limitation (correction 1) and modified constant for the velocity divergence term (correction 2) [101]. None of the computations accurately predict the upstream influence in the surface pressure. This behavior is typical of zero- and two-equation turbulence model predictions for 2-D/axisymmetric and 3-D shock wave turbulent boundary layer interactions [102, 103]. For the 2-D/axisymmetric shock wave turbulent boundary layer interaction generated by a compression ramp, for example, the separation shock is observed to be unsteady with gross displacement on the order of the incoming boundary layer thickness δ, while the computations indicate a stationary shock system [102, 104]. Possibly, the discrepancy between the computed and experimental surface pressure in Fig. 22 may be attributable to unsteadiness in the experimental separation shock; however, there is no mention of unsteadiness in the experiment [105].

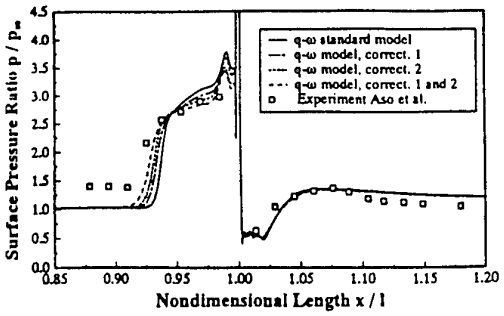

Figure 22: Surface pressure for wall jet (from [101])

15.7 Supersonic Curved Compression Ramp

An adverse pressure gradient supersonic turbulent boundary layer is created by a curved surface as shown in Fig. 23. The upstream Mach number $M_\infty = 2.87$, the Reynolds number $Re_\delta = 1.58 \times 10^6$, and the ratio of incoming boundary layer thickness δ to the radius of curvature R_c of the surface is 0.02 (Case 1) and 0.10 (Case 2). Experiments were performed by Smits and his colleagues [106, 107]. Computations were performed by Lee *et al* [108] using the Baldwin-Lomax, $k-\epsilon$ and Lee-Taulbee-Holden Reynolds Stress Equation models [108].

In Fig. 24, the computed and experimental surface skin friction coefficient c_f is presented for Case 2. The experimental c_f is determined by two different methods (Preston tube and velocity extrapolation). The computed c_f is within the experimental uncertainty.

In Figs. 25 and 26, the computed and experimental turbulent normal and shear stress are shown. The Lee-Taulbee-Holden Reynolds Stress Equation model displays closer agreement with the normal Reynolds stress than the $k-\epsilon$ model; however, the opposite holds for the Reynolds shear stress over most of the boundary layer.

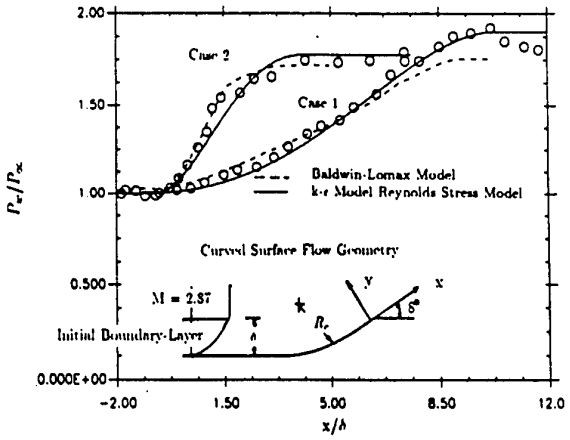

Figure 23: Geometry and surface pressure for curved compression ramp (from [108])

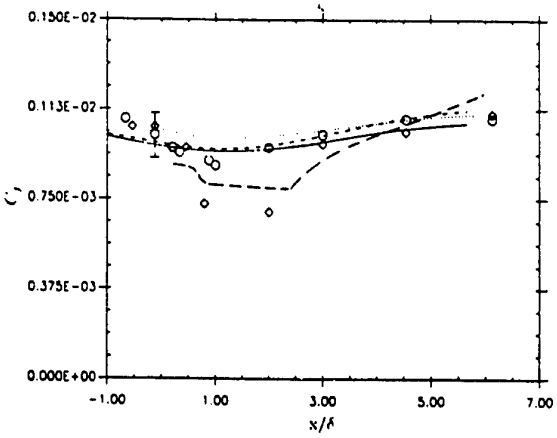

Figure 24: Skin friction *vs* x/δ for supersonic curved compression ramp (Case 2). ○ Experiment (Preston tube), ◇ Experiment (velocity profile extrapolation), — Reynolds Stress Equation ('Mass' version), - - Reynolds Stress Equation ('Standard' version), ··· $k-\epsilon$ model, – – Baldwin-Lomax model (from [108])

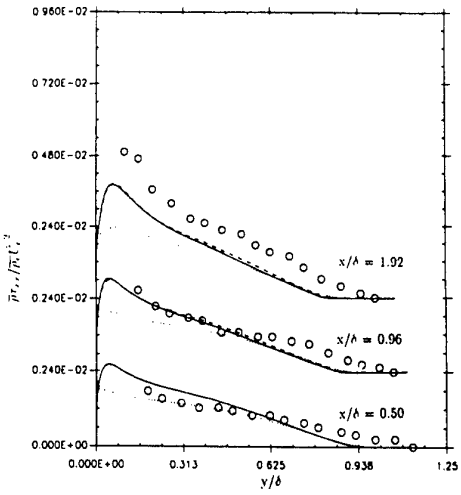

Figure 25: Turbulent normal stress for supersonic curved compression ramp (Case 2). ○ Experiment, — Reynolds Stress Equation ('Mass' version), - - Reynolds Stress Equation ('Standard' version), ··· $k-\epsilon$ model (from [108])

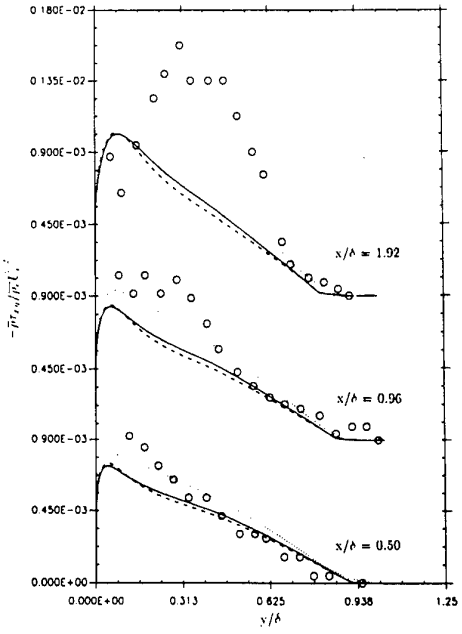

Figure 26: Turbulent shear stress for supersonic curved compression ramp (Case 2). ○ Experiment, — Reynolds Stress Equation ('Mass' version), - - Reynolds Stress Equation ('Standard' version), ··· $k-\epsilon$ model (from [108])

15.8 Supersonic Compression Corner

The supersonic compression corner generates a shock wave turbulent boundary layer interaction as shown in Fig. 27. The upstream Mach number $M_\infty = 2.87$ and the Reynolds number $Re_\delta = 1.82 \times 10^6$. Experiments were performed by Smits and Muck [109] for corner angles $\alpha = 8°, 16°$ and $20°$. Computations [77] are presented for the Zhang-So-Gatski-Speziale model [76].

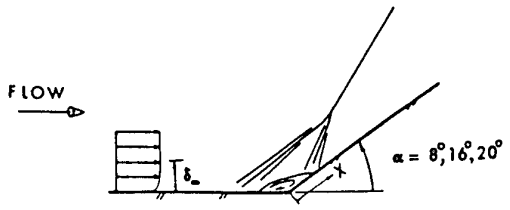

Figure 27: Supersonic compression corner

In Fig. 28, the mean velocity parallel to the surface is shown for the $\alpha = 8°$. This flow is unseparated [109]. The agreement is excellent. The normal Reynolds stress is displayed in Fig. 29. Upstream of the interaction, ($s = -0.0508$), the agreement between the computation and experiment is very good. Downstream of the interaction, differences are evident although the computation shows similar trends as the experiment. A similar conclusion holds for the Reynolds shear stress (Fig. 30). Additional results are presented in [77] for the 16° and 20° cases. The conclusions are similar to the 8° case. Also, the predicted mean velocity profile shows significant differences from experiment in the vicinity of the corner for the 20° (separated) case.[50]

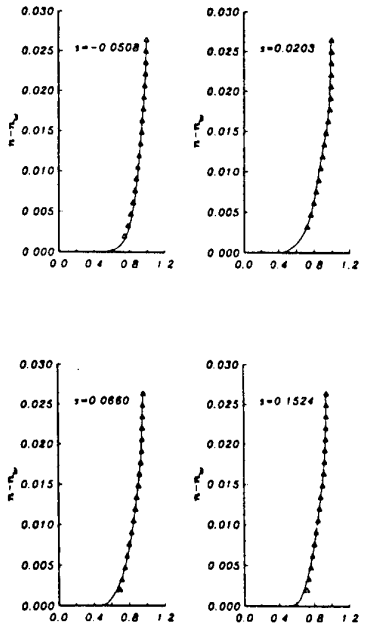

Figure 28: Mean velocity (parallel to surface) for 8° supersonic compression ramp (from [77])

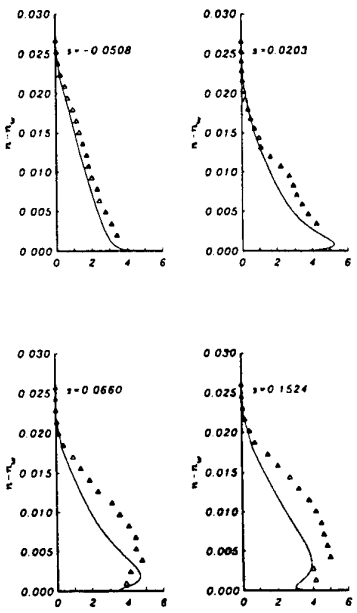

Figure 29: Normal Reynolds stress $\tau_{ss} \times 10^3$ for 8° supersonic compression ramp (from [77])

[50] It should be noted that experimental data indicates that the separation shock for the $\alpha = 20°$ case is unsteady with streamwise excursions of $\mathcal{O}(\delta)$.

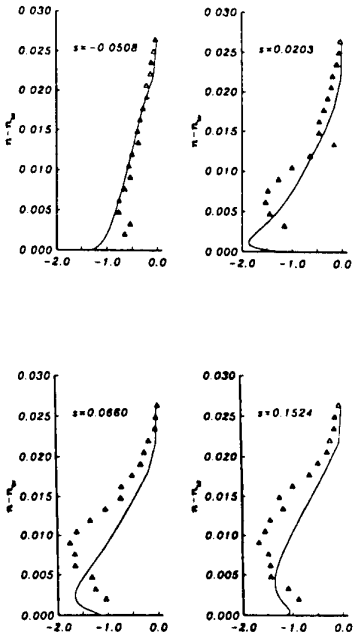

Figure 30: Reynolds shear stress $\tau_{sn} \times 10^3$ for 8° supersonic compression ramp (from [77])

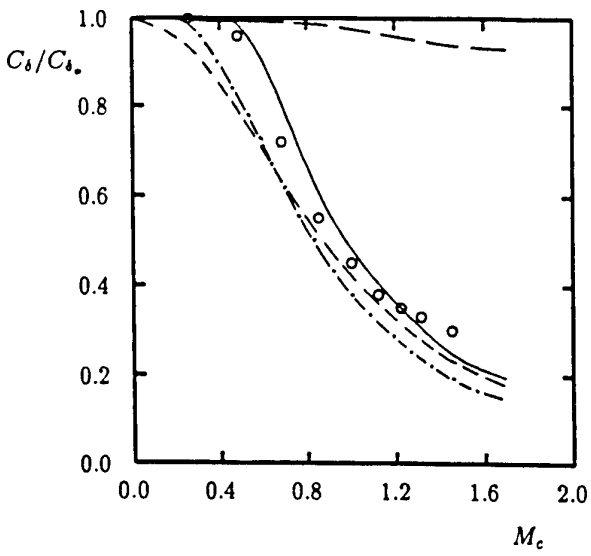

Figure 32: Growth rate for compressible mixing layer *vs* M_c – – unmodified $k-\omega$ model, — Wilcox $\xi^* = 3/2$, - - Sarkar $\xi^* = 1$, - · - Zeman $\xi^* = 3/4$, ○ experiment (from [15])

15.9 Mixing Layer

The compressible mixing layer (Fig. 31) is formed by two compressible streams with different velocities and temperatures. Experiments [110, 111] have demonstrated that the growth rate of the compressible mixing layer is reduced relative to the incompressible case, and correlates with the convective Mach number M_c defined by

$$M_c = \frac{u_1 - u_2}{a_1 + a_2} \tag{195}$$

where a is the speed of sound.

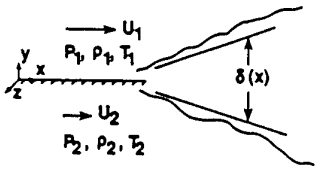

Figure 31: Compressible shear layer (from [112])

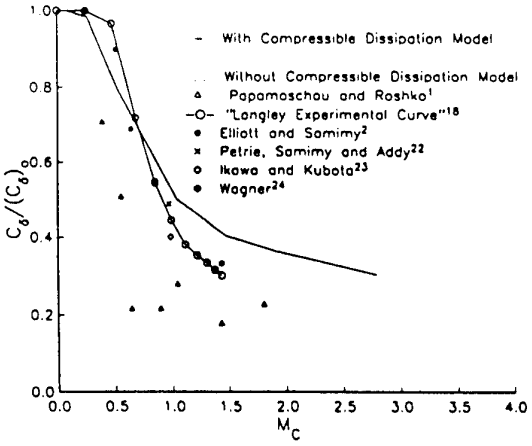

Figure 33: Growth rate for compressible mixing layer *vs* M_c (from [112])

Various compressibility modifications to two-equation and Reynolds Stress Equation models have been proposed to improve agreement between the computed and experimental growth rate as a function of M_c. The width of the shear layer $\delta(x)$ is observed to vary linearly[51] with x and is given by

$$\frac{d\delta}{dx} = C_\delta \left(\frac{u_1 - u_2}{u_1 + u_2} \right) \tag{196}$$

where C_δ is a function of M_c.

In Figs. 32 and 33, the ratio of the compressible to incompressible growth rate C_δ / C_{δ_o} *vs* M_c is displayed for several variants of the Wilcox $k-\omega$ model [15] and the Reynolds Stress Equation model of Sarkar *et al* [112]. The effect of compressibility on the growth rate is accurately predicted.

15.10 Jet

The supersonic jet in a quiescent fluid is a compressible free shear flow. Thies and Tam [69] performed a series of computations for jet Mach numbers $M_j = 0.4$ to 2.0 and temperature ratios from 1.0 to 4.0 using the $k-\epsilon$ model with the corrections[52] of Pope [70] and Sarkar [71]. Moreover, Thies and Tam proposed a new set of values for the constants in the $k-\epsilon$ model (see Table 8), on the basis of the argument that the large scale eddies are dependent on the flow geometry, and hence no single set of turbulence constants in a Reynolds-averaged Navier-Stokes model can be expected to yield accurate results for all types of turbulent flows.

In Fig. 34, computed and experimental mean velocity profiles are displayed for the cold, Mach 0.4 axisymmetric jet configuration of Schreck *et al* [113]. The agreement is excellent. In Fig.

[51] Outside an inception region near the trailing edge of the splitter plate in Fig. 31.

[52] The correction of Pope [70] was developed to correct the observed inability of the $k-\epsilon$ model to accurately predict the spreading rate of an incompressible round jet. In the absence of the Pope correction, the $k-\epsilon$ model overestimates the spreading rate of the incompressible round jet by 40% [70]. The correction of Sarkar *et al* was developed to correct the observed inability of a Reynolds Stress Equation model to accurately predict the spreading rate of a compressible free shear layer as described in the previous section.

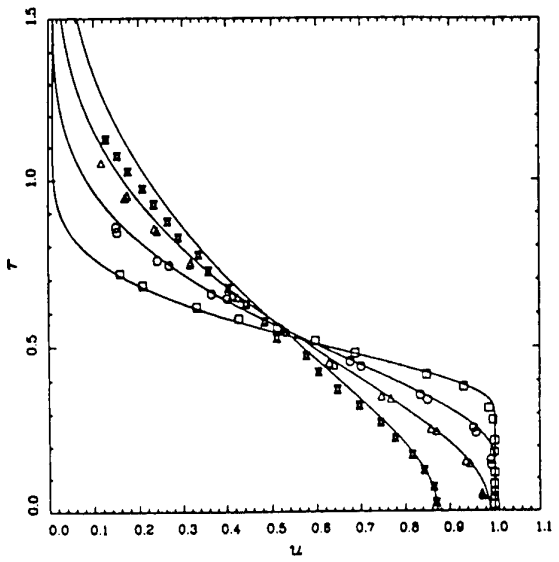

Figure 34: Axial velocity for cold, Mach 0.4 axisymmetric jet. Experimental data from Schreck *et al* [113] at □ $x = 2.0$, ○ $x = 4.0$, △ $x = 6.0$, XX $x = 8.0$. — computed (from [69])

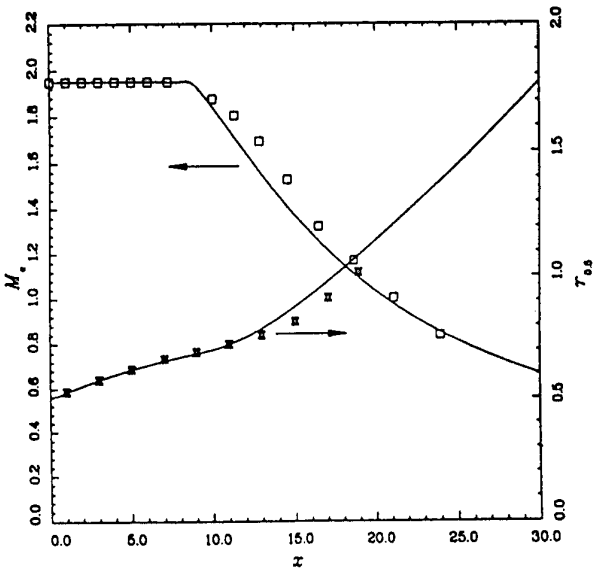

Figure 35: Centerline Mach number and half-velocity point distributions for cold, Mach 2.0 axisymmetric jet. Experimental data from Seiner *et al* [114] for □ centerline Mach number, XX half-velocity radius. — computed (from [69])

35, the computed and experimental centerline Mach number and half-velocity point distributions are shown for the cold, Mach 2.0 axisymmetric jet configuration. Again, the agreement is very good.

15.11 Afterbody

The axisymmetric afterbody flow is a separated free shear flow (Fig. 36). Experiments were performed by Herrin and Dutton [115, 116, 117] for a cylindrical afterbody at a Mach number $M_\infty = 2.46$ and Reynolds number[53] $Re_d = 3.3 \times 10^6$ based on the cylinder diameter d. Computations were performed by Sahu [118] using the Baldwin-Lomax, Chow and $k-\epsilon$ Chien models and by Tucker and Shyy [119] using two different variants of the $k-\epsilon$ model.

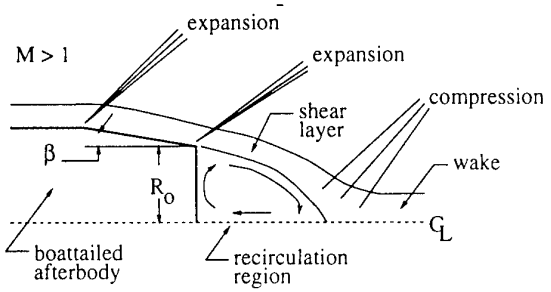

Figure 36: Afterbody geometry and flow structure

In Figs. 37 and 38, the computed and experimental pressure on the afterbody base is shown. None of the turbulence models accurately predict the experimental profile.

In Figs. 39 and 40, the mean streamwise velocity and turbulence kinetic energy are shown at $x/D = 1.42$ which is slightly downstream of the end of the recirculation region ($x/D = 1.3$). The $k-\epsilon$ model displays good agreement with experiment,[54] while the other predictions are in significant disagreement. The predicted turbulence kinetic energy at the same location (Fig. 40) shows significant disagreement with experiment.

[53] The Reynolds number $Re_\delta = 1.66 \times 10^5$ based on the boundary layer thickness δ immediately upstream of the base.

[54] Although larger discrepancies are evident at other x locations [118].

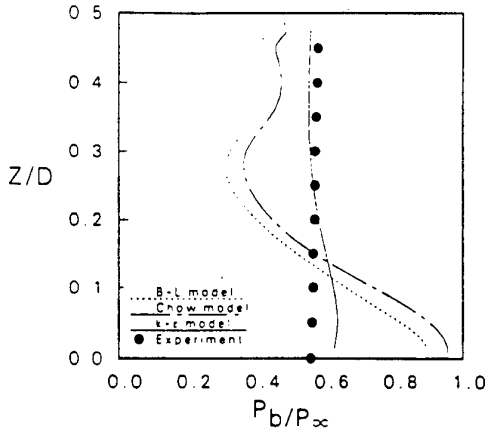

Figure 37: Base pressure for cylindrical afterbody flow ··· Baldwin-Lomax, – · – Chow, — $k-\epsilon$, • experiment (from [118])

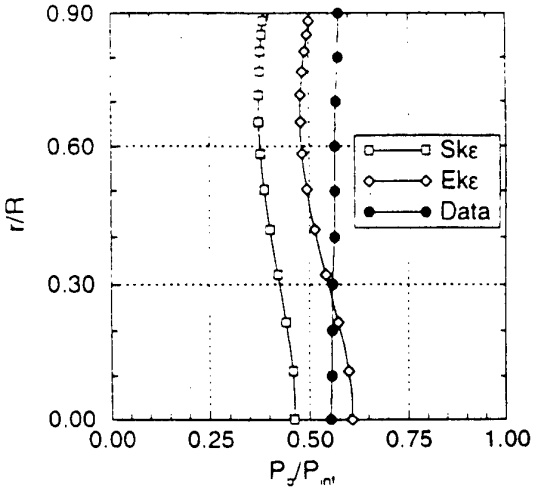

Figure 38: Base pressure for cylindrical afterbody flow (from [119])

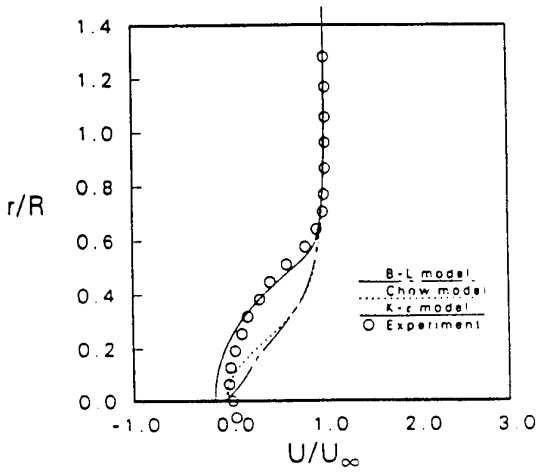

Figure 39: Streamwise mean velocity for cylindrical afterbody flow at $x/D = 1.42$ $-\cdot-$ Baldwin-Lomax, $\cdots$ Chow, — $k-\epsilon$, o experiment (from [118])

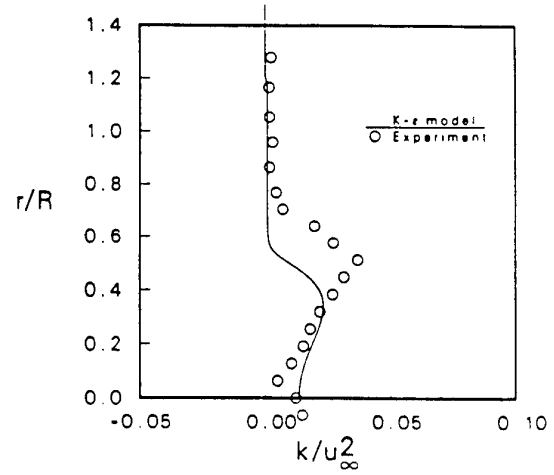

Figure 40: Turbulence kinetic energy for cylindrical afterbody flow at $x/D = 1.42$ $-\cdot-$ Baldwin-Lomax, $\cdots$ Chow, — $k-\epsilon$, o experiment (from [118])

15.12 Cylinder-Offset-Flare

The cylinder-offset-flare generates a 3-D shock wave turbulent boundary layer interaction. The configuration, shown in Fig. 41, is formed by a cylinder and an offset 20° half-angle conical flare. The axis of the conical flare is parallel to the axis of the cylinder, but offset by a distance equal to one-fourth of the diameter of the cylinder. Experiments were performed by Wideman *et al* [120] at a freestream Mach number $M_\infty = 2.89$ and Reynolds number $Re_\delta = 1.65 \times 10^5$ based on the turbulent boundary layer thickness immediately upstream of the interaction. Computations were performed by Gaitonde *et al* [121] using the zero-equation Baldwin-Lomax model, the one-equation Baldwin-Barth [53] and Spalart-Allmaras [55] models, and the two-equation $k-\epsilon$ model. Computations were also performed by Edwards and Chandra [122] using the one-equation models of Baldwin-Barth [53], Baldwin-Barth-Goldberg-Ramakrishnan [123], Edwards-McRae [122] and Spalart-Allmaras [55].

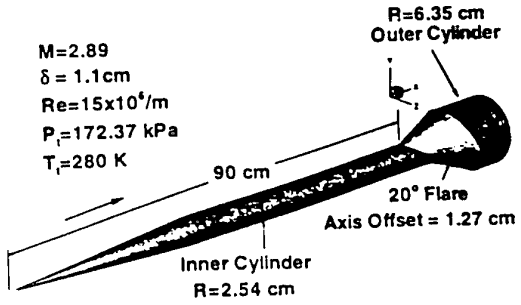

Figure 41: Cylinder-Offset-Flare (from [121])

The surface pressure in shown in Figs. 42 and 43 where $\theta = 0°$ is the upper surface and $\theta = 180°$ is the lower surface. The location of the initial pressure rise is accurately predicted by all models except Baldwin-Barth-Goldberg-Ramakrishnan.[55] However, all mod-

[55]It should be noted that the experimental shock system was stationary for this flow [120]. For 2-D separated turbulent compression ramp flows [102], the computed and experimental surface pressure generally display significant disagreement upstream and in the separated region, likely due to the inability of the RANS computations to predict the unsteady shock motion observed in the experiments.

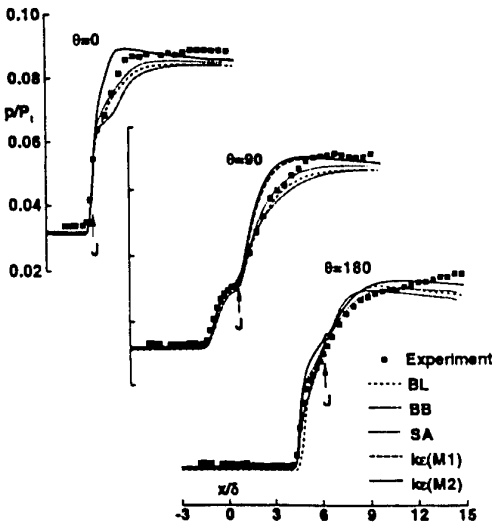

Figure 42: Surface pressure for cylinder-offset-flare. BL Baldwin-Lomax, BB Baldwin-Barth, SA Spalart-Allmaras, $k\epsilon$ (M1) $k-\epsilon$ (mesh 1), $k\epsilon$ (M2) $k-\epsilon$ (mesh 2), J juncture location at particular θ. (from [121])

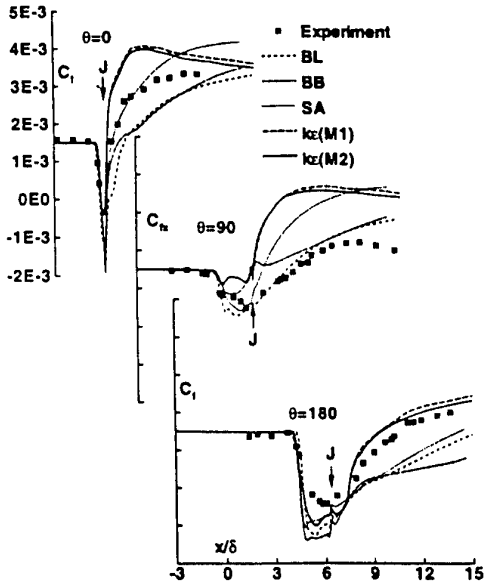

Figure 44: Surface skin friction for cylinder-offset-flare. BL Baldwin-Lomax, BB Baldwin-Barth, SA Spalart-Allmaras, $k\epsilon$ (M1) $k-\epsilon$ (mesh 1), $k\epsilon$ (M2) $k-\epsilon$ (mesh 2), J juncture location at particular θ. (from [121])

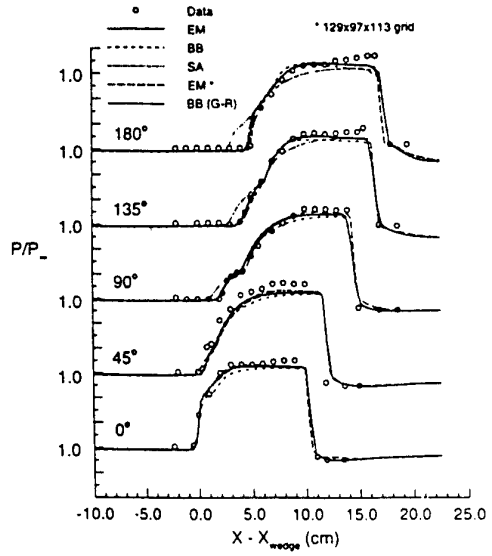

Figure 43: Surface pressure for cylinder-offset-flare. EM Edwards-McRae, BB Baldwin-Barth, SA Spalart-Allmaras, BB(GR) Baldwin-Barth-Goldberg-Ramakrishnan (from [122])

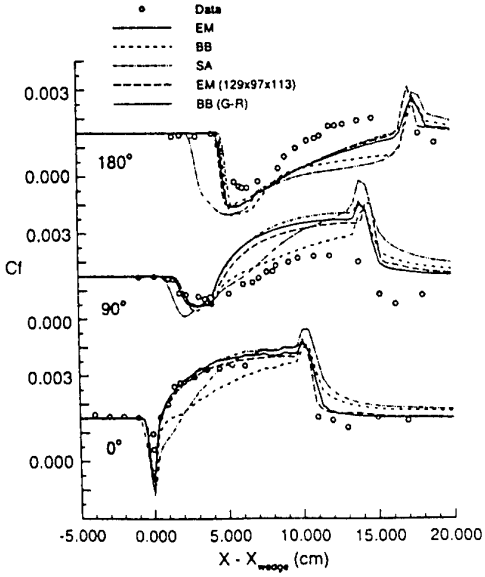

Figure 45: Surface skin friction for cylinder-offset-flare. EM Edwards-McRae, BB Baldwin-Barth, SA Spalart-Allmaras, BB(GR) Baldwin-Barth-Goldberg-Ramakrishnan (from [122])

els display some disagreement with experiment downstream.

The skin friction coefficient c_f is displayed in Figs. 44 and 45. The location of the initial drop in c_f is accurately predicted by all models except Baldwin-Barth-Goldberg-Ramakrishnan; however, there are significant discrepancies for all models within and downstream of the interaction region.

The surface oil flow pattern is displayed in Fig. 46 for the one-equation Baldwin-Barth, Edwards-McRae and Spalart-Allmaras models, and the experiment. The lines of separation (LS) and attachment (LA) are predicted with reasonable accuracy by all models; however, the detailed features within the separated region differ between the computations and experiment, and in particular between the computations themselves.

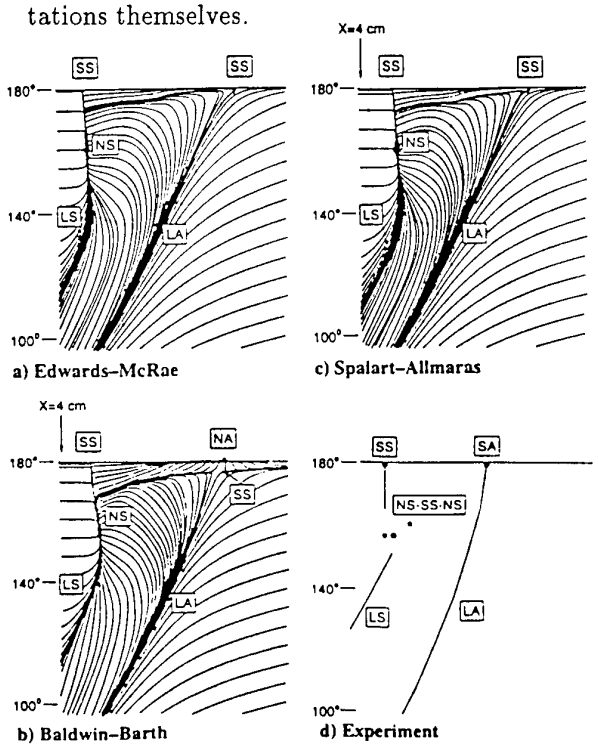

Figure 46: Surface oil flow pattern for cylinder-offset-flare near $\theta = 180°$. LA line of attachment, NA node of attachment, SS saddle of separation, LS line of separation, NS node of separation, SA saddle of attachment (from [121]). For a discussion of the topology of 3-D separated flows, see Tobak and Peake [124].

15.13 Single Fin

The single fin geometry is a wedge of angle α attached normal to a flat plate (Fig. 47) on which an equilibrium turbulent boundary layer has developed. The wedge generates an oblique shock wave which interacts with the turbulent boundary layer on the flat plate. The fin is assumed semi-infinite in height and length. A detailed assessment of several turbulence models for several different configurations of the single fin geometry is described in Knight and Degrez [125]. Herein we present results for a single configuration for Mach number $M_\infty = 4.0$, fin angle $\alpha = 20°$ and Reynolds number $Re_\delta = 2.1 \times 10^5$ based on the boundary layer thickness δ immediately upstream of the interaction. The experimental data was obtained by Kim *et al* [126]. Computations were performed by Edwards [122] (using the Spalart-Allmaras-Edwards model [122]), Horstman [127] (using the $k-\epsilon$ model), Knight [127](using the Baldwin-Lomax model) and Panaras [51] (using the Baldwin-Lomax-Panaras model).

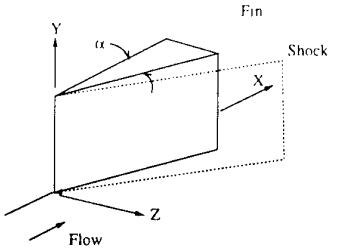

Figure 47: Single fin geometry

The surface pressure[56] is shown in Fig. 48. The Baldwin-Lomax-Panaras and Spalart-Allmaras-Edwards models are the most accurate. Both models predict the surface pressure in the plateau region ($36° \leq \beta \leq 47°$) within 5% to 10%. Also, both models display a pressure trough at $\beta = 32°$, in agreement with experiment, although the predictions differ from the experimental value by 30%. Both models overestimate the peak pressure in the vicinity of the corner by 11%. The predictions of the Baldwin-

[56]The abscissa $\beta = \tan^{-1}[(z-z_o)/(x-x_o)]$ is the angle on the flat plate measured relative to the freestream direction. Outside an initial inception region near the fin leading edge associated with the virtual conical origin at (x_o, z_o), the surface pressure is conical (for a physical description, see [128, 129]) and thus depends only on the angle β.

Lomax and $k-\epsilon$ models exhibit the general trends of the experiment, but are less accurate.

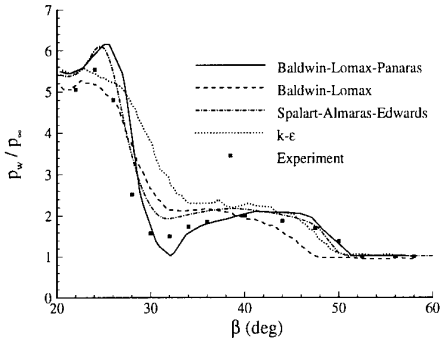

Figure 48: Surface pressure for single fin

The surface streamline angle on the flat plate is displayed in Fig. 49. The Baldwin-Lomax-Panaras is again the most accurate, with the Spalart-Allmaras-Edwards model providing nearly comparable results. The principal difference between the two predictions is in the region of the secondary separation at $\beta = 40°$. Again, the Baldwin-Lomax and $k-\epsilon$ models show general agreement with experiment, but are less accurate.

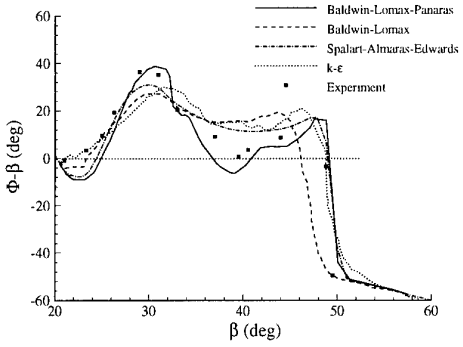

Figure 49: Surface streamline angle for single fin

The skin friction coefficient is displayed in Fig. 50. The Baldwin-Lomax-Panaras and Spalart-Allmaras-Edwards models predict a peak in the vicinity of the corner which is not evident in the experiment;[57] in particular, their computed values at the experimental location $\beta = 26.5°$ are substantially above the experiment. Additional measurements in the region $22° < \beta < 26°$ would be helpful in determining whether a peak appears.[58] Elsewhere, all four models provide generally good agreement with experiment.

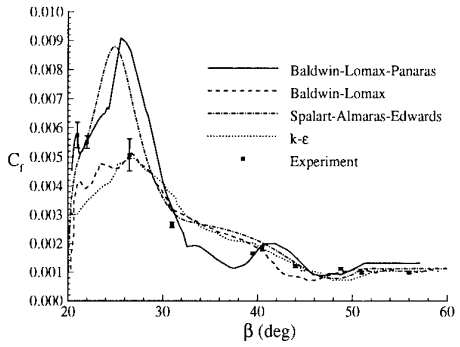

Figure 50: Skin friction coefficient for single fin

15.14 Double Fin

The double fin ("crossing shock") geometry consists of two wedges of angles α_1 and α_2 affixed normal to a flat plate (Fig. 51) on which an equilibrium turbulent boundary layer has developed. The wedges generate intersecting oblique shock waves which interact with the boundary layers on the flat plate and inner fin surfaces. The flow parameters are the Mach number M_∞, Reynolds number Re_{δ_∞}, fin angles α_1 and α_2, contraction ratio L_2/L_1, throat middle line offset L_3/L_1, boundary layer to throat width ratio δ_∞/L_2, and wall temperature ratio T_w/T_{aw}. The fins are assumed semi-infinite in height. For the symmetric double fin, $L_3 = 0$. A detailed assessment of several turbulence models for several different configurations of the double fin is described in Knight and Degrez [125]. Results are presented for a single configuration for Mach number $M_\infty = 4.0$, $\alpha_1 = 7°$, $\alpha_2 = 11°$, and $Re_\delta = 3.0 \times 10^5$. The experimental data was obtained by Zheltovodov *et al* [130]. Computations were performed by Edwards (using the Spalart-Allmaras-Edwards model [122]), Gnedin [131] (using the k–ϵ variant of Knight [68]), Hassan and Alexopoulos (using the $k-\omega$ model), Knight (using the $k-\epsilon$ Chien model), Sekar (using the Baldwin-Lomax model) and Zha (using the Reynolds Stress Equation model of Knight [81]).

[57] Corrected data for $\beta = 22°$ and $26.5°$, provided by Prof. G. Settles, is included in Fig. 50.

[58] Note that the attachment line is $\beta = 26°$ [128].

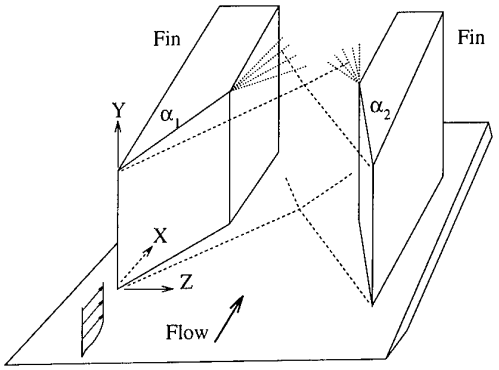

Figure 51: Double fin geometry

In Figs. 52 and 53, the computed surface skin friction lines using the $k-\epsilon$ Chien model and $k-\epsilon$ Knight models, respectively, are shown. The experimental surface visualization in displayed in Fig. 54. The incident separation lines originating from the fin leading edges (**1** and **2**) can be seen in both computations and experiment. The computed separation line angles are within 10% of the experiment. The $k-\epsilon$ Chien results display a coalescence of the incident separation lines into a narrow band (**3**) offset to the left side, in agreement with experiment. This line represents the surface image of the boundary between the left and right vortices generated by the incident single fin interactions. The $k-\epsilon$ Chien results also show a second line of coalescence form alongside on the right and farther downstream (**4**) associated with a secondary separation underneath the left side of the right vortex [132], and a line of divergence alongside the right fin (**5**). A similar line of divergence (unmarked) is near the left fin.

For the $k-\epsilon$ Knight model (Fig. 53), the incident separation lines do not coalesce near the center of the region, but rather continue further downstream almost in parallel until they converge at $x \approx 110$ mm to form a narrow band of skin friction lines (**3**), which is offset to the left side of the channel. This represents the surface image of the boundary between the left and right vortices generated by the incident single fin interactions. Lines of divergence are also apparent near the right fin (**4**) and left fin (**5**) associated with the incident single fin interaction. The second line of coalescence observed in the $k-\epsilon$ Chien results (**4** in Fig. 52) is not present in this computation. Consequently, the $k-\epsilon$ Knight model does not predict a secondary separation underneath the left side of the right vortex.[59]

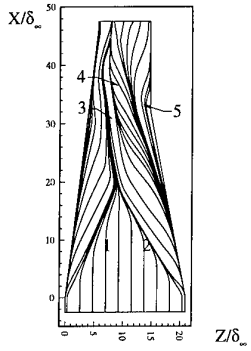

Figure 52: Computed skin friction lines $k-\epsilon$-Chien model for double fin
1 Left incident separation line
2 Right incident separation line
3 Left downstream coalescence line
4 Right downstream coalescence line
5 Line of divergence (similar line near left fin)

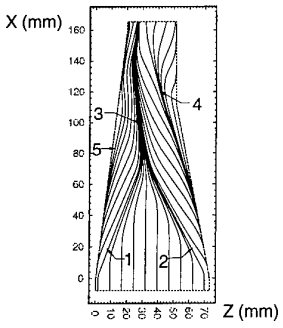

Figure 53: Computed skin friction lines $k-\epsilon$-Knight model for double fin
1 Left incident separation line
2 Right incident separation line
3 Left downstream coalescence line
4,5 Lines of divergence

In Figs. 55 and 56, the surface pressure along the Throat Middle Line[60] (TML) is displayed. The computed and experimental surface pressure on TML are in good agreement for $x < 135$ mm for all models, although the computations slightly underestimate the extent of the upstream influence. The computed results in Fig. 55 do not accurately predict the pressure rise

[59] For a detailed explanation, see [125].

[60] The Throat Middle Line is the intersection of the flat plate with the streamwise plane which bisects the throat.

Figure 54: Experimental surface flow for double fin

(beginning at $x = 145$ mm) associated with the shock reflection from the 7° fin, since the computations omit the boundary layers on the fin surfaces. The computed and experimental surface pressure at $x = 46$ and 79 mm are displayed in Figs. 57 to 60. Close agreement is again observed between the predictions of all models and experiment.

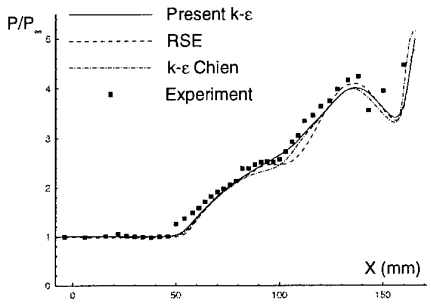

Figure 55: Wall pressure on TML for double fin

The surface heat transfer coefficient C_h is shown in Figs. 61 to 64. On the Throat Middle Line (Figs. 61 and 62), all turbulence models overpredict the heat transfer by approximately a factor of two downstream of the intersection of the shocks (which occurs at $x = 93.7$ mm). At $x = 112$ mm (Figs. 63 and 64), located within the strongly three-dimensional region of the flow, all models show significant disagreement with experiment. The overprediction in C_h represents an overestimate in q_w, since a series of studies [81, 133] have demonstrated that the computed q_w is proportional to the computed $T_w - T_{aw}$. A possible explanation [131] is that the turbulence models overestimate the effects of the shock-boundary layer interaction on the

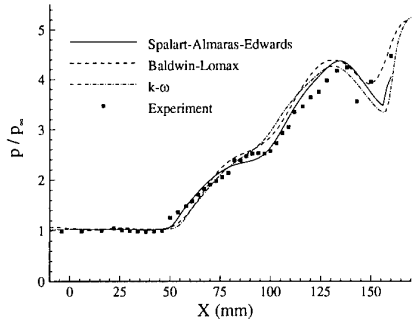

Figure 56: Wall pressure on TML for double fin

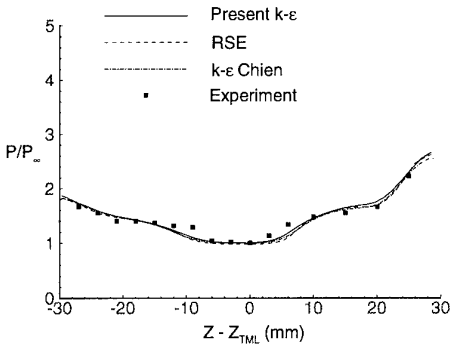

Figure 57: Wall pressure at $x = 46$ mm for double fin

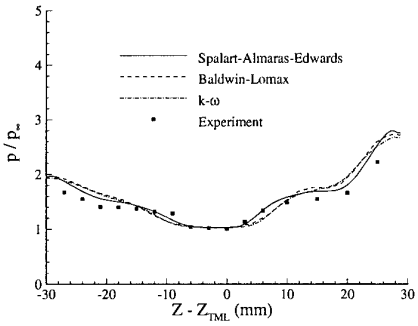

Figure 58: Wall pressure at $x = 46$ mm for double fin

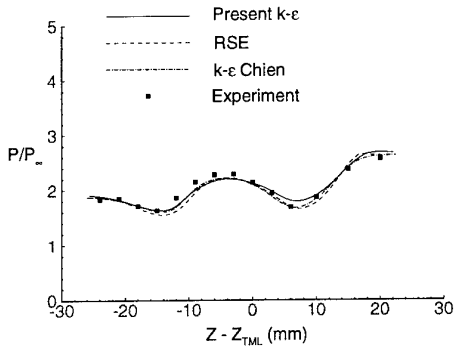

Figure 59: Wall pressure at $x = 79$ mm for double fin

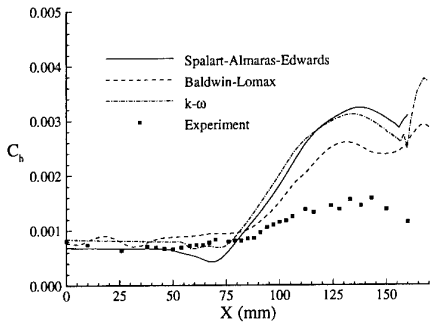

Figure 62: C_h on TML for double fin

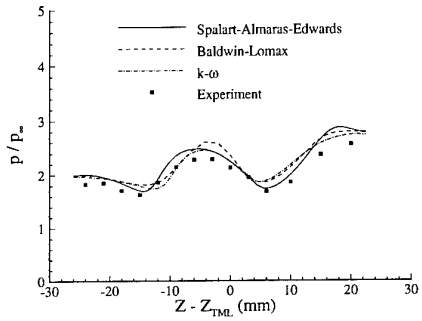

Figure 60: Wall pressure at $x = 79$ mm for double fin

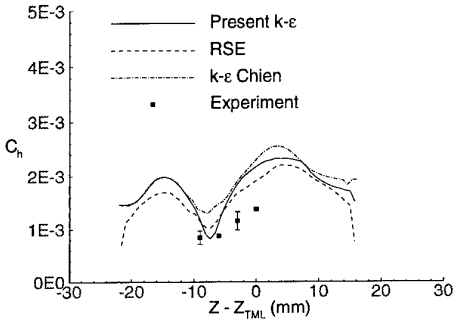

Figure 63: C_h at $x = 112$ mm for double fin

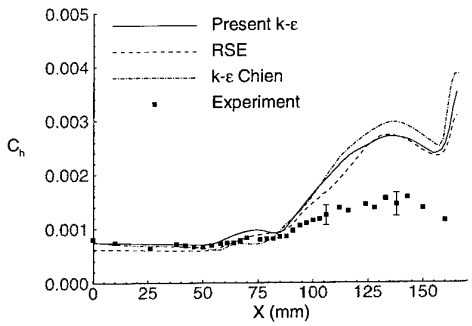

Figure 61: C_h on TML for double fin

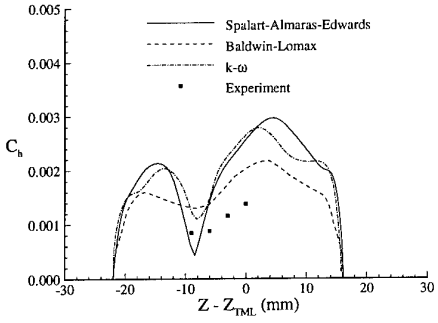

Figure 64: C_h at $x = 112$ mm for double fin

turbulence production, thereby generating excessive turbulence kinetic energy and turbulent eddy viscosity, and thus overestimating the turbulent thermal conductivity.

The adiabatic wall temperature T_{aw}/T_∞ is shown in Figs. 65 to 68, respectively. The $k-\epsilon$ Knight and $k-\omega$ models display closest agreement with experiment.

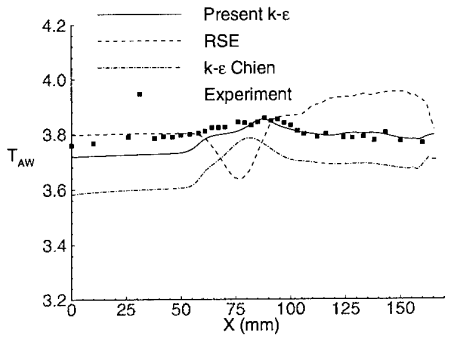

Figure 65: T_{aw} on TML for double fin

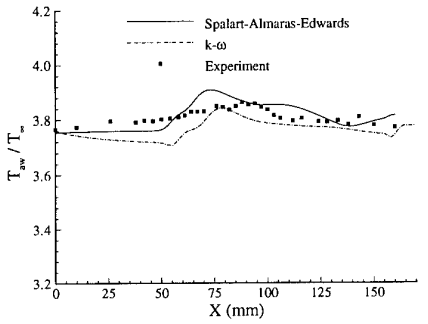

Figure 66: T_{aw} on TML for double fin

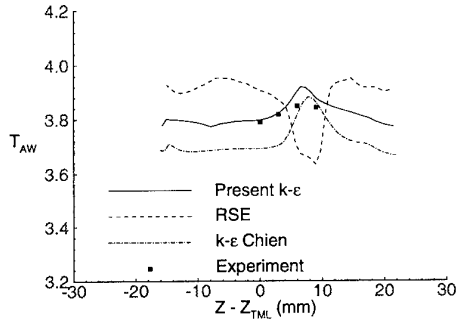

Figure 67: T_{aw} at $x = 112$ mm for double fin

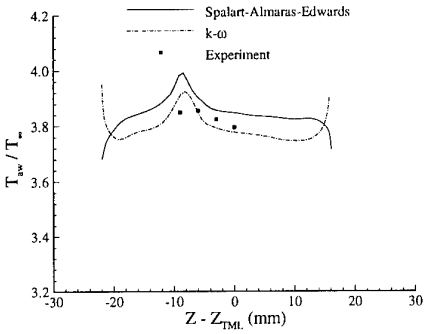

Figure 68: T_{aw} at $x = 112$ mm for double fin

16 CONCLUSIONS

The extraordinary wide range of scales in most compressible turbulent flows of engineering interest precludes direct numerical simulation using the Navier-Stokes equations. Consequently, an averaged form of the Navier-Stokes equations is employed. Two basic approaches have been developed. The first is the Reynolds-averaged Navier-Stokes equations (RANS), based on ensemble averages of the Navier-Stokes equations. The second is Large Eddy Simulation, based on a spatial filtering of the Navier-Stokes equations. The first approach, discussed in this paper, has led to a wide range of models from zero-equation to full Reynolds Stress Equation methods. Comparison of computed and experimental results for a wide variety of compressible turbulent flows leads to the following conclusions. First, no single RANS model has been demonstrated to provide close agreement with experimental data for all cases considered. Second, the higher order models tend to provide better agreement with experiment, although this is not uniformly true. Third, the best agreement is achieved with RANS models customized to a specific type of flow (*e.g.*, the k–ϵ model of Thies and Tam for jet flows which employed a different set of constants than the standard $k-\epsilon$ model, or the Johnson-King model which was specially developed for transonic airfoils with embedded shocks). Fourth, the surface pressure distribution (and, consequently, the mean aerodynamic loads on a vehicle) can be predicted with reasonable accuracy.[61] Fifth, the surface heat trans-

[61] For 2-D shock wave boundary layer interactions with separation, the turbulence model has a strong influence on the prediction, and certain turbulence models (*e.g.*,

fer distribution (and, consequently, the mean aerothermodynamic loads on a vehicle) cannot be accurately predicted for shock wave turbulent boundary layer interactions. Sixth, the principal features of the flow separation (as deduced from surface streamlines) can be reasonably predicted; however, detailed features of the surface streamline pattern can be strongly influenced by the choice of turbulence model and may not be accurate.

With regards to future work, RANS models will likely continue to be developed, with greater emphasis on customization for specific types of flows. From an engineering standpoint, the development of multiple versions of a two-equation model, for example, for different types of flows can be a very practical near-term solution to simulation requirements. This is already a practice in industry.

Large Eddy Simulation (LES) will become more common in simulation of compressible turbulent flows. Unlike RANS models, LES computes the dynamic motion of the large scale structures (which are geometry and hence problem dependent), while modeling the small scale structures (which tend to be more isotropic and hence universal). In principle, therefore, LES may be more capable of accurate simulation of a wide range of compressible turbulent flows without resort to customization of model constants. Moreover, the continued rapid growth in microprocessor performance (*i.e.*, the current doubling of microprocessor speeds every eighteen to twenty four months [134]) and development of software standards for parallel computing languages (*e.g.*, MPI [135]) offers the opportunity for use of LES in engineering design in the near future.[62]

Johnson-King) are clearly superior. For 3-D shock wave boundary layer interactions, the turbulence model has a somewhat weaker influence on the prediction. For further discussion of the latter, see Knight and Degrez [125].

[62] By way of example, the CDC 6600, introduced in 1964, was the first computer to employ functional parallelism as a major design feature [136]. Its clock speed was 10 MHz. The CDC 6600 was used for 2-D RANS simulations using eddy viscosity models. Its performance on the LINPACK benchmarks [137] (which tests sustained performance in solving a 100×100 system of linear equations) was 0.48 MFlops. The SGI Power Challenge / Power Onyx R10000, introduced in 1996, provides up to 18 CPUs operating at 200 MHz. Its performance on the LINPACK benchmarks is 126 MFlops on one processor, an increase by a factor of 263 over the CDC 6600.

17 ACKNOWLEDGMENTS

This research is supported by AFOSR Grant F49620-96-1-0389, monitored by Dr. Len Sakell. Numerous figures have been reproduced with permission of the American Institute of Aeronautics and Astronautics. Figures 5 and 32 are reproduced with permission of DCW Industries, Inc.

References

[1] W. Reynolds. Computation of Turbulent Flows. In *Annual Review of Fluid Mechanics*, volume 8, pages 183–208. Annual Reviews, Inc., 1976.

[2] B. Lakshminarayana. Turbulence Modeling for Complex Shear Flows. *AIAA Journal*, 24(12):1900–1917, December 1986.

[3] C. Speziale. Analytical Methods for the Development of Reynolds Stress Closure Models in Turbulence. In *Annual Review of Fluid Mechanics*, volume 23, pages 107–157. Annual Reviews, Inc., 1991.

[4] J. Marvin. Perspective on Computational Fluid Dynamics Validation. *AIAA Journal*, 33(10):1778–1787, October 1995.

[5] H. Fernholz, P. Finley, J. Dussauge, and A. Smits. A Survey of Measurements and Measuring Techniques in Rapidly Distorted Compressible Turbulent Boundary Layers. Technical Report AGARDograph 315, NATO, 1989.

[6] G. Settles and L. Dodson. Hypersonic Shock / Boundary Layer Interaction Database. Technical Report PSU-ME-90/91-003, Gas Dynamics Laboratory, Department of Mechanical Engineering, Penn State University, December 1990.

[7] F. White. *Viscous Fluid Flow.* McGraw-Hill, New York, 1974.

[8] P. Crickmore. *F-15 Eagle.* Smithmark, New York, 1992.

[9] H. Tennekes and J. Lumley. *A First Course in Turbulence.* The MIT Press, Cambridge, MA, 1972.

[10] J. Dussauge, R. Smith, A. Smits, H. Fernholz, P. Finley, and E. Spina. Turbulent Boundary Layers in Subsonic and Supersonic Flow. Technical Report AGARD AG 335, NATO, July 1996.

[11] W. Reynolds. The Potential and Limitations of Direct and Large Eddy Simulations. In J. Lumley, editor, *Whither Turbulence ? Turbulence at the Crossroads*, pages 313–343. Springer-Verlag, 1990. Lecture Notes in Physics, Vol. 357.

[12] R. Antonia. Conditional Sampling in Turbulence Measurement. In *Annual Review of Fluid Mechanics*, volume 13, pages 131–156. Annual Reviews, Inc., 1981.

[13] A. Monin and A. Yaglom. *Statistical Fluid Mechanics: Mechanics of Turbulence*, volume 1. The MIT Press, Cambridge, Massachusetts, 1971.

[14] E. Van Driest. Turbulent Boundary Layer in Compressible Fluids. *Journal of the Aeronautical Sciences*, 18(3):145–160 & 216, 1951.

[15] D. C. Wilcox. *Turbulence Modelling for CFD.* DCW Industries, 1993.

[16] A. Favre. Equations des Gaz Turbulents Compressibles. *Journal de Mecanique*, 4(3):361–390, 1965.

[17] J. Lee, D. Taulbee, and M. Holden. A Study of Turbulence on a Compression Ramp with k–ϵ and Reynolds Stress Models. AIAA Paper 90-1582, 1990.

[18] C. Speziale. Second-Order Closure Models for Supersonic Turbulent Flows. AIAA Paper 91-0217, 1991.

[19] M. Rubesin. Extra Compressibility Terms for Favre-Averaged Two-Equation Models of Inhomogeneous Turbulent Flows. Technical Report NASA CR 177556, NASA, June 1990.

[20] S. Sarkar, G. Erlebacher, M. Hussaini, and H. Kreiss. The Analysis and Modelling of Dilatational Terms in Compressible Turbulence. *Journal of Fluid Mechanics*, 227:473–493, 1991.

[21] O. Zeman. Dilatation Dissipation: The Concept and Application in Modelig Compressible Mixing Layers. *Physics of Fluids A*, 2:178–188, 1990.

[22] J. Ristorcelli. A Pseudo-Sound Constitutive Relationship for the Dilatational Covariances in Compressible Turbulence: An Analytical Theory. Technical Report ICASE Report No. 95-22, NASA Langley Research Center, March 1995. NACA CR 195064.

[23] J. Hinze. *Turbulence.* McGraw Hill, New York, 1959.

[24] L. Kovasznay. Turbulence in Supersonic Flow. *Journal of the Aeronautical Sciences*, 20:657–674, 1953.

[25] R. Panton. *Incompressible Flow.* John Wiley & Sons, New York, second edition, 1996.

[26] A. Favre, editor. *The Mechanics of Turbulence.* Gordon & Breach, New York, 1964.

[27] P. Bradshaw. Compressible Turbulent Shear Layers. In *Annual Review of Fluid Mechanics*, volume 9, pages 33–54. Annual Reviews, Inc., 1977.

[28] A. Kistler. Fluctuation Measurements in a Supersonic Turbulent Boundary Layer. *Physics of Fluids*, 2(3):290–296, May-June 1959.

[29] J. Boussinesq. Essai sur la Théorie des eaux Courantes. *Mém. preés. par div. savants á l'Acad. Sci.*, 23(1):1–680, 1887.

[30] G. Batchelor. *An Introduction to Fluid Dynamics.* Cambridge University Press, Cambridge, 1970.

[31] H. Schlichting. Recent Progress in Boundary-Layer Research. *AIAA Journal*, 12:427–440, 1974.

[32] J. Shang. Computation of Hypersonic Turbulent Boundary Layers with Heat Transfer. *AIAA Journal*, 12:883–884, 1974.

[33] R. Simpson, D. Whitten, and R. Moffatt. An Experimental Study of the Turbulent Prandtl Number of Air with Injection and Suction. *International Journal of Heat Transfer*, 13:125–143, 1970.

[34] S. Pope. A More General Effective Viscosity Hypothesis. *Journal of Fluid Mechanics*, 72:331–340, 1975.

[35] T. Gatski and C. Speziale. On Explicit Algebraic Stress Models for Complex Turbulent Flows. *Journal of Fluid Mechanics*, 254:59–78, 1993.

[36] R. Abid, J. Morrison, T. Gatski, and C. Speziale. Prediction of Aerodynamic Flows with a New Explicit Algebraic Stress Model. *AIAA Journal*, 34(12):2632–2635, December 1996.

[37] V. Yakhot and S. Orszag. Renormalization Group Analysis of Turbulence. I. Basic Theory. *Journal of Scientific Computing*, 1:3–51, 1986.

[38] L. Martinelli and V. Yakhot. RNG-Based Turbulent Transport Approximation with Applications to Transonic Flows. AIAA Paper 89-1950, 1989.

[39] A. Yakhot, E. Shalman, O. Igra, and Y. Yadlin. An Algebraic-Q_4 Turbulence Model for Transonic Airfoil Flows. AIAA Paper 95-0358, 1995.

[40] T. Cebeci, A. Smith, and G. Mosinskis. Calculation of Compressible Adiabatic Turbulent Boundary Layers. *AIAA Journal*, 8(11):1974–1982, November 1970.

[41] T. Cebeci. Calculation of Compressible Turbulent Boundary Layers with Heat and Mass Transfer. *AIAA Journal*, 9(6):1091–1097, June 1971.

[42] T. Cebeci and A. Smith. *Analysis of Turbulent Boundary Layers.* Academic Press, New York, 1974.

[43] N. Buleev. Theoretical Model of the Mechanism of Turbulent Exchange in Fluid Flows. Atomic Energy Research Establishment, Hartwell, England, AERE Translation 957, 1963.

[44] B. Baldwin and H. Lomax. Thin Layer Approximation and Algebraic Model for Separated Flows. AIAA Paper 78-257, 1978.

[45] B. York and D. Knight. Calculation of Two-Dimensional Turbulent Boundary Layers Using the Baldwin-Lomax Model. *AIAA Journal*, 23(12):1849–1850, December 1985.

[46] D. Knight, C. Horstman, B. Shapey, and S. Bogdonoff. Structure of Supersonic Turbulent Flow Past a Sharp Fin. *AIAA Journal*, 25:1331–1337, 1987.

[47] M. Visbal. *Numerical Simulation of Shock Turbulent Boundary Layer Interactions over 2-D Compression Corners.* PhD thesis, Department of Mechanical and Aerospace Engineering, Rutgers University, New Brunswick, NJ, October 1983.

[48] D. Coles. The Young Person's Guide to the Data. In *AFOSR-IFP-Stanford Conference on Computation of Turbulent Boundary Layers*, 1968.

[49] M. Visbal and D. Knight. The Baldwin-Lomax Turbulence Model for Two-Dimensional Shock-Wave / Turbulent Boundary-Layer Interactions. *AIAA Journal*, 22(7):921–928, July 1984.

[50] D. Degani and L. Schiff. Computation of Turbulent Supersonic Flows Around Pointed Bodies Having Crossflow Separation. *Journal of Computational Physics*, 66:173–196, September 1986.

[51] A. Panaras. Algebraic Turbulence Modelling for Swept Shock Wave / Turbulent Boundary Layer Interactions. Technical Report IB 223-96 A 22, Deutsche Forschungsanstalt für Luft- und Raumfahrt e.V., March 1996.

[52] A. Smits and D. Wood. The Response of Turbulent Boundary Layers to Sudden

Perturbations. In *Annual Review of Fluid Mechanics*, volume 17, pages 321–58. Annual Reviews, Inc., 1985.

[53] B. Baldwin and T. Barth. A One-Equation Turbulence Transport Model for High Reynolds Number Wall-Bounded Flows. AIAA Paper 91-0610, 1991.

[54] D. Johnson and L. King. A New Turbulence Closure Model for Boundary Layer Flows with Strong Adverse Pressure Gradients and Separation. AIAA Paper 84-0175, 1984.

[55] P. Spalart and S. Allmaras. A One-Equation Turbulence Model for Aerodynamic Flows. AIAA Paper 92-0439, 1992.

[56] D. Johnson and L. King. A Mathematically Simple Turbulence Closure Model for Attached and Separated Turbulent Boundary Layers. *AIAA Journal*, 23(11):1684–1692, November 1985.

[57] D. Johnson. Transonic Separated Flow Predictions with an Eddy-Viscosity / Reynolds-Stress Closure Model. *AIAA Journal*, 25(2):252–259, February 1987.

[58] D. Johnson and T. Coakley. Improvements to a Nonequilibrium Algebraic Turbulence Model. *AIAA Journal*, 28(11):2000–2003, November 1990.

[59] A. Perry and W. Schofield. Mean Velocity and Shear Stress Distributions in Turbulent Boundary Layers. *Physics of Fluids*, 16:2068–2081, December 1973.

[60] A. Kolmogorov. Equations of Turbulent Motion of an Incompressible Fluid. *Izvestia Academy of Sciences, USSR; Physics*, 6(1 and 2):56–58, 1942.

[61] P. Saffman. A Model for Inhomogeneous Turbulent Flow. *Proceedings of the Royal Society, London*, A317:417–433, 1970.

[62] D. Wilcox and I. Alber. A Turbulence Model for High Speed Flows. Proc. of the 1972 Heat Transfer and Fluid Mechanics Institute, Stanford University, 1972.

[63] S. Sarkar and L. Balakrishnan. Application of a Reynolds Stress Turbulence Model to the Compressible Shear Layer. NASA Contractor Report 182002, ICASE Report No. 90-18, February 1990.

[64] W. Jones and B. Launder. The Prediction of Laminarization with a Two-Equation Model of Turbulence. *Int. Journal of Heat and Mass Transfer*, 15:301–304, 1972.

[65] B. Launder and B. Sharma. Application of the Energy Dissipation Model of Turbulence to the Calculation of Flow Near a Spinning Disc. *Letters in Heat and Mass Transfer*, 1(2):131–138, 1974.

[66] K.-Y. Chien. Predictions of Channel and Boundary Layer Flows with a Low Reynolds Number Turbulence Model. *AIAA Journal*, 20:33–38, January 1982.

[67] C. Lam and K. Bremhorst. Modified Form of $k-\epsilon$ Model for Predicting Wall Turbulence. *ASME Journal of Fluids Engineering*, 103:456–460, 1981.

[68] C. Becht and D. Knight. A Simple Low Reynolds Number Modification for the Compressible $k-\epsilon$ Model. Part I. Boundary Layer Flows. AIAA Paper 95-2218, 1995.

[69] A. Thies and C. Tam. Computation of Turbulent Axisymmetric and Nonaxisymmetric Jet Flows Using the $k-\epsilon$ Model. *AIAA Journal*, 34(2):309–316, February 1996 1996.

[70] S. Pope. An Explanation of the Turbulent Round-Jet / Plane-Jet Anomaly. *AIAA Journal*, 16(3):279–181, March 1978.

[71] S. Sarkar, G. Erlebacher, M. Hussaini, and H. Kreiss. The Analysis and Modeling of Dilatational Terms in Compressible Turbulence. Technical Report ICASE Report 89-79, NASA Langley Research Center, 1989.

[72] T. Coakley. Turbulence Modelling Methods for the Compressible Navier-Stokes Equations. AIAA Paper 83-1693, 1983.

[73] T. Coakley and T. Hsieh. A Comparision Between Implicit and Hybrid Methods for the Calculation of Steady and Unsteady Inlet Flows. AIAA Paper 85-1125, 1985.

[74] S. Vuong and T. Coakley. Modeling of Turbulence for Hypersonic Flows With and Without Separation. AIAA Paper 87-0286, 1987.

[75] T. Coakley and P. Huang. Turbulence Modelling for High Speed Flows. AIAA Paper 92-0436, 1992.

[76] H. Zhang, R. So, T. Gatski, and C. Speziale. In R. So, C. Speziale, and B. Launder, editors, *Proceedings of the International Conference on Near-Wall Turbulent Flows*. Elsevier Publishers B. V., 1993.

[77] J. Morrison, T. Gatski, T. Sommer, H. Zhang, and R. So. Evaluation of a Near Wall Turbulence Closure Model in Predicting Compressible Ramp Flows. In R. So, C. Speziale, and B. Launder, editors, *Proceedings of the International Conference on Near Wall Turbulent Flows*, 1993.

[78] M. Gnedin and D. Knight. A Reynolds Stress Equation Model for Compressible Turbulent Flows. Part I: Flat Plate Boundary Layers. AIAA Paper 95-0860, 1995.

[79] B. Launder, G. Reece, and W. Rodi. Progress in the Development of a Reynolds Stress Turbulence Closure. *Journal of Fluid Mechanics*, 68:537–566, 1975.

[80] J. Rotta. Recent Attempts to Develop a Generally Applicable Calculation Method for Turbulent Shear Flows. AGARD CP-93, 1972.

[81] G. Zha and D. Knight. Computation of 3D Asymmetric Crossing Shock Wave / Turbulent Boundary Layer Interaction Using a Full Reynolds Stress Equation Turbulence Model. AIAA Paper 96-0040, 1996.

[82] C.-C. Sun and M. Childs. Wall Wake Velocity Profile for Compressible Adiabatic Flows. *AIAA Journal*, 14(6):820–822, June 1976.

[83] P. Saffman and D. Wilcox. Turbulence-Model Predictions for Turbulent Boundary Layers. *AIAA Journal*, 12:541–546, 1974.

[84] G. Carrier, M. Krook, and C. Pearson. *Functions of a Complex Variable*. McGraw Hill, New York, 1966.

[85] F. Jacon and D. Knight. A Navier-Stokes Algorithm for Turbulent Flows Using an Unstructured Grid and Flux Difference Splitting. AIAA Paper 94-2292, 1994.

[86] D. Spalding and S. Chi. The Drag of a Compressible Turbulent Boundary Layer on a Smooth Flat Plate With and Without Heat Transfer. *Journal of Fluid Mechanics*, 18(1):117–143, 1964.

[87] E. Winkler and M. Cha. Investigation of Flat Plate Hypersonic Turbulent Boundary Layers with Heat Transfer at Mach 5.2. Technical Report NAVORD Report 6631, Naval Ordnance Lab, White Oaks, MD, September 1959.

[88] E. Hopkins and M. Inouye. An Evaluation of Theories for Predicting Skin Friction and Heat Transfer on Flat Plates at Supersonic and Hypersonic Mach Numbers. *AIAA Journal*, 9(6):993–1003, June 1971.

[89] W. Bachalo and D. Johnson. Transonic Turbulent Boundary-Layer Separation Generated on an Axisymmetric Flow Model. *AIAA Journal*, 24(3):437–443, March 1986.

[90] C. Horstman and D. Johnson. Prediction of Transonic Separated Flows. *AIAA Journal*, 22(7):1001–1003, July 1984.

[91] I. Abbott and A. von Doenhoff. *Theory of Wing Sections*. Dover Publications, Inc., New York, 1949.

[92] T. Coakley. Numerical Simulation of Viscous Transonic Airfoil Flows. AIAA Paper 87-0416, 1987.

[93] L. King. A Comparison of Turbulence Closure Models for Transonic Flows About Airfoils. AIAA Paper 87-0418, 1987.

[94] P. Cook, M. McDonald, and M. Firmin. Aerofoil RAE 2822 - Pressure Distributions and Boundary Layer and Wake Measurements. Technical Report AGARD AR 138, NATO.

[95] W. Haase, F. Brandsma, F. Elsholz, M. Leschziner, and D. Schwamborn, editors. *EUROVAL - A European Initiative on Validation of CFD-codes*. Vieweg Verlag, 1993. Notes on Numerical Fluid Mechanics.

[96] T. Hellstrom, L. Davidson, and A. Rizzi. Reynolds Stress Transport Modelling of Transonic Flow Around the RAE2822 Airfoil. AIAA Paper 94-0309, 1994.

[97] J. Delery. Investigation of Strong Shock Turbulent Boundary Layer Interaction in 2-D Transonic Flows with Emphasis on Turbulence Phenomena. AIAA Paper 81-1245, 1981.

[98] G. Degrez, K. Hadriche, E. Solakoglu, and D. Vandromme. Computation of a Shock Wave Boundary Layer Interaction in a Nozzle with Different Algorithms and Turbulence Models. AIAA Paper 91-1757, 1991.

[99] J. Greene. Interactions between Shock Waves and Turbulent Boundary Layers. In *Progress in Aerospace Science*, volume 11, pages 235–340. Pergammon Press, 1970.

[100] S. Aso, S. Okuyama, and M. Kawai. Experimental Study on Mixing Phenomena in Supersonic Flows with Slot Injection. AIAA Paper 91-0016, 1991.

[101] P. Gerlinger, J. Algermissen, and D. Brüggemann. Numerical Simulation of Mixing for Turbulent Slot Injection. *AIAA Journal*, 34(1):73–78, January 1996.

[102] D. Dolling. Problems in the Validation of CFD Codes through Comparison with Experiment. AGARD Symposium on Theoretical and Experimental Methods in Hypersonic Flows, Turin, Italy, 1992.

[103] D. Knight. Numerical Simulation of 3-D Shock Wave Turbulent Boundary Layer Interactions. In *AGARD/VKI Special Course on Shock-Wave Boundary-Layer Interactions in Supersonic and Hypersonic Flows*, pages 3–1 to 3–32. Von Karman Institute for Fluid Dynamics, May 1993. AGARD R-792.

[104] D. Dolling. Unsteady Phenomena in Shock - Wave / Boundary Layer Interaction. In *AGARD/VKI Special Course on Shock-Wave Boundary-Layer Interactions in Supersonic and Hypersonic Flows*, pages 4–1 to 4–46. Von Karman Institute for Fluid Dynamics, May 1993. AGARD R-792.

[105] S. Aso, S. Okuyama, and Y. Ando. Experimental Study on Interacting Flow Fields Induced by Normally Injected Secondary Flow through a Slot Nozzle into Supersonic Flow. *Memoirs of the Faculty of Engineering, Kyushu University*, 51(1):53–62, 1991.

[106] M. Taylor and A. Smits. The Effects of a Short Region of Concave Curvature on a Supersonic Turbulent Boundary Layer. AIAA Paper 84-0169, 1984.

[107] M. Jarayam, M. Taylor, and A. Smits. The Response of a Compressible Turbulent Boundary Layer to Short Regions of Concave Surface Curvature. *Journal of Fluid Mechanics*, 175(1):343–362, 1986.

[108] J. Lee, D. Taulbee, and M. Holden. Study of Turbulence on Supersonic Compression Surfaces Using Reynolds Stress Model. *AIAA Journal*, 30(7):1738–1746, July 1992.

[109] A. Smits and K. Muck. Experimental Study of Three Shock Wave / Turbulent Boundary Layer Interactions. *Journal of Fluid Mechanics*, 182:291–314, September 1987.

[110] S. Birch and J. Eggers. A Critical Review of the Experimental Data for Developed Free Turbulent Shear Layers. Technical Report NASA SP-321, NASA, 1972.

[111] D. Papamoschou and A. Roshko. The Compressible Turbulent Shear Layer: An Experimental Study. *Journal of Fluid Mechanics*, 197:453–477, 1988.

[112] S. Sarkar and B. Lakshmanan. Application of a Reynolds Stress Turbulence Model to the Compressible Shear Layer. *AIAA Journal*, 29(5):743–749, May 1991.

[113] S. Schreck, C. Ho, and R. Sarmiento. Noise Radiated from Axisymmetric and

Asymmetric Jets. AIAA Paper 92-02-044, 1992.

[114] J. Seiner, D. McLaughlin, and C. Liu. Supersonic Jet Noise Generated by Large-Scale Instabilities. Technical Report NASA TP 2072, NASA, September 1982.

[115] J. Herrin and J. Dutton. An Experimental Investigation of the Supersonic Axisymmetric Base Flow Behind a Cylindrical Afterbody. Technical Report UILU 91-4004, University of Illinois, Urbana-Champaign, May 1991.

[116] J. Herrin and J. C. Dutton. Supersonic Base Flow Experiments in the Near-Wake of a Cylindrical Afterbody. AIAA Paper 93-2924, 1993.

[117] J. Herrin and J. C. Dutton. Supersonic Base Flow Experiments in the Near Wake of a Cylindrical Afterbody. *AIAA Journal*, 32:77–83, 1994.

[118] J. Sahu. Numerical Computations of Supersonic Base Flow with Special Emphasis on Turbulence Modelling. Ballistic Research Lab Interim Memorandum Report No. 971, 1992.

[119] P. Kevin Tucker and W. Shyy. A Numerical Analysis of Supersonic Flow Over an Axisymmetric Afterbody. AIAA Paper 93-2367, 1993.

[120] J. Wideman, J. Brown, J. Miles, and O. Özcan. Skin-Friction Measurements in a Three-Dimensional Supersonic Shock-Wave / Boundary Layer Interaction. *AIAA Journal*, 33(5):805–811, May 1995.

[121] D. Gaitonde, J. Shang, and J. Edwards. Performance of Eddy-Viscosity-Based Turbulence Models in Three-Dimensional Turbulent Interactions. *AIAA Journal*, 34(4):844–847, April 1996.

[122] J. Edwards and S. Chandra. Comparison of Eddy Viscosity-Transport Turbulencd Models for Three-Dimensional, Shock-Separated Flowfields. *AIAA Journal*, 34:756–763, 1996.

[123] U. Goldberg and S. Ramakrishnan. A Pointwise Version of the Baldwin-Barth Turbulence Model. AIAA Paper 93-3523, 1995.

[124] M. Tobak and D. Peake. Topology of Three-Dimensional Separated Flows. In *Annual Review of Fluid Mechanics*, volume 14, pages 61–85. Annual Reviews, Inc., 1982.

[125] D. Knight and G. Degrez. Shock Wave Boundary Layer Interactions in High Mach Number Flows – A Critical Survey of Current CFD Prediction Capabilities. AGARD AR-319, Volume 2 (to appear), 1997.

[126] K. Kim, Y. Lee, F. Alvi, G. Settles, and C. Horstman. Laser Skin Friction Measurements and CFD Comparison of Weak-to-Strong Swept Shock / Boundary Layer Interactions, 1990. AIAA Paper 90-0378.

[127] D. Knight, C. Horstman, and G. Settles. Three Dimensional Shock Wave - Turbulent Boundary Layer Interactions Generated by a Sharp Fin at Mach 4. AIAA Paper 91-0648, 1991.

[128] F. Alvi and G. Settles. Physical Model of the Swept Shock / Boundary Layer Interaction Flowfield. *AIAA Journal*, 30:2252–2258, September 1992.

[129] A. Zheltovodov. Physical Features and Some Properties of Two and Three-Dimensional Separated Flows at Supersonic Velocities. *Izvestiya AN SSSR, Mekhanika Zhidkosti i Gaza*, 3:42–50, 1979.

[130] A. Zheltovodov, A. Maksimov, A. Shevchenko, S. Vorontsov, and D. Knight. Experimental Study and Computational Comparison of Crossing Shock Wave - Turbulent Boundary Layer Interaction. In *Proceedings of the International Conference on Methods of Aerophysical Research - Part 1*, pages 221–230, August 1994. Russian Academy of Sciences, Siberian Division.

[131] M. Gnedin, D. Knight, A. Zheltovodov, A. Maksimov, A. Shevchenko, and S. Vor-

ontsov. 3-D Crossing Shock Wave Turbulent Boundary Layer Interaction. AIAA Paper 96-2001, 1996.

[132] D. Knight, T. Garrison, G. Settles, A. Zheltovodov, A. Maksimov, A. Shevchenko, and S. Vorontsov. Asymmetric Crossing-Shock Wave / Turbulent Boundary Layer Interaction. *AIAA Journal*, 33(12):2241–2249, Dec 1995.

[133] M. Gnedin. *Numerical Simulation of 3-D Shock Wave Turbulent Boundary Layer Interaction Using a Two Equation Model of Turbulence.* PhD thesis, Rutgers University, May 1996.

[134] B. Berkowitz. Information Age Intelligence. *Foreign Policy*, (103):35–50, 1996.

[135] P. Pacheco. *Parallel Programming with MPI.* Morgan Kaufmann Publishers, Inc., San Francisco, CA, 1997.

[136] R. Hockney and C. Jesshope. *Parallel Computers.* Adam Hilger, Bristol, England, 1981.

[137] J. Dongarra. Performance of Various Computers Using Standard Linear Equation Software. Technical Report CS-89-85, University of Tennessee and Oak Ridge National Laboratory, January 1997.

[138] E. Fernando and A. Smits. A Supersonic Turbulent Boundary Layer in an Adverse Pressure Gradient. *Journal of Fluid Mechanics*, 211:285–307, 1990.

[139] E. Spina, A. Smits, and S. Robinson. The Physics of Supersonic Turbulent Boundary Layers. In *Annual Review of Fluid Mechanics*, pages 287–319. Annual Reviews, Inc., New York, 1994.

A TURBULENCE KINETIC ENERGY

In Section 11, it was stated that the Boussinesq concept of a turbulent eddy viscosity μ_t, together with the assumption of a constant turbulent Prandtl number Pr_t, reduced the closure of the system of equations (72) to (75) to the determination of μ_t. This is not precisely correct due to the appearance of the turbulence kinetic energy k in the definitions of the Reynolds Stress (80) and total energy (31). If a one- or two-equation turbulence model is used, then an additional equation for k is typically prescribed, and therefore the system of equations is close. If an algebraic turbulence model is employed, no additional equation for k is specified. In such cases, the contribution of k to (80) and (31) is ignored. This may be justified in certain flows as follows. Consider the magnitude of the terms in (31)

$$\tilde{e} = c_v \tilde{T} + \tfrac{1}{2}\, \tilde{u}_i \tilde{u}_i + k \tag{197}$$

Now

$$\tilde{e} = c_v \tilde{T} \left[1 + \frac{\gamma(\gamma-1)}{2} \left(M^2 + M_t^2 \right) \right] \tag{198}$$

where $M = \sqrt{\tilde{u}_i \tilde{u}_i}/a$ is the mean flow Mach number and $M_t = \sqrt{2k}/a$ is the turbulence Mach number. The turbulence kinetic energy k in (31) can be neglected if

$$M_t \ll M \tag{199}$$

and

$$M_t \ll \sqrt{\frac{2}{\gamma(\gamma-1)}} = 1.89 \text{ for air} \tag{200}$$

These conditions generally hold for adiabatic non-hypersonic boundary layers. Using an analysis similar to Appendix B, it can be shown that

$$\sqrt{\overline{M'^2}} = \frac{\sqrt{\overline{u'^2}}}{\bar{a}} \left[1 + \frac{(\gamma-1)}{2} \overline{M}^2 \right] \tag{201}$$

where $\overline{M} = \bar{u}/\bar{a}$ is the mean Mach number, and $\bar{a} = \sqrt{\gamma R \bar{T}}$ is the mean speed of sound. Fernando and Smits [138] measured turbulence statistics in a 2-D adverse pressure gradient adiabatic turbulent boundary layer [138] (Fig. 69). The upstream Mach number $M_\infty = 2.92$, and the Reynolds number based on the incoming boundary layer $Re_\delta = 1.67 \times 10^6$. Over a significant portion of the boundary layer, their data indicates that $\overline{u'^2} \approx 2\,\overline{v'^2}$. Assuming further that $\overline{w'^2} \approx \overline{v'^2}$, then from (201),

$$M_t \approx \frac{\sqrt{2\overline{M'^2}}}{\left[1 + \frac{(\gamma-1)}{2} \overline{M}^2 \right]} \tag{202}$$

For the same conditions [139], $\sqrt{\overline{M'^2}} \approx 0.2$, and thus $M_t \approx 0.1$. Thus, conditions (199) and (200) are satisfied, and k may be neglected in (31). Now the term $\frac{2}{3}\rho k$ which appears in (80) can be combined with the mean pressure $\bar{p}$ in (40) and (41), and since

$$\frac{\frac{2}{3}\bar{\rho}k}{\bar{p}} = \frac{\gamma}{3}M_t^2 \tag{203}$$

then for adiabatic non-hypersonic boundary layers it is clear that $\frac{2}{3}\rho k$ can be ignored in (80). For hypersonic boundary layers, and for free shear flows, these arguments may not hold[63] and the importance of k in (80) and (31) must be examined on an case-by-case basis.

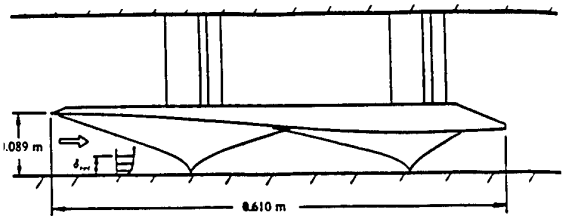

Figure 69: Adverse pressure gradient flow (from [138])

B ON THE RELATION BETWEEN FAVRE AND CONVENTIONAL REYNOLDS STRESSES

The relationship between the Favre and conventional averages is important for comparison between computation and experiment. Using (12) and (14) it is possible to show that

$$-\overline{\rho u_i'' u_j''} = \underbrace{-\bar{\rho}\,\overline{u_i' u_j'}}_{I} \underbrace{-\overline{\rho' u_i' u_j'}}_{II} + \underbrace{\frac{(\overline{\rho' u_i'})(\overline{\rho' u_j'})}{\bar{\rho}}}_{III} \tag{204}$$

It is interesting to compare the relative magnitude of terms I, II and III for the Reynolds shear stress $-\overline{\rho u'' v''}$ in a 2-D supersonic turbulent boundary layer. Fernando and Smits [138] measured turbulence statistics in a 2-D adverse pressure gradient adiabatic turbulent boundary layer (Fig. 69). Under these conditions, the relationships (66) and (70) deduced from Morkovin's hypotheses are valid. Thus

$$\rho' \approx (\gamma-1)\,M^2 \bar{\rho}\frac{u'}{\bar{u}} \tag{205}$$

where $M = \bar{u}/\sqrt{\gamma R \bar{T}}$ is the local Mach number. The fluctuations u' and v' are roughly comparable[64] and therefore

$$\overline{\rho' u' v'} \approx \frac{\bar{\rho}\bar{u}}{c_p \bar{T}}\overline{u'^3} \tag{206}$$

Assuming[65] that $\overline{u'^3} \approx \left(\overline{u'^2}\right)^{3/2}$ then the ratio of II to I is

$$\frac{\overline{\rho' u' v'}}{\bar{\rho}\,\overline{u' v'}} \approx (\gamma-1)\,M^2 \frac{\sqrt{\overline{u'^2}}}{\bar{u}} \tag{207}$$

According to the experimental data of Fernando and Smits [138],

$$(\gamma-1)\,M^2 \frac{\sqrt{\overline{u'^2}}}{\bar{u}} \leq 0.15 \tag{208}$$

By a similar argument, the ratio of III to I is

$$\frac{\overline{\rho' u'}\,\overline{\rho' v'}}{\bar{\rho}}\left[\bar{\rho}\,\overline{u' v'}\right]^{-1} \approx \left[(\gamma-1)\,M^2 \frac{\sqrt{\overline{u'^2}}}{\bar{u}}\right]^2 \tag{209}$$

Thus,

$$-\overline{\rho u'' v''} \approx -\bar{\rho}\,\overline{u' v'} \tag{210}$$

to within approximately 17% or less for the experiment of Fernando and Smits. This is within the experimental uncertainty in the measurement of $-\bar{\rho}\,\overline{u' v'}$.

[63] For example, the rms fluctuating Mach number $\sqrt{\overline{M'^2}}$ may be as large as one in a hypersonic turbulent boundary layer [139].

[64] The experimental data [138] indicates $\overline{u'^2} \leq 2\overline{v'^2}$ for $y/\delta \geq 0.2$.

[65] Within a factor which is $\mathcal{O}(1)$.

Case Studies of Applications of Turbulence Models in Aerospace

W. Haase
Daimler–Benz Aerospace AG
Department LMT63, Building 213
Rechliner Strasse
D–85077 Manching
Germany

1. SUMMARY

Validation of CFD methods is an ongoing process and it strongly depends on an assessment of flow–physics models employed in this process. On the basis of reliable numerical methods whether they are of boundary layer type or thin–layer or full Navier–Stokes approaches, predictive capabilities of turbulence models have to be validated in order to achieve accurate answers on the simulation of complex flow phenomena.

Results are presented and discussed for two–dimensional and three–dimensional flow cases and for a variety of turbulence models that are nowadays in use in the field of aeronautics and, more specifically, in the aeronautics industry. Moreover, some aspects of transition region modelling, hence enabling in general a continuous growth of turbulence – in contrast to merely "switching on" the desired eddy–voscosity turbulence model "abruptly" – are discussed.

Additionally, attention is paid on problems related to accuracy and efficiency of a proper validation of turbulence models and numerical methods.

2. INTRODUCTION

Cost effective aircraft design requires extensive work in the area of aerodynamics. As a consequence of rapid developments in computer technology, numerical mathematics, mesh generation and turbulence modelling, computational fluid dynamics (CFD) plays an increasingly important role in the design context of new and/or advanced aircraft by both lowering costs, reducing the amount of design cycles and providing information on critical flow processes which are difficult to measure in the wind tunnel. Moreover, the economic viability of the proposed design for a future large aircraft will depend strongly on its aerodynamic characteristics, especially those contributing to fuel consumption and load–carrying capacity (Hirschel et al, 1994).

For a successful design, aiming at cost– and time–effectiveness, both excellent ground facilities (wind tunnels) and accurate computer–based prediction procedures must be available. In most circumstances, the aeronautical engineer has to exploit both tools to arrive at a design offering characteristics close to those defined by technological and/or market requirements. The value of theoretical approaches lies in their ability to provide predictions, economically, rapidly and flexibly, in areas where measurements are difficult to conduct and where insight into details of the flow structure can contribute to decisions on design details.

It is known, however, that CFD is not an exact technology. While its basic framework consists of a well–established set of partial differential equations describing fluid motion, this (Reynolds–averaged) framework is not self–contained (closed) and must be combined with approximate theoretical models describing the physical processes in question. Turbulence and – associated with it – transition from laminar to turbulent flow are central phenomena, and a proper prediction of these phenomena is a prerequisite to accuracy improvements of any numerical method. Further important uncertainties arise from the geometric approximation of the solid components – including surface representation and mesh resolution aspects – and the transformation of the differential laws into algebraic equivalents by means of approximate discretisation technique but also from non–trivial treatments of (physically) correct boundary conditions.

Theoretical models feeding into the above framework always arise as a synthesis of fundamental physical laws, empirical input and – very often – intuition. "Engineering" intuition, of course, when aiming at accurate simulation results is correlated to a "pre"–knowledge about the desired (specific) flow case and has to find input into the simulation process when generating a very first mesh.

Normally, turbulence models respecting flow physics are 'calibrated' by reference to non–complex flows (only), dominated by one or the other flow feature (strong shear, strong compression, rotation, separation, etc.) and mostly applied to flows over generic non–complex geometries. Whether any particular model is likely to perform well in complex, practical situations is a question which can only be answered through a broad–ranging test program, usually involving model improvement and optimisation. This 'validation' effort is not merely concerned with predictive realism, but includes issues such as numerical realizability, stability, convergence and computational efficiency.

Validation has been – and still is – a key contributor to the steady increase in the level of confidence placed on CFD. While CFD is normally used as a means of exploring the response to conceptual or evolutionary design changes and obtaining insight into complex flow processes, it comes, in certain circumstances, close to constituting an often called "numerical wind tunnel". Validation is especially important when CFD is to be applied to physically complex three–dimensional flows, involving strong shocks, turbulence, shear, separation and unsteady phenomena, all features routinely encountered in aircraft aerodynamics. As a 'bonus', well–validated methods for aircraft–related flows contribute to the solution of a range of problems peripheral to external aerodynamics, such as noise, turbomachine performance, gas emissions, aircraft–ground interaction and environmental aspects.

Because a computational procedure for fluid–flow prediction is an amalgam of many building blocks, most being highly

Paper presented at the AGARD FDP Special Course on "Turbulence in Compressible Flows", held at the von Kármán Institute for Fluid Dynamics (VKI) in Rhode-Saint-Genèse, Belgium, 2-6 June 1997, and in Newport News, Virginia, USA, 20-24 October 1997, and published in R-819.

non–linear and interactive, any related validation process is rarely straightforward. Its validity and benefits depend on pedantic attention paid to consistency of model implementation, boundary conditions, geometric representation of the flow domain, the disposition of the influence of the numerical grid supporting the solution, error control and the inclusion of all relevant flow phenomena.

During the last years and in line with worldwide investigations on transition and turbulence modelling, two projects funded by the European Commission – EUROVAL (Haase et al, 1993) and ECARP/Validation–UVII (Haase et al, 1997) – were particularly dedicated to validation and assessment of turbulence models for a variety of – very well defined – applications. Although restricted at a first glance to sub– and transonic flows, the lessons learnt did not only improve the knowledge about what turbulence model to use preferably in what application, but provided also an increased insight in the physics of the corresponding flow.

Whatever will be carried out to assess flow–physics models, it is the outcome of a thorough validation process that is dictating whether a model will be eventually employed in an improved industrial design methodology.

Nowadays, it might be a contradiction in itself to achieve accurate results with robust turbulence models, however, current (and future) investigations show a drastic increase in both accuracy and robustness, an indispensible requirement for engineering use in the aerospace industry. The process of flow–physics model assessment has not yet been finished, moreover, it must be continued in future initiatives and projects – in order to assemble the already available "parts of the flow–physics model puzzle" properly.

The present paper provides results from those lessons learnt. It is trying to demonstrate – on the basis of the aformentioned European collaborative projects – the capabilities reached on one hand and will show the detected model shortcomings and deficiencies on the other hand on the basis of a set of Navier–Stokes solutions for compressible flows. Although this contribution is far from providing a complete overview, results are going to be presented for algebraic, half–, one–equations and two–equations turbulence models as well as Reynolds–stress turbulence models, hence covering (nearly) the whole range of turbulence models used in the aeronautics industry.

3. THE GOVERNING EQUATIONS

3.1 General Remarks

As turbulence consists of random fluctuations of the flow properties, the well–known statistical approach by Reynolds (1895) is used to express all quantities as the sum of mean values and fluctuating parts. The most relevant averaging forms are the time averaged, ensemble averaged and spatial averaged ones. Most often, applications are concerned by a time–averaged description of the flow of interest, therefore, the Reynolds–averaged equations of motion are considered with the statistical means replaced by the temporal one, i.e. the time–averaged equations are normally equated with the Reynolds–averaged equations. In this Reynolds averaging, strictly applicable to stationary turbulence, the time–averaged flow variable is to be expressed by (assuming incompressible flows with velocity and pressure fluctuations):

$$A = \overline{A} + A' \quad with \quad \overline{A'} = 0$$

and the mean value

$$\overline{A}(\vec{x}, t) = \frac{1}{T} \int_{-T/2}^{+T/2} A(\vec{x}, t + \tau)\, d\tau \quad .$$

Applied to incompressible flow, the equations for the mean properties are similar to the non–averaged equations apart from the correlation term $\overline{u'_i u'_j}$, the so–called Reynolds–stress term.

However, in compressible flow, where significant density changes occur, even when pressure changes are small, additional density and temperature fluctuations have to be taken into account. The Reynolds–averaging procedure – applied to the equations describing compressible flow – is producing extra terms for desity and temperature, ϱ' and T', fluctuations which are both difficult to handle and model. Favre (1965) has introduced mass–averaged quantities according to

$$\tilde{A} = \frac{\overline{\rho A}}{\overline{\rho}}$$

with

$$A = \tilde{A} + A'' \quad \text{and} \quad \overline{\rho A''} = 0$$

Although this approach leads to a more compact form of the governing equations, the resulting turbulent terms cannot be identified with measured quantities. With the knowledge that the difference between Reynolds averaged and Favre averaged variables is small for "moderate" Reynolds numbers, this conflict is often circumvented by using again or instead the Reynolds averaged equations. In this approach – which is applied to all the results discussed below – compressibility effects are considered by taking into account a variable mean density, $\overline{\rho}$.

Recalling Morkovin's hypothesis that compressibility effects on the wall–bounded eddies are relatively small for Mach numbers lower than 5 (and perhaps higher), the Favre averaging is applied for the velocity components and the total energy – as well as the Reynolds averaging is applied for the density and pressure. Although the majority of turbulence–model applications for high–speed flows are derived from incompressible turbulence modelling, it is noticeable that modifications have beeen done and still are needed to be improved further to take compressibility effects – in the presence of solid walls – into account. To this end, local Mach number (Zeman, 1992) or the gradient thereof (Sarkar, 1995) are employed in various classes of turbulence models to account for compressible flows (Dervieux, 1997).

A considerable part of developments in turbulence models is based on the eddy–viscosity assumption, by adopting the Boussinesq approximation which relates the turbulent stresses to the mean strain rate. In the same way, the Boussinesq law relates the the molecular stresses to the instantaneous strain rate of the Navier–Stokes equations.

Assuming that the Boussinesq approximation is valid, i.e. (only) eddy–viscosity turbulence models are concerned, the Reynolds stress tensor

$$\tau_{ij} = -\overline{\rho u'_j v'_i}$$

is given by

$$-\overline{\rho u'_j u'_i} = \mu_T S_{ij} - \frac{2}{3}\rho k \delta_{ij} , \quad k = \frac{1}{2}\overline{u'_i u'_i}$$

with μ_T being the eddy viscosity and k the turbulent kinetic energy. S_{ij} denotes the strain rate tensor.

Reducing – just for simplicity – the full three–dimensional problem to a two–dimensional boundary layer, the Reynolds stress tensor reduces to

$$-\overline{u'v'} = \nu_t \frac{\partial U}{\partial y}$$

and – to describe the eddy viscosity – one can introduce Prandtl's mixing layer concept

$$\nu_t = l_m^2 \left|\frac{\partial U}{\partial y}\right|$$

where the mixing length, l_m, is an unknown.

A combination of Prandtl's mixing length concept with the van Driest assumption for the mixing length,

$$l_m = \kappa y \left\{ 1 - \exp\left(- \frac{y(\tau_W/\rho)^{1/2}}{A^+ \nu_W} \right) \right\} \quad with \quad A^+ = 26 ,$$

now provides an equation for the turbulent eddy viscosity given above. This approach is often used for the inner part of the boundary layer.

For the outer part of the boundary layer, Clauser's concept for the eddy viscosity reads

$$\nu_t = k \, U_e \, \delta_i^*$$

with the Clauser parameter, k=0.0168. U_e denotes the velocity at the boundar layer edge and δ_i^* is the incompressible displacement thickness

$$\delta_i^* = \int_0^\delta \left[1 - \frac{u}{U_e} \right] dy .$$

When combining the definitions for the inner layer eddy viscosity and the outer layer eddy viscosity, one has (simultaneously) derived a two–layer turbulence model, in particular the basic Cebeci–Smith (1974) algebraic turbulence model.

One of the major requirements for a turbulence model, namely to define turbulence by a "*minimum amount of complexity*" (Wilcox, 1993), is definitely fulfilled by the Cebeci–Smith model, however, Wilcox's follow–on comment, "*while capturing the essence of the relevant physics*", does, unfortunately, not hold for all kinds of flows. Nevertheless, the Cebeci–Smith turbulence model can be applied with good predictive accuracy to attached flows, as it can be recognized by some of the results presented below.

Although the deduction of the Cebeci–Smith model was said to be based on boundary layer assumptions, all classes of algebraic turbulence models deal with this derivation which also holds for the application of these models in Navier–Stokes approaches.

3.2 Summary of CFD (Navier–Stokes) Methods Used

3.2.1 Dornier 2D Method

The Navier–Stokes equations describing two–dimensional, unsteady and compressible flows in conservation form, are solved by means of a finite volume approach using a Runge–Kutta time–stepping method with multigrid acceleration.

This code, a single–block version, utilises blended second and fourth order filtering to prevent odd–even decoupling. For the three–stage scheme, filtering is applied only once to provide the best damping properties. Numerical dissipation is minimized by taking the eigenvalues in x– and y–direction independently, and filtering is switched off in the boundary layer region by scaling the filter value with the ratio of local to free–stream Mach number. For more detailed information regarding method descriptions, the reader is referred to Haase et al (1983).

The Jameson–based schemes employ residual averaging and a variable timestep approach. Moreover, a multigrid approach is employed. In most of the 2D calculations, the steady state is defined to be reached if the force coefficients and the sum of pressure along airfoil (and wake) or in a channel does not vary by more than 0.01%. Typically, this leads to an L2–norm reduction of about 5 decades in the coarsest and further 3 decades in a very fine mesh (results in sections 7.1, 7.2, 7.3 and 7.4).

3.2.2 DLR FLOWer Code

For the three–dimensional flows presented in sections 7.5 and 7.7, the FLOWer code (Kroll et al, 1996) has been utilized, a Jameson–type solver written in cell–vertex form, i.e. the flow variables are associated with the cell vertices of the mesh. This code solves the Navier–Stokes equations for time–dependent compressible flow. Similar to the above mentioned two–dimensional codes, local time–stepping, implicit residual averaging and multigrid is employed for accelerating convergence of the solution. The multigrid implementation follows the approach of Jameson (1985) and Radespiel et al (1990).

The FLOWer code is a block–structured code in order to handle complex geometries. It ensures second order accuracy at block interfaces by using two rows of interface cells (a switch for using just one cell is also implemented).

3.2.3 BAe DELPHIS Method

The BAe cell vertex code DELPHIS – applied for the RAE2822 results using the Kalitzin–Gould turbulence model in section 7.1 – uses a 3D, finite–volume, multiblock approach to solve the full Navier–Stokes equations. The dependent variables are stored at the grid vertices and steady state solutions are obtained using a Lax–Wendroff time–marching iteration procedure. The procedure is explicit, using local time steps, and requires the addition of artificial viscosity to suppress "checkerboard" mode instabilities. The Lax–Wendroff scheme is based on that version proposed by Ni (1982) and Davis et al. (1984) which is second order accurate.

The viscous terms require the evaluation of stresses, which in turn require gradients for velocity and temperature. These gradients are calculated at the centre of each cell by integrating around the cell using the primary flow variables

located at the vertices. The stresses are then averaged back to the vertices and the complete Navier–Stokes equations can be integrated around each cell. The final updates are distributed in a weighted fashion back to the cell vertices, such that each vertex receives an update from each of the eight surrounding cells. This procedure provides a compact stencil, while ensuring second order spatial accuracy even on distorted meshes.

The artificial dissipation is similar to the popular second–fourth order differencing procedure proposed by Jameson, Schmidt and Turkel (1981). The differences are taken along grid lines and not in the coordinate directions. A "pressure switch" in the form of local second differences of pressure is used to restrict the first order smoothing to shock waves and allow the third order terms to be applied elsewhere.

A multigrid scheme is used to accelerate convergence. This is an extension of the method by Ni and Bogoian (1989) where the residuals are propagated over progressively coarser meshes. The multigrid is implemented in such a way that different levels can be selected in different coordinate directions.

3.2.4 Dornier PNS Method

The results for a cone at incidence, going to be presented in section 7.6, have been obtained by using the Dornier PNS (Parabolized Navier–Stokes) method, Rieger (1986 and 1987).

This method solves the (Euler and) Navier–Stokes equations in parabolized form by using a finite–volume method together with an implicit Beam–Warming scheme. The space–marching scheme is similar to a central difference scheme with the consequence that some artificial dissipation is needed. According to Jameson, second and fourth order damping is applied with the latter switched off at shocks – downgrading the numerical method to first order in that area. All necessary boundary conditions are treated implicitly as well as the second order dissipation operator – to improve the stability of the scheme.

The new results presented in section 7.6 utilized an improvement of the method described. Computations were run in "step–back" mode. This approach enables very accurate solution at particular cross sections by "setting back" the solution of one cross section to the previous one, i.e. "iterating" the solution at a particular station. The advantage is an increased overall accuracy and the additional possibility to get very accurate starting conditions.

4. TURBULENCE MODELS

A variety of turbulence models from algebraic over 1/2–equation to 2–equation models has been applied and assessed on different two–dimensional and three–dimensional test cases. The most often used models will be presented briefly in the following; for a more comprehensive description, the reader is referred to the original publications or to the already mentioned ECARP book (Haase et al, 1997).

The algebraic turbulence models described hereafter are two–layer eddy–viscosity models, i.e. different definitions are employed for the near wall and the outer region of the boundary layer.

According to the eddy–viscosity concept, in the stress terms of the Navier–Stokes equations, the molecular (laminar) viscosity μ is replaced by

$$\mu = \mu_l + \rho\nu_t$$

while in the heat–flux terms, $k/c_p = \mu/Pr$ is replaced by

$$\frac{\mu}{\mathrm{Pr}} = \frac{\mu_l}{\mathrm{Pr}_l} + \frac{\rho\nu_t}{\mathrm{Pr}_t}$$

with the kinematic turbulent viscosity, $\nu_t=\mu_t/\varrho$. The Prandtl numbers are chosen to be Pr_l=0.72 for laminar and Pr_t=0.90 for turbulent flows.

The second coefficient of viscosity,

$$\lambda = -\frac{2}{3}\mu$$

which is related to a zero value for the bulk viscosity, is often treated differently. Sometimes the eddy–viscosity concept is applied also to λ, following a replacement of λ by the molecular viscosity μ, in other cases the second coefficient of viscosity is left unchanged, i.e. the molecular viscosity is used in the definition of λ.

4.1 Cebeci–Smith Model

4.1.1 The Original Model

In general, the (basic) algebraic Cebeci–Smith turbulence model has been already presented in section 3.1, however, the computed outer–layer eddy viscosity is normally multiplied by the Klebanoff intermittency function,

$$F_{Kleb} = \left[1 + 5.5\ (y/\delta)^6\right]^{-1} .$$

This function accounts for the turbulence becoming intermittant when – at the boundary ledge – the free stream is approached and when only for a fraction of the time the flow is turbulent. The Klebanoff function was introduced to avoid that on–and–off character (Cebeci&Smith, 1974) and offers a correct derivation of the boundary layer thickness.

A so–called "modified version" of the Cebeci–Smith model is taking into account separated flow areas by changing the definition of the incompressible displacement thickness in the following way:

$$\delta_i^* = \int_{y_{u/U_e=0}}^{\delta} \left[1-\frac{u}{U_e}\right] dy \quad ,$$

i.e. the displacement thickness is integrated by taking the edge of the separation region as the lower bound for integration rather than the wall (with y=0).

4.1.2 The Granville Modification

Granville (1989) has modified the definition for the mixing length by using a pressure gradient parameter in the exponential term of the mixing length equation,

$$l = k\, y\sqrt{\tau^+}\left(1 - e^{-y^+\sqrt{1+b\hat{p}^+}/26}\right)$$

with b=14.0 for $p^+>0$ and p=16.4 for $p^+<0$. The shear stress profile τ^+ is given by

$$\tau^+ = 1 + p^+ y^+$$

and

$$p^+ = \frac{\nu_e}{\rho_w u_\tau^3} \frac{dp}{dx} \rightarrow -\frac{\mu}{\rho} \frac{U_e}{u_\tau^3} \frac{dU_e}{dx}$$

Although history effects can now be taken into account, the influence on the global flow behaviour – especially if flow separation has to be treated – is small. The reason might be that for separated flows the amount of the outer–layer eddy viscosity has more influence on the flow than the inner–layer eddy viscosity.

4.2 Baldwin–Lomax Model

4.2.1 The Original Model

The Baldwin–Lomax turbulence model (Baldwin–Lomax, 1978) is also a two–layer algebraic eddy–viscosity model, patterned after the Cebeci–Smith model. The success of this model related to its extensive application to various kinds of turbulent flows – particularly for three–dimensional ones – is based on the fact that it avoids the need of finding the edge of the boundary layer and the corresponding displacement thickness. The eddy viscosity, ν_t, is given by

$$\nu_t = \begin{cases} \nu_{ti} & for \quad y \le y^* \\ \nu_{to} & for \quad y > y^* \end{cases}$$

where y^* is the wall–nearest value of the wall–normal direction, y, at which the eddy–viscosity values from the inner and outer region are identical. In the inner region, the Prandtl–van Driest formulation is used. To allow for an easy use in three–dimensional Navier–Stokes applications, the derivative of the wall–normal velocity profile, *du/dy*, is replaced by the magnitude of the vorticity and ν_{ti} reads:

$$\nu_{ti} = l^2 \, |\omega|$$

with the mixing length

$$l = \kappa \, y \, [1 - e^{-y^+/A^+}] \, .$$

The dimensionless sublayer–scaled distance, y^+, is in fact a Reynolds number based on the friction velocity, u_τ,

$$y^+ = \frac{\sqrt{\rho_w \, |\tau_w|} \; y}{\mu_w} = \frac{y \, u_\tau}{\nu} \quad .$$

The constants in the mixing length equation are the von Kármán constant, κ=0.4, and the van Driest damping constant, A^+=26. The subscript 'w' denotes values to be taken at walls. For the outer layer, the eddy viscosity is proposed as

$$\nu_{to} = k \, C_{CP} \, F_{Kleb} \, F_{WAKE}$$

with two alternate expressions for F_{WAKE},

$$F_{WAKE} = Min \, [y_{max} \, F_{max} \, , \quad C_{WK} \, y_{max} \, U_{Diff}^2 / F_{max}]$$

and the constants C_{CP}=1.6 and C_{WK}=0.25.

It should be mentioned that the original value for C_{WK} (=0.25), as it has been defined in the original version of the Baldwin–Lomax (1978) model, is sometimes changed to C_{WK}=1.0. Although this higher value yields considerably stronger interaction – and very often provides a positive tendency on the numerical convergence – its usefulness is reversed in case of separated flows. The reason is that an increase in C_{WK} results in an increase in the outer eddy viscosity, thus diminishing the (already originally) underpredicted separated domain.

U_{Diff} is the difference between maximum and minimum velocity in the profile,

$$U_{Diff} = U_{max} - U_{min} \, ,$$

where *Umin* is taken to be zero except in wakes.

The Clauser parameter, k, is again assigned to be a constant with k=0.0168, although one should consider that it varies slightly in the low–momentum Reynolds number range. A possible modification to the Clauser constant has been presented by Granville, see below.

The quantities F_{max} and y_{max} are determined from the function

$$F = y \, |\omega| \, [1 - e^{-y^+/A^+}]$$

with the exponential term set to zero in wakes.

The quantity F_{max} is the maximum value of F that occurs in the velocity profile and, consequently, y_{max} defines the y location where F equals F_{max}.

Additionally, the Klebanoff intermittency factor, F_{Kleb}, is given by

$$F_{Kleb} = \left[1 + 5.5 \left(C_{Kleb} \frac{y}{y_{max}} \right)^6 \right]^{-1}$$

with C_{Kleb}=0.3.

4.2.2 The Granville Modification

Granville has shown that the Klebanoff coefficient, C_{Kleb}, should be a function of the Coles' wake factor, Π. In addition, the C_{CP} value, a constant in the Baldwin–Lomax model, then depends on C_{Kleb} in the following way:

$$C_{Kleb} = \frac{4}{9} \left(\frac{1 + 6 \, \Pi}{1 + 4 \, \Pi} \right)$$

with

$$C_{CP} = \frac{3 - 4 C_{Kleb}}{2 C_{Kleb} \, (2 - 3 C_{Kleb} + C_{Kleb}^3)} \, .$$

The last two equations have been obtained from a comparison between the outer layer formulations of the Baldwin–Lomax and the Cebeci–Smith turbulence model, assuming an outer similarity law for the turbulent boundary layer, (Granville, 1976), and its validity up to the wall.

For equilibrium pressure gradients, Π remains constant in the streamwise direction and can be empirically correlated to the Clauser pressure–gradient parameter. Granville has fitted the latter to the Baldwin–Lomax model and derived an explicit formula for C_{Kleb} as a function of a modified Clauser pressure–gradient parameter, β, where

$$C_{Kleb} = \frac{2}{3} - \frac{0.01312}{0.1724 + \beta}$$

with

$$\beta = - \frac{y_{max}}{u_\tau} \frac{dU_e}{dx}$$

with U_e denoting again the velocity at the boundary layer edge. Hence, the equations presented above are providing

the possibility of introducing flow–dependent variables of C_{Kleb} and C_{CP} into the Baldwin–Lomax model, which are indirectly based on – experimentally – confirmed similarity laws.

For low–Reynolds–number flows, Granville has proposed an additional modification to the equation for the outer–layer eddy–viscosity by changing the normally–kept–constant Clauser constant to

$$k = 0.0168 \left[1 + (1100 \frac{\nu}{C_{CP}} F_{WAKE})^2 \right]$$

with the kinematic viscosity, ν. F_{WAKE} is identical to the original equation for the Baldwin–Lomax model. The improved Clauser "factor", k, now varies with the displacement–thickness Reynolds number, $Re_\Theta = u\delta^*/\nu$.

A thorough examination of the original Baldwin–Lomax constants and the Granville modification shows that even for a zero–pressure–gradient flow, e.g. flat plate flow, the original Baldwin–Lomax values and the Granville–corrected values do not compare:

	Baldwin–Lomax	Granville Correction
C_{Kleb}	0.3	0.591
C_{CP}	1.6	1.24

This result clearly indicates the reduced outer–layer eddy viscosity and the improved damping in the outer part of the boundary layer when the Granville correction is applied. Thus, in case of flow separation the Granville correction provides much better results than the original Baldwin–Lomax model and can be easily implemented without increasing the model complexity.

4.2.3 The Degani–Schiff Modification

Another modification to the Baldwin–Lomax model for three–dimensional applications containing large regions with cross–flow separation that are caused by strong longitudinal vortices, has been given by Degani–Schiff (1983). It can be used with some success for those (vortical) flows and is restricting the y_{max} search in the original Baldwin–Lomax model to the first maximum reached. In addition, the search for y_{max} on subsequent stations is smoothed by taking into account the y_{max} value derived at the neighboring upstream station in order to avoid drastic changes in y_{max} from one station to another. This procedure is, by the way, also used in the Dornier 2D Navier–Stokes methods.

4.3 Johnson–King Model

The Johnson–King (1985) model accounts for convection and diffusion effects of the Reynold shear stress. Although an algebraic eddy–viscosity distribution is used across the boundary layer, this formulation is based on an ordinary differential equation that is derived from the turbulent kinetic energy equation.

The model incorporates again a two–layer approach, but uses an exponential blending between the inner and outer layer:

$$\nu_t = \nu_{to}[1 - \exp(\nu_{ti}/\nu_{to})]$$

The outer eddy viscosity distribution equals that of the Cebeci–Smith model, except for an additional non–equilibrium parameter, $\sigma(s)$, which is a measure for how far the flow is away from equilibrium – which is achieved for $\sigma(s)=1$, with s representing the streamwise direction. The outer eddy viscosity formulation reads

$$\nu_{to} = k\, U_e\, \delta_i^*\, F_{kleb} * \sigma(s) , \qquad k = 0.0168$$

The inner formulation in the Johnson–King model differs from that proposed by Cebeci–Smith by taking the maximum turbulent shear stress as a velocity scale

$$\nu_{ti} = D^2 \kappa y (-\overline{u'v'}_m)^{1/2} , \quad with\ \kappa = 0.4$$

Instead of using the wall friction velocity, Johnson (1987) uses the turbulent shear stress also for the damping term

$$D = 1 - \exp[-y(-\overline{u'v'}_m)^{1/2}/\nu A^+], \quad A^+ = 15.$$

From the equation of the turbulent kinetic energy, Johnson–King derived an ordinary equation for the maximum shear stress assuming that the path for the maximum kinetic energy is (nearly) aligned to the main flow direction. The ODE reads

$$(-\overline{u'v'}_m)^{1/2} = L_m[(\frac{\partial u}{\partial y})_m - \frac{C_{dif}(-\overline{u'v'}_m)^{1/2}}{a_1(0.7\delta - y_m)} |1 - \sigma(x)^{1/2}| - \frac{u_m}{a_1(-\overline{u'v'}_m)} \frac{d(-\overline{u'v'}_m)}{dx}]$$

From left to right, the terms in the ODE represent dissipation, production, diffusion and convection. The index m denotes quantities to be evaluated at the position of maximum shear stress and L_m denoted the dissipation length scale defined by

$$L_m = 0.4 y_m \qquad y_m \le 0.225\delta$$
$$L_m = 0.09\delta \qquad y_m > 0.225\delta$$

The constants a_1 and C_{dif} in the ODE are normally set to $a_1=0.25$ and $C_{dif}=0.5$.

Assuming equilibrium, the last two terms in the ODE cancel such that $L_m|\partial u/\partial y|_m$ can be interpreted as the equilibrium value of the maximum shear stress. Setting σ to unity and replacing the maximum shear stress by its equilibrium value, yields

$$\nu_{t,eq} = \nu_{to,eq}[1 - \exp(\nu_{ti,eq}/\nu_{to,eq})]$$
$$\nu_{to,eq} = 0.0168\, U_e\, \delta_i^*\, F_{kleb}$$
$$\nu_{ti,eq} = D^2 \kappa y (-\overline{u'v'}_{m,eq})^{1/2}$$

Comparing the definition for equilibrium and non–equilibrium gives the definition for σ:

$$\sigma = \nu_{to} / \nu_{to,eq}$$

For the ease of use, Johnson–King proposed a substitution for the ODE and a two–step iteration to obtain a new σ value from the implicit formulation. In the results discussed below, the Johnson–King model has been used by utilizing an Aitken iteration instead of the originally proposed two–step iteration. This allows for getting closer to accurate results for one particular time–step and is speeding up the rate of convergence. Apart from initial time steps, between 3 and 5 internal Aitken iterations are usually necessary to get down to an error norm of less than 1% for the eddy viscosity profile.

4.4 Johnson Coakley Model

When applying the Johnson–King model to transonic flows, often results have been achieved with shock positions appearing to much upstream – in contrast to the algebraic models where the shock position is found too much downstream. The latter also holds for the Johnson–King model if it is run in equilibrium mode, i.e. as a purely algebraic model. Most of the Johnson–Coakley (1990) modifications to the (original) Johnson–King model affect the eddy viscosity of the inner layer. A new velocity scale was formulated, based on the assumption that the law–of–the–wall is more valid in the neighbourhood of the wall for attached flow than the originally used mixing length theory.

The inner layer eddy viscosity now reads

$$\nu_{ti} = D^2 \kappa y U_s$$

with the new velocity scale

$$u_s = \sqrt{\rho_w/\rho}\, u_\tau \,[1 - \tanh(y/L_c)] + \sqrt{\rho_m/\rho}\, u_m \tanh(y/L_c)$$

where L_c is based on the dissipation length scale, L_m, according to

$$L_c = \frac{\sqrt{\rho_w}\, u_\tau}{\sqrt{\rho_w}\, u_\tau + \sqrt{\rho_m}\, u_m} L_m$$

For computational purposes, a lower limit of L_c=0.005 should be imposed in order to prevent "overflow errors" in the tanh calculation if u_τ reaches zero at separation.

Two additional modifications have been introduced by Johnson–Coakley, firstly a hyperbolic blending between inner and outer layer and, secondly, the diffusion term in the ODE is set to zero if σ becomes less than unity, i.e. $|1-\sigma^{1/2}|$ is replaced by $\max(0,\sigma^{1/2}-1)$.

Although the new formulation should reduce essentially to the original one in case of separation, computational results in the subsonic regime with pressure induced separation show a deficit for the Johnson–Coakley model with a clear advantage for the (original) Johnson–King model (Haase et al, 1997).

4.5 Abid et al Model – A 3D Extension of the Johnson–King model

This 3D extension of the Johnson–King model utilizes the original exponential blending of the Johnson–King model with an equivalent to the inner layer formulation

$$\nu_{ti} = D^2 \kappa y\, \tau_m^{1/2}$$

with

$$\tau_m = \nu_t\, |\omega|$$
$$D = 1 - \exp(-y u_\tau / \nu A^+)$$
$$u_t = \max(\tau_m/\rho_m,\ \tau_w/\rho_w)$$

where the indices m and w denote the maximum–shear–stress and wall conditions, respectively. The constant A^+ is set to A^+=17. The outer layer has been reset to the Baldwin–Lomax formulation in order to circumvent the calculation of the boundary layer thickness and the resulting displacement thickness. However, the outer layer eddy viscosity formulation (by Baldwin–Lomax) has been multiplied again by the non–equilibrium factor, σ:

$$\nu_{to} = 0.0168 C_{CP}\, F_{Wake}\, F_{Kleb}\, \sigma$$

with C_{CP}=1.6. The original ODE changes into a linear partial differential equation (PDE) that can be considered in a time–dependent form in order to utilize the time stepping algorithm – which is already in use for the momentum equations:

$$\frac{\partial g}{\partial t} + u_m \frac{\partial g}{\partial y} + v_m \frac{\partial g}{\partial z} + w_m + \Gamma = 0, \quad g = \tau_m^{1/2}$$

with

$$\Gamma = \frac{a_1}{2L_m}\left[\left(\frac{g}{g_{eq}} - 1\right) - \frac{C_{dif}\, L_m\, |1 - \sigma^{-1/2}|}{a_1\,(0.7\delta - y_m)}\right]$$

To resolve for non–equilibrium, the authors propose the time–dependent relation

$$\sigma^{t+\Delta t} = \sigma^t \left(\frac{\tau}{\nu\, \omega}\right)_m$$

to be updated during the iteration or time–stepping process rather than using the originally proposed Johnson–King two–step algorithm.

4.6 General Remarks on 2–Equation Turbulence Models

Turbulence models presented so far are using algebraic relations to describe the eddy viscosity. In addition, the non–equilibrium models are accounting for convection and diffusion effects of the Reynolds shear stress utilizing an ordinary differential equation. Models strongly rely on terms related to wall–distance, thus performing well on flows with clear boundary layer character. The situation, however, becomes more critical on flows which are both more complex from a physical and geometrical point of view. Concerning the latter first, the application of the models presented need special treatment already in the case of a corner flow where two different boundary layers are merging and where wall distance cannot be calculated straightforward. In those cases, differential turbulence models – and preferably those which do not rely on wall–distance terms – can be used more successively. Of course, differential models, accounting for non–equilibrium effects by incorporating convection, diffusion, production and dissipation (as already the 1/2–equation models are doing), exhibit a much better performance compared to the purely equilibrium ones.

The models presented in the following are so–called low Reynolds number models, i.e. a description of the turbulence processes is provided across the entire flow domain including the (low–Re) near wall region. In contrast to that, high–Re turbulence models need auxiliary wall models/definitions for a proper description of that area. Those wall laws are derived on the assumption of a logarithmic velocity distribution close to the wall.

In the class of 2–equation models, the length scale (or a related variable) is governed by a transport equation that has to be solved additionally to that describing the turbulent kinetic energy, k. In the k–ε models, the length scale variable is ε which is the turbulent dissipation rate. The eddy viscosity is given as a rationale of $f_m C_m \cdot k^2/\varepsilon$ where a transport equation is needed for k and ε, or more general, for a length or a time scale.

The Boussinesq approximation is leading to a linear relation between stresses and strains and, more recently, so–called non–linear 2–equation turbulence models have been devel-

oped with quadratic and/or cubic terms in the stress–strain relation. Concerning a proper turbulence representation of leading edge flows, these models reduce the often unphysical turbulence production rate which is one of the major weaknesses of the linear (k–ε) turbulence models.

4.7 Chien k–ε Model

The 2–equation Chien k–ε turbulence model is described by

$$\frac{\partial(\rho k)}{\partial t} + \frac{\partial(\rho U_i k)}{\partial x_j} = \tau_{ij}\frac{\partial U_i}{\partial x_j} - \rho\tilde{\epsilon} - \frac{2\mu k}{y^2} + \frac{\partial}{\partial x_j}\left[(\mu + \sigma^*\mu_T)\frac{\partial k}{\partial x_j}\right]$$

$$\frac{\partial(\rho\tilde{\epsilon})}{\partial t} + \frac{\partial(\rho U_i\tilde{\epsilon})}{\partial x_j} = C_1\frac{\tilde{\epsilon}}{k}\tau_{ij}\frac{\partial U_i}{\partial x_j} - \frac{2\mu\tilde{\epsilon}}{y^2}exp(-C_4y^+) - C_2\frac{\rho\tilde{\epsilon}^2}{k}\left[1 - 0.22\exp\left(-(R_t/6)^2\right)\right] + \frac{\partial}{\partial x_j}\left[(\mu + \sigma\mu_T)\frac{\partial\omega}{\partial x_j}\right]$$

taking a modified dissipation rate

$$\tilde{\epsilon} = e - 2\nu\left(\frac{\partial k^{1/2}}{\partial x_i}\right)^2$$

that vanishes at the wall because ε approaches the second term in that equation. For the Chien model, however, the wall dissipation is held to

$$\tilde{\epsilon} = e - 2\nu\frac{k}{x_i^2}$$

and

$$R_t = \rho k^2/\mu\tilde{\epsilon}$$
$$y^+ = \rho U_\tau y/\mu$$

denote the turbulent Reynolds number, R_t. The dimensionless wall distance, y^+, a Reynolds number based on the wall shear velocity, is defined as above.

The eddy viscosity is now evaluated from

$$\mu_t = \rho f_\mu C_\mu k^2/\tilde{\epsilon}$$

with

$$f_\mu = 1 - \exp(-C_3\, y^+)$$

The constants appearing in the model take the following values:

σ^*=1, σ=1.3, C_μ=0.09, C_1=1.35, C_2=1.8, C_3=0.0115, C_4=0.5 .

4.8 Wilcox, k–ω Model

In the k–ε models, the length scale variable is ε, in the *k–ω* model, however, ω stands for the turbulent vorticity – with a dimension 1/time. ω is defined by:

$$\omega = \frac{\rho\, k}{\mu_t} \quad .$$

Wilcox (1993) claimed that the use of ω instead of ε allows for an integration (of the partial differential equations) down to the wall – through the viscous sublayer – without the use of terms which are sensitive to viscosity with respect to the corrsponding turbulent Reynolds number. In particular, Wilcox proposes the following set of equations.

$$\frac{\partial(\rho k)}{\partial t} + \frac{\partial(\rho U_i k)}{\partial x_j} = \tau_{ij}\frac{\partial U_i}{\partial x_j} - \beta^*\rho k\omega + \frac{\partial}{\partial x_j}\left[(\mu + \sigma^*\mu_T)\frac{\partial k}{\partial x_j}\right]$$

$$\frac{\partial(\rho\omega)}{\partial t} + \frac{\partial(\rho U_i\omega)}{\partial x_j} = \alpha\frac{\omega}{k}\tau_{ij}\frac{\partial U_i}{\partial x_j} - \beta\rho k\omega^2 + \frac{\partial}{\partial x_j}\left[(\mu + \sigma\mu_T)\frac{\partial\omega}{\partial x_j}\right]$$

with

$$\epsilon = \beta^*\omega\, k \qquad l = \frac{k^{1/2}}{\omega}$$

and the following closure coefficients

$$\alpha=5/9,\ \beta=3/40,\ \beta^*=9/100,\ \sigma=1/2,\ \sigma^*=1/2.$$

In general, the Wilcox model performs well in flow cases with adverse pressure gradients, however, the wall–boundary condition for ω is somewhat difficult to handle for general aerodynamic flow problems. An additional problem might be seen in the sensitivity of the model to the free–stream values of ω. An alternative – although the free–stream dependence is still not solved completely, is to re–write the ω–equation in terms of τ, the turbulent time scale, or an equivalent of that as it is shown in the following description of the Kalitzin–Gould model.

4.9 Kalitzin–Gould k–g Model

By substituting in a first step the specific dissipation rate, ω, with the time scale τ, i.e. writing

$$\tau = \frac{k}{\epsilon} = \frac{1}{\omega\,\beta^*} \ ,$$

the boundary problem in the Wilcox model can be overcome because the boundary condition for τ becomes zero at walls. Moreover, the decoupling of k and ω, leading to strong far–field dependence, does not exist (at least not to that extent) in the k–τ model, i.e. even in the case that the local level of turbulence is rather small, a solution for τ will be found. However, the far–field dependence problem is not completely solved, the value of τ has still an influence on the boundary layer itself.

On the other hand it is well know that τ tends to zero according to y^2 (instead of just y; y being the wall normal distance) and this knowledge is guiding to the Kalitzin–Gould model which offers good predictive accuracies in various two– and three–dimensional flows.

The new variable now introduced is $\tau^{1/2}$ instead of τ. The transport equations then read

$$\frac{\partial(\rho k)}{\partial t} + \frac{\partial(\rho U_i k)}{\partial x_j} = \tau_{ij}\frac{\partial U_i}{\partial x_j} - \rho\frac{k}{g^2} + \frac{\partial}{\partial x_j}[(\mu + \sigma^*\mu_T)\frac{\partial k}{\partial x_j}]$$

$$\frac{\partial(\rho g)}{\partial t} + \frac{\partial(\rho U_i g)}{\partial x_j} = -\frac{\alpha}{2}\frac{g}{k}\tau ij\frac{\partial U_i}{\partial x_j} - (\mu + \sigma\mu_t)\frac{3}{g}\frac{\partial g}{\partial x_i}\frac{\partial g}{\partial x_i} + \frac{\beta\rho}{2g\beta^*} + \frac{\partial}{\partial x_j}\left[(\mu + \sigma\mu_T)\frac{\partial g}{\partial x_j}\right]$$

with the eddy viscosity being

$$\mu_t = \beta^*\rho k g^2 \ .$$

The closure coefficients for the Kalitzin–Gould turbulence model are the same as those presented above for the Wilcox model, namely

$$\alpha=5/9,\ \beta=3/40,\ \beta^*=9/100,\ \sigma=1/2 \text{ and } \sigma^*=1/2.$$

4.10 How to Derive the Boundary Layer Thickness from Navier–Stokes Calculations

In Navier–Stokes computations, the calculation of boundary layer integral values is not straightforward because it proves difficult to accurately derive the boundary layer thickness and all boundary layer integral values directly from the velocity field distribution. An approach for handling this problem had been proposed by Stock&Haase (1987, 1989) that is briefly described in the following.

The method to be considered relies on the assumption that computed Navier–Stokes velocity profiles can be correlated to Coles' boundary layer profiles. For these velocity profiles it can be shown that $[y(du/dy)]_{max}$ occurs at the same relative wall distance inside the viscous layer for all attached and separated flows. Using this feature when analysing the Navier–Stokes data and evaluating the wall distance y_{max} for which y|du/dy| – equivalent to the F–function in the Baldwin–Lomax turbulence model – becomes a maximum, delivers the boundary layer thickness to be

$$\delta = 1.936\ y_{max}$$

Consequently, with the knowledge of the boundary layer thickness itself, all boundary layer integral values can be easily computed by numerical integration.

For three–dimensional applications, it was proposed in EUROVAL (Haase et al, 1993), to derive the boundary layer thickness, δ, by

1. searching for the wall–normal distance, y_{max}, in each velocity profile where the maximum of the resultant velocity, $|u_{max}|$, is found,
2. calculating the maximum value for the vorticity, $|\omega_{max}|$, and
3. scanning the vorticity distribution in order to check where

$$|\omega|>0.001\cdot|\omega_{max}| \quad \text{for} \quad y<y_{max}$$

is found.

The boundary layer thickness is then described by the wall–normal distance where $|\omega|>0.001\cdot|\omega_{max}|$ is found. This approach provides reasonable results at least for wing–type flows.

5. SOME ASPECTS OF TRANSITION AREA MODELLING

The class of eddy–viscosity turbulence models presented so far are linear models with two major weaknesses. They can neither predict the onset of transition nor the length of the transition region.

Prediction of the onset of transion is an important factor for accurately simulating flows that have not been tripped in the experiment, i.e. where transition from laminar to turbulent flow has not been forced by special devices. Two strong factors – the streamwise pressure gradient and the free–stream turbulence – are influencing the position of transition. Careful computations, however, need to compute the growth of disturbances that build up in the boundary layer until they reach the condition where transition really occurs. Michel (1951) and Granville (1953) suggested methods that base on the transition momentum–thickness Reynolds number. More recently, Arnal (1989) and Stock&Haase (1996) proposed methods that can be used for analysing boundary layer and Navier–Stokes results by means of linear stability theory.

Transition–area modelling, i.e. simulation of that area where the flow is transitioning from laminar to fully turbulent flow, is the second important weakness of (linear) eddy–viscosity models. Moreover, models often massively overpredict the eddy viscosity in the region of leading edges (e.g. of an airfoil). At the onset of transition, turbulence models are normally "switched on" without taking into account the finite distance of the transition region. Moreover, in the case of turbulence models employed that do not have the capability of predicting or estimating transition onset, as e.g. the higher–order 2–equation turbulence models, the question of a smooth transition from laminar to turbulent flow is often not considered at all.

However, just "switching on" the turbulence model at the measured or suggested position of transition onset might not be a valuable approach, as it is demonstrated for the transition–sensitive hypersonic ramp flow in section 7.4.

In the following, three classes of easy–to–employ transition models are presented that are related to firstly switching off eddy viscosity in the expected transition region (Baldwin–Lomax) and secondly, and more precisely, using intermittancy functions that provide – when multiplied to the tentatively computed eddy viscosity – a smooth variation from laminar to turbulent flow.

5.1 Baldwin–Lomax

For Navier–Stokes calculations, Baldwin–Lomax proposed to very simply simulate transition from laminar to turbulent flow by setting ν_t equal to zero everywhere in the wall–normal eddy viscosity profile, for which the (tentatively) computed maximum value of ν_t is less than a pre–specified value. This results in:

$$\rho\nu_t = 0 \quad if \quad (\rho\nu_t)_{maximum\ in\ profile} < \mu_\infty C_{MUTM}$$

with a proposed value of C_{MUTM}=14.

5.2 Cebeci

Cebeci (1974) pointed out that substantial errors occur if transition modelling is inadequate. Considering e.g. the (boundary layer) flow past a compressor blade, the extent of the transition region can be correlated according to Chen and Thyson (1971) by

$$R_{\Delta x} = \mathrm{Re}_{x_t} - \mathrm{Re}_{x_{tr}} = C R_{x_{tr}}^{2/3}$$

where $R_{\Delta x}$ describes the extent of the transition area. Re_{x_t} is the Reynolds number based on the completion of the transition and $\mathrm{Re}_{x_{tr}}$ is the Reynolds number based to the start of transition. C is an empirical expression reading

$$C = 60 + 4.86\ M_e^{1.92} \qquad 0 < M_e < 5.$$

where M_e denotes the Mach number at the boundary layer edge. Depending on the (turbine blade) Reynolds number

and the onset of transition this approach might lead to large transition areas often extending to the trailing edge.

5.3 Dhawan&Narasimha

Another estimate, used for the hypersonic ramp flow in section 7.4, is the transition length estimate by Dhawan&Narasimha (1958) which is based on an examination of experimental data to deduce the (probable) existance of a relation between the transition Reynolds number and the rate of production of the turbulent spots. Application of an observed statistical similarity in the transition distributions together with Emmons' (1951) spot theory results in a single universal intermittency function

$$\gamma_{tr} = 1 - exp(-0.412\xi^2)$$

with ξ being the normalized streamwise coordinate in the transition zone,

$$\xi = (x - x_{tr})/\lambda_{tr}$$

and λ_{tr} being a measure of the extent of the transition region, characterized by

$$\lambda_{tr} = x_{(\gamma_{tr}=0.75)} - x_{(\gamma_{tr}=0.25)}$$

where x_{tr} denotes the onset of transition.

One has to be aware of the situation that the two "free" parameters to be specified in the transition length model, x_{tr} and λ_{tr}, have to be taken from experiment, see result for the hypersonic ramp flow in section 7.4.

6. REQUIREMENTS FOR ACCURATE AND EFFICIENT MODELLING OF TURBULENCE

6.1 DNS Requirements

The most accurate way simulating turbulent flows is of course the use of Direct Numerical Simulation (DNS). Nowadays, the major problem is that the requested computer performance is not available, thus restricting the use of DNS to low(er) Reynolds numbers in the order of $O(10^4)$.

Knowing that in boundary layers an energy transport is taking place from larger to smaller eddies and dissipation is related to viscosity, the ratio of spacial dimensions between small to large eddies is equivalent to a Reynolds number of $Re^{3/4}$. In case of three–dimensional flows this is resulting in $(Re^{3/4})^3$ degrees of freedom. Assuming that the time being necessary for the energy transport (from the larger) to the smaller eddies is equivalent to $Re^{3/4}$ as well and that a number of (mathematical) operations needed is in the order of O(1),

$$O(Re^{9/4}) \text{ memory} \quad \text{and}$$
$$O(Re^3) \text{ numerical operations}$$

have to be carried out. In other words, doubling the Reynolds number results in an increase of computer capacity by one magnitude. Getting now back to the first paragraph of this section, the latter might provide an answer to the mentioned limitations on Reynolds numbers being in the order of $O(10^4)$ for DNS computations of turbulent flow.

Although for "real" applications the desired Reynolds numbers are much higher, DNS results obtained at still lower Reynolds numbers bear a very good capability of directly supporting flow–physics–modelling aspects. On the other hand, it becomes quite evident that computational fluid dynamics for "real" applications at high Reynolds numbers still rely on the utilization of turbulence models.

6.2 Turbulence Model Requirements

If – due to computer limitations – DNS computations cannot be applied to flow cases governed by Reynolds numbers greater $O(10^4)$, the question arise what the needs are for accurately predicting flow on the basis of using turbulence models.

Assuming that an estimated size of eddies in a boundary layer is in the order of 1/5 of the boundary layer thickness and that 10 mesh points are needed to resolve one eddy, 50 points are needed in total within the boundary layer. Assuming, furthermore, that the boundary layer thickness is about 1% of the chord of an airfoil, 5,000 points are needed in chordwise direction. Extending this to three–dimensional flow with the same mesh spacing in all three directions for a wing with an aspect ratio of 10, an amount of 50,000 points is needed. Summing up in space,

$$12.5 \times 10^9 \text{ mesh points}$$

might form a proper basis for an accurate discretization of the considered boundary layer domain.

Allowing waves, when assuming time–dependent flow, to travel just through one mesh interval per time step and to allow for a total time equivalent for those waves to travel three times the length of the chord for a converged solution, results in 15,000 time steps. Hence, a (computer) performance is needed that is beyond the teraflop and adds up to

$$>10^{14} \text{ operations per second.}$$

This is, of course, a rather pessimistic guess (for an assumed explicit numerical method), however, it reflects at least some needs for mesh fineness in order to get close to results that can be termed as mesh independent ones. By the way, the figures derived above, are based on a mesh that is merely resolving the *upper–surface boundary layer* of a wing and does neither take into account the lower surface nor the farfield of the computational mesh ... !

7. APPLICATIONS

In the following, applications for two– and three–dimensional compressible flows will be presented and discussed with respect to flow–physics modelling aspects.

7.1 RAE 2822 airfoil

The most popular test case treated by the majority of people investigating transonic (two–dimensional) flow is the RAE 2822 airfoil, (Cook, McDonald, Firmin, 1979). The cases going to be discussed are Case 9 and 10, respectively. Both cases consider transonic flow with shock strengths causing flow with either approaching separation or showing incipient separation. The major problems are related to shock/boundary layer interaction that is difficult to treat by the turbulence models used.

In order to carry out any – reliable – validation process, emphasis on mesh dependence aspects must be placed initially. For the RAE 2822, Case 9, application, a comprehensive grid–dependence study has been undertaken in a GARTEUR initiative (Williams, 1994). The flow parameters for Case 9 read Ma = 0.734, Re = $6.5 \cdot 10^6$, $\alpha = 2.54^o$ with transition at 0.03 chord on lower and upper surface. The flow parameters have been corrected according to recommendation by the experimentalists (Haase et al, 1993).

Results of the GARTEUR study are given in Table 1 and are based on a use of the Baldwin–Lomax turbulence model coded in the original version.

Table 1 Force coefficients for RAE 2822, Case 9. A mesh dependence study using the Baldwin–Lomax turbulence model. The mesh structure for the 256x64 mesh is presented in Fig. 1.

Meshpoints	Drag c_D	Lift c_L	Moment c_M
64x16	0.032682	0.85812	–0.13794
128x32	0.022277	0.85316	–0.12068
256x64	0.018891	0.83565	–0.11121
512x128	0.017665	0.82207	–0.10638
1024x256	0.017291	0.81445	–0.10490
Experiment	0.016800	0.80300	–0.09900

It can be seen from Table 1 that variations in lift and moment coefficients are much smaller compared to the drag coefficient on the different mesh levels; drag variation is close to 100% between finest and coarsest mesh. Although the finest–mesh results show the best agreement with experiments, two further items should be made as clear as possible: First, as mentioned above, results obtained for that study have been carried out using the original Baldwin–Lomax model, a turbulence model that does not precisely describe shock/boundary layer interaction. Second, one can recognize easily that between the fine grid (512x128) and the finest one (1024x256) a difference of still four drag counts has been calculated. However, in the context of an accurate design (say of a complete wing) this might be still too much.

It should be noted at this point that the difference between measurement and computation is not the most crucial issue aspects of validation, errors are evident on both sides, but grid independent results should be obtained in all cases in order to predict the "deltas" between a variety of solutions accurately.

Results going to be discussed in the following have been obtained using a mesh with 512x128 volumes. Moreover, it should be mentioned that the mesh has been adapted to the measured shock location. However, in order to provide reliable results for different turbulence models with corresponding slightly differently predicted shock locations, shock aligned mesh adaptation has been applied moderately (for the upper airfoil surface) as it is shown in Fig. 1 for the second mesh level (256x64) of the RAE 2822 airfoil mesh.

As already mentioned, in the fine mesh 512 volumes are located in the wrap–around–direction and 128 volumes are used to discretise the wall–normal–direction. 64 volumes have been taken from the 512 for wake representation, i.e. 384 volumes are distributed on the airfoil surface according to the C–type mesh structure. The first volume height (adjacent to the airfoil surface) is selected to be between 3.5×10^{-7} chords in the apex region and about 6.0×10^{-6} in the trailing–edge part on lower and upper surface, respectively. This results in calculations that exhibit in the finest (512x128) mesh 50–78 mesh points in the boundary layer, starting with 50 points (volumes) in the stagnation point area and reaching 56 points in the lower trailing edge and 71 (78) for Case 09 (Case10) in the upper trailing edge boundary layer.

The following discussion of the RAE 2822 test cases will now concentrate on Case 10, a test case being more sensitive with respect to different turbulence model applied. The flow parameters are Ma = 0.754, Re = $6.2 \cdot 10^6$ and α = 2.81° with transition at 0.03 chord on lower and upper surface. The grid dependence that has been carried out, exhibits y^+–values in the fine meshes, i.e. in both the 256x64 and the 512x128 mesh, that are lower than unity.

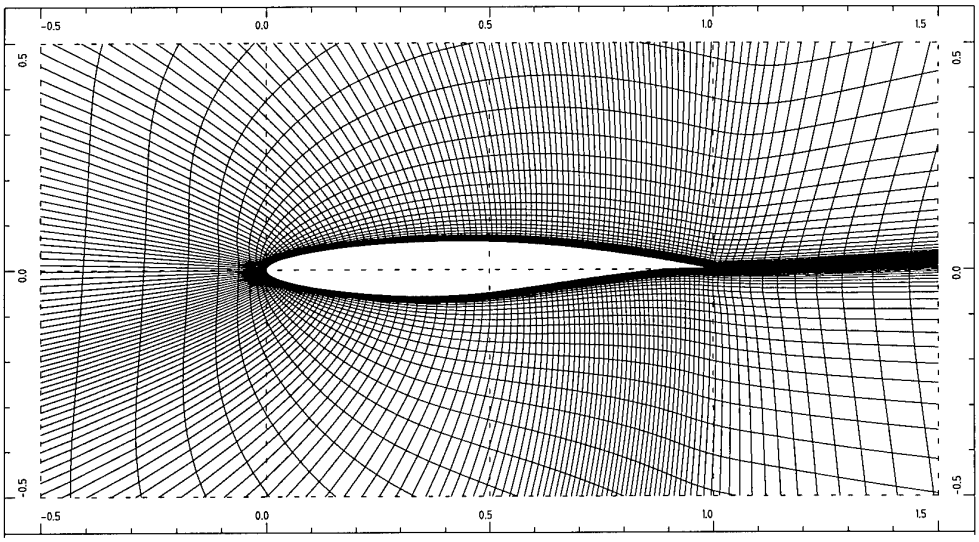

Figure 1 Mesh for RAE 2822 airfoil with 256x64 cells

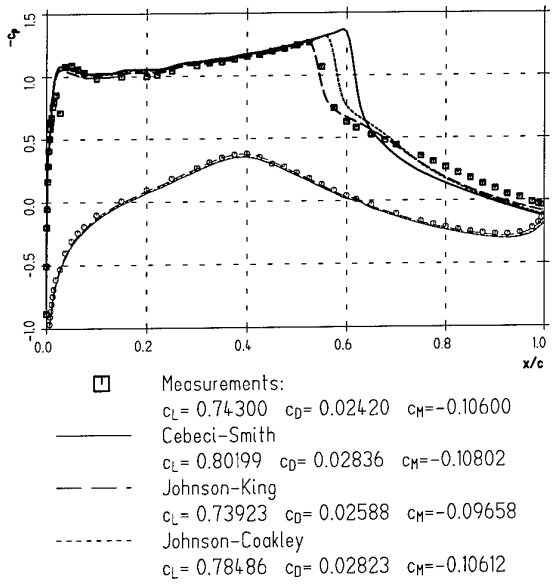

Figure 2 Pressure distributions for RAE 2822, Case 10, and different turbulence models, mesh level 512x128

In Fig. 2, for the Cebeci–Smith, Johnson–King and Johnson–Coakley turbulence models, pressure coefficient distributions are presented and, additionally, the computed force coefficient are given. As "usual", the algebraic model – but this holds also for the Baldwin–Lomax model – is shifting the shock more downstream, in contrast to the Johnson–King model which (often) positions the shock more upstream in alignment with a reduced shock strength. The Johnson–Coakley model ameliorates the shock location by the introduction of the modified inner layer formulation. This holds for nearly all transonic test cases, as it will be shown also in section 7.2 for the MBB–A3 airfoil.

The thinner lines in all figures of this section correspond to the lower airfoil surface distributions, the thicker ones to the upper surface.

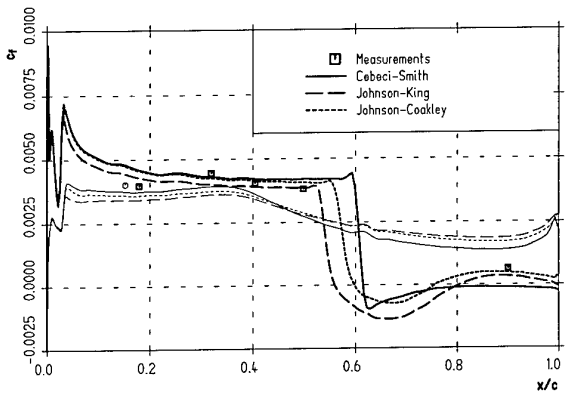

Figure 3 Skin friction distributions for the RAE 2822, Case 10, and different turbulence models

Fig. 3 depicts the corresponding skin friction distributions for the three selected turbulence models. It becomes very clear, that in the area where the flow remains attched, all three models are producing similar results, however, in the shock and post–shock regions, major differences occur. The algebaic model returns (shock induced) separation down to the trailing edge, whereas the 1/2–equation models provide more reliable results showing reattachment in the rear part of the upper airfoil surface.

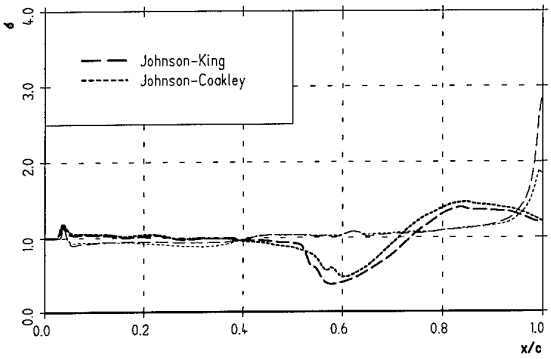

Figure 4 RAE2822, Case 10, non–equilibrium effects using Johnson–King and Johnson–Coakley 1/2–equation turbulence models

The advantage of the 1/2–equation models with respect to the algebraic model is due to the fact that the non–equilibrium models are taking boundary layer history effects into account by solving an ordinary differential equation. The σ distribution shown is – as described above in section 4.3 – the ratio between the (outer) eddy viscosity for the non–equilibrium and equilibrium approach,

$$\sigma = \nu_{t,outer} \,/\, \nu_{t,outer,equilibrium} \quad .$$

For the upper surface of the RAE 2822 airfoil, Fig. 4, the flow well upstream of the shock is close to its equilibrium state, whereas in the vicinity of the shock – initiated already some boundary layer thicknesses ahead of it – the non–equilibrium eddy viscosity is smaller. This situation is reversed aft of the shock and σ reaches a near–equilibrium state at the trailing edge again. On the lower surface, where the flow (thinner lines in Fig. 4) is accelerated towards the trailing edge (due to the rear loading of the airfoil), the non–equilibrium eddy viscosity is dominating, too.

A disadvantage of the 1/2–equation models when "switched on" at the desired onset of transition is that they often produce high unphysical non–equilibrium values for σ. Assuming that the turbulent boundary layer is closer to equilibrium in that area than to non–equilibrium, this local maximum can be reduced by using a relaxation between the eddy viscosity calculated on a equilibrium and non–equilibrium model basis. This is forcing the flow (and consequently the eddy viscosity) to stay near to equilibrium at least along some percent of the chord when "switching on" the turbulence model right at transition onset.

More precise answers about the predictive accuracy of any Navier–Stokes computation provides an inspection of the boundary layer behaviour. The boundary layer displacement thickness, presented in Fig. 5, has been derived by using the approach by Stock&Haase (1989) that has been briefly described in section 4.10. Fig. 5 exhibits the displacement thickness for Case 10 on upper and lower surface (thin lines), respectively. The various shock locations can be easily detected, causing a rather different post–shock boundary layer behaviour. Again, the Johnson–Coakley model gives favourable results – when compared to the measurements.

This can be underlined by the velocity profiles plotted at x/c=0.65 and x/c=1.0 presented in Figs. 6 and 7.

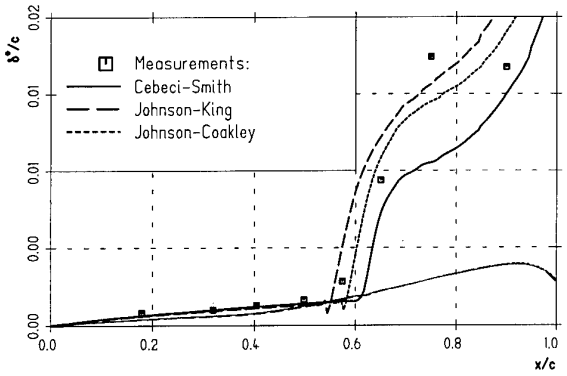

Figure 5 RAE 2822, Case 10, displacement thickness distributions

However, one has to be cautious in interpreting the results shown in Fig. 6 and 7, in particular the results for x/c=0.65 because different shock locations produce correspondingly different velocity profiles at fixed chord–wise positions. The x/c=0.65–profile lies in the post–shock area for all models but the boundary layer history at this station is different due to the different positions of the shock upstream of that location. The 1/2–equation models show well separated flow with reasonable shapes of velocity, while the algebraic (Cebeci–Smith) model exhibits a "feature" which holds for nearly all algebraic models, namely to produce spiky, i.e. unphysical, near wall profile shapes in separation zones.

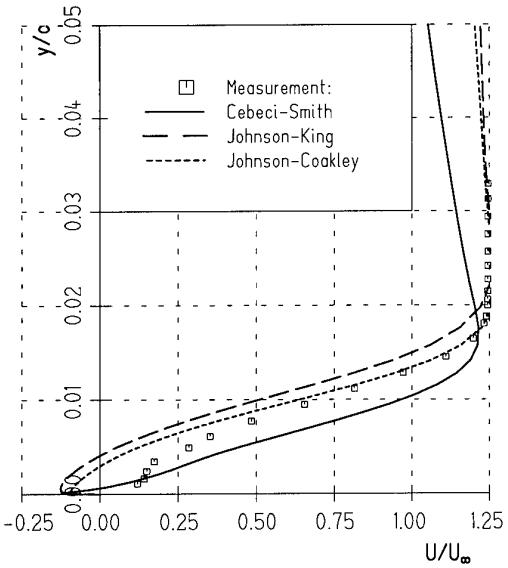

Figure 6 RAE 2822, Case 10, velocity profiles at x/c=0.65 on upper surface

Although pressure distributions compare fairly well for the different turbulence models tested, larger differences in the velocity profiles can be detected from Fig. 6 and 7. Apart from the situation that the algebraic model is unable to predict reattachment behind the shock in that very case, as it can be taken from the skin friction distribution in Fig. 3, only the Johnson–Coakley model provides at least a qualitative agreement with the experimental findings.

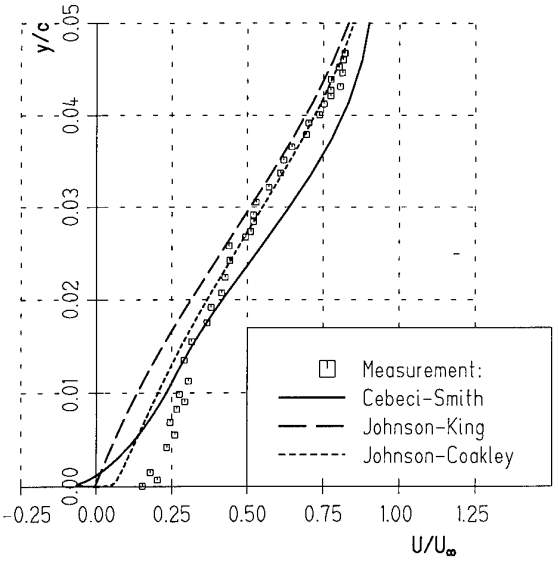

Figure 7 RAE 2822, Case 10, velocity profiles at x/c=1.0 on upper surface

Results for three different 2–equation models can be taken from Fig. 8 and 9, presenting pressure coefficient and skin friction distributions for the Lien–Leschziner (1991), the Chien (1982) and the Kalitzin (1995) k–τ model. The latter is the modified Wilcox k–ω model expressing the eddy viscosity as a function of the turbulent kinetic energy and the time scale, $\tau=k/\varepsilon$.

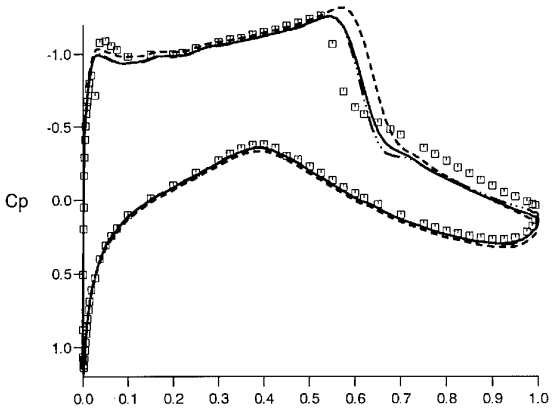

Figure 8 RAE 2822, Case 10, pressure coefficient distributions for 2–equation models, for legend see Fig. 9 (by courtesy of G. Kalitzin)

Computations of pressure, Fig. 8, and skin friction, Fig. 9, exhibit a trend that is recognized in many 2–equation turbulence models, in particular to underpredict pressure induced separation caused by adverse pressure gradients or dismissing separation at all. Unfortunately, the results discussed so far do not provide a proper basis for being able to distinguish between model sophistication and accuracy, however, the advantage of the 2–equation models, being more effectively applicable to complex geometric shapes, still holds.

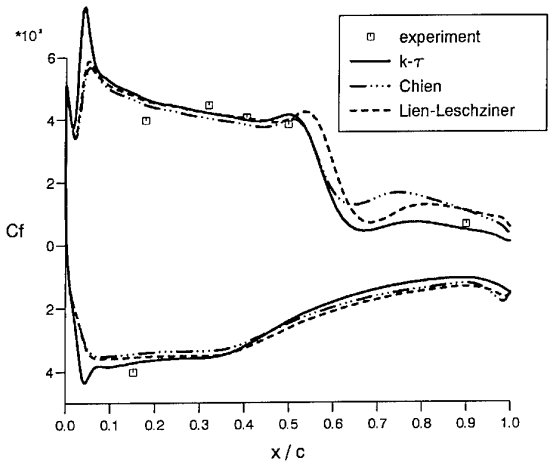

Figure 9 RAE 2822, Case 10, skin friction distributions for 2–equation models (by courtesy of G. Kalitzin)

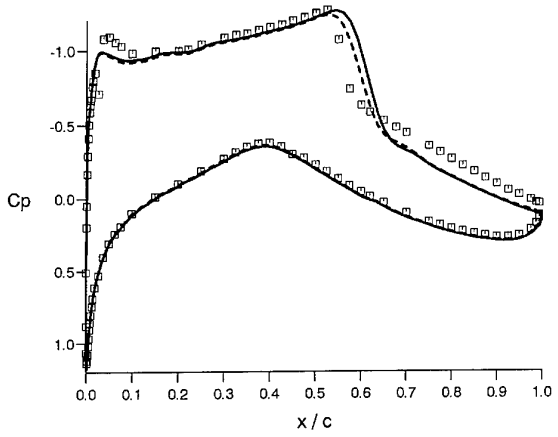

Figure 10 RAE 2822, Case 10, pressure coefficient distributions for k–τ (——) and k–τ–SST (– – –) model (by courtesy of G. Kalitzin)

The adoption of Menter's (1994) SST approach, i.e. reducing the amount of outer layer eddy viscosity, is ameliorating the pressure result, as it can be taken from Fig. 10. Additionally, the flow is further approaching separation but not really separating. In general, the SST approach was found to predict separated flows or flows approaching separation much better. The pressure "plateau" on the upper surface (upstream of the shock), however, is slightly more underpredicted (pressure in fact is overpredicted, $-c_p$ is plotted) by using the SST approach. As a gift in return, the slightly lower (favourable) pressure results in a more upstream shock location and the shift of the shock position is caused by the slightly different boundary layer history.

It has been shown in the ECARP project (Haase et al, 1997) that even more improvements on 2–equation turbulence models can be achieved by taking into account second (or third) order effects in the stress–strain relation.

7.2 MBB–A3 airfoil

Flow over the MBB–A3 airfoil (Bucciantini et al, 1979) is similar to what has been discussed in the previous section. However, the increased Mach number is causing a more pronounced shock/boundary layer interaction and will exhibit some further problems in flow prediction on the lower side of the airfoil. Results for the MBB–A3 airfoil, Case 113, are presented to demonstrate the encountered weaknesses.

Concerning mesh generation for the MBB–A3 airfoil, a similar effort as for the RAE 2822 airfoil has been placed on achieving mesh independent results. The mesh (in)dependence study has revealed a mesh with a first volume height (adjacent to the airfoil surface) of 3.4×10^{-7} chords in the apex region and 7.0×10^{-6} in the trailing–edge part on lower and upper surface, respectively. This leads to y^+ values at the wall of less than 0.5. Computations for test case "113" exhibit between 45 to 67 mesh points across the boundary layer in the finest (512x128) mesh, starting with 45 points at the stagnation point and reaching 59 in the lower–surface and 67 on the upper–surface trailing edge region.

Compared – when different turbulence models are considered – to the already sensitive test case RAE 2822, Case 10, an even more critical flow simulation is achieved for the MBB–A3 airfoil due to much larger deviations in shock locations when using different turbulence models. This test case that has been thoroughly investigated in the European ETMA project (ETMA: Efficient Turbulence Modelling for Aeronautical Applications, Dervieux, 1997).

The flow parameters for the "113" test case read: Ma=0.85, $Re=6.08 \cdot 10^6$, $\alpha=1.78$ with transition at 0.4 chords on the lower surface and at 0.03 chords on the upper surface, respectively. The major problem, and this underlines again the strong need for having precisely defined and comprehensive experiments at hand, is that transition was not fixed in the measurements. For the present computations, transition location on lower and upper surface has been "derived" from the experiment itself by taking the pressure distribution as an initial guess. This more than rough estimate is checking where favourable pressure gradients change into adverse ones and has no relation to a serious investigation of transition onset.

Pressure distributions, shown in Fig. 11, using the same set of turbulence models as for the RAE 2822 cases – Cebeci–Smith, Johnson–King and Johnson–Coakley – exhibit drastic deviations on both upper and lower (!) surface of the airfoil. For the upper surface, the same answers given for the RAE 2822 are still valid, although the differences obtained between the chosen turbulence models are much bigger. On the lower surface, no real explanation can be given for the gap between experiment and computation. The measurements do not exhibit a supersonic region – the c_p^* line defines the critical pressure coefficient where the flow becomes supersonic – whereas the computational results show a clear tendency for a supersonic bucket. Setting transition on the lower surface to x/c=0.03, according to the detected small area of adverse pressure in that region, does not really change the flow behaviour on the lower airfoil surface.

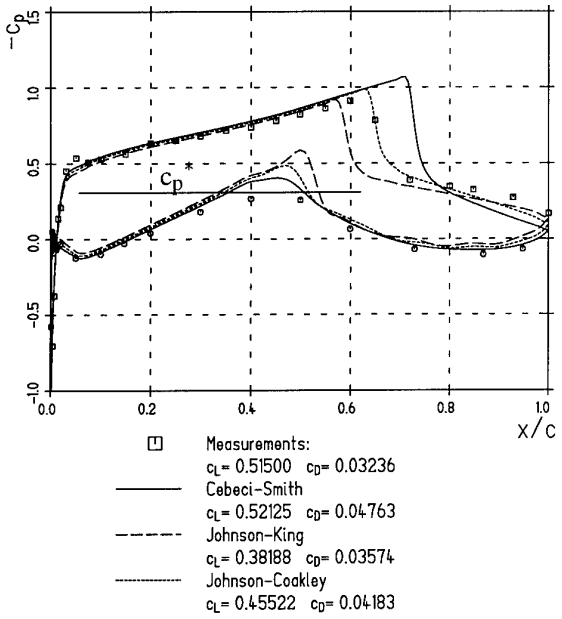

Figure 11 MBB–A3, Case 113, pressure coefficient distributions for different turbulence models

It should be mentioned additionally, and this again shows the importance of the undertaken grid–dependence study, that the algebraic turbulence model on the very fine mesh produces similar results – with respect to the shock position – as the Johnson–Coakley model is predicting on the coarser mesh. Thus, the MBB–A3 "113" test case has not only been presented to demonstrate weaknesses but even more to encourage further investigations.

7.3 ONERA channel bump flow

In contrast to simulating exteriour flows, channel flows offer the possibility of achieving more accurate results by precisely taking measuremental flow conditions (inflow, outflow, correct boundary conditions due to limited computational domain) into account. Moreover, for the ONERA bump test, Case A, it is possible to computationally "shift" the shock directly into that streamwise position where it was measured, hence enabling a very good basis for properly comparing different turbulence models in the shock area itself. It allows for directly comparing boundary layer profile data at fixed positions. However, fixing the shock computationally, causes the disadvantage of additional calculations as the exit pressure is driving the flow field behaviour – and the shock position.

The flow parameters used in that study are: In–flow Mach number Ma=0.68, total pressure p_t=0.96·10^{5}N/m^2, total temperature T_t=300K and the experimental pressure ratio being p_t/p_{exit}=1.522. The isentropic Mach number target on the lower wall – that has to be fulfilled by all computations – has been set to Ma=1.047 at x=0.158m.

The mesh that has been used mandatorily in the EUROVAL project (Haase et al, 1993) is presented in Fig. 12. It shows the refined shock area and allows for y^+ values at the wall being less than unity.

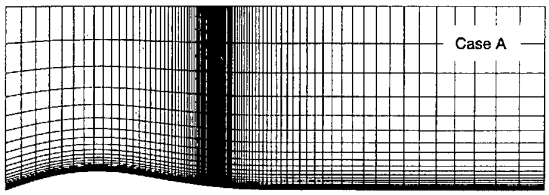

Figure 12 ONERA bump, Case A, mesh structure

Based on the flow parameters given above and the mesh in Fig. 12, flow field results for a variety of turbulence models are presented as Mach number contours in Fig. 13. At a first glance, most of the solutions obtained look rather similar whether algebraic, 1/2–equation, 2–equation or algebraic Reynolds stress models are concerned. Apart from some oscillatory behaviour in the post–shock area and slight differences in the contour shapes at the inlet boundary due to variations in implemention (e.g. the Dornier results have been obtained by extrapolating the velocity components u and v under the constraint that v never violates the "kinematic limit", i.e. the computed density remains positive), the shock position, mandatorily adjusted to the experimental value, is well captured by all computations. However, closer inspection of the near–wall shock area itself exhibits a variety of shock/boundary layer interference aspects with varying λ–shock structures which are caused by over(under)prediction of post–shock separation when using the different turbulence models.

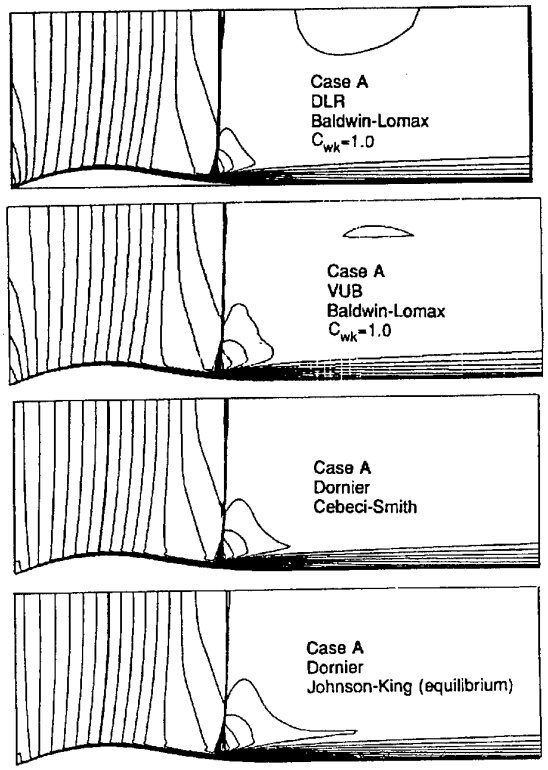

Figure 13 ONERA bump, Case A, Mach number contours for different turbulence models

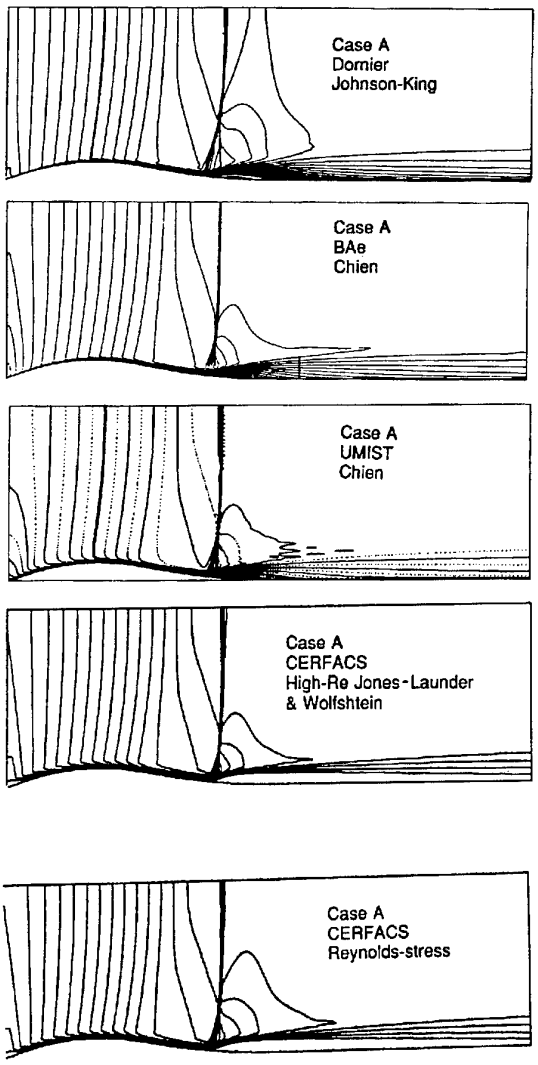

Figure 13 (cont.) ONERA bump, Case A, Mach number contours for different turbulence models

The two following figures, Fig. 14 and 15, present a better insight into what was discussed up to now. Up to the shock, the isentropic Mach number at the tunnel wall, Fig. 14, is in perfect agreement with the experimental findings, i.e. all turbulence models involved return the attached–boundary–layer features correctly. The marked Mach number, (⇦), indicating the correct shock location (to be met mandatorily by all computations), has been well captured. The computed exit pressure ratios that were necessary for the different turbulence models to fix the shock at the desired position, varied from p_t/p_{exit}=1.520 to 1.529, see legend in Figs. 14 and 15.

Concerning the flow prediction in the aft shock region, the non–equilibrium Johnson–King model provides the best performance, although it is overpredicting separation, as it can be recognized from Fig. 13. It is important to note, particularly with respect to a thorough validation work, that the discrepancy in the area well behind the shock, i.e. the gap between the experimental and computed Mach number level must not be related to weaknesses in flow–physics (turbulence) modelling but was reported as a three–dimensional effect in the measurements.

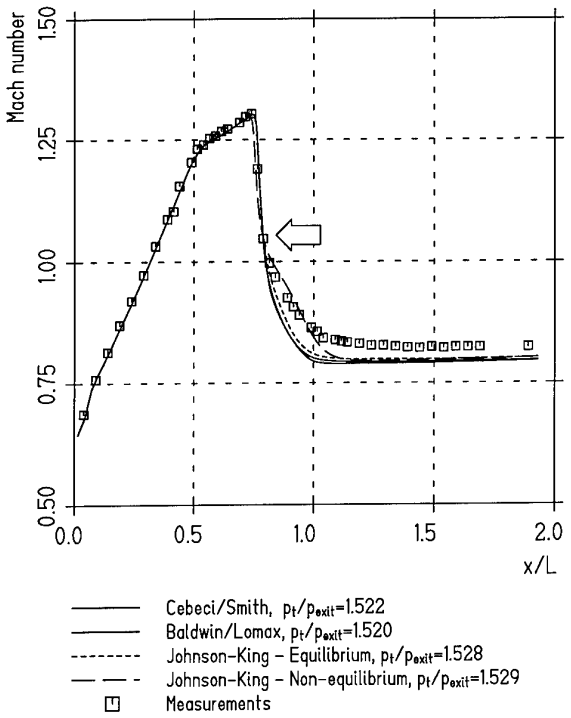

Figure 14 ONERA bump, Case A, Isentropic wall Mach number for different turbulence models

But even when "global" flow features are in line with the measurements, a thorough investigation of the boundary layer provides a better indicator on the predictive accuracy as it is presented in Fig. 15, showing distributions for the boundary layer displacement and momentum thicknesses. Concerning computed momentum–thickness distribution one should be aware of the importance for any CFD method to predict momentum thickness accurately.

Fig. 15 seems to indicate – concerning the displacement and momentum thicknesses – that the algebraic models which do not predict pressure in the close vicinity of the aft–shock region accurately, are in better agreement with the experimental findings. However, the algebraic models do not predict either the maximum displacement thickness or the downstream conditions correctly. Moreover, the Baldwin–Lomax model clearly underpredicts momentum thickness downstream of the shock. Unfortunately, the Johnson–King model drastically overpredicts momentum and displacement thickness due to an overprediction of shock induced separation which can be related to a non–equilibrium outer eddy viscosity being by far too small in that area.

It should be recalled that this flow is presumably attached, as suggested by the experimental velocity distributions, there is, however, no conclusive evidence that separation is completely suppressed, as there are no experimental data for skin friction available.

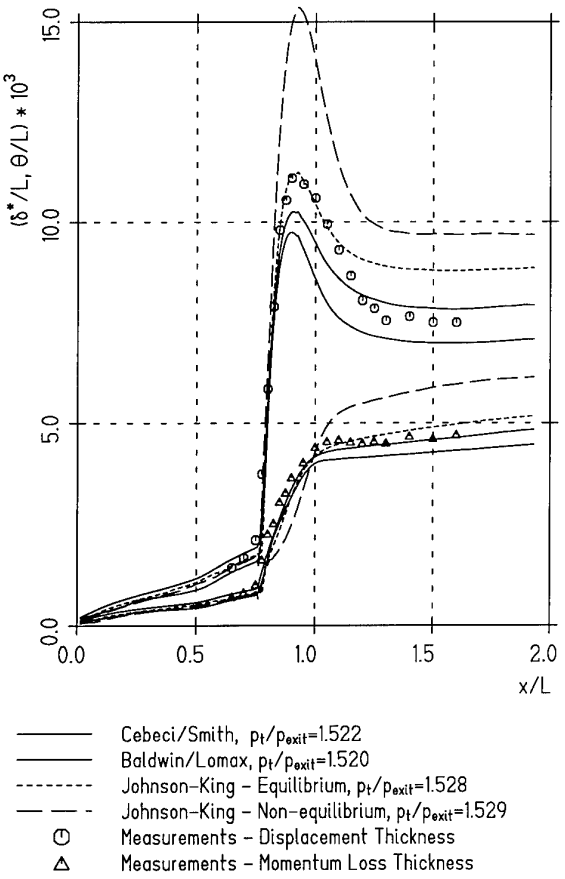

Figure 15 ONERA bump, Case A, displacement and momentum thickness for different turbulence models

7.4 Hypersonic ramp flow

Initiated at the Hypersonic Workshop (Désidéri et al, 1991), emphasis was placed on the calculation and validation of hypersonic re–entry problems, particularly aiming at the simulation of flows over deflected control surfaces (e.g. Simeonides&Haase, 1995). However, when starting work on test cases and comparing to available measurements drastic mismatches between heat transfer measurements and the corresponding computations have been achieved.

Generally spoken and this does hold for all experimental investigations, they are playing a prominent role in the validation of aerospace design tools and in a thorough understanding of fluid dynamics. Moreover, they play a key role in CFD development. However, expectations for using CFD as an accurate flow analysis and engineering tool places more stringent requirements on experiments supporting code development, improvement and validation (Marvin, 1995).

After thoroughly discussing all issues concerning the specific test cases with the experimentalists, it was commonly stated that measurements, expected to be in the fully laminar flow regime, were in fact transitional. New calculations have been carried out, dealing with both modelling of transition and turbulence. Strong shock wave/laminar boundary layer interactions, exhibiting large separated regions, were found additionally. The reattaching boundary layer on the ramp was significantly thin and was transitioning to a turbulent one right after reattachment.

Results of two different test cases are going to be discussed below on a basis of heat transfer distributions with various settings for transition onset, including transition modelling itself and "forced" tripping of the originally laminar boundary layer.

The mesh used for this investigation was a very fine one, adapted to the viscous layers and the shock position, with 352x160 mesh points in the main–flow and wall–normal direction. The mesh has been intensively tested in order to allow for grid independent results. 109 (!) cells had been stretched across the boundary layer with almost 66 cells in the subsonic layer measured at the onset of (laminar) separation. The advantage of this extremely refined mesh is of course a high resolution of the boundary layer which in turn proved necessary to predict heat transfer rates accurately and – as a gift in return – made it more conveniant to use the algebraic Cebeci–Smith turbulence model. Moreover, due to the fact that turbulent flow was initiated in the very close vicinity of flow reattachment, only attached turbulent boundary layers had to be taken into account. The Cebeci–Smith model could be appropriately used, together with the (above described) method by Stock&Haase for deriving the boundary layer displacement thickness. In the case of fully turbulent flow which does not show any separation at all, the Cebeci–Smith model has been used, too.

The first test case for a 0.07m hinge, i.e. a flat plate with a length of 0.07m upstream of the ramp, at Ma=14.1, $Re_{unit}=6.5\cdot10^6$/m, $T_\infty=58.8$K, $T_{Wall}=290$K and a ramp angle of 15°, exhibits a considerable length of the transition region. The "normally" applied approach of "switching on" the desired turbulence model at transition onset failed completely with respect to an accurate flow prediction in the transition region, Fig. 16. In order to overcome this failure, the transition model by Dhawan&Narasimha, described in section 5.3, has been applied by choosing the two "free" parameters to be

$$\lambda_{tr}=0.06\text{m} \quad \text{and} \quad x_{tr}=0.12\text{m} \ .$$

Heat transfer distributions in the form of a modified Stanton number

$$c_H = \frac{q}{\rho_\infty U_\infty c_{p_\infty}(T_0 - T_{Wall})}$$

are presented in Fig. 16 for laminar, transitional and fully turbulent flow together with the experimental values and results obtained by the reference temperature method (Simeonides, 1992). Obviously, the same niveau of turbulent heat transfer is achieved on the ramp whether the flow is laminar, transitional or fully turbulent. Apart from a modest gap between computation and measurements, even those calculations with a "switched on" turbulence model – i.e. without making use of the transition model – are reaching the same turbulent heat transfer level as the fully turbulent computations. The advantage of is that the Navier–Stokes method can be used to predict at least the *maximum turbulent heat transfer* correctly, independently of the chosen onset of transition. However, an accurate prediction of transition from laminar to turbulent flow – with a transition taking place well after the interaction – needs, as it is shown, more thorough investigations.

The second test case concerned again a 15° ramp but now with a flat plate length ahead of the hinge line of 0.2m. The flow parameters are: Ma=14.1, $Re_{unit}=13.0 \cdot 10^6$/m, $T_\infty=58.8$K and $T_{Wall}=290$K. In this case – where transition occurs very close to the reattachment point of the boundary layer – computations with transition setting at 0.24m are in good agreement with the measurements performed without tripping the boundary layer. The modest underprediction of the (laminar) heat transfer data upstream of the hinge line may be attributed to the experimental finite leading edge thickness of the flat plate, an effect that had not been taken into account for the computations.

Whenever transition had been set to a location well in the separation region or upstream of it, as it had been carried out by setting transition to 0.06m, it resulted in a fully attached flow with heat transfer transitioning directly from the fully–laminar to the fully–turbulent level. Additionally, and very important from an engineering point of view, it becomes obvious from Fig. 17 that transition initiated in the close vicinity of the reattachment point results in good estimates for the highest turbulent heat transfer (peak heating) on the deflected control surface.

In order to obtain a proper basis for comparing with the fully–turbulent computations, an experimental "attempt" was carried out, tripping the laminar flat plate boundary layer for receiving "fully" turbulent flow.

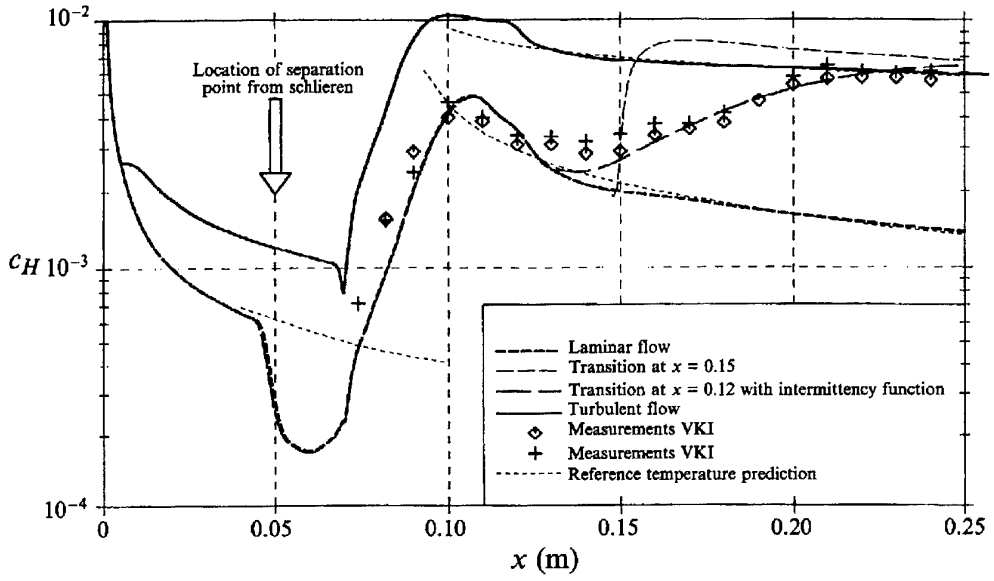

Figure 16 Heat transfer rates for hypersonic laminar, transitional and turbulent 0.07m–ramp flow

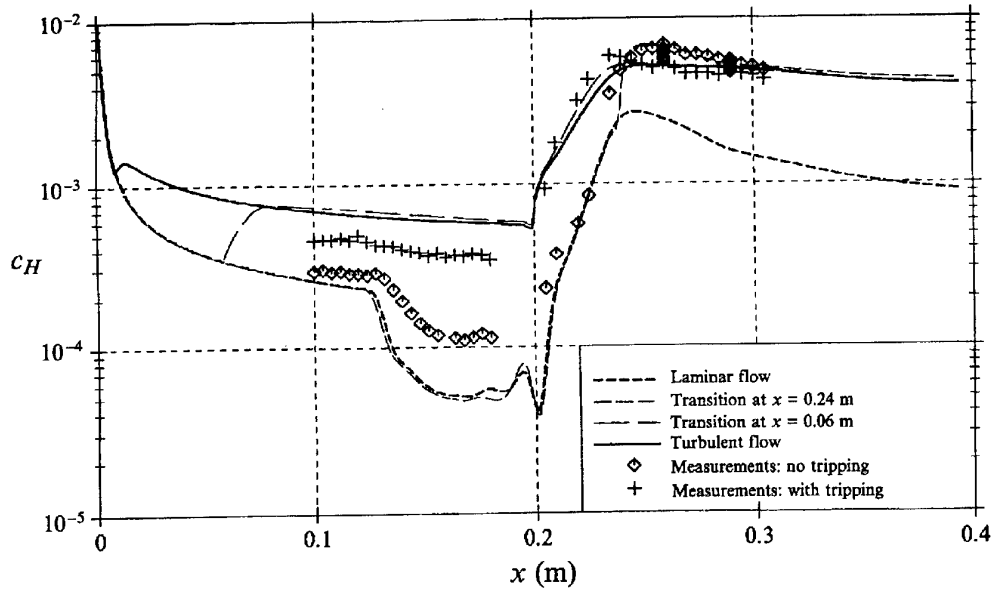

Figure 17 Heat transfer rates for hypersonic laminar, transitional and turbulent 0.20m–ramp flow

In Fig. 18, Schlieren pictures for the non–tripped (transitional) and tripped (turbulent) flow are presented. In addition, for the non–tripped flow, computed density contours are provided, revealing a good comparison with the Schlieren photo given below. In the tripped flow case, however, in view of the high level of stability of hypersonic boundary layers and their strong restistance to transition (Arnal, 1989), 3mm diameter tripping devices has been used. Hence, it is not certain that an equilibrium turbulent boundary layer was attained on the flat plate part of the model. Nevertheless, the tripping caused a fully attached, non–separating, boundary layer, and a fully turbulent boundary layer on the ramp. This is confirmed by the fully turbulent computations which are in close agreement with the experimental findings.

It should be mentioned once more that the Cebeci–Smith turbulence model did behave well in all transitional and turbulent computations due to the fact that this model has been applied in regions of attached flow only. It is well known that the Cebeci–Smith turbulence model has a good predictive accuracy when attached flows are concerned, provided a correct calculation of the boundary layer displacement thickness has been performed.

Computed density contours for transitional flow

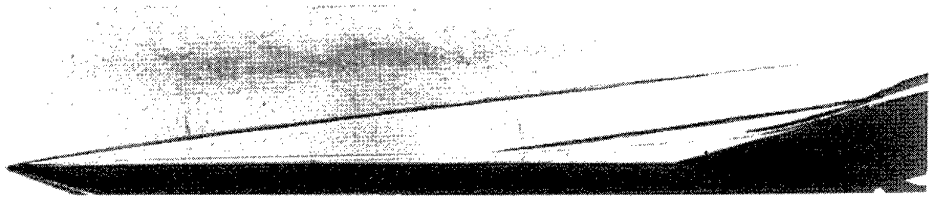

Schlieren picture for transitional (untripped) flow

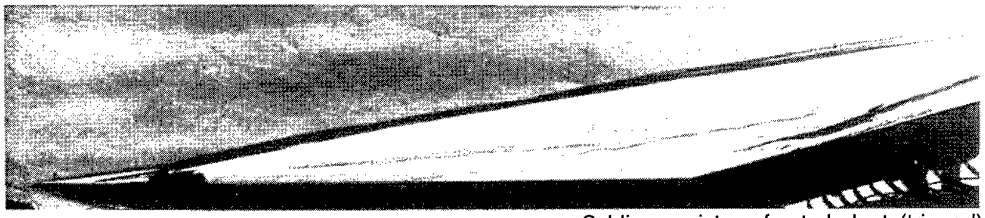

Schlieren picture for turbulent (tripped) flow

Figure 18 Density contours and Schlieren pictures for hypersonic transitional (non–tripped) and turbulent (tripped) flow over the 0.20m ramp

7.5 Flow about DLR–F4

Validation of flow around the DLR–F4 wing–body (airplane) combination was one of the major challenges in the ECARP project. Results obtained by several investigators are presented in Haase et al (1997).

The mesh that had been mandatorily used, consisted of 1.1 million mesh points and was moderately adapted with respect to the boundary layer thickness and the shock location. "Moderately" means that mesh lines were concentrated in the shock area more weakly in order to allow for slightly different locations in the various computations. In particular, boundary layer calculations have been carried out on the basis of preliminary Navier–Stokes pressure results in order to analyse the mesh on the wing. Approximately 30 grid points are found across the boundary layer with y^+ values at the wing surface in the order of O(1). On should note, however, that the chosen 1.1 million mesh points were still insufficient in so far, as the mesh on the fuselage was still rather coarse, hence, a complete computation – being precise on both wing and body – would have required many more grid points in total. Nevertheless, due to the main interest in three–dimensional flow simulations over the wing using different turbulence models, the mentioned grid was mandatorily adopted for the considered validation work.

The flow parameters read: Ma=0.75, Re=$3.0 \cdot 10^6$ (based on the mean aerodynamic chord length) with an angle of attack of 0.93°. Transition was fixed at 15% and 25% on upper and lower wing, respectively. Flow over the fuselage was assumed to be fully turbulent, i.e. starting at the apex with turbulent flow already. As indicated by some computations, the chosen flow parameters result in flows just approaching separation but not really running into separation. The experiments for this test case did not reveal the appearance of shock induced separation.

Fig. 19 is representing at least some of the problems one can discover when validating various types of turbulence models. Apart from the ONERA contribution, shown at the right hand side of that figure, that uses a non–Navier–Stokes approach – namely a VII (viscous–inviscid interaction) method togther with a special 2–half–equation model (LeBalleur, 1981) – a variety of results have already been achieved by just using the Baldwin–Lomax model.

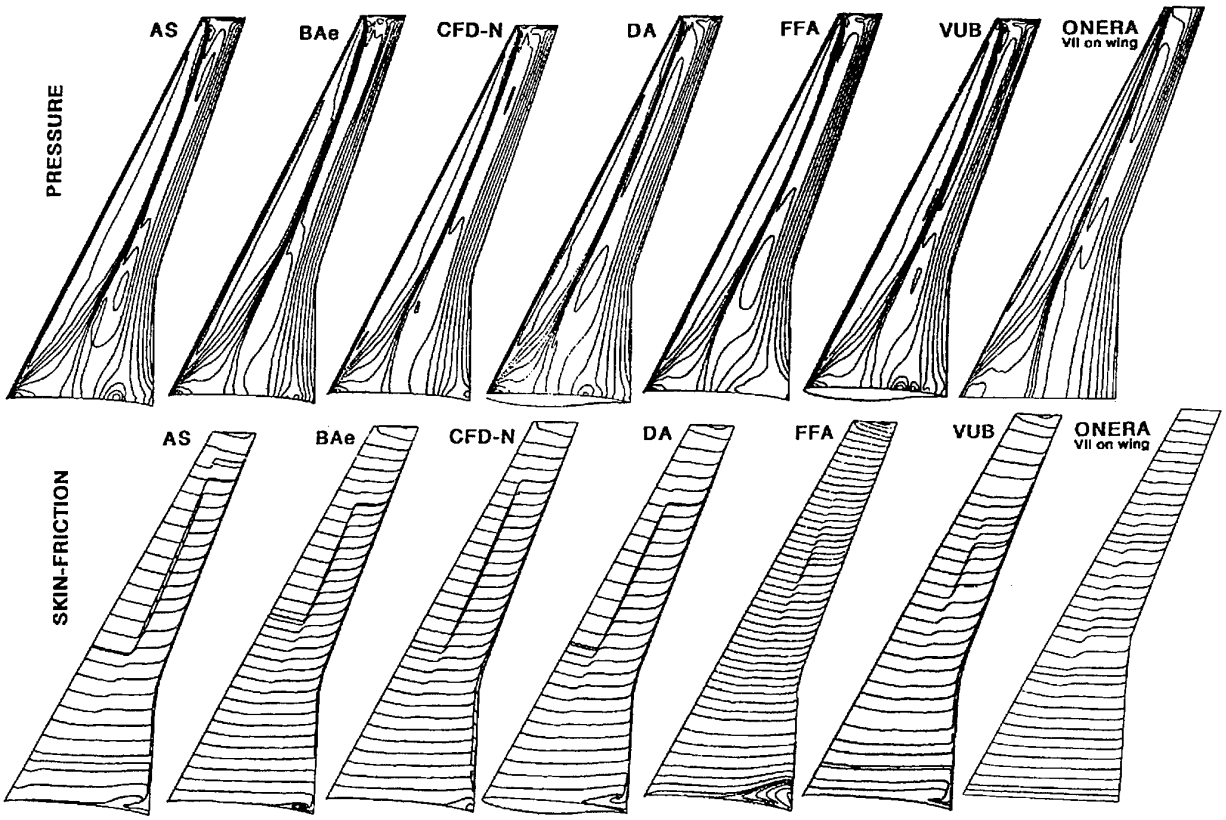

Figure 19 Pressure contours and skin friction patterns on the upper wing for Baldwin–Lomax turbulence model and VII solution

It was related to the diversification in these results that a decision was taken by the ECARP consortium to collect from each and every partner a concise report on implementation and coding issues of the turbulence models employed in the CFD codes, in order to shed more light to this problem. *Although the complete report is an internal ECARP consortium report, ECARP/Validation partners have agreed on a free dissemination (Haase, 1994).*

The different results for the Baldwin–Lomax model should be related to the numerical method itself – and, of course, to the coding and parametrization of the Baldwin–Lomax turbulence model itself. As mentioned before, flow parameters and mesh have been fixed mandatorily for all ECARP partners.

The results with respect to pressure distributions can be claimed to be acceptable – and in reasonable agreement with each other.

Comparing skin friction distributions, different flow situations have been computed covering the whole range from shock–induced separation to still attached flow. The ONERA results, Fig. 19, seem to be more accurate, unfortunately, these are wing–alone computations not taking into account the three–dimensional vortex footprint at the wing–body junction. Once again, the variety of results obtained very clearly indicate the strong need for any validation process to reveal exact information about the numerical method, the mesh and the coding and implementation of models, before getting to conclusions about the (different) results.

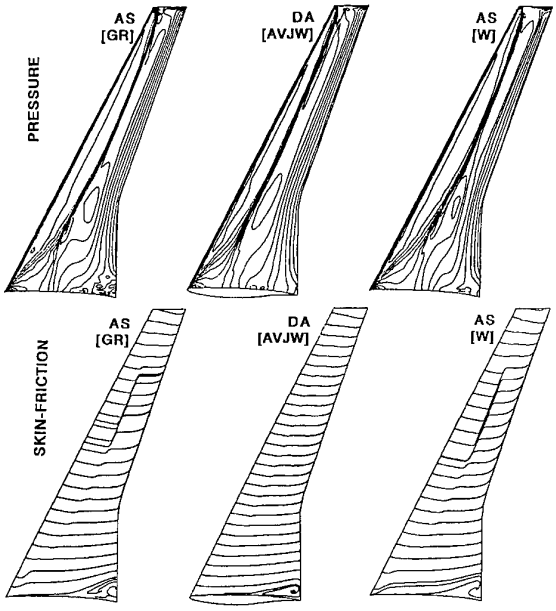

Figure 20 Pressure contours and skin friction patterns on the upper wing for Granville, 1/2– and 1–equation models

Additional to results for the Baldwin–Lomax model presented in Fig. 19, Fig. 20 is providing results for the Granville (1987) modification to the Baldwin Lomax model [GR], the three–dimensional extension of the half–equation Johnson–King model by Abid et al (1989) [AVJW] and the one–equation Wolfshtein (1969) model [W]. As the Johnson–King turbulence model for two–dimensional applications with adverse pressure gradients, the three–dimensional extension of the Johnson–King model by Abid et al is providing a similar accuracy, recalling that no separation on the wing was found in the experiments. The Granville and Wolfshtein models do predict a smaller area of shock induced separation compared to most of the Baldwin–Lomax results. Hence, the Granville modification to the Baldwin–Lomax model shows a clear improvement – as suggested.

Fig. 21 is presenting a comparison of pressure and skin friction distributions on four wing sections using the Baldwin–Lomax and the Abid et al turbulence model. Additionally, the experimental pressures are given. The computed pressure results are in very good agreement with the measurements on both lower and upper surface. The shock has been resolved properly by means of the slight mesh adjustment in that area. As already seen from the skin friction contour lines, major differences with respect to the turbulence model used also show up in the section skin friction. The Baldwin Lomax model tends to predict separation according to a slightly more downstream location of the shock and a correspondingly increased shock strength. The over–interpretation of adverse pressure effects by the Baldwin–Lomax model can also be extracted from the lower surface skin friction behaviour – where the flow is approaching separation in the aft (rear–loaded) part of the wing.

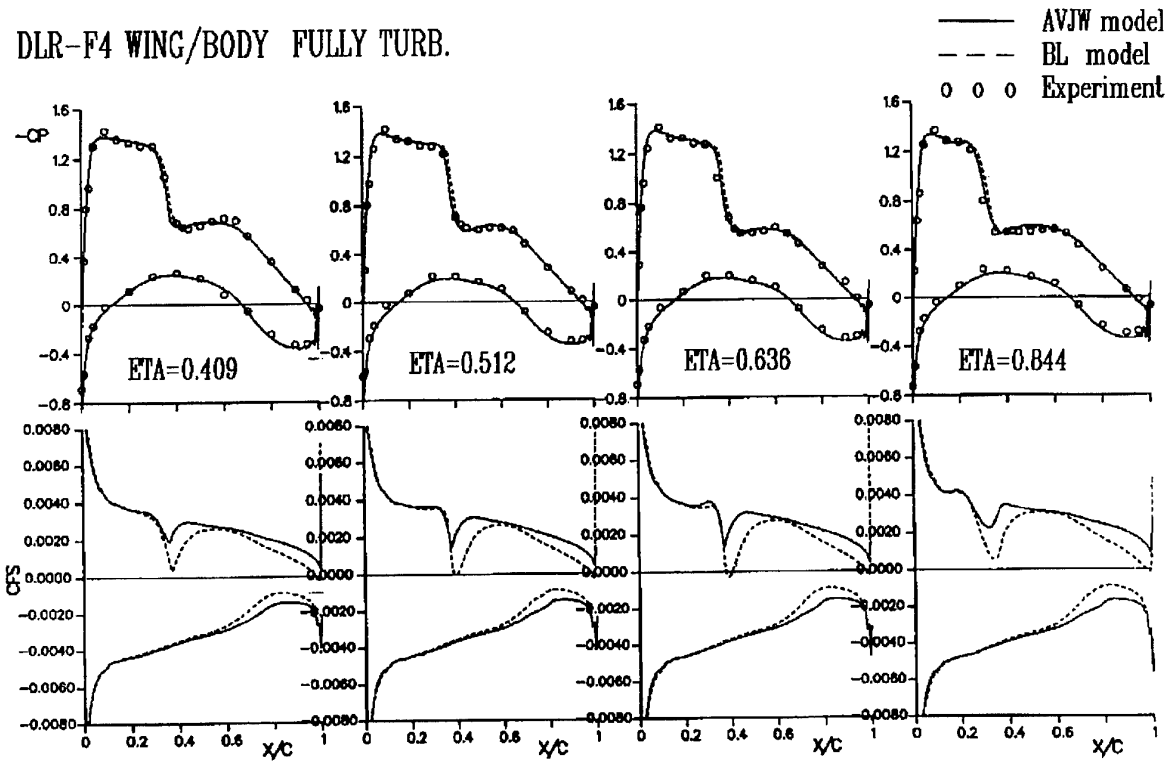

Figure 21 Pressure and skin friction distributions on upper and lower wing at various span–wise sections comparing Baldwin–Lomax and AVJW models (by courtesy of E. Elsholz, Dasa–DA)

Results for various 2–equation models are presented in Fig. 22. In particular, the models of Chen–Patel (1987), Chien (1982), Kalitzin–Gould (1996) – in the k–τ version, an earlier development of the k–g model as presented in section 4.9 – and the Chien model plus a modified length scale are concerned. Again, for three different partners using the Chien model, three different solutions have been obtained. Moreover, the results obtained by one contributor do not show the vortex footprint at all – even for the Chien model – although the same numerical method exhibited a wing–body junction vortex when using the Baldwin–Lomax turbulence model.

To draw a conclusion from these varying results is in fact not simple, nevertheless, one might argue that in general the relevant flow features have been successively computed. The influence of artificial dissipation has been recognized as being negligible, however, mesh dependence together with boundary layer resolution and treatment of farfield conditions should be investigated further. Again, the major differences in results by choosing different turbulence models might be related to unresolved issues on different implementation, interpretation and coding of these models.

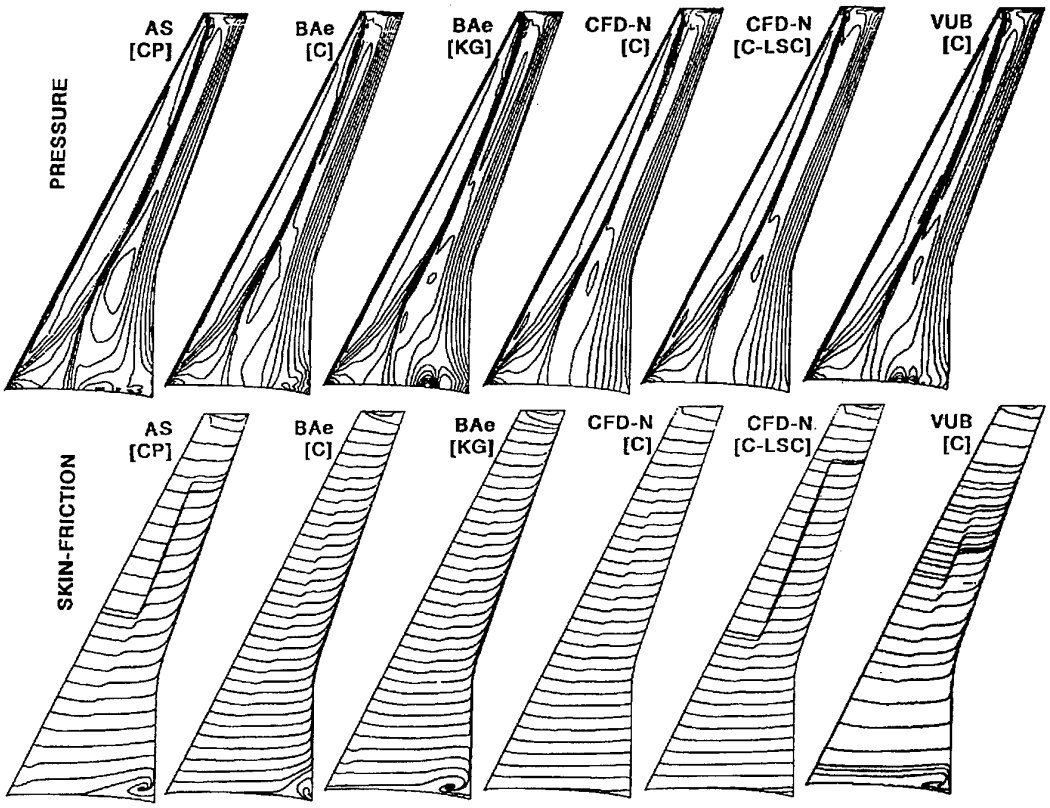

Figure 22 Pressure contours and skin friction patterns on the upper wing for a variety of 2–equation models

7.6 Flow Over a Cone – A Solution of the Parabolized Navier–Stokes Equations

In order to show that algebraic turbulence models – the Baldwin–Lomax model in this particular case – can provide a reasonable predictive accuracy, results are presented for the flow over the Rainbird (1968) cone (Rieger, 1968, 1987, 1997). For this flow simulation which is governed by vortical flow exhibiting primary and secondary vortex sheet separation, the Degani–Schiff modifications to the Baldwin–Lomax model have been utilized together with a procedure that is taking boundary layer history effects into account. For that, local y_{max} positions in the Baldwin–Lomax model are smoothed out by using a relaxation based on the y_{max} station that has been obtained at the previous flow station. Thus, the difficulties encountered in determining F and consequently F_{WAKE} values in the Baldwin–Lomax model, becoming apparent when considering vortical flows, have been overcome.

The experimental setup consisted of a 12.5° half–angle cone model with the following test conditions: Ma=1.8, total (tunnel) pressure of 25psia and a total (tunnel) temperature of approximately 70°F. This corresponds to a Reynolds number of 25 million based on the axial length of the model. Experimental surface–pressure distributions were obtained at x/L=0.85 or x=0.88m.

In the attached flow region, including the complete windward side, where the vortex sheet remains attached, the obtained results are in very good agreement with the experimental findings, as it can be easily taken from Fig. 23 where computed and experimental circumferential pressure distributions are presented for the 0.88m cross section.

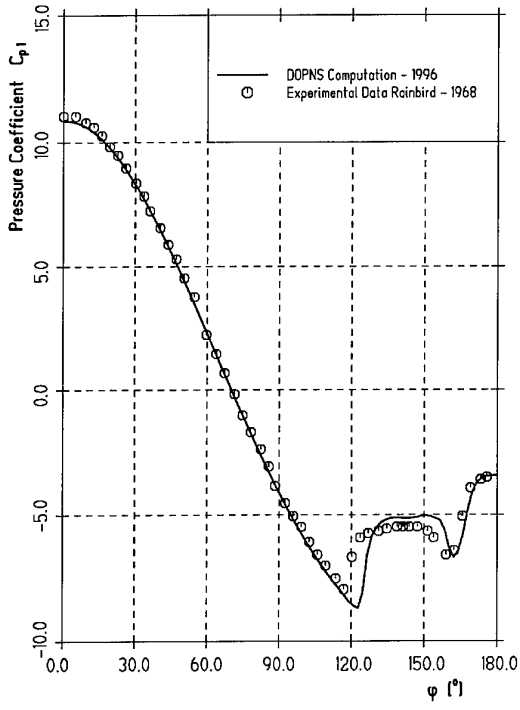

Figure 23 Circumferential pressure distribution for Rainbird cone at 0.88m cross section

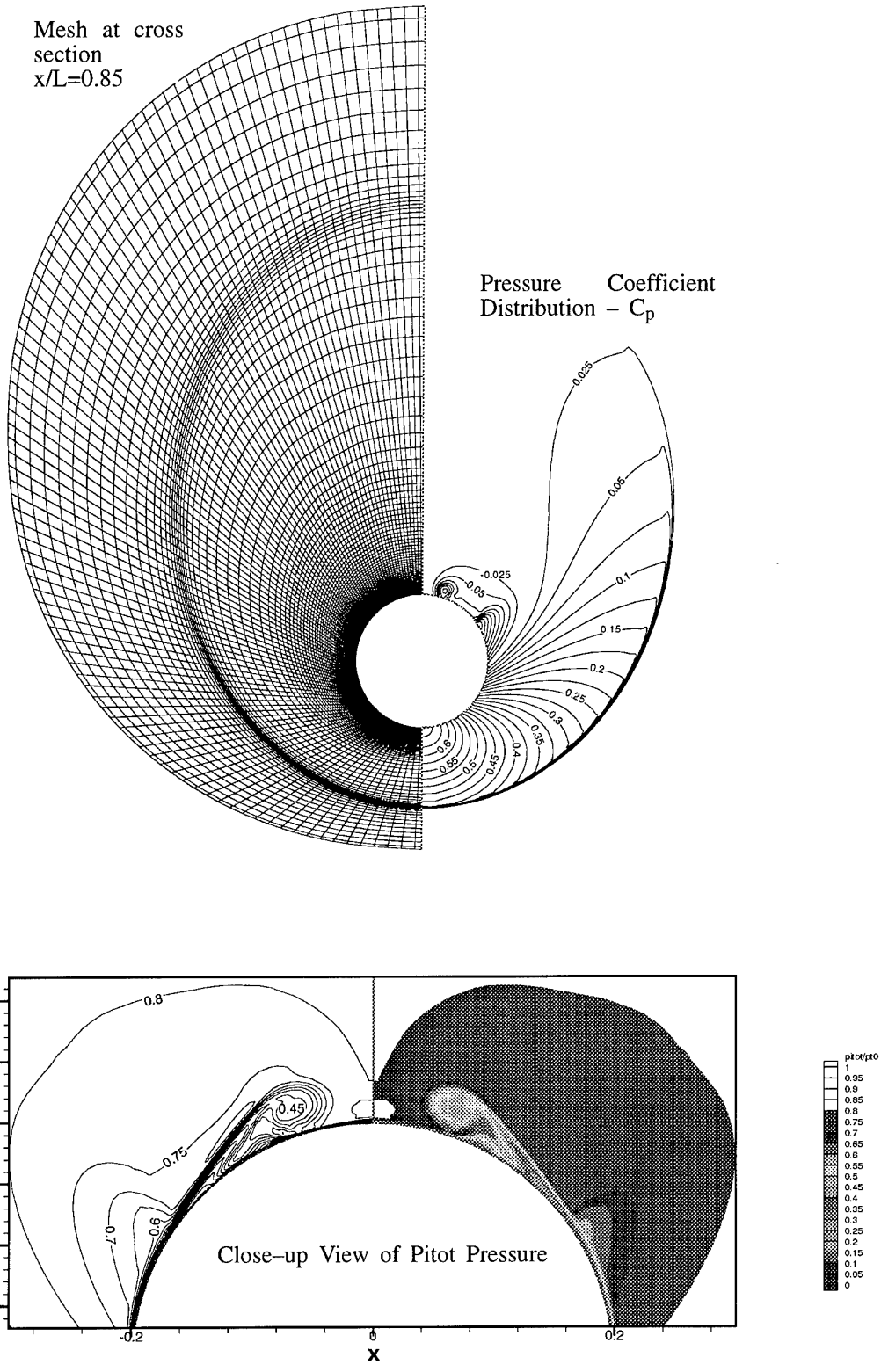

Figure 24 Mesh formation and pressure distributions and upper–surface details for the Rainbird Cone

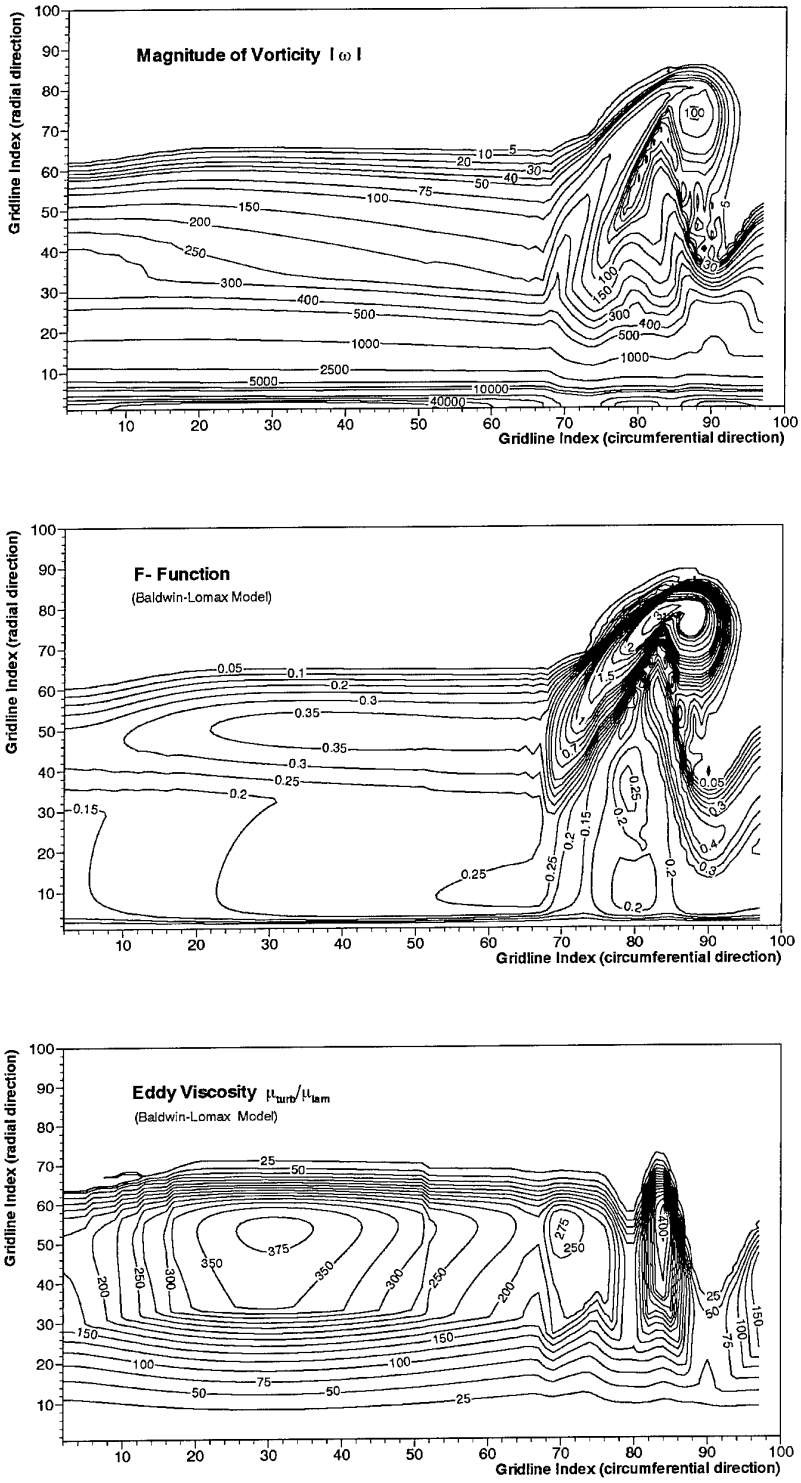

Figure 25 Distribution of characteristic quantities for the application of the Baldwin–Lomax turbulence model for the Rainbird Cone

Although primary separation is slightly delayed, vortex sheet separation is well predicted as well as the (circumferential) length between primary and secondary separation.

Fig. 24 is presenting the chosen mesh and the computed pressure coefficient distribution at x=0.88m. Pitot pressures are plotted as near–wall details. It becomes obvious that the mesh has been adapted with respect to shape and position of the shock to account for accurate post–shock relations and additionally allows for a proper resolution of the viscous near wall region. It consisted of 97x151 mesh points per cross section in circumferential and wall–normal direction. With the step–back mode, approximately 3000 steps have been performes to compute along the complete cone, 700–800 might be sufficient.

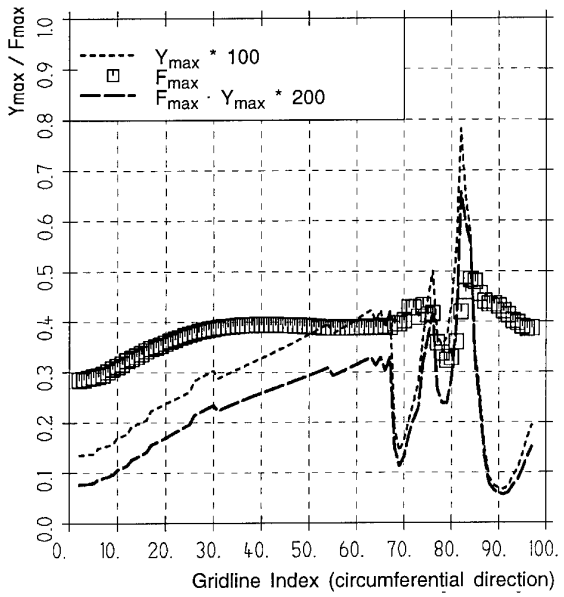

Figure 26 Resulting F_{max}, y_{max} and $F_{max}{\cdot}y_{max}$ distributions for application of the Baldwin–Lomax turbulence model with Degani–Schiff modifications for the Rainbird Cone

A good insight into the performance of the Baldwin–Lomax turbulence model together with the Degani–Schiff modifications is provided by Fig. 25 on the previous page. For the 0.88m cross section, this figure presents a correlation between the vorticity, the F–function and the resulting eddy–viscosity. The latter is given as the ratio between turbulent and laminar viscosity, i.e. a value of unity denotes an eddy–viscosity which has the same amount as the laminar one. The influence of primary and secondary separation on the F–function can be clearly detected and it is demonstrated that the model is producing – despite of the Degani–Schiff modifications – a rather unphysical absolute maximum in between primary and secondary separation. Another interesting feature of the F–function can be taken from the contour plot, a feature that might be caused by the (physical) behaviour of the supersonic boundary layer. This is the F–function "plateau" in the inner half of the boundary layer with values varying only between F=0.2 and F=0.25. The vorticity is reduced by more than one magnitude in that area which is directly compensated by the increase in the wall–normal distance. Obviously, this "plateau" is causing the problem of possibly detecting local maxima in the F function close(r) to the wall making a search for y_{max} (as a function of F_{max}) a "random walk".

In addition to Fig. 25, y_{max}, F_{max} and $y_{max}{\cdot}F_{max}$ distributions are presented in Fig. 26, providing another insight into the sensitivity of the Baldwin–Lomax turbulence model. The F_{max} distribution is "amplified" by the wall–normal distance, in other words, the computed y_{max} value is the driving force for the resultant eddy viscosity and, hence, the model performance. While the two minima in F_{max} and $F_{max}{\cdot}y_{max}$ can be closely related to the position of primary and secondary separation, the maximum can be correlated to the overshoot in the eddy viscosity in between, compare again with Fig. 25.

7.7 Flow about a delta–wing

The last application presented in this paper is the flow about a cropped delta wing at Ma=0.4, Re=3.1 million and an angle of attack of α=9.0 (Fritz, 1997). This low–speed experiment has been carried out in the DLR–Braunschweig wind tunnel by Loeser (1996). Although this measurement is termed a low–speed experiment (because other measurements at higher speeds have been carried out additionally), the Mach number of Ma=0.4 is indicating a speed range being already in the compressible regime, at the lower limit, of course.

This delta wing with a 65° skew angle has a sharp leading edge – promoting a leading edge vortex – that is transitioning to a round edge in the cropped rear part of the wing. The cropped part of the wing is initiated at 85% of the total chord length.

The mesh that has been used for this test case is a very fine C–O mesh (C type in main–flow direction and O type in spanwise direction) with more than 2 million mesh points. 193 mesh points have been distributed in the main flow direction, 129 in spanwise and 81 in the wall–normal direction. Mesh lines are emanating orthogonally from the wing surface in order to allow for an as–proper–as–possible application of turbulence models and resolution of the boundary layer.

Two different turbulence models have been tested, the algebraic Baldwin–Lomax model, again in conjunction with the Degani–Schiff modification, and the 2–equation Wilcox k–ω model.

Fig. 27 presents total–pressure losses and eddy–viscosity contours for the 80% cross section, the cross section located just 5% upstream of the cropped part. Total–pressure losses indicate the boundary layer thickness distribution and provide an insight into the vortex structure, showing a primary and secondary vortex. The extent and shape of these vortices are obviously influenced by the eddy viscosity distribution – given in the lower part of that figure. Although the Degani–Schiff modification has been applied to more properly account for vortical flow, the corresponding contour plot exhibits a somewhat strange distribution in the area of the vortices while the attached flow region shows a reasonable behaviour. Recalling the results obtained for the cone flow in the previous section, a similar turbulence model deficiency has been obtained with F–function maxima near the wing leading edge computed well outside of the boundary layer and, hence, being unphysical.

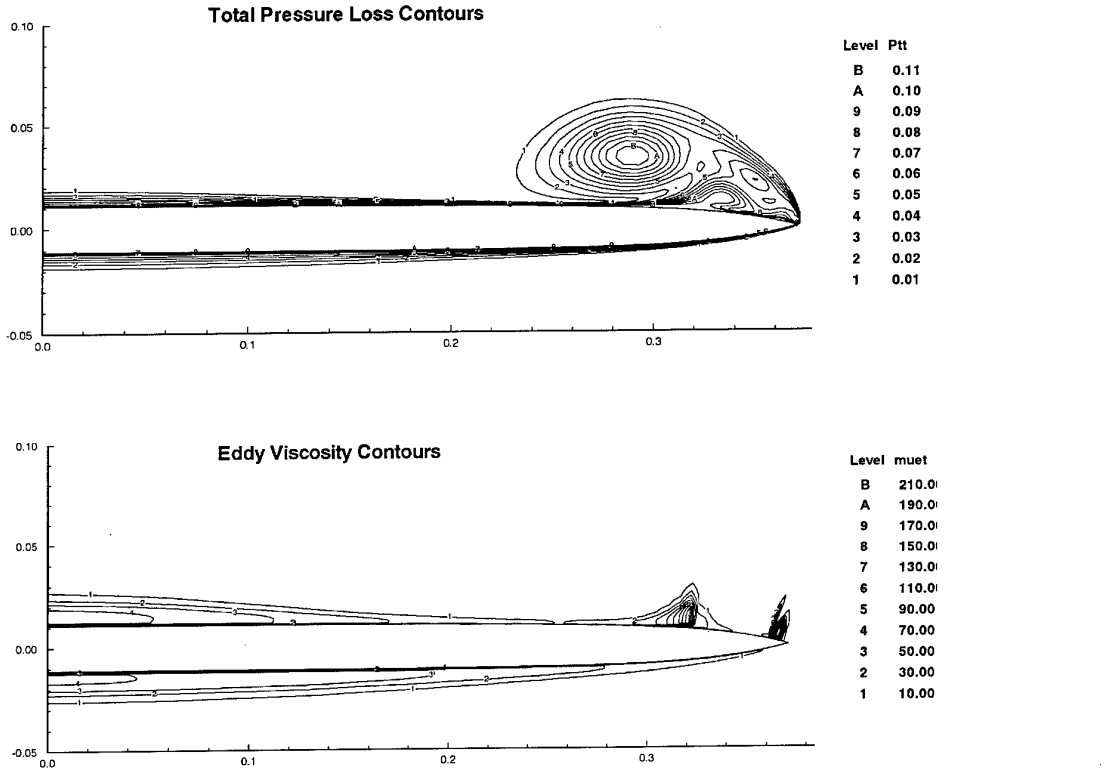

Figure 27 Total pressure losses and eddy viscosity contours for the cropped delta wing at 80% chord using the Baldwin–Lomax turbulence model with the Degani–Schiff extension

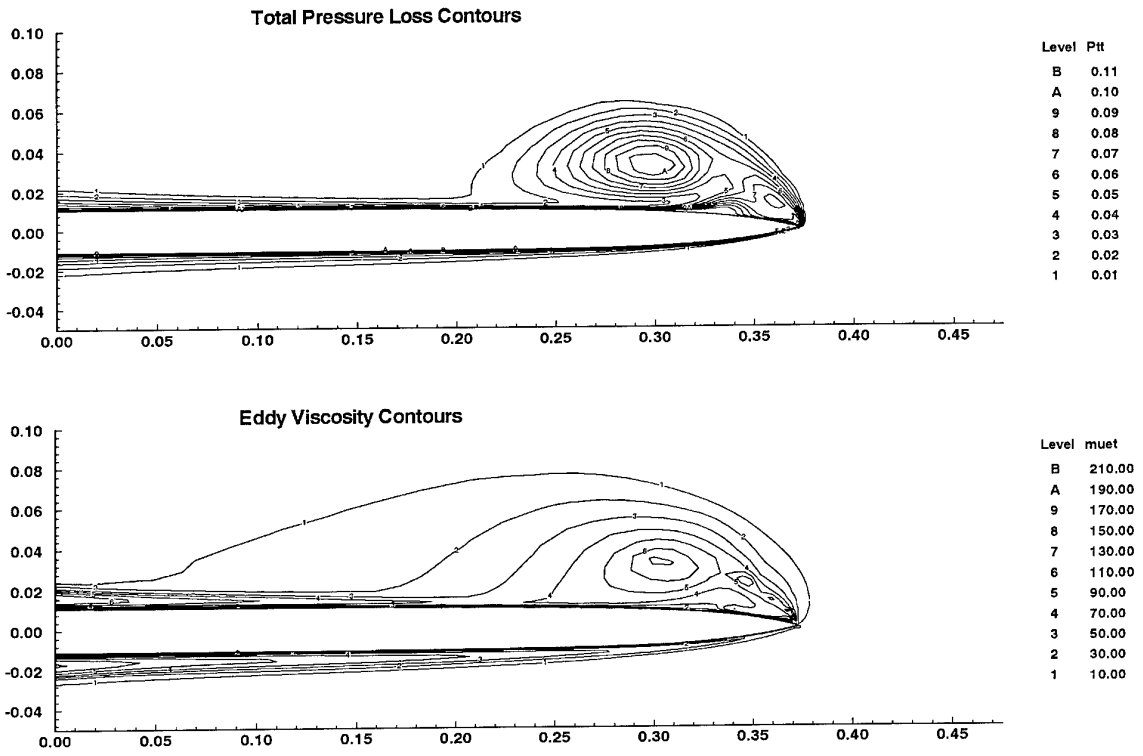

Figure 28 Total pressure losses and eddy viscosity contours for the cropped delta wing at 80% chord using the Wilcox k–ω turbulence model

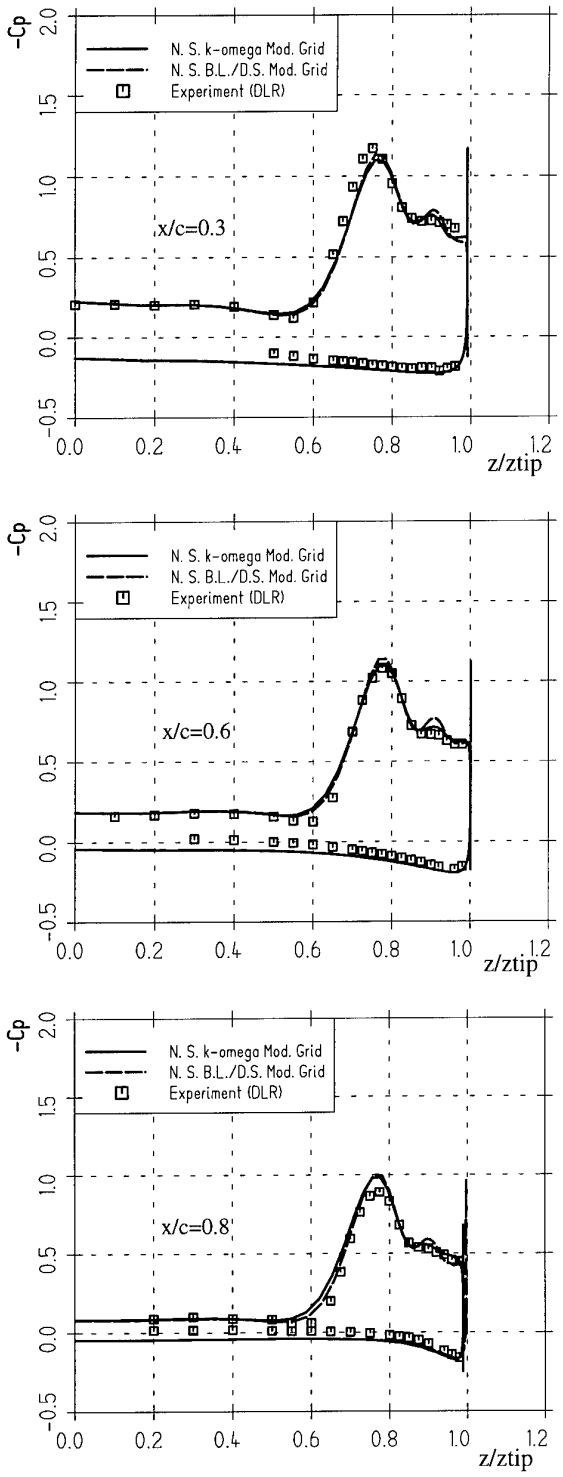

Figure 29 Pressure distributions on delta wing at various cross sections for Baldwin–Lomax+Degani–Schiff and Wilcox k–ω turbulence model

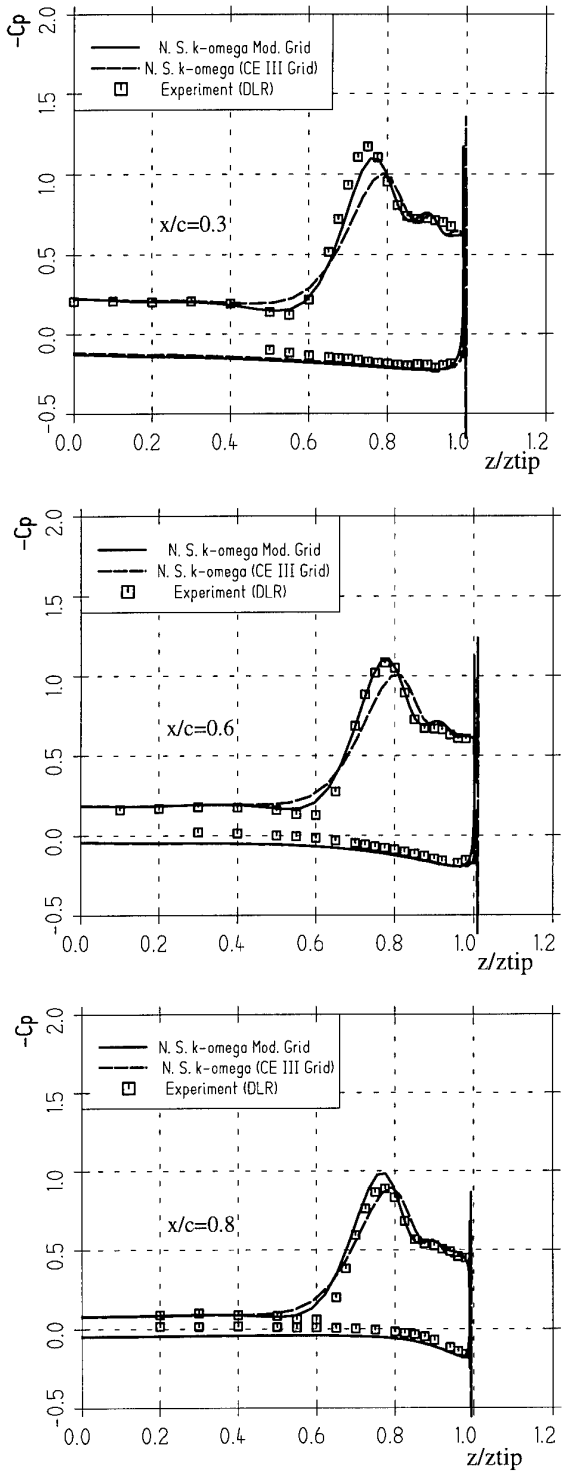

Figure 30 Pressure distributions on delta wing at various cross sections demonstrating mesh dependence; Wilcox k–ω turbulence model

Comparing these results with those obtained by utilizing the Wilcox model, Fig. 28, exhibits a rather different structure for the eddy–viscosity contours. Viscosity in the region of the vortices is much more spread out into the flow field, the outermost line denotes an eddy viscosity which is still 10 times bigger than the corresponding laminar viscosity. Although the eddy viscosity in the attached boundary layer region looks similar for both turbulence models, the maximum eddy–viscosity intensity in the boundary layer part for the Wilcox model is about 50% higher compared to the Baldwin–Lomax model – of course not in the leading edge region where the Baldwin–Lomax model predicted an unphysical behaviour. The plotted contour lines have same contour levels in Fig. 27 and 28.

The more "diffusive" eddy viscosity distribution obtained with the Wilcox turbulence model might be due to the already mentioned sensitivity of the Wilcox model to the freestream values of ω. An examination of the total pressure contours in Figs. 27 and 28 exhibits the influence of the different eddy–viscosity distributions on the shape and structure of the two vortices, in particular on the size of the secondary vortex.

The difference in pressure between computation and experiment on the lower side of the delta wing is related to the mounting device. The keel–like shape is inluencing the pressure by a lot, hence, the disagreement between clean–wing computations and measurement is reasonable.

Although the influence of the two chosen turbulence models on the computed pressure distribution is rather small, the different extent of the secondary vortex can be also detected from the pressure distributions given in Fig. 29. For three different cross sections, pressure results for the two turbulence models are more or less identical, apart from the area at z/ztip=0.9 where the secondary vortex appears. Here, the Baldwin–Lomax model is underpredicting pressure ($-c_p$ plotted) resulting in a more pronounced secondary vortex. As expected and to be seen at x/c=0.8, the eddy–viscosity obtained for the Wilcox model is producing a slightly more "viscous" pressure gradient at about 0.65 z/ztip.

As mentioned above, results presented so far have been obtained on a high–quality grid with very good resolution in the close vicinty of the sharp leading edge. Fig. 30 provides a comparison of the above presented results with those achieved with a more coarse grid containing 97x81x49 mesh points (CEIII grid of the common validation exercise). It can be seen clearly that the shape and the location of the primary vortex (and logically that of the secondary vortex) is very much affected by the resolution of the different meshes. The suction peak is shifted towards the edge of the wing, more precisely, the coarse–grid suction peak is rather close to that position one would obtain when running an Euler calculation, i.e. the primary vortex – initiated by the sharp leading edge of the delta wing – is dominated by "inviscid" mechanisms.

8. NEEDS FOR VALIDATION AND ASSESSMENT OF TURBULENCE MODELS

Concluding from the discussion of results provided in chapter 7, a proper validation and assessment of turbulence and/or transition models should place emphasis on a list of items given in the following and should, particularly, take seriously care of

- the numerical method whether it is a structured or unstructed approach with central, upwind, cell–centered or cell–vertex methods employed,
- the meshes used for the validation purpose with respect to the type of mesh, the resolution and/or the level of adaptation to the real existing physical problem,
- the correctly specified – and for the validation procedure fixed – flow parameters whether they are the experimentally given values or in some sense adjusted ones,
- the original turbulence models, i.e. one should not talk about model "A" without mentioning modifications at all,
- the numerical coding and implementation of turbulence model,
- the parametrisation of turbulence models by fixing the model constants to the original values – or at least to mention accurately what has been changed in the model, why and with what success.

However, in the "real" world of applying CFD tools to particular flow situations, it might be nearly impossible (and expensive) to take care of all the items mentioned above. The attempt to achieve reliable results, however, needs to take into account at least the knowledge about these items because it really does not help a lot to compare results and to validate codes and turbulence models on an insufficient and in fact non–comparable basis – CFD people should talk the same language.

The best thing one can achieve when validating flow physics models is to achieve a proper knowledge about the predictive accuracy of turbulence models in a per–test–case manner, i.e. to mention types of applications where certain models provide reliable results and where not. To obtain such recommendation is a laborious task and needs thorough and accurate numerical studies, guided by comprehensive measurements. An attempt for such "rating" of turbulence models has been performed in the "European Computational Aerodynamics Research Project" – ECARP (Haase et al, 1997).

9. CONCLUSION

It has been shown that a proper validation of CFD codes is a challenging process and depends most of all on an assessment of turbulence and transition models describing the physics of the flow. Results have been provided for two–dimensional and three–dimensional flows and for a variety of turbulence models that are in current use in the aeronautics industry. In addition, requirements for both predictive accuracy and validation/assessment of turbulence models have been discussed.

Recently developed non–linear two–equation turbulence models appear to have a better performance, however, the fact that there are several completely different sets of coefficients in the literature implies that there is reduced chance of a generalised version. Those models bear the possibilities of predicting laminar–to–turbulent transition, although a correct location can not be predicted right now. Non–linear k–ε models can give performance close to best Reynolds–

stress models, depending on precisely specified variants. Compared to linear k–ε models, only marginally higher computation costs have to be accepted.

The major improvements are related to the second moment closures, which remove assumptions such as the eddy viscosity and provide for the first time, a truly three–dimensional modelling capability. In these models, certain key source terms can be modelled "exactly" and a more realistic prediction of the transition region – without the need for incorporating additional criteria – is possible. Of course, there are some numerical and technical difficulties because these models are complex and not very straightforward to implement. Moreover, they sometimes require modifications to give close agreement with measurements. However, compared to predictive accuracy, the application of Reynolds stress models may provide the most reliable results.

It can be concluded that the CFD methods used nowadays exhibit a good predictive accuracy, however, the overall accuracy, robustness and reliability has to be improved. A major keypoint for this is seen in flow–physics modelling issues. It is obvious that implementation and coding aspects are a major drawback in the context of a more general assessment of turbulence and transition models and that certain changes in the models themselves can ameliorate the predictive accuracy of a particular model in use for a specific application. Unfortunately, this can be reversed if the same model with the same parametrization is considered for other flow cases.

In order not to waste time and money, future challenges and strategies on both an assessment and improvement (or new developments) on how to model turbulence and transition will definitely rely on comprehensive and properly carried out validation studies which have to be supported by one important item: All investigators should talk the same language – at least when parametrization, coding and implementation issues of flow–physics models are concerned.

10. ACKNOWLEDGEMENT

The author gratefully acknowledges the help by his colleagues at Dasa–LM (W. Fritz and H. Rieger) and by G. Kalitzin (Stanford) and E. Elsholz (Dasa–Airbus) for providing results. Moreover, thanks are due to M. Braza (IMFT) and H.W. Stock (DLR) for valuable comments on this manuscript and to all partners from the European projects mentioned.

11. REFERENCES

Abid, R., Vatsa, V.N., Johnson, D.A., Wedan, B.W. (1989): Prediction of separated transonic wing flows with a non–equilibrium algebraic model. AIAA Journal, **28**, no. 8, pp. 1426–1431.

Arnal, D. (1989): Laminar–turbulent transition problems in supersonic and hypersonic flows. AGARD–FDP/VKI Special course on aerothermodynamics of hypersonic vehicles, AGARD Rep. 761.

Arnal, D. (1993): Boundary layer transition predictions based on linear theory. AGARD Rep. 793.

Baldwin, B.S., Barth, T.J. (1990): A one–equation turbulence transport model for high Reynolds number wall bounded flows. NASA TM, 102847.

Baldwin, B.S., Lomax, H. (1978): Thin layer approximation and algebraic model for separated turbulent flow, AIAA Paper 78–257.

Buccantini, G., Oggiani, M.S. Onorato, M. (1979): Supercritical airfoil MBB–A3 surface pressure distributions, wake and boundary condition measurements. AGARD AR 138, A8 1–25.

Cebeci, T., Smith, A.M.O. (1974): Analysis of turbulent boundary layers. Ser. in Appl. Math. & Mech., XV, Academic Press, London.

Chen, H.C., Patel, V.C. (1887): Practical near–wall turbulence models for complex flows including separation. AIAA–Paper 87–1300.

Chen, K.K., Thyson, N.A. (1971): Extension of Emmons' spot theory to flows on blunt bodies. AIAA Journal, **5**, 821.

Chien K.–Y. (1982): Predictions of channel and boundary–layer flows with a low–Reynolds–number turbulence model, AIAA Journal, **20**, No. 1, pp. 33–38.

Coles, D.E. (1956): The law of the wake in turbulent boundary layers. – JFM, **1**, part 2, 1956.

Cook, P.H., McDonald, M.A., Firmin, M.C.P. (1979): Aerofoil RAE 2822 – Pressure distributions, and boundary layer and wake measurements. AGARD–AR–138.

Degani, D., Schiff, L.B. (1983): Computation of supersonic viscous flows around pointed bodies at large incidence. AIAA Paper 83–0034.

Dervieux, A. (1997): The European ETMA (Efficient Turbulence Modelling for Aeronautical Applications) project. To appear in: Notes on Numerical Fluid Mechanics, Vieweg Verlag.

Désidéri, J.–A., Glowinski, R., Périaux, J. (eds.) (1991): Hypersonic flows for reentry problems. Springer Verlag.

Dhawan, S., Narasimha, R. (1958): Some properties of boundary layer flow during the transition from laminar to turbulent motion. J. Fluid Mech., **4**, pp. 418–436.

Driest, E.R. van (1956): On Turbulent Flow Near a Wall. Journal of the Aeronautical Sciences, **23**, p. 1007.

Fritz, W. (1997): Berechnungsverfahren in der Aerothermodynamik, WEAG–TA 15. Dasa–LM Report Dasa/S/R/1702.

Granville, P.S. (1953): The calculation of the viscous drag of bodies of revolution. The David. W. Taylor Model Basin Rep. No. 849.

Granville, P.S. (1976): A modified law of the wake for turbulent shear flows. ASME J. of Fluids Engineering, **98**, pp. 578–580.

Granville, P.S. (1987): Baldwin–Lomax factors for turbulent boundary layers in pressure gradients. AIAA J., **25**, No.12, pp. 1624–1627.

Granville, P.S. (1989): A modified van Driest Formula for the mixing length of turbulent boundary layers in pressure gradients. Transactions of the ASME, **94**, Vol. 111.

Haase, W. (1994): ECARP – Task 2.1, Maximum lift for (mandatory) A–airfoil. Mid–Term Report.

Haase, W. (ed.) (1994): ECARP–Validation Area: Intermediate Report on Turbulence Models Used by Partners – Modifications to Original Models and Description of Implementation and Coding.

Haase, W., Brandsma, F., Elsholz, E., Leschziner, M., and Schwamborn, D. (1993): EUROVAL, A European initiative on validation of CFD codes, Notes on Numerical Fluid Mechanics, **42**, Vieweg Verlag.

Haase, W., Wagner, B., Jameson, A. (1983): Development of a Navier–Stokes Method Based on a Finite Volume Tech-

nique for the Unsteady Euler Equations. In: Notes on Numerical Fluid Mechanics, Vieweg Verlag, **7**, pp. 99–107.

Haase, W., Chaput, E., Elsholz, E., Leschziner, M.A., Müller, U.R. (eds.) (1997): ECARP – European Computational Aerodynamics Research Project: Validation of CFD codes and assessment of turbulence models. Notes on Numerical Fluid Mechanics, **58,** Vieweg Verlag.

Hirschel, E.H., Haase, W., Elsholz, E. (1994): Turbulence Modelling for aeronautical applications. Dasa–LM Report DASA/LME12/S/PUB/0538; also in: Proceedings of 5th European Turbulence Conference, 1994, Kluwer Academic Publications.

Horton, H.P. (1990): A non–equilibrium model for turbulent boundary layers. Queen Mary & Westfield College, University of London.

Horton, H.P. (1994): Invariant imbedding algorithms for inverse boundary layer problems, Queen Mary&Westfield College, University of London, UK, Faculty of Engineering Paper QMW–EP–1102.

Jameson A. (1985): Multigrid algorithms for compressible flow calculations. MAE Report 1743, Priceton University.

Jameson A. (1993): Artificial diffusion, upwind biasing, limiters and their effect on accuracy and multigrid convergence in transonic and hypersonic flow, AIAA paper 93–3359, AIAA 11th Computational Fluid Dynamics Conference

Jameson, A., Schmidt, W. and Turkel, E (1981): Numerical solutions of the Euler equations by finite volume methods using Runge–Kutta time–stepping schemes. AIAA–Paper 81–1259.

Johnson, D.A., Coakley, T.J. (1990): Improvements to a non–equilibrium algebraic turbulence model. AIAA J., **28**, No. 11, pp. 2000–2003.

Johnson, D.A., King, L.S. (1985): A mathematical simple turbulence closure model for attached and separated turbulent boundary layers. AIAA Paper 84–0175.

Kalitzin, G. (1995): Validation and development of turbulence models. Final (technical) report on the specific training to ECARP. Contract No. AER2–CT93–5006H.

Kalitzin, G., Gould, A.R.B., Benton, J.J. (1996): Application of two–equation turbulence models in aircraft design, AIAA–Paper 96–0327.

Kroll, N. (1996): Installation and user handbook for the project FLOWer. Doc.–Nr. MEGAFLOW–1001, DLR.

Le Balleur, J.C. (1981): Strong matching method for computing transonic viscous flows including wakes and separations. Lifting airfoils. La Recherche Aerospatiale 1981–3, p.21–45, English and French editions.

Lien, F.S., Leschziner, M.A. (1991): Second–moment modelling of recirculating flow with a non–orthogonal collocated finite–volume algorithm. Proceedings of the 8. Symposium of Turbulent Shear Flows, TU Munich, Paper 20–5.

Löser, Th. (1996): Dynamic force and pressure measurements on an oscillating delta wing at low speeds. DLR Report IB 129–96/6

Marvin, J.G. (1995): Perspective on computational fluid dynamics validation. AIAA Journal, **33**, No. 10.

Menter F.R. (1994): Two–equation eddy viscosity turbulence models for engineering applications, AIAA Journal, **32**, No. 8, August 1994.

Michel, R. (1951): Etude de la transition sur les profiles d'aile; establissment d'un critere de determination de point de transition ae calcul de la trainée de profile incompressible. ONERA Rep. 1/1578A.

Ni, R.–H., Bogoian, J. (1989): Prediction of a 3–D multistage turbine flow field using a multiple– grid Euler solver. AIAA–Paper, 89–0203.

Radespiel, R., Rossow, C.–C., Swanson, R.C. (1990): Efficient cell–vertex multigrid scheme for the three–dimensional Navier–Stokes equations. AIAA Journal, **28**, No. 8.

Rainbird, J.R. (1968): Turbulent boundary layer growth and separation on a yawed cone. AIAA Journal, **6**, pp. 2410–2416.

Reynolds, O. (1895): On the dynamical theory of incompressible viscous fluids and the determination of the criterion. Philosophical Transactions of the Royal Society of London, Series A, **186**, p. 123.

Rieger, H. (1986): Thermische Aufheizung von Flugkörpern bei hohen Geschwindigkeiten. Dornier Bericht BF 7/86 B.

Rieger, H. (1987): Solution of some 3D viscous and inviscid supersonic flow problems by finite–volume space–marching schemes. AGARD CP 428.

Rieger, H. (1987): Private communication

Sarkar (1995): The stabilizing effect of compressibility in turbulent shear flow. J. Fluid Mechanics, 282, pp. 163–186.

Simeonides, G. (1992): Hypersonic shock wave boundary layer interactions over compression corners. PhD Thesis, University of Bristol/von Karman Institute.

Simeonides, G., Haase, W. (1995): Experimental and computational investigations of hypersonic flow about compression ramps. J. Fluid Mech., **283**, pp.17–42.

Speziale, Ch.G., Abid, R., Anderson, E.C. (1992): Critical evaluation of two–equation models for near–wall turbulence. AIAA Journal, **30**, No.2.

Stock, H.W., Haase, W. (1987): The determination of turbulent length scales in algebraic turbulence models for attached and slightly separated flows using Navier–Stokes methods. AIAA Paper 87–1302.

Stock, H.W., Haase, W. (1989): Determination of length scales in algebraic turbulence models for Navier–Stokes methods. AIAA Journal, **27**, No. 1, pp. 5–14.

Stock, H.W., Haase, W. (1996): Some aspects of linear stability calculations in industrial applications. Transitional Boundary Layers in Aeronautics, Henkes, R.A.W.M., van Ingen, J.L., (eds), North–Holland, Scientific Publishers. pp. 225–238.

Willliams, B.R. (1994): Computations of 2D Navier–Stokes equations. GARTEUR/TP–067.

Wilcox, D.C. (1993): Turbulence modeling for CFD. DCW Industries, Inc.

Wilcox, D.C. (1994): Simulation of transition with a two–equation turbulence model, AIAA Journal, **32**, No. 2.

Wolfshtein, M. (1969): The velocity and temperature distribution in one–dimensional flow with turbulence augmentation and pressure gradient.Int. J. Heat Mass Transfer, **12**, pp. 139–163.

Zeman, O. (1990): Dilatation dissipation – the concept and application in modelling compressible mixing layers. Phys. Fluids, A, **2**, pp. 178–188.

REPORT DOCUMENTATION PAGE

1. Recipient's Reference	2. Originator's Reference	3. Further Reference	4. Security Classification of Document
	AGARD-R-819	ISBN 92-836-1057-1	UNCLASSIFIED/ UNLIMITED

5. Originator Advisory Group for Aerospace Research and Development
North Atlantic Treaty Organization
7 rue Ancelle, 92200 Neuilly-sur-Seine, France

6. Title
Turbulence in Compressible Flows

7. Presented at/sponsored by
The course held at the von Kármán Institue for Fluid Dynamics (VKI) in Rhode-Saint-Genèse, Belgium, 2-6 June 1997, and in Newport News, Virginia, USA, 20-24 October 1997.

8. Author(s)/Editor(s)	9. Date
Multiple	June 1997
10. Author's/Editor's Address	**11. Pages**
Multiple	308

12. Distribution Statement There are no restrictions on the distribution of this document. Information about the availability of this and other AGARD unclassified publications is given on the back cover.

13. Keywords/Descriptors

Turbulence	Turbulent boundary layer
Compressible flow	Computerized simulation
Computational fluid dynamics	Mathematical models
Turbulent flow	Eddies
Laminar flow	Combustion
Transition flow	Case studies

14. Abstract

Lecture notes for the AGARD Fluid Dynamics Panel (FDP) Special Course on "Turbulence in Compressible Flows" have been assembled in this report. The following topics were covered: Compressible Turbulent Boundary Layers, Compressible Turbulent Free Shear Layers, Turbulent Combustion, DNS/LES and RANS Simulations of Compressible Turbulent Flows, and Case Studies of Applications of Turbulence Models in Aerospace.

The material assembled in this report was prepared under the combined sponsorship of the AGARD Fluid Dynamics Panel, the Consultant and Exchange Program of AGARD, and the von Kármán Institute (VKI) for Fluid Dynamics.

AGARD

NATO OTAN

7 RUE ANCELLE • 92200 NEUILLY-SUR-SEINE

FRANCE

Télécopie 0(1)55.61.22.99 • Télex 610 176

DIFFUSION DES PUBLICATIONS

AGARD NON CLASSIFIEES

Aucun stock de publications n'a existé à AGARD. A partir de 1993, AGARD détiendra un stock limité des publications associées aux cycles de conférences et cours spéciaux ainsi que les AGARDographies et les rapports des groupes de travail, organisés et publiés à partir de 1993 inclus. Les demandes de renseignements doivent être adressées à AGARD par lettre ou par fax à l'adresse indiquée ci-dessus. *Veuillez ne pas téléphoner.* La diffusion initiale de toutes les publications de l'AGARD est effectuée auprès des pays membres de l'OTAN par l'intermédiaire des centres de distribution nationaux indiqués ci-dessous. Des exemplaires supplémentaires peuvent parfois être obtenus auprès de ces centres (à l'exception des Etats-Unis). Si vous souhaitez recevoir toutes les publications de l'AGARD, ou simplement celles qui concernent certains Panels, vous pouvez demander à être inclu sur la liste d'envoi de l'un de ces centres. Les publications de l'AGARD sont en vente auprès des agences indiquées ci-dessous, sous forme de photocopie ou de microfiche.

CENTRES DE DIFFUSION NATIONAUX

ALLEMAGNE
Fachinformationszentrum Karlsruhe
D-76344 Eggenstein-Leopoldshafen 2

BELGIQUE
Coordonnateur AGARD-VSL
Etat-major de la Force aérienne
Quartier Reine Elisabeth
Rue d'Evere, 1140 Bruxelles

CANADA
Directeur - Gestion de l'information
(Recherche et développement) - DRDGI 3
Ministère de la Défense nationale
Ottawa, Ontario K1A 0K2

DANEMARK
Danish Defence Research Establishment
Ryvangs Allé 1
P.O. Box 2715
DK-2100 Copenhagen Ø

ESPAGNE
INTA (AGARD Publications)
Carretera de Torrejón a Ajalvir, Pk.4
28850 Torrejón de Ardoz - Madrid

ETATS-UNIS
NASA Center for AeroSpace Information (CASI)
800 Elkridge Landing Road
Linthicum Heights, MD 21090-2934

FRANCE
O.N.E.R.A. (Direction)
29, Avenue de la Division Leclerc
92322 Châtillon Cedex

GRECE
Hellenic Air Force
Air War College
Scientific and Technical Library
Dekelia Air Force Base
Dekelia, Athens TGA 1010

ISLANDE
Director of Aviation
c/o Flugrad
Reykjavik

ITALIE
Aeronautica Militare
Ufficio del Delegato Nazionale all'AGARD
Aeroporto Pratica di Mare
00040 Pomezia (Roma)

LUXEMBOURG
Voir Belgique

NORVEGE
Norwegian Defence Research Establishment
Attn: Biblioteket
P.O. Box 25
N-2007 Kjeller

PAYS-BAS
Netherlands Delegation to AGARD
National Aerospace Laboratory NLR
P.O. Box 90502
1006 BM Amsterdam

PORTUGAL
Estado Maior da Força Aérea
SDFA - Centro de Documentação
Alfragide
2700 Amadora

ROYAUME-UNI
Defence Research Information Centre
Kentigern House
65 Brown Street
Glasgow G2 8EX

TURQUIE
Millî Savunma Başkanliği (MSB)
ARGE Dairesi Başkanliği (MSB)
06650 Bakanliklar-Ankara

Le centre de distribution national des Etats-Unis ne détient PAS de stocks des publications de l'AGARD.
D'éventuelles demandes de photocopies doivent être formulées directement auprès du NASA Center for AeroSpace Information (CASI) à l'adresse ci-dessous. Toute notification de changement d'adresse doit être fait également auprès de CASI.

AGENCES DE VENTE

NASA Center for AeroSpace Information
(CASI)
800 Elkridge Landing Road
Linthicum Heights, MD 21090-2934
Etats-Unis

The British Library
Document Supply Division
Boston Spa, Wetherby
West Yorkshire LS23 7BQ
Royaume-Uni

Les demandes de microfiches ou de photocopies de documents AGARD (y compris les demandes faites auprès du CASI) doivent comporter la dénomination AGARD, ainsi que le numéro de série d'AGARD (par exemple AGARD-AG-315). Des informations analogues, telles que le titre et la date de publication sont souhaitables. Veuiller noter qu'il y a lieu de spécifier AGARD-R-nnn et AGARD-AR-nnn lors de la commande des rapports AGARD et des rapports consultatifs AGARD respectivement. Des références bibliographiques complètes ainsi que des résumés des publications AGARD figurent dans les journaux suivants:

Scientific and Technical Aerospace Reports (STAR)
publié par la NASA Scientific and Technical
Information Division
NASA Langley Research Center
Hampton, Virginia 23681-0001
Etats-Unis

Government Reports Announcements and Index (GRA&I)
publié par le National Technical Information Service
Springfield
Virginia 22161
Etats-Unis
(accessible également en mode interactif dans la base de données bibliographiques en ligne du NTIS, et sur CD-ROM)

Imprimé par le Groupe Communication Canada Inc.
(membre de la Corporation St-Joseph)
45, boul. Sacré-Cœur, Hull (Québec), Canada K1A 0S7

AGARD

NATO OTAN

7 RUE ANCELLE • 92200 NEUILLY-SUR-SEINE

FRANCE

Telefax 0(1)55.61.22.99 • Telex 610 176

DISTRIBUTION OF UNCLASSIFIED

AGARD PUBLICATIONS

AGARD holds limited quantities of the publications that accompanied Lecture Series and Special Courses held in 1993 or later, and of AGARDographs and Working Group reports published from 1993 onward. For details, write or send a telefax to the address given above. *Please do not telephone.*

AGARD does not hold stocks of publications that accompanied earlier Lecture Series or Courses or of any other publications. Initial distribution of all AGARD publications is made to NATO nations through the National Distribution Centres listed below. Further copies are sometimes available from these centres (except in the United States). If you have a need to receive all AGARD publications, or just those relating to one or more specific AGARD Panels, they may be willing to include you (or your organisation) on their distribution list. AGARD publications may be purchased from the Sales Agencies listed below, in photocopy or microfiche form.

NATIONAL DISTRIBUTION CENTRES

BELGIUM
Coordonnateur AGARD — VSL
Etat-major de la Force aérienne
Quartier Reine Elisabeth
Rue d'Evere, 1140 Bruxelles

CANADA
Director Research & Development
Information Management - DRDIM 3
Dept of National Defence
Ottawa, Ontario K1A 0K2

DENMARK
Danish Defence Research Establishment
Ryvangs Allé 1
P.O. Box 2715
DK-2100 Copenhagen Ø

FRANCE
O.N.E.R.A. (Direction)
29 Avenue de la Division Leclerc
92322 Châtillon Cedex

GERMANY
Fachinformationszentrum Karlsruhe
D-76344 Eggenstein-Leopoldshafen 2

GREECE
Hellenic Air Force
Air War College
Scientific and Technical Library
Dekelia Air Force Base
Dekelia, Athens TGA 1010

ICELAND
Director of Aviation
c/o Flugrad
Reykjavik

ITALY
Aeronautica Militare
Ufficio del Delegato Nazionale all'AGARD
Aeroporto Pratica di Mare
00040 Pomezia (Roma)

LUXEMBOURG
See Belgium

NETHERLANDS
Netherlands Delegation to AGARD
National Aerospace Laboratory, NLR
P.O. Box 90502
1006 BM Amsterdam

NORWAY
Norwegian Defence Research Establishment
Attn: Biblioteket
P.O. Box 25
N-2007 Kjeller

PORTUGAL
Estado Maior da Força Aérea
SDFA - Centro de Documentação
Alfragide
2700 Amadora

SPAIN
INTA (AGARD Publications)
Carretera de Torrejón a Ajalvir, Pk.4
28850 Torrejón de Ardoz - Madrid

TURKEY
Millî Savunma Başkanliği (MSB)
ARGE Dairesi Başkanliği (MSB)
06650 Bakanliklar-Ankara

UNITED KINGDOM
Defence Research Information Centre
Kentigern House
65 Brown Street
Glasgow G2 8EX

UNITED STATES
NASA Center for AeroSpace Information (CASI)
800 Elkridge Landing Road
Linthicum Heights, MD 21090-2934

The United States National Distribution Centre does NOT hold stocks of AGARD publications.
Applications for copies should be made direct to the NASA Center for AeroSpace Information (CASI) at the address below.
Change of address requests should also go to CASI.

SALES AGENCIES

NASA Center for AeroSpace Information
(CASI)
800 Elkridge Landing Road
Linthicum Heights, MD 21090-2934
United States

The British Library
Document Supply Centre
Boston Spa, Wetherby
West Yorkshire LS23 7BQ
United Kingdom

Requests for microfiches or photocopies of AGARD documents (including requests to CASI) should include the word 'AGARD' and the AGARD serial number (for example AGARD-AG-315). Collateral information such as title and publication date is desirable. Note that AGARD Reports and Advisory Reports should be specified as AGARD-R-nnn and AGARD-AR-nnn, respectively. Full bibliographical references and abstracts of AGARD publications are given in the following journals:

Scientific and Technical Aerospace Reports (STAR)
published by NASA Scientific and Technical
Information Division
NASA Langley Research Center
Hampton, Virginia 23681-0001
United States

Government Reports Announcements and Index (GRA&I)
published by the National Technical Information Service
Springfield
Virginia 22161
United States
(also available online in the NTIS Bibliographic
Database or on CD-ROM)

Printed by Canada Communication Group Inc.
(A St. Joseph Corporation Company)
45 Sacré-Cœur Blvd., Hull (Québec), Canada K1A 0S7

ISBN 92-836-1057-1